Advances in ATOMIC, MOLECULAR, and OPTICAL PHYSICS

Serial Edited by
Ennio Arimondo
Paul R. Berman
Chun C. Lin

Volume 60

Advances in

ATOMIC, MOLECULAR, AND OPTICAL PHYSICS

VOLUME 60

ADVANCES IN

ATOMIC, MOLECULAR, AND OPTICAL PHYSICS

Edited by

E. Arimondo
PHYSICS DEPARTMENT
UNIVERSITY OF PISA
PISA, ITALY

P. R. Berman
PHYSICS DEPARTMENT,
UNIVERSITY OF MICHIGAN
ANN ARBOR, MI, USA

C. C. Lin
DEPARTMENT OF PHYSICS,
UNIVERSITY OF WISCONSIN,
MADISON, WI, USA

Volume 60

ELSEVIER

AMSTERDAM • BOSTON • HEIDELBERG • LONDON • NEW YORK
OXFORD • PARIS • SAN DIEGO • SAN FRANCISCO • SINGAPORE
SYDNEY • TOKYO

Academic Press is an imprint of Elsevier

Academic Press is an imprint of Elsevier
525 B Street, Suite 1900, San Diego, CA 92101-4495, USA
225 Wyman Street, Waltham, MA 02451, USA
32 Jamestown Road, London NW1 7BY, UK

First edition 2011

ISBN: 978-0-12-385508-4

ISSN: 1049-250X

Printed and bound in USA

11 12 13 14 10 9 8 7 6 5 4 3 2 1

Contents

CONTRIBUTORS

Numbers in parentheses indicate the pages on which the author's contributions begin.

GEORGE C. KING (1), School of Physics and Astronomy and Photon Science Institute, University of Manchester, Manchester, M13 9PL, UK

JOHN J. CURRY (65), National Institute of Standards and Technology, Gaithersburg, MD 20899, USA

WALTER P. LAPATOVICH (65), 51 Pye Brook Lane, Boxford, MA 01921, USA

ALBERT HENINS (65), National Institute of Standards and Technology, Gaithersburg, MD 20899, USA

B. BARRETT (119), Department of Physics & Astronomy, York University, 4700 Keele St., Toronto, ON M3J 1P3, Canada

I. CHAN (119), Department of Physics & Astronomy, York University, 4700 Keele St., Toronto, ON M3J 1P3, Canada

C. MOK (119), Department of Physics & Astronomy, York University, 4700 Keele St., Toronto, ON M3J 1P3, Canada

A. CAREW (119), Department of Physics & Astronomy, York University, 4700 Keele St., Toronto, ON M3J 1P3, Canada

I. YAVIN (119), Department of Physics & Astronomy, McMaster University, 1280 Main St. W, Hamilton, Ontario, Canada L8S 4M1

A. KUMARAKRISHNAN (119), Department of Physics & Astronomy, York University, 4700 Keele St., Toronto, ON M3J 1P3, Canada

S. B. CAHN (119), Department of Physics, Yale University, New Haven, CT 06511, USA

T. SLEATOR (119), Department of Physics, New York University, New York, NY 10003, USA

HARUKA TANJI-SUZUKI (201), Department of Physics, MIT-Harvard Center for Ultracold Atoms, and Research Laboratory of Electronics,

Massachusetts Institute of Technology, Cambridge, MA 02139, USA; Department of Physics, Harvard University, Cambridge, MA 02138, USA

IAN D. LEROUX (201), Department of Physics, MIT-Harvard Center for Ultracold Atoms, and Research Laboratory of Electronics, Massachusetts Institute of Technology, Cambridge, MA 02139, USA

MONIKA H. SCHLEIER-SMITH (201), Department of Physics, MIT-Harvard Center for Ultracold Atoms, and Research Laboratory of Electronics, Massachusetts Institute of Technology, Cambridge, MA 02139, USA

MARKO CETINA (201), Department of Physics, MIT-Harvard Center for Ultracold Atoms, and Research Laboratory of Electronics, Massachusetts Institute of Technology, Cambridge, MA 02139, USA

ANDREW T. GRIER (201), Department of Physics, MIT-Harvard Center for Ultracold Atoms, and Research Laboratory of Electronics, Massachusetts Institute of Technology, Cambridge, MA 02139, USA

JONATHAN SIMON (201), Department of Physics, Harvard University, Cambridge, MA 02138, USA

VLADAN VULETIĆ (201), Department of Physics, MIT-Harvard Center for Ultracold Atoms, and Research Laboratory of Electronics, Massachusetts Institute of Technology, Cambridge, MA 02139, USA

PHILIP H. BUCKSBAUM (239), PULSE Institute and Departments of Physics, Applied Physics, and Photon Science, Stanford University, Stanford, CA 94305, USA; SLAC National Accelerator Laboratory, Menlo Park, CA 94025, USA

RYAN COFFEE (239), Linac Coherent Light Source; SLAC National Accelerator Laboratory, Menlo Park, CA 94025, USA

NORA BERRAH (239), Western Michigan University Physics Department, Kalamazoo, MI 49008, USA

GIUSEPPE VALLONE (291), Museo Storico della Fisica e Centro Studi e Ricerche "Enrico Fermi", Via Panisperna 89/A, Compendio del Viminale, I-00184 Roma, Italy; Dipartimento di Fisica, Università Sapienza di Roma, I-00185 Roma, Italy; Department of Information Engineering, University of Padova, I-35131 Padova, Italy

PAOLO MATALONI (291), Dipartimento di Fisica, Università Sapienza di Roma, I-00185 Roma, Italy; Istituto Nazionale di Ottica (INO-CNR), Largo E. Fermi 6, I-50125 Florence, Italy

MARK SADGROVE (315), Institute for Laser Science, The University of Electro-communication, 1-5-1 Chofugaoka, Chofu, Japan

SANDRO WIMBERGER (315), Institut für Theoretische Physik, Universität Heidelberg, Philosophenweg 19, 69120 Heidelberg, Germany

FRANCESCA CALEGARI (371), Politecnico di Milano, Department of Physics, Istituto di Fotonica e Nanotecnologie, IFN-CNR, Piazza Leonardo da Vinci 32, 20133 Milano, Italy

FEDERICO FERRARI (371), Politecnico di Milano, Department of Physics, Istituto di Fotonica e Nanotecnologie, IFN-CNR, Piazza Leonardo da Vinci 32, 20133 Milano, Italy

MATTEO LUCCHINI (371), Politecnico di Milano, Department of Physics, Istituto di Fotonica e Nanotecnologie, IFN-CNR, Piazza Leonardo da Vinci 32, 20133 Milano, Italy

MATTEO NEGRO (371), Politecnico di Milano, Department of Physics, Istituto di Fotonica e Nanotecnologie, IFN-CNR, Piazza Leonardo da Vinci 32, 20133 Milano, Italy

CATERINA VOZZI (371), Politecnico di Milano, Department of Physics, Istituto di Fotonica e Nanotecnologie, IFN-CNR, Piazza Leonardo da Vinci 32, 20133 Milano, Italy

SALVATORE STAGIRA (371), Politecnico di Milano, Department of Physics, Istituto di Fotonica e Nanotecnologie, IFN-CNR, Piazza Leonardo da Vinci 32, 20133 Milano, Italy

GIUSEPPE SANSONE (371), Politecnico di Milano, Department of Physics, Istituto di Fotonica e Nanotecnologie, IFN-CNR, Piazza Leonardo da Vinci 32, 20133 Milano, Italy

MAURO NISOLI (371), Politecnico di Milano, Department of Physics, Istituto di Fotonica e Nanotecnologie, IFN-CNR, Piazza Leonardo da Vinci 32, 20133 Milano, Italy

ANDREI DEREVIANKO (415), Department of Physics, University of Nevada, Reno, NV 89557, USA

SERGEY G. PORSEV (415), Department of Physics, University of Nevada, Reno, NV 89557, USA; Petersburg Nuclear Physics Institute, Gatchina, Leningrad district, 188300, Russia

VANJA DUNJKO (461), Department of Physics, University of Massachusetts Boston, Boston MA 02125, USA

MICHAEL G. MOORE (461), Department of Physics and Astronomy, Michigan State University, East Lansing, MI 48824, USA

THOMAS BERGEMAN (461), Department of Physics and Astronomy, University of Stony Brook, SUNY, Stony Brook, NY 11794-3800, USA

MAXIM OLSHANII (461), Department of Physics, University of Massachusetts Boston, Boston, MA 02125, USA

PREFACE

Volume 60 of the *Advances* Series contains ten contributions, covering a diversity of subject areas in atomic, molecular, and optical physics.

Measurements of the full angular variation of electron scattering cross sections are of great importance in understanding electron-atom interactions. The conventional experimental method using electrostatic hemispherical analyzers has only a limited range, typically up to 135°, making it very difficult to obtain reliable data on backward scattering. This problem, however, has been circumvented with the use of *magnetic angle changers* developed by researchers at University of Manchester. A localized magnetic field in the scattering region is introduced to deflect the electrons in a controlled way. This results in a shift of the effective angular range of the conventional spectrometer by a fixed amount so that the previously inaccessible region of 135°–180° is shifted into a lower angle range. George King discusses the principles of operation of this novel device, along with examples that illustrate how it can be used for coincidence measurements of electron-impact excitation and ionization and for photoelectron studies.

Although laser-induced fluorescence has long been a powerful tool for detecting atomic species, only in the last decade has x-ray-induced fluorescence emerged as a tool for diagnostic studies of commercial high-intensity discharge lamps. As an introduction to industrial lamp technology, John Curry, Walter Lapatovich, and Albert Henins present a brief account of the operation of metal-halide lamps, where the metal component includes alkali and rare-earth metals. The use of x-ray, rather than other light sources, is necessitated by the nature of the lamps and the impediments to the traditional optical techniques raised by the physical size and construction of commercial lamps. The x-rays probe inner-shell electrons and give number densities of specific nuclei, which are particularly useful for monitoring metal additives. Included in the discussion are a number of diagnostic studies that exemplify the connections between advanced developments in atomic physics and industry.

In their chapter, Brynle Barrett, Iain Chan, Carson Mok, Adam Carew, Itay Yavin, A. Kumarakrishnan, Sidney Cahn, and Tycho Sleator present an overview of time-domain atom interferometry. By applying two or more off-resonant, standing-wave fields to a cold atomic vapor and monitoring the atomic response, they obtain a signal that is analogous

to one that is obtained in optical interferometry using phase gratings. Alternatively, they can release atoms from an optical lattice to simulate an amplitude grating. The theory of a time-domain atom interferometer is developed, and it is shown how the signal can be used as a sensitive measure of such quantities as the atomic recoil frequency, the acceleration of gravity, and rotation rates. The dependence of the interferometric signal on magnetic fields, spontaneous emission, and laser beam profile is modeled theoretically and studied experimentally.

Haruka Tanji-Suzuki, Ian Leroux, Monika Schleier-Smith, Marko Cetina, Andrew Grier, Jonathan Simon, and Vladan Vuletić discuss the problem of coupling between an applied optical field, an atom or an ensemble of atoms in a cavity, and the cavity field. In a novel approach, all fields are considered classical and the atoms are modeled as classical dipole oscillators. They show that results obtained in a quantized cavity field, quantized atom approach, are reproduced in this classical description. In other words, phenomena such as mode "vacuum Rabi splitting," cavity cooling, cavity spin squeezing, and electromagnetic-induced transparency can be explained within the context of the classical model. The applied optical field can be directed either perpendicular to or aligned with the cavity field. A key parameter in the analysis is the so-called cooperativity parameter that characterizes the atom-field interaction.

Philip Bucksbaum, Ryan Coffee, and Nora Berrah report on the first experiments at the Stanford Linac Coherent Light Source (SLCLS), an ultrafast x-ray source at the Stanford Linear Accelerator (SLAC). The various properties of the SLCLS beam are described and potential applications to atomic, chemical, and biological studies are examined. The theory of ionization of atoms in strong pulsed x-ray fields is reviewed, and the roles played by core-level photoionization, Auger relaxation, and valence photoionization are described. Experimental results on the multiple photoionization of neon are presented that provide evidence for nonsequential multiphoton ionization. Intense x-ray-induced ionization and dissociation of molecular nitrogen is also studied. The first optical pump, x-ray probe time-resolved experiments at SLCLS were also carried out using molecular nitrogen as the target. The chapter concludes with some exciting prospects for future work at SLCLS.

In recent years, photonic entangled states have received a great deal of attention for both fundamental tests of quantum mechanics and applications to quantum information and quantum communication. The entanglement of two particles involving more than one degree of freedom, namely their hyperentanglement, allows for an expanded use of the possibilities offered by quantum mechanics. Giuseppe Vallone and Paolo Mataloni survey the most relevant experimental and theoretical investigations of hyperentangled multiqubit photon states based on the use of different degrees of freedom of the photon. Applications to quantum

nonlocality tests, Bell state analysis, dense coding and quantum computation are reviewed. The principle advantage of using hyperentangled states is the ability to engineer and detect multiqubit, very high-purity entangled states at a relatively high rate

The kicked rotor, a model system in the study of chaos, is physically embodied by a *Gedankenexperiment* in which a rigid pendulum experiences momentum "kicks" resulting from a periodic train of delta-function gravitational pulses and evolves freely between those pulses. Given its status as a paradigm system, it is natural that studies of the quantum dynamics of chaotic systems have focused heavily on the quantized standard map or, equivalently, the quantum kicked rotor. The kicked rotor was realized experimentally using cold noninteracting atoms exposed to a pulsed optical standing wave. The application of effective delta-like kicks created a very good experimental realization of the standard map. Mark Sadgrove and Sandro Wimberger review both theoretical and experimental advances in the atom-optics kicked rotor problem. The theory concentrates on the concept and applications of a pseudoclassical approximation to the resonant dynamics of an atom kicked by a pulsed, periodic potential. This powerful method allows them to derive analytical results in the deep quantum limit of the kicked rotor. The method is applied to interpret atom-optics kicked rotor experiments in which there are well-controlled driving forces

Recent progress in attosecond technology has resulted in an increasing interest in the application of attosecond pulses as a probe of atomic, molecular and solid state physics. In addition, novel techniques have been introduced for the generation of subfemtosecond pulses and their applications. Francesca Calegari, Federico Ferrari, Matteo Lucchini, Matteo Negro, Caterina Vozzi, Salvatore Stagira, Giuseppe Sansone, and Mauro Nisoli report on recent advances in attosecond science, with particular emphasis on the generation and use of isolated attosecond pulses produced using high-order harmonic generation in gases. The authors analyze various temporal gating techniques that allow the harmonic generation process to be fully implemented using a single pulse. In addition, the principle applications of isolated attosecond pulses to atomic, molecular and solid state physics are presented.

Atomic clocks based on the ultranarrow intercombination optical transitions in divalent atoms offer the potential to achieve a new level of timekeeping accuracy and stability. Compared with microwave atomic clocks, such as the present-day cesium frequency standard, the optical clocks have an advantage of much higher frequency and resonance quality factors. Andrei Derevianko and Sergey Porsev present a rigorous formalism for evaluating various atomic-structure parameters affecting performance and ultimate accuracy of optical lattice-based atomic clocks. They evaluate a number of important parameters, such as the hyperfine-induced

width of the clock transition, the static polarizabilities, the multipolar and vector dynamic polarizabilities, the "magic" trapping wavelengths, the hyperfine-induced g-factors, and the blackbody radiation shifts. Accurate numerical calculations of these parameters are carried out for several divalent atoms presently under investigation, with a particular emphasis on the ytterbium clock.

Confinement-induced resonances arise when particle scattering takes place in the presence of an external potential that spatially confines the motion of the particles. These resonances are obtained in the limit that the scattering cross section reaches the unitary limit which can occur for some combination of the scattering energy, the confining potential, and the interatomic potential. Although those resonances properly belong to the physics of two-particle scattering, they were discovered and investigated within the context of many-body physics of ultracold atomic gases. Vanja Dunjko, Michael Moore, Thomas Bergeman, and Maxim Olshanii review the types of confinement-induced resonances that have been studied theoretically and experimentally. In addition they provide details on one paradigmatic case of resonance.

The Editors would like to thank all the contributing authors for their contributions and for their cooperation in assembling this volume. They would also like to express their appreciation to Ms. Gayathri Venkatasamy at Elsevier for her invaluable assistance.

Ennio Arimondo
Paul Berman
Chun Lin

CHAPTER 1

The Use of the Magnetic Angle Changer in Atomic and Molecular Physics

George C. King

School of Physics and Astronomy and Photon Science Institute, University of Manchester, Manchester, M13 9PL, UK

Contents

Advances in Atomic, Molecular, and Optical Physics, Volume 60, Copyright © 2011 Elsevier Inc.
ISSN 1049-250X, DOI: 10.1016/B978-0-12-385508-4.00001-2.

Abstract The magnetic angle changer (MAC) is a system of solenoids that produces a localized and shaped magnetic field, which can change the direction of an electron beam in a controlled way. When it is used in conjunction with a conventional electron spectrometer employing hemispherical deflector analyzers, it can extend the angular range of the spectrometer. In particular, it enables the spectrometer to view the complete back-scattering hemisphere up to and including scattering angles of 180°. The principles of operation of the MAC are described, and practical examples of it are presented. The use of the MAC is described in measurements of differential cross sections in elastic and inelastic electron scattering in atoms and molecules, including the observation of resonance structures in these cross sections. Applications of the MAC to coincidence measurements of electron impact excitation and ionization and to photoelectron studies are also described. Comparisons of experimental measurements with theoretical predictions are presented where applicable.

1. INTRODUCTION AND BACKGROUND

1.1 Introduction

There is a wide range of experiments in atomic and molecular physics in which the angular behavior of charged particles is investigated. In particular, this includes collision studies using electron impact excitation. Examples are measurements of elastic and inelastic differential scattering cross sections, studies of negative ion resonances (Buckman and Clark, 1994; Schulz, 1973a,b) and correlation studies involving (e, 2e) and electron–photon coincidence measurements (Andersen et al., 1988; McCarthy & Weigold, 1995). In addition, photoionization studies often involve the measurement of the angular behavior of ejected photoelectrons (Becker & Shirley, 1996). In order to obtain the maximum information from an experiment, it is invariably necessary to investigate the full angular range of the reaction products. For example, in measurements of angle-differential

cross sections, it is advantageous to detect the scattered electrons over the full angular range from 0° to 180°, so that total and momentum transfer cross sections can be determined: the data that are required for technological, atmospheric, and plasma applications. And of course, the complete angular range is required for full comparison with theory. However, the angular range of experimental measurements is often limited by the mechanical constraints of the apparatus. Very large scattering angles are not accessible to instruments using electrostatic hemispherical analyzers, the largest angles being typically 135°: scattering angles approaching 180° are inaccessible because the analyzer bumps into the monochromator. (In addition, although small angles are mechanically available, angles close to 0° are difficult because the unscattered electron beam enters the analyzer causing large spurious background signals.) Theory, of course, does not suffer from these physical constraints, and many important and interesting effects are predicted for electron scattering processes in the backward hemisphere. It is here, for example, that exchange and spin orbit effects may be especially important for small-parameter collisions. This region should therefore provide particularly sensitive tests of theory and so it is extremely valuable to have experimental access to the backward scattering hemisphere for detailed comparison. There are some experimental techniques that provide limited access to the backward scattering hemisphere as described in section 1.2. However, their angular ranges are limited and are generally confined to a scattering angle of 180°: they do not provide continuous access across the whole backward hemisphere. The magnetic angle changer (MAC) has changed all this and does allow continuous access, without gaps, to the full angular range in the backward hemisphere. The way it achieves this and how it has been employed in various experimental studies are described in this chapter. The MAC was invented and initially developed by Read and King and their collaborators at the University of Manchester (Zubek et al., 1996; Read & Channing, 1996). It first arose from the measurement of elastic differential cross sections and the need to extend the measurements continuously to 180°.

The MAC works by the application of a localized magnetic field at the scattering region of a conventional electron spectrometer. This magnetic field is produced by a system of solenoids (coils), and it deflects the electrons in a controlled way. Briefly, the two main principles of the MAC are as follows. First, the magnetic field produced by the system of solenoids is highly localized so that it does not disturb the operation of the electron spectrometer in which the MAC is housed. This is achieved by cancelling the overall dipole moment of the system of solenoids so that the magnetic field falls off as at large distances r as r^{-5}. (Higher-order magnetic moments can also be cancelled, depending on the number of solenoids and the geometry of the solenoid system). Second, the system

of solenoids is axially symmetric, so that the axial component of the generalized momentum of an electron in the magnetic field is a conserved quantity. This component is zero at the axis of the solenoid system, and it is zero in the field-free region far away from the axis for electrons that are initially directed toward the axis. Consequently, any such electrons change direction in the magnetic field but still pass through the axis of the solenoid system, where the interaction region is located. Similarly, electrons that originate from the interaction region move radially away from it once they reach the field-free region. The operation of the MAC is described in more detail in section 2.

1.2 Alternative Techniques for Accessing the Backward Hemisphere in Electron Scattering

As noted above, conventional electron spectrometers based on hemispherical deflector analyzers have a limited angular range of detection. To gain access to larger scattering angles, and in particular to the case of electron scattering through 180°, several experimental techniques have been developed. These techniques are usually based on the trochoidal monochromator of Stamatovic and Schultz (1970). In this device, an electron beam is collimated by an axial magnetic field and is passed through a region containing an electric field that is perpendicular to the electron beam direction and the magnetic field. The combined electric and magnetic fields cause the electrons to drift in a direction at right angles to their axial velocity and if a small aperture is placed at the exit of the region, an energy selected beam is obtained. This beam can then be used for collision studies. A characteristic of the motion of the electrons in the crossed electric and magnetic fields is that the drift direction is independent of the direction of the axial motion. Thus, a second small aperture can be placed in the backward direction in the monochromator to pass electrons backscattered into the monochromator through 180° and separate them from the primary beam (Burrow & Sanche, 1972). It may be noted that the angular acceptance of the device for backward scattering is strongly dependent on the energy of the electrons. Using a magnetically collimated electron impact spectrometer, Asmis and Allan (1997) have described a novel scheme for the measurement of inelastic differential cross sections (DCS) at 180°. In this instrument, the backward scattered electrons are reflected into the forward direction by a potential barrier and enter the energy analyzer located at 0°. Pulsed incident electron beam and time of flight detection are used to differentiate the backward and forward scattered electrons. The instrument yields the ratio of the forward and backward DCS. These data are then normalized to the absolute DCS at 0°, measured with a conventional spectrometer to yield the DCS at 180°. Greenwood et al. (1995a,b) have described a technique for measuring partial cross

sections integrated over the angular range 90° to 180° in elastic scattering from Ar^+. Their technique is again based on a trochoidal analyzer. This analyzer is operated at a high pass energy in a nondispersive mode, so that back-scattered electrons with axial velocities from almost zero up to the full collision energy are transmitted with no attenuation and are detected. The yield of detected electrons therefore corresponds to a partial cross section, integrated over the backward scattering hemisphere.

None of the above techniques, however, enables angular differential measurements to be made over the whole of the backward scattering hemisphere. The MAC does so by using its localized magnetic field to shift the effective angular range of a conventional spectrometer by a fixed amount, for example by 70°. The angular defining characteristics of the spectrometer and also the mechanical means of varying the measured angle are preserved but the entire range is shifted magnetically, in this case from say −10° to 135° to the range 60° to 205°, so that the mechanical constraints of the apparatus are overcome.

1.3 Applicability of the Magnetic Angle Changer (MAC)

The MAC is universally applicable to both elastic and inelastic electron (and positron) scattering. However, the small magnetic deflection produced for the much heavier atomic and molecular ions makes the MAC of limited practical use for ion experiments. So far it has been used for studies of elastic, inelastic, and superelastic electron scattering, resonances in electron scattering, for (e, 2e) experiments, and also for photoelectron spectroscopy. For a given magnetic field distribution, the deflection θ of an electron depends on the strength of the magnetic field B and the energy E of the electron as

$$\theta \propto \frac{B}{\sqrt{E}}. \tag{1}$$

The magnetic deflection required in the MAC technique is of the order of tens of degrees. The value of B that can be produced using turns of wire in a vacuum system is limited by heat dissipation, and this has limited most applications to electron energies less than about 100 eV. At the other extreme, the MAC has been used successfully with electron energies as low as ∼100 meV. One way to increase the magnetic field, without recourse to larger solenoid currents, is to use iron-cored solenoids. Cubric et al. (2000), for example, have done this and were able to increase the value of B by a factor of 5 compared to a solenoid system without an iron core. This increases the range of electron energy by a factor of 25: potentially to the keV range. An important feature of the MAC is that it can be fitted to an existing electron spectrometer. It is compact in size, typically ∼25 mm in diameter and length. Moreover, the magnetic field produced

by the MAC is well confined: the field drops to a negligible value within a radial distance of a few tens of mm ensuring that it does not adversely effect the operation of the electron spectrometer.

2. PRINCIPLES OF OPERATION OF THE MAC AND PRACTICAL REALIZATIONS OF IT

2.1 Principles of Operation of the MAC

Here are described the basic principles of the MAC: the localization of its magnetic field and its action on an electron beam. The production and properties of an unscreened but localized magnetic field have been described by Read and Channing (1996). The basic arrangement of the MAC is illustrated schematically in Figure 1. It consists of four coaxial solenoids that are arranged as two pairs, namely an inner and an outer pair, of radii R_1 and R_2, respectively. The two members of each pair are separated by a narrow gap, which allows passage of the electron beam. The electron scattering plane is perpendicular to the central axis of the solenoids, the z-axis in Figure 1, and passes through the centre of the gap. The first important feature of the MAC is that the magnetic field it produces is localized so that it does not disturb the action of the electrostatic devices that are used for energy selection or analysis. (In the operation of such devices, precautions are usually taken to ensure residual magnetic fields in their vicinity are kept to a value below about 5×10^{-4} mT.) This condition is accomplished by making the overall magnetic dipole moment of the solenoid system equal to zero. Because the

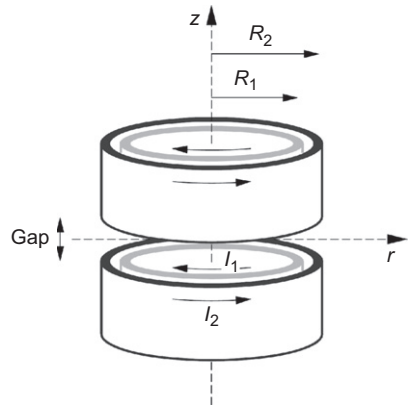

Figure 1 Basic arrangement of the MAC, consisting of two pairs of coaxial solenoids of radii R_1 and R_2, respectively, separated by a narrow gap to allow passage of the electron beams. The scattering plane of the electrons is perpendicular to the central axis of the MAC and passes through the middle of the gap.

overall magnetic quadrupole moment of a system of cylindrical solenoids is automatically zero, the magnetic field then falls off at large radial distances r as r^{-5}. The magnetic dipole moment for a set of circular loops or solenoids is zero when

$$\sum_i n_i I_i R_i^2 = 0 \tag{2}$$

where I_i is the current, R_i is the radius of the solenoid, n_i is the number of turns in the solenoid, and the subscript i labels the solenoids. The attainment of a zero magnetic dipole moment can therefore be achieved with two solenoids of different radii having the appropriate number of turns and with currents flowing in *opposite* directions, as indicated in Figure 1. The resultant magnetic field produced by the set of solenoids is cylindrically symmetric about the axis of the solenoids and so is perpendicular to the scattering plane of the electrons. These electrons are therefore deflected by the magnetic field but remain in the scattering plane. Figure 2 illustrates the typical shape of the variation of the axial component B_z of the magnetic field with radial distance that is obtained with a MAC. B_z has a value of typically several mT at the axis, changes direction at a particular point, and falls to a negligible value within a radial distance of a few tens of mm.

The second important feature of the MAC is that an electron beam that is initially directed toward the central axis of the system of solenoids still passes through that axis after deflection by the magnetic field. Similarly, electrons originating at the axis will move radially away from the axis when in the external field-free region. The reason for this is that for an axially symmetric field, the generalized momentum

$$\pi_\phi = m\rho^2\dot{\phi} + e\rho A_\phi \tag{3}$$

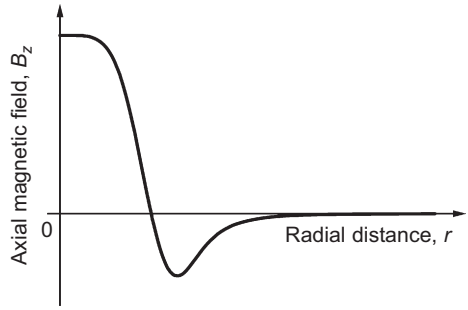

Figure 2 The typical shape of the variation of the axial component B_z of the magnetic field with radial distance r from the central axis of a MAC. B_z has a value of typically several mT at the axis, changes direction at a particular point, and falls to a negligible value within a radial distance of a few tens of mm.

is a conserved quantity, where the magnetic vector potential is $\boldsymbol{A}(r)$ and cylindrical polar coordinates, ρ, z, ϕ are used (Read & Channing, 1996). Both terms on the right-hand side of this equation are zero for an electron that starts or finishes by moving radially in a region of zero A_ϕ, i.e., in the external field-free region, and both terms are zero on the axis of the MAC. This action of the MAC for elastic scattering of electrons is illustrated in Figure 3. The MAC is placed at the interaction region of an electron spectrometer, so that the interaction region is at the middle of the gap on the axis of the MAC, and the scattering plane of the electrons is perpendicular to it. The magnetic field deflects the incident electron beam by the angle θ before it reaches the interaction region, as shown. Since the electrons are elastically scattered, the outgoing electrons from the interaction region are deflected by the same amount, so that the total deflection angle is 2θ. From Figure 3, it is clear that electrons scattered in the backward direction, through 180° in the example shown, would be accessible to an electron energy analyzer. Moreover, the presence of the localized magnetic field does not require any realignment of the electron source or analyzer. The above example shows the situation for elastic scattering. The MAC can also be used for inelastic electron scattering. Now the scattered electrons will have less energy that the incident electrons and so their magnetic deflection will be greater. However, this can be readily taken into account.

It is also possible to make a solenoid system that has a zero dipole moment and also a zero octupole moment. In this case, the magnetic field

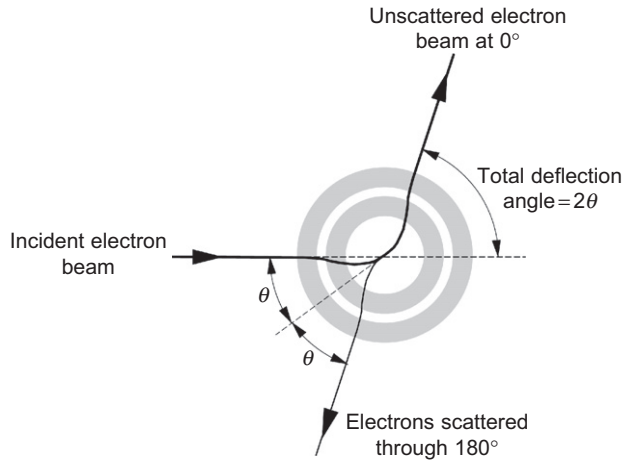

Figure 3 The action of a MAC on elastically scattered electrons. The incident electron beam and the scattered electrons are deflected through the same angle θ by the magnetic field, since they have the same energy, giving a total deflection of 2θ. This action enables an energy analyzer to view electrons scattered in the backward hemisphere.

falls of with radial distance as r^{-7}, since the first nonzero magnetic moment would then be the 32-dipole moment. The dipole and octupole moments can both be made zero if there are three or more pairs of solenoids and if the additional condition

$$\sum_i n_i I_i R_i^4 = 0 \tag{4}$$

is satisfied. A MAC using three solenoids has been described by, for example, Zubek et al. (1999). Alternatively, the dipole and octupole moments can both be made zero by having solenoids of different but appropriate lengths (Read & Channing, 1996). A "conical" solenoid system based on this approach has been described by Linert et al. (2004a,b). Read and Channing also considered the general deflecting and focusing properties and the associated aberrations of a particular system of solenoids. The MAC has the effect of increasing the angular and spatial extent of the transmitted electron beam. However, by careful design of the solenoids and by not employing excessively large magnetic deflections, these effects can be minimized.

The MAC can be operated in a variety of modes. In one mode, the MAC is adjusted to give a particular value of total deflection angle, say 70°. The electron energy analyzer is then mechanically rotated about the target region in the normal way. If its angular range without the MAC is −10° to 135°, then with the MAC it would be 60° to 205°. In a second mode of operation, the electron energy analyzer is fixed in position at a particular angle, say 120°, and the magnetic deflection produced by the MAC is varied by suitably varying the solenoid currents. This is a useful mode for computer control of the experiment. Both modes of operation have been successfully employed.

2.2 Practical Examples of the MAC

2.2.1 Prototype Manchester Design

The first practical realization of the MAC, at Manchester, consisted of two pairs of cylindrical solenoids. The magnetic properties of this solenoid system were designed and optimized using the CPO-3D computer simulation program (Read & Bowring, 2010). The inner and outer solenoids had diameters of 20 mm and 25 mm, respectively, and a length of 36 mm, which allowed the MAC to fit into the interaction region of an existing electron spectrometer. The gap between the two pairs of solenoids was chosen to be 8 mm. This allowed passage of the electron beam without striking the edges of the solenoids, minimizing spurious scattering from these edges. It was also found useful to coat, with colloidal graphite, those surfaces of the solenoids exposed to the electron beam. The solenoid formers were made of aluminium, and the inner former was bored so that

the nozzle for the target gas could be positioned along the solenoid axis. Each of the solenoids consisted of 240 turns of silver-plated solid copper wire of 0.25 mm diameter, with a PTFE coating for vacuum compatibility. The successful operation of the Manchester prototype was demonstrated by observing elastic electron scattering in argon over the angular range 30° to 180° for an incident energy of 10 eV, with a total deflection angle of 95° (Zubek et al., 1996). However, the strength of the magnetic field that could be produced by the solenoids, and hence the ranges of deflection angle and electron energy, was limited by heat dissipation in the solenoids in the vacuum environment. This lead to the realization that it is possible to make the solenoids shorter than their radius as the magnetic field in the small gap between the coils is not increased significantly by making the coils any longer. This in turn leads to a reduction in heat dissipation in the solenoids.

Following the Manchester prototype, several different MAC designs have been developed by various research groups. These designs offer various advantages including the following: reduced heat dissipation in the solenoids permitting the use of higher electron energies, a zero magnetic field at the axis of the MAC, a more rapid decrease in magnetic field with radial distance, the use of iron pole pieces to increase the magnetic field, and reduced surface areas in the MAC construction to minimize spurious background contributions. Representative examples of these designs are now presented.

2.2.2 High Transparency MAC

The construction of a MAC that is nearly optically transparent has been described by Allan (2000). This is achieved by having the inner and outer coils made of a single layer of thin copper tubing. This makes the MAC highly transparent to the target gas emanating from the interaction region, and particularly advantageous for supersonic expansion sources. This MAC is illustrated in Figure 4. The four coils are wound from a single piece of copper tubing of 0.63 mm outer diameter and 0.22 mm inner diameter and are self-supporting. Cooling water is passed through the copper tubing which permits a solenoid current of up to about 8 A. This provides magnetic fields that are strong enough to measure elastic scattering of 100 eV electrons at 180°. The coils are insulated by a PTFE tubing which is covered with colloidal graphite to provide a conductive surface. The individual coils are designed so as to provide good compensation of the magnetic field outside the structure with the same current passing through both the inner and outer coils. The design of the current and coolant leads is thus greatly simplified as is the arrangement of the power supplies, which makes computer control of the MAC much more convenient. The MAC is used in conjunction with a high-resolution electron spectrometer whose analyzer can be rotated up to an angle of 135°.

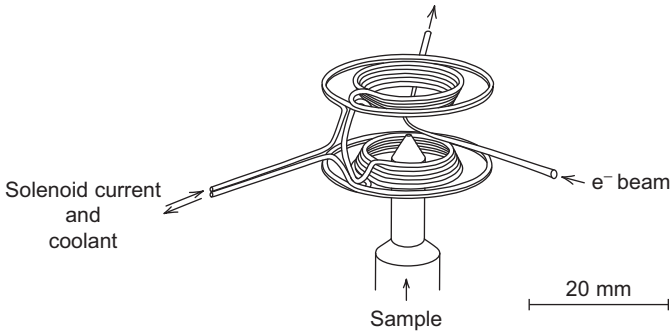

Figure 4 The high transparency MAC of Allan (2000). The four coils are wound from a single piece of copper tubing and are self-supporting. Cooling water is passed through the copper tubing, which permits a solenoid current of up to about 8 A. This provides magnetic fields that are strong enough to measure elastic scattering of 100 eV electrons at 180°. Reproduced from Allan (2000).

This means that a deflection of only 22.5° is required for the incident and for the scattered electrons to measure elastic scattering at 180°, reducing any undesired focusing effects of the magnetic field. The dependence of the deflection angle on the solenoid currents was determined empirically by measuring the deflection angle of the unscattered electron beam using a Faraday cup that could be rotated about the interaction region. This empirical calibration was in good agreement with the prediction of the numerical simulations of the CPO-3D program (Read & Bowring, 2010). The first use of this MAC was to measure energy-differential and angle-differential cross sections for the excitation of the 2^3S state in helium from threshold to 24 eV. In the case of energy-differential cross sections, the cross section is measured as a function of electron energy at fixed scattering angles. For this mode of operation, the solenoid current is continuously adjusted under computer control during each scan so as to keep the scattering angle constant as the incident and scattered electron energies vary.

2.2.3 Iron-Cored System of Solenoids

One approach to increase the magnetic field of a MAC while still preserving field localization is to incorporate iron cores in the solenoids. This approach was taken by Cubric et al. (2000). These authors started with two pair of solenoids using the usual requirement to have a zero magnetic dipole moment, Equation (2). Their approach to the iron-cored design was more pragmatic but it was still expected that Equation (2) would provide an indication of the required solenoid currents. Figure 5 shows a cross section through their iron-cored design. Only a quarter of the system is shown for the sake of clarity. The material used was soft iron with a

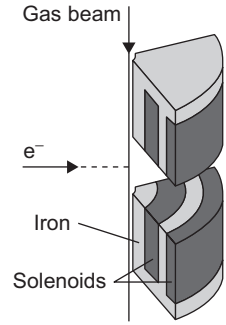

Figure 5 The figure illustrates the iron-cored solenoid system described by Cubric et al. (2000). Only one quarter of the solenoid system is shown for the sake of clarity. The directions of the gas and electron beams are also shown. Reproduced from Cubric et al. (2000).

magnetic permeability of approximately 1000. Cubric et al. calculated the resultant magnetic field variation this pair of solenoids would have in the absence of the iron core, using the analytic expression:

$$B_z(z,\rho,R,I) = \frac{\mu_o I}{4\pi}\int_0^{2\pi} \frac{R^2 - \rho R\cos\phi}{[\rho^2 + z^2 + R^2 - 2\rho R\cos\phi]^{3/2}}\mathrm{d}\phi \qquad (5)$$

where R is the radius of a loop, and z and ρ are cylindrical coordinates representing, respectively, the axial and radial distances to the centre of the loop. The result for the iron-free system is presented as the dashed curve in Figure 6. It shows the axial component B_z of the magnetic field across the gap for the system using Equation (5) and summing over the separate turns of the solenoid. This result has been multiplied by a factor of 5 with respect to its actual strength. The positions of the two solenoids are represented at the top of Figure 6, and the directions of the electric currents are indicated. Also shown on Figure 6 is the magnetic field obtained with the complete system consisting of coils and iron cores. The positions of the iron cores are shown at the top of the figure by grey rectangles. The magnetic field in the gap was measured experimentally using a small magnetometer probe. It can be seen that the variation of the magnetic field with radial distance is similar for the two configurations. Essentially, the use of the iron core multiplies the magnetic field by a factor of 5 while preserving field localization. Since the curvature of the trajectory of a charged particle of kinetic energy E depends on the magnetic field B it experiences as $B/\sqrt{E}$, Equation (1), it follows that the iron-core system is capable of handling electron energies 25 times larger than a similar system without iron cores. This increases the maximum electron energy of the MAC to a

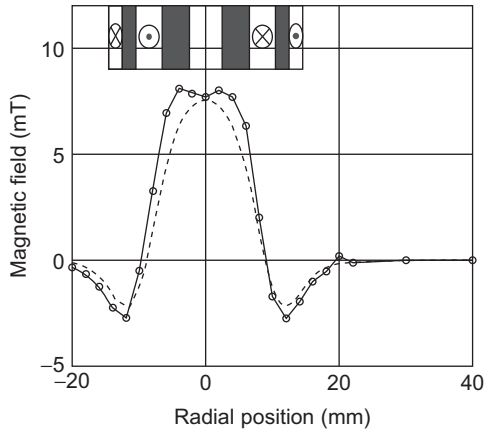

Figure 6 The axial component B_z as a function of the radial distance from the central axis of the iron-cored MAC described by Cubric et al. (2000). The dashed curve shows the result using Equation (5) and summing over the separate turns of the solenoid, in the absence of the iron cores. This result has been multiplied by a factor of 5 with respect to its actual strength. Also shown is the actual magnetic field in the gap, with the iron cores present. Essentially the use of the iron core multiplies the magnetic field by a factor of 5 while preserving field localization. Grey and white rectangles represent the iron cores and solenoid positions, respectively. Reproduced from Cubric et al. (2000).

few keV, depending on the magnitude of the desired change in angle. The performance of the iron-cored MAC was tested by making electron impact excitation studies of the $n = 2$ states of helium, at an incident energy of 120 eV. The energy analyzer was kept at 90° with respect to the incident electron beam direction, and appropriate currents were applied to the solenoids to produce an angular deflection of ±90°. These currents were well below the 5 A limit imposed by the solenoids overheating.

Other authors have incorporated magnetic materials in their versions of the MAC. Trantham et al. (1997) used high permeability pole pieces and a unique coil arrangement to further minimize external stray magnetic fields (see also Cho et al., 2000), while Cho et al. have also described a MAC with iron cores for use in elastic scattering experiments, for example, see Cho et al. (2003b).

2.2.4 Conical Solenoid Design

It was noted in section 2.1 that a system of solenoids of different lengths also allows cancellation of the octupole moment of the magnetic field of the system, and consequently a very rapid decrease of the magnetic field with radial distance. In addition, it can provide a very open structure so that the target gas can be efficiently pumped away from the interaction

region. A MAC design with solenoids of a conical geometry has been described and used by Linert et al. (2004a,b). This system is shown in Figure 7. The inner and outer coils are indicated by full black and full grey circles, respectively. Each inner solenoid contains six layers of turns with four layers in each outer solenoid. The required ratio of currents in both solenoids to obtain zero magnetic dipole moment of the system satisfies the following relationship:

$$I_1 \sum_{i=1}^{6} n_i R_i^2 + I_2 \sum_{i=7}^{10} n_i R_i^2 = 0 \tag{6}$$

where I_1 and I_2 are the currents flowing in the inner and outer solenoids, respectively, n_i the number of turns in the layer, and R_i its radius. The arrangement used by Linert et al. used a value of the ratio of the currents in the inner and outer coils of $1 : -0.327$, with the two currents flowing in opposite directions. The width of each layer (a_{2i}–a_1), see Figure 7, is related to its radius R_i through the geometric condition

$$a_1^2 + a_1 a_{2i} + a_{2i}^2 = \frac{3}{4} R_i^2 \tag{7}$$

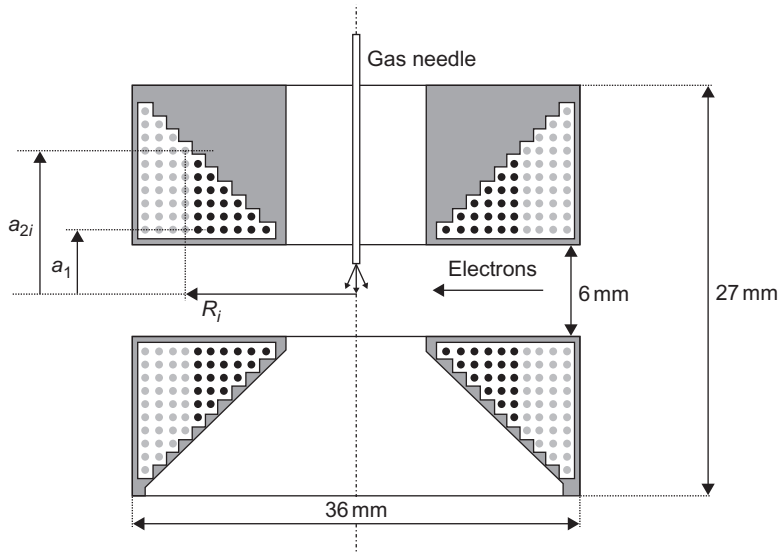

Figure 7 A MAC with a conical solenoid system (to scale). The inner and outer coils are indicated by full black and full grey circles, respectively. R_i is the radius of the i-th layer of turns. a_1 and a_{2i} are the distances of the turns from the plane of symmetry. Reproduced from Linert et al. (2004a).

(Read & Channing, 1996). Here, a_1 gives the position of the first turn in all layers with respect to the scattering plane and a_{2i} is the position of the last turn in layer i (see Figure 7). As noted previously, a MAC has the effect of increasing the angular and spatial extent of the transmitted electron beam, and the ratio of the number of layers in the inner to the outer coils was adjusted to minimize these spreading effects. In this MAC design, relatively low currents are required to obtain the required deflection at a given energy. For example, a 70° deflection of electrons of 10 eV is achieved with a current $l_1 = 0.83$ A in the inner coils. The magnetic field reaches 0.1% of its maximum value at a radial distance of 40 mm. For an electron energy E, the angle of deflection α in the magnetic field is given by

$$\alpha = a \arcsin\left(\frac{cI_1}{\sqrt{E}}\right) \tag{8}$$

with $a = 98.3°$ and $c = 2.50\,\mathrm{A}^{-1}$. The deflection angle of an electron beam of energy 10 eV as a function of inner solenoid current I_1 was measured empirically and is shown in Figure 8. The observed dependence, which for small α is approximately linear agrees very well with the analytical expression, Equation (8). It can be seen from Equation (8) that for a given deflection angle, the magnetic field and therefore the currents in the coils have to be scaled as the square root of the electron energy E. Equation (8)

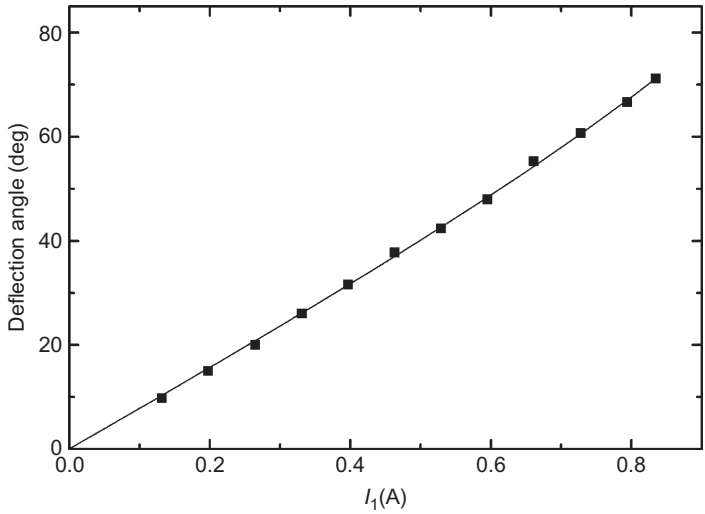

Figure 8 Magnetic deflection angle of an electron beam of energy 10 eV, measured as a function of the inner solenoid current I_1. The experimental points (full squares) were fitted with the analytical expression, Equation (8). Reproduced from Linert et al. (2004a).

also shows how the deflection angle α depends on E for fixed solenoid currents. This conical design has been adopted and successfully applied by several research workers.

2.2.5 Multisolenoid Systems

One property of a MAC consisting of two pairs of solenoids is that a finite magnetic field exists at the central axis of the device, cf. Figures 2 and 6. This may be of no consequence and indeed, it may be usefully applied in some circumstances: for example, to split atomic energy levels. However, there are experiments where the presence of the magnetic field may have important consequences. Murray et al. (2008) have presented theoretical modeling of resonant laser excitation of atoms in a magnetic field, which is relevant to the use of a MAC. A zero magnetic field at the axis of a MAC can be achieved, while still maintaining a highly localized magnetic field, by using three pairs of solenoids instead of two. Such a three-solenoid system has been described by Zubek et al. (1999). The solenoids are each 15.3 mm long with a gap of 9 mm between the solenoids in each pair. Each solenoid consists of four layers each of 16 turns of copper wire covered by PTFE insulation. The layers are tightly wound on aluminium formers whose diameters are 5 mm for the inner solenoids, 14 mm for the middle solenoids, and 23 mm for the outer solenoids. The currents in the inner, middle, and outer solenoids are maintained in the ratios, $1.000 : -0.927 : 0.298$, with the current in the middle solenoids being in the opposite direction to those of the other solenoids. These currents satisfy the requirements of a zero resultant magnetic field in the interaction region and a zero overall magnetic dipole moment. This MAC was used by Zubek et al. to study resonances in the rare gases. The solenoid currents were set to produce an angular deflection of 35° for electrons of energy 11 eV. For this application, the incident energy was varied over a range of typically less than 0.6 eV. Since the electron analyzer was held at a fixed position and the solenoid currents were also held constant, changes in the electron energy introduce an uncertainty in the scattering angle but this uncertainty is only small, typically $\pm 0.5^\circ$. More recently, Klosowski et al. (2007) have described a MAC design that has 10 pairs of coaxial coils of specially designed shape. This design provides large angles of magnetic deflection (up to 60° for 100 eV electrons), and a magnetic field in the scattering region that is very close to zero. Moreover, the spatial profile of the magnetic field introduces a relatively small divergence of the electron beam, which does not significantly decrease the angular resolution of the measurements. The MAC dissipates typically 25 W of power and so is water cooled. Klosowski et al. have demonstrated the application of the MAC to electron–photon coincidence experiments.

3. ELASTIC ELECTRON SCATTERING AND VIBRATIONAL EXCITATION

3.1 Elastic Electron Scattering in Atoms

3.1.1 Introduction

The most widely used application of the MAC has been to measure elastic differential cross sections (DCS) in atoms and molecules. There already existed a large body of both experimental and theoretical work devoted to the study of elastic DCS, but the experimental work did not encompass the full backward hemisphere. Interest in the backward region is motivated by both fundamental scientific reasons and by practical applications of DCS data. An exact knowledge of the differential cross section for electron scattering over the complete scattering angle range from 0° to 180° is crucial to the understanding of the dynamics of electron scattering from atoms and molecules. This is particularly the case at low electron energies. In addition, elastic DCS over the full range of scattering angle are required to obtain integral and momentum transfer cross sections, which are important for the simulation of natural and technological plasmas. Previously, measurements of DCS for electron elastic scattering had usually been performed over a typical angular range of 10° to 135° although some workers had achieved angles close to 160° (e.g., Panajotovic et al., 1997; Sweeny & Shyn, 1996). The maximum angle is limited by the mechanical constraints of the electron spectrometer, while close to 0°, the elastically scattered electrons cannot be separated from the unscattered electron beam. On the other hand, DCS for elastic scattering are provided by theoretical calculations over the full range of scattering angle. These theoretical data have been extensively used to extrapolate the experimental data over the missing angular gaps at low and high scattering angles to estimate integral and momentum transfer cross sections. However, a comparison of calculated DCS in the range of high scattering angles up to 180° shows that different theoretical approaches may predict results that differ by a factor of up to two. Moreover, it appears that various theoretical approaches usually predict integral cross sections for elastic scattering that lie at or above the upper limit of the range of values obtained in the measurements of total cross sections. The MAC technique provides access to the backward hemisphere and can fill the gap at the higher angles. However, it also cannot separate the elastically scattered electron at 0° from the unscattered beam, so that extrapolation of the data is still required at angles close to 0°. The first measurements of elastic DCS using the MAC were reported by Zubek et al. (1996) for the case of argon. Since then several groups have adopted the MAC technique to measure elastic DCS in the rare gases and in a range of diatomic and polyatomic molecules. However, experimental results in

the backward hemisphere are still rather scarce, especially at low incident electron energies.

3.1.2 Apparatus and Experimental Methods

Elastic DCS are measured using the combination of a MAC and a high-resolution electron spectrometer. (Indeed, this combination of a MAC and spectrometer is also used for the measurement of inelastic DCS and for resonance studies.) A typical experimental arrangement is shown in Figure 9, which is taken from Cubric et al. (1999), see also, for example, Linert and Zubek (2006). The electron spectrometer consists of a fixed electron monochromator and an electron energy analyzer that can be rotated about the target region through the angular range 10° to 120° with respect to the incident electron beam. Both the monochromator and energy analyzer employ hemispherical energy selectors. Electrons leaving the energy monochromator are accelerated and focused onto the interaction region by electrostatic lenses, and the incident electron current is measured using a deep Faraday cup placed beyond the interaction region. Scattered electrons from the target are decelerated and focused onto the entrance aperture of the energy analyzer by another set of electrostatic lenses. Electrons transmitted by the analyzer are detected by a position

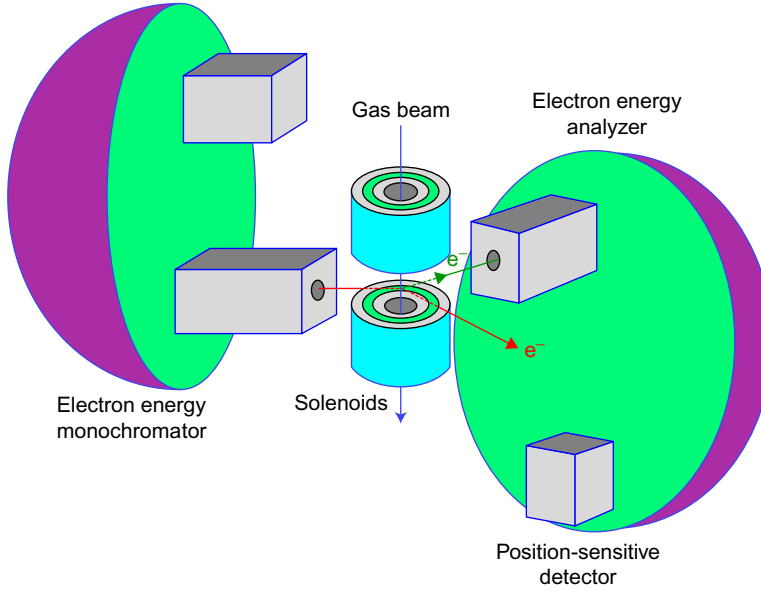

Figure 9 Schematic diagram of the combination of an electron spectrometer and a MAC for use in measurements of angle-resolved DCS. Reproduced from Cubric et al. (1999).

sensitive detector, which allows a range of electron energies to be detected simultaneously. The overall energy resolution of the spectrometer is typically 70 meV, which is more than sufficient to resolve elastically scattered electrons from those that are inelastically scattered. The target gas beam is produced by a single narrow capillary. The MAC consists of two pairs of solenoids and produces a localized magnetic field that is perpendicular to the scattering plane at the interaction region. The gap in the solenoids allows passage of the electrons and the scattering plane lies at the midpoint of this gap. The MAC is used to produce a total deflection of typically 70°. Coupled with the angular range of the rotatable analyzer, this allows the detection of scattered electrons over the full backward scattering hemisphere, including 180°.

The experimental methods that are used to measure the DCS are described, for example, by Linert et al. (2006). The incident electron energy is calibrated against the positions of temporary negative ion resonances that occur in the elastic cross sections at well-know energies, e.g., the ^2S negative ion resonance in helium at 19.366 eV (Brunt et al., 1977; but also see Gopalan et al. (2003) for a more recent measurement), with an uncertainty of typically ±30 meV. The angular scale of the measurements is calibrated by observing the maximum in the elastic DCS of argon that occurs at 180° and the deep minimum close to 120°. Linert et al. give a total uncertainty in the angular scale of ±2° and estimate their angular resolution to be 4°. The angular response of the analyzer is taken into account by simultaneously measuring the DCS of helium and using the calculated cross section in helium (Nesbit, 1979). The measured relative DCS are made absolute using the relative flow technique, which has been described in detail by Khakoo and Trajmar (1986). In order to maintain high operational stability of the electron spectrometer, both the gas under investigation and the helium calibrant gas are always present simultaneously in the vacuum chamber. The measurements usually cover the backward scattering hemisphere but are extended to overlap the angular regions of conventional measurements in the forward direction, which are now quite well established. In this way, accurate elastic DCS measurements are obtained over the widest possible angular range. The uncertainties in the measured values of the absolute DCS arise from the determination of the relative flow rates of the two gases, the scattered electron yields, and the incident electron current. There is also an uncertainty in the theoretical DCS for helium, which is quoted as 1%. From the statistical distribution of several series of measurements, Linert et al. give an overall uncertainty in their measured DCS of typically 15%.

Despite the availability of the MAC, the measurement of DCS at very small and very large angles remains far from trivial, as emphasized by Allan (2005). Elaborate strategies are required to ensure the optimum overlap of the incident electron beam and the analyzer acceptance cone as

the electron energies and the scattering angles are changed, and to determine the response function of the spectrometer for all the energies and angles required. The methods to achieve this are discussed extensively by Allan. One issue that has arisen in using a MAC is the occurrence of spurious noise contributions arising from the incident electron beam. This beam will also be deflected by the MAC. If this deflected beam subsequently strikes a metal surface in the vicinity of the target region, it may be reflected back into the MAC. The MAC may then direct it into the analyzer, leading to spurious background signals. In practice, such contributions may be eliminated by minimizing the amount of solid surface area near the target region and by suitable angular positioning of the electron energy analyzer and judicious use of the deflection angle of the MAC.

3.1.3 Elastic DCS in the Rare Gases

The ability to calculate accurate elastic DCS represents a fundamental test of our understanding of the dynamics of electron–atom interactions: the large amount of theoretical effort applied to these calculations attests to their importance. Producing sufficiently accurate experimental data to test the various theories presents challenges to the experimentalist, and for detailed comparison with theory, measurements over the full range angular scattering 0°–180° are required. The rare gases have attracted most of the theoretical effort. Various different interactions become dominant as the mass of the atom increases. Moreover, the rare gases provide the basis upon which to proceed to open-shell atoms and to molecular systems. The elastic DCS in helium is well described by theory, Nesbit (1979), and indeed its role has been to normalize the experimental data in the other rare gases. Elastic DCS in the rare gases, neon, argon, krypton, and xenon have been measured using the MAC technique. This has mainly involved two experimental collaborations: the Manchester/Gdansk collaboration and the collaboration between Buckman, Cho, and coworkers. This has usefully allowed comparison between different sources of DCS experimental data. More recently in joint experimental–theoretical work, Allan, Hotop, Bartschat, and coworkers have produced elastic DCS data in the rare gases in their studies of Feshbach resonances.

3.1.3.1 Elastic DCS in Neon

The scattering of electrons by neon has particular importance because its relative simplicity makes it more amenable to theoretical calculation than heavier atoms. Experimentally, the need for accurate absolute DCS in neon has been emphasized by suggestions (Gulley et al., 1994; Shi & Burrow, 1992) that it can be used as a secondary standard, after helium in the determination of DCS of other gases. Theoretical studies of elastic electron scattering by neon atoms have been more extensive than the

experimental studies. The general aim of these theoretical works was to develop a description of the polarization and exchange interactions between the target atom and the incident electron. The first measurement of the elastic DCS in neon in the backward direction was made by Linert et al. (2006), who also summarized the theoretical work. They measured the DCS at incident energies of 7, 10, and 15 eV, i.e., below the first excitation threshold. This range was extended by Cho et al. (2008) who used incident energies of 5, 10, 20, and 50 eV: the two higher energies lying above the first excitation threshold. The elastic DCS in neon, including the backward scattering hemisphere, has also been reported by Allan et al. (2009), at an incident energy of 18 eV, together with theoretical calculations. An example of a measured elastic DCS in neon, at an energy of 10 eV, from Linert et al. (2006), is shown in Figure 10. This figure also shows previous experimental cross sections and the results from several theoretical calculations. The previous experimental work relates to the angular range below 140°, although the much earlier work of Ramsauer and Kollath (1932) employed a technique, which could reach up to 167.5°. The results of Linert et al. cover the angular range 110°–180°,

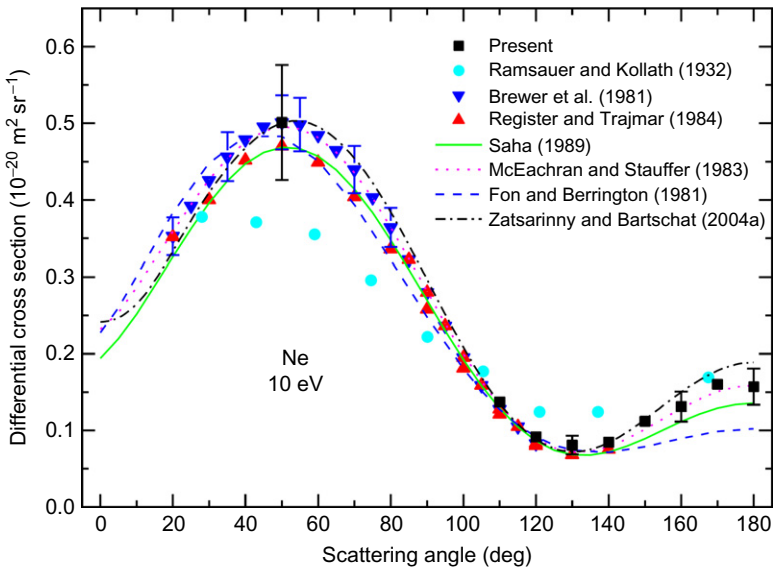

Figure 10 DCS for electron elastic scattering in neon at the energy of 10 eV, obtained by Linert et al. (2006), shown as full black squares. Also shown are experimental results of Ramsauer and Kollath (1932), Brewer et al. (1981), Register and Trajmar (1984) and the theoretical results of Saha (1989), McEachran and Stauffer (1983), Fon and Berrington (1981), and Zatsarinny and Bartschat (2004a). Reproduced from Linert et al. (2006).

while the theoretical calculations cover the complete angular range, 0° to 180°. There is some overlap in the angular range 110°–130° between the MAC data and the studies of Brewer et al. (1981) and Register and Trajmar (1984). In this region of overlap, there is good agreement between all the recent experimental data including the MAC data. Over the angular range 110°–130°, the theoretical calculations are also in agreement with each other and in agreement with the experimental data. In the angular range below 110°, the calculated DCS tend to deviate from each other by a small amount (∼10%). The experimental results of Brewer et al. and Register and Trajmar show differences, which increase to 10% at an angle of 50°. A measurement made at 50° using the MAC is in excellent agreement with that of Brewer et al. For the angular range above 130°, the MAC results rise to a maximum at 180°. Over this angular range, there are significant discrepancies between the results of the various calculations. This emphasizes the usefulness of the MAC to test theory in this angular range. The best agreement with the MAC results comes from the calculations of McEachran and Stauffer (1983) and Dasgupta and Bhatia (1984), which coincide with each other. The results of Saha (1989) and in particular of Fon and Berrington (1981) are considerably lower than the experimental DCS, while the results of Zatsarinny and Bartschat (2004a) are about 20% higher than the experimental values. Cho et al. (2008) have also measured the elastic DCS in neon at 10 eV using a MAC and so a direct comparison can be made. Above 130°, the data of Cho et al. lie below those of Linert et al. but still above the results of Fon and Berrington.

3.1.3.2 Elastic DCS in Argon

There has been a considerable amount of theoretical work on elastic scattering in argon, and these have been summarized by Mielewska et al. (2004). These works differ most significantly in their various approaches to account for long-range polarization and short-range correlation interactions in the electron scattering process. Mielewska et al. measured the elastic DCS in argon at energies of 5, 7.5, and 10 eV, where correlation and polarization interactions between the target and incident electron are expected to play dominant roles. In a comparison of their data with the available theoretical calculations, these authors find that in general the theoretical results lie above the experimental values for high scattering angles. Furthermore, although the various theoretical calculations are in fair agreement with each other over the range of intermediate scattering angles, they display significant differences in the region of high scattering angle. Mielewska et al. suggest that the discrepancies may be ascribed to difficulties in modeling the polarization–correlation interaction (cf. Gianturco & Rodriguez-Ruiz, 1993). Cho and Park (2009) have also used a MAC to measure elastic DCS in argon, at energies from 5 to 50 eV, including 10 eV. Their results are shown in Figure 11 and allow direct

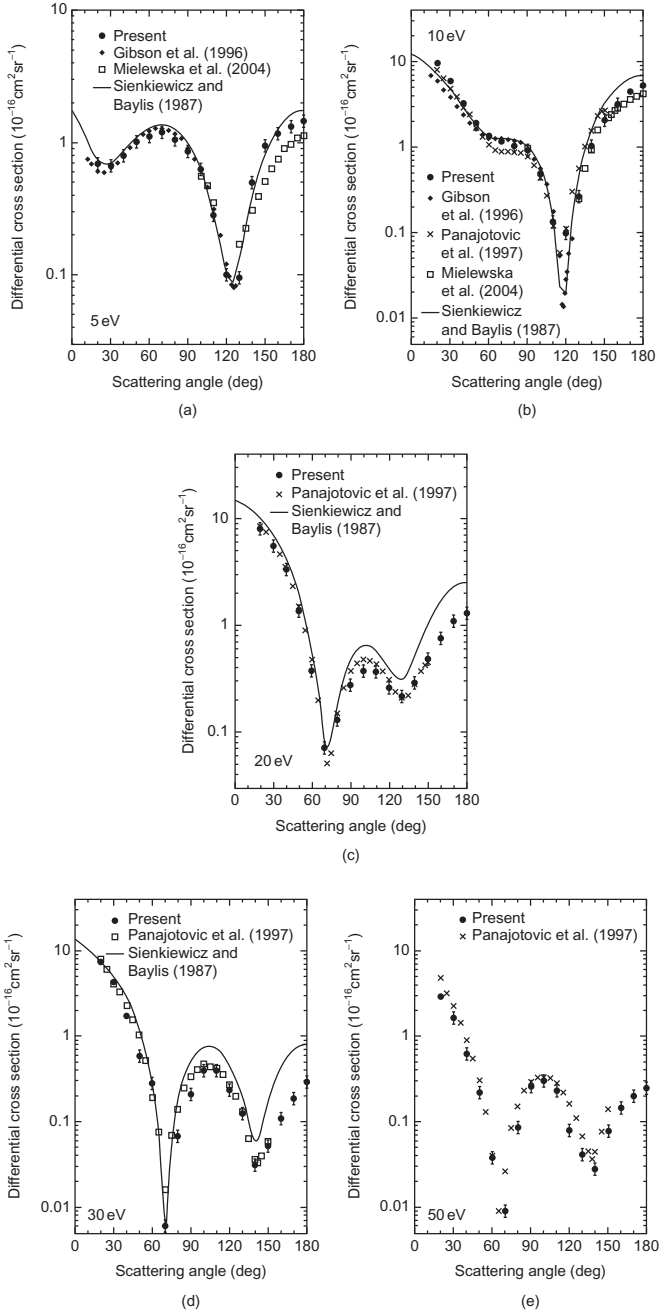

Figure 11 Absolute DCS for elastic scattering in argon, obtained by Cho and Park (2009). Also shown for: Mielewska et al. (2004), Gibson et al. (1996), Panajotovic et al. (1997), and Sienkiewicz and Baylis (1987). Reproduced from Cho and Park (2009).

comparison with the results of Mielewska et al. It can be seen that the agreement between the two sets of data is good at 10 eV while it is less good at 5 eV. Also shown for comparison is the theoretical calculation of Sienkiewicz and Baylis (1987) who used a model potential with two parameters to account for the dipole and quadrupole correlation polarization.

3.1.3.3 Elastic DCS in Krypton and Xenon

Analogous measurements of elastic DCS using a MAC have been made for krypton (Cho et al., 2003a, 2004; Hoffmann et al., 2010; Linert et al., 2010) and for xenon (Cho et al., 2006; Linert et al., 2007). In their work, Cho and coworkers have investigated the role of absorption in the intermediate energy range. These various studies compare in some detail the experimental data from the various groups and the predictions of the various theoretical predictions. Cho et al., Linert et al., and Hoffmann et al. all report measurements of the DCS in krypton at or close to the energy of 10 eV, and so a useful comparison can be made between measurements obtained using different MAC designs. It is found that the agreement between the three measurements is good to excellent, except in the region around the minimum in the DCS, which is strongly influenced by the angular resolution of the experiments. These elastic studies of electron scattering by the heavier rare gases in the low energy region are particularly important from the view of developing adequate theoretical models for correlation–polarization interactions and relativistic effects. Having a full set of elastic DCS for the rare gases has allowed some comparisons to be made. Linert et al. (2010) analyzed the DCS of the three heavier rare gases argon, krypton and xenon as a function of their polarizabilities at the scattering angles of 30°, 80°, and 180° and electron energies in the range 5–30 eV. They find that at lower energies 5 and 7.5 eV, the DCS tend to rise with increasing atomic polarizability, indicating significant contribution of long-range dipole polarization interaction. That dependence becomes weaker or disappears at higher energies, possibly as a result of nonadiabatic effects.

3.1.4 Integral and Momentum Transfer Cross Sections

Elastic DCS can be used to deduce integral and momentum transfer cross sections by integrating the DCS over the full scattering range 0°–180°. However, we reiterate that the elastic cross section cannot be measured close to 0° since the elastically scattered electrons cannot be distinguished from the unscattered electron beam. Furthermore, the maximum angle that can be observed in a conventional spectrometer is limited by mechanical constraints. Previously, this meant that measured DCS data had to be

extrapolated to low and high scattering angles. The MAC allows measurements, continuously up to 180° so that extrapolation to higher angles is avoided, although it is still necessary to extrapolate the DCS close to 0°.

An example of the determination of integral and momentum transfer cross sections is provided by the work of Linert et al. (2010). These authors determined these cross sections for krypton at energies of 5, 7.5, and 10 eV. Both were obtained by extrapolating the measured DCS from 30° down to 0° and then integrating the DCS over the complete angular range 0°–180°. In the extrapolation procedure for the 0°–30° range the angular dependencies of the theoretical data of Bell et al. (1988) were taken, which were normalized to the measured DCS at 30°. The uncertainty in the integral and momentum transfer cross sections because of this extrapolation procedure is estimated to be less than 2% and 1%, respectively. Linert et al. estimate the associated uncertainties in their elastic integral and momentum transfer cross sections to be 17% and 15%, respectively. In Figure 12, the integral cross sections of Linert et al., obtained at 5, 7.5 and 10 eV, are compared with cross sections determined from other measured DCS and with the results of theoretical calculations. At 10 eV, the very small contribution (2%) because of the excitation cross section of the first excited state 5s[3/2]^o at 9.915 eV is neglected. Very good agreement is found with the experimental total cross sections, which usually

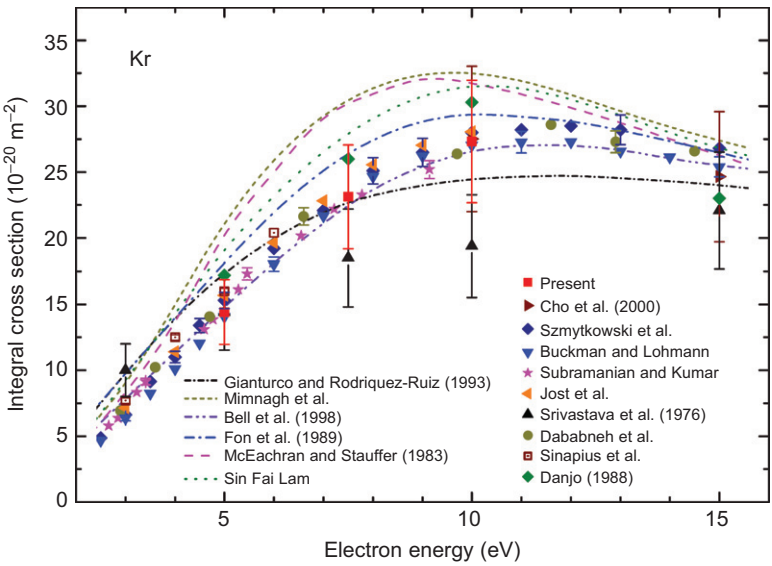

Figure 12 Integral cross sections for elastic scattering in krypton, reproduced from Linert et al. (2010), whose data are given by the full squares. See Linert et al. (2010) for full details of previous experimental and theoretical results.

have a higher degree of accuracy than DCS measurements. There is agreement also with the results of Cho et al. (2003a) who also used a MAC to determine the integral cross section. Above 5 eV, the results of Danjo (1988) overestimate the integral cross section whereas those of Strivastava et al. (1981) largely underestimate it. These differences may, to some extent, arise from the extrapolation of their results over the wide scattering range 130°–180° which is avoided with the MAC. The momentum transfer cross sections determined at 5, 7.5, and 10 eV by Linert et al. are shown in Figure 13 and compared with those determined from previous DCS measurements, with swarm experiments and with the preferred cross sections given by Buckman et al. (2000). The cross sections agree very well with those obtained by swarm experiments by Hunter et al. (1988) and Suzuki et al. (1989). However, the preferred momentum cross sections given by Buckman et al. appear to be underestimated above 7 eV. The integrated results of Strivastava et al. (1981) and Danjo (1988) deviate from the measurements of Linert et al. In the integration procedure, the 130°–180° angular range gives a significant (40%–60%) contribution to the momentum transfer cross section, which therefore relies heavily on an accurate determination of the DCS in the backward scattering direction. With respect to the theoretical results, the *R*-matrix calculations of Bell et al. (1988) are in best accord with the experimental cross sections.

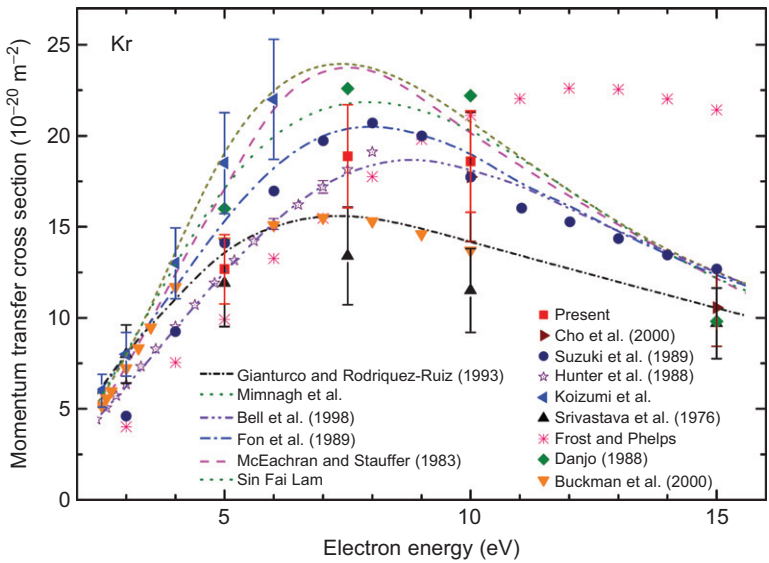

Figure 13 Momentum transfer cross sections in krypton, reproduced from Linert et al. (2010), whose data are given by the full squares. See Linert et al. (2010) for full details of previous experimental and theoretical results.

3.2 Elastic Electron Scattering and Vibrational Excitation in Molecules

The MAC is finding increasingly wide application in the measurement of cross sections for elastic scattering and vibrational excitation in molecules because of its ability to make measurements in the backward scattering hemisphere. Although there is a large body of both theoretical and experimental work in the literature on elastic DCS in molecules, there is much less on DCS for vibrational excitation. The scattering of low-energy electrons by molecules is an accepted test ground for developing an accurate description of electron–molecule interactions, and an important role is played by detailed comparison of the results of theory and experiment. Comparison is especially important to understand the roles of short- and long-range correlation (polarization) and exchange interactions. Consequently, the MAC has been used to measure elastic DCS and vibrational excitation in the diatomic molecules N_2 (Allan, 2005; Linert & Zubek, 2009; Zubek et al., 2000), O_2 (Linert et al., 2004a,b; Linert & Zubek, 2006), and CO (Allan, 2010). Elastic scattering and vibrational excitation cross sections are also required in the modeling of atmospheres, in the development of gas etching processes, and in the study of radiation damage in biological molecules and their analogues. Moreover, the interest in electron-induced chemical processes at low energies has recently been renewed by the discovery that electrons at sub-ionization and even sub-excitation energies can damage DNA. Thus, the MAC has been used to measure elastic and vibrational cross sections in sulfur hexaflouride SF_6 (Cho et al., 2000), which is an important gas for insulation in the electrical industry; in ethane (Allan et al., 2008) and methane CH_4 (Curkic et al., 2008), which is important in a wide variety of technological and atmospheric applications; in tetrahydrofuran (Allan, 2007; Dampc et al., 2007a,b), which serves as convenient model for the sugar ring in the DNA backbone; and in the flourocarbons CF_3H and CF_3I (Cho et al., 2010), which are important in the field of plasma processing.

3.2.1 Elastic Electron Scattering and Vibrational Excitation in Molecular Nitrogen

Molecular nitrogen, after molecular hydrogen, is probably the most studied target for investigations of electron–molecule collisions and for measurements of scattering cross sections. It plays an important role in atmospheric processes and in electrical discharges in various physical environments. Moreover, its relatively simple electronic configuration represents a suitable target for fundamental tests of electron–molecule interactions. Recently, Linert and Zubek (2009) have measured DCS for elastic electron scattering and vibrational $v = 1$ excitation in N_2 from 5 to

20 eV over the angular range 10°–180° using a MAC. The apparatus they used is described in detail by Linert and Zubek (2006). The aims of the work were to resolve discrepancies between earlier measurements using a MAC (Allan, 2005; Zubek et al., 2000), and to extend previous experimental work to higher energies and a wider range of scattering angles. Linert and Zubek also summarize the previous experimental and theoretical works. The DCS obtained for elastic electron scattering at energies of 5, 10, 15, and 20 eV are presented and compared with other available previous experimental and theoretical results in Figures 14(a)–(d). The statistical uncertainties are estimated to be 13% for 5 eV, 10% for 10 eV and 15 eV, and 15% for 20 eV. Perhaps, the DCS of most interest in the present context is the one obtained at the energy of 5 eV, since direct comparison can be made with the measurements of Allan et al. (2005) who also used a MAC. It is also the case that experimental measurements at such low energies are particularly challenging to the experimentalist. It can be seen that in the angular range 60°–120°, there is very good agreement with Allan (and also with the earlier results of Srivastava et al. (1976), later renormalized by Trajmar et al. (1983)). The agreement with the results of Allan extends beyond 120°; above 160°, the results of Linert and Zubek are slightly below those of Allan, although within the experimental uncertainty. In the region below 50°, measurements from the different laboratories show differences. At 30°, the cross section of Linert and Zubek lies between the results of Allan (2005) and Brennan et al. (1992), the differences being 15% and 8%, respectively. The best agreement with theory in the range 60°–120° is with the calculations of Feng et al. (2003) and Sun et al. (1995), which both treat polarization–correlation effects in most detail. In the region below 60°, most of the calculations display the experimental angular dependencies, but appear to overestimate the cross section.

For the measurement of vibrational excitation, Linert and Zubek (2009) recorded energy loss spectra for fixed incident electron energies at each scattering angle. From the energy loss spectra, using a peak fitting procedure, ratios of intensities of the $v = 1$ peak to those of the elastic peak were determined. Absolute DCS for excitation of the $v = 1$ level were derived from these ratios using their values for the absolute elastic cross sections. The energy loss spectra above 90° were measured using a MAC. This introduced an additional uncertainty in the angular scale of 1.5° at 5 eV and less than 1° at higher energies, resulting in a total uncertainty for vibrational excitation of ±3.5° at 5 eV and less than ±3° at other energies. The DCS for vibrational ($v = 0 \rightarrow 1$) excitation measured at 5, 10, 15, and 20 eV are shown in Figure 15, where they are compared with available experimental and theoretical data.

The statistical uncertainties in the DCS at 5 eV are estimated to be 22% in the angular range 25°–40° and 19% in the remaining angular range. The uncertainties at 10, 15, and 20 eV are 17%, 14%, and 18%, respectively, over

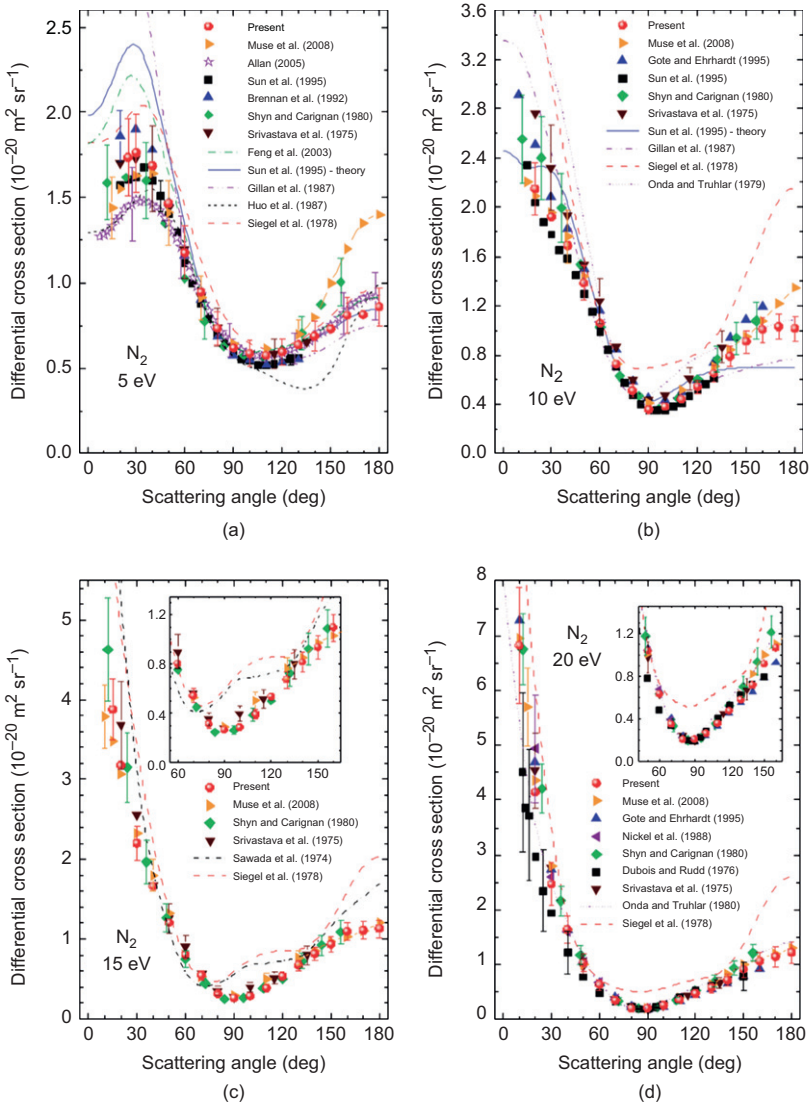

Figure 14 DCS for elastic scattering in molecular nitrogen, at incident energies of (a) 5, (b) 10, (c) 15, and (d) 20 eV. Reproduced from Linert and Zubek (2009), where full details of the previous experimental and theoretical works can be found.

the whole angular range. At 5 eV, the DCS of Linert and Zubek display two minima, at 55° and 125°, and it is asymmetric with respect to a maximum at about 85°. It is in best agreement with the results of Brennan et al. (1992) measured up to 130°. The DCS of Allan (2005) show a more

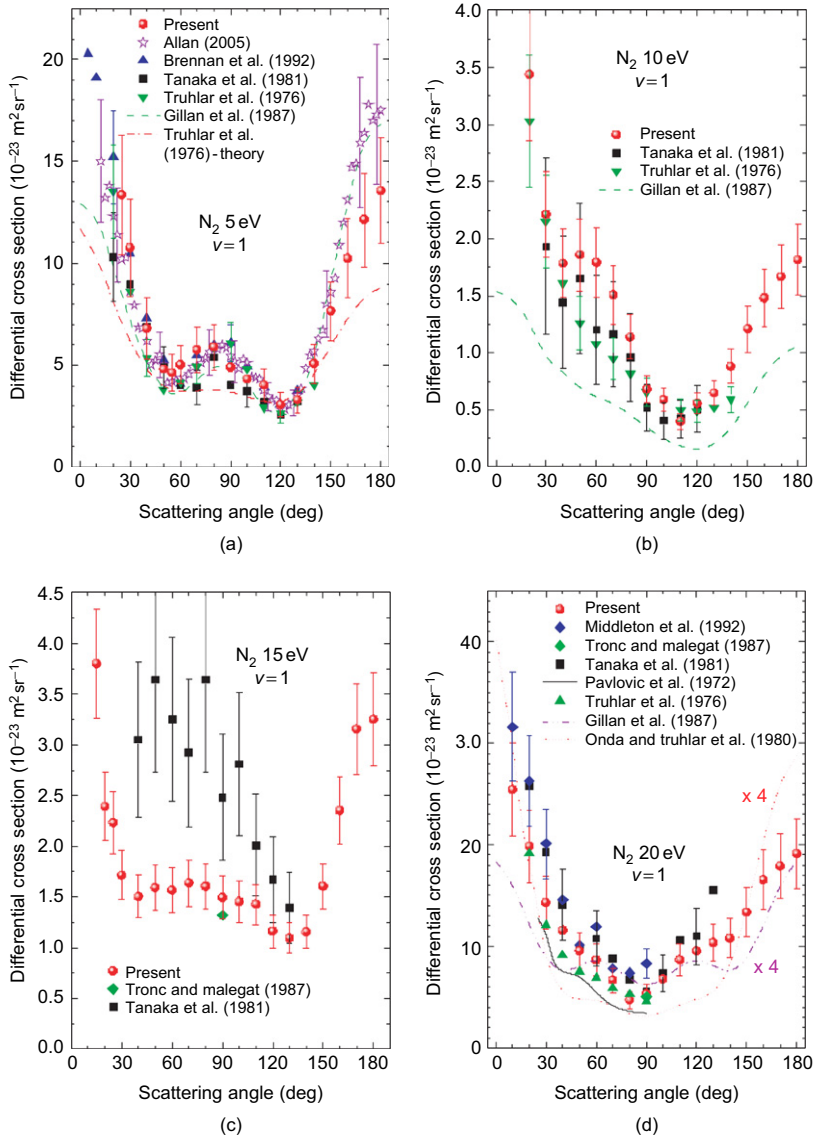

Figure 15 DCS for excitation of the $v = 1$ level of molecular nitrogen, at incident energies of (a) 5, (b) 10, (c) 15, and (d) 20 eV. Note that in (d), the results of the theoretical calculations have been multiplied by a factor of 4. Reproduced from Linert and Zubek (2009), where full details of the previous experimental and theoretical works can be found.

symmetric shape with respect to 85°. However, the differences between both results at 25° and 180° are within the uncertainty limits. These results indicate considerable contribution from the $^2\Pi_g$ resonance at 5 eV. The

R-matrix calculations of Gillan et al. (1987), which apart from $^2\Pi_g$ symmetry also accounted for five other scattering symmetries, generated lower cross sections in forward than in backward scattering. At other values of incident energy, it can be seen that agreement between available data is less satisfactory. This may be due to the extrapolation techniques used to extend the DCS toward 180°, which is avoided with the use of a MAC. Linert and Zubek also integrated their cross sections for elastic scattering and vibrational excitation to obtain integral and momentum-transfer cross sections. In the case of elastic scattering, the cross sections were extrapolated down to 0°. A linear extrapolation was used at 10, 15, and 20 eV and at 5 eV, and the theoretical data of Sun et al. (1995) were employed. The integration and extrapolation procedures introduced uncertainties of less than 0.5%.

4. INELASTIC ELECTRON SCATTERING

The physical principles of the MAC also apply to the case of inelastic electron scattering: the magnetic field is localized so that the operation of the electrostatic spectrometer is not impaired; the incident electrons change their incident angle but still pass through the interaction region and the scattered electrons change their direction but still move radially away from the interaction region once they reach the field-free region. Of course, the incident and inelastically scattered electrons are deflected by different amounts but these magnetic deflections can readily be determined either by computer simulations of the MAC or from experimental measurements. There is, however, an additional advantage of the MAC for measurements of inelastic scattering. The trajectories of the inelastically scattering electrons are separated from the unscattered electron beam because they are deflected through different angles, as illustrated in Figure 16, which is adapted from Cubric et al. (1999). The inelastic yield at and near 0° can therefore be accurately determined, unlike the elastic scattering case. Furthermore, the backward scattered electrons follow different trajectories to those of the incident electron beam. The MAC therefore allows inelastic measurements to be made over the complete angular range from 0° to 180°, and integral cross sections can be obtained without recourse to any extrapolation procedures. It also follows that electron energy loss spectra can be obtained at all angles in the backward scattering hemisphere including 180°.

4.1 DCS for Inelastic Electron Scattering

The first application of a MAC for inelastic electron scattering was made by Cubric et al. (1999) who measured DCS for excitation of the $n = 2$ states of helium over the complete angular range from 0° to 180°, at energies of 30, 40, and 50 eV. There had been numerous previous measurements of

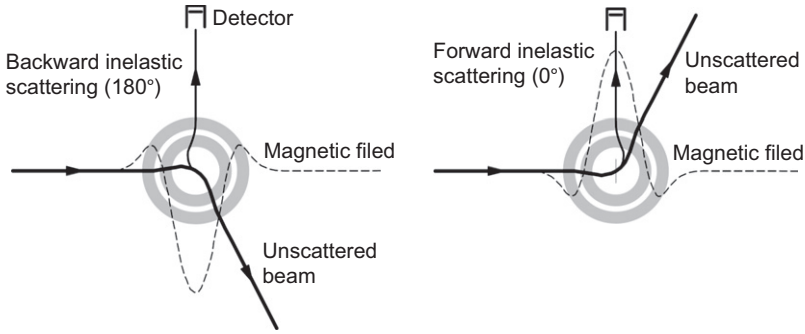

Figure 16 Cross sections through a MAC showing computed trajectories for the detection of backward (180°) and forward (0°) scattered inelastic electrons, where the incident and scattered electrons have energies of 30 and 10 eV, respectively. Also shown, for each case, is the variation of the axial magnetic field with distance from the centre. Adapted from Cubric et al. (1999).

these DCS, with the most complete coverage of scattering angles being achieved by Asmis and Allan (1997). These authors used a conventional spectrometer to cover the range 0° to 135° and a magnetically focused spectrometer, used in connection with the "electron mirror" technique, to measure the DCS at the two specific angles of 0° and 180°. It was the measurements of Asmis and Allan that were the first that were able to show the discrepancies between theory and experiment at the extremes of scattering angle. Cubric et al. used two pairs of short solenoids in conjunction with a conventional electron spectrometer. The total change in angle α caused by the MAC depends on the magnitude and direction of the field and the energies, E_1 and E_2 of the incident and scattered electrons. Cubric et al. maintained a constant ratio for the currents I_1 and I_2 in the inner and outer solenoids and measured the dependence of α on I_1 using sharp structures in the DCS of the 2^1P state of helium at 40 eV. They also computed it using the CPO program (Read & Bowring, 2010) and found that the two methods were in agreement. A parameterization that is accurate to within 1% is

$$\alpha = a\left[\arcsin\left(b\frac{I_1}{\sqrt{E_1}}\right) + \arcsin\left(b\frac{I_1}{\sqrt{E_2}}\right)\right] \tag{9}$$

where a and b are empirical constants. Cubric et al. used a two-dimensional scanning technique, in which energy loss spectra were recorded at a series of incremented values of I_1, while the analyzer was kept at a fixed position. To extract the DCS of a particular state, the sum of all counts under the corresponding peak was taken for each value of I_1, which was converted to the relevant scattering angle using Equation (9).

This provided relative DCS. To put these on an absolute scale, the authors used the accurate measurements of Trajmar et al. (1992) and the CCC calculations of Fursa and Bray (1997) for the excitation of the optically allowed 2^1P state; the CCC calculations being chosen because of the established accuracy of this method over a wide range of states and energies. The angular resolution of the MAC technique is affected by the curvature of the trajectories of the incident electrons as they transverse the scattering region. This curvature gives rise to a range of scattering angles received by the analyzer and the spread is greatest for backward scattering. Using the CPO program, Cubric et al. estimated that in their measurements the rms spread in angles from this effect is $\pm 6^\circ$ for scattering through 180°. This magnetic spread has to be added in quadrature to the estimated conventional spread of $\pm 3^\circ$ caused by the finite range of angles in the incident beam and the finite angular acceptance of the analyzer. At a scattering angle of 130°, the magnetic and conventional spreads have the same magnitude, while at scattering angles less than approximately 100° the magnetic spread can be ignored. Cubric et al. give a total uncertainty of 8% in the magnitude of the measured DCS, although they note that this may be larger at some scattering angles. The measured and calculated DCS for the $n = 2$ states of helium are shown in Figure 17. The DCS of the 2^1S state show a sharp minimum between 45° and 55° at all the three impact energies. The fact that such a deep and sharp is observed confirms the estimate of the experimental angular resolution of the measurements. The DCS of the 2^1P state matches the CCC results because of the normalization procedure. The agreement between theory and experiment for the DCS of the other states is generally good at all three impact energies but there are discrepancies, particularly at the angles that were previously inaccessible. The largest discrepancies, by factors in the range 2–7, between the measured and calculated results and between the calculated results themselves, occur for the 2^3P state at the lower impact energies and at the lowest and highest scattering angles. The disagreement for this state at small angles may be partially explicable in terms of the slight overlap between the 2^3P and 2^1P peaks in the energy loss spectra, but this would affect the results at 40 and 50 eV much more than those at 30 eV, where in fact the disagreement is largest. The disagreements at large angles are partly due to the spread in acceptance angle in the MAC technique as discussed above, but by convoluting the theoretical results with the experimental angular function this is found to account for less than 15% of the difference. The experimental data for the triplet cross sections also exhibit some discontinuities, for example, near 25° at 30 eV. It is considered that these arise from the arrival at the detector of electrons from the incident beam that have undergone various reflections and deflections. Such contributions have been removed from all the singlet DCS in the procedures used to analyze the data but the discontinuities remain in the triplet DCS even when more elaborate analyses were employed.

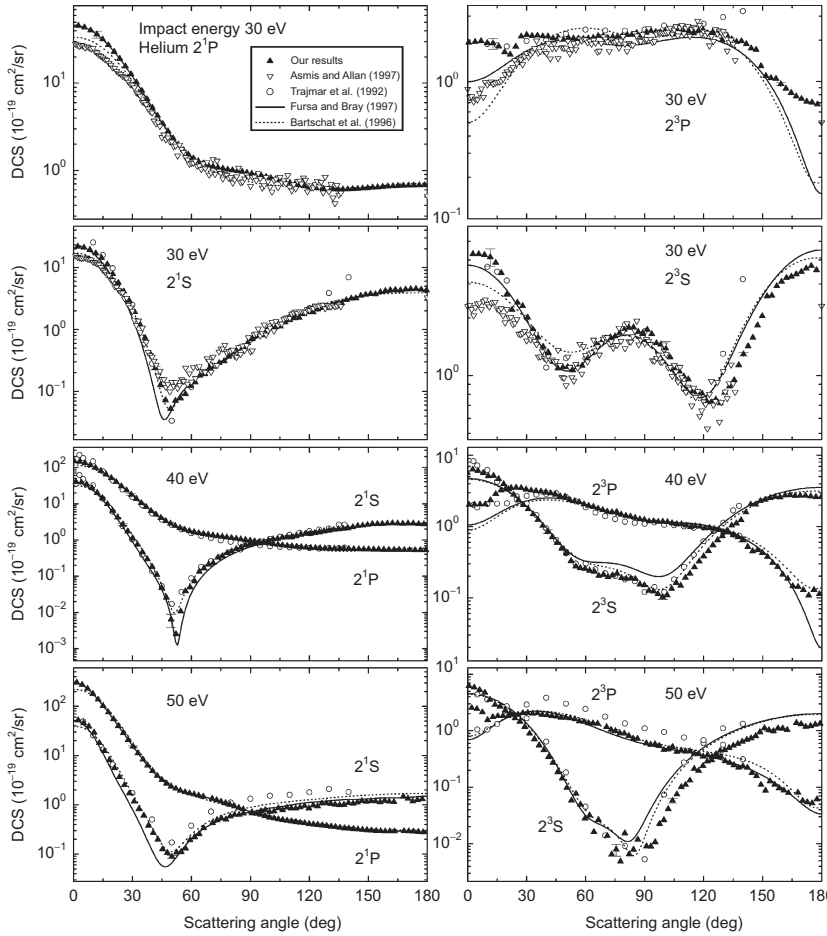

Figure 17 Measured and calculated DCS for the $n = 2$ states of helium at incident electron energies of 30, 40, and 50 eV. Reproduced from Cubric et al. (1999).

Subsequently, Allan (2000) measured the DCS of the 2^3S state of helium from threshold to 24 eV and presented spectra at scattering angles from 0° to 180°. As noted previously, the MAC devised by Allan readily allows the incident energy to be continuously varied in the measurement of a DCS. The measured DCS of the 2^3S state of helium is shown in Figure 18. The spectra recorded at 45°, 90°, and 135° were recorded without magnetic deflection. The spectrum at 180° was recorded with the analyzer set at 135° and a corresponding magnetic deflection. The spectra at 0° and 180° agree well with those Asmis and Allan (1997) with the magnetically focused mirror spectrometer, mutually validating the two techniques. The spectrum at 90° agrees with that of Allan (1992) although there are

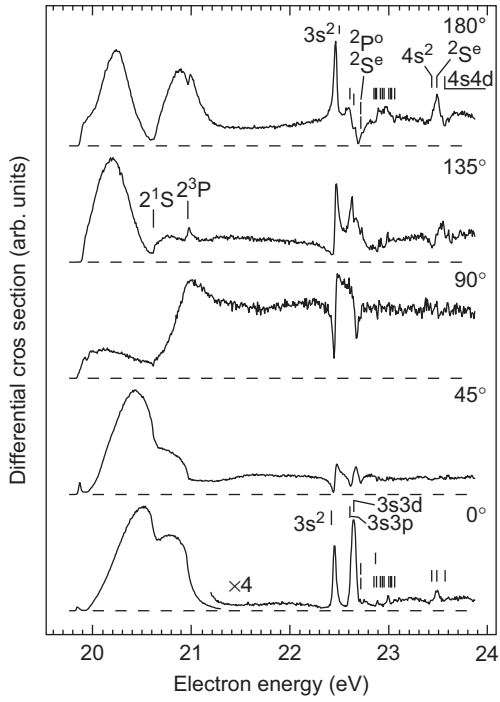

Figure 18 Measured DCS of the 2^3S state of helium from threshold to 24 eV, at scattering angles spanning the entire sphere. The vertical lines above the spectra in the 22–24 eV range indicate the energies of ridge resonances as calculated by Fon et al. (1989). Reproduced from Allan (2000).

some differences within the first few hundred meV above threshold. The spectra show that the shape of the sharp resonant structures, i.e., the interference of the resonant scattering amplitude with the underlying background varies dramatically with scattering angle. The results of Allan also reveal interesting details of narrow ridge resonances surrounding the deep minimum of the angular distribution at 22 eV for backward scattering angles.

More recently, in joint experimental and theoretical investigations, use of the MAC has been made to measure absolute DCS for electron impact excitation of neon (Allan et al., 2009) and krypton (Hoffmann et al., 2010). In particular, studies were made of the energy regions just above the first excitation thresholds where the excitation process is dominated by prominent resonance structure. In addition to the experimental measurements, the *B*-spline *R*-matrix method (Zatsarinny & Bartschat, 2004a,b, 2005) has been used to calculate the cross sections. In the example of neon, absolute DCS of excitation to the four $2p^5 3s$ levels and to selected $2p^5 3p$ levels were determined as a function of electron energy up to 3.5 eV above threshold

at specific angles from 0° to 180°. In addition, cross sections were recorded as a function of scattering angle from 0° to 180° at 18 eV for the $2p^5 3s$ levels and at 19.3 eV for the $2p^5 3p$ levels, respectively. The cross sections were also determined theoretically using the *B*-spline *R*-matrix methods with nonorthogonal orbit sets. Very good agreement was found both in terms of absolute values and in terms of the energies and widths of the numerous resonance features, thereby allowing for (re)classifications with significantly improved accuracy compared to earlier work. This work is further discussed in the section on resonances (section 5).

4.2 Electron Energy Loss Spectroscopy

Electron energy loss spectroscopy is a powerful technique to investigate the excited states of atoms and molecules. Since the mass of the electrons can be neglected compared to the mass of the atomic or molecular target, the energy lost by the inelastically scattered electrons gives directly the energies of the excited states. Moreover, energy loss spectroscopy has some valuable advantages compared to conventional photoabsorption measurements. The optical selection rules may become considerably relaxed when the incident energy approaches the excitation threshold of an excited state and when the scattering angle of the scattered electron is large. This is where the ability of the MAC to access large scattering angles becomes important, making it valuable in spectroscopic measurements. So far, the application of the MAC to specifically measure energy loss spectra for spectroscopic reasons has been limited, although energy loss spectra have been obtained in the rare gases as a prelude to measuring the DCS of excited states (Allan et al., 2009; Hoffmann et al., 2010).

Linert et al. (2004a) have studied electron impact excitation of molecular oxygen using a MAC and have presented an energy loss spectrum of O_2 at a scattering angle of 180°. Oxygen is interesting because of the important role it plays in fundamental physical phenomena in the Earth's atmosphere and in gaseous plasmas. In addition, it is an important example of a molecule with an open-shell structure. Providing an adequate description of the interactions of incoming electrons with such open-shell molecules is a testing challenge for theoretical methods. Particular attention has been paid to elastic scattering, vibrational excitation of the ground state, and excitation of the lowest $a^1\Delta_g$ and $b^1\Sigma_g^+$ electronic states of oxygen in the energy range 5 to 20 eV (see Linert et al. for details of previous work). Apart from initiating studies of the excitation of molecular oxygen at backward scattering angles, the aim of the study by Linert et al. was to resolve inconsistencies in the experimental DCS for vibrational excitation and excitation of the $a^1\Delta_g$ and $b^1\Sigma_g^+$ states and to provide DCS data for comparison with theoretical calculations. Their energy loss spectrum of oxygen at an incident energy of 10.4 eV and at a scattering angle of 180°

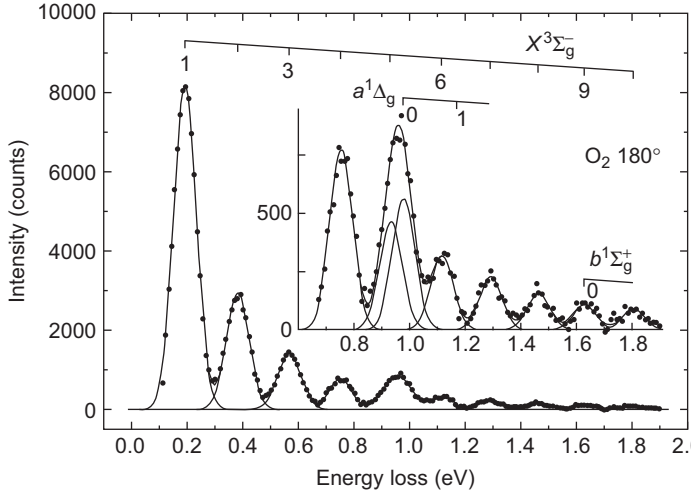

Figure 19 Energy loss spectrum of oxygen at an incident energy of 10.4 eV and a scattering angle of 180°. The energy loss peaks were fitted with Gaussian curves, which are shown by the full lines. A smoothly varying background has been subtracted from the original spectrum. Reproduced from Linert et al. (2004a).

is shown in Figure 19. The corresponding spectrum was also obtained at 90°. The energy loss peaks were fitted to Gaussian profiles having a width (FWHM) of 80 meV, corresponding to the apparatus resolution. In both spectra, the $v = 0$–10 vibrational levels of the ground state together with excitation of the $v = 0$ level of the $a^1\Delta_g$ state are identified. The most important difference between the two spectra is the observation of the $v = 0$ level of the $b^1\Sigma_g^+$ state in the 90° spectrum at 1.63 eV but its absence in the180° spectrum. This observation is in agreement with the predication of vanishing cross section at 180° for the $\Sigma^- \leftrightarrow \Sigma^+$ transition, and the spectrum of Figure 19 is the first test of this theoretical rule. Linert et al. also report DCS for the $v = 3$ level of the ground state and for excitation of the $v = 0$ level of the $a^1\Delta_g$ state which represents about 95% of the electronic excitation of the $a^1\Delta_g$ state.

5. RESONANCES IN ELECTRON IMPACT EXCITATION OF ATOMS AND MOLECULES

5.1 Resonances in Elastic Electron Scattering

5.1.1 Resonances in Rare Gas Atoms

The formation of resonances (or temporary negative ions) is one of the fundamental phenomena that are observed in electron scattering from

atoms and molecules. Since the first observation of such a state by Schultz in helium (1963), many resonances have been observed in a range of different targets (for reviews see Buckman and Clark, 1994; Schulz, 1973a,b). Resonances appear as structure in the elastic scattering cross section, and the shapes of these structures vary with the scattering angle. Studies of the shapes of the resonance structures and their angular dependencies are important for determining the energy positions, i.e., the spectroscopy of the resonances and also in the determination of their symmetries. Until the last decade or so, however, resonance structures in atoms and molecules had been observed over limited angular ranges. This has changed with the application of the MAC, which has allowed the structures to be observed for the first time over the full backward scattering hemisphere. In the case of atoms, the observed shapes and their angular dependencies allow the determination of the phase shifts of the partial waves involved in the scattering process. Measurements at large angles are important for the determination of these phase shifts since at the scattering angle of 180° all partial waves that contribute have the same magnitude (modulus) of unity for their Legendre polynomials. Moreover, measurements in the backward direction are especially useful for the heavier rare gas atoms where more partial waves are present than for the lighter atoms helium and neon.

The use of the MAC to observe resonances in the backward direction was first demonstrated by Zubek et al. (1996), who observed resonance structures in elastic scattering for argon at angles of 110°, 150°, and 180°. In this experiment, the yield of scattered electrons was measured as a function of incident electron energy over the energy range of 10.9–11.4 eV. This first observation was followed by a fuller study of resonance structures in elastic electron scattering from helium, neon, argon, krypton, and xenon, over the range of angles from 100° to 180° (Zubek et al., 1999). The subject of the studies was the $2s^2\,{}^2S$ resonance in He^- and the $np^5(^2P_{3/2,1/2})(n+1)s^2(^1S)$ resonances in Ne^-, Ar^-, Kr^-, and Xe^- where $n = 2, 3, 4$, and 5, respectively. These states are positioned below the first excitation threshold of the respective atoms, or in the case of the higher-lying states of krypton and xenon, just above. The lowest resonances can only decay to the respective ground states and are among the sharpest of features in electron scattering. The resonances may be considered as two spin-paired Rydberg electrons surrounding a relatively compact core. For these measurements, Zubek et al. employed the electrostatic spectrometer described by Zubek and King (1994) in combination with a MAC. The overall energy resolution of the measurements was approximately 30 meV. The MAC consists of three pairs of short, coaxial solenoids, and the solenoid currents are set to produce a zero magnetic field at the scattering centre. This ensures that the electron-atom scattering takes place in a field-free region. The currents in the solenoids were set to produce a total angular

displacement of 70° at an incident energy of 11 eV. The unscattered electron beam is deflected in the direction away from the angular view of the analyzer, which is then able to detect electrons that are scattered within the angular range 60°–190°. The currents in the solenoids were adjusted for other values of incident energy E_i to maintain the above range of scattering angles for each value of energy, by scaling each of the solenoid currents as $E_i^{1/2}$. The angular scale of the spectrometer was calibrated at the mean value of each energy range studied by observing the positions of the maximum of the DCS of argon at 180° and the second minimum close to 120°. The angular scale determined by this procedure is considered accurate to ±1°. Since the analyzer was held fixed in position at the scattering angle of interest, and the magnetic field strength was also held constant, changes in the incident energy introduce a small uncertainty in the scattering angle. This uncertainty is estimated to be ±0.5°, and the total uncertainty in the scattering angle is taken to be ±1.5°. The angular acceptance of the electron spectrometer is 4° as determined by the acceptance angle for scattered electrons. An example of the resonance structure observed by Zubek et al. (1999) is shown in Figure 20, for the $^2P_{3/2}$ resonance in xenon at various scattering angles in the backward direction. The observed structures were analyzed using a standard phase-shift formulation (see, for example, Zubek et al. (1995)) to obtain information on the resonance energies and widths. The calculated phase shifts of Sienkiewicz and Baylis (1989) were used as a starting point. The calculated cross sections were convoluted with a Gaussian function of width corresponding to the energy resolution of the spectrometer. The best agreements with experiment were obtained after adjustment of the $l = 1$ phase shifts, although the final values did not differ by more than 10% from the theoretical ones. The full curve shows the best fit obtained for the measured resonance structures. The energy and width of the $^2P_{3/2}$ resonance were found to be 7.901 ±0.016 eV and 4.0 ±1.0 meV, respectively.

5.1.2 High-Resolution Studies of Feshbach Resonances in Krypton

Recently, in a joint experimental and theoretical investigation (Hoffmann et al., 2010), the low lying Kr^- ($4p^5 5s^2\ ^2P_{3/2}$) Feshbach resonances have been studied in elastic scattering from krypton. Absolute DCS were measured over the energy range 9.3 to 10.3 eV, which contains the resonances, at scattering angles between 10° and 180°. The very high resolution (13 meV) of the measurements has allowed for improved determinations of the resonance positions and widths. In order to obtain additional physical insights, *B*-spline *R*-matrix calculations of the DCS were performed. In the case of krypton, the fine splitting between the two Kr^- ($4p^5 5s^2\ ^2P_{3/2,1/2}$) resonances is sufficiently large that the higher lying resonance lies above the first inelastic threshold. The lower lying resonance can only decay to

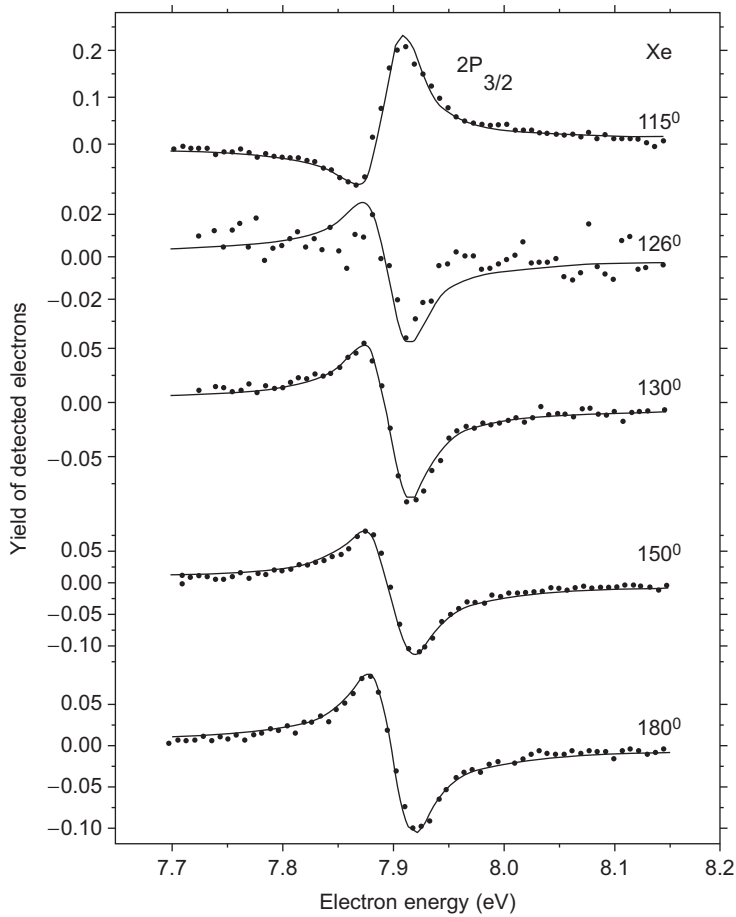

Figure 20 Elastic scattering spectra in xenon for various values of angle in the backward direction showing the $^2P_{3/2}$ resonance. The scale of the yield of scattered electrons shows the size of the $^2P_{3/2}$ resonance with respect to the nonresonant yield. Reproduced from Zubek et al. (1999).

the Kr ($4p^6\ ^1S_0$) ground state but the higher lying resonance can decay into three exit channels, namely, to the ground state and to the two excited Kr ($4p^5\ 5s\ ^3P_{2,1}$) levels (energies of 9.915 eV and 10.032 eV, respectively). Correspondingly, the width of the Kr^- ($4p^5 5s^2\ ^2P_{1/2}$) resonance is much larger than the Kr^- ($4p^5 5s^2\ ^2P_{3/2}$) resonance width. Figure 21 shows the measured energy dependence of the DCS over the energy range encompassing both Kr^- ($4p^5 5s^2\ ^2P_{3/2,1/2}$) resonances, where the difference in the two resonance widths is apparent. The properties of the Kr^- ($4p^5 5s^2\ ^2P_{1/2}$) resonance were accurately determined through a standard partial-wave

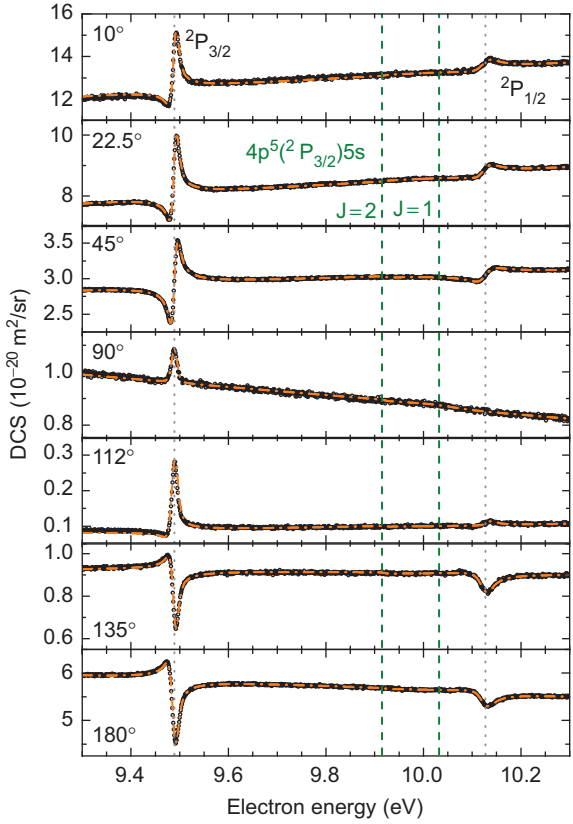

Figure 21 DCS for elastic electron scattering in krypton in the vicinity of the Kr^- ($4p^55s^2\,^2P_{3/2,1/2}$) resonances (open circles: experiment). The chain curves represent the result of a phase-shift analysis for the $4p^55s^2\,^2P_{3/2}$ resonance and Fano-type profiles with appropriate background for the $4p^55s^2\,^2P_{1/2}$ resonance. Reproduced from Hoffmann et al. (2010).

analysis. The measured data were fitted by a resonance profile calculated from a few sets of phase shifts and adjustable values of the resonance width and the experimental energy resolution. The weighted mean of the different fits results in a value of 3.58 (20) for the width of the ($4p^55s^2\,^2P_{3/2}$) resonance. The width of the higher lying Kr^- ($4p^55s^2\,^2P_{1/2}$) was determined from Fano-type fits to the experimental data using Shore profiles (1968), which were convoluted with a Gaussian apparatus function. This gave a total width of 33(5) meV. This width again reflects the fact that the decay of this resonance into the two nearby excited Kr ($4p^5\ 5s\ ^3P_{2,1}$) levels is almost ten times more rapid than that to the ground state. The measurements also gave accurate values for the positions of the two resonances.

Accompanying calculations were performed with the semirelativistic *B*-spline *R*-matrix (BSR) program of Zatsarinny (2006) as well as a fully relativistic version (Zatsarinny & Bartschat, 2008). An important feature of this code is the ability to define nonorthogonal sets of one-electron orbitals, which generally allow for a highly accurate target description with relatively low configuration-interaction expansions. Results were presented from a semirelativistic 47-state model (BSR47) and from a fully relativistic model with 31 states plus a pseudostate to ensure the dipole polarizability of the ground state (DBSR31p). The DBSR31p model gave a value of 2.9 meV for the width of the Kr^- ($4p^5 5s^2\ ^2P_{3/2}$) resonance, while the BSR47 model gave a value of 2.7 meV. There is consistency between the two very independent calculations but these widths appear to be too small. For the width of the Kr^- ($4p^5 5s^2\ ^2P_{1/2}$) resonance, once again the BSR47 model gives a significantly smaller total width for this resonance (15.4 meV) than the DBSR31p calculation (31.9 meV), which accounts for long-range polarization effects and is in good agreement with experiment. The large difference in the calculated widths indicates a strong sensitivity of the results on the details of the model which makes a theoretical description very challenging. The two models were also used to calculate the angular dependence of the resonance profiles. Here it was found that the variation of the experimentally deduced line shapes is well recovered by the BSR calculations, now with a preference for the BSR47 results. Hoffmann et al. (2010) conclude that further high-resolution experiments as well as continued theoretical efforts are necessary to fully understand the intricacies of these collision processes.

5.1.3 Resonances in Electron–Molecule Scattering

The formation of resonances is also of much importance in electron–molecule collisions. Again, the study of the resonance shapes as a function of scattering angle is important in determining the energy positions and hence spectroscopy of the negative ion resonances and also in the determination of the symmetries of the states. As seen in section 5.1.2, resonances with relatively large intensity are observed in elastic electron scattering by the rare gases. In the case of diatomic molecules, such high-intensity structures have also been detected in elastic scattering above the first electronic excitation threshold and about 0.5 eV below the excitation threshold of the first Rydberg states. However, here, measurements are rather scarce and have been obtained over limited angular ranges. In addition, no formalism similar to analyze these molecular structures, similar to that used for atoms, has been developed. Mielewska et al. (1999) have reported the use of the MAC to observe resonance structures corresponding to the $(3s\sigma)^2\ ^2\Sigma^+$ state in CO and the $(3s\sigma_g)^2\ ^2\sigma_g^+$ state in N_2, in elastic scattering over the angular range from 95° to 180°. For this study, they used

the apparatus described by Zubek et al. (1999). The resonance structure observed for the $^2\Sigma_g^+$ state in molecular nitrogen is shown in Figure 22. This structure appeared on top of a background that varied with energy. This background was approximated by a second order polynomial, which

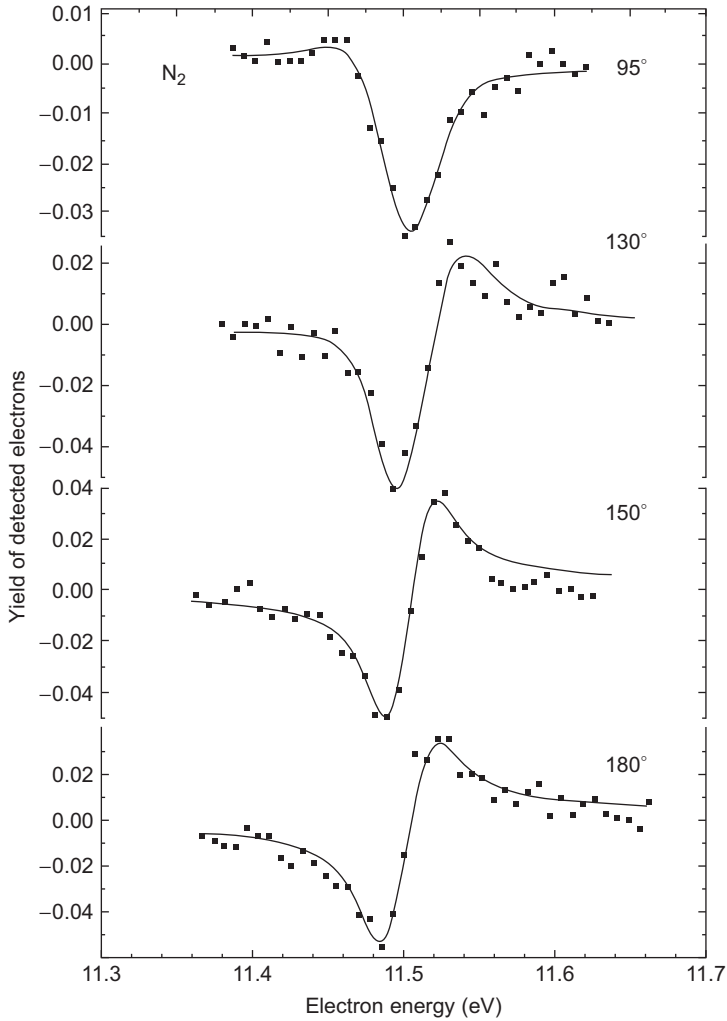

Figure 22 Resonance curves corresponding to the $^2\Sigma_g^+$ state in molecular nitrogen, observed in elastic electron scattering for various values of scattering angle in the backward direction. The scale of the detected yield shows the size of the resonance structures with respect to the nonresonant background. The full curves show the best fit obtained for the measured resonance structures using a Shore parameterization. Reproduced from Mielewska et al. (1999).

was fitted to the regions below and above the resonance structures and then subtracted from the measured spectrum. The detected yield in the presented spectrum shows the size of the structure with respect to the nonresonant background. The observed structures were analyzed using a fitting program bases on the Shore parameterization (1968), where the calculated spectrum has been convoluted with a Gaussian apparatus function of width 35 meV. The best fit is shown in Figure 22. The resonance had been previously measured in elastic scattering only at scattering angles of 40° and 85°. At 45°, the structure has the shape of dip while at 85° it becomes a symmetric structure of a peak followed by a dip. As shown in shown in Figure 22, which covers the range of scattering angle from 95° to 180°, the resonance structure evolves gradually to form an asymmetric dip-peak structure at 180°. This change in shape is more dramatic than for the corresponding $^2\Sigma^+$ state in carbon monoxide. Mielewska attributed this difference to the result of a d-wave contribution besides the main s-wave in the potential scattering by the nitrogen molecule and the influence of a small dipole moment of carbon monoxide in electron scattering.

The formation of shape resonances in molecules, which can dominate the elastic and vibrational excitation cross sections, has also been investigated with the use of a MAC. For example, Allan (2005) has observed the $^2\Pi_g$ shape resonance in N_2 at angles up to 180°. The shape of the elastic cross section depends substantially on scattering angle because of the coherent superposition of the direct and resonant contributions. More recently, Allan (2010) has investigated elastic and vibrational cross sections in CO at scattering angles extending to 180° and at energies between 0.2 and 5 eV, the energy region that contains a strong resonant contribution from the $^2\Pi$ shape resonance.

5.2 Resonances in Inelastic Electron Scattering

It has been emphasized that the scattering of electrons represents a test of our understanding of electron–atom interactions and the theoretical treatments of these processes. A particularly sensitive test is provided by near-threshold excitation where the excitation process is dominated by resonance structure. A particular point of interest is the coupling of the various resonance states to specific final states. This was noted in section 5.1.2 for the $^2P_{1/2}$ Feshbach resonances in the rare gases. Consequently, a fruitful way to investigate resonances is to measure energy-differential cross sections for the various final states, i.e., to measure their excitation functions and to observe the resonance structures over the complete range of scattering angle, as enabled by a MAC. For the measurement of excitation functions, the incident electron energy E_i is

linearly increased from the threshold of the excited state. Simultaneously, the collection energy E_c of the energy analyzer is linearly increased in synchronism with the incident energy so that the difference between the two is maintained equal to the excitation energy E_{ex} of the state under study, i.e., $E_i - E_c = E_{ex}$. When a MAC is used in such measurements, the solenoid currents must be changed to take account of the change in the incident and scattered electron energies, i.e., that the deflection angle is constant for changes in E_i and E_c.

5.2.1 Observation of Resonance Structure in the Angle-Differential Excitation Cross Sections of the $2p^5 3s$ Levels of Neon

Absolute angle-differential cross sections for electron impact excitation of the $2p^5 3s$ and $2p^5 3p$ levels of neon have been investigated in a joint experimental and theoretical collaboration (Allan et al., 2009). The theoretical work involved the *B*-spline *R*-matrix method with nonorthogonal orbit sets. This work extended an earlier investigation on a subset of these data on Ne $2p^5 3s$ excitation (Allan et al., 2006). The energy resolution of the incident beam was 10 meV (FWHM), and the energy loss peaks had a width of 14 meV, thus permitting the resolution of the four Ne ($2p^5 3s$) levels and the majority of the Ne ($2p^5 3p$) levels. DCS were measured as a function of electron energy at the scattering angles of 0°, 45°, 90°, 135°, and 180°, the angles of 0° and 180° being obtained with the use of a MAC. To obtain absolute cross sections, absolute elastic cross sections were first determined at energies in the range of the resonance positions, by normalizing to helium using the relative flow technique. Energy loss spectra containing both the elastic and inelastic peaks were then recorded at the same incident energies. Absolute inelastic values were determined from the relative elastic and inelastic signal intensities after correction for the analyzer response function. The associated uncertainties in the inelastic cross sections are reported to be ±20% for energies greater than 0.3 eV above threshold and increasing gradually to 50% very near to threshold. As an example, Figure 23 shows the experimental cross section for excitation of the four $2p^5 3s$ levels in neon, obtained at a scattering angle of 180°, together with the corresponding predictions of the *B*-spline *R*-matrix approach. The absolute magnitude of the experimental results was determined independently of the theoretical results. Overall, theory and experiment agree remarkably well on the shapes, widths, and energies of the narrow resonant features in the 18.3–19.0 eV range of incident energies. The difference becomes larger close to threshold which may be due to the difficulty of determining the response function of the spectrometer in this region.

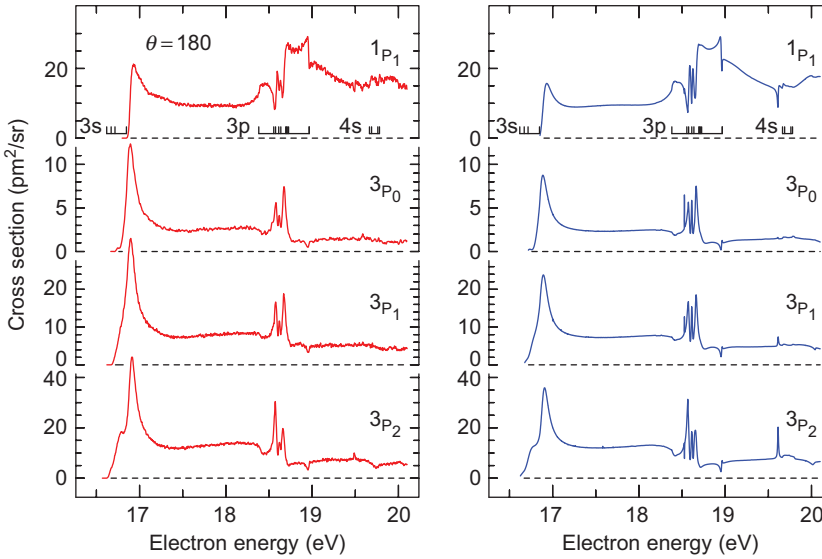

Figure 23 Absolute cross sections for excitation of the four $2p^5 3s$ levels in neon obtained at a scattering angle of 180°. The experimental data are in the left and the theoretical predictions in the right panel. Reproduced from Allan et al. (2009).

6. COINCIDENCE STUDIES IN ELECTRON IMPACT EXCITATION AND IONIZATION

6.1 Introduction

We have seen that electron impact excitation of atoms and molecules provides fundamental processes that allow accurate and detailed comparison between experiment and theory. These comparisons allow models of the collision process to be refined and enhanced with the ultimate goal being the development of a general theory that is applicable over all collision energies. These considerations also apply to electron impact ionization of atoms and molecules. Comparison with theory is most exact when, the momenta and character of the incident electron and the collision products are measured, since the full differential cross section can then be determined. In the case of excitation, the scattered electron can be correlated in time with photons emitted from the excited state in an electron–photon coincidence experiment (e.g., King et al., 1972; Eminyan et al., 1973). In the case of ionization, there are three electrons involved: the incident, the scattered, and the ejected electrons. In an (e, 2e) experiment, the momenta of all three electrons are well defined, and the scattered and ejected electrons are detected in coincidence (Andersen et al., 1988; McCarthy & Weigold, 1995). Such coincidence experiments can provide the most detailed data

on electron collision processes for comparison with theory. In both these types of experiment, the outgoing electrons need to be measured over as wide a range of angles as possible, ideally extending over the complete backward hemisphere where the most significant discrepancies between various theoretical models usually exist. In order to achieve this, MAC devices have been incorporated into several coincidence apparatus. This has allowed theory to be tested in angular ranges that were previously inaccessible to experiment.

6.2 (e, 2e) Experiments

A conventional (e, 2e) apparatus typically consists of an unselected electron gun and two angle-resolving analyzers, which can be rotated about the interaction region, as illustrated schematically in Figure 24. In this figure, the electron gun and the two analyzers lie in the same plane in the so called coplanar geometry. Analyzer 1 is fixed in position at angle θ_a while the angle θ_b of analyzer 2 is varied. The coincidence count rate between electrons detected in the two analyzers is then measured a function of the moveable analyzer to determine the triple-differential cross section. Clearly, the angular range of the moveable analyzer is constrained by the presence of the electron gun and the fixed analyzer. However, the MAC allows the angular range to be increased by deflecting the trajectories of the electrons. Of course, the incident, scattered, and ejected electrons will in general have different energies and be deflected by different amounts by the MAC. However, these deflection angles can be predicted either by computer simulation and/or empirical measurements and so the required positions of the two analyzers can be readily determined.

Stevenson and Lohmann (1996) and Murray et al. (2006) have applied the MAC in (e, 2e) experiments. Stevenson and Lohmann measured the triple-differential cross section for electron impact ionization of argon 3s

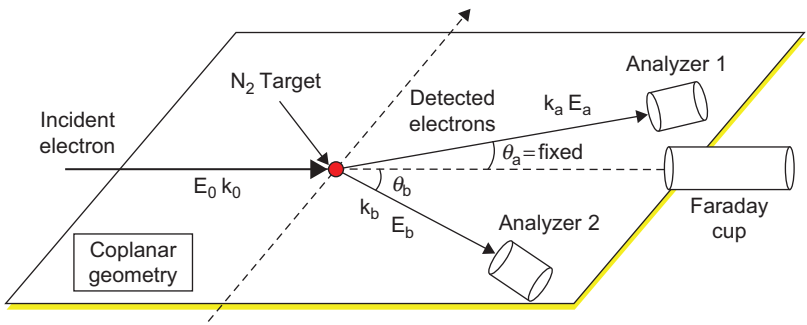

Figure 24 The coplanar geometry in an (e, 2e) coincidence experiment, where one analyzer is fixed in space. Reproduced from Murray et al. (2006).

in the backward direction. Murray et al. (2006) made ionization measurements from the $3\sigma_g$ and $2\sigma_u^*$ states of molecular nitrogen. The aim of the work of Murray et al. was to look for a Young's type interference effect in the fully differential cross sections for ionization of the $3\sigma_g$ and $2\sigma_u^*$ states at large scattering angles as predicted by Gao et al. (2005). The theoretical prediction is that there should be a strong interference peak for the $3\sigma_g$ ionization at an angle of 180°, when the scattered electron leaves the interaction region at a small angle with respect to the incident electron beam, i.e., that the coincidence yield should show a maximum when θ_a is small and θ_b is close to 180°. The (e, 2e) spectrometer used by Murray et al. has a range for θ_b of 22° to 140° without the MAC. With the inclusion of the MAC, the range of θ_b is extended from near 0° to about 170°, thus allowing the theoretical prediction to be tested. Figure 25 shows the ionization differential cross section for the $3\sigma_g$ state of N_2, measured without the use of the MAC. These data were collected with $\theta_a = 22°$ and θ_b ranging from 30° to 140° as mechanically constrained by the spectrometer. Here, the incident electron energy is 75.6 eV, and both outgoing electrons have an energy of 30 eV. Figure 26 shows the experimental data with the MAC switched on. Again $\theta_a = 22°$ but now the range of θ_b has been extended to 10° to 170°. The experimental results do show a peak in the vicinity near 180° in addition to the normal binary peak. Moreover, by including polarization effects in the theoretical description, the predicted interference peak is approximately the same size as the measured cross

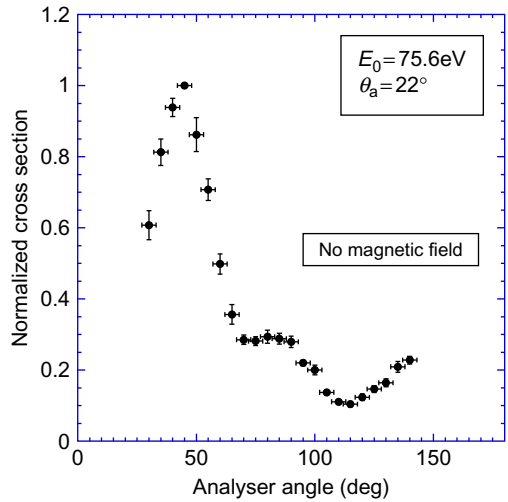

Figure 25 Ionization differential cross section for the $3\sigma_g$ state of N_2, measured without the use of the MAC. The forward scattering angle is 22° and the incident energy is 75.6 eV. Both electrons have an energy of 30 eV. Reproduced from Murray et al. (2006).

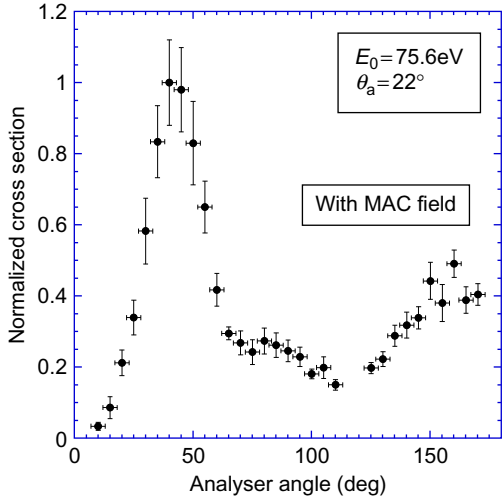

Figure 26 Ionization differential cross section for the $3\sigma_g$ state of N_2, measured with the use of the MAC. Reproduced from Murray et al. (2006).

section. The results of the experiment support the possibility of a Young's type interference effect in this case. Although the results using the MAC are very similar to those collected with the magnetic field switched off, small differences can be seen. In particular, the minimum at $\theta_b \approx 115^\circ$ is not as deep when the field is absent, and there is a slight enhancement of the cross section for scattering angles in the range from 125° to 140°.

6.3 The Electron–Photon Coincidence Technique and Superelastic Scattering

As mentioned in section 6.1, the electron–photon coincidence technique gives very detailed information about electron impact excitation processes. In this technique, the scattered electron is detected at a given angle and is time correlated with a photon emitted from the excited target. The momenta of the incident and scattered electrons define the scattering plane, and the polarization of the correlated photon is determined, so that a complete description of the radiated light is determined. The coincidence technique therefore effectively selects a small subset of all possible scattering events, allowing accurate comparison with theory. Klosowski et al. (2007) have described a MAC for use in electron–photon coincidence measurements and tested its performance on the 2^1P_1 state of helium at an electron energy of 100 eV. Of note is that their MAC design has a nearly zero magnetic field at its axis, i.e., at the interaction region, which avoids any influence of the field on the evolution of the excited state or on the coincidence measurements. Klosowski et al. found that

results obtained with and without the use of the MAC were in good agreement where comparison could be made. Subsequently, Klosowski and coworkers reported further measurements of the electron-impact coherence parameters for electron–helium scattering over the full range of scattering angles (Klosowski et al., 2009).

Although the electron–photon coincidence technique is a very powerful method for the determination of detailed cross sections, it suffers from low detection efficiencies as do other coincidence methods. This is because they are by their very nature highly selective in the energy and momentum of the process under study. In the case of the electron–photon coincidence technique, the atom that scatters the detected electron may not radiate to the photon detector, in which case no event registers. An alternative method that provides equivalent information is the superelastic experiment, which can be considered as the "time reversal" of the electron–photon coincidence technique. In the superelastic technique, the atom is initially excited using laser radiation of well-defined polarization, which is directed orthogonal to the scattering plane. The incident electrons are directed in the opposite direction to those detected in the corresponding coincidence experiment (Farrell et al., 1988), while the electron detector is located where the source would be. The detector measures superelastically scattered electrons that have equal energy to the incident electrons in the corresponding coincidence experiment. Data are accumulated by counting the rate of superelastically scattered electrons as a function of the laser polarization. The signal counting rates from superelastic scattering experiments are many times greater than those from coincidence measurements because the laser photons are directed in a single, well-defined direction. The apparatus used by Hussey et al. (2007, 2008) for superelastic measurements is shown in Figure 27. It combines an angle-resolving electron spectrometer with a MAC and enabled Hussey et al. to investigate superelastic scattering in the backward scattering hemisphere for the first time. They studied electron impact of the 4^1P_1 state of calcium from near 0° to 180°, over the energy range 45 to 55 eV. The calcium beam is produced by a well-collimated oven. The exciting laser enters the vacuum chamber through a window in the top flange and is accurately directed through the interaction region. For excitation of a P state, the parameters of interest are the angular momentum L_{perp} transferred to the charge cloud during the interaction, the angle γ of the charge cloud with respect to the incident electron direction and P_{lin} which defines the "length" to "width" of the charge cloud. L_{perp} is determined from the ratio of superelastically scattered electrons produced by changing the handedness of circularly polarized laser radiation, whereas γ and P_{lin} are determined using linear radiation. Without the MAC, the angular range of the analyzer is from near 0° to 145° whereas application of the MAC extends this to range to greater than 180°. One consequence of the MAC is that the excited substates of the target atom are no longer

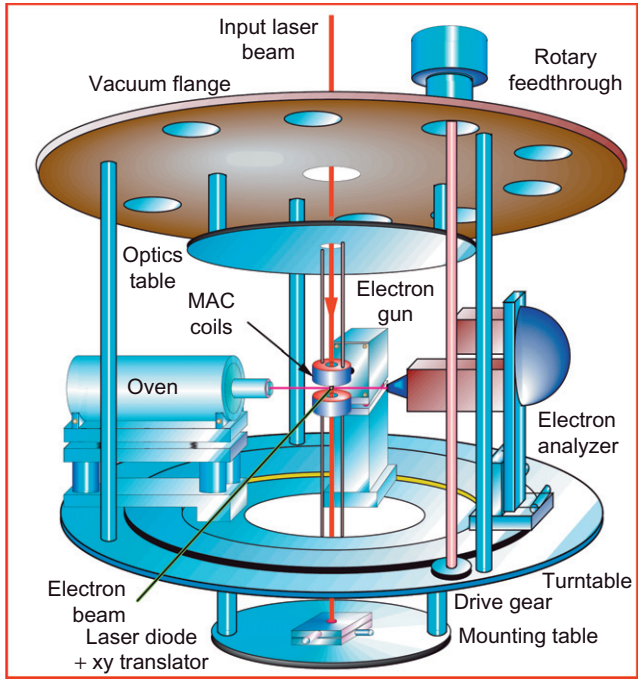

Figure 27 The superelastic apparatus described by Hussey et al. (2007). Calcium atoms emitted from the oven are laser excited by the input laser beam. The electron gun is located next to the oven, and the analyzer rotates on a turntable driven by a rotary feedthrough. The MAC solenoids surround the interaction region as shown. Reproduced from Hussey et al. (2007).

degenerate, and this had to be taken into account in tuning the laser wavelength and analyzing the data. Figure 28 shows the results of the experiment and the derived values of the angular momentum parameter L_{perp} for outgoing electron energies of 45 and 55 eV. These results include data taken with and without the application of the MAC as indicated. The results with and without the MAC operating are in close agreement where overlap exists. At 45 eV, the results are compared to the superelastic scattering data of Law and Teubner (1995) and the earlier coincidence measurements of Kleinpoppen and coworkers (El-Fayoumi et al., 1988). It is clear that the quality of the superelastic measurements is much greater than that of the coincidence measurements, which have difficulties with low counting rates and long data accumulation times. Also shown are the measurements at 55 eV, which required a larger magnetic field. The DWBA calculations of Stauffer and coworkers (Chauhan et al., 2005), convoluted with the experimental angular response, are also shown for comparison. It is clear that this model is in very good agreement with the superelastic data, apart from the minimum close to 60°, which is underestimated, and

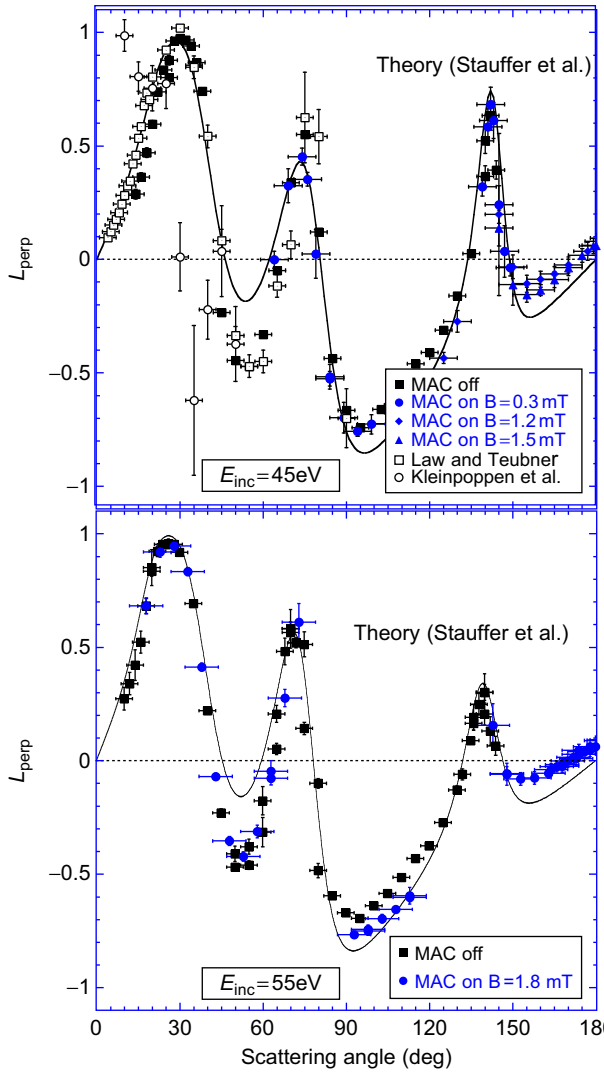

Figure 28 Derived values of the angular momentum parameter L_{perp} for outgoing electron energies of 45 and 55 eV, for scattering angles from 0° to 180°. The results include data taken with and without the application of the MAC as indicated. At 45 eV, the results are compared to the superelastic scattering data of Law and Teubner (1995) and the coincidence measurements of Kleinpoppen and coworkers (El-Fayoumi et al., 1988). The theoretical calculations of Stauffer and coworkers (Chauhan et al., 2005) are also shown. Reproduced from Hussey et al. (2007).

also the minima at the higher angles, which are overestimated. The maxima and their positions are well reproduced. In particular, the sharp peak at 150°, which is observed for the first time experimentally, is in very good agreement with theory.

7. PHOTOELECTRON SPECTROSCOPY

7.1 Advantages of the MAC for Photoelectron Spectroscopy

So far, the use of the MAC for electron impact studies has been described. Another important application is its use in photoelectron spectroscopy of atoms and molecules. This technique provides spectroscopic information for atomic and molecular ions, giving a direct measurement of the binding energies of electron orbitals. In addition, the angle of ejection of the photoelectrons provides information about the symmetry of the orbitals. Traditionally, angle-resolved photoelectron spectroscopy is performed with an energy analyzer that rotates about the interaction region of the gas and photon beams and measures the photoelectron intensity at various angles of emission. For synchrotron radiation sources, unlike for UV laboratory sources, the analyzer usually rotates in the plane perpendicular to the photon beam direction. Consequently, the energy analyzer is able to rotate over most of the 0° to 360° angular range in that plane, constrained only by the presence of the target gas nozzle. However, even here, the MAC offers valuable advantages. With the MAC there is no longer the need to rotate the analyzer, and so mechanical movement of the analyzer in the vacuum system is avoided. Instead, the angular behavior of the photoelectrons can be determined by varying the solenoid currents, and this can readily be done under computer control. Moreover, the use of an energy analyzer with a large mean radius is facilitated if the analyzer is not required to move in the vacuum system. The energy resolution of a hemispherical deflector analyzer depends on the ratio of the size of the entrance aperture and mean radius of the hemispheres. Consequently, higher energy resolution is obtained when the mean radius is increased. A fixed analyzer also means that it can be fitted with a bulky detector, for example, a Mott detector for spin analysis of the detected photoelectrons. It is also the case that there are studies where it is useful to measure the photoelectron angular distribution in the plane containing the photon beam direction, including photoelectron spectroscopic studies with UV lamps. With conventional spectrometers, it is not possible to move the energy analyzer into the direction of the photon beam. However, the MAC does allow this, in an analogous way to its use in electron impact studies.

7.2 Photoelectron Spectroscopy

7.2.1 Photoelectron Spectroscopy of Atoms: The Study of Autoionizing Resonances

The first use of the MAC in photoionization experiments was made by Cubric et al. (1997) who measured photoelectron angular distributions in xenon. In particular, they determined the angular distribution pattern for

the $Xe^+ {}^2P_{3/2}$ ionic state in the region of the $5s^2\ 5p^6 \rightarrow 5s5p^5\ np$ autoionizing resonances. These resonances correspond to highly excited neutral states where an electron is promoted from a subvalence shell to an unfilled orbital. Subsequently, Cubric and coworkers made analogous measurements of resonances lying between the ${}^2P_{3/2,1/2}$ states of Kr^+ and Xe^+ (Cooper et al., 2000). The autoionizing resonances of the rare gases are of interest because they are crucial to the understanding of the coupling of bound states with underlying ionization continuum. The heavier rare gases are particularly fruitful for study because of the dominant roles played by relativistic and correlation effects. The use of photoelectron spectroscopy in the study of these resonances brings several important advantages. The resonances invariably decay to more than one final ion state, and the use of photoelectron spectroscopy allows these various channels to be isolated and individual, partial ionization cross sections to be measured. These partial ionization cross sections can be markedly different from each other, especially for the heavier rare gases. Moreover, the angular distributions of the photoelectrons provide particularly sensitive and detailed information about the resonances. The differential cross section for photoionization of an atom by partially polarized radiation, in the dipole approximation, is given by

$$\frac{d\sigma}{d\Omega} = \frac{\sigma}{4\pi}\left[1 + \frac{1}{4}\beta(1 + 3P\cos 2\theta)\right] \tag{10}$$

where θ is the angle between the photon electric field vector and the direction of photoelectron ejection, σ is the partial cross section for photoionization, and P is the degree of linear polarization of the photon beam. β is the angular distribution asymmetry parameter. Its value can be deduced using Equation (10) by measuring the ratio of the photoelectron intensity at two values of θ. β depends on relative phases as well as magnitudes of photoionization amplitudes. Comparisons of theoretical predictions of β with experiment therefore place additional constraints on theory beyond those for cross section comparisons and are an important avenue to understand the finer details of the ionization process.

The apparatus initially used by Cubric and coworkers (Cooper et al., 2000; Cubric et al., 1997) consists of a compact electron spectrometer based on a 127° cylindrical deflector analyzer (Hall et al., 1992) coupled with a three-solenoid MAC system. The spectrometer provides the necessary range of photoelectron kinetic energy at an energy resolution of typically 50 meV and an angular resolution 10°. The experiments were carried out at the Daresbury Laboratory SRS using a 5-m McPherson monochromator, which provided photons over the range of interest with a resolution of typically 15 meV. The measurements were made as continuous functions of both photon energy and photoelectron ejection angle. Interestingly, this work involved photoelectron energies down to typically 100 meV. Even

at these relatively low kinetic energies, the MAC performed as computer simulations predicted and the measurements demonstrated the successful operation of the MAC in near-threshold photoionization studies. To test the performance of the apparatus, the angular distribution of the He^+ $N = 1$ state was measured, which has $\beta = 2$ for all photon energies. The results, obtained at a photon energy of 27.6 eV, are shown in Figure 29.

The open circles correspond to the measurements obtained with the spectrometer operating in the conventional mode, where the analyzer was rotated mechanically. The full circles correspond to the measurements obtained using the MAC. In this latter mode of operation, the analyzer is placed at a fixed angle of 45° with respect to the polarization axis of the photon beam as illustrated in Figure 30. Magnetic deflections of ±45° are then obtained by passing appropriate currents through the solenoids and reversing the polarity of the voltages applied to the solenoids. This gives observation angles of 0° and 90°, respectively, and ensures that any asymmetries in the magnetic field cancel out in the deduced value of the intensity ratio. It can be seen from Figure 29 that the two sets of data are in good agreement with the full curve, which corresponds to the expected distribution for $\beta = 2$ and the polarization of the photon beam $P = 0.6$. The small disagreements in this data set were attributed to deflector settings in the electron optics system, which were subsequently corrected in the experiments on krypton and xenon. The variation of the β-parameter and the partial ionization cross section for the $^2P_{3/2}$ state of Xe^+ (Cooper et al., 2000) is shown in Figure 31. This covers the energy region from the 7d′/9s′ autoionizing resonances up to and beyond the Xe^+ $^2P_{1/2}$ ionization threshold at 13.44 eV. The sharp step-like feature in the partial ionization cross section is attributed to the new ionization channel opening, but no dramatic feature in the β-parameter variation occurs at this threshold. The

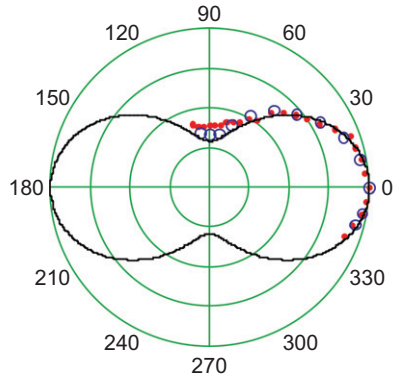

Figure 29 Angular distribution measurements of the He^+ $N = 1$ state at a photon energy of 27 eV. The open circles show the results obtained with the analyzer rotated mechanically and the full circles show the results obtained using the MAC. Reproduced from Cubric et al. (1997).

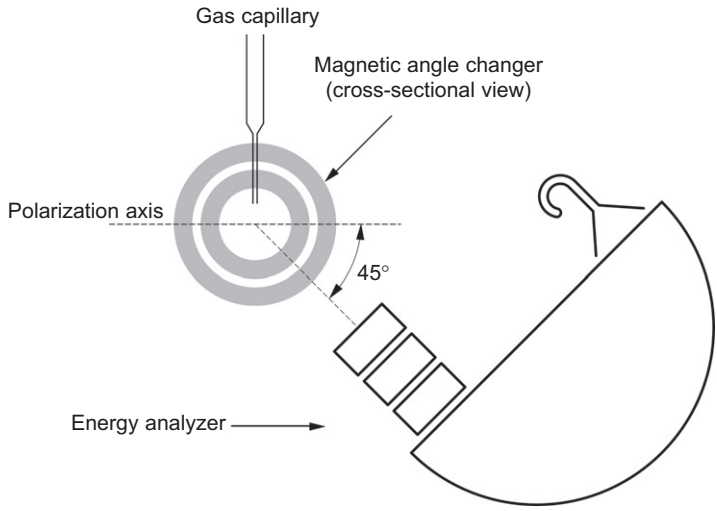

Figure 30 The relative positions of the MAC and the hemispherical deflector analyzer for the measurement of photoelectron angular distributions. The analyzer is fixed in position and at an angle of 45° with respect to the polarization axis of the photon beam.

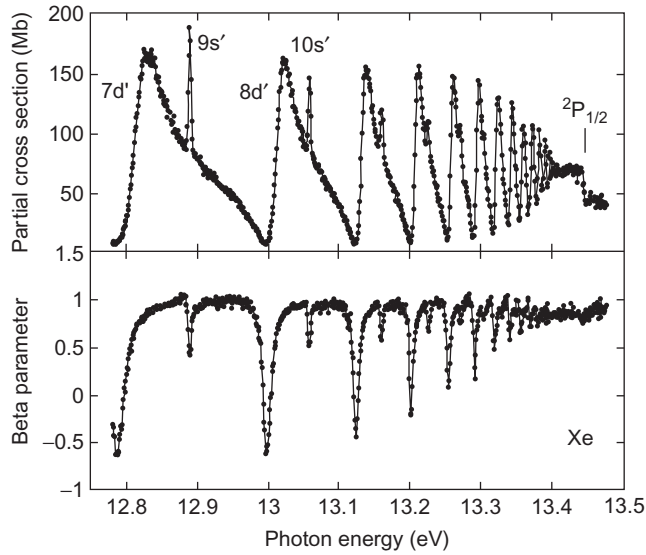

Figure 31 The variation of the β-parameter and the partial ionization cross section for the $^2P_{3/2}$ state of Xe^+, from the 7d′/9s′ resonances up to and beyond the $Xe^+{}^2P_{1/2}$ ionization threshold at 13.44 eV. Reproduced from Cooper et al. (2000).

β-parameter data have improvements in both statistical accuracy and in photon energy resolution over previous studies and extend the previous work up to the $^2P_{1/2}$ ionization threshold. Interestingly, the β-parameter spectrum shows up features that are not visible in the partial ionization cross section. For example, it is possible to see the 14s' resonance only in the β-parameter spectrum. A full interpretation of the β-parameter, based on experimental data alone, is not straightforward since, for example, there are significant spin-orbit and configuration-interaction effects, and there is a strong need for further theoretical work.

7.2.2 High-Resolution Photoelectron Studies of H_2

Cubric and coworkers subsequently developed a photoelectron spectrometer consisting of a three-solenoid MAC and a fixed hemispherical deflector analyzer with a large mean radius of 165 mm (Cubric et al., 2002). The analyzer is coupled with a four-element cylindrical lens that transports the photoelectrons to the entrance slit of the analyzer. In particular, the large radius of the analyzer provides a high energy resolution of ~10 meV. Juarez et al. (2005) have used this spectrometer to measure for the first time with full rotational selection, photoelectron angular distributions in H_2 and their dependence on photon energy. In particular, the transitions $X^1\Sigma_g(v=0, N=0) \rightarrow X^2\Sigma_g^+(v^+=0, N^+=0,2)$ were studied over the energy range 15.47 to 15.75 eV, where resonance structure dominates the direct ionization continuum. The experiment was undertaken at the Gasphase beamline at the Elettra Synchrotron Radiation Source, Italy, which provides the high photon resolution (~3 meV), high light intensity, and high degree of linear polarization (~100%) that is necessary for the experiment. This rotational state-selective work involved the delivery of para-H_2 gas to the target region, which was cooled by liquid nitrogen. This resulted in a target region surrounded by bulky mechanical components where the ability to use a fixed-position energy analyzer was a great advantage.

7.2.3 Photodouble Ionization

With the advent of synchrotron radiation sources, which provide tunable UV radiation, attention has increasingly been focused on the process of photodouble ionization in atoms and molecules. In photodouble ionization, two photoelectrons are ejected simultaneously and a major aim of the work is to study the correlations between these two outgoing electrons (e.g., Briggs & Schmidt, 2000; King & Avaldi, 2000). The electron–electron correlations are reflected in the angular behavior of the two photoelectrons. These behaviors can be investigated in an apparatus containing two angle-resolving analyzers. Here, the two photoelectrons are detected in coincidence in a (γ, 2e) experiment, in an analogous way to (e, 2e) experiments in electron impact ionization. In addition to the

advantages listed for single photoionization experiments, the MAC brings an additional advantage to these photodouble ionization studies, since an important case occurs where the two photoelectrons are ejected in the same direction. Then, the Coulomb interaction between them is strongest. This case cannot be viewed using a conventional setup of two analyzers but it can be with the inclusion of a MAC so long as the energies of the two photoelectrons are unequal. So far, this advantage does not seem to have been exploited in photodouble ionization experiments.

8. CONCLUSIONS

The MAC was invented for the measurement of DCS in elastic electron scattering over the complete backward hemisphere. Since then its use has been extended to a variety of experimental studies in atoms and molecules, including inelastic electron scattering and vibrational excitation, resonances in electron scattering, coincidence measurements in electron impact excitation and ionization, and photoelectron spectroscopy. The MAC has enabled measurements to be made in angular regions, which were previously inaccessible to conventional electron spectrometers that employ hemispherical deflector analyzers. In turn, this has allowed more complete comparisons of theory with experiment. In addition, the MAC has enabled DCS measurements to be integrated over an extended (or even complete) angular range to produce more accurate determinations of integral and momentum transfer cross sections, which are important in a variety of technological applications. It may be expected that the MAC will continue to be an important experimental tool in these areas, but there may be other applications where a localized magnetic field is useful. The focusing properties and aberrations of the MAC have been investigated for electrons that lie in the plane perpendicular to the central axis of the MAC. Less attention has been paid to the focusing properties of the MAC for electrons that move out of this plane. Further computational simulation studies would be beneficial in this respect.

REFERENCES

Allan, M. (1992). Measurement of differential cross-sections for excitation of helium by electron-impact within the first 4 eV above threshold. *Journal of Physics B: Atomic, Molecular and Optical Physics*, *25*, 1559–1575.

Allan, M. (2005). Measurement of the elastic and $v = 0 \rightarrow 1$ differential electron-N_2 cross section over a wide angular range. *Journal of Physics B: Atomic, Molecular and Optical Physics*, *38*, 3655–3672.

Allan, M. (2007). Absolute angle-differential elastic and vibrational excitation cross sections for electron collisions with tetrahydrofuran. *Journal of Physics B: Atomic, Molecular and Optical Physics*, *40*, 3531–3544.

Allan, M. (2010). Electron collisions with CO: elastic and vibrational excitation cross sections. *Physical Review A*, *81*, 042706-9.

Allan, M., Winstead, C., & McKoy, V. (2008). Electron scattering in ethane: excitation of the $\tilde{a}^3B_{1u}$ state, elastic scattering and vibrational excitation. *Physical Review A*, *77*, 042715-7.

Allan, M. (2000). Excitation of the 2^3S state of helium by electron impact from threshold to 24 eV: measurements with the "magnetic angle changer." *Journal of Physics B: Atomic, Molecular and Optical Physics*, *33*, L215–L220.

Allan, M., Franz, K., Hotop, H., Zatsarinny, O., & Bartschat, K. (2006). Absolute angle-differential cross sections for electron-impact excitation of neon atoms from threshold to 19.5 eV. *Journal of Physics B: Atomic, Molecular and Optical Physics*, *39*, L139–L144.

Allan, M., Franz, K., Hotop. H., Zatsarinny, O., & Bartschat, K. (2009). Absolute angle-differential cross sections for electron-impact excitation of neon within the first 3.5 eV above threshold. *Journal of Physics B: Atomic, Molecular and Optical Physics*, *42*, 044009-20.

Andersen, N., Gallagher, J. W., & Hertel, I. V. (1988). Collisional alignment and orientation of atomic outer shells 1. Direct excitation by electron and atom impact. *Physics Reports*, *165*, 1–188.

Asmis, K. R., & Allan, M. (1997). Measurement of absolute differential cross sections for the $n = 2$ states of helium at 0° and 180°. *Journal of Physics B: Atomic, Molecular and Optical Physics*, *30*, 1961–1974.

Becker, U., & Shirley, D. A. (1996). *VUV and X-ray Photoionization*. New York: Plenum Press.

Bell, K. L., Berrington, K. A., & Hibbert, A. (1988). Elastic-scattering of electrons by krypton and the free absorption-coefficient of Kr^-. *Journal of Physics B: Atomic and Molecular Physics*, *21*, 4205–4216.

Brennan, M. J., Alle, D. T., Euripedes, P., Buckman, S. J., & Brunger, M. J. (1992). Elastic electron-scattering and rovibrational excitation of N_2 at low incident energies. *Journal of Physics B: Atomic and Molecular Physics*, *25*, 2669–2682.

Brewer, D. F. C., Newell, W. R., Harper, S. F. W., & Smith, A. C. H. 1981. Elastic-scattering of low-energy electrons by neon atoms. *Journal of Physics B: Atomic and Molecular Physics*, *14*, L749–L754.

Briggs, J. S., & Schmidt, V. (2000). Differential cross sections for photo-double-ionization of the helium atom. *Journal of Physics B: Atomic, Molecular and Optical Physics*, *33*, R1–R48.

Brunt, J. N. H., King, G. C., & Read, F. H. (1977). Resonance structure in elastic electron-scattering from helium, neon and argon. *Journal of Physics B: Atomic and Molecular Physics*, *10*, 1289–1301.

Buckman, S. J., & Clark, C. W. (1994). Atomic negative-ion resonances. *Reviews of Modern Physics*, *66*, 539–655.

Buckman, S. J., Cooper, J. W., Elford, M. T., Inokuti, M., Itikawa, Y., & Tawara, H. (2000). *Landolt-Borstein, photon and electron interaction with atoms, molecules and ions, group I*, Y. Itikawa (Ed.), (Vol. 17A). Berlin: Springer.

Buckman, S. J., & Lohmann, B. (1987). The total cross section for low-energy electron scattering from krypton. *Journal of Physics B: Atomic and Molecular Physics, 20,* 5807–5816.

Burrow, P. D., & Sanche, L. (1972). Elastic-scattering of low-energy electrons at 180 degrees in CO_2. *Physical Review Letters*, *28*, 333–336.

Chauhan, R. K., Srivastava, R., & Stauffer, A. D. (2005). Electron impact excitation of the 4^1P_1 state of calcium. *Journal of Physics B: Atomic, Molecular and Optical Physics*, *38*, 2385–2394.

Cho, H., Gulley, R. J., & Buckman, S. J. (2003a). Elastic electron scattering from krypton at backward angles. *The Journal of the Korean Physical Society*, *42*, 71–75.

Cho, H., Gulley, R. J., Trantham, K. W., Uhlmann, L. J., Dedman, C. J., & Buckman, S. J. (2000). Elastic electron scattering from sulfur hexaflouride. *Journal of Physics B: Atomic, Molecular and Optical Physics*, *33*, 3531–3544.

Cho, H., Lee, H., & Park, Y. S. (2003b). Electron spectrometer with a magnetic angle-changing device for the measurement of cross sections at backward angles. *The Journal of the Korean Physical Society*, *43*, 40–44.

Cho, H., McEachran, R. P., & Buckman, S. J. (2008). Elastic electron scattering from neon at backward angles. *Physical Review A*, *78*, 034702-4.

Cho, H., McEachran, R. P., Buckman, S. J., Filipovic, D. M., Pejcev, V., Marinkovic, B. P., et al. (2006). Absorption effects in intermediate energy elastic scattering from xenon. *Journal of Physics B: Atomic, Molecular and Optical Physics*, *39*, 3781–3790.

Cho, H., McEachran, R. P., Tanaka, H., & Buckman, S. J. (2004). The role of absorption in intermediate energy elastic scattering from krypton. *Journal of Physics B: Atomic, Molecular and Optical Physics*, *37*, 4639–4645.

Cho, H., & Park, Y. S. (2009). Low-energy electron scattering from argon. *The Journal of the Korean Physical Society*, *55*, 459–462.

Cho, H., Song, M. Y., Yoon, J. S., Hoshino, M., & Tanaka, H. (2010). Elastic electron scattering from CF_3H and CF_3I. *Journal of Physics B: Atomic, Molecular and Optical Physics*, *43*, 135205-8.

Cooper, D. R., Cubric, D., Thompson, D. B., Bolognesi, P., Lopes, M. C. A., & King, G. C. (2000). Measurements of photoelectron angular distributions between the $^2P_{3/2,1/2}$ states of Kr^+ and Xe^+ using a new magnetic angle-changing technique. *The Journal of Electron Spectroscopy*, *112*, 129–136.

Cubric, D., Juarez, A. M., Bowring, N. J., Read, F. H., & King, G. C. (2002). Spin-orbit selective measurements of photoelectron angular distributions across the H $^3\Pi_u$ ($v = 6$) resonance in molecular oxygen. *The Journal of Electron Spectroscopy*, *123*, 133–141.

Cubric, D., Mercer, D. J. L., Channing, J. M., King, G. C., & Read F. H. (1999). A study of inelastic electron scattering in He covering the compete angular range from 0° to 180°. *Journal of Physics B: Atomic, Molecular and Optical Physics*, *32*, L45–L50.

Cubric, D., Thompson, D. B., Cooper, D. R., King, G. C., & Read, F. H. (1997). A study of photoelectron angular distributions in xenon using a new magnetic angle-changing technique. *Journal of Physics B: Atomic, Molecular and Optical Physics*, *30*, L857–L864.

Cubric, D., Ward, R., King, G. C., & Read, F. H. (2000). Iron-cored coil system for the measurement of angular distributions of charged particles. *Review of Scientific Instruments*, *71*, 3323–3325.

Curkic, R., Carsky, P., & Allan, M. (2008). Vibrational excitation of methane by slow electrons revisited: theoretical and experimental study. *Journal of Physics B: Atomic, Molecular and Optical Physics*, *41*, 115203-7.

Dababneh, M. S., Kauppila, W. E., Downing, J. P., Laperriere, F., Pol, V., Smart, J. H., & Stein, T. S. (1980). Measurements of total scattering cross sections for low-energy positrons and electrons colliding with krypton and xenon. *Physical Review A, 22,* 1872–1877.

Dampc, M., Linert, I., Milosavljevic, A. R., & Zubek, M. (2007a). Vibrational excitation of tetrahydrofuran by electron impact in the low energy range. *Chemical Physics Letters*, *443*, 17–21.

Dampc, M., Milosavljevic, A. R., Linert, I., Marinkovic, B. P., & Zubek, M. (2007b). Differential cross sections for low-energy elastic electron scattering from tetrahydrofuran in the angular range 20° – 180°. *Physical Review A*, *75*, 042710-7.

Danjo, A. (1988). Electron-scattering from Kr.1. Differential cross-section for elastic-scattering. *Journal of Physics B: Atomic, Molecular and Optical Physics*, *21*, 3759–3766.

Dasgupta, A., & Bhatia, K. A. (1984). Scattering of electrons from neon atoms. *Physical Review A*, *30*, 1241–1246.

DuBois, R. D., & Rudd, M. E. (1976). Differential cross sections for elastic scattering of electrons from argon, neon, nitrogen and carbon monoxide. *Journal of Physics B: Atomic and Molecular Physics, 9,* 2657–2667.

El-Fayoumi, M. A. K., Hamdy, H., Beyer, H.-J., Eid, Y., Shahin, F., & Kleinpoppen, H. (1988). Electron impact coherence parameters for the excitation of the 4^1P_1 state of Ca. *Atomic Physics*, *11*, 173.

Eminyan, M., MacAdam, K. B., Slevin, J., & Kleinpoppen, H. (1973). Measurements of complex excitation amplitudes in electron-helium collisions by angular correlations using a coincidence method. *Physical Review Letters*, *31*, 576–579.

Farrell, P., MacGillivary, W. R., & Standage, M. C. (1988). Quantum-electrodynamic calculation of hyperfine-state populations in atomic sodium. *Physical Review A*, *37*, 4240–4251.

Feng, H., Sun, W., & Morrison, M. A. (2003). Parameter-free nonadiabatic correlation-polarization potential for vibrational excitation in electron-molecule scattering: application to e-N_2 collisions. *Physical Review A*, *68*, 062709-14.

Fon, W. C., & Berrington, K. A. (1981). The elastic-scattering of electrons from inert-gases.2. Neon. *Journal of Physics B: Atomic and Molecular Physics*, *14*, 323–334.

Fon, W. C., Berrington, K. A., Burke, P. G., & Kingston, A. E. (1989). A 19-state *R*-matrix investigation of resonances in e^-–He scattering. I. The resonance widths and positions. *Journal of Physics B: Atomic and Molecular Physics*, *22*, 3939–3949.

Frost, L. S., & Phelps, A. V. (1964). Momentum-transfer cross sections for slow electrons in He, Ar, Kr, and Xe from transport coefficients. *Physical Review A, 13,* 1538–1545.

Fursa, D. V., & Bray, I. (1997). Convergent close-coupling calculations of electron-helium scattering. *Journal of Physics B: Atomic, Molecular and Optical Physics*, *30*, 757–785.

Gao, J., Madison, D. H., & Peacher, J. L. (2005). Interference effects for low-energy electron-impact ionization of nitrogen molecules. *Physical Review A*, *72*, 032721-5.

Gianturco, F. A., & Rodriguez-Ruiz, J. A. (1993). Correlation forces in electron-scattering processes via density-functional theory: Electron collisions with closed-shell atoms. *Physical Review A*, *47*, 1075–1086.

Gibson, J. C., Gulley, R. J., Sullivan, J. P., Buckman, S. J., Chan, V., & Burrows, P. D. (1996). Elastic electron scattering from argon at low incident energies. *Journal of Physics B: Atomic, Molecular and Optical Physics*, *29*, 3177–3195.

Gillan, C. J., Nagy, O., Burke, P. G., Morgan, L. A., & Noble, C. J. (1987). Electron-scattering by nitrogen molecules. *Journal of Physics B: Atomic, Molecular and Optical Physics*, *20*, 4585–4603.

Gopalan, A., Bommels, J., Gotte, S., Landwehr, A., Franz, K., Ruf, M.-W., et al. (2003). A novel electron scattering apparatus combining a laser photoelectron source and a triply differentially pumped supersonic beam target: characterization and results for the He^- ($1s\,2s^2$) resonance. *European Physical Journal D*, *22*, 17–29.

Gote, M., & Ehrhardt, H. (1995). Rotational excitation of diatomic molecules at intermediate energies: absolute differential state-to-state transition cross sections for electron scattering from N_2, Cl_2, CO and HCl. *Journal of Physics B: Atomic, Molecular and Optical Physics, 28,* 3957–3986.

Greenwood, J. B., Williams, I. D., & McGuiness, P. (1995a). Large angle elastic scattering of electrons from Ar^+, 1995. *Physical Review Letters*, *75*, 1062–1065.

Greenwood, J. B., Williams, I. D., Srigengan, B., Newell, W. R., Geddes, J., & O'Neill, R. W. (1995b). Low energy backscattering of electrons from Ar^+. *Journal of Physics B: Atomic, Molecular and Optical Physics*, *28*, L307–L311.

Gulley, R. J., Alle, D. T., Brennan, M. J., Brunger, M. J., & Buckman, S. J. (1994). Differential and total electron-scattering from neon at low incident energies. *Journal of Physics B: Atomic, Molecular and Optical Physics*, *27*, 2593–2611.

Hall, R. I., McConkey, A., Ellis, K., Dawber, G., Avaldi, L., MacDonald, M. A., & King, G. C. (1992). A penetrating field electron-ion coincidence spectrometer for use in photoionization studies. *Measurement Science and Technology*, *3*, 316–324.

Hoffmann, T. H., Ruf, M.-W., Hotop, H., Zatsarinny, O., Bartschat, K., & Allan, M. (2010). New light on the $Kr^-(4p^5 5s^2)$ Feshbach resonances: high-resolution electron scattering experiments and *B*-spline *R*-matrix calculations. *Journal of Physics B: Atomic, Molecular and Optical Physics*, *43*, 085206-11.

Hunter, S. R., Carter, J. G., & Christophorou, L. G. (1988). Low-energy electron drift and scattering in krypton and xenon. *Physical Review A*, *38*, 5539–5551.

Huo, W. M., Lima, M. A. P., Gibson, T. L., & McKoy, V. (1987). Correlation effects in elastic e-N_2 scattering. *Physical Review A, 36,* 1642–1648.

Hussey, M., Murray, A., MacGillivray, W., & King, G. C. (2007). Superelastic electron scattering within a magnetic angle changer: determination of the angular momentum transferred during electron excitation over all scattering angles. *Physical Review Letters*, *99*, 133202-4.

Hussey, M., Murray, A., MacGillivray, W., & King, G. C. (2008). Low energy super-elastic studies of calcium over the complete angular range using a magnetic angle changing device. *Journal of Physics B: Atomic, Molecular and Optical Physics*, *41*, 055202-10.

Jost, K., Bisling, P. G. F., Eschen, F., Felsmann, M., & Walther, L. (1983). In J. Eichler (Ed.), *Proceedings of the 13th Int. Conf. on the Physics of Electronic and Atomic Collisions (Berlin)*, (p. 91). Amsterdam, North-Holland.

Juarez, A. M., Sokell, E., Bolognesi, P., King, G. C., Cubric, D., De Simone, M., et al. 2005. β-parameter measurements of state-selected rotational transitions near the $v^+ = 0$ threshold of *para*-H_2^+. *Journal of Physics B: Atomic, Molecular and Optical Physics*, *38*, 2109–2118.

Khakoo, M. A., & Trajmar, S. (1986). Elastic electron scattering cross sections for molecular hydrogen. *Physical Review A*, *34*, 138–145.

King, G. C., Adams, A., & Read, F. H. (1972). Polarization studies using electron photon coincidence technique. *Journal of Physics B: Atomic, Molecular and Optical Physics*, *12*, L254–L257.

King, G. C., & Avaldi, L. (2000). Double-excitation and double-escape processes studied by photoelectron spectroscopy near threshold. *Journal of Physics B: Atomic, Molecular and Optical Physics*, *33*, R215–R284.

Klosowski, L., Piwinski, M., Dziczek, D., Pleskacz, K., & Chwirot, S. (2009). Coincidence measurements of electron-impact coherence parameters for *e*-He scattering in the full range of scattering angles. *Physical Review A*, *80*, 062709-4.

Klosowski, L., Piwinski, M., Dziczek, D., Wisniewska, K., & Chwirot, S. (2007). Magnetic angle changer – a new device allowing extension of electron-photon coincidence measurements to arbitrary electron scattering angles. *Measurement Science and Technology, 18*, 3801–3810.

Koizumi, T., Shirakawa, E., & Ogawa, I. (1986). Momentum transfer cross sections for low-energy electrons in krypton and xenon from characteristic energies. *Journal of Physics B: Atomic, Molecular and Optical Physics, 19,* 2331–2342.

Law, M. R., & Teubner, P. J. O. (1995). Orientation of the $4P_1$ state in calcium by electron-impact. *Journal of Physics B: Atomic, Molecular and Optical Physics*, *28*, 2257–2267.

Linert, I., King, G. C., & Zubek, M. (2004a). A study of electron impact excitation of molecular oxygen at a scattering angle of 180°. *Journal of Electron Spectroscopy and Related Phenomena*, *134*, 1–8.

Linert, I., King, G. C., & Zubek, M. (2004b). Measurements of differential cross sections for elastic scattering in the backward direction by molecular oxygen. *Journal of Physics B: Atomic, Molecular and Optical Physics*, *37*, 4681–4691.

Linert, I., Mielewska, B., King, G. C., & Zubek, M. (2006). Elastic electron scattering in neon in the 110°–180° scattering angle range. *Physical Review A*, *74*, 042701-6.

Linert, I., Mielewska, B., King, G. C., & Zubek, M. (2007). Differential cross sections for elastic electron scattering in xenon in the energy range from 5 to 10 eV. *Physical Review A*, *76*, 032715-6.

Linert, I., Mielewska, B., King, G. C., & Zubek, M. (2010). Elastic electron scattering in krypton in the energy range from 5 to 10 eV. *Physical Review A*, *81*, 012706-7.

Linert, I., & Zubek, M. (2006). Differential cross sections for electron impact vibrational excitation of molecular oxygen in the angular range 15°–180°. *Journal of Physics B: Atomic, Molecular and Optical Physics*, *39*, 4087–4095.

Linert, I., & Zubek, M. (2009). Differential cross sections for electron elastic scattering and vibrational $v = 1$ excitation in nitrogen in the energy range from 5 to 20 eV measured over an angular range of 10°–180°. *Journal of Physics B: Atomic, Molecular and Optical Physics*, *42*, 085203-8.

McCarthy, I. E., & Weigold, E. (1995). *Electron atom collisions* (Vol. 1). Cambridge, UK: Cambridge University Press.

McEachran, R. P., & Stauffer, A. D. (1983). Positron excitation of the 2^1S state of helium. *Journal of Physics B: Atomic, Molecular and Optical Physics*, *16*, 4023–4038.

Middleton, A. G., Brunger, M. J., & Teubner, P. J. O. (1992). Vibrational excitation in isoelectronic molecules by electron impact: CO and N_2. *Journal of Physics B: Atomic, Molecular and Optical Physics, 25,* 3541–3549.

Mielewska, B., King, G. C., Read, F. H., & Zubek, M. (1999). A study of resonance structures in elastic scattering by carbon monoxide and molecular nitrogen in the backward direction. *Chemical Physics Letters*, *311*, 428–432.

Mielewska, B., Linert, I., King, G. C., & Zubek, M. (2004). Differential cross sections for elastic electron scattering in argon over the angular range 130°–180°. *Physical Review A*, *69*, 062716-8.

Mimnagh, D. J. R., McEachran, R. P., & Stauffer, A. D. (1993). Elastic electron scattering from the noble gases including dynamic distortion. *Journal of Physics B: Atomic, Molecular and Optical Physics, 26,* 1727–1741.

Murray, A. J., Hussey, M. J., Gao, J., & Madison, D. H. (2006). (e,2e) ionization measurements from the $3^\circ\sigma_g$ and $2\sigma_u^*$states of N_2: comparison between experiment and theoretical predictions of the effects of exchange, polarization and interference. *Journal of Physics B: Atomic, Molecular and Optical Physics*, *39*, 3945–3956.

Murray, A. J., MacGillivray, W. R., & Hussey, M. (2008). Theoretical modeling of resonant laser excitation of atoms in a magnetic field. *Physical Review A*, *77*, 013409-12.

Muse, J., Silva, H., Lopes, M. C. A., & Khakoo, M. A. (2008). Low energy elastic scattering of electrons from H_2 and N_2. *Journal of Physics B: Atomic, Molecular and Optical Physics, 41,* 095203.

Nesbit, R. K. (1979). Variational calculations of accurate e^-–He cross sections below 19 eV. *Physical Review A*, *20*, 58–70.

Nickel, J. C., Mott, C., Kanik, I., & McCollum, D. C. (1988). Absolute elastic differential electron scattering cross sections for carbon monoxide and molecular nitrogen in the intermediate energy region. *Journal of Physics B: Atomic, Molecular and Optical Physics, 21,* 1867–1877.

Onda, K., & Truhlar, D. G. (1979). State-to-state cross sections for electron impact on N_2. Close coupling and polarized Born calculations for rotational and vibrational excitation and pure elastic scattering at nonresonant energies. *Journal of Chemical Physics, 71,* 5107–5124.

Onda, K., & Truhlar, D. G. (1980). State-to-state cross sections for elastic and inelastic electron scattering by N_2 at 20-35 eV, including resonant enhancement of vibrational excitation. *Journal of Chemical Physics, 72,* 5249–5263.

Panajotovic, R., Filipovic, D., Marinkovic, B., Pejcev, V., Kurepa, M., & Vuskovic, L. (1997). Critical minima in elastic electron scattering by argon. *Journal of Physics B: Atomic, Molecular and Optical Physics*, *30*, 5877–5894.

Pavlovic, Z., Boness, M. J. W., Herzenberg, A., & Schulz, G. J. (1972). Vibrational excitation in N_2 by electron impact in the 15-35-eV region. *Physical Review A, 6,* 676–685.

Ramsauer, C., & Kollath, R. (1932). Die Winkelverteilung bei der Streuung langsamer Elektronen an Gasmolekülen, *Annalen der Physik*, *12*, 529–535.

Read, F. H., & Bowring, N. J. (2010). Email: cpo@electronoptics.com. Die Winkelverteilung bei der Streuung langsamer Elektronen an Gasmolekülen.

Read, F. H., & Channing, J. M. (1996). Production and optical properties of an unscreened but localised magnetic field. *Review of Scientific Instruments*, *67*, 2372–2377.

Register, D. F., & Trajmar, S. (1984). Differential, integral, and momentum-transfer cross sections for elastic electron scattering by neon: 5 to 100 eV. *Physical Review A*, *29*, 1785–1792.

Saha, H. P. (1989). Low-energy elastic scattering of electrons from neon atoms. *Physical Review A*, *39*, 5048–5061.

Sawada, T., Ganas, P. S., & Green, A. E. S. (1974). Elastic scattering of electrons from N_2. *Physical Review A, 9,* 1130–1135.

Schulz, G. (1963). Resonance in the elastic scattering of electrons in helium. *Physical Review Letters*, 10, 104–105.

Schulz, G. (1973a). Resonances in electron impact on atoms. *Reviews of Modern Physics*, *45*, 378–422.

Schulz, G. (1973b). Resonances in electron impact on diatomic molecules. *Reviews of Modern Physics*, *45*, 423–486.

Shi, X., & Burrow, P. D. (1992). Differential scattering cross-sections of neon at low electron energies. *Journal of Physics B: Atomic, Molecular and Optical Physics*, *25*, 4273–4279.

Shore, B. W. (1968). Parametrization of absorption-line profiles. *Physical Review*, *171*, 43–54.

Shyn, T. W., & Carignan, G. R. (1980). Angular distribution of electrons elastically scattered from gases: 1.5-400 eV on N_2. II. *Physical Review A, 22,* 923–929.

Siegel, J., Dill, D., & Dehmer, J. L. (1978). Differential elastic electron scattering cross sections for N_2 from 0 to 30 eV. *Physical Review A, 17,* 2106–2109.

Sienkiewicz, J. E., & Baylis, W. E. (1987). A relativistic approach to the elastic-scattering of electrons by argon. *Journal of Physics B: Atomic, Molecular and Optical Physics*, *20*, 5145–5156.

Sienkiewicz, J. E., & Baylis, W. E. (1989). Low-energy elastic e-Xe scattering - the effect of exchange in the polarization potential. *Journal of Physics B: Atomic, Molecular and Optical Physics*, *22*, 3733–3745.

Sin Fai Lam, L. T. (1982). Relativistic effects in electron scattering by atoms. III. Elastic scattering by krypton, xenon and radon. *Journal of Physics B: Atomic and Molecular Physics, 15,* 119–142.

Sinapius, G., Raith, W., & Wilson, W. G. (1980). Scattering of low-energy positrons from noble-gas atoms. *Journal of Physics B: Atomic and Molecular Physics, 13,* 4079–4090.

Srivastava, S. K., Chutjian, A., & Trajmar, S. (1976). Absolute elastic differential electron-scattering cross-sections in intermediate energy region. 2. N_2. *Journal of Chemical Physics*, *64*, 1340–1344.

Stamatovic, A., & Schultz, G. J. (1970). Characteristics of trochoidal electron monochromator. *Review of Scientific Instruments*, *41*, 423–427.

Stevenson, M. A., & Lohmann, B. (1996). Triple-differential cross section measurements of electron impact ionization of argon 3s in the backward direction. *Physical Review A*, *73*, 020701-4.

Strivastava, S. K., Tanaka, H., Chutjian, A., & Trajmar, S. (1981). Elastic scattering of intermediate-energy electrons by Ar and Kr. *Physical Review A*, *23*, 2156–2166.

Subramanian, K. P., & Kumar, V. (1987). Total electron scattering cross sections for argon, krypton and xenon at low electron energies. *Journal of Physics B: Atomic and Molecular and Physics, 20,* 5505–5515.

Sun, W., Morrison, M. A., Isaacs, W. A., Trail, W. K., Alle, D. T., Gulley, R. J., et al. (1995). Detailed theoretical and experimental analysis of low-energy electron-N_2 scattering. *Physical Review A*, *52*, 1229–1256.

Suzuki, M., Taniguchi, T., & Tagashira, H. (1989). Momentum transfer cross section of krypton deduced from electron drift velocity data. *Journal of Physics D*, *22*, 1848–1855.

Sweeny, C. J., & Shyn, T. W. (1996). Measurement of inelastic electron impact on ozone: absolute differerential cross sections for excitation of the Hartley band. *Physical Review A*, *53*, 1576–1580.

Szmytkowski, C., Maciag, K., & Karwasz, G. (1996). Absolute electron-scattering total cross section measurements for noble gas atoms and diatomic molecules. *Physica Scripta, 54,* 271–280.

Trajmar, S., Register, D. F., Cartwright, D. C., & Csanak, G. (1992). Differential and integral cross-sections for electron-impact excitation of the n^3S, n^1S and n^3P ($n = 2, 3$) levels in He. *Journal of Physics B: Atomic, Molecular and Optical Physics*, *25*, 4889–4910.

Trajmar, S., Register, D. F., & Chutjian, A. (1983). Electron scattering by molecules II. Experimental methods and data. *Physics Reports*, *97*, 219–356.

Trantham, K. W., Dedman, C. J., Gibson, J. C., & Buckman, S. J. (1997). Absolute electron scattering cross section measurements at backward angles. *Bulletin of the American Physical Society*, *42*, 1727.

Tronc, M., & Malegat, L. (1984). Shape resonances in electron-polyatomic molecules collisions. In F. A. Gianturco & G. Stefani (Eds.), *Wavefunctions and mechanisms from electron scattering processes* (Lecture Notes in Chemistry, Vol. 35, pp. 24–31). Berlin: Springer.

Truhlar, D. G., Brandt, M. A., Chutjian, A., Srivastava, S. K., & Trajmar, S. (1976). Electron scattering by N_2 at 5 and 10 eV: rotational-vibrational close coupling calculations and crossed beam studies of vibrational excitation. *Journal of Chemical Physics, 65,* 2962–2970.

Zatsarinny, O. (2006). BSR: *B*-spline atomic *R*-matrix codes. *Computer Physics Communications*, *174*, 273–356.

Zatsarinny, O., & Bartschat, K. (2004a). *B*-spline Breit-Pauli *R*-matrix calculations for electron collisions with neon atoms. *Journal of Physics B: Atomic, Molecular and Optical Physics*, *37*, 2173–2189.

Zatsarinny, O., & Bartschat, K. (2004b). *B*-spline Breit-Pauli *R*-matrix calculations for electron collisions with argon atoms. *Journal of Physics B: Atomic, Molecular and Optical Physics*, *37*, 4693–4706.

Zatsarinny, O., & Bartschat, K. (2005). Benchmark calculations for electron collisions with zinc atoms. *Physical Review A*, *71*, 022716-8.

Zatsarinny, O., & Bartschat, K. (2008). Relativistic *B*-spline *R*-matrix method for electron collisions with atoms and ions: Application to low-energy electron scattering from Cs. *Physical Review A*, *77*, 062701-7.

Zubek, M., Danjo, A., & King, G. C. (1995). Differential cross-sections for elastic electron-scattering by mercury in the energy-range 9 to 25 eV. *Journal of Physics B: Atomic, Molecular and Optical Physics*, *28*, 4117–4127.

Zubek, M., Gulley, N., King, G. C., & Read, F. H. (1996). Measurements of elastic electron scattering in the backward hemisphere. *Journal of Physics B: Atomic, Molecular and Optical Physics*, *29*, L239–L244.

Zubek, M., & King, G. C. (1994). Differential cross-sections for electron-impact excitation of the $C\,^3\Pi_u$, $E\,^3\Sigma_g^+$ and $a''\,^3\Sigma_g^+$ states of N_2. *Journal of Physics B: Atomic, Molecular and Optical Physics*, *27*, 2613–2624.

Zubek, M., Mielewska, B., Channing, J., King, G. C., & Read, F. H. (1999). A study of resonance structures in elastic electron scattering from helium, neon, argon, krypton and xenon over the angular range from 100° to 180°. *Journal of Physics B: Atomic, Molecular and Optical Physics*, *32*, 1351–1363.

Zubek, M., Mielewska, B., & King, G. C. (2000). Absolute differential cross sections for electron elastic scattering and vibrational excitation in nitrogen in the angular range from 120° to 180°. *Journal of Physics B: Atomic, Molecular and Optical Physics*, *33*, L527–L532.

CHAPTER 2

X-ray Methods in High-Intensity Discharges and Metal-Halide Lamps: X-ray Induced Fluorescence

John J. Curry[a], **Walter P. Lapatovich**[b], and **Albert Henins**[a]

[a]*National Institute of Standards and Technology, Gaithersburg, MD 20899, USA*

[b]*51 Pye Brook Lane, Boxford, MA 01921, USA*

Contents

Abstract

We describe the use of x-ray induced fluorescence to study metal-halide high-intensity discharge lamps and to measure equilibrium vapor pressures of metal-halide salts. The physical principles of metal-halide lamps, relevant aspects of

Advances in Atomic, Molecular, and Optical Physics, Volume 60, Copyright © 2011 Elsevier Inc.
ISSN 1049-250X, DOI: 10.1016/B978-0-12-385508-4.00002-4.

x-ray–atom interactions, the experimental method using synchrotron radiation, and x-ray induced fluorescence measurements relevant to metal-halide lamps are covered.

1. INTRODUCTION

Just over 10 years ago, x-ray induced fluorescence (XRIF) was used for the first time to measure and map gas-phase densities in a commercial high-intensity discharge (HID) lamp (Curry et al., 2001). This work opened up a new window on important processes affecting lamp performance. It may also have been the first successful use of XRIF to measure vapor densities below 10^{17} cm^{-3}. The success of those measurements owed much to an x-ray source that had just become available at the then relatively new Advanced Photon Source. Since then, XRIF has been used several more times to further explore the physics of metal-halide high-intensity discharge lamps and related processes. This chapter describes that work, all of which has been in collaboration with the lighting industry.

High-intensity discharges, also referred to as high-pressure arcs, play a role in many technologies including general purpose lighting, materials processing, sterilization, environmental remediation, and spectrochemistry. The focus here will be on high-intensity discharges used for lighting applications. Metal-halide high-intensity discharge (MH-HID) lamps, or metal-halide lamps for short, are among the most advanced general purpose light sources available (Hong et al., 2002 and 2005). These lamps combine a high luminous efficacy[1] with excellent color rendering[2] and are used in a number of places where intense sources are needed.[3] The desires of lighting companies to produce more profitable lamps, of government agencies and public utilities to reduce energy consumed by lighting, and of scientists to improve general knowledge of plasma physics have made metal-halide lamps a topic of considerable scientific and engineering interest for at least the last few decades (ALITE, 2006; ICF, 2006). This interest has motivated the development and refinement of a number diagnostic methods in search of better and more detailed information about these complex systems. Diagnostics utilizing x rays are a small subset of the available methods, but a very powerful subset.

The combination of terms "x ray" and "high-intensity" frequently produces an initial misconception that the "x rays" are produced by

[1] A quantitative measure of the illuminating efficiency of a light source (see Luminous efficacy in the Glossary for more detail).
[2] A quantitative measure of the ability of a light source to properly render all colors (see Color rendering in the Glossary for more detail).
[3] Metal-halide lamps are used to illuminate streets and parking lots, buildings and monuments, stadiums, large indoor spaces, and even high-end retail merchandise.

the "high-intensity" discharge; one thinks of laser-produced plasmas or pulsed-power discharges, from which x rays are indeed emitted by the plasma and are also used for diagnostic purposes. High-intensity discharges are high-pressure plasmas in which electrons and heavy particles have the same or nearly the same temperature, with that temperature generally being less than a few electronvolts. In metal-halide lamps, these temperatures are usually less than one-half an electronvolt,[4] far too low to generate a substantial amount of ultraviolet radiation, to say nothing of x rays. The x-ray methods used to study high-intensity discharges and metal-halide lamps utilize external sources of x rays. X-ray absorption imaging has been demonstrated with both synchrotron radiation (Curry et al., 2004) and with commercial x-ray tubes (Curry et al., 1998), whereas x-ray induced fluorescence (XRIF) relies on synchrotron radiation (Curry et al., 2003b). The latter is the subject of the present discussion.

XRIF is neither new nor unfamiliar to the broader scientific community, but its application to the study of metal-halide lamps is novel and presents some special challenges. The densities of atoms being detected are small compared to typical applications; we are interested in densities as low as 10^{15} cm^{-3}. Such sensitivities are made possible by the availability of third-generation synchrotron sources, such as the Advanced Photon Source (APS) at Argonne National Laboratory. It is possible to obtain spatially resolved measurements of relatively low vapor densities in a matter of tens of seconds.

An intense, laser-like beam of high-energy photons like that obtainable at the APS is not required for XRIF measurements but is so powerful that it makes measurements with lesser sources relatively insignificant. Unfortunately, the considerable effort and resources required to competitively obtain access to and operate a remote experiment at an appropriate synchrotron facility put such measurements beyond the reach of many. Most synchrotrons are publicly funded institutions with a responsibility and mission to serve scientific and industrial endeavors, but they are still a limited resource.

X-ray methods are far from being the answer to all questions in metal-halide lamps. They are, however, a considerably different set of tools with capabilities that are both powerful and complementary to existing methods. As will be seen, they can answer questions that are important and cannot be answered with other methods. In some ways, the significance of the answers they provide has not been fully appreciated because the theoretical approaches and interpretations have for so long been focused

[4]The electronvolt (eV) is a non-SI unit of energy equal to $1.60217733 \times 10^{-19}$ J. It is accepted for use with the International System of Units (SI) by the International Committee for Weights and Measures (CIPM).

on the answers that are provided by existing methods. This situation has changed slowly, but we hope the change will continue.

At present, the lighting industry is undergoing somewhat of a revolution in technology. The development of blue, green, and even ultraviolet light-emitting diodes (LEDs) has led to the development of LEDs as general purpose light sources to compete with other traditional technologies like metal-halide, fluorescent, halogen, and incandescent lamps. There are a number of medium- to low-wattage LED lamps on the market that exhibit good luminous efficacy and color rendering. Much of the excitement in the industry and the public arises from the rapid rate of improvement in LED lamps over the last decade and the hope that eventually LEDs can be fabricated to meet any desired performance specification at competitive cost. If that hope becomes reality, LEDs may displace all existing technologies. Although LEDs have already made significant inroads into the lamp market and will probably continue that trend for some time as additional advances occur, a complete displacement of all existing technologies is no closer than a couple of decades and, in our opinion, is not likely to ever happen. The historical lesson in the lighting industry is that the market has always been diverse, matching the diverse performance of various light sources to the exacting requirements of customers. Candles and oil lamps, as an extreme example, are still made and marketed for their ambiance as well as muted illumination.

There is still much that can be learned about high-intensity discharges and metal-halide lamps. X-ray methods have and will continue to play a role in that process. Furthermore, the techniques themselves are not static and will experience development. It is our hope that this chapter encourages more work in this area.

We begin this chapter by discussing metal-halide high-intensity discharge lamps; the motivation for the use of XRIF and x-ray methods in general derives directly from the characteristics of the lamps themselves. An understanding of the physical structure and operational regimes of the lamps will enable an appreciation for many of the points to be made regarding XRIF. This is followed by a review of the atomic physics relevant to understanding how the technique works. Finally, we review applications of XRIF to measurements in operating metal-halide lamps and to the measurement of equilibrium vapor pressures of metal halides in vapor cells.

2. HIGH-INTENSITY DISCHARGES AND METAL-HALIDE LAMPS

High-intensity discharges (HID) are arc-like plasmas formed by a relatively intense concentration of power in a high-pressure vapor (typically

the ambient pressure and above). The term is frequently associated with lamps and electroded discharges but rightfully applies to a more general class that also includes some electrodeless radio-frequency excited discharges and other plasma sources not used for lighting. In fact, electrodeless high-intensity discharges found use in atomic spectroscopy (Corliss et al., 1953) before metal-halide lamps became commercially available in the 1960s (Reiling, 1964). More recently, the lighting industry has seen the development and patenting of electrodeless HID lamps (Hochi et al., 2001; Palmer & Lapatovich, 2000; Turner et al., 1997), but they have not yet been developed into widespread products because of limitations on available power electronics.

High-intensity discharges for practical lighting applications include mercury arc lamps, high-pressure sodium (HPS) lamps, and metal-halide lamps. The vapor in all of these lamps is primarily mercury but also includes a lesser amount of a rare gas such as argon, which plays an important role during startup. Mercury arc lamps have no further additives and, as such, are somewhat inefficient and prone to producing a bluish-white light with rather poor color rendering properties. HPS lamps contain sodium metal in addition to mercury, and the rare gas used is xenon. These are very efficient lamps with luminous efficacies of 120–150 lm/W. However, the radiated light is largely from the pressure-broadened wings of the yellow sodium "D" lines. At 589 nm and 590 nm, these lines closely match the peak of the eye sensitivity curve (see Figure 1) near 550 nm, accounting for the high luminous efficacy. The domination of the yellow "D" lines gives HPS lamps poor color rendering (30 to 40) (de Groot & van Vliet, 1986).

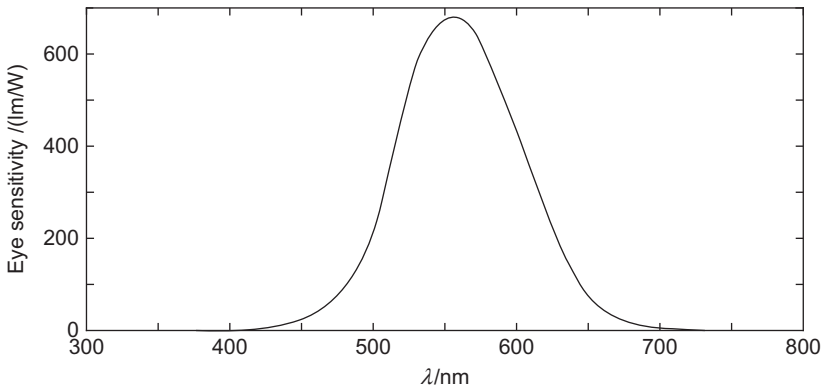

Figure 1 The eye sensitivity curve defines the number of lumens produced by 1 W of light at a given wavelength. It represents the response of a human eye to electromagnetic radiation.

Metal-halide lamps are a particular type of high-intensity discharge lamp widely used in general illumination applications where high illumination levels or exceptional color rendering are necessary. These lamps contain, in addition to elemental mercury and a rare gas, some metal-halide salts.[5] Metal-halide salts are a mechanism for introducing various metals into the discharge for the purpose of improving the luminous efficacy and color rendering of the lamp. Metal-halide salts are used in preference to elemental metals themselves because the vapor pressures of the salts are much higher than that of the metals. This permits the metal-halide lamp to operate at lower temperatures than would otherwise be necessary. The iodide salts are almost exclusively used in electroded lamps because of the limited reactivity of iodine with metal electrode components. In electrodeless lamps, bromides, chlorides, interhalogenated compounds, and oxyhalides may be used since there are no metallic electrodes in the discharge with which to react.

Our work has been focused on metal-halide lamps, and therefore this chapter will be as well. Much of what is discussed, however, may be applied to the broader class of high-intensity discharges. There are a number of excellent general articles on the operation and characteristics of metal-halide lamps (Ingold, 1987; Lister & Waymouth, 2002; Sugiura, 1993; Waymouth, 1971, 1991). A particularly good one is the general review of discharge lamps by Lister et al. (2004). An older article by Dakin et al. (1989) titled "Anatomy of a vertical metal-halide discharge" is also highly recommended.

A schematic of a typical, modern metal-halide lamp appears in Figure 2. The heart of a metal-halide lamp is the ceramic or vitreous silica arc tube. Lamps with the latter are often referred to as quartz lamps. Ceramic arc tubes are almost always constructed of densely sintered alumina grains with an average size between 0.02 mm and 0.05 mm. The sintered material is called polycrystalline alumina (PCA). Its hexagonal crystal structure results in a translucent arc tube. In contrast, vitreous silica makes a transparent glass arc tube. For applications requiring a transparent ceramic arc tube, cubic material such as yttrium oxide or dysprosium oxide may be sintered to transparency (Rhodes & Reid, 1979; Wei et al., 2008).

The arc tube is a sealed vessel, equipped with two opposing electrodes as shown in Figure 2. Before the tube is sealed, it is dosed with several milligrams of mercury, a few milligrams of a combination of metal-halide salts, and approximately 10^4 Pa of a rare gas. The arc tube is mounted

[5]Hg-free metal-halide lamps have been developed and are commercially available but have a much smaller market share than mercury-based metal-halide lamps.

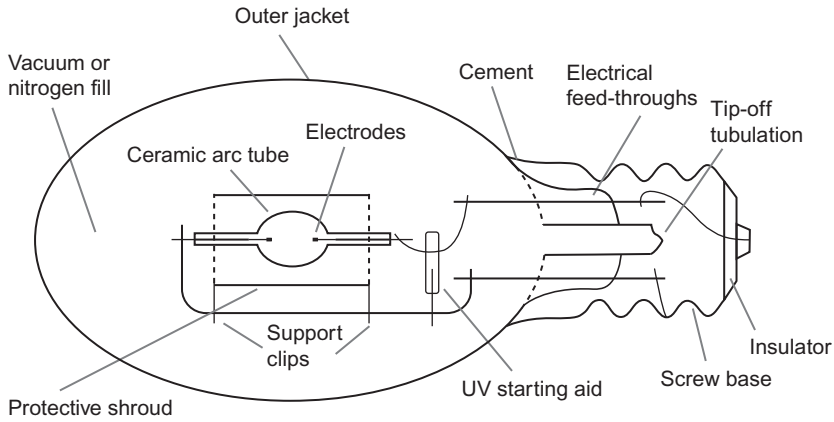

Figure 2 Schematic of a typical low to medium wattage metal-halide high-intensity discharge lamp.

inside a hard glass jacket that absorbs ultraviolet radiation (produced during startup), provides thermal management for the arc tube, and provides some mechanical protection in case of failure of the arc tube. Sometimes, an internal shroud is used in close proximity to the arc tube to provide additional control and safety. The UV starting aid shown in Figure 2 shortens lamp ignition times by producing ultraviolet photons that enter the arc tube and ionize a few rare gas atoms, thus providing the initial electrons for discharge breakdown.

Modern metal-halide lamps are almost entirely driven by electronic ballasts that ignite the discharge with a high-voltage pulse or radio-frequency pulse train and drive the discharge with an audio frequency square wave or modified square wave. Some ballasts employ sinusoidal driving waveforms at a few MHz. The lamps are made and marketed in a wide range of sizes, from 10 W to 10s of kilowatts.

The vapor pressure of mercury at room temperature is a few tenths of a pascal, so if the lamp is ignited under these conditions, the discharge is initially a low pressure Hg glow discharge, much like that in a fluorescent lamp. At low pressure, Hg emits copious amounts of ultraviolet light at 254 and 185 nm (this is the basis for the fluorescent lamp). Ultraviolet protection by the glass jacket is absolutely essential if the lamp is located near people. The voltage across the discharge is relatively low at this point, so the power deposited is not at its full value. Nevertheless, heat from the discharge is sufficient to evaporate additional mercury, thereby increasing the mercury vapor pressure and consequently the power deposited in the discharge. At some point (usually when the mercury pressure is above 10^5 Pa and at wall temperatures of around 800 K), the diffuse

low-pressure discharge will constrict and transition to a high-pressure arc or high-intensity discharge. Before the lamp reaches final operating temperature, the mercury is typically completely evaporated, with final pressures in the arc tube in the range of a few or more times atmospheric pressure, depending on the lamp design. As the temperature continues to increase ($>$900 K), the arc tube becomes hot enough to raise the metal-halide vapor pressures to significant levels. The metal-halide molecules evaporate from the solid or liquid salt and diffuse into the discharge. The introduction of the metal-halide salts into the arc stream alters the discharge in many ways. The average ionization energy of the plasma species decreases, and the plasma core temperature drops. This results in reduced heat flux to the wall, and the arc tube temperature begins to level off. The cold spot, or cold zone, temperature reaches a steady state at approximately 1200 K. More importantly, the radiation output increases (more electrical power is converted to light and less into heat) and the color changes from the "blue-white" characteristic of mercury to a more pleasing "warm-white" with greatly improved color rendering as radiation from the metal additives fills out the spectrum.

Electric power is deposited along the axis of the lamp, between the electrode tips, where the electrical conductivity is highest. This establishes a radial temperature gradient in the approximately cylindrical lamp geometry as the input power is partitioned between thermal energy and radiation that escapes the lamp. In warmer regions of the discharge, salt molecules are dissociated to varying degrees. In the core of the arc, where temperatures are the highest ($\leq$5300 K), the molecules are completely dissociated, releasing metal atoms into the vapor. Temperatures are even high enough to ionize a large fraction of the metal atoms. Those free metal atoms and their ions are largely responsible for the high luminous efficacies and excellent color rendering characteristic of metal-halide lamps.

Specific metals are used in the salts because of their strong emission in the visible range of the spectrum. Some common examples of metal-halide salts appearing in commercial lamps are given in Table 1. The rare-earth elements are prominently represented because they have rich visible spectra. Dysprosium, holmium, thulium, and scandium have been widely used for at least a couple of decades. More recently, cerium has produced dramatic improvements in luminous efficacies. A number of one- or two-electron type atoms such as sodium, cesium, calcium, and indium are also used. These atoms tend to have strong resonance transitions as opposed to the complex spectra of the rare earths. Typically, a combination of these salts is used in a given lamp to optimize luminous efficacy and color rendering or produce a certain color temperature. The operation of a lamp depends strongly on the vapor pressures of the salts. These vapor pressures are often strongly modified by the presence of other salts in the melt

Table 1 Some common metal-halide salts used in metal-halide lamps and comments on their function.

Metal-Halide Salt	Comments
NaI	Resonance emission near peak of eye sensitivity curve; improves efficacy; reduces core temperature.
DyI_3	Multiline atomic spectrum and molecular continuum; improves efficacy and color rendering; reduces core temperature.
HoI_3	Multiline atomic spectrum and molecular continuum; adjusts color temperature; improves efficacy.
TmI_3	Multiline atomic spectrum and molecular continuum; adjusts color temperature; improves efficacy.
CeI_3	Multiline atomic spectrum and molecular continuum; dramatically improves efficacy and color rendering.
CaI_2	Dilution agent and filler; adjusts viscosity of liquid fill.
ZnI_2	Alternative to Hg for high electrical impedance.

and in the vapor phase. Formation of complexes (weakly-bound combinations of molecules) between different metal halides in the vapor phase can increase the vapor pressures of some salts sufficiently to improve spectral output or modify temporal behavior (warm-up time) of the lamp.

The temperature in the core of the discharge in a metal-halide lamp is in the same range as the photosphere of the Sun: 4500–6000 K, with the lower end being more typical of lamps having a high alkali content. Moving outside the core, into the mantle of the discharge, temperatures decrease rapidly—approximately quadratically—and the lamp geometry is chosen so that temperatures at the wall do not exceed the capability of the arc tube while it is under the extreme pressures produced by the mercury vapor. For polycrystalline alumina (PCA) arc tubes, the maximum wall temperature is about 1300 K. For fused quartz, it is only 1120 K. In a vertically operating lamp, the metal-halide salts eventually accumulate in the coolest parts of the arc tube, usually in a lower corner, or in the sealing area where the electrode enters the arc tube. The liquid salts are viscous and wet the interior surface of the arc tube but have a consistency more like honey. Droplets of salt can adhere to regions of the arc tube and resist gravity. The lamps are symmetrical with respect to the geometrical equator, so the colder areas near the lower electrode are replicated near the upper electrode seal region despite internal convection. The notion of a cold *spot* is too simplistic as the salts are always observed to cover a substantial area within the arc tube. The salts reside in a cold *zone* with a distribution of temperatures. Consequently salts are frequently observed in the upper and lower portions of the arc tube, although gravity tends to pool the salts in the lower part of the tube. Temperatures in the cold

zones are typically in the range of 1020–1200 K. The highest cold zone temperature determines the vapor pressures of the metal-halide salts in the surrounding volume. If the lamp were in complete equilibrium, these vapor pressures would be a constant throughout. Plasma and hydrodynamic effects frequently conspire to produce spatially dependent vapor pressures, as well as differences between various metals. The latter phenomenon is referred to as demixing and is almost always detrimental to the operation of the lamp.

Mercury, being at high pressure, is the most abundant constituent in the metal-halide arc. However, it produces only a small fraction of the radiation because temperatures in the core are too low to excite the resonance levels of mercury. The role of mercury is to increase the electrical and thermal resistivities of the arc. A large electrical resistivity makes it possible to dissipate a high level of power in the arc without increasing current. Mercury's relatively large electron impact momentum transfer cross section enhances the electrical resistance of the arc. The large cross section also facilitates equilibration of kinetic energy between heavy particles and electrons. Although some work has shown a modest divergence of electron and heavy particle temperatures (Elloumi et al., 1999; Karabourniotis, 2002, and references therein) in some regions of metal-halide arcs, the massive particles can be considered to be in local thermal equilibrium with each other. Mercury's low thermal conductivity reduces thermal transport across the large thermal gradients between the core and the arc tube wall, thereby reducing a significant power loss mechanism.

An essential aspect of metal-halide lamp design is the regenerative halogen cycle. This cycle begins with a parent molecule, e.g., DyI_3, being vaporized from a liquid condensate in the cold zone and entering the discharge; as the molecule diffuses into warmer regions of the arc, the molecule dissociates to varying degrees; in the core of the arc, where temperatures are highest, the metal atom is completely liberated and may even be ionized; the metal atoms and ions are excited to radiating states by collisions with electrons and subsequently produce radiation. When the metal atom migrates to cooler regions, it recombines with halogen atoms; if a reassembled parent molecule comes in contact with a liquid condensate, it may recondense back into the liquid, ready to begin the cycle again.

Recombination near the wall is assisted by the high density of neutral Hg atoms, which act as collision partners to absorb the binding energy of the forming polyatoms. The latter is often viewed as an effective increase of radial thermal conductivity in the mantle. The halogen, after dissociation, rarely participates in the radiation process since its excitation potential is generally similar to or greater than that of Hg.

The halogen cycle is essential to the lifetime of metal-halide lamps. Processes that interrupt this regeneration can drastically reduce life

and performance. For example, reactions of electrode components with dissociated halogens remove halogens from the vapor and produce a metal–rich plasma. If the metal cannot find halogen partners with which to recombine, it will condense on the arc tube wall. The temperature of the wall is insufficient to vaporize the pure metals, and these atoms are forever lost to the discharge. The presence of rare-earth metals on the alumina surface may precipitate formation of rare-earth aluminates, reducing the lifetime of the arc tube. Continued sequestering of halogens eventually depletes the discharge of metals entirely. Iodide salts are commonly used since iodine is the least reactive of the halogens.

The high pressures in metal-halide arcs lead to a high degree of radiation trapping in some regions of the spectrum. When the vapor is optically thick in a given wavelength range and local spatial volume, the radiation field equilibrates with the massive particles. This leads to radiation levels that saturate at the blackbody curve of the local vapor temperature. This is particularly true in the wavelength range surrounding the 254-nm resonance line of Hg, for which the mean free path is on the order of microns. Radiation emitted by the lamp in this range can only come from the very edge of the arc, but the temperature there is too low to allow any significant blackbody emission. Thus, ultraviolet radiation is greatly suppressed. This effect occurs to lesser extent in other regions of the spectrum, depending on the constituents of the vapor. Infrared radiation losses are not as effectively suppressed by optical opacity because the infrared blackbody limit is less severe than the ultraviolet limit.

3. WHY X-RAY METHODS?

The development and use of optical diagnostics to study high-intensity discharge lamps have been long and successful (see Lister et al., 2004 for a review). The reasons for this are quite obvious. The metal atoms in the discharge are chosen specifically because they and their singly-charged ions have radiative transitions in the visible range of the optical spectrum, and conditions in the discharge are engineered to maximize excitation of those transitions. Atoms, ions, and molecules of other species are also active in the optical range and may exhibit strong emission or absorption of optical radiation.

Optical emission spectroscopy has been used to confirm the presence or absence of particular species, obtain discharge temperatures (Herd & Lawler, 2007; Karabourniotis, 1986; Schneidenbach & Franke, 2008), and even measure Hg densities (Lawler, 2004). Excitation of optical transitions with an external continuum source (Bonvallet & Lawler, 2003) or a laser (Beks et al., 2008) has been used to measure densities and distributions of

particular species. Many other optical measurements can be found in the literature.

It will become clear in the following pages that x-ray techniques require a somewhat different set of knowledge than the optical methods cited earlier and also require equipment that is not normally present in the laboratory of a lighting scientist. In fact, for XRIF, one has the additional burden of applying for beam time and conducting an experiment at a remote facility in order to access synchrotron radiation. Given these hurdles, one might be led to ask the question "Why is it useful to go to such lengths?"

The primary motivations for the use of x-ray diagnostics to study high-intensity discharge lamps arise from the nature of the lamps themselves and the impediments the lamps raise to traditional methods. Most HID lamps are relatively small. They contain the high-intensity discharge inside a sealed arc tube that is made of translucent PCA or fused silica that is generally not of optical quality; optical access is limited by the strong curvature and optical defects of the arc tube, with practically no spatial resolution being possible in PCA arc tubes, which are translucent. The sharp gradients in temperature restrict optical emission to the core of the arc where temperatures are sufficiently high; the mantle of the discharge is largely dark.

The need to "see through" the translucent PCA of most modern metal-halide lamps while still maintaining good spatial resolution is a strong motivation for the use of x rays. X-ray methods have also proved very capable in quartz arc lamps. In fact, it is possible to pull an arbitrary metal-halide lamp off a store shelf and make excellent x-ray measurements without the need for any modifications to the lamp. This makes it possible to study and learn about real lamps, not just model lamps. This is possible because high-energy x rays can penetrate both the glass jacket and arc tube with only a small amount of scattering and no additional deformation of the x-ray beam.

As will be discussed in the following section, x rays are used to probe inner shell electrons, electrons whose quantum states are not much perturbed by external conditions, such as valence excitation or binding with other atoms in a molecule. As an important consequence, x-ray techniques can be used to measure and understand what is happening in all regions of the arc, even in the dark regions where little optical excitation occurs; they are spatially comprehensive diagnostics.

A third important motivation follows from the preceding discussion: x rays are not just another way to measure the same parameters that traditional methods might be used to measure if not impeded by the limitations cited earlier. Instead of measuring the density of a particular valence level of a particular molecular species, both x-ray absorption and x-ray induced fluorescence measure the number densities of specific

nuclei (mercury, dysprosium, iodine, etc.). This is particularly useful for measuring metal additives in metal-halide lamps where the metal may be distributed over many molecular and atomic species. X-ray induced fluorescence is complementary to optical spectroscopy in this regard.

4. INTERACTION OF X RAYS WITH ATOMS

All of the optical methods discussed in the preceding section are based on interactions between radiation and valence electrons with binding energies of a few electronvolts or less. In contrast, the x-ray methods discussed in this chapter are based on the interaction of high-energy radiation with core electrons; electrons whose binding energies are several thousand electon volts and higher! This fact has two important, and favorable, consequences for the study of metal-halide lamps. First, the photon energies are orders of magnitude greater than anything produced by the high-intensity discharge. Thus, the isolation of the x-ray signal from the intense optical radiation produced by the discharge and from the noise of the thermal background is excellent. Second, the problem of translucent or poor optical quality arc tubes is avoided. Although scattering of high-energy x rays does occur, such interactions are much weaker than optical refraction. This enables x-ray methods to achieve good spatial resolution in lamps with translucent PCA or fused quartz arc tubes of poor optical quality.

There are three principal types of interactions between x rays and atoms that are relevant to the work described in this chapter. All of them involve interactions with the electrons orbiting atoms. They are photoelectric absorption, Compton scattering, and coherent scattering. The basis of XRIF is photoelectric absorption, but Compton and coherent scattering also have an impact on measurements. All three of these processes will be described in more detail in this section.

Figure 3 is a spectroscopic energy level diagram that may be used to visualize excitation of core electrons. Potassium is chosen as an example because it is simpler than, though not qualitatively different from, the heavier atoms that are typically of interest in metal-halide lamps. At the very bottom of the diagram is the ground level, corresponding to the lowest electronic energy levels filled by the 19 atomic electrons of the neutral potassium atom. This ground level and the bound valence levels (short horizontal lines in the expanded diagram) between it and the $4s_{1/2}$ ionization limit at 4.3 eV form the traditional level diagram of optical spectroscopy. These levels are excited when a valence orbital is occupied by the electron initially in the $4s_{1/2}$ orbital. The 4s ionization limit, on the other hand, corresponds to the energy required to eject the 4s electron from the atom. All of the levels between the ground level and the 4s level

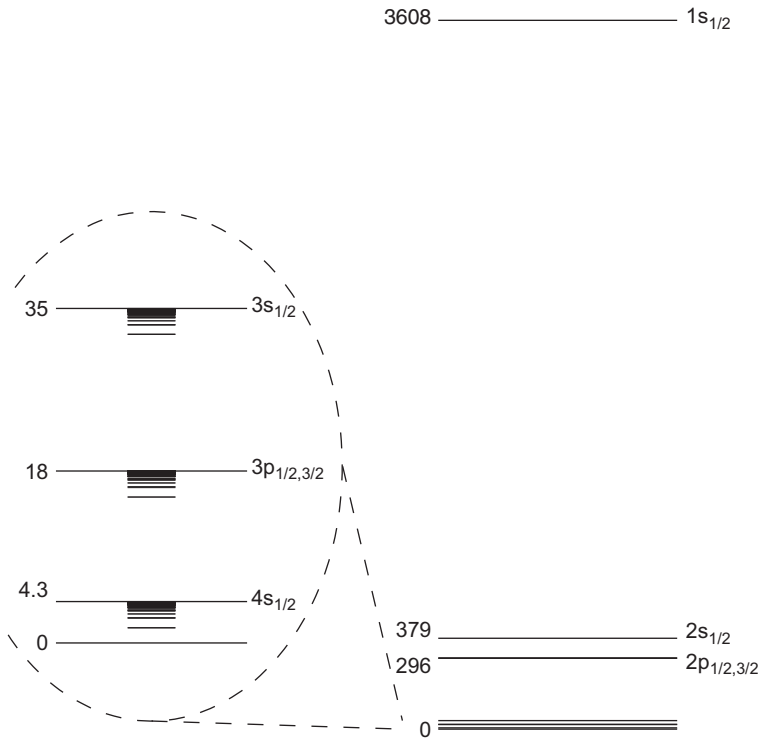

Figure 3 Excited levels of the potassium atom, whose ground configuration is $1s^2 2s^2 2p^6 3s^2 3p^6 4s$, arising from excitation of a bound electron. The wide lines are ionization energies for each of the bound electrons; the initial orbital is given on the right of each line and the ionization energy in electronvolts is given on the left. It is also possible to excite one of the electrons to a valence orbital; these are indicated in the expanded view on the left of the figure by short lines; they are too close to the ionization limits to be visible on the right. Excitation of any of the levels above the 4s limit corresponds to an empty core orbital. (Deslattes et al., 2003; Ralchenko et al., 2010; Thompson et al., 2001).

correspond to an empty 4s orbital. The next higher set of levels is qualitatively similar in appearance and corresponds to excitation or ionization, not of the 4s electron, but of a $3p_{3/2}$ electron. All of these levels correspond to an empty $3p_{3/2}$ orbital.

Above the 4s and $3p_{3/2}$ ionization limits lie additional, similar sets of energy levels that correspond to single excitation of the other core electrons that lie increasingly deeper in the Coulomb potential of the nucleus. Other core orbitals in the potassium atom include $3p_{1/2}$, $3s_{1/2}$, $2p_{3/2}$, $2p_{1/2}$, $2s_{1/2}$, and $1s_{1/2}$. Values of $n = 1, 2, 3, \ldots$ are often referred to by the letters

$K, L, M, \ldots$, and excitation of one of the two $1s_{1/2}$ electrons is referred to as K-shell excitation. Excitation of closely spaced levels just below the ionization limits (short horizontal lines in the expanded diagram) produces the near-edge fine structure observed in some x-ray spectra.

The levels in Figure 3 can be excited by sufficiently energetic photons or by impact with sufficiently energetic massive particles. The former process is referred to as photoelectric absorption. The photon is annihilated and any excess energy is imparted to the ejected electron. Figure 4 gives the photoabsorption cross section σ for dysprosium as a function of photon energy E. The general dependence of the cross section on energy follows from some of the principles already discussed. Discontinuous jumps in the cross section occur at the minimum (threshold) energy required to eject an inner shell electron from the atom. Edges due to the three nondegenerate orbitals of the L-shell ($L_1 \leftrightarrow 2s_{1/2}$, $L_2 \leftrightarrow 2p_{1/2}$, $L_3 \leftrightarrow 2p_{3/2}$) are visible. The K-shell presents only one edge corresponding to the two degenerate $1s_{1/2}$ orbitals. Not visible in this graph is the fine structure just below each threshold energy that corresponds to excitation of a core electron to a valence orbital.

The photoabsorption cross section decreases relatively slowly with energy ($\sim E^{-7/2}$) above each threshold because the electron is ejected into

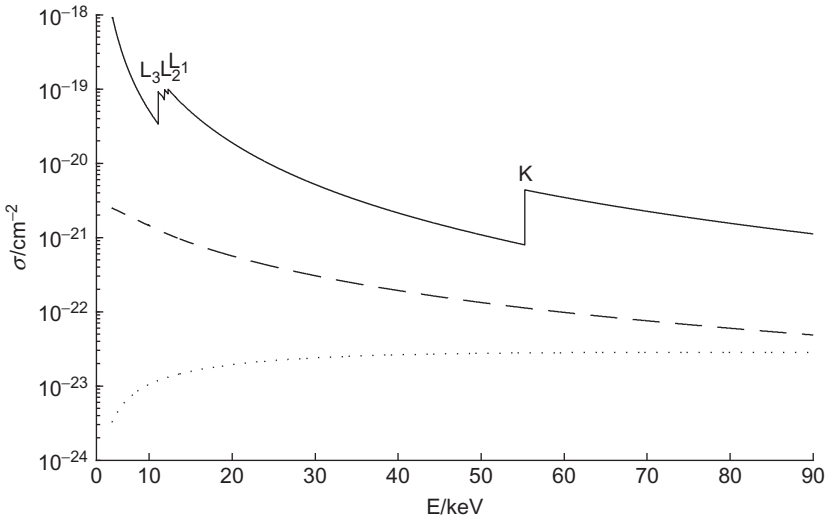

Figure 4 Cross sections for photoabsorption (—), coherent scattering (- -), and Compton scattering (· · ·) of high energy photons by a dysprosium atom as a function of photon energy. The L_i-edges ($i = 1, 2, 3$) and K-edge in photoabsorption are noted. (Berger et al., 1998).

the continuum and can absorb any excess energy. This slow falloff has the effect that a monochromatic beam of x rays can simultaneously excite a large number of atoms and transitions, provided the photon energy is above the corresponding edges. Thus, several species can be observed simultaneously with XRIF.

The curve in Figure 4 gives the total cross section for photoabsorption. For photon energies above the K-shell threshold, this includes the cross section for absorption by all the other shells as well. The ratio of the K-shell cross section to that for all other shells is approximately independent of energy and may be determined at the K-edge.

All of the levels above the 4s ionization limit correspond to creation of an empty orbital, or hole, in the core. These levels will typically relax spontaneously to the 4s ionization limit, the ground level of the singly charged ion. The hole in the core is filled by some combination of three major processes that rearrange the remaining bound electrons. These processes are spontaneous radiative relaxation, Auger decay, and the Koster–Kronig process. The relative importance of these three processes is determined by the atomic number of the atom and the principal quantum number (n) of the excited level. Only the first of these, radiative decay, is of interest here because it is the process that produces characteristic fluorescence and is the basis of x-ray induced fluorescence.

Figure 5 shows the energy level diagram for dysprosium with the major radiative transitions from an excited K-shell, along with the traditional notation for the various lines. The radiative transitions involving core orbitals are subject to the same selection rules as optical transitions, so the most probable decay paths are electric-dipole transitions, i.e., transitions for which $\Delta l = \pm 1$ and $\Delta j = \pm 0, 1$. Thus, radiative decay from the 1s level is dominated by transitions to $n\mathrm{p}_{1/2,3/2}$ levels. Overlap of the orbitals is also a factor in the strength of transitions, so $\Delta n = 1$ transitions are stronger than the corresponding $\Delta n > 1$ transitions. The $K\alpha_1$ line is stronger than the $K\alpha_2$ line because the degeneracy $g = 2j + 1$ of the $3\mathrm{p}_{3/2}$ level is greater than that of the $3\mathrm{p}_{1/2}$ level. (Since excitation of levels in this diagram corresponds to a hole in the indicated orbital, the initial level for the electron involved in spontaneous decay is the lower level.)

The probability that a core-shell excitation will decay radiatively is referred to as the fluorescence yield. Figure 6 shows that the K-shell fluorescence yield Y increases with atomic number Z and for atoms heavier than $Z = 55$, $Y > 0.9$. The relative probabilities of the different radiative transitions originating in a given level are referred to as branching fractions. Branching fractions for major K-shell lines as a function of atomic number are given in Figure 7.

Photoabsorption involving K-shell electrons in heavy elements is only weakly affected by the valence electron(s). The so-called chemical effects

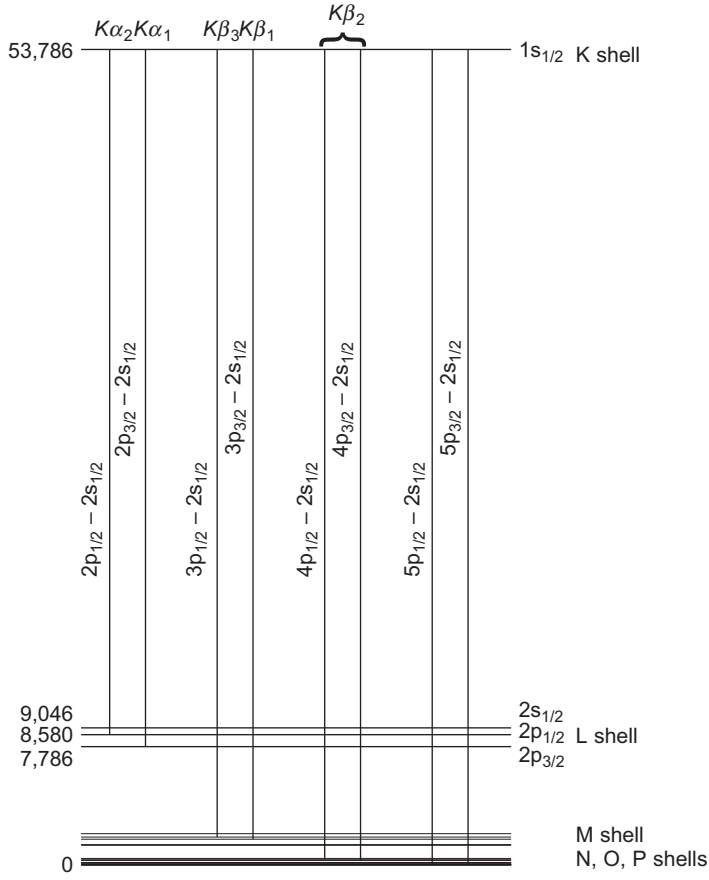

Figure 5 Radiative electric-dipole transitions from a K-shell excited dysprosium atom. (Deslattes et al., 2003).

(arising from molecular bonding) typically affect the absorption cross sections only near edges, where virtual transitions to valence states can have a noticeable influence. Observation of near-edge structure, and shifts in this structure due to molecular bonding and ionization of the valence electron, typically requires spectral resolutions of order 1 eV or better. The work described here has employed a much coarser energy resolution ($\approx$ 100 eV) and has avoided absorption edges.

The considerations in the preceding paragraph lead to a very important point regarding the densities measured by XRIF. Since the inner shell processes are not significantly influenced by chemical bonding or ionization, XRIF is proportional to the density of atoms of a particular atomic number Z, *regardless of the range of chemical states in which those atoms*

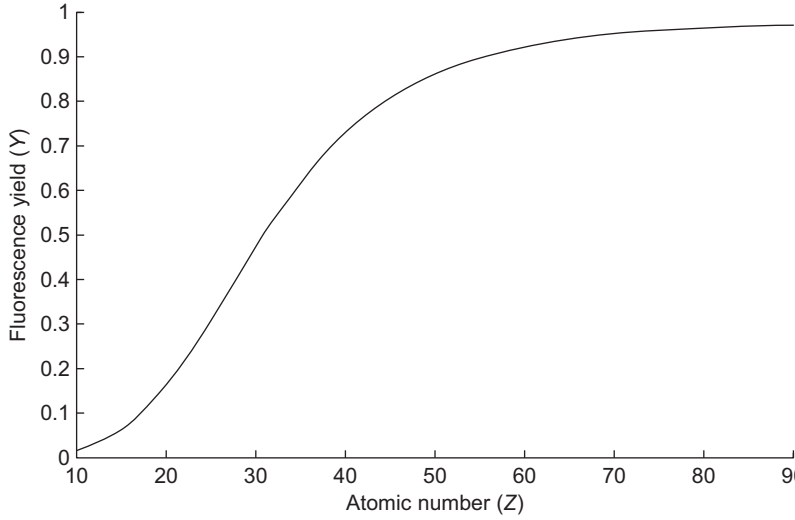

Figure 6 K-shell fluorescence yield as a function of atomic number. (Krause, 1979).

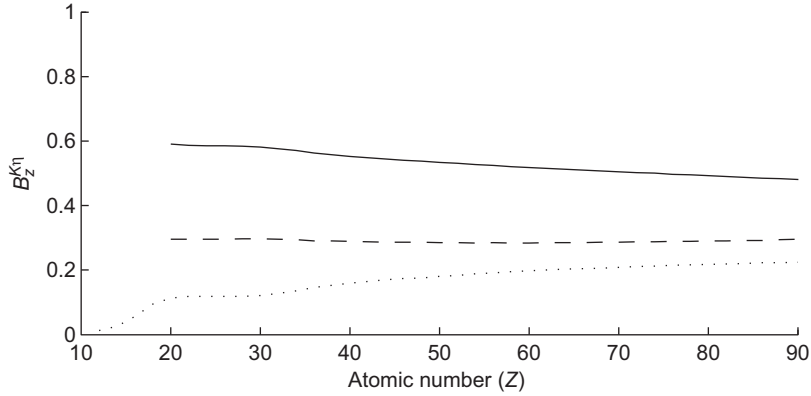

Figure 7 Branching fractions for K-shell fluorescence lines η as a function of atomic number: $\eta = \alpha_1$ (—), $\eta = \alpha_2$ (- -), and $\eta = \beta = \sum_i \beta_i$ ($\cdots$). (Salem et al., 1974).

may find themselves! Thus, our measured densities $n_{\Sigma Z}$ are summations over all molecular and ionic species M that contain an atom of atomic number Z,

$$n_{\Sigma Z} = \sum_i c_{Zi} M_i \tag{1}$$

where c_{Zi} is the relevant stoichiometric coefficient. The $n_{\Sigma Z}$ are sometimes referred to as elemental densities, and for clarity, we usually replace the subscript Z with the one- or two-letter symbol for the element.

Coherent scattering and Compton scattering are generally of no significance for the atoms we are interested in observing with XRIF. However, scattering from the solid arc tube can be important. First, scattering causes a small, but finite, reduction in the transmission of x rays through the arc tube. Second, scattering from the arc tube into the detector can easily overwhelm the fluorescence signal being observed. This occurs because the density of the arc tube is many orders of magnitude higher than the vapor densities in the arc.

Compton scattering describes the interaction between a high-energy photon and a free electron. Electrons bound to an atom can react as free electrons to some extent if the photon energy is greater than the electron binding energy. Compton scattering is typically more of a problem than coherent scattering. The Compton cross section is generally larger and the shift in photon energy that accompanies Compton scattering often leads to interference between scattered photons and fluorescence lines in the observed spectrum.

Considering only the conservation of momentum and energy during the relativistic interaction between a high-energy photon and a free electron, it is relatively easy to derive the scattered photon energy E_f as a function of the scattering angle θ and the incident energy E_0,

$$E_f = \frac{E_0}{1 + \alpha(1 - \cos\theta)} \tag{2}$$

where $\alpha = E_0/m_0c^2$ is the ratio of the incident photon energy to the electron rest energy. This shows that the change in energy is small when the photon energy is relatively small compared with the electron rest energy of approximately 500 keV. A more complete treatment of the photon–electron interaction including the electric field of the photon leads to the Klein–Nishina formula for the cross section for Compton scattering of polarized radiation by a free electron (Evans, 1958). Additionally, the bound electrons of an atom react as free electrons only to the extent that the incident photon energy exceeds each electron's binding energy. The binding energy has a small effect on the energy shift, but the cross section can be modified considerably. In addition, the kinetic energy of the bound electrons broadens the energy distribution of scattered photons. The effect of binding energy on the cross section must be calculated separately for each type of atom and is accounted for by multiplying the Klein–Nishina result with the incoherent scattering function $S(\theta)$ (Hubbell et al., 1975).

The differential Compton cross section then has the form

$$\frac{d^2\sigma}{d\Omega} = \left(\frac{r_e}{1+\alpha(1-\cos\theta)}\right)^2 \left[1 - \sin^2\theta\cos^2\phi + \frac{\alpha^2}{2}\cdot\frac{(1-\cos\theta)^2}{1+\alpha(1-\cos\theta)}\right] S(E,\theta) \tag{3}$$

where r_e is the classical electron radius, ϕ is the azimuthal angle about the incident photon wave vector with $\phi = 0$ parallel to the direction of polarization, and $d\Omega = \sin\theta\, d\theta\, d\phi$ is the differential solid angle. A surprising result is that the cross section does not go to zero along the direction of polarization, although it is a minimum.

Figure 8 gives the total Compton cross section for an Al_2O_3 unit cell as a function of incident photon energy. For photon energies greater than about 45 keV, Compton scattering is the dominant interaction. At approximately 3×10^{-23} cm^2, the Compton cross section for PCA is about two orders of magnitude smaller than the photoabsorption cross section for Dy. However, the density of PCA (and of fused quartz) is about five orders of magnitude larger than the vapor densities of interest. As a result, Compton scattering from arc tubes and vapor cells can have greater intensity than fluorescence if it is not minimized by an appropriate detection geometry.

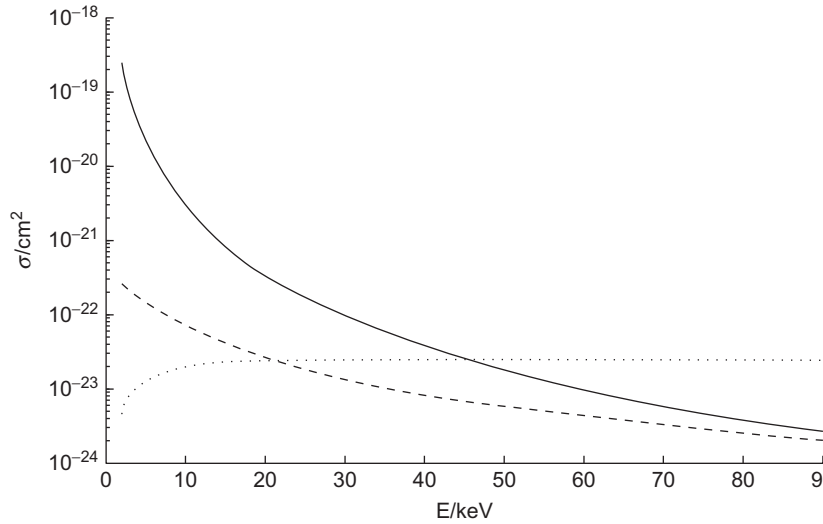

Figure 8 Cross sections for photoabsorption (—), coherent scattering (- -), and Compton scattering (· · ·) of high-energy photons from a unit cell of Al_2O_3 as a function of photon energy. (Berger et al., 1998).

Coherent scattering describes the correlated response of atomic electrons to an electromagnetic wave. As photon energy becomes comparable to and exceeds the binding energy of an electron, that electron ceases to contribute to the coherent response, so coherent cross sections decrease with photon energy. In addition, there is no significant shift in energy of the scattered photon. Cross sections for coherent scattering from dysprosium and PCA are given in Figures 4 and 8, respectively.

5. X-RAY INDUCED FLUORESCENCE SPECTROSCOPY (XRIF)

5.1 Density Measurements

X-ray induced fluorescence measurement of vapor-phase densities in metal-halide lamps was first attempted by Fohl et al. (1993). They reported having successfully measured iodine fluorescence signals, but they did not report iodine densities. Fohl et al. did not use photon energies high enough to detect the lanthanide rare-earth metals. The first reported densities measured with XRIF in a metal-halide lamp did not come until 2001 (Curry et al., 2001). Since then, XRIF has been used to measure densities of metal additives, iodine, and Hg in operating metal-halide lamps (Curry et al., 2003a,b; Nimalasuriya et al., 2007). More recently, XRIF has been used to measure equilibrium vapor pressures of metal-halide salts in vapor cells (Curry et al., 2011). All of this work has involved lighting industry scientists, including work done as part of the two Electric Power Research Institute-sponsored ALITE consortia that existed between 1995 and 2005 (ALITE, 2006). All of the cited measurements, except those by Fohl et al., were conducted at the Advanced Photon Source, Argonne National Laboratory because of the ideal source parameters that are available on Beamline 1-ID.

Beamline 1-ID combines an undulator and Si crystal double monochromator (Shastri et al., 2002) to produce a laser-like x-ray beam with high intensity, narrow bandwidth, wide tunability, low divergence, and small size. The beam photon energy can be tuned anywhere in the range between 50 keV and 130 keV with an energy resolving power of better than 600. A typical photon flux at the experiment is $\Phi = 10^{12}\ \mathrm{s}^{-1}$ with horizontal and vertical divergences of $\leq 10\,\mu\mathrm{rad}$.[6] Without focusing, the beam cross section is approximately 1 mm by 1 mm and polarization is >95% in the horizontal plane. The tunability of the beam photon energy makes it possible to observe atoms as heavy as thallium (90 keV) or to maximize the absorption cross section of lighter elements with photon energies as low as 50 keV.

[6] A 60 keV photon flux of $10^{12}\ \mathrm{s}^{-1}$ gives an average beam power of approximately 10 mW.

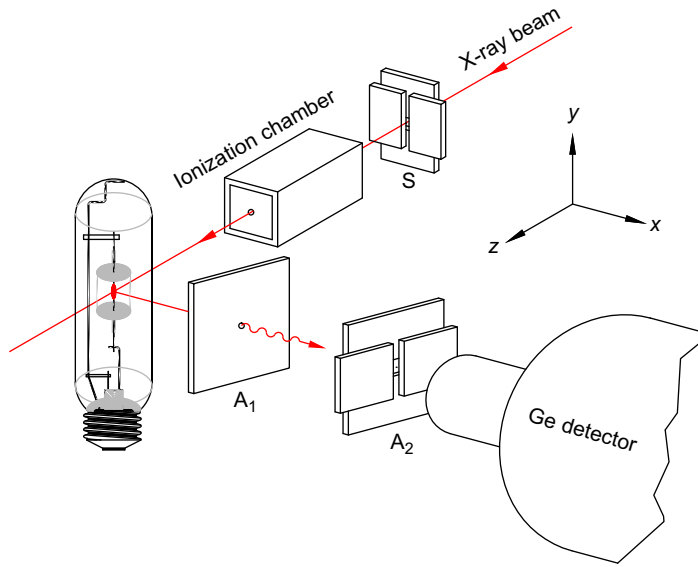

Figure 9 Apparatus for x-ray induced fluorescence measurements in a high-intensity discharge lamp, including a pair of crossed tungsten slits (S) and apertures (A_1 and A_2) defining the field of view of the detector. The coordinate system used in this chapter is also defined.

The tabletop arrangement for an XRIF measurement of densities in a metal-halide lamp is shown in Figure 9. A pair of crossed, electronically-adjustable tungsten slits (S) is used to eliminate any halo around the beam and can be used to reduce the beam size. (Halos arise from scattering by air molecules and windows, as well as imperfections in beamline optics.) Next, an atmospheric pressure nitrogen ionization chamber measures the photon flux transmitted by the slits. A small number of photons transiting the ionization chamber are absorbed or scattered by the nitrogen atoms, creating electron-ion pairs in the gas. A pair of electrodes collects the resulting current, which can be calibrated to determine absolute fluxes. Immediately following the ionization chamber is the test lamp, mounted on a five-dimensional translation stage that allows the lamp to be moved in the three orthogonal linear dimensions, as well as rotation around the two horizontal axes. Rotation is sometimes required to improve the vertical alignment of the lamp and arc tube.

The fluorescence signal induced by the x-ray beam in the lamp discharge is observed by a solid-state Ge detector. The detector consists of a cryogenically cooled Ge crystal across which a voltage is applied. When a photon is absorbed by the crystal, the electrodes collect the charge pairs created by the deposited energy and the resulting current pulse is amplified and fed to a pulse height analyzer. Ideally, the pulse

height is proportional to the energy of the absorbed photon. By processing a number of sequentially absorbed photons, a spectrum is constructed count-by-count. The energy scale for such a spectrum must be determined independently. ^{109}Cd, which produces an 88-keV γ ray and Ag characteristic x-ray fluorescence between 22 keV and 25 keV, has proved useful for this purpose.

Ge detectors typically have a flat response curve for a range of energies that extend from below 10 keV to about 90 keV, depending on the specific detector being used. The low energy cutoff is determined by the transmission of the window in front of the crystal, usually beryllium, sometimes polyimide. The detector response at high energy begins to decrease when the mean free path for photoelectric absorption becomes comparable to the crystal, and photons have a finite probability of passing through the crystal without interaction. A thicker crystal can extend this range but also reduce the maximum count rate because it increases the "dead time," or time required to collect the charge created by a photon. Dark current is greatly reduced by keeping the crystal at cryogenic temperatures.

Limitations of a finite crystal size, a finite pulse processing time, and crystal imperfections lead to spectral artifacts, limited spectral resolution, and noise (Knoll, 2000). Sometimes, so-called escape peaks can be seen in fluorescence spectra, and care must be taken to avoid misidentification. Escape peaks are created when some of the energy of the absorbed photon escapes the crystal as Ge K-shell fluorescence. A count is registered at an energy equal to the difference between the absorbed photon energy and the Ge fluorescence energy, instead of the absorbed photon energy. Pulse processing time is adjustable, with longer times producing better energy resolution but longer dead times. For high count rates, corrections must be made to account for dead time (Knoll, 2000). A typical energy resolution is a couple of hundred electronvolts.

The Ge detector is aligned to observe fluorescence emitted along the direction of polarization of the beam. This orientation suppresses scattering from the vapor into the detector. The detector's field of view is defined by two apertures, one at the detector and one close to the lamp. The detector aperture is formed by a pair of crossed, adjustable tungsten slits, typically open several millimeters wide. The lamp aperture is placed as close to the beam as possible, allowing just enough room for the lamp over its full range of movement. This aperture is typically a submillimeter circular hole in a 2-mm-thick tungsten plate. Because the lamp aperture is much smaller than the detector aperture, the field of view of the detector can be approximated as a projection of the detector aperture through the pinhole of the lamp aperture. This projection is shown in Figure 10 for some typical dimensions. The intersection of the field of view with the beam determines what will be referred to as the viewing volume, i.e., the volume from which fluorescence is collected by the detector. Typically, this volume is approximately 1 mm by 1 mm by 1 mm, although it has been

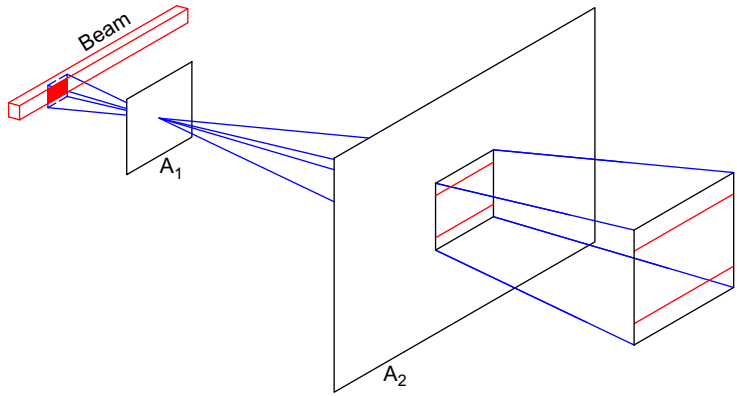

Figure 10 Fluorescence collection optics and x-ray beam. The detector (represented by a circle) sits to the right of A_2. The field of view of the detector can be approximated by projecting A_2 back through the pinhole A_1. The intersection of the field of view with the x-ray beam determines the viewing volume V, the region of space from which XRIF is observed by the detector.

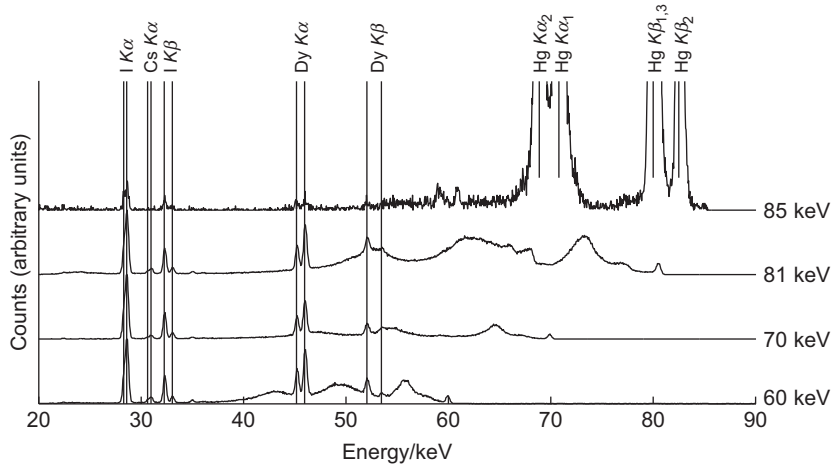

Figure 11 Fluorescence spectra acquired from a metal-halide lamp with different beam photon energies.

substantially less on occasion because of a smaller beam size. Obviously, the axis of the field of view must be aligned to intersect the beam. Spatially resolved XRIF spectra are obtained by step scanning an operating lamp in the $x - y$ plane.

A few typical spectra are shown in Figure 11 for beam photon energies of 60 keV, 70 keV, 81 keV, and 85 keV. The data were acquired from a

lamp containing Hg, DyI_3, and CsI (Curry et al., 2003b). In all the spectra, narrow fluorescence lines from I and Dy are seen. In the spectrum excited by 85 keV, very strong fluorescence lines from Hg are also present. The Hg K-edge occurs at 83.102 keV; the lower beam energies are insufficient to excite Hg. The considerably larger magnitude of Hg fluorescence relative to Dy and I is mostly due to the much greater abundance of Hg, 2 to 3 orders of magnitude greater than I. Additionally, the photoabsorption cross section for Hg is about 4 times larger than that for I. Not labeled, but also present in each spectrum are fluorescence lines from Cs. The $K\alpha$ lines for Cs appear between the I $K\alpha$ and I $K\beta$ peaks and are most apparent in the spectrum excited by 60-keV photons. All of these fluorescence lines appear at the same energy regardless of the excitation energy. Weak escape peaks originating from the Hg $K\alpha$ lines appear near 59 and 61 keV, the energies of Hg $K\alpha_1$ and $K\alpha_2$ minus the energies of Ge $K\alpha_1$ and $K\alpha_2$.

Scattered photons are also apparent in each of the spectra. The narrow peaks at each of the beam photon energies are due to coherent scattering. The broad, multipeaked features that extend over many kilo-electronvolts are the result of Compton scattering from the arc tube. Figure 12 shows a cross section of the arc tube cylinder and the four possible paths by which photons can scatter into the detector with only two scattering events. (Single Compton scattering from the arc tube into the detector cannot occur because the field of view, beam, and arc tube do not all overlap at

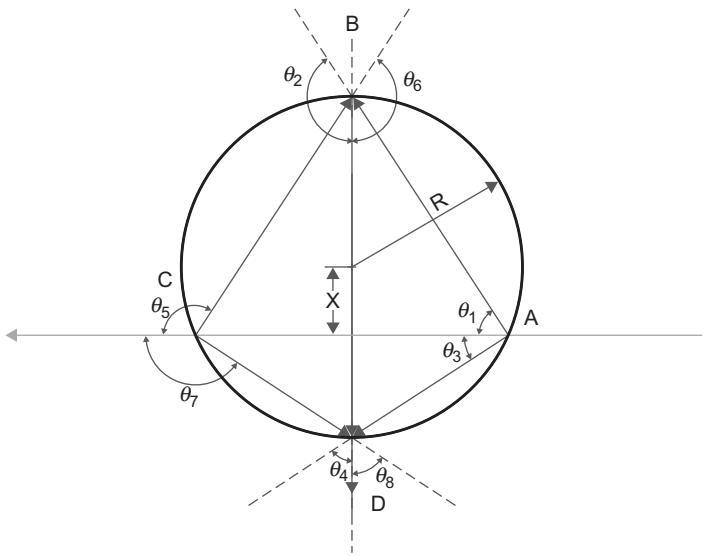

Figure 12 The four possible paths involving double scattering from a cylindrical arc tube that can lead to a beam photon entering the detector.

any point in space.) One path involves scattering from point A through angle θ_1 followed by scattering from point B through angle θ_2; another from point A through θ_3 followed at point D through θ_4; another from points C and B through θ_5 and θ_6, respectively; and the last from points C and D through θ_7 and θ_8, respectively. The final photon energy after such sequential scatters is

$$E_{ij} = \frac{E_0}{[1+\alpha(1-\cos\theta_i)]\left[1+\alpha(1-\cos\theta_j)\right]} \tag{4}$$

where the cosines of each of the eight angles, as well as x and R, are defined in Figure 12. Thus,

$$\begin{aligned}
\cos\theta_1 &= \frac{1}{\sqrt{2}}\sqrt{(1-\rho)} \\
\cos\theta_2 &= -\frac{1}{\sqrt{2}}\sqrt{(1+\rho)} \\
\cos\theta_3 &= \frac{1}{\sqrt{2}}\sqrt{(1+\rho)} &&= -\cos\theta_2 \\
\cos\theta_4 &= \frac{1}{\sqrt{2}}\sqrt{(1-\rho)} &&= \cos\theta_1 \\
\cos\theta_5 &= -\frac{1}{\sqrt{2}}\sqrt{(1-\rho)} &&= -\cos\theta_1 \\
\cos\theta_6 &= -\frac{1}{\sqrt{2}}\sqrt{(1+\rho)} &&= \cos\theta_2 \\
\cos\theta_7 &= -\frac{1}{\sqrt{2}}\sqrt{(1+\rho)} &&= \cos\theta_2 \\
\cos\theta_8 &= \frac{1}{\sqrt{2}}\sqrt{(1-\rho)} &&= \cos\theta_1
\end{aligned}$$

with $\rho = x/R$. Only three Compton peaks are produced because E_{12} and E_{78} are always the same. Figure 13 plots the energies of the 3 peaks for $E_0 = 70\,\text{keV}$ as a function of ρ, and Figure 14 plots the Compton-shifted energies as a function of E_0 for $\rho = 0$. These calculations do not take into account the broadening of the energy distribution of the scattered photons arising from the kinetic energy distribution of the scattering electrons and from the range of possible scattering angles due to the finite field of view of the detector. Figure 11 shows that the Compton peaks are quite broad compared with fluorescence lines, with each Compton peak having a different shape. It can also be seen that increasing the beam energy is not very

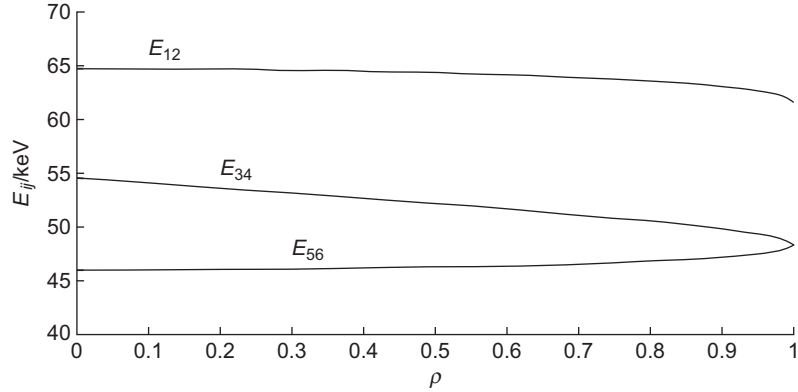

Figure 13 Final energies for 70-keV photons doubly scattered from a cylindrical arc tube along the paths shown in Figure 12 as a function of ρ, the distance between the beam and arc axis, normalized by the radius of the arc tube.

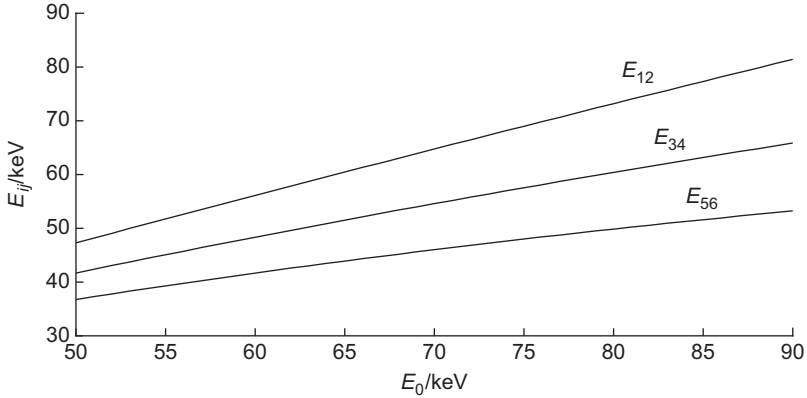

Figure 14 Final energies for photons doubly scattered from a cylindrical arc tube along the paths shown in Figure 12 as a function of beam photon energy E_0 for $\rho = 0$, the beam intersecting the arc axis.

effective in reducing interference with fluorescence lines, but just spreads the Compton peaks over a wider spectral range. Fortunately, the breadth of the Compton features is a considerable help in separating scattering from characteristic fluorescence.

The count rate C observed by the detector within a given K-shell fluorescence line $K\eta$ is

$$C_Z^{K\eta} = \frac{\Phi}{A}\,\sigma_Z^K(E_0)\,Y_Z^K\,B_Z^{K\eta}\,\frac{\Omega}{4\pi}V\,T(E_0)\,T(E_Z^{K\eta})\,Q_d(E_Z^{K\eta})\,n_{\Sigma Z} \tag{5}$$

where Φ is the incident photon flux, A is the beam cross-sectional area, $\sigma_Z^K(E_0)$ is the K-shell photoabsorption cross section for an atom of atomic number Z at the energy of the incident beam photons E_0, Y^K is the K-shell fluorescence yield, $B^{K\eta}$ is the branching fraction for the K-shell η line, Ω is the solid angle observed by the detector, V is the viewing volume (see Figure 10), T is the transmission of x rays of fluorescence energy $E_Z^{K\eta}$ through the arc tube, or other, wall, Q_d is the detector efficiency, and $n_{\Sigma Z}$ is the number density defined by Equation 1.

Equation (5) allows the determination of elemental densities $n_{\Sigma Z}$ from the intensity of observed fluorescence lines. The values for the atomic parameters σ, Y, and B have been discussed in Section 4. The beam flux density Φ is continuously measured during the experiment by the ionization chambers as the beam passes through them. Transmission of beam and fluorescence photons through the arc tube wall is determined from cross sections of the relevant materials. Transmission through 1 mm of fused silica and transmission through 1 mm of PCA are shown in Figure 15 as a function of energy. Attenuation of beam photons is typically small because their energy is usually greater than 60 keV. Attenuation of fluorescence photons, however, can be more severe and gets larger as the element being observed gets lighter and the fluorescence energy decreases. There is no hard cutoff for what can be observed, but as the fluorescence photon energy decreases, the measurement signal-to-noise ratio decreases. In addition, the correction factor for finite transmission becomes larger and more sensitive to the exact thickness and density of the arc tube or cell wall. It is difficult, in practice, to observe elements with atomic numbers less than $Z = 40$ inside the types of arc tubes and cells being used and

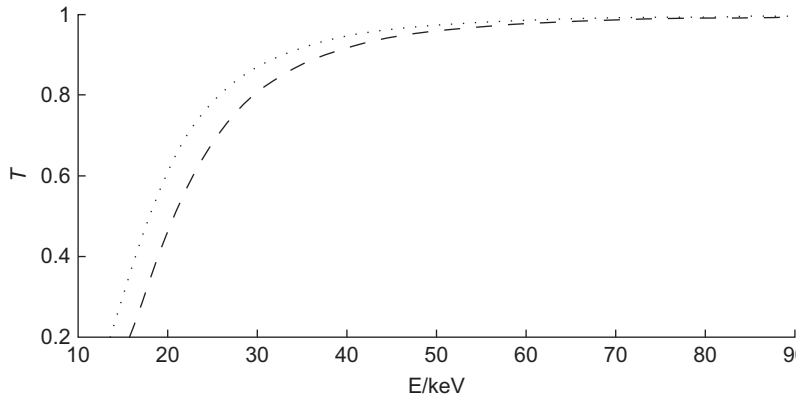

Figure 15 Transmission through 1 mm of PCA (- -) and fused silica (· · ·) as a function of photon energy, not including scattering.

at the densities typical of metal additives in MH-HID lamps. This precludes observation of the important additives sodium and scandium, or the mercury substitute zinc in Hg-free lamps.

The transmission curves in Figure 15 reflect attenuation due to photoabsorption only. An additional attenuation results from coherent and Compton scattering. This component must be calculated for each situation because a significant fraction of scattered photons is scattered at such small angles that the event is irrelevant. The fraction of photons scattering from 1 mm of PCA is shown by the top curve in Figure 16. This is an upper limit on the attenuation due to scattering. The lower curve gives the fraction of photons scattered by Compton scattering only. The atomic form factor concentrates coherent scattering in the forward direction, while the incoherent scattering function goes to zero in the forward direction (Curry, 2010). Consequently, the Compton cross section gives a reasonable first approximation for attenuation by scattering, which is increasingly accurate with increasing energy.

The measured value C is the count rate in a fluorescence line. Lineshapes for spectra measured by a Ge detector depend on a number of factors including processing time and photon energy (Knoll, 2000). As a result, C may be just as accurately obtained by straight integration as by line fitting if care is taken to integrate over the entire line and to adequately account for the baseline. Figure 17 demonstrates how this can be done using the Dy $K\alpha_1$ and $K\alpha_2$ doublet blended with a Compton feature as an example. The background, including the Compton signal, is determined by fitting a single second-order polynomial to the noncontiguous baseline segments on each side of the fluorescence line. These regions are indicated

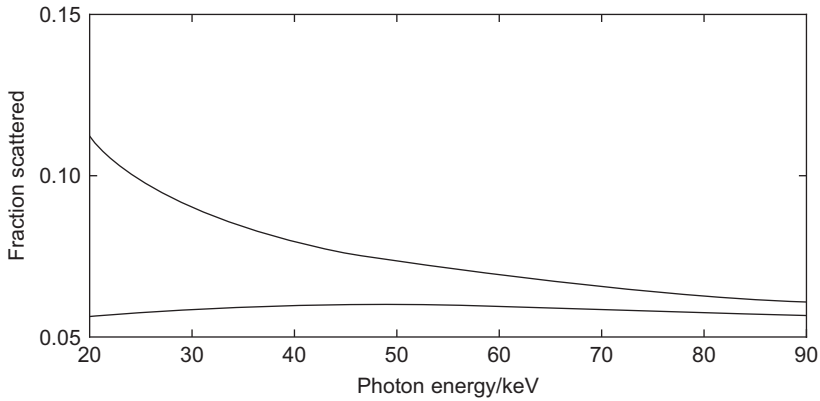

Figure 16 Fraction of photons scattered by 1 mm of PCA as a function of photon energy. The top curve includes both Compton and coherent scattering. The bottom curve includes only Compton scattering.

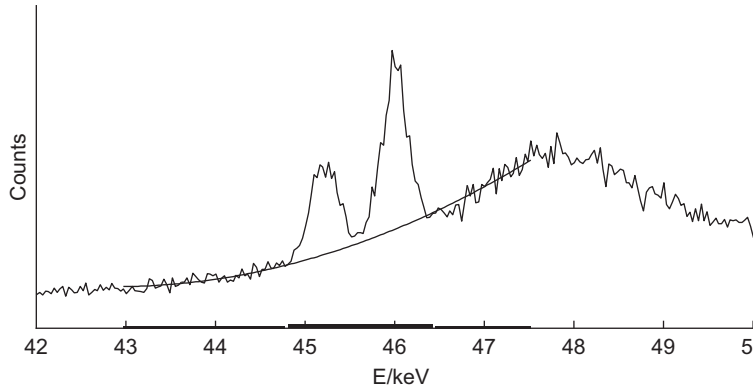

Figure 17 Finding the baseline under Dy $K\alpha$ lines. The thin horizontal lines indicate the ranges over which a second-order polynomial is fit to the baseline on each side of the fluorescence peaks. The thick horizontal line indicates the range over which the spectrum is integrated after the fitted baseline (shown) is subtracted.

in the figure by thin horizontal black lines. Contributions from Compton scattering, as can be seen in Figure 11, change slowly over the width of most fluorescence features. The fitted background is subtracted from the entire spectral region, and the line feature is integrated. The region of integration is shown in the figure by a thick horizontal black line. The regions of integration and baseline fitting can be chosen individually for each line but should remain the same across all spectra. The statistical uncertainty σ_C in the number of counts can be estimated as

$$\sigma_C = \sqrt{p\,\sigma_{\text{fit}}^2 + q} \tag{6}$$

where p is the number of points over which the integration is performed, σ_{fit} is the rms deviation of the data from the fit in the fitting regions, and q is the number of counts in the line integral. The first term in the radical is an estimate of the statistical error due to fluctuations in the true baseline, whereas the second term represents shot noise in the line integral. For Figure 17, the measured density is 6.7×10^{15} cm^{-3} and the statistical uncertainty is about 2%. The data were acquired with an integration time of 600 seconds.

The concept of two separable geometric parameters Ω and V is only an approximate way of representing geometric effects in Equation (5). In fact, Ω is a complicated function of position and should be integrated over the volume V. Nevertheless, one can deal with these parameters in an exact way by comparison of fluorescence signals from a lamp to fluorescence signals from a known standard. Fused silica cells or PCA cells filled with

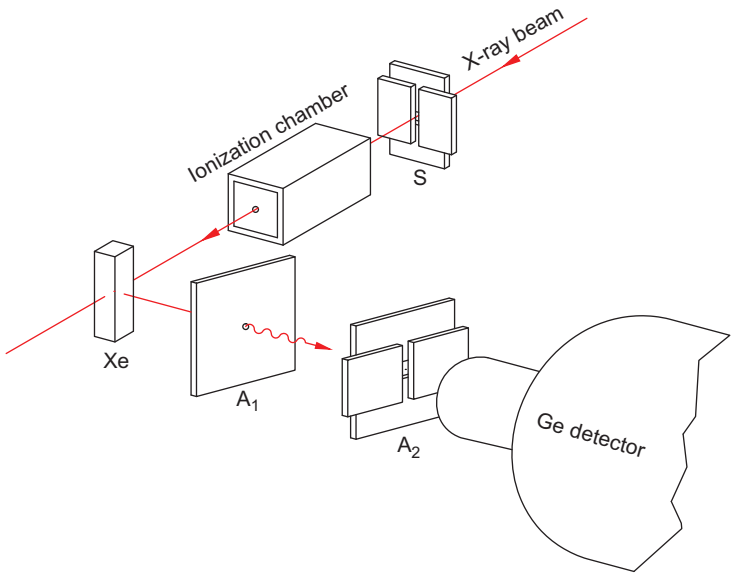

Figure 18 Schematic of x-ray induced fluorescence measurements in a gas-filled calibration cell.

a comparable density of Xe have proven to be useful for this purpose. The measured lamp is simply replaced by a calibration cell as in Figure 18, and a fluorescence spectrum is acquired in the same manner as for the lamp. A ratio of counts then leads to an absolute density

$$n_{\Sigma Z} = \frac{C_Z^{K\eta}}{C_{Xe}^{K\alpha}} \frac{\Phi_{Xe}}{\Phi_Z} \frac{\sigma_{Xe}^K(E_0)}{\sigma_Z^K(E_0)} \frac{Y_{Xe}^K}{Y_Z^K} \frac{B_{Xe}^{K\alpha}}{B_Z^{K\eta}} \frac{T_{cell}(E_0)}{T_{lamp}(E_0)} \frac{T_{cell}(E_{Xe}^{K\alpha})}{T_{lamp}(E_Z^{K\eta})} \tag{7}$$

if the Xe $K\alpha$ lines are used for calibration and the detector efficiency is flat over the range of energies considered.

Typically, lamp measurements are entirely automated, and the lamp position will be stepped through a predetermined matrix of positions such that the desired spatial range is covered. Once the lamp has settled at each position, data acquisition is triggered and persists for a predetermined period, usually for a period in the range of 10–100 seconds. At the end of this period, a time-integrated spectrum and a time-integrated incident flux are electronically saved along with all other relevant measurement parameters. Though changes in the beam intensity over tens of seconds are generally quite small, any changes that do occur are automatically taken into account because the flux signal and fluorescence signal are integrated simultaneously.

Some examples of XRIF measurements of density distributions in a metal-halide lamp appear in Figure 19. These include essentially complete spatial distributions of the principle components of a lamp containing 16 mg of Hg, 6.8 mg of DyI_3, 1.2 mg of CsI, and 12 kPa (90 Torr) of Ar (Curry et al., 2003b). The only component not measured was Ar because the K-shell fluorescence lines of Ar have energies of less than 3.2 keV,

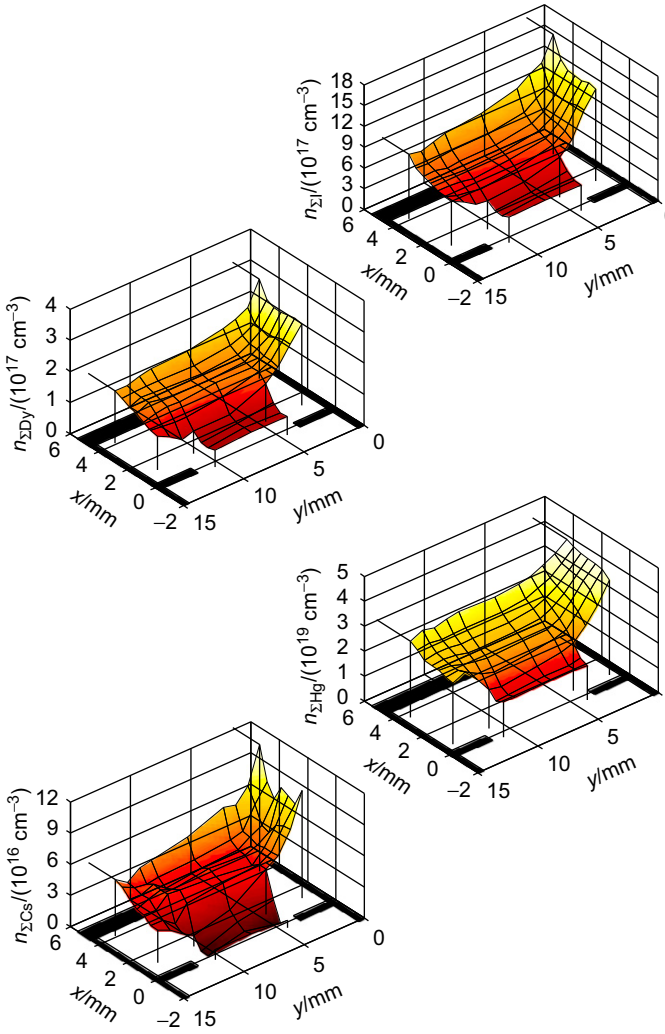

Figure 19 Density distributions measured by XRIF in a metal-halide high-intensity discharge lamp containing 16 mg of Hg, 6.8 mg of DyI_3, 1.2 mg of CsI, and 12 kPa (90 Torr) of Ar (Curry et al., 2003b). The coordinate system is defined in Figure 9.

too low to be observed through an arc tube. It is worth noting that this lamp was equipped with an outer glass jacket in addition to a translucent ceramic arc tube. The x-ray transmission of the jacket must be taken into account but represents no serious impediment to XRIF measurements.

The measurements in Figure 19 were acquired at the vertices of the grid superposed on the data. The spatial resolution for each measurement was $\Delta x \approx 1\,\text{mm}$, $\Delta y \approx 1\,\text{mm}$, and $\Delta z \approx 1$ mm. Measurements were not acquired over the full range of $-x$ because of the assumption of cylindrical symmetry. In the figure, the positions of the electrodes and arc tube walls are shown in blue on the $n_{\Sigma Z} = 0$ plane. The arc tube was operated vertically with the bottom of the arc tube at $y = 0$ on the right side of each graph. The range of densities measured in this lamp extends from 1×10^{16} to 5×10^{19} cm^{-3}.

The density of Hg is the largest of any constituent of the arc, more than an order of magnitude larger than the second most abundant constituent, iodine. Cs has the smallest density of all. Its presence in the arc is primarily to broaden the main current channel. Two properties of Cs help achieve this goal. First, the ionization potential of Cs is lower than that of Dy. Therefore, Cs is ionized at larger radii than Dy. Second, resonance radiation produced by Cs in the core is heavily self-absorbed, thereby heating the vapor by collisional de-excitation wherever atomic Cs exists. Such broadening or fattening of the arc is necessary in lamps containing strong multiline radiators like the rare earths. Metals like Dy are so efficient at producing and emitting radiation that they cool the vapor in the core of the arc. In order to maintain sufficient ionization for a given input power, the volume of the current channel must decrease. If the current channel becomes too thin, magnetic instabilities begin to make the arc precess slowly about the arc axis like a vertical jump rope. Such an effect is highly detrimental to lamp appearance and performance and is avoided by adding a small amount of Cs or a similar resonance radiator.

5.2 Temperature Distributions

The primary contributor to the shapes of the density distributions in Figure 19 is the temperature variation in the arc. As the measurements make clear, Hg is the dominant component. It exists almost completely in monatomic form. Thus, the relationship of the Hg density $n_{\Sigma\text{Hg}}$ to the vapor temperature T can be described by the Ideal Gas Law

$$p = n_{\Sigma\text{Hg}}(\vec{r})kT(\vec{r}) \tag{8}$$

where p is the total vapor pressure, $\vec{r}$ is spatial location, and k is Boltzmann's constant. Spatial variation does occur in the total vapor pressure, either because of convective flow or in the form of acoustic waves driven

by the alternating current in the arc. Pressure variations associated with convective flows are too small to be of significance in this context (Lowke, 1979; Zollweg, 1978). Pressure variations from acoustic waves are of order 1% and occur at frequencies exceeding 10 kHz (Baumann et al., 2009; Dreeben, 2008). The time-averaged vapor pressure is constant and spatially homogeneous in a normally operating lamp. As a result, the spatially dependent arc temperature may be determined if the Hg density and vapor pressure are both known

$$T(\vec{r}) = \frac{p}{kn_{\Sigma \mathrm{Hg}}(\vec{r})}. \tag{9}$$

Alternatively, the temperature of core of the arc can be determined from optical emission measurements (Karabourniotis, 1986). The spatially independent vapor pressure is determined from the combination of a local Hg density and the corresponding local temperature. Then, spatially comprehensive temperature maps can be obtained from Hg density distributions. Some examples can be found in Curry et al. (2005) and Curry et al. (1998). Using a design operating pressure of 10^6 Pa (10 atm), the Hg density shown in Figure 19 is converted to the temperature distribution in Figure 20. Optical determination of core temperatures in ceramic lamps has been discussed in the literature (Karabourniotis & Drakakis, 2002) but was not applied to this lamp.

The density distributions in Figure 19 and the temperature distribution in Figure 20 show that the arc is hottest in the core where the electrical

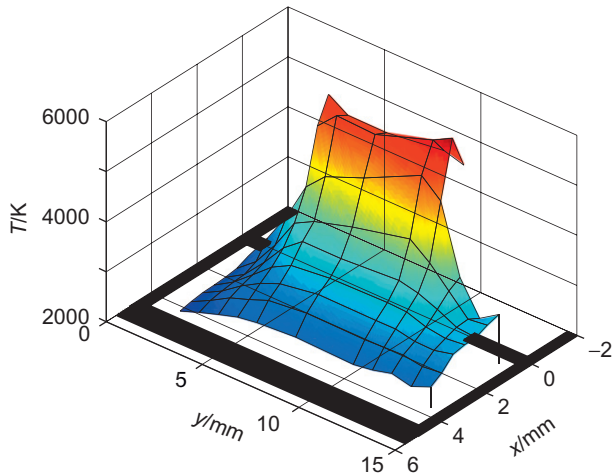

Figure 20 Temperature distribution derived from the Hg density distribution in Figure 19 using a design operating pressure of 10^6 Pa (≈10 atm). The coordinate system is defined in Figure 9.

current provides direct heating of the gas. Somewhat less apparent is the general trend of increasing temperature from bottom to top as the heated gas rises. Within a couple of hundred microns or less of each electrode, the temperature distribution is determined by different factors. The convergence of the current to meet the electrode tip produces a relatively rapid increase in the gas temperature, but the temperature of the tungsten electrode tip itself cannot exceed the melting point of tungsten. These two effects produce a local maximum in excess of 5000 K in front of each electrode, followed by a steep drop to 3683 K or less at the tip. These near-electrode effects are more clearly seen from high-resolution x-ray imaging of the Hg density (Curry et al., 1998) than in the lower resolution XRIF measurements.

Temperatures in the core of the arc are typically in the range of 4500–6000 K, depending on the lamp. Outside the core, the temperature must drop quickly to the maximum operating temperature of the arc tube wall material, 1100–1400 K. The shape of the temperature drop depends greatly on the type and density of radiating species in the core. If radiation trapping is sufficiently large, the temperature distribution becomes fatter and most of the temperature drop occurs in the outer third of the discharge radius. This leads to very large temperature gradients near the wall. Another important area for lamp operation is the area below the bottom electrode. This is often the coolest part of the arc because the cooler, heavier gas sinks to the bottom. The greater densities in this region are clearly seen in the distributions of Figure 19. The metal-halide salts also reside in this region, and the temperatures here determine the equilibrium vapor pressures of the salts.

Temperatures throughout the core of the arc can be obtained directly from optical emission measurements. However, optical emission is of little help for regions outside the core where the temperature is too low to produce significant emission in the visible. Thus, comprehensive temperature maps, as in Figure 20, are practically impossible to obtain by any method other than x rays. Such complete maps are essential to determining and understanding the chemical distribution in the arc. Although the dark region of the lamp contributes no visible radiation to the lamp output and would appear to be of little interest, the molecular species that exist in these regions can have a substantial impact on infrared radiation transport and do play an important role in the transport of metal additives into the core. The latter can be a determining factor in the luminous efficacy and color rendering.

5.3 Chemical Partitioning

As pointed out earlier in this chapter, the densities shown in Figure 19 and those obtained by XRIF are elemental densities, a summation over all atomic and molecular species. In the lamp of Figure 19, there are only five

elements present, the four shown and Ar. What are not shown are the 10 or more significant molecular species into which these elements may combine over the range of temperatures that occur in the lamp. A few of these species may be detected by optical means. Given a temperature distribution, densities of a few more may be inferred from optical measurements. Alternatively, one may infer all of the species densities by combining the elemental densities with the corresponding temperature map. For a system in thermal equilibrium, the partitioning of elements across different species is a function only of the elemental densities present, the equilibrium temperature, and the thermodynamic parameters of all possible atomic and molecular species. Although lamp discharges are not in full equilibrium, a local chemical equilibrium *is* achieved. The densities of individual molecular species are those that are mutually consistent and minimize the free energy of the system. Those densities can be determined for a given set of input parameters by an iterative calculation (Cruise, 1964). As an example, the chemical distribution for a system containing a Hg number density of 3×10^{19} cm^{-3}, a DyI_3 density of 1×10^{17} cm^{-3}, and a CsI density of 5×10^{16} cm^{-3} has been calculated as a function of temperature and is shown in Figure 21. The shift from heavy molecular species at the lower temperatures to lighter molecular species at increasing temperatures, then to atoms, and eventually to electrons and ions at the highest temperatures is evident.

In contrast to Figure 21 where the elemental densities are held constant, the elemental densities and temperature in a lamp will be a function of position. An example of the chemical partitioning in a real lamp appears

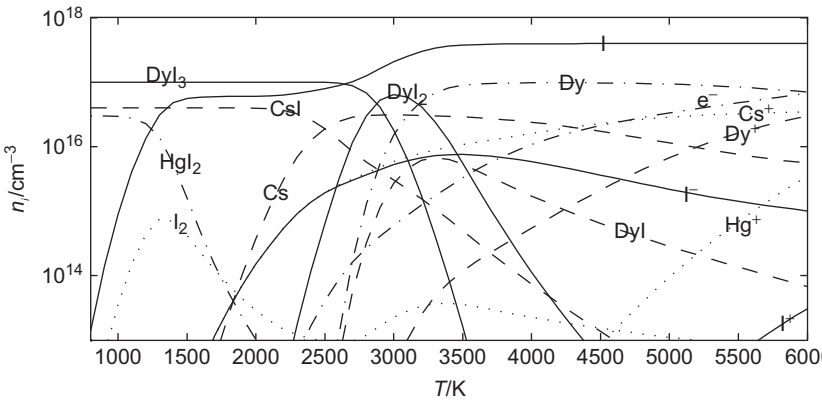

Figure 21 An example of equilibrium molecular densities as a function of temperature for a system containing a Hg number density of 3×10^{19} cm^{-3}, a DyI_3 number density of 1×10^{17} cm^{-3}, and a CsI number density of 5×10^{16} cm^{-3}. (Curry et al., 2003a).

in Figure 22 (Curry et al., 2003a). These are the equilibrium molecular densities in the midplane of the arc calculated from the measured elemental densities in Figure 19 and the temperature distribution in Figure 20. This figure illustrates the complexity of the chemistry of a metal-halide high-intensity discharge, even though only the major Dy species are plotted. It is interesting to note the localization of certain molecular species like DyI_2. Given sufficient atomic data, the radiative output of the discharge could be calculated from the information presented in this graph. Practically, the calculation of radiation production and transport remains a challenge because of the large size of the parameter space and the nonlocal nature of some portion of the radiation transport.

The measurements and calculations behind Figure 22 are a way to determine a comprehensive picture of the chemical distribution in a metal-halide lamp. The weakness of such calculations is the lack of experimental measurements of thermodynamic parameters for many of the species of interest, at least at the temperatures relevant to lamps. Free energies can, in principle, be calculated from basic principles and spectroscopic data in a straightforward way (Chase, 1998). However, the key to accurate results at higher temperatures lies in the appropriate treatment of the lowering of ionization energy for each species. This is where different calculations begin to diverge, and experimental measurements are needed to distinguish the most accurate methods. In Section 5.5, we will discuss the use

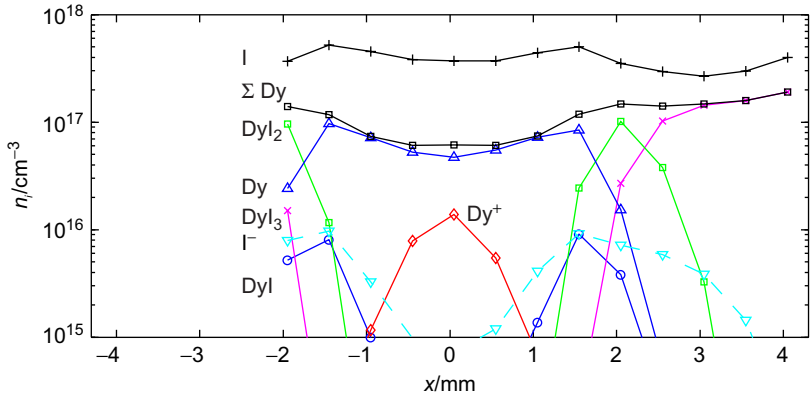

Figure 22 Equilibrium molecular densities calculated from measured elemental densities and the inferred temperature distribution in the mid-plane of a metal-halide lamp. The elemental densities are from Figure 19 and the temperature distribution is from Figure 20. The total Dy density (black, □) is given along with the major Dy molecular species DyI_3 (×), DyI_2 (gray, □), DyI (○), Dy (△), and Dy^+(◇). Also shown are monatomic I (+) and the negative ion I^- (▽) (Curry et al., 2003a). The coordinate system is defined in Figure 9.

of XRIF to measure some of the needed basic thermochemical data. Without experimentally confirmed data, thermochemical calculations can still be useful in clarifying the relative importance of different species and processes.

5.4 Demixing

An interesting phenomenon that can be observed in some metal-halide high-intensity discharge lamps is demixing of the metal additives (Dakin & Shyy, 1989; Fischer, 1976; Stormberg, 1981). The impact of demixing on lamp performance is deleterious. Severe cases that are immediately obvious to any observer may produce color and brightness variations along the length of a lamp (Nimalasuriya et al., 2007). Less severe demixing may not be apparent to the naked eye but still have a negative impact on luminous efficacy and color rendering.

Demixing refers to the segregation of minority constituents to different parts of the discharge. Molecular and atomic species are, of course, segregated simply because certain molecular species are thermodynamically preferred at certain temperatures, and a wide range of temperatures exists within a high-intensity discharge lamp. Demixing is the much more comprehensive spatial segregation of an elemental constituent that extends across all of the atomic and molecular forms in which that element may be found. Thus to observe demixing, the densities across all such species must be measured. It is also necessary to measure the overall density of the vapor because demixing is a relative change in density. Large changes in absolute density are always present for all elements in a high-intensity discharge because of the large range of temperatures. Demixing has a much smaller impact on absolute densities than do temperature variations. The most obvious way of observing demixing is to look at the so-called mixing ratios (Dakin et al., 1989; Shaffner, 1971), that is, the ratios of the elemental densities to the Hg density, the latter being an excellent approximation to the overall vapor density. The mixing ratios are independent of chemical partitioning and of the overall density variation of the vapor. Spatial variations in the mixing ratios represent demixing. XRIF, as discussed already, directly measures the elemental densities required to determine the mixing ratios, something difficult to achieve with other methods.

Mixing ratios for Dy, Cs, and I obtained from the data in Figure 19 are shown in Figure 23. These plots give the radial variations of the mixing ratios in the midplane of the arc, along with the temperature profile (Figure 20). Radial demixing is evident for the metal additives Dy and Cs, being most pronounced for the latter. On and near the discharge axis, the metal atoms have been significantly depleted. A depletion of this kind generally reduces luminous efficacy, simply because there are fewer

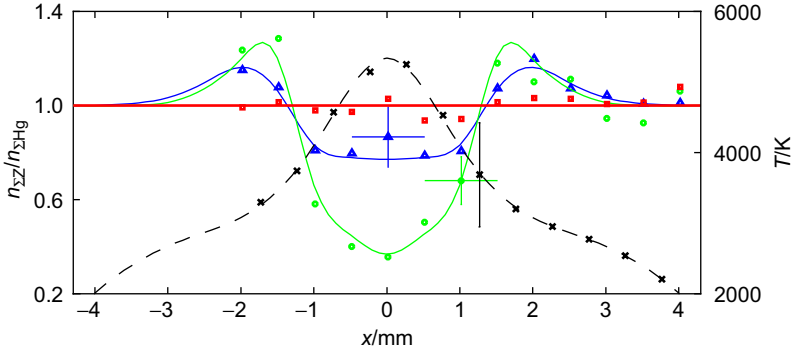

Figure 23 Mixing ratios in a ceramic metal-halide lamp for Dy (△), Cs (○), and I (□), as well as the temperature distribution (×) obtained from the data in Figure 19 and an estimated lamp pressure of 10^6 Pa. The ratios have been normalized so that their asymptotic value at the wall is 1. The coordinate system is defined in Figure 9.

radiators present. Outside the core near $|x| = 2\,\text{mm}$, there is a relative enhancement in the mixing ratio of both Dy and Cs as compared with the asymptotic value at the wall. I, on the other hand, shows little or no demixing.

The origin of demixing is the differences in diffusion velocities for different atomic and molecular species and the range of temperatures present in a high-intensity discharge. Two principal classes of demixing are referred to as radial demixing and axial demixing. The former involves radial transport velocities, whereas the latter involves both radial and axial (convection) transport.

The radial depletion seen in Figure 23 can be explained by considering the different types of radial transport at work. Considering Dy in Figure 22 near the axis as an example, singly ionized dysprosium Dy^+ has a density maximum on axis and diffuses away from the axis due to that density gradient. Dy, DyI, and DyI_2 have a minimum on axis and diffuse toward the axis. In steady state, the net transport rate is zero and the inflow of neutral molecules must balance the outflow of the ion

$$\Sigma_i D_i \nabla n_i(\vec{r}) = -D_+ \nabla n_+(\vec{r}) \tag{10}$$

where the summation is over all the neutral particles i, D is the diffusion coefficient, and n_+ is the ion density. If the diffusion coefficients of all species are the same and the spatial dependence of the coefficients is ignored, this leads to

$$n_{\Sigma\text{Dy}}(r) = n_{\Sigma\text{Dy}}(0). \tag{11}$$

In other words, the dysprosium elemental density is independent of r and there is no demixing.

When the diffusion coefficients are different for different species, the picture changes. The diffusion coefficient for the Dy ion is generally much larger than the coefficients for the neutral particles because of the presence of the radial ambipolar electric field. Such a field arises in finite-sized plasmas in order to balance the loss of positive charge and negative charge. The lighter, more mobile electrons escape at a faster rate than the more massive positive ions, creating a space-charge electric field. The field grows until it is large enough to balance the loss of positive and negative charges by speeding up the loss of positive charges and slowing down the loss of negative charges. When ion and electron temperatures are the same, the ambipolar field has the effect of doubling the diffusion coefficient for positive ions over its value in the absence of a field (Krall & Trivelpiece, 1986).

The larger diffusion coefficient for positive ions increases the transport rate of ions away from the axis resulting in a relative depletion of the elemental density near the axis if an element is ionized there. The solution of Equation (10) is then

$$n_{\Sigma \mathrm{Dy}}(r) = n_{\Sigma \mathrm{Dy}}(0) + n_{+}(0) - n_{+}(r). \tag{12}$$

The elemental density of Dy is clearly a function of r if $n_{+}(r)$ is. In addition, it is also clear that the elemental density on axis is less than the elemental density at the wall ($r = R$)

$$n_{\Sigma \mathrm{Dy}}(R) > n_{\Sigma \mathrm{Dy}}(0) \tag{13}$$

as long as the ion density on axis $n_{+}(0)$ is greater than the ion density at the wall $n_{+}(R)$. This simplified analysis does not take into account the change in temperature between the axis and the wall, nor the differences in diffusion coefficients for different molecules, but those effects do not qualitatively change the conclusions drawn.

The extent of ambipolar depletion experienced by an element increases with ion density on axis, with the result that more easily ionized species will see a greater level of demixing. Accordingly, Cs having an ionization potential 35% lower than Dy exhibits a greater level of depletion on axis. Iodine, with an ionization potential 75% larger than Dy, shows very little or no depletion on axis.

Both Dy and Cs, in addition to exhibiting depletion on axis, show a local maximum in their mixing ratios just outside the core of the arc. This feature is not explained by the reasoning in the preceding paragraphs, nor has such a feature been previously observed. Curry et al. (2003a)

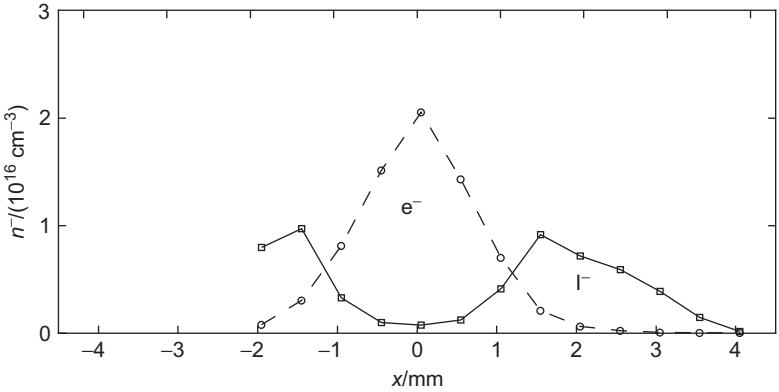

Figure 24 Distribution of negative charge corresponding to the densities and temperatures in Figure 23. The coordinate system is defined in Figure 9.

calculated the chemical equilibrium from their measured elemental densities and temperatures and found that the distribution of negative charge was as shown in Figure 24. The negative charge in the core is dominated by electrons, but off axis, where the temperature begins to drop, the negative charge consists primarily of I^-, negative iodine ions. The iodine ions do not have the light mass of the electrons; their mass is only slightly smaller than that of Dy and Cs ions. Therefore, the ambipolar field must quickly disappear where the negative charge becomes dominated by I^-, and so must the excess transport that leads to depletion. A detailed explanation of the observed maxima remains to be provided.

Axial demixing involves the radial diffusion mechanisms described earlier but also involves axial convective flow. Axial demixing can often be observed in lamps for which convective and radial diffusion velocities are comparable. A major convective cell that rises along the axis and falls along the arc tube wall circulates the mercury vapor and entrained additives axially. At the same time, radial diffusion transports constituents between the upward and downward flowing parts of the convective cell. If radial transport is faster in the outward direction than the inward, and comparable to convective transport, constituents riding the upward flowing vapor on axis will short-circuit the convective cell by diffusing outward to the downward flowing vapor before they reach the top (see Figure 25). This leads to a steady state in which the constituents subject to strong radial depletion will also show depletion at the top of the arc, whereas elements less subject to radial demixing are relatively more abundant there. Axial demixing is considerably reduced if the convective velocity is either much smaller than or much larger than radial diffusion velocities. Fischer (1976) showed that there is a convective velocity for

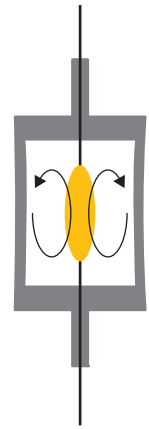

Figure 25 Typical convective flow in an HID lamp.

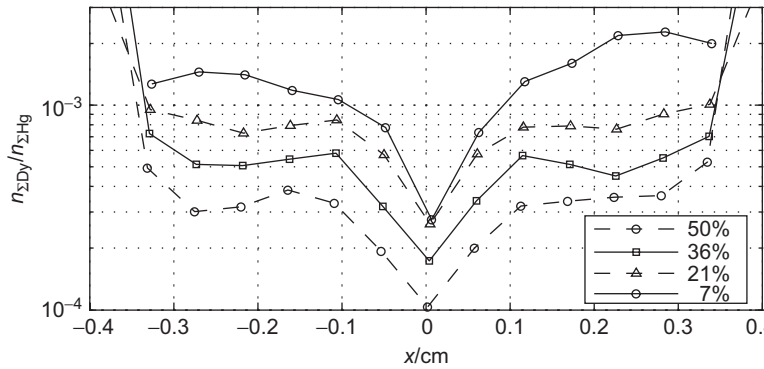

Figure 26 The mixing ratio for Dy in a DyI_3-Hg metal-halide lamp plotted versus radial coordinate for several axial positions. The percentages given in the key are the percentages of the total distance from the lower electrode to the upper electrode. Data points at each wall are off the scale of the figure. Both radial and axial demixing are apparent. The coordinate system is defined in Figure 9. (Nimalasuriya et al., 2007).

which axial demixing is a maximum. Larger convective velocities reduce, rather than increase, demixing because additives are transported upward faster than they can be transported away from the axis by radial diffusion.

A study of axial demixing was made by Nimalasuriya et al. (2007) using both XRIF to measure elemental densities and laser absorption to obtain distributions of atomic Dy (Flikweert et al., 2005). The XRIF measurements showed clear examples of both radial and axial demixing (Figure 26). In addition, the two complementary diagnostic techniques made it possible to evaluate specific terms in the radial diffusion equation presented there.

5.5 Equilibrium Vapor Pressures

After seeing the capabilities of XRIF in the measurement of metal and iodine densities in metal-halide lamps, Walter Lapatovich (then of OSRAM SYLVANIA INC) suggested that XRIF might be a solution to the longstanding problem of obtaining accurate measurements of the equilibrium vapor pressures of metal-halide salts. By "equilibrium vapor pressure," we mean the pressure that equilibrates with a solid or liquid condensate when the vapor and condensate are in a closed system in full thermodynamic equilibrium. Although the observations of demixing, discussed already, make clear that actual vapor pressures in metal-halide lamps are not everywhere in equilibrium with a condensate, those pressures are a strong function of the equilibrium vapor pressures of the salts. Ab initio numerical modeling of metal-halide lamps must incorporate reasonably accurate values for equilibrium vapor pressures, even though small errors are self-correcting.[7] Unfortunately, very few, if any, of the relevant vapor pressures have been measured anywhere in the temperature range of interest for metal-halide lamps (>1000 K). The calculated and/or extrapolated values currently used may be in error by an unacceptable amount.

In addition to the need for the equilibrium vapor pressures of simple metal-halide salts, knowledge of the vapor pressures in equilibrium with salt *mixtures* has become increasingly important. The lighting industry has sought to exploit the phenomenon of vapor-phase complexing between dissimilar salts to increase the density of the radiating metal in the arc at a given temperature, or equivalently, obtain the same density at a lower temperature.

Complexing refers to a relatively weak bonding of two or more stable molecules, which may be identical (homocomplex) or different (heterocomplex) (Hastie, 1975). The use of complexing in lamps typically involves pairing a high vapor pressure salt with a low vapor pressure salt in order to increase the partial pressure of the metal atoms in the lower vapor pressure salt. Thermochemical calculations suggest that some combinations of salts can produce increases in the partial pressures of some metals by up to two orders of magnitude (Lapatovich & Baglio, 2001). Again, very few or no measurements have been made of this effect in the temperature range relevant to metal-halide lamps.

The principal impediment to obtaining measurements of equilibrium vapor pressures in the temperature range of interest is the difficulty in not only reaching those high temperatures but also in making accurate

[7] For example, a slightly too high vapor pressure leads to greater radiative losses, a cooling of the lamp, and hence a lowering of the vapor pressure.

measurements in that pressure range. The Knudsen cell method is based on the measurement of time-integrated mass loss from a small hole in an equilibrium vapor cell. The hole must be small enough that the flow of vapor does not substantially perturb the vapor pressure in the cell, i.e., the mean free path of the molecules must be much greater than the diameter of the hole. The technique is often referred to as the effusion method. This requirement typically limits the maximum pressures that may be investigated to something of the order of 100 Pa and less. The pressure range relevant to metal-halide lamps is 10^2 Pa to 10^4 Pa.

The Knudsen method also involves an open system in which some of the vapor is lost through the effusion aperture. When measuring salt mixtures whose components have greatly different vapor pressures, this involves a change in the system content with time.

The use of XRIF for the measurement of equilibrium vapor pressures has many aspects in common with the measurement of metal distributions in operating arc lamps. The metal-halide salts are typically the same. The vapor densities are in the same range. And one can use vapor cells identical or similar to the arc tubes used in lamps. There are some critical differences, however. First, one would like to measure equilibrium vapor pressures over the widest range possible. Hence, there is an incentive to increase the dynamic range of XRIF as much as possible. Second, if one intends to obtain quality reference values for the measured vapor pressures, absolute accuracy and understanding of systematic errors becomes essential. (In lamps, relative pressures can be of great importance.) Thus, the measurement of equilibrium vapor pressures tests the limits of XRIF.

The sensitivity of XRIF measurements in operating lamps is limited by Compton scattering of beam photons from the arc tube into the detector. These Compton features frequently interfere with fluorescence lines in observed spectra. Although the broad shape of those Compton features makes it possible to distinguish them from line fluorescence, the Compton counts contribute to statistical noise in integrated line intensities. In Section 5.1, we described the paths by which photons scattered from an arc tube can reach the detector. These paths all require at least two scattering events. A vapor cell geometry that reduces Compton scattering further by requiring at least three scattering events to reach the detector is shown in Figure 27. Except for a several millimeter long, sealed filling stem, the PCA cell is cylindrically symmetric. It is surrounded by a cylindrical tantalum jacket whose primary purpose is to absorb scattered photons. It also serves the purpose of providing reasonably good heat conduction along the outside wall of the cell, thus reducing temperature gradients when the cell is heated in the oven. The jacket has two holes to accommodate the entrance and exit of the beam, and a third hole through the side of the cylinder through which x-ray fluorescence is observed. This hole is one of the defining apertures determining the solid angle from which

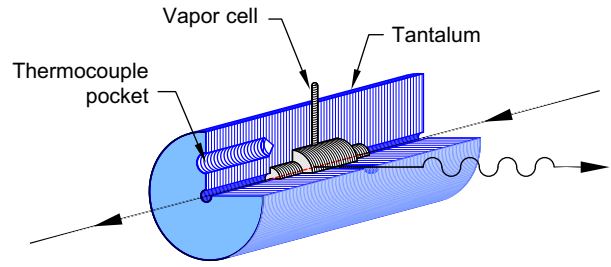

Figure 27 The PCA vapor cell and tantalum jacket used for vapor pressure measurements with XRIF.

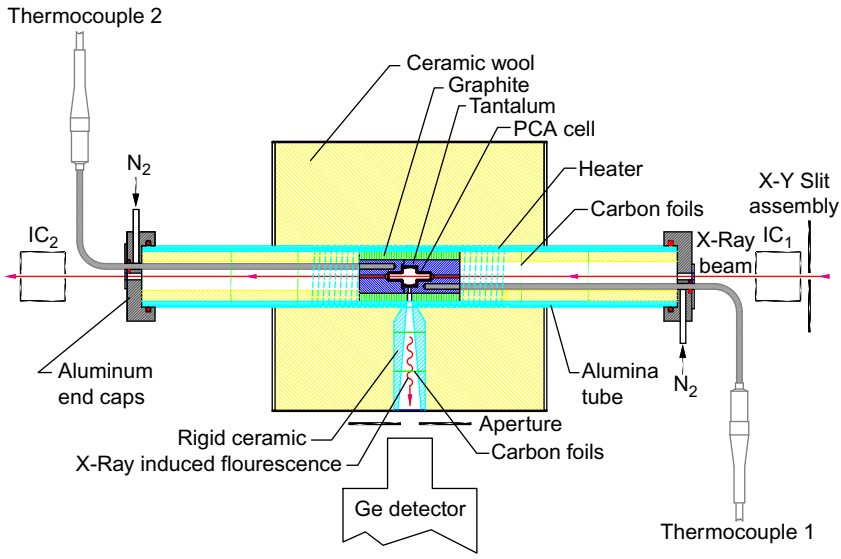

Figure 28 Schematic of the oven used for measuring equilibrium vapor pressures of metal-halide salts with XRIF.

photons are collected by the detector. The jacket has two holes (only one is visible in Figure 27), which accommodate thermocouples for monitoring the cell and jacket temperature.

Measurement of equilibrium vapor pressures with XRIF was recently demonstrated using the vapor cell described above (Curry et al., 2011). Several vapor cells were dosed with a salt or salt mixture and filled with 500 Pa of Ar. They were sealed by fusing a PCA plug into the filling tube with a frit. A vapor cell and the tantalum jacket were fit into a graphite bushing and placed into a cylindrical oven as shown schematically in Figure 28. The experimental arrangement shown there is not too different

from that used for measurements in a metal-halide lamp discussed in Section 5.1. The oven is aligned so that the x-ray beam travels unobstructed through the oven. The detection of fluorescence remains along the direction of polarization of the incident beam to minimize scattering directly from the vapor into the detector. The field of view of the detector is determined by the viewing hole in the tantalum jacket and the crossed slits in front of the detector. Nitrogen-filled atmospheric pressure ionization chambers monitor the beam flux immediately preceding and following the oven and are used to normalize the measured fluorescence signal and determine corrections for attenuation of the beam by the vapor at the highest vapor pressures.

Absolute vapor densities are obtained by comparison with fluorescence observed from calibration cells containing a known pressure of xenon (see Section 5.1). These cells are placed in the oven in the same manner as the salt-filled cells. Vapor pressures $p(T)$ corresponding to the measured densities $n(T)$ are then determined from the Ideal Gas Law

$$p(T) = n(T)kT \tag{14}$$

where T is the temperature of the cell as determined by thermocouple measurements. It is important to remember that $n(T)$ is defined by Equation (1). Accordingly, the corresponding vapor pressures $p(T)$ have sometimes been referred to as elemental vapor pressures.

A weakness of the calibration approach described earlier is the susceptibility to movement of the tantalum jacket and the limiting aperture through which fluorescence is observed, particularly as the oven changes temperature. A remedy may be to dose each vapor cell with a calibration gas so that the calibration is obtained simultaneously with each measurement.

Measurements of equilibrium vapor pressures for Dy over DyI_3 and Tm over TmI_3 are shown in Figures 29 and 30 where the logarithm base 10 of the pressure P is plotted versus $1/T$ (Curry, 2010). Plotting in this manner allows one to compare the data visually against the expected linear dependence predicted by

$$\ln P = \frac{\Delta S}{k} - \frac{\Delta H}{kT} \tag{15}$$

where ΔS and ΔH are the changes in entropy and enthalpy under standard conditions when a mole of molecules evaporates, and k is Boltzmann's constant (Mahan, 1975). A distinct change in slope in each graph occurs at or near the predicted melting point of each salt shown by a vertical dashed line. Such a change is expected since the enthalpy of evaporation from a solid should be more than that from a liquid.

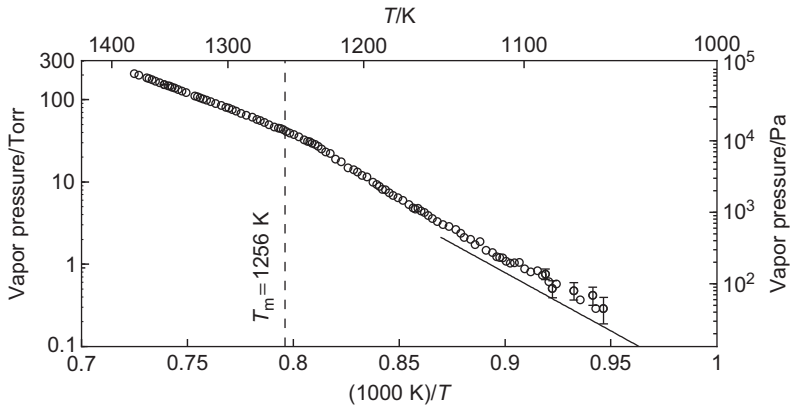

Figure 29 Equilibrium vapor pressure of Dy over DyI_3 as measured with XRIF (Curry, 2010). The solid line is an analytic expression for the vapor pressure, and the dashed line is the melting temperature, both given by Hansen et al. (1998, 2000).

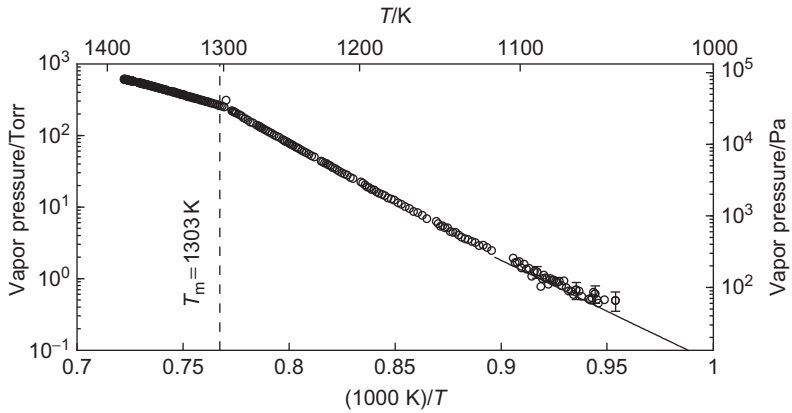

Figure 30 Equilibrium vapor pressure of Tm over TmI_3 as measured with XRIF (Curry, 2010). The solid line is an analytic expression for the vapor pressure, and the dashed line is the melting temperature, both given by Hansen et al. (1998, 2000).

The dynamic range of these measurements extends over nearly three orders of magnitude. At the upper end of the range, the vapor density is high enough to produce significant absorption of the x-ray beam and corrections were made for this effect. The lower end of the range overlaps with the upper end of the range of applicability of the effusion method, and several measurements of the vapor pressure of both DyI_3 and TmI_3 have been made for pressures below 100 Pa. These existing measurements have been compiled by Hansen et al. (1998, 2000) who have produced recommended analytic expressions for the vapor pressures of

the triiodide molecule over each salt. These expressions are also shown in Figures 29 and 30 by solid lines for their range of expected applicability. The XRIF results are 50% and 10% higher for DyI_3 and TmI_3, respectively. At this point, sufficient work has not been completed to understand possible systematic errors and their origins. The XRIF results are for the total Dy vapor pressure, summed over all possible molecules, as opposed to Hansen's expressions for the triiodide molecular vapor pressure, but there is no expected significant difference in these two values in the range of temperatures where the comparison is being made.

Now that the use of XRIF to measure equilibrium vapor pressures has been demonstrated, a more thorough understanding of the absolute accuracy of the method is needed. There are many possible sources of systematic error. Chief among these are: (1) possible contamination of the metal-halide salts and/or cells during preparation, (2) an inaccurate filling of the Xe pressure in the calibration cells, and (3) variations in fluorescence collection efficiency due to movement of the tantalum jacket with temperature or when cells are changed. Inconsistencies in initial data indicate errors in the range of 20%. Discrepancies with Hansen's recommended values indicate errors may be larger.

5.6 Accuracy

Some of the data presented already have statistical error bars associated with many of the XRIF measurements. These are frequently dominated by photon statistics. Thus, smaller uncertainties could, in most cases, be obtained by integrating for a longer period of time. Harder to understand are systematic errors. With respect to measurements on lamps, there has not been a strong incentive to make measurements with uncertainties less than 5%. For measurement of basic data, such as vapor pressures, there is always merit in reducing uncertainties, if not for present applications, then for future ones.

Calibration of XRIF signals using a gas-filled standard is a primary source of systematic uncertainty because independent measurements of the pressures of the standards have not been made. The densities of Xe, for example, have been determined entirely by a single pressure and temperature measurement of the cell maker prior to sealing of the cell. The process of sealing a cell opens the possibility of significant changes in the density from the measured value. Independent measurements of Xe densities could be made in sealed cells using x-ray absorption. Such measurements should give a good scale for the consistency and accuracy with which standard cells can be made.

There are several atomic parameters in Equation (7) including absorption cross sections, fluorescence yields, and branching fractions. These values are almost always based on semiempirical or ab initio calculations

rather than direct measurements. Thus, their uncertainty is not always a matter of common agreement. Nevertheless, a few points can be made. Uncertainties in the cross sections are largest for photon energies close to energy edges where resonances can have a large impact. Uncertainties are generally much smaller away from the edges. The cross sections appearing in most tabulations are total cross sections, meaning the cross section for energies greater than the K-shell threshold includes absorption by the L- and lower shells. In order to obtain the K-shell only cross section, the ratio of cross sections at the K-edge is taken as a constant and used to determine the K-shell component at higher energies. This inevitably involves additional error. Thus, it may be wise to consider the K-shell photoelectric cross section values to be no better than 5%. Veigele (1973) puts uncertainties for some of the rare-earth K-shell cross sections as high as 10%. The branching fractions used here are estimated to have errors between 2% and 5% (Salem et al., 1974). Uncertainties in the relevant fluorescence yields are estimated as 1% to 2% depending on the atomic number (Krause, 1979).

Determination of the transmission factors T in Equation (7) follows from total absorption cross sections of the relevant material, so the discussion in the preceding paragraph applies here as well. In addition, there is Compton and coherent scattering from the materials, which also effectively attenuates the x-ray beam. The treatment of scattering was discussed in Section 5.1 where the total effect was shown to be 11% at 20 keV, decreasing to less than 7% at 90 keV. The suggested approximation of using Compton scattering but ignoring coherent scattering probably cuts the error by more than a factor of two.

Measurements of beam flux under normal conditions are not likely to be a significant source of error, mostly because it is the ratio of fluxes that enter into the calibration [Equation (7)]. Statistical fluctuations in the flux measurements are typically negligible.

6. SUMMARY

We have described the use of high-energy x rays to study the low temperature plasmas in high-intensity discharge lamps and to measure equilibrium vapor pressures at high temperatures. X-ray induced fluorescence (XRIF) is a well-known technique used for analysis in many fields, but its application to low-density vapors, as described in this chapter, appears to be unique. Spatially resolved vapor densities of less than 10^{16} cm^{-3} have been measured, in a reasonable time, with the use of high-flux synchrotron radiation.

Additive densities, temperature distributions, mixing ratios, and equilibrium vapor pressures have all been measured with a straightforward

application of XRIF. More sophisticated variants of XRIF could prove useful in the future. These include nuclear resonance fluorescence for observing lighter elements, resolving near-edge fine structure to determine chemical bonding, looking at the very weak effect of the x rays on the plasma current to understand transport and equilibration times, and using Ge detector arrays to increase measurement sensitivity.

GLOSSARY

Ambipolar field The weak electric field arising from unequal loss rates of positive and negative charges in a finite-sized plasma.

Coherent scattering The scattering of electromagnetic radiation produced by the coherent response of all the bound electrons in an atom. This process is sometimes referred to as Rayleigh scattering.

Color rendering The color rendering index is a quantitative measure of the ability of a light source to render all colors properly as compared to an ideal source, such as daylight. The color rendering index can have values between 0 and 100, with 100 indicating a perfect match between source and reference.

Complex A molecule formed from the relatively weak association of two or more smaller molecules.

Compton scattering The scattering of electromagnetic radiation by a free electron. The low-energy limit of Compton scattering is sometimes referred to as Thomson scattering. The response of a bound atomic electron has a Compton component if the photon energy is larger than the binding energy of the electron.

Demixing The relative spatial separation of elements in metal-halide high-intensity discharge lamp.

Elemental density The total number density of atoms of a particular element summed over all atomic and molecular species.

Equilibrium vapor pressure The vapor pressure of a substance that is in equilibrium with a condensate in a closed system in full thermal equilibrium.

Escape peak An anomalous signal from a crystal x-ray detector arising from the excitation and loss of the crystal material's characteristic fluorescence. It produces relatively small peaks that differ in energy from real signal peaks by an energy equal to the characteristic fluorescence energy.

HID High-intensity discharge.

HPS High-pressure sodium.

Luminous efficacy Luminous efficacy is a measure of the illumination a light source provides per unit of input power. It typically has the units of lumens/watt and is defined as the wavelength integral of the product of the eye sensitivity curve (lumens per watt of optical power) and the optical power per unit wavelength radiated by the lamp, all divided by the electrical power consumed by the lamp. The maximum luminous efficacy for a full-color white light source is generally considered to be in the range of 300 lm/W to 350 lm/W, depending on what is considered full-color.

XRIF X-ray induced fluorescence.

REFERENCES

ALITE. (2006). Program on technology innovation: advanced light source research: ALITE-II: losses in high-intensity discharge light sources. Tech. rep., Electric Power Research Institute, Palo Alto, CA, Philips Lighting Company, Somerset, NJ, General Electric Company, Niskayuna, NY, Osram Sylvania, Beverly, MA. Retrieved July 16, 2011, from www.epri.com

Baumann, B., Wolff, M., Hirsch, J., Antonis, P., Bhosle, S., & Barrientos, R. V. (2009). Finite element estimation of acoustical response functions in hid lamps. *Journal of Physics D: Applied Physics*, *42*, 225209.

Beks, M. L., Flikweert, A. J., Nimalasuriya, T., Stoffels, W. W., & van der Mullen, J. J. A. M. (2008). Competition between convection and diffusion in a metal halide lamp, investigated by numerical simulations and imaging laser absorption spectroscopy. *Journal of Physics D: Applied Physics*, *41*, 144025.

Berger, M. J., Hubbell, J. H., Seltzer, S. M., Chang, J., Coursey, J. S., Sukumar, R., et al. (1998). NIST Standard Reference Database 8: Photon cross sections database. Retrived July 16, 2011, from http://www.nist.gov/pml/data/xcom/index.cfm

Bonvallet, G. A., & Lawler, J. E. (2003). Optical absorption spectroscopy on a metal-halide high intensity discharge arc lamp using synchrotron radiation. *Journal of Physics D: Applied Physics*, *36*, 1510.

Chase, M. W. (1998). NIST-JANAF Thermochemical Tables, fourth edition, part I, Al-Co. *Journal of Physical and Chemical Reference Data*, *Monograph No. 9*, 17.

Corliss, C. H., Bozman, W. R., & Westfall, F. O. (1953). Electrodeless metal-halide lamps. *Journal of the Optical Society of America*, *43*, 398.

Cruise, D. R. (1964). Notes on the rapid computation of chemical equilibria. *Journal of Physical Chemistry*, *68*, 3797.

Curry, J. J. (2010). Monte carlo simulation of photon scattering in x-ray absorption imaging of high-intensity discharge lamps. *Journal of Physics D: Applied Physics*, *43*, 234001.

Curry, J. J., Adler, H. G., Lee, W.-K., & Shastri, S. D. (2003a). Direct observation of de-mixing in a ceramic metal-halide arc lamp. *Journal of Physics D: Applied Physics*, *36*, 1529.

Curry, J. J., Adler, H. G., MacPhee, A., Narayanan, S., & Wang, J. (2004). X-ray absorption imaging of Hg vapour in a ceramic metal-halide lamp using synchrotron radiation. *Plasma Sources Science and Technology*, *13*, 403.

Curry, J. J., Adler, H. G., Shastri, S. D., & Lawler, J. E. (2001). Minority additive distributions in a ceramic metal-halide arc lamp using high-energy x-ray induced fluorescence. *Applied Physics Letters*, *79*, 1974.

Curry, J. J., Adler, H. G., Shastri, S. D., & Lee, W.-K. (2003b). X-ray induced fluorescence measurement of density distributions in a metal-halide lighting arc. *Journal of Applied Physics*, *93*, 2359.

Curry, J. J., Estupiñan, E. G., Henins, A., Lapatovich, W. P., & Shastri, S. D. (2011). Measurement of vapor pressures using x-ray induced fluorescence. *Chemical Physics Letters*, *507*, 52.

Curry, J. J., Sakai, M., & Lawler, J. E. (1998). Measurement of the Hg distribution in a high-pressure arc lamp by x-ray absorption. *Journal of Applied Physics*, *84*, 3066.

Curry, J. J., Sansonetti, C. J., & Wang, J. (2005). Temperature profiles and thermal losses in 150 W high-intensity discharge lamps. *Journal of Physics D: Applied Physics*, *38*, 3086.

Dakin, J. T., Rautenberg, T. H., Jr., & Goldfield, E. M. (1989). Anatomy of a vertical metal halide discharge. *Journal of Applied Physics*, *66*, 4074.

Dakin, J. T., & Shyy, W. (1989). The prediction of convection and additive demixing in vertical metal halide discharge lamps. *Journal of the Electrochemical Society*, *136*, 1210.

de Groot, J. J., & van Vliet, J. A. J. M. (1986). *The high pressure sodium lamp*. London: MacMillan Education LTD.

Deslattes, R. D., Kessler, E. G., Jr., Indelicato, P., de Billy, L., Lindroth, E., & Anton, J. (2003). X-ray transition energies: new approach to a comprehensive evaluation. *Rev. Mod. Phys. 75*, 35, also available as NIST Standard Reference Database 128: X-ray Transition Energies. Retrieved from July 16, 2011, from http://www.nist.gov/pml/data/xraytrans/index.cfm

Dreeben, T. D. (2008). Modelling of fluid mechanical arc instability in pure-mercury HID lamps. *Journal of Physics D: Applied Physics*, *41*, 144023.

Elloumi, H., Kindel, E., Schimke, C., & Zissis, G. (1999). Experimental investigation of deviations from local thermodynamic equilibrium in high-pressure mercury discharges. *Journal of Applied Physics*, *86*, 4134.
Evans, R. D. (1958). *Compton effect in Encyclopedia of Physics* (Vol. 34, p. 218). Berlin: Springer-Verlag, Ch. Compton Effect.
Fischer, E. (1976). Axial segregation of additives in mercury metal-halide arcs. *Journal of Applied Physics*, *47*, 2954.
Flikweert, A. J., Nimalasuriya, T., Grothuis, C. H. J. M., Kroesen, G. M. W., & Stoffels, W. W. (2005). Axial segregation in high intensity discharge lamps measured by laser absorption spectroscopy. *Journal of Applied Physics*, *98*, 073301.
Fohl, T., Kramer, J. M., & Lester, J. E. (1993). X-ray measurements of mercury density in arc discharge lamps during warm-up and following extinction. *Journal of Applied Physics*, *73*, 46.
Hansen, S., Getchius, J., & Brumleve, T. R. (1998). *Vapor pressure of metal bromides and iodides, with selected metal chlorides and metals*. Urbana, Illinois: APL Engineered Materials, Inc.
Hansen, S., Steward, R., Getchius, J., & Brumleve, T. (2000). *Supplement to vapor pressure of metal bromides and iodides*. Urbana, Illinois: APL Engineered Materials, Inc.
Hastie, J. W. (1975). *High temperature vapors: science and technology*. New York: Academic Press.
Herd, M. T., & Lawler, J. E. (2007). Infrared continuum radiation from metal-halide high-intensity discharge lamps. *Journal of Physics D: Applied Physics*, *40*, 3386.
Hochi, A., Hashimotodanl, K., & Katash, K. (2001). Vane-type electrodeless HID lamp. *Matsushita Technical Journal*, *47*, 42.
Hong, E., Conroy, L. A., & Scholand, M. J. (2002 and 2005). U. S. lighting market characterization (Vols. i and ii). Tech. rep., Navigant Consulting, Inc., Washington, DC.
Hubbell, J. H., Veigele, W. J., Briggs, E. A., Brown, R. T., Cromer, D. T., & Howerton, R. J. (1975). Atomic form factors, incoherent scattering functions, and photon scattering cross sections. *Journal of Physical and Chemical Reference Data*, *4*, 471.
ICF. (2006). High-intensity discharge lighting technology: workshop report. Tech. rep., Prepared for the U.S. Department of Energy by ICF Consulting. Retrieved July 16, 2011, from http://apps1.eere.energy.gov/buildings/publications/pdfs/corporate/hid_workshop-report.pdf.
Ingold, J. H. (1987). Radiative processes in discharge plasmas. Physics Volume 149 of NATO Advanced Study Institute Series B (p. 347). New York: Plenum Press, Ch. Metal-halide Sources.
Karabourniotis, D. (1986). Self-reversed emission lines in inhomogeneous plasmas. In J. M. Proud & L. H. Leussen (Eds.), *Radiative processes in discharge plasmas* (pp. 171–247). Plenum, New York: Proceedings of a NATO Advanced Study Institute.
Karabourniotis, D. (2002). Non-equilibrium excited-state distribution of atoms in dense mercury plasmas. *Journal of Applied Physics*, *92*, 25.
Karabourniotis, D., & Drakakis, E. (2002). Electron temperature and density in a metal-halide discharge lamp. In *2002 IEEE international conference on plasma science. Vol. Banff, Canada of IEEE conference record - abstracts* (p. 315). Piscataway, NJ: IEEE.
Knoll, G. F. (2000). *Radiation detection and measurement* (3rd ed.). New York: John Wiley and Sons.
Krall, N. A., & Trivelpiece, A. W. (1986). *Principles of plasma physics* (Chap. 6.8). San Francisco: San Francisco Press, Inc.
Krause, M. O. (1979). Atomic radiative and radiationless yields for K- and L-shells. *Journal of Physical and Chemical Reference Data*, *8*, 307.
Lapatovich, W. P., & Baglio, J. A. (2001). Chemical complexing and effects on metal-halide lamp performance. In *Proceedings of the 9th International Symposium on the Sci. and Tech. of Light Sources, 12–16 Aug* (p. 91). Ithaca, NY: Cornell University.
Lawler, J. E. (2004). Resonance broadening of Hg lines as a density diagnostic in high intensity discharge lamps. *Plasma Sources Science and Technology*, *13*, 321.
Lister, G. G., Lawler, J. E., Lapatovich, W. P., & Godyak, V. A. (2004). The physics of discharge lamps. *Reviews of Modern Physics*, *76*, 541.
Lister, G. G., & Waymouth, J. F. (2002). *Encyclopedia of Physical Science and Technology* (3rd ed., Vol. 8, p. 557). San Diego: Academic Press, Ch. Light Sources.

Lowke, J. J. (1979). Calculated properties of vertical arcs stabilized by natural convection. *Journal of Applied Physics*, *50*, 147.
Mahan, B. H. (1975). *University chemistry* (3rd ed., Chap. 8.). Reading, MA: Addison-Wesley.
Nimalasuriya, T., Curry, J. J., Sansonetti, C. J., Ridderhof, E. J., Shastri, S. D., Flikweert, A. J., et al. (2007). X-ray induced fluorescence measurement of segregation in a DyI_3-Hg metal-halide lamp. *Journal of Physics D: Applied Physics*, *40*, 2831.
Palmer, F. L., & Lapatovich, W. P. (2000). Coaxial applicators for electrodeless high-intensty discharge lamps. U. S. Patent 6,107,752 and associated patents.
Ralchenko, Y., Kramida, A. E., Reader, J., & the NIST ASD Team. (2010). NIST Standard Reference Database 78: Atomic spectra database. Retrieved July 16, 2011, from http://www.nist.gov/pml/data/asd.cfm
Reiling, G. H. (1964). Characteristics of mercury vapor-metal iodide arc lamps. *Journal of the Optical Society of America*, *54*, 532.
Rhodes, W. H., & Reid, J. (1979). Transparent yttria ceramics containing magnesia and magnesium aluminate. U. S. Patent 4,174,973.
Salem, S. I., Panossian, S. L., & Krause, R. A. (1974). Experimental K and L relative x-ray emission rates. Atomic Data and Nuclear Data Tables, *14*, 91.
Schneidenbach, H., & Franke, S. (2008). Basic concepts of temperature determination from self-reversed spectral lines. *Journal of Physics D: Applied Physics*, *41*, 144016.
Shaffner, R. O. (1971). Theoretical properties of several metal halide arcs assuming LTE. *Proceedings of the IEEE*, *59*, 622.
Shastri, S. D., Fezzaa, K., Mashayekhi, A., Lee, W.-K., Fernandez, P. B., & Lee, P. L. (2002). Cryogenically-cooled bent double-Laue monochromator for high-energy undulator x rays (50-200 keV). *Journal of Synchrotron Radiation*, *9*, 317.
Stormberg, H. P. (1981). Axial and radial segregation in metal-halide arcs. *Journal of Applied Physics*, *52*, 3233.
Sugiura, M. (1993). Review of metal-halide discharge lamp development 1980–1992. *IEE Proceedings A*, *140*, 443.
Thompson, A. C., Attwood, D. T., Gullikson, E. M., Howells, M. R., Kortright, J. B., Robinson, A. L., et al. (2001). *X-ray data booklet*. Berkeley, CA: Technical and Electronic Information Department, Lawrence Berkeley National Laboratory.
Turner, B. P., Ury, M. G., Leng, Y., & Love, W. G. (1997). Sulfur lamps: progress in their development. *Journal of the Illuminating Engineering Society*, *26*, 10.
Veigele, W. J. (1973). Photon cross sections from 0.1 keV to 1 MeV for elements $Z = 1$ to $Z = 94$. *Atomic Data*, *5*, 51.
Waymouth, J. F. (1971). Metal-halide lamps. *Proceedings of the IEEE*, *59*, 629.
Waymouth, J. F. (1991). LTE and near-LTE lighting plasmas. *IEEE Transactions on Plasma Science*, *19*, 1003.
Wei, G. C., Lapatovich, W. P., Browne, J., & Snellgrove, R. (2008). Dysprosium oxide ceramic arc tube for HID lamps. *Journal of Physics D: Applied Physics*, *41*, 144014.
Zollweg, R. J. (1978). Convection in vertical high-pressure mercury arcs. *Journal of Applied Physics 49*, 1077.

This page intentionally left blank

CHAPTER 3

Time-Domain Interferometry with Laser-Cooled Atoms

B. Barrett[a], **I. Chan**[a], **C. Mok**[a], **A. Carew**[a], **I. Yavin**[b], **A. Kumarakrishnan**[a], **S. B. Cahn**[c], and **T. Sleator**[d]

[a]*Department of Physics & Astronomy, York University, 4700 Keele St., Toronto, ON M3J 1P3, Canada*
[b]*Department of Physics & Astronomy, McMaster University, 1280 Main St. W, Hamilton, Ontario, Canada L8S 4M1*
[c]*Department of Physics, Yale University, New Haven, CT 06511, USA*
[d]*Department of Physics, New York University, New York, NY 10003, USA*

Contents

Advances in Atomic, Molecular, and Optical Physics, Volume 60, Copyright © 2011 Elsevier Inc.
ISSN 1049-250X, DOI: 10.1016/B978-0-12-385508-4.00003-6.

Abstract A single-state grating echo interferometer offers unique advantages for time-domain studies of light–matter interactions using laser-cooled atoms, including applications that involve precision measurements of atomic recoil, rotation, and gravitational acceleration. To illustrate the underlying physics, we first discuss the output signal of the interferometer in the absence of spontaneous emission. The influence of spontaneous emission, magnetic sublevels, and the spatial profile of excitations beams on matter wave interference in a two-pulse interferometer is described, followed by a discussion of transit time limited experiments using a multipulse technique that offers several advantages. We also examine the enhancement in signal size achieved by a lattice interferometer. The sensitivity of the interferometer to magnetic gradients and gravitational acceleration is discussed along with extensions to frequency-domain studies of atomic recoil and rotation. Applications of coherent transient effects and echo techniques associated with internal state labeled interferometers that utilize magnetic sublevels of a single hyperfine state are considered for precise measurements

of magnetic interactions such as atomic g-factor ratios. The article concludes with an overview of the suitability of the traditional two-pulse photon echo technique for measurements of atomic lifetimes and studies of superradiant emission in laser-cooled samples.

1. INTRODUCTION AND DESCRIPTION OF TWO-PULSE STANDING WAVE INTERFEROMETER

1.1 Introduction

Matter wave interference has intrigued scientists since the early days of quantum mechanics. It was not until the late 1980s, however, that the field of atom interferometry was born. There have been a series of beautiful experiments carried out over the past two decades that have probed the fundamental nature of matter wave interference using atom interferometers (Berman, 1997). These include interference of "large" objects and of biomolecules (Hackermüller et al., 2004), interference of independently prepared particles (Andrews et al., 1997), and the origin of quantum mechanical complementarity (Durr et al., 1998). Advances in microfabrication techniques and the development of laser-cooling and trapping for neutral atoms has opened up many new possibilities for constructing atomic interferometers (Keith et al., 1988; Weiss et al., 1993). Besides testing the fundamental nature of matter wave interference, atom interferometers play an essential role in many high-precision measurements of fundamental constants, such as the fine structure constant α and the Newtonian constant of gravity. They offer an independent method for determining these constants that expands our understanding of the fundamental nature of physical laws (Cladé et al., 2006; Fixler et al., 2007; Weiss et al., 1993). Moreover, precise measurements of quantities such as the local gravitational field hold promise for technological advances in navigation and mineral exploration (McGuirk et al., 2002).

This article discusses the physics and various extensions of a particular atom interferometer design developed at New York University (NYU) in the mid-1990s (Cahn et al., 1997). The interferometer involves the interaction of a set of pulsed laser fields with a sample of laser-cooled Rb atoms in a magneto-optical trap. A schematic of the experimental setup of this interferometer is shown in Figure 1. The principle of the NYU interferometer is that the interaction of an off-resonant optical standing-wave pulse (made up of traveling waves with k-vectors $\boldsymbol{k}_1$ and $\boldsymbol{k}_2$) with a two-level atomic system effectively modulates the atomic ground-state energy with a spatial period $2\pi/q$, with $\boldsymbol{q} = \boldsymbol{k}_2 - \boldsymbol{k}_1$. The pulse therefore acts as

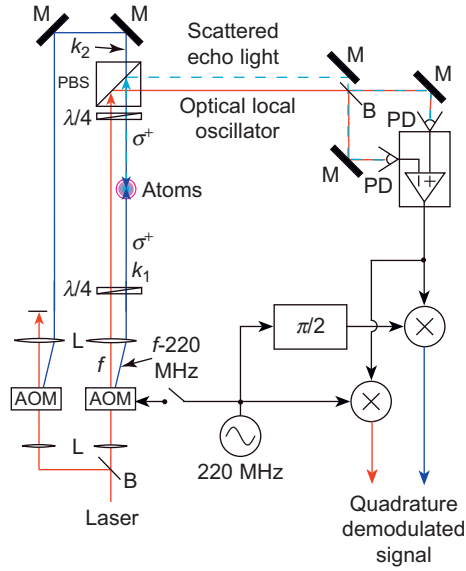

Figure 1 Schematic diagram of the experimental setup (for σ^+-polarized sw experiment). M = mirror, B = beamsplitter, PD = photodiode, AOM = acousto-optic modulator, $\lambda/4$ = quarter-wave plate, L = lens, PBS = polarizing beam splitter.

a phase grating for atomic de Broglie waves, and an initial atomic plane-wave is scattered into a set of diffraction orders differing by multiples of momentum $\hbar\boldsymbol{q}$. A second standing-wave pulse, separated from the first by a time T, produces further diffraction orders, and at various times after the second pulse, these diffraction orders interfere to produce a spatial modulation in the atomic density that can be observed by the scattering of a traveling wave pulse with wavevector $\boldsymbol{k}_2$ into the direction $\boldsymbol{k}_1$. An important property of this interferometer is that a high degree of "collimation" of the atoms is not necessary. This is because, for various times after the second pulse (called *echo* times), the relative phase between interfering diffraction orders is independent of the initial atomic velocity. An interferometer that is based on the cancelation of this Doppler phase is referred to as an *echo* interferometer, in analogy with the spin echo (Hahn, 1950a), or the photon echo (Abella et al., 1965). Another important feature of this interferometer is that the measured signal results from coherences involving a single atomic ground state, making the interference signal relatively insensitive to external electric and magnetic fields.

Like many of the atom interferometers developed over the past two decades, this interferometer can be used to make measurements of various physical quantities of interest to high precision. Examples are the atomic recoil frequency $\omega_q = \hbar q^2/2M$ (M is the mass of the test atom), which is

useful for determining the fine-structure constant α, and inertial effects such as acceleration and rotation.

The original experiments (Cahn et al., 1997) were carried out with counter-propagating beams having identical circular polarizations, as shown in Figure 1. The $\boldsymbol{k}_1$ and $\boldsymbol{k}_2$ beams were independently controlled with acousto-optic modulators (AOMs). In the experiment, the $\boldsymbol{k}_1$ and $\boldsymbol{k}_2$ beams are simultaneously pulsed at time $t = 0$ for a duration of about 100 ns, followed by a second standing-wave pulse a time T later. Then, at a later time in the vicinity of $t = (N + 1)T$ for integer N, the resulting atomic grating is probed by switching on only the traveling wave along $\boldsymbol{k}_2$ and measuring the (complex) amplitude of the light wave scattering into the direction $\boldsymbol{k}_1$. The scattered wave is detected by beating it with an optical local-oscillator in a balanced heterodyne arrangement (see Figure 1). The local oscillator is derived from the light passing undiffracted through the AOM used to switch the $\boldsymbol{k}_1$ beam. During the experiment, the echo beat signal is further mixed down by a 220-MHz reference from the rf oscillator using a quadrature demodulator. The two outputs of this demodulator represent the real and imaginary parts of the scattered light field, where the real part is in phase with the $\boldsymbol{k}_1$ field (which is *not* on during detection), and the imaginary part is $\pi/2$ out of phase with $\boldsymbol{k}_1$. The phase of the signal is stabilized against mirror motion in between experiments (where an "experiment" consists of 90% trapping [sample preparation] time and 10% standing-wave pulse excitation and detection time), by phase-shifting the rf local oscillator.

1.2 Calculation of the Signal

We model the system as a two-level atom interacting with an off-resonant optical standing wave (Cahn et al., 1997; Dubetsky, 1997). We assume, first, that the detuning $\Delta = \omega - \omega_0$ is sufficiently large that the atom always remains in the ground state and that spontaneous emission can be neglected. Here ω is the laser frequency and ω_0 is the resonance frequency of the atom. The effects of spontaneous emission are discussed in Section 2. We also assume that, during the standing-wave pulse, the kinetic energy term in the Hamiltonian can be neglected (Raman–Nath approximation). This approximation is valid when $\omega_q \tau \ll 1$ and $\sqrt{\omega_q \chi}\, \tau \ll 1$ for two-photon Rabi frequency χ and standing-wave pulse duration τ.

For $\sigma^+ - \sigma^+$ or Lin–Lin illumination, we treat the separate transitions as independent two-level systems. For a single two-level system, we can adiabatically eliminate the excited state (Berman & Malinovsky, 2011) to obtain an effective Hamiltonian for the atomic ground state

$$H = \frac{\boldsymbol{p}^2}{2M} + V(\boldsymbol{r}, t), \tag{1}$$

where

$$V(\boldsymbol{r},t) = \hbar\chi(t)\cos(\boldsymbol{q}\cdot\boldsymbol{r}). \tag{2}$$

The time-dependent two-photon Rabi frequency is $\chi(t) = \Omega_0^2/2\Delta$, where $\Omega_0(t) = -\boldsymbol{\mu}\cdot\boldsymbol{E}(t)/\hbar$ is the on resonance Rabi frequency, $\boldsymbol{\mu}$ is a matrix element of the dipole moment operator, and $\boldsymbol{E}_0(t)$ is the electric field amplitude.

To calculate the signal, we first find the signal for a single atomic momentum state $\hbar\boldsymbol{k}_0$, and then sum that signal over all the initial momentum states. We therefore assume that just before the first standing-wave pulse, the atomic state is given by

$$\psi(\boldsymbol{r},0^-) = \mathrm{e}^{i\boldsymbol{k}_0\cdot\boldsymbol{r}}. \tag{3}$$

We will now apply the pulse to get

$$\psi(\boldsymbol{r},0^+) = \exp[iu_1\cos(\boldsymbol{q}\cdot\boldsymbol{r}) + i\boldsymbol{k}_0\cdot\boldsymbol{r}], \tag{4}$$

where $u_1 = \int_0^\tau \chi(t)\mathrm{d}t$ is a pulse area and τ is the duration of the pulse. Expanding Equation (4) in a Fourier series, we have

$$\psi(\boldsymbol{r},0^+) = \sum_n i^n J_n(u_1)\mathrm{e}^{i(n\boldsymbol{q}+\boldsymbol{k}_0)\cdot\boldsymbol{r}}, \tag{5}$$

which is a sum of plane waves with momenta differing by integer multiples of $\hbar\boldsymbol{q}$.

Each of the momentum states in Equation (5) oscillates at the frequency $\hbar(\boldsymbol{k}_0 + n\boldsymbol{q})^2/2M$, so the wave function at time t is given by

$$\psi(\boldsymbol{r},t) = \mathrm{e}^{i(\boldsymbol{k}_0\cdot\boldsymbol{r}-\omega_{k_0}t)}\sum_{n_1} i^{n_1}J_{n_1}(u_1)\mathrm{e}^{in_1\boldsymbol{q}\cdot(\boldsymbol{r}-\boldsymbol{v}_0t)}\mathrm{e}^{-in_1^2\omega_q t}, \tag{6}$$

where $\omega_{k_0} = \hbar k_0^2/2M$ and $\omega_q = \hbar q^2/2M$ is the two-photon recoil frequency.

As an aside, we compute the expected signal immediately after the first pulse. The atomic density after the pulse is given by $\rho(\boldsymbol{r},t) = \psi(\boldsymbol{r},t)\psi^*(\boldsymbol{r},t)$, and for a given initial velocity $\boldsymbol{v}_0$ is

$$\rho_{\boldsymbol{v}_0}(\boldsymbol{r},t) = \sum_{n_1,n_1'} i^{n_1-n_1'}J_{n_1}(u_1)J_{n_1'}(u_1)\mathrm{e}^{i(n_1-n_1')\boldsymbol{q}\cdot(\boldsymbol{r}-\boldsymbol{v}_0t)}\mathrm{e}^{-(n_1^2-n_1'^2)\omega_q t}. \tag{7}$$

In the experiment, we apply a laser field along the direction $\boldsymbol{k}_2$ and observe a scattered field along the direction $\boldsymbol{k}_1$ (see Figure 1). This signal

is proportional to the spatial Fourier component of the atomic density involving $e^{iq\cdot r}$ for which $n_1 - n_1' = 1$:

$$\rho_{q,v_0}(\boldsymbol{r},t) = \sum_{n_1} iJ_{n_1}(u_1)J_{n_1+1}(u_1)e^{-iq\cdot v_0 t}e^{-i(2n_1-1)\omega_q t}. \tag{8}$$

The expression can be summed using the identity (Watson, 1980)

$$i^v J_v\,[2u\sin(\alpha/2)] = \sum_{l=-\infty}^{\infty} e^{iv\alpha/2}J_{l+v}(u)J_l(u)e^{il\alpha}, \tag{9}$$

resulting in a density

$$\rho_{q,v_0}(t) = J_1[2u_1\sin(\omega_q t)]e^{-iq\cdot v_0 t}. \tag{10}$$

After summing over the initial Maxwellian velocity distribution, we find

$$\rho_q(t) = J_1[2u_1\sin(\omega_q t)]\langle e^{-iq\cdot v_0 t}\rangle = J_1[2u_1\sin(\omega_q t)]e^{-(q\sigma_v t/2)^2}, \tag{11}$$

where σ_v is the e^{-1} width of the velocity distribution.

Figure 2 shows data (Cahn, 1997) and a theoretical fit based on Equation (11). In the experiment, a short standing-wave pulse made up of counter-propagating fields with wave vectors $\boldsymbol{k}_1$ and $\boldsymbol{k}_2$ is applied. Immediately after the pulse, a traveling wave is applied along $\boldsymbol{k}_2$, and the scattered signal along $\boldsymbol{k}_1$ is detected. A physical picture of the data shown in Figure 2 can be understood as follows. Before the pulse the atomic density is uniform. The effect of the standing-wave pulse is a momentum kick

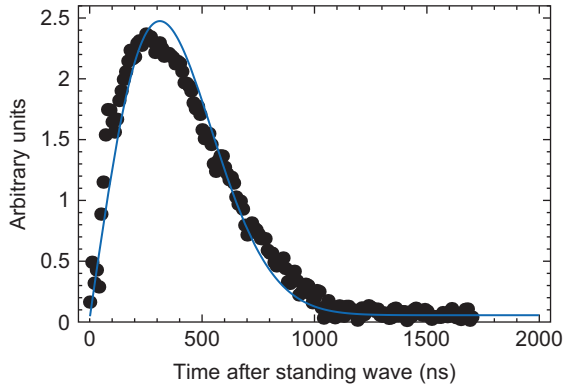

Figure 2 Doppler-broadened Kapitza-Dirac effect.

to the atoms in a direction toward the minima of the potential defined by the standing wave. Immediately after the pulse, there is no scattered signal, since the atoms have had no time to move from their initial position. With time, the atoms move toward the potential minima, creating a grating in atomic density, which scatters the light. Since there is a spread in initial velocities, the grating will wash out because of the fact that gratings produced by different velocity classes will dephase from one another on a time scale $t \sim d/\sigma_v$, where σ_v is the initial velocity spread and $d = \lambda/2$ is the period of the grating.

At time $t = T$, we apply a second pulse with area u_2. The result is that each atomic plane wave generated by the first pulse is split into a set of plane waves, and the wave function after the second pulse is given by

$$\psi(\boldsymbol{r},t) = \mathrm{e}^{i(\boldsymbol{k}_0\cdot\boldsymbol{r}-\omega_{k_0}t)}\sum_{n_1,n_2} i^{n_1+n_2}J_{n_1}(u_1)J_{n_2}(u_2) \times \mathrm{e}^{-in_1\boldsymbol{q}\cdot\boldsymbol{v}_0T}\mathrm{e}^{i(n_1+n_2)\boldsymbol{q}\cdot[\boldsymbol{r}-\boldsymbol{v}_0(t-T)]}\,\mathrm{e}^{-in_1^2\omega_qT}\mathrm{e}^{-i(n_1+n_2)^2\omega_q(t-T)}. \tag{12}$$

We find that the resulting density $\rho_{v_0}(\boldsymbol{r},t) \equiv \psi^*(\boldsymbol{r},t)\psi(\boldsymbol{r},t)$ is

$$\rho_{\boldsymbol{q},v_0}(\boldsymbol{r},t) = \sum_{n_1,n_1',n_2,n_2'} i^{n_1+n_1'+n_2+n_2'}J_{n_1}(u_1)J_{n_1'}(u_1)J_{n_2}(u_2)J_{n_2'}(u_2) \times \mathrm{e}^{-i(n_1-n_1')\boldsymbol{q}\cdot\boldsymbol{v}_0T}\mathrm{e}^{i[(n_1+n_2)-(n_1'+n_2')]\boldsymbol{q}\cdot[\boldsymbol{r}-\boldsymbol{v}_0(t-T)]} \times \mathrm{e}^{-i(n_1^2-{n_1'}^2)\omega_qT}\mathrm{e}^{-i[(n_1+n_2)^2-(n_1'+n_2')^2]\omega_q(t-T)}. \tag{13}$$

Since the experiment measures the scattering of the light field with wave-vector $\boldsymbol{k}_1$ into wave-vector $\boldsymbol{k}_2$, we are interested only in the $\mathrm{e}^{i\boldsymbol{q}\cdot\boldsymbol{r}}$ Fourier component of the atomic density. We therefore consider only the terms in Equation (13) for which $(n_1 + n_2) - (n_1' + n_2') = 1$. In addition, we define $\bar{N} \equiv n_1' - n_1$, and find

$$\rho_{\boldsymbol{q},v_0}(\boldsymbol{r},t) = \sum_{n_1,n_1',n_2,n_2'} i^{n_1+n_1'+n_2+n_2'}J_{n_1}(u_1)J_{n_1'}(u_1)J_{n_2}(u_2)J_{n_2'}(u_2) \times \mathrm{e}^{-i\boldsymbol{q}\cdot\boldsymbol{v}_0[t-(\bar{N}+1)T]}\mathrm{e}^{i(n_1+n_1')\bar{N}\omega_qT}\mathrm{e}^{-i[2(n_1+n_2)+1]\omega_q(t-T)}. \tag{14}$$

This expression, when averaged over initial velocities $\boldsymbol{v}_0$, will be equal to zero unless the Doppler phase, $\phi_D = \boldsymbol{q}\cdot\boldsymbol{v}_0[t-(\bar{N}+1)T] \approx 0$. Thus, for a given value of $\bar{N}$, no signal will be observed unless $|t - t_{\bar{N}}| < 1/q\sigma_v$, where $t_{\bar{N}} = (\bar{N}+1)T$ is the echo time. We now apply Equation (9) to Equation (14) twice to get

$$\rho_q(t) = (-1)^{\bar{N}+1}J_{\bar{N}}[2u_1\sin(\omega_q\Delta t)]J_{\bar{N}+1}[2u_2\sin(\bar{N}\omega_qT+\omega_q\Delta t)]\langle\mathrm{e}^{-i\boldsymbol{q}\cdot\boldsymbol{v}_0t}\rangle, \tag{15}$$

where $\Delta t = t - t_{\text{echo}}$. This equation can be simplified further by replacing $\langle e^{-i\mathbf{q}\cdot\mathbf{v}_0 t}\rangle$ with $e^{-(q\sigma_v t/2)^2}$, and realizing that the velocity spread of the laser-cooled atoms is much larger than the recoil velocity, so that a signal will be observed only when $\omega_q \Delta t \ll 1$. With this approximation, we can write

$$\rho_{\mathbf{q}}(t) \sim (\Delta t)^{\bar{N}} J_{\bar{N}+1}[2u_2 \sin(\bar{N}\omega_q T)] e^{-(q\sigma_v t/2)^2}, \tag{16}$$

Figures 3a and b show the echo signal as a function of Δt for $\bar{N} = 1$ and $\bar{N} = 2$, respectively. We see that for $\bar{N} = 1$, the signal is linear at the time $\Delta t = 0$, and for $\bar{N} = 2$, the signal is quadratic, which is consistent with Equation (16).

Figure 3c and d show the amplitude of the echo signal as a function of T, for $\bar{N} = 1$ and $\bar{N} = 2$, respectively. In this case, the signal is periodic with a period equal to $2\pi/\omega_q \sim 32.4\,\mu s$. We point out here that an accurate measurement of this periodicity would allow one to make an accurate determination of the recoil frequency, and hence $\hbar/M$. The precision $d\omega_q$ with which one can determine the recoil frequency is given approximately by $dT/T_{\max}$, where dT is the uncertainty in the time of the zeros of the signal and $T_{\max}$ is the maximum value of T that yields a significant signal. As will be discussed further in Section 2, a precision measurement of ω_q would allow a precise determination of the fine structure constant.

Since the development of the time-domain de Broglie wave interferometer discussed earlier, a number of extensions of the basic interferometer design have been carried out by various groups. At NYU, the theory has been extended to an arbitrary sequence of short pulses, and data have been taken for a three-pulse interferometer (Strekalov et al., 2002).

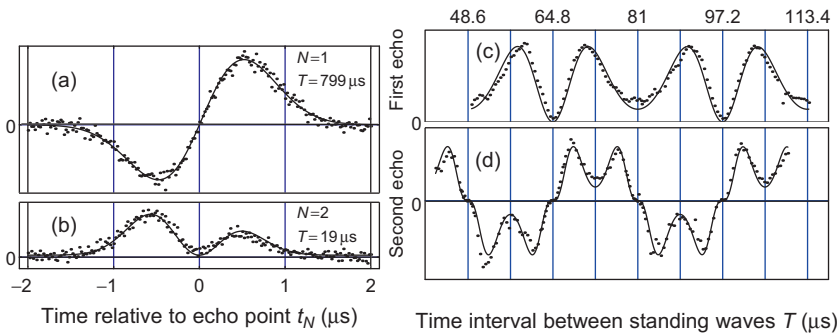

Figure 3 (a), (b) First two echoes as a function of Δt. (c), (d) First two echoes as a function of T. In all the plots, data are represented by solid dots. The solid curves in (a) and (b) are fits based on Equation (15). In (c) and (d) the solid curves are fits based on Equation (16).

At MIT, an interferometer of the type described here has been demonstrated with a Bose–Einstein condensate (BEC) (Gupta et al., 2002). At NIST in Gaithersburg, output coupling of BECs was also demonstrated using a standing-wave interferometer (Hagley et al., 1999). Other pioneering studies at MIT and Duke University have examined the role of atomic collisions on echo interferometers and developed techniques for phase-space imaging using coherent transient effects (Bacon et al., 1994; Forber et al., 1990; Thomas & Wang, 1995). Recent studies of the kicked-rotor in a magnetically guided trap for investigations of quantum dynamics and for applications to precision measurements have also used internal-state interferometers of this type (Tonyushkin & Prentiss, 2010; Tonyushkin et al., 2009a; Wu et al., 2005, 2009). At York University, the focus has been on precision measurements of atomic recoil (Beattie et al., 2009b). A complete understanding of mechanisms affecting the two-pulse interferometer was developed on the basis of analytical calculations and numerical simulations (Barrett et al., 2010; Cahn, 1997; Dubetsky, 1997) including effects such as spontaneous emission, magnetic sublevels, and standing-wave pulse parameters (rise time, duration, detuning, intensity). Systematic effects on the recoil frequency (angle between excitation beams, sample density, and index of refraction) have also been investigated. A multipulse interferometer was also developed, which has significant advantages for precision measurements (Beattie et al., 2009a). The theoretical description of this interferometer was developed using the wave function evolution approach discussed in Strekalov et al. (2002) and, separately, using the coherence function approach shown in Mandel (1979). The coherence function approach resulted in an understanding of the complete recovery of contrast in the interferometer using pulsed standing waves and the partial recovery of contrast using pulsed traveling waves and continuous wave light. The results of these studies of traveling-wave excitation were similar to the results of atomic beam experiments carried out by several pioneering groups (Chapman et al., 1995; Kokorowski et al., 2001; Pfau et al., 1994; Uys et al., 2005).

The outline of this chapter is as follows. Section 2 provides a physical description of the two-pulse interferometer described earlier and its application for precision measurements. It also presents an analysis of the effects of spontaneous emission and magnetic sublevels on the interferometer signal. The sensitivity of the interferometer to magnetic gradients and gravitational acceleration, g, is also discussed. This is followed by a description of the multipulse interferometer and a review of recent experimental results at the transit-time limit. Section 3 presents a modification to the techniques outlined earlier, in that instead of the first pulse, the atoms are cooled in an optical lattice potential, and at time $t = 0$, suddenly released. At time T a pulse of the optical lattice is applied and, at times close to $t = (\bar{N} + 1)T$, an echo is observed by the scattering of a

traveling wave. In addition, Section 3 discusses the behavior of the system if the applied pulse is of very long duration, in extreme violation of the Raman–Nath condition. Section 4 discusses frequency-domain techniques for measurements of atomic recoil and rotation. Section 5 includes a discussion of techniques for measurements of g using the two-pulse interferometer and presents recent results that show the potential for high-precision measurements. Section 6 presents techniques for measuring magnetic interactions using an internal state labeled interferometer that utilizes magnetic sublevels in a single ground state. Section 7 shows the suitability of the traditional two-pulse photon echo technique for precision measurements of atomic lifetimes. The article concludes with Section 8, which is a review of recent studies of superradiant emissions in laser-cooled atoms.

2. TIME-DOMAIN ATOM INTERFEROMETER EXPERIMENTS—ATOMIC RECOIL

2.1 Introduction

During the last 20 years, the field of precision measurements has focused on new determinations of fundamental constants. In particular, there has been renewed emphasis on independent measurements of the atomic fine structure constant, α, to test quantum electrodynamics (QED). Experiments based on the electron g-factor (Hanneke et al., 2008) and helium fine structure (Smiciklas & Shiner, 2010) rely on QED to define α. In contrast, precision measurements of α using atom interferometers (AIs) have relied on the following relationship (Taylor, 1994)

$$\alpha^2 = \left(\frac{2R_\infty}{c}\right)\left(\frac{m_p}{m_e}\right)\left(\frac{M}{m_e}\right)\left(\frac{h}{M}\right), \tag{17}$$

where R_∞ is the Rydberg constant, c is the speed of light, m_p (m_e) is the mass of the proton (electron), h is Planck's constant, and M is the mass of the test atom. Since R_∞ and the mass ratios have been measured with a precision greater than 0.1 parts per billion (ppb), AIs are well suited for precision measurements of α. Importantly, an AI-based measurement of α does not rely on QED and the precision in determining h/M is better than the precision with which h and M can be measured independently (Taylor, 1994).

AIs involving Raman transitions between hyperfine ground states have exploited the properties of laser-cooled atoms for a variety of experiments related to precision measurements and inertial sensing (Chiow et al., 2009; Dubetsky & Kasevich, 2006; Gupta et al., 2002; Lamporesi et al., 2008; McGuirk et al., 2002; Müller et al., 2010; Peters et al., 1999; Weiss et al.,

1993; Wicht et al., 2002). Recent AI-based work using Bloch oscillations in cold optical lattices (Cadoret et al., 2008) have also produced competitive measurements of α.

In this section, we review two time-domain echo-type AI techniques (Barrett et al., 2010; Beattie et al., 2009a,b, 2008; Cahn et al., 1997) that are ideal for precise measurements of the atomic recoil frequency, $\omega_q = \hbar q^2/2M$, where $\hbar q$ is the two-photon momentum transfer from counter-propagating laser fields. The different techniques for extracting ω_q are introduced briefly, followed by a more detailed discussion of signal formation.

2.1.1 Physical Description of the AI

The AI functions on the basis of phase modulation of the atomic wave function due to the interaction with standing-wave (sw) pulses. Although this phase modulation is directly connected to the recoil energy, the functional form of the signal has a complicated dependence on a number of mechanisms that we explore in the following subsections. These include the dynamic population of magnetic sublevels, phase shifts due to spontaneous and stimulated processes, excitation of multiple momentum states, and the spatial profile of the excitation beams. Recent work has successfully modeled the signal shape on the basis of analytical calculations as well as numerical simulations (Barrett et al., 2010; Beattie et al., 2008).

The AI uses a cold gas of rubidium atoms. The sample is excited by sw pulses that satisfy the Raman–Nath criterion and are far-detuned from the excited state. Each such pulse results in the diffraction of atoms into a superposition of momentum states separated by $\hbar q = 2\hbar k$ (as shown in Figure 4a), where $k = 2\pi/\lambda$ is the wavenumber of the traveling wave components of the sw. Each pulse transfers momenta in integer multiples of $\hbar q$, due to scattering of radiation between the two traveling-wave components of the sw field. After excitation, the sample evolves into a superposition of momentum states corresponding to the same internal ground state—which can have several magnetic sublevels.

The recoil phase of momentum state $|p = n\hbar q\rangle$ scales as $n^2\omega_q t$, where n is an integer denoting the number of two-photon transitions induced by the sw pulse. The Doppler phase of these states evolves as nqv_0t, where v_0 is the initial atomic velocity. The modulation of the wave function occurs on a timescale $\tau_q = \pi/\omega_q$ ($\sim$32 μs for ^{85}Rb). This occurs because atoms differing in velocity by the recoil velocity, $v_q = \hbar q/M$, are displaced relative to one another by one grating period ($\lambda/2$) in a time τ_q. This time scale should be compared to the coherence time, $\tau_{\mathrm{coh}} \sim 2/q\sigma_v$, of the atomic density grating induced by the sw potential. Here, $\sigma_v = \sqrt{2k_{\mathrm{B}}\mathcal{T}/M}$ is the e^{-1} width of the velocity distribution and $\mathcal{T}$ is the temperature of the sample. This is the time scale on which the temporal modulation of the wave

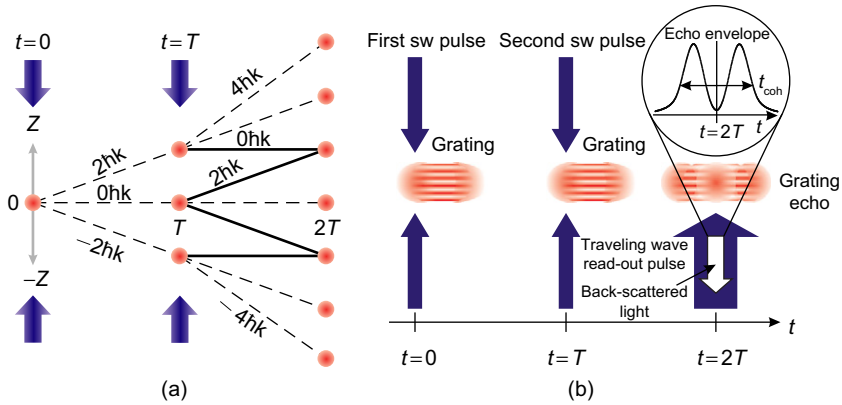

Figure 4 (a) Recoil diagram for the two-pulse AI. Center-of-mass momentum states are shown as dots. Standing-wave pulses are applied at $t = 0$ and $t = T$ to diffract the momentum states of the atom into multiples of the two-photon recoil momentum $2\hbar k$. Only the zeroth-order and the $\pm$ first-order diffractions from each sw pulse are drawn for simplicity. Two pairs of interfering momentum states are shown as solid lines. (b) Pulse timing diagram for the experiment. After each sw pulse, a modulation in atom density forms and then decays in a time τ_{coh} because of Doppler dephasing. At time $t = 2T$, the grating echo forms as a result of the interference between different momentum states. A traveling-wave read-out pulse coherently scatters light from the grating at this time. The intensity of this light is detected as the signal.

function decoheres because of Doppler dephasing from the finite velocity distribution of the sample.

For BEC conditions with $\mathcal{T} \sim 10^{-8}$ K, the dephasing time can be much longer than the modulation period of the wave function. In this case, the recoil modulation can be observed with a single sw pulse, as discussed in detail in Section 2.3.

The theoretical expression for the recoil signal in the two-pulse regime was originally derived in Cahn et al. (1997). The treatment in (Beattie et al., 2008) addressed the role of spontaneous emission (SE) on the recoil signal. A comprehensive study of effects on the two-pulse AI related to both stimulated and spontaneous processes between magnetic sublevels in the ground and excited states was carried out using numerical simulations in Barrett et al. (2010). An analytical model of the two-pulse AI including both SE and magnetic sublevels was also derived in this work. We discuss these issues in Section 2.4.

An alternative technique for measuring ω_q, described in Section 2.5, involves excitation with a third sw pulse applied at $t = T + \delta T$. One then observes the influence of this pulse on the echo at $t = 2T$. Figure 5 shows the timing diagrams for both the two-pulse and three-pulse AI techniques. In the absence of SE, the contrast at $t = 2T$ can be recovered when δT is

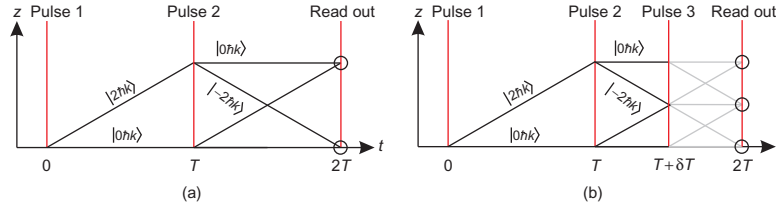

Figure 5 Recoil diagram for the two-pulse AI (a) and the three-pulse AI (b). The grating contrast at $t = 2T$ is measured by varying the pulse separation, T, in the two-pulse AI. In the case of the three-pulse AI, T is held fixed and the time of the third pulse, δT, is varied. The contrast exhibits a periodic revival when δT is an integer multiple of the recoil period, τ_q.

an integer multiple of τ_q, due to constructive interference of phase-shifted momentum states produced by the third pulse, as shown in Figure 5b. The basic signal shape produced by this AI can be described by a coherence function (Beattie et al., 2009b; Mandel, 1979)—a Fourier transform of the atomic momentum distribution produced by a sw pulse. A more detailed quantum mechanical calculation of the echo formation (Beattie et al., 2009a; Strekalov et al., 2002) predicts certain scaling laws for the fringe width as a function of the area of the third pulse which can be exploited to improve the precision of a measurement of ω_q.

In contrast, if the third pulse is a traveling wave, the quasi-periodic contrast cannot be fully recovered because of decoherence from SE. The contrast as a function of δT in this case can also be described using a coherence function, as in atomic beam experiments (Chapman et al., 1995; Kokorowski et al., 2001; Pfau et al., 1994; Uys et al., 2005) and in time-domain experiments in cold atoms (Beattie et al., 2009a).

2.2 Experimental Work

Although the timescale and precision associated with the recoil experiment should be limited only by the transit time of the atoms through the region of interaction, in practice it is necessary to eliminate the effects of decoherence due to atomic collisions and background light. Magnetic field gradients also cause amplitude oscillations that must be eliminated (Weel et al., 2006). A plot of the signal decay as a function of the pulse separation, T, is shown in shown in Figure 6a. The decrease in signal with T is mainly due to residual magnetic field gradients and the loss of atoms from the region of interaction defined by the excitation beams.

An interesting aspect of using the echo technique is that the Doppler phases accumulated by momentum states cancel at the echo times. As a result, the experiment does not rely on velocity selection. Although velocity selection is not required for the grating echo AI, sub-Doppler cooling

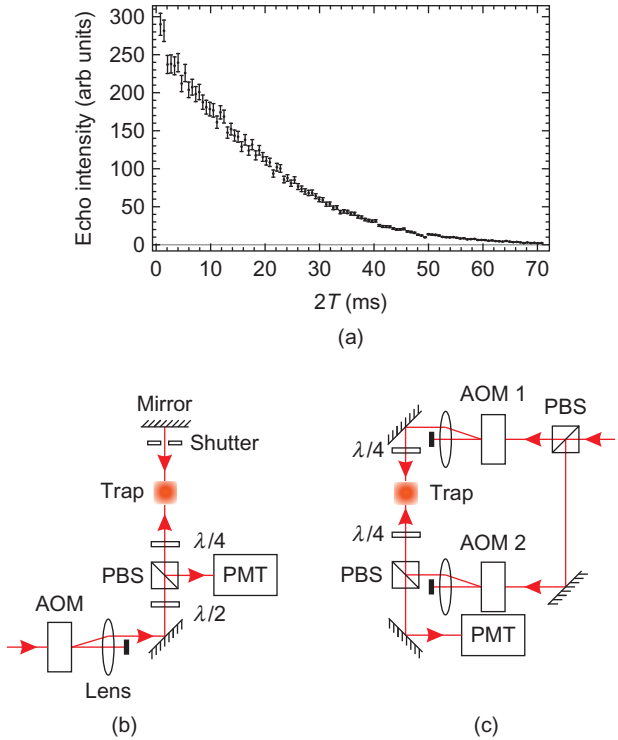

Figure 6 (a) Signal decay of the two-pulse AI as a function of pulse separation, T. The first pulse is held fixed while the second pulse and read-out pulse are moved out in integer units of the recoil period, τ_q, and twice the recoil period, respectively. The loss of signal is primarily due to atoms leaving the region of interaction. (b) Experimental setup used for the two-pulse recoil experiment and (c) for the three-pulse experiment.

of the sample is necessary to extend the transit time, which is the primary limitation for the timescale of the experiment.

Experiments involving the two-pulse technique (Beattie et al., 2008) were carried out in a stainless steel vacuum chamber. The light used for atom trapping and atom interferometry is derived from a Ti:Sapphire ring laser and from a semiconductor tapered amplifier seeded by light from the Ti:Sapphire laser. Approximately 10^8 ^{85}Rb atoms are loaded into a magneto-optical trap (MOT) in ∼200 ms. The temperature of the sample was typically ∼50 μK (Vorozcovs et al., 2005).

The excitation pulses for the AI are derived from a chain of acousto-optic modulators (AOMs) controlled by transistor-transistor logic (TTL) switches that ensure an extinction ratio for the radio frequency (RF) power of ∼40 dB. Pulsing a chain of AOMs ensures that excitation and read-out pulses have on/off contrast greater than 10^6 : 1, thereby minimizing

decoherence due to background light. The last AOM in this chain operates at 250 MHz and is shown in Figure 6b. The diffracted beam from this AOM serves as the excitation beam. A beam diameter of ∼0.5 cm was used, which is comparable to the initial cloud diameter of ∼0.6 cm. The mirror shown at the top of Figure 6c is used to retro-reflect the traveling-wave pulses from the AOM and produce the sw excitation pulses used for the AI. A shutter with a closing time of ∼600 μs is used to block the retro-reflection at the time of the read-out pulse.

The grating contrast is detected using a read-out pulse that has the same polarization and detuning as the excitation pulses. The scattered light from the sample due to the read-out pulse is detected using a gated photomultiplier tube (PMT). Owing to jitter in the shutter closing time of ∼200 μs, the smallest pulse separation, T, for which the echo can be recorded using this technique is ∼1 ms. The grating contrast is determined by integrating the echo envelope over the signal duration of ∼2 μs.

For recent experiments with the three-pulse technique, a glass vacuum system was used. Here, the trap loads $\sim 10^9$ atoms in ∼300 ms. Both the MOT laser beams and the magnetic field gradient are switched off prior to the AI experiment. Three pairs of coils, one pair along each direction, are used to cancel residual magnetic fields and field gradients. These coils remain on continuously. Under these conditions, the magnetic field at the time of the echo experiment is canceled at the level of ∼1 mG over the volume of the trap. The AI excitation pulses are derived from two off-resonant, circularly polarized, traveling wave beams. They are overlapped at the location of the trap to form a sw along the vertical direction. The AI beams have a Gaussian intensity profile and are collimated to a diameter of ∼1 cm. Two separate AOMs operating at 250 MHz were used to generate counter-propagating traveling-wave pulses as shown in Figure 6c. This arrangement allowed the shutter to be eliminated so that the time separation between the standing-wave excitation pulses, T, could be reduced to a few microseconds.

2.3 One-Pulse Atom Interferometer

In order to fully understand the origin of the signal used in the experiments, a quantum theory of matter wave interference is essential. Such a theory is governed by the quantization of the atomic center-of-mass motion and is analogous to the diffraction of light in classical optics.

The simplest signal is presented first, namely the recoil signal produced by one sw pulse. In order to observe interference between momentum states after one pulse, the velocity distribution of the sample must be very narrow ($\sigma_v/v_q \ll 1$) such that the coherence of the sample is preserved much longer than the onset time of recoil modulation (τ_q). The calculation of the signal is then carried out in two stages. First, the Schrödinger equation is solved for the ground-state amplitude of the atomic wave

function using the two-level Hamiltonian for a sw laser field. The Hamiltonian assumes that the sw pulse is short (Raman–Nath regime) such that the motion of the atoms along the axis of the sw can be neglected during the interaction. It also assumes that the pulse is far off-resonance ($|\Delta| \gg \Omega_0, \gamma$) such that the excited state is not significantly populated. This leads to Kapitza-Dirac diffraction of the atomic wave function into a superposition of momentum states. Here, $\Delta \equiv \omega - \omega_0$ is the detuning of the laser frequency, ω, from the atomic resonance frequency, ω_0, $\Omega_0 \equiv \mu_{eg} E_0/\hbar$ is the Rabi frequency, μ_{eg} is a dipole matrix element, E_0 is the electric-field amplitude of each traveling-wave component of the sw, and $\gamma = \Gamma/2$, where Γ is the spontaneous emission rate.

In the second stage of the calculation, after the pulse has turned off, the atom is allowed to evolve in free space for a time t, which results in a modification of the phase of the ground-state amplitude. In an experiment involving a BEC, a traveling-wave read-out pulse with wavelength λ can be applied to the atomic sample and the back-scattered electric field can be detected as the signal (Gupta et al., 2002). The amplitude of the scattered field is proportional to the $\lambda/2$-periodic component of the atomic density modulation (the $2k = q$-Fourier harmonic) produced by the sw interaction. For a long read-out pulse, the scattered signal would exhibit temporal modulation proportional to the contrast of the atomic density distribution.

For a two-level atom, the Hamiltonian in the field-interaction representation is (Berman & Malinovsky, 2011)

$$\mathcal{H} = \hbar \begin{pmatrix} -\Delta - i\gamma & \Omega(\boldsymbol{r}) \\ \Omega(\boldsymbol{r}) & 0 \end{pmatrix}, \tag{18}$$

where $\Omega(\boldsymbol{r}) = \Omega_0 \cos(\boldsymbol{k} \cdot \boldsymbol{r})$ for a sw laser field. The energy is defined to be zero for the ground state and $-\hbar\Delta$ for the excited state. The $-i\hbar\gamma$ term is a phenomenological constant added to account for SE during the interaction, which gives rise to amplitude decay of the excited state. For the moment, the effects due to SE are ignored by setting $\gamma = 0$ in Equation (18). These effects are discussed in a later section.

The ground-state density produced after the interaction with one sw pulse is

$$\rho_g^{(1)}(\boldsymbol{r}, t) = \frac{1}{V} \sum_{\nu=-\infty}^{\infty} \chi_\nu^{(1)}(t) e^{-i\nu \boldsymbol{q} \cdot \boldsymbol{r}}, \tag{19a}$$

$$\chi_\nu^{(1)}(t) = i^\nu e^{i\nu \boldsymbol{q} \cdot \boldsymbol{v}_0 (t - T_1)} \sum_n J_n(u_1) J_{n+\nu}(u_1) e^{i\nu(2n+\nu)\omega_q (t - T_1)}. \tag{19b}$$

Here, $\chi_\nu^{(1)}(t)$ is the amplitude of the $\nu\boldsymbol{q}$-Fourier harmonic of the density distribution and the superscript (1) denotes that this is valid for one sw

pulse. The field scattered from the density grating is proportional to $\chi_1^{(1)}(t)$ and can be shown to be (Barrett et al., 2010)

$$E^{(1)}(t) \propto -J_1\left[2u_1 \sin \omega_q (t - T_1)\right], \tag{20}$$

where T_1 is the onset time of the pulse, ω_q is the recoil frequency and u_1 is the pulse area, which, for a pulse duration of τ_1, is given by

$$u_1 = \frac{\Omega_0^2}{2\Delta}\tau_1. \tag{21}$$

Figure 7 shows the atomic density (obtained using Equation [19a]) and corresponding scattered field amplitude (obtained using Equation [20]) for two different pulse areas.

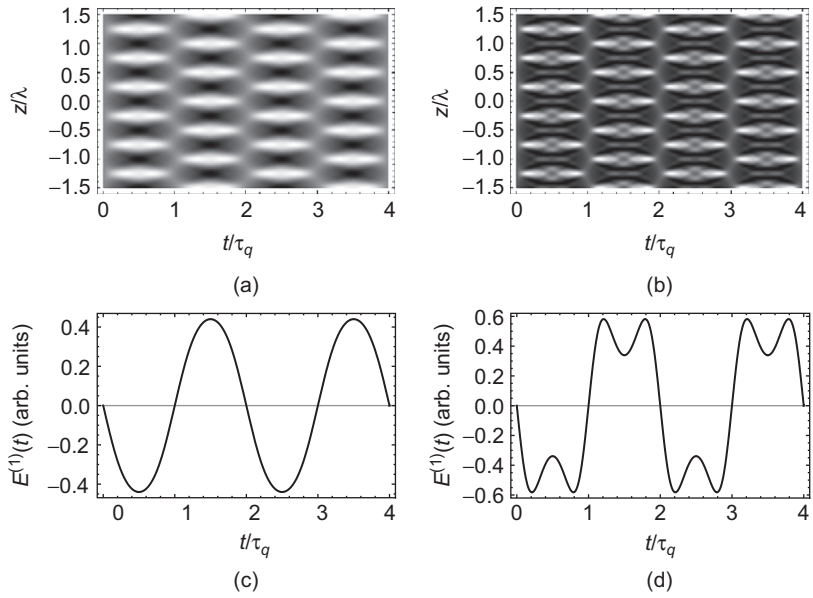

Figure 7 Density distribution, $\rho_g^{(1)}(z,t)$, and corresponding back-scattered electric field amplitude, $E^{(1)}(t)$, for an atomic sample after the interaction with a weak sw pulse (a, c) and a strong sw pulse (b, d). In plots (a) and (b), z is the distance along the sw field. Dark portions correspond to low density while light portions correspond to high density. $\rho_g^{(1)}(z,t)$ shows spatial modulation that is periodic at integer multiples of $\lambda/2$, and shows temporal modulation at integer multiples of $2\omega_q$ as the pulse area increases. Equation (19a) was used to produce plots (a) and (b) with pulse area $u_1 = 0.5$ and 1.5, respectively. In plots (c) and (d), Equation (20) was used with the same respective pulse areas. The zeroes in the contrast of the density modulation correspond to the zeroes in $E^{(1)}(t)$.

The recoil signal in the one-pulse regime is the intensity of the scattered field, which is proportional to the square of Equation (20): $s^{(1)}(t) \propto |E^{(1)}(t)|^2$.

2.4 Two-Pulse Atom Interferometer

Here, the two-pulse atom interferometer is discussed, along with the qualitatively new features that arise in this case. When the velocity dispersion of the sample is large, that is, $\sigma_v/v_q > 1$, the grating in Equation (19a) is washed out. By subjecting the sample to a second sw pulse, the grating is reformed at a later time. The grating echoes occur only at times where the Doppler phase cancels, (as shown in Figure 8)

$$t_{\text{echo}}^{(2)} = T_2 + \bar{N}(T_2 - T_1) = (\bar{N} + 1)T, \tag{22}$$

for pulse onset times of $T_1 = 0$ and $T_2 = T$.

The first echo time where all momentum states interfere is $t_{\text{echo}}^{(2)} = 2T$, corresponding to $\bar{N} = 1$, which will be the focus of most of this work. The scattered field amplitude in the vicinity of the $\bar{N}$th- order echo time is

$$\begin{aligned} E_{\bar{N}}^{(2)}(\Delta t; T) \propto (-1)^{\bar{N}+1} \mathrm{e}^{-(\Delta t/\tau_{\text{coh}})^2} J_{\bar{N}}\big(2u_1 \sin(\omega_q \Delta t)\big) \\ \times J_{\bar{N}+1}\big(2u_2 \sin[\omega_q(\Delta t + \bar{N}T)]\big), \end{aligned} \tag{23}$$

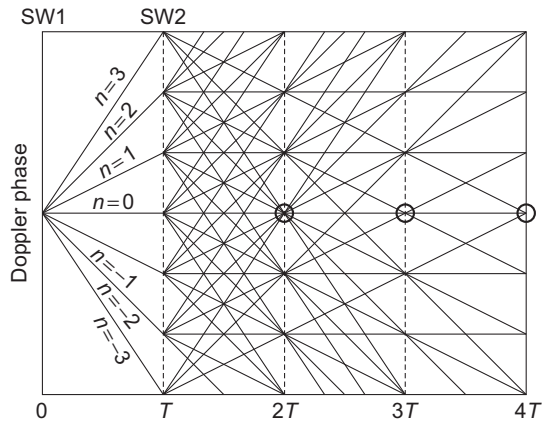

Figure 8 Two-pulse recoil diagram: Doppler phase as a function of time for momentum states $|n\hbar q\rangle$. Only $n = -3, \ldots, 3$ are shown for simplicity. The first sw pulse (SW1) is applied at $t = 0$, while the second (SW2) is applied at $t = T$. Echo times (given by Equation [22]) are marked by circles. The number of crossings at each echo time is proportional to the contrast of the $\lambda/2$-periodic density grating formed at those times.

where $\Delta t = t - t^{(2)}_{\text{echo}}$, with $t^{(2)}_{\text{echo}}$ given by Equation (22). From this expression, it is clear that the scattered field amplitude is periodic at multiples of the recoil frequency as a function of the pulse separation T. It is interesting to note that, for the $\bar{N}$th-order echo, the scattered field amplitude changes at frequency $\bar{N}\omega_q$, which is advantageous for a precision measurement of ω_q. However, the maximum contrast of the $\bar{N}$th-order echo is reduced by a factor of $\sim J_{\bar{N}-1}(2u_1)/J_{\bar{N}}(2u_1) \sim (2u_1)^{-1}$ relative to the $(\bar{N}-1)$th order echo, which manifests as a loss in the signal to noise ratio in the experiment.

In the experiment, the measurable quantity is the relative contrast of the atomic density grating in the vicinity of the echo. This quantity—defined as the recoil signal—is obtained by integrating the scattered field intensity over the duration of the echo, which can be written as

$$s^{(2)}_{\bar{N}}(T) \propto J^2_{\bar{N}+1}\big(2u_2 \sin(\bar{N}\omega_q T)\big), \tag{24}$$

where the superscript (2) denotes the number of pulses used to produce the signal and the subscript $\bar{N}$ denotes the order of the echo.

2.4.1 Effects due to Spontaneous Emission

Spontaneous emission during the sw interaction strongly affects the recoil signal (Beattie et al., 2008). Taking it into account, the expression for the scattered field in the case of both one and two pulses is modified as follows:

$$E^{(1)}(t) \propto -J_1\left(2u_1\sqrt{\sin(\phi^{(1)}_1+\theta)\sin(\phi^{(1)}_1-\theta)}\right)\left(\frac{\sin(\phi^{(1)}_1-\theta)}{\sin(\phi^{(1)}_1+\theta)}\right)^{1/2}, \tag{25a}$$

$$\begin{aligned} E^{(2)}_{\bar{N}}(\Delta t;T) \propto{}& (-1)^{\bar{N}+1}\mathrm{e}^{-(\Delta t/\tau_{\text{coh}})^2} \\ &\times J_{\bar{N}}\left(2u_1\sqrt{\sin(\phi^{(2)}_1+\theta)\sin(\phi^{(2)}_1-\theta)}\right) \\ &\times J_{\bar{N}+1}\left(2u_2\sqrt{\sin(\phi^{(2)}_2+\theta)\sin(\phi^{(2)}_2-\theta)}\right) \\ &\times \left(\frac{\sin(\phi^{(2)}_1+\theta)}{\sin(\phi^{(2)}_1-\theta)}\right)^{\bar{N}/2}\left(\frac{\sin(\phi^{(2)}_2-\theta)}{\sin(\phi^{(2)}_2+\theta)}\right)^{(\bar{N}+1)/2}. \end{aligned} \tag{25b}$$

Here, the recoil phases for each pulse are defined as

$$\phi^{(1)}_1 = \omega_q(t-T_1), \tag{26a}$$

$$\phi^{(2)}_1 = \omega_q[t - T_2 - \bar{N}(T_2-T_1)] = \omega_q\Delta t, \tag{26b}$$

$$\phi^{(2)}_2 = \omega_q(t-T_2) = \omega_q[\Delta t + \bar{N}(T_2-T_1)], \tag{26c}$$

where T_j is the onset time of pulse j, u_j is the magnitude of the complex pulse area, $\Theta_j = u_j e^{i\theta}$, given by

$$u_j = \frac{\Omega_0^2 \tau_j}{2\Delta}\left[1 + \left(\frac{\Gamma}{2\Delta}\right)^2\right]^{-1/2}, \tag{27}$$

and θ is a phase that represents the degree to which SE contributes to the signal:

$$\theta = \tan^{-1}\left(-\frac{\Gamma}{2\Delta}\right). \tag{28}$$

There are two main features that are observed when SE is present. First, within a single period, the signal develops an *asymmetry* about the zeroes. Second, there is a temporal shift of the zeroes toward earlier times relative to the zeroes expected without SE. Both of these features are best demonstrated when the pulse area is large—causing the double-peak structure within each period of the recoil signal. This is illustrated in Figure 9a for the one-pulse case, and has been observed experimentally in the two-pulse case as shown in Figure 9b.

In the absence of SE the signal develops multiple peaks within each period for large pulse areas (compare Figure 7c to Figure 7d). This

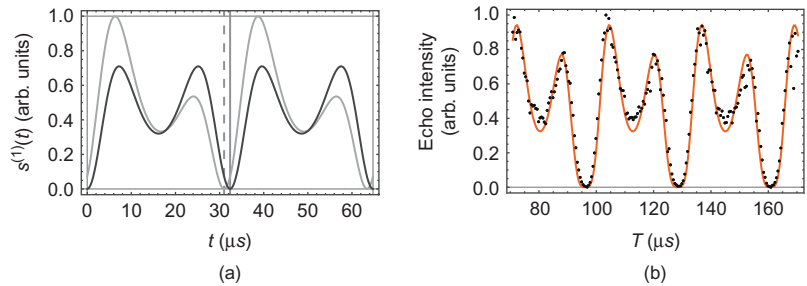

Figure 9 (a) Comparison of recoil curves (scattered field intensity as a function of time after the sw pulse) predicted by the one-pulse theory (square of Equation [25a]) with and without SE. The black curve corresponds to a SE-free system ($\Gamma = 0 \rightarrow \theta = 0$), while the gray curve corresponds to a system where SE is present ($\Gamma = \Gamma_N \rightarrow \theta = -0.133$ rad). The solid vertical line shows the first zero in the signal after $t = 0$ in the absence of SE, while the dashed vertical line shows the zeroes shift by a temporal amount $\delta t = \theta/\omega_q$ in the presence of SE. Pulse parameters: $\Delta = 7.5\,\Gamma_N$; $\Omega_0 = 1.5\,\Gamma_N$; $\tau_1 = 250$ ns; pulse area $u_1 \sim 1.43$. (b) Data from the two-pulse recoil experiment fitted to the square of Equation (25b)—solid line. The data exhibit a similar asymmetric shape to that predicted by the theory. Pulse parameters: detuning $\Delta \sim 50$ MHz; intensity $I \sim 50$ mW/cm^2; pulse durations $\tau_1 = 300$ ns, $\tau_2 = 70$ ns; circular polarization.

structure is due to the interference of higher order momentum states which become more populated as the pulse area increases. In the absence of any phase shifts of the individual harmonics, the shape of the recoil signal ($s^{(1)}(t) = |E^{(1)}(t)|^2$) is symmetric (black curve in Figure 9a).

On the other hand, when SE is present the phases of the individual harmonics comprising the signal are shifted by a phase $\phi_n^{(1)} \approx |n|\theta - n\pi/2$ (Barrett et al., 2010), as a result of the decay of the excited state into the ground state. Here, n is an integer denoting the momentum states that are interfering ($\langle n\hbar q \,|\, (n+1)\hbar q\rangle$) to produce each harmonic of the signal. Since the signal is a coherent sum over all the harmonics, it exhibits more constructive interference on one side of its zeroes than the other, giving rise to an asymmetry in the peak amplitude within each recoil period. It also results in an overall temporal shift of the waveform equal to $\delta t = \theta/\omega_q$.

2.4.2 Effects due to Magnetic Sublevels

In the experiment ^{85}Rb is used, which is a multilevel atom. If only the $F = 3 \rightarrow F' = 4$ transition is considered, there are $2F + 1 = 7$ ground-state magnetic sublevels and nine excited state sublevels. These energetically degenerate sublevels have a significant effect on the response of the AI.

The coupling strength between states $|g\rangle = |n_g J_g m_g\rangle$ and $|e\rangle = |n_e J_e m_e\rangle$ is determined by the dipole matrix element

$$\mu_{eg} = -e\,\langle e \,|\, \hat{\epsilon}_{q_L} \cdot \boldsymbol{r}\, |g\rangle = -e\langle n_e J_e \| r \| n_g J_g\rangle C^{J_g\ 1\ J_e}_{m_g\ q_L\ m_e}, \tag{29}$$

where n_g, n_e are the principal quantum numbers, J_g, J_e are the total angular momenta, and m_g, m_e are the magnetic sublevels of the ground and excited states, respectively. In our case, $J_g = F = 3$ and $J_e = F' = 4$. The unit vector $\hat{\epsilon}_{q_L}$ represents the polarization of the laser field. Linear and circular polarization states are denoted by q_L. Here, $q_L = 0$ for linearly polarized light along the quantization axis, $\hat{z}$ ($\boldsymbol{k} \parallel \hat{z}$), and $q_L = \pm 1$ for $\sigma^{\pm}$ polarizations in the xy-plane ($\boldsymbol{k} \perp \hat{z}$). The factor $\langle n_e J_e \| r \| n_g J_g\rangle$ in Equation (29) is the reduced matrix element associated with the radial part of the wave functions—the magnitude of which is unimportant for this treatment and will be absorbed into the Rabi frequency, $\Omega_0 = \mu_{eg} E_0/\hbar$. The factor $C^{J_g\ 1\ J_e}_{m_g\ q_L\ m_e}$ is the Clebsch-Gordan coefficient, which describes how strongly two states are coupled by the photon and depends on the particular transition. We are concerned only with electric dipole transitions that obey the selection rules: $J_e = J_g + 1$ and $m_e = m_g + q_L$.

From Equation (29), it is apparent that each degenerate m-level interacts with a sw pulse (of a given polarization) with a different coupling strength—which is proportional to the Rabi frequency for each transition: $C^{J_g\ 1\ J_e}_{m_g\ q_L\ m_e}\,\Omega_0$. In the experiment, this differential coupling causes the

population of the m-levels to become unbalanced after the interaction with the sw pulse (optical pumping). The degree of the imbalance is determined by Ω_0, Δ, and the pulse durations. In the analytical treatment that follows, optical pumping is not taken into account. We assume that the population of each m-level remains constant during the sw pulses. However, optical pumping effects can be taken into account using numerical simulations of the AI, which will be discussed later.

The area of a given sw pulse, denoted by index j, is given by

$$u_j^{(m_g)} = \frac{\Omega_0^2 \tau_j}{2\Delta}\left[1+\left(\frac{\Gamma}{2\Delta}\right)^2\right]^{-1/2}\left(C^{J_g\ 1\ J_e}_{m_g\ q_L\ m_e}\right)^2. \tag{30}$$

For the first-order echo of the two-pulse recoil signal ($\bar{N}=1$), the total scattered field amplitude is a sum over the fields scattered by each state $|J_g\, m_g\rangle$ (Barrett et al., 2010)

$$\begin{aligned} E_1^{(2)}(\Delta t;T) \propto e^{-(\Delta t/\tau_{coh})^2}&\left(\frac{\sin(\phi_1^{(2)}+\theta)}{\sin(\phi_1^{(2)}-\theta)}\right)^{1/2}\left(\frac{\sin(\phi_2^{(2)}-\theta)}{\sin(\phi_2^{(2)}+\theta)}\right)\\ &\times\sum_{m_g}\left(C^{J_g\ 1\ J_e}_{m_g\ q_L\ m_e}\right)^2 J_1\left(2u_1^{(m_g)}\sqrt{\sin(\phi_1^{(2)}+\theta)\sin(\phi_1^{(2)}-\theta)}\right)\\ &\times J_2\left(2u_2^{(m_g)}\sqrt{\sin(\phi_2^{(2)}+\theta)\sin(\phi_2^{(2)}-\theta)}\right), \end{aligned} \tag{31}$$

where the $\phi_j^{(2)}$ are recoil phases given by Eqs. (26b) and (26c). The extra factor of $\left(C^{J_g\ 1\ J_e}_{m_g\ q_L\ m_e}\right)^2$ in Eq. (31) arises because of the coupling of states $|J_g\, m_g\rangle$ and $|J_e\, m_e\rangle$ by the traveling-wave read-out pulse (assuming that the scattered field has the same polarization as the read-out pulse).

The form of Equation (31) allows for interference between scattered fields from each m-level. This additional interference from magnetic sublevels strongly affects the shape of the recoil signal. Figure 10a shows a comparison of two-pulse recoil signals predicted by the simple two-level theory (square of Equation [25b]) and the theory including multiple sublevels (square of Equation [31]). The two-level theory predicts extra zeroes in the signal shape that are not observed experimentally. In contrast, for the same set of pulse parameters, the multilevel theory correctly predicts that these extra zeroes should not be present. Their absence is due to the interference of back-scattered light from each magnetic sublevel.

Indeed, as Figure 10b shows, data from the two-pulse recoil experiment strongly support the multilevel model described by Equation (31). In particular, the multilevel theory successfully models the asymmetry

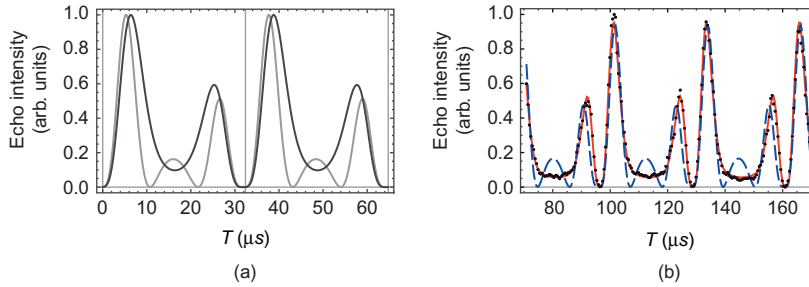

Figure 10 (a) Two-pulse recoil curves predicted by the two-level theory (square of Equation [25b]—gray curve) and the theory including magnetic sublevels (square of Equation [31]—black curve). The *m*-level populations were assumed to be equally distributed among the seven levels of the $J_g = 3$ ground state of ^{85}Rb. Pulse parameters: $\Delta = 10\,\Gamma_N$; $\Omega_0 = 2.5\,\Gamma_N$; $\Gamma = \Gamma_N$, $\tau_2 = 250$ ns. (b) Data from the two-pulse recoil experiment. Data are fitted to the two-level expression (square of Equation [25b]—dashed line), and the multilevel expression (square of Equation [31]—solid line). Pulse parameters: detuning $\Delta \sim 50$ MHz; intensity $I \sim 50$ mW/cm^2; polarization state $|q_L| = 1$; first pulse durations $\tau_1 = 300$ ns, $\tau_2 = 98$ ns.

and the broad valleys between zeroes that occur as the area of the second pulse is increased. Fits using the multilevel theory show a factor of ~10 improvement in the χ^2/dof compared to that of the two-level theory, which corresponds to a factor of ~3 improvement in the relative uncertainty of the recoil frequency. Thus, the multilevel model is necessary for precision measurements of ω_q using the two-pulse technique.

2.4.3 Spatial Profile

Another complication in modeling the AI is that magnetic sublevels and the spatial intensity profile of the excitation beams can be shown to produce similar effects on the signal shape. For the data presented earlier, the beam diameter (~1 cm) was larger than the diameter of the atomic cloud (~0.6 cm). Under these conditions, magnetic sublevels played the dominant role on the response of the AI. However, when the beam diameter is comparable to the size of the atomic cloud, these effects are indistinguishable.

Figure 11 shows a typical measurement of ω_q using the two-pulse technique. The echo intensity is recorded over two widely separated periods. The fit to the data shown in both plots is based on a phenomenological treatment including the effects due to SE and the spatial profile of excitation beams (Beattie et al., 2008) and gives an error for ω_q of ~3 parts per million (ppm). This is a factor of ~3 more precise than the fits using models without accounting for the spatial profile.

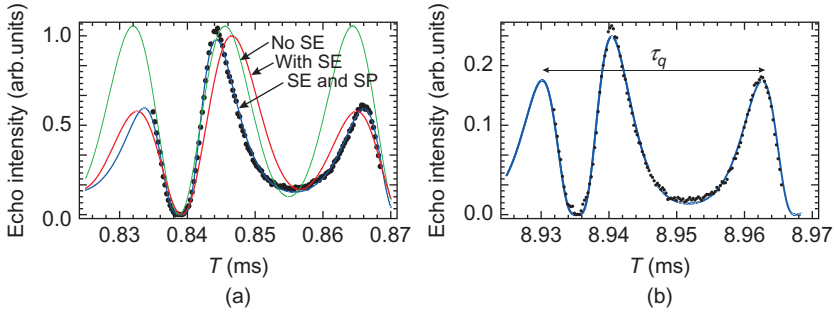

Figure 11 Grating contrast as a function of T for the two-pulse experiment shown at (a) $T \sim 1$ ms and (b) $T \sim 9$ ms. Part (a) shows three fits to the data, one based on the theory of echo formation ignoring effects due to SE (labeled "No SE"), one including SE (labeled "With SE"), and one based on a phenomenological treatment including both SE and the spatial profile of excitation beams (labeled "SE and SP"). Part (b) shows only the fit based on the phenomenological model. This fit gave a single measurement of ω_q precise to ~3 ppm.

In either case of small or large beam diameter, the importance of including both SE and magnetic sublevels/spatial profile in the model of the signal is quite significant for precision measurements.

2.4.4 Effects due to B-Field Gradients and Gravity

The effect of a constant acceleration on the interferometer manifests itself as a phase shift of the atomic grating, and therefore of the back-scattered electric field. Here, the modification of the scattered field amplitude due a constant force is presented. Two physical examples are considered: the force due to gravity and the force on the atom due to the presence of a uniform magnetic field gradient (Weel et al., 2006). Both of these forces can be written in the form $\hat{U}(z) = -\hat{\mathcal{M}}z$, where $\hat{\mathcal{M}}$ is an operator that commutes with both the position (z) and momentum (p) operators, and acts on the basis states $|F\, m_F\rangle$. In the case of gravity, $\hat{\mathcal{M}} = \mathcal{F}\hat{I}$, with $\mathcal{F} = -Mg$ and identity matrix $\hat{I}$ since gravity acts equally on all magnetic sublevels. In the case of a magnetic field gradient, the potential is

$$\hat{U}(z) = -\boldsymbol{\mu} \cdot \boldsymbol{B}(z) = -g_F \mu_B G \frac{\hat{F}_z}{\hbar} z, \tag{32}$$

where g_F is the Landé g-factor, μ_B is the Bohr magneton, and $\boldsymbol{B}(z) = Gz$, where $G = \partial B/\partial z$ is a uniform magnetic field gradient along z, and $\hat{F}_z$ is the projection operator for total angular momentum, $\boldsymbol{F}$. In this case, $\hat{\mathcal{M}} = \mathcal{F}\hat{F}_z/\hbar$ and $\mathcal{F} = g_F \mu_B G$.

The total scattered field from all magnetic sublevels in the presence of a gradient G can be shown to be

$$E^{(2)}_{\bar{N},G}(\Delta t;T) = E^{(2)}_{\bar{N}}(\Delta t;T)\sum_{m_F}|\alpha_{m_F}|^2 e^{im_F\phi^{(2)}_G}, \tag{33}$$

where $E^{(2)}_{\bar{N}}$ is given by Equation (23) and the phase due to the gradient is

$$\phi^{(2)}_G(\Delta t;T) = \frac{qg_F\mu_B G}{2M}\left[\bar{N}(\bar{N}+1)T^2 + 2(\bar{N}+1)\Delta tT + \Delta t^2\right]. \tag{34}$$

From Equation (33), it is clear that the scattered field amplitude from state $|F\,m_F\rangle$ exhibits phase modulation as a function of the pulse spacing, T, at a frequency $m_F\omega^{(2)}_G(T)$ due to the presence of the gradient, where $\omega^{(2)}_G(T) = \partial\phi^{(2)}_G/\partial T$. This frequency depends linearly on the value of T (since the phase scales as T^2) and the magnetic quantum number, m_F. For an arbitrary set of m-level populations, $\{|\alpha_{m_F}|^2\}$, the total scattered field contains all the allowed harmonics of frequency $\omega^{(2)}_G(T)$. If more than one sublevel is populated, this effect can be detected in the signal intensity ($|E^{(2)}_{\bar{N},G}(t)|^2$), since interference between differentially oscillating sublevels would manifest as an amplitude modulation. However, if the system is optically pumping into a single sublevel, the modulation only affects the phase of the electric field—which cannot be observed using intensity detection. Instead, one can use a balanced heterodyne detector to measure the in-phase and in-quadrature components of the electric field amplitude to obtain the phase.

Taking into account the phase evolution of the wave function due to gravity, the scattered field can be shown to be

$$E^{(2)}_{\bar{N},g}(\Delta t;T) = E^{(2)}_{\bar{N}}(\Delta t;T)e^{i\phi^{(2)}_g}, \tag{35}$$

where $\phi^{(2)}_g(T) \sim -qg\bar{N}(\bar{N}+1)T^2/2$. Since gravity acts equally on all states, its effect is a modification of the phase of the density grating. This phase is then imprinted on the electric field scattered by the grating from the read-out pulse and cannot be detected from the intensity of the scattered light.

If the system is optically pumped into a single magnetic sublevel, other than $m_F = 0$, then a magnetic field gradient will affect only the phase of the scattered electric field in the same manner as gravity. Since both forces affect the phase of the scattered field in a similar manner, some care must be taken to isolate one effect or the other in an experiment. By performing the echo experiment in the horizontal direction, for example, one can eliminate the effect of gravity and isolate the effect of a magnetic field gradient. Similarly, by performing the experiment along the vertical direction

and canceling field gradients along all other directions, or by optically pumping into the $m_F = 0$ state, it is possible to eliminate the effect of B-field gradients in order to isolate the acceleration due to gravity.

The scale of these two physical mechanisms is also quite different. The force due to gravity on a ^{85}Rb atom is $\mathcal{F}_g \sim 1.4 \times 10^{-24}$ N. To achieve this same force with a B-field gradient, an atom in the $|F = 3, m_F = 3\rangle$ state would have to be exposed to a gradient of $G \sim 15$ Gauss/cm. In the lab, gradients as small as $G \sim 10^{-5}$ Gauss/cm can be applied to the atoms. Experimental timescales of $2T \sim 60$ ms have been achieved in a glass vacuum chamber with gradients at this level. At a pulse separation of $T \sim 30$ ms, amplitude modulation of the grating contrast due to a gradient of this size oscillates at a frequency of $m_F \omega_G^{(2)}(T) \sim 1$ Hz for $m_F = 3$ and $\bar{N} = 1$.

Figure 12 shows the recoil signal decay in the presence of a magnetic field gradient. The signal is modulated by the phase, $m_F \phi_G(T)$, for each sublevel $|F\, m_F\rangle$. By fitting the data to a model based on Equation (33), we measure the gradient to be $G = (23.9 \pm 0.09) \times 10^{-3}$ Gauss/cm, which is within a factor of two of the estimate of the applied gradient: $G \sim 0.05$ Gauss/cm.

Related studies of the effects of magnetic gradients involving guided atom interferometers are described in Wu et al. (2005).

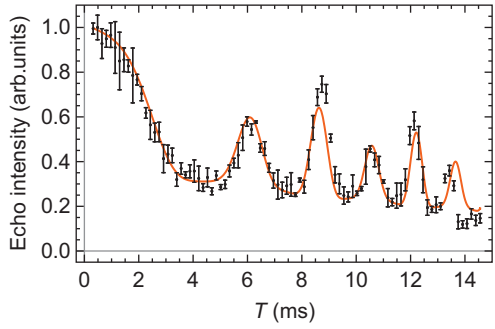

Figure 12 Data showing the effect of a magnetic field gradient on the recoil signal decay. Here, a gradient is applied to the atomic sample during the time of the experiment. The pulse separation, T, is varied in integer multiples of the recoil period, τ_q, so as to avoid any modulation due to recoil. The echo intensity is recorded at the first-order echo time, $t_{\text{echo}}^{(1)} = 2T$. Error bars represent the standard deviation of a set of three measurements of the echo intensity at the same T. The signal is modulated by the phase, $m_F \phi_G(T)$, for each sublevel $|F\, m_F\rangle$. The data are fitted to the function: $A[\alpha_0^2 + (\alpha_1 \cos \omega_G T + \alpha_2 \cos 2\omega_G T + \alpha_3 \cos 3\omega_G T)^2] e^{-T/\tau}$, shown as the solid line. From the fit we extract the gradient to be $G = (23.86 \pm 0.09) \times 10^{-3}$ Gauss/cm. The m-level populations are also measured to ~1% as $|\alpha_{m_F}|^2 = \{0.51, 0.46, 0.01, 0.02\}$, from $m_F = 0$ on the left to $m_F = 3$ on the right.

2.5 Multi-pulse atom interferometer

For the purposes of a precision measurement of ω_q, the two-pulse technique has one significant drawback: the signal exhibits a complicated, asymmetric shape as a function of T due to the different effects discussed earlier. A different technique for measuring ω_q with this interferometer—which makes use of multiple sw pulses—eliminates this difficulty.

It is relatively straightforward to generalize the expression of the scattered field for two sw pulses (Equation [23]) to N-pulses by applying a succession of phase gratings to the ground-state wave function (Beattie et al., 2009a; Strekalov et al., 2002). Work related to quantum kicked-rotors, which also use multiple-pulse AIs (Tonyushkin & Prentiss, 2009; Tonyushkin et al., 2009b; Wu et al., 2009), have also demonstrated sensitivity to atomic recoil.

Assuming that the jth pulse has a duration τ_j, complex pulse area $\Theta_j = u_j e^{i\theta}$ (where u_j and θ are given by Equations [27] and [28], respectively), and onset time $T_j > T_{j-1}$, followed by a period of free evolution $T_{j+1} - T_j$ before the $(j+1)$th pulse, the velocity averaged atomic density can be expressed as

$$\langle \rho_g^{(\boldsymbol{l})}(\boldsymbol{r}, t; \boldsymbol{T}) \rangle = \frac{1}{V} \sum_{l_N} \chi_{l_N}^{(\boldsymbol{l})}(t; \boldsymbol{T}) e^{-i l_N \boldsymbol{q} \cdot \boldsymbol{r}}, \tag{36}$$

where $\chi_{l_N}^{(\boldsymbol{l})}(t; \boldsymbol{T})$ is the amplitude of the $(l_N \boldsymbol{q})$-Fourier harmonic of the density distribution. Here, N is the number of pulses, $\boldsymbol{l} = \{l_1, l_2, \ldots, l_N\}$ denotes the set of interfering momentum states after the pulse sequence, and $\boldsymbol{T} = \{T_1, T_2, \ldots, T_N\}$ is the set of pulse onset times. The amplitude of each spatial component of the density is

$$\begin{aligned} \chi_{l_N}^{(\boldsymbol{l})}(t; \boldsymbol{T}) = - \sum_{l_1, \ldots, l_{N-1}} & e^{-\left[l_N \left(t - t_{\text{echo}}^{(\boldsymbol{l},\boldsymbol{T})}\right)/\tau_{\text{coh}}\right]^2} \\ & \times \prod_{j=1}^{N} J_{(l_j - l_{j-1})}(w_j) \left(\frac{\sin(\phi_j - \theta)}{\sin(\phi_j + \theta)} \right)^{(l_j - l_{j-1})/2}, \end{aligned} \tag{37}$$

where $\tau_{\text{coh}} = 2/q\sigma_v$ and ϕ_j is the recoil phase due to pulse j:

$$\phi_j = \omega_q \sum_{k=j}^{N} l_k (T_{k+1} - T_k), \tag{38a}$$

$$w_j = 2u_j \sqrt{\sin(\phi_j + \theta) \sin(\phi_j - \theta)}. \tag{38b}$$

In Equations (37) and (38a), $l_0 = 0$ and $T_{N+1} = t$. The echo times, $t_{\text{echo}}^{(\boldsymbol{l},\boldsymbol{T})}$, occur at temporal locations where the Doppler phase cancels and are determined by the set of interferences, $\boldsymbol{l}$, and onset times, $\boldsymbol{T}$, that satisfy

$$t_{\text{echo}}^{(\boldsymbol{l},\boldsymbol{T})} = T_N - \frac{1}{l_N}\sum_{j=1}^{N-1} l_j(T_{j+1} - T_j). \tag{39}$$

Owing to the detection technique typically employed in experiments, one is sensitive only to the amplitude of the q-Fourier harmonic of the density distribution, which corresponds to $\chi_1^{(\boldsymbol{l})}$ ($l_N = 1$). The scattered field amplitude for N-pulses is therefore given by

$$E^{(N)}(t;\boldsymbol{T}) \propto \chi_1^{(\boldsymbol{l})}(t;\boldsymbol{T}). \tag{40}$$

Setting $N = 2$ and $l_1 = -\bar{N}$ in Equation (40) gives the expression for the two-pulse scattered field at the $\bar{N}$th-order echo time (Equation [25b]).

An interesting feature of the N-pulse echo signal is that, in the absence of spontaneous emission ($\theta = 0$), the contrast of the grating at $t = t_{\text{echo}}^{(\boldsymbol{l},\boldsymbol{T})}$ is zero. There is a scattered field only at times $\sim\tau_{\text{coh}}/l_N$ about the echo times, just as in the two-pulse case. Thus, the echo technique produces conditions in the atomic sample at the echo times that are similar to those at $t = 0$, namely an absence in density modulation.

2.5.1 Three-Pulse Atom Interferometer

As an illustrative example, one can consider three sw pulses applied in the following sequence: $T_1 = 0$, $T_2 = T$, and $T_3 = T + \delta T$, and a read-out pulse applied at $t_{\text{echo}} = (\bar{N}+1)T$ to detect the $\bar{N}^{\text{th}}$-order echo. Just as in the two-pulse sequence considered in previous sections, the first two pulses cause all the momentum states to interfere in the vicinity of the echo time. However, only those states that differ by $\hbar\boldsymbol{q}$ are detected. The third pulse diffracts all the momentum states once more, as shown in Figure 13, but effectively converts the difference between those states that interfere at $(\bar{N}+1)T$ from $m\hbar\boldsymbol{q}$ ($m > 1$) to $\hbar\boldsymbol{q}$. Equivalently, the third pulse displaces the $\bar{N}$th-order echo from $(\bar{N}+1)T$ to $(\bar{N}+1)T + \delta T$. However, there is still an echo at $(\bar{N}+1)T$ provided δT is an integer multiple of τ_q. In this way, the role of the third pulse is different from the first two pulses, whose sole purpose is to produce an echo at $(\bar{N}+1)T$.

The detected signal in this three-pulse scheme (as a function of δT) is sensitive to more sets of interferences than in the two-pulse sequence. As a result, the shape of the signal differs significantly from the two-pulse signal. One should expect periodic revivals in grating contrast as a function of δT, with maxima occurring when δT is an integer multiple of the recoil period, $\tau_q = \pi/\omega_q$.

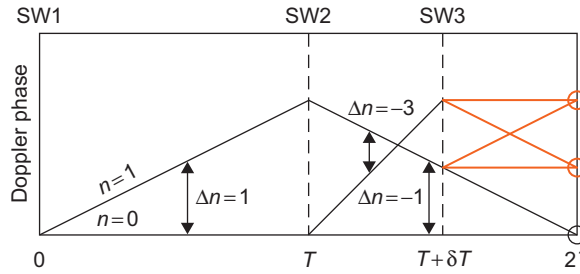

Figure 13 Simplified recoil diagram for the three-pulse signal. Two momentum states that differ by $|\Delta n| = 3$ ($|-\hbar q\rangle$ and $|2\hbar q\rangle$) interfere at $2T$ (gray circles) because of diffraction from the third pulse. This shows an example of how the third pulse can convert the difference between interfering states from $|\Delta n| > 1$ to $|\Delta n| = 1$.

Using Equation (39) with $l_1 = -\bar{N}$ and $l_2 = 1$, the three-pulse recoil signal can be approximated by

$$s^{(3)}(\delta T) \propto J_0^2\left(2u_3\sqrt{\sin(\omega_q\delta T + \theta)\sin(\omega_q\delta T - \theta)}\right), \tag{41}$$

where θ is a phase caused by spontaneous emission during the pulses, δT is varied between 0 and $\bar{N}T$, and T is held fixed. The signal as a function of δT is shown in Figure 14a for various pulse lengths, τ_3. The shape of the three-pulse signal is considerably different from that of the two-pulse signal. Its symmetric, periodic peak-shaped structure is particularly advantageous for precision measurements of ω_q. Furthermore, it can be shown that the full-width at half-maximum (FWHM) of the peaks is $\sim 1/u_3\omega_q$. This implies that by increasing the area of the third pulse (increasing the field intensity, pulse duration or decreasing the detuning) one can decrease the width of the peaks. This improves the determination of a given peak center and therefore the measurement of ω_q. This scaling law has been confirmed experimentally and shown in Figure 14b.

It is possible to reduce the fringe width even further by increasing the number of perturbation pulses (Beattie et al., 2009a). In order for each additional perturbation pulse to rephase momentum states at the echo time, they must be separated from all other perturbation pulses by a multiple of the recoil period, τ_q. Assuming that all perturbation pulses have the same pulse area, u_3, each additional pulse contributes to the signal shape an additional factor of $s^{(3)}(\delta T)$ from Equation (41). This effectively narrows each recoil fringe by a factor of $N^{-1/2}$ such that the FWHM scales as $\sim 1/\sqrt{N}u_3\omega_q$. Figure 14c shows the theoretically predicted and experimentally observed $(2 + N)$-pulse recoil signals. The scaling of the FWHM with N has been confirmed experimentally and is shown in Figure 14d.

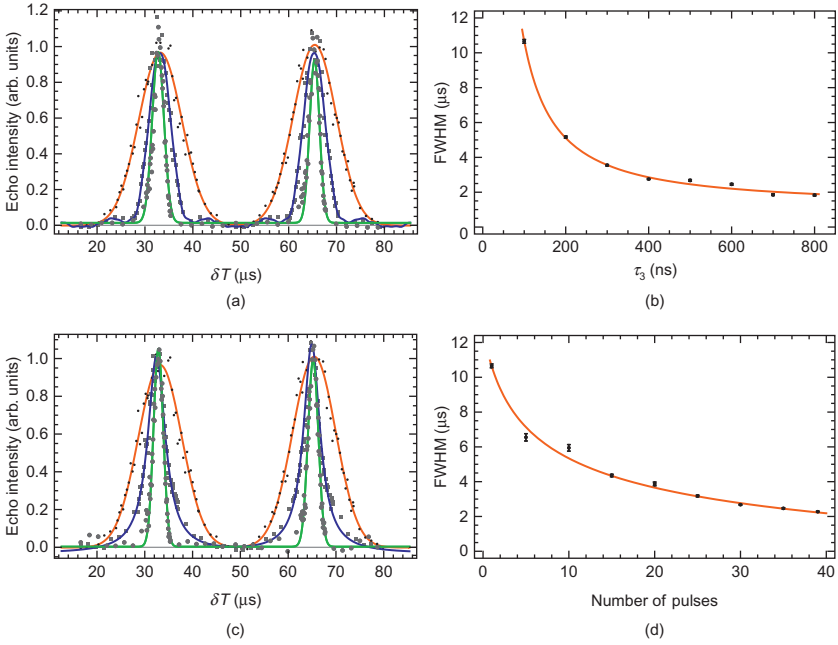

Figure 14 (a) Data from the three-pulse recoil experiment as a function of onset time, δT, for various pulse durations, τ_3. Dots: $\tau_3 = 100$ ns; squares: $\tau_3 = 200$ ns; circles: $\tau_3 = 500$ ns. (b) Scaling of the peak FWHM as a function of τ_3. Data is fitted to the function $A(\tau_3 - \tau_0)^{-n} + B$. The power was found to be $n = 1.18 \pm 0.88$. (c) Data from the $(2 + N)$-pulse recoil experiment as a function of onset time, δT, for various numbers of pulses, N, each with a duration of 100 ns. Dots: $N = 1$; squares: $N = 15$; circles: $N = 35$. (d) Scaling of the peak FWHM as a function of N. Data are fitted to the function $A(N - N_0)^{-n} + B$. The power was found to be $n = 0.32 \pm 0.47$. In both (a) and (c), data are fitted to different lineshapes (shown as solid lines) to guide the eye. The FWHM of the peaks was obtained from these fits. Other pulse parameters: $\Delta \sim 255$ MHz, $I \sim 250$ mW/cm^2, $\tau_1 = 700$ ns, $\tau_2 = 200$ ns.

In work relating to quantum kicked-rotors (Tonyushkin et al., 2009b), a large number of pulses was used, each with pulse area $u_j \ll 1$, for a measurement of ω_q. An appreciable loss in contrast and subsequent revival was observed when N was increased. For the technique described in Tonyushkin et al. (2009b), the time scale increases linearly with N. The prediction that the FWHM of each recoil fringe scales as $N^{-1/2}$ above is equivalent to the $N^{-3/2}$ scaling predicted in Tonyushkin et al. (2009b), since a factor of N^{-1} is related to the linear increase in time scale with an increase in N.

Figure 15a and b show a measurement of atomic recoil using the three-pulse technique. The sw pulses of the AI are separated by ~24 ms. The

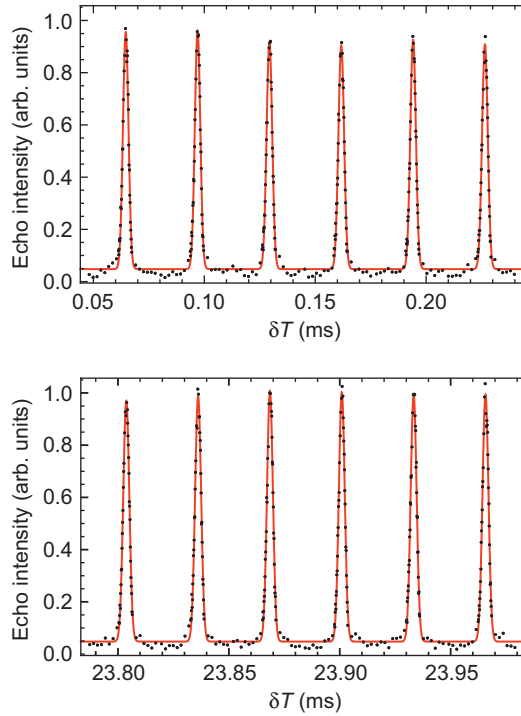

Figure 15 Recoil measurement using the three-pulse technique. Two windows are shown, one at $\delta T \sim 0.1$ ms (a) and one at $\delta T \sim 24$ ms (b). The solid line is a fit to the data consisting of a sum of Gaussians (one for each peak) that yields a measurement of the recoil frequency precise to ~350 ppb. Pulse parameters: $\tau_1 = 1100$ ns, $\tau_2 = 300$ ns, $\tau_3 = 400$ ns, $\Delta = 210$ MHz, intensity $I \sim 200$ mW/cm^2.

data were acquired in ~1 hour. A fit based on a sum of Gaussian lineshapes results in a measurement of ω_q precise to ~350 ppb. An interesting aspect of using a third pulse to measure ω_q is that the effect of signal decay due to the transit time of cold atoms is avoided because T is fixed.

In summary, the multiple-pulse technique is better suited for a precision measurement of ω_q than the two-pulse technique because the signal exhibits a simple, narrow-featured shape. Further improvements in the single measurement precision to the level of ~50 ppb appear to be attainable by improving the signal to noise ratio and exploiting scaling laws that can reduce the fringe width. Since the precision scales inversely proportional to the timescale of the experiment, additional improvements in precision can be achieved by increasing the transit time of cold atoms through the region of interaction with a larger excitation beam diameter. Studies of systematic effects in a precision measurement will include the angle between traveling-wave components of the standing wave and the

index of refraction of the atomic sample (Campbell et al., 2005), which is affected by both the atomic density and the frequency of the excitation beams.

3. LATTICE INTERFEROMETRY

3.1 Introduction

In the interferometer considered so far in this chapter, a set of off-resonant standing-wave pulses are applied to a cloud of cold atoms. One of the characteristic features of this interferometer is that at the exact times of the echoes (when the Doppler phase difference between interfering amplitudes is zero), the amplitude of the echo signal is zero. As discussed in Strekalov et al. (2002), this property applies to an interferometer of the type discussed here consisting of an arbitrary sequence of pulses—each satisfying the Raman–Nath condition—and is due to cancelation of the recoil phases of the amplitudes contributing to the echo signal at the same instant that the Doppler phases cancel. This cancelation is related to the fact that immediately after the first standing-wave pulse, the density of the atomic cloud is uniform, since, under the Raman–Nath condition, the atoms have not had time to move during the pulse. Consequently, one must observe the echo at times other than the exact echo time, where Doppler dephasing has reduced the size of the signal. A solution would be to cool the atoms further, for example using a BEC (Gupta et al., 2002) to achieve a subrecoil velocity spread. But this is technically more difficult and is likely to give rise to systematic errors due to interactions between atoms in the condensate.

In this section, we discuss a closely related type of echo-interferometer, which we refer to as a "lattice interferometer" (Andersen & Sleator, 2009), that doesn't suffer from the issue mentioned earlier. It uses atoms initially laser-cooled, then loaded into a one-dimensional (1D) optical lattice potential where it is further cooled in the potential, then released and later exposed to a pulse of the lattice potential. As is discussed below, one consequence of cooling the atoms in the lattice is that at the moment of release, the atomic density is strongly modulated with the period of the lattice potential. Consequently, at the exact echo times, the signal is a maximum, yielding a signal (in our measurements) more than a factor of four greater than obtained in the interferometer of Cahn et al. (1997). This interferometer shares the robustness against vibrations, accelerations, rotations, magnetic field gradients, and differences of AC Stark shifts between internal levels of the echo-type time-domain interferometers described in Section 1, and in Cahn et al. (1997).

In addition, we discuss how this interferometer performs when the optical lattice pulse violates the "short" pulse or Raman–Nath limit

(a regime not previously investigated in related interferometers), and find that a moderate violation of this limit can enhance the performance of the interferometer. We show that the interferometer reveals information on the quantum dynamics of atoms in an optical lattice potential, and thereby may be useful for the study of driven 1D systems (Raizen, 1999). Furthermore, we find that for specific pulse lengths, a coherent signal can occur at times that differ from the expected echo time by as much as $10\,\tau_{\mathrm{coh}}$, where $\tau_{\mathrm{coh}} = 2/q\sigma_v$ is the coherence time expected from the initial momentum spread of the atoms.

3.2 Description of the Interferometer

Figure 16 shows a timeline of the experiment, which uses a vapor cell loaded MOT of ^{85}Rb atoms loaded for 40 ms. An optical molasses stage of 7 ms further cools the atoms and loads them into the optical lattice, which is formed by two vertically polarized horizontally propagating laser beams with wave vectors $\boldsymbol{k}_1$ and $\boldsymbol{k}_2$, angled apart by 162°, and detuned 395 MHz above the $|5S_{1/2}, F = 3\rangle$ to $|5P_{3/2}, F' = 4\rangle$ transition. The lattice laser beams are clipped Gaussian beams with a diameter larger than the MOT cloud, so all the atoms in the MOT are loaded into the lattice. After the molasses stage, which cools the atoms to ~36 μK, the repump laser remains on for 100 μs to prepare the atoms in the $F = 3$ ground state. Acousto-optic modulators control the optical lattice beams. At time $t = 0$ (~10 μs after the turn-off of the repump light) we abruptly (in ~20 ns) turn off the optical lattice. After leaving the atoms in darkness for a time T, we pulse the optical lattice on for a short time τ. Later we detect the amplitude of atomic density modulations with period $2\pi/q$, where $\boldsymbol{q} = \boldsymbol{k}_1 - \boldsymbol{k}_2$, by applying a weak off-resonant optical field along direction

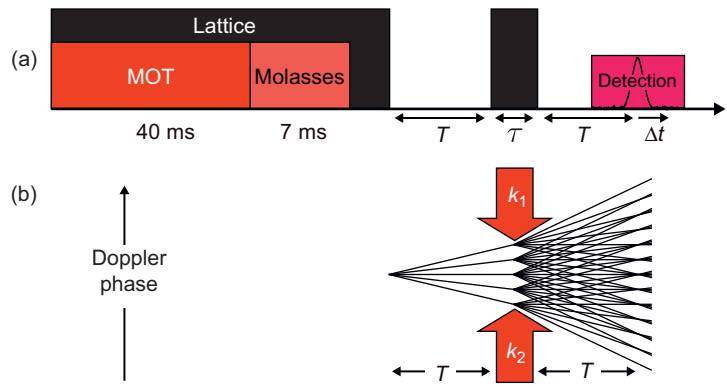

Figure 16 (a) Timeline of the experimental cycle. (b) Doppler phase diagram for atoms released from the optical lattice.

$\boldsymbol{k}_1$ and measuring the amplitude of the field Bragg scattered off of the atomic density modulation along the direction $\boldsymbol{k}_2$ using the heterodyne technique described in Section 1 and in Cahn et al. (1997).

3.3 Calculation of the Signal

To calculate the expected signal we assume that the atoms are in thermal equilibrium in the optical lattice, and localized to narrow regions near the potential minima, so they form a periodic density distribution and effectively experience a harmonic oscillator potential. Since the temperature of the atoms is $\sim$36 μK, their thermal de Broglie wave coherence length is much shorter than the period of the optical lattice. Under these conditions, it can be shown that the state of the atomic system can be closely approximated by an incoherent mixture of states identical to the ones obtained by an atomic plane wave of momentum $\boldsymbol{k}_0$ impinging on a periodic array with period $\boldsymbol{a} = (2\pi/q)\hat{\boldsymbol{q}}$ of Gaussian transmission functions, each with width σ (the width of the atomic density distribution in a single minimum in the lattice). Thus, we can write $\psi_{k_0}(\boldsymbol{r}) = \psi_0(\boldsymbol{r})e^{i\boldsymbol{k}_0\cdot\boldsymbol{r}}$, where

$$\psi_0(\boldsymbol{r}) = \frac{1}{(2\pi\sigma^2)^{1/4}} \sum_m \exp[-(\boldsymbol{r} - m\boldsymbol{a})^2/4\sigma^2]. \tag{42}$$

We would like to express Equation (42) as a sum of momentum eigenstates, so we write

$$\psi_0(\boldsymbol{r}) = \sum_{n_1} A_{n_1} e^{in_1\boldsymbol{q}\cdot\boldsymbol{r}}, \tag{43}$$

with

$$A_n = \frac{1}{a}\int_{a/2}^{a/2} \psi_0(x)e^{-in_1qx}dx \approx \frac{1}{a}\int_{\infty}^{\infty} \frac{e^{-x^2/4\sigma^2}}{(2\pi\sigma^2)^{1/4}} e^{-in_1qx}dx \tag{44}$$

$$\approx \left(\sqrt{2}/a\right)(2\pi\sigma^2)^{1/4}\, e^{-n_1^2(q\sigma)^2}, \tag{45}$$

where the integral is along the direction of $\boldsymbol{a}$. This gives, up to a constant factor,

$$\psi_{k_0}(\boldsymbol{r}, t=0) = \sum_{n_1=-\infty}^{\infty} e^{-n_1^2(q\sigma)^2} e^{i(\boldsymbol{k}_0 + n_1\boldsymbol{q})\cdot\boldsymbol{r}}. \tag{46}$$

Each state ψ_{k_0} contributes to the mixture with a weight given by the momentum ($\hbar\boldsymbol{k}_0$) distribution of a gas of atoms in thermal equilibrium.

The experimental signal can be computed by first calculating the signal resulting from the system initially in state $\psi_{k_0}(\boldsymbol{r}, 0)$ and then summing this signal over the weighted distribution of $\boldsymbol{k}_0$.

After the lattice is turned off at $t = 0$, each plane wave, $\exp[i(\boldsymbol{k}_0 + n_1\boldsymbol{q}) \cdot \boldsymbol{r}]$, in Equation (46) acquires a phase $\phi = (\omega_{k_0} + n_1^2\omega_q + n_1\boldsymbol{q} \cdot \boldsymbol{v}_0)\, t$, where $\omega_q = \hbar q^2/2M$ is the (two-photon) recoil frequency and $n_1\boldsymbol{q} \cdot \boldsymbol{v}_0 t$ is the Doppler phase, which is proportional to the initial atomic velocity $\boldsymbol{v}_0 = \hbar\boldsymbol{k}_0/M$, and $\omega_{k_0} = \hbar k_0^2/2M$ contributes to an overall phase that can be ignored. The optical lattice pulse, turned on at time $t = T$, diffracts each plane wave into a set of plane waves with wave vectors differing by integer multiples of $\boldsymbol{q}$. If τ is so short that atomic motion can be neglected during the pulse (Raman–Nath condition), no Doppler phase evolution occurs during this time. Figure 16(b) shows a diagram of the Doppler phase evolution of various amplitudes as a function of time in the interferometer. Crossing lines in the diagram occur at times when different momentum states have the same Doppler phase, and atomic fringe patterns are produced at these times. In particular, fringe patterns with period $2\pi/q$ are produced close to times $t_{\bar{N}} = (\bar{N} + 1)T$ for positive integer $\bar{N}$ (the $t_{\bar{N}}$ are called echo times). A detailed calculation similar to the one in outlined in Section 1, which assumes that the interaction during the pulse is given by $H = \hbar\chi \cos(\boldsymbol{q} \cdot \boldsymbol{r})$, gives a signal

$$S(\Delta t) \propto \mathrm{e}^{-(q\sigma_v \Delta t/2)^2} \mathrm{e}^{-\frac{1}{2}\bar{N}^2(q\sigma)^2} J_{\bar{N}+1}\{2u \sin[\omega_q(\bar{N}T + \Delta t)]\}. \tag{47}$$

where $\sigma_v = \sqrt{2k_B\mathcal{T}/M}$, k_B is Boltzmann's constant, $\mathcal{T}$ the temperature of the atoms, $\Delta t \equiv t - t_{\bar{N}}$, and $u \sim \chi\,\tau$ is the area of the lattice pulse.

3.4 Experimental Results

Figure 17a shows the signal obtained at around $T = 81\,\mu\mathrm{s}$ with a short pulse of duration $\tau = 350\,\mathrm{ns}$ (solid curve). All data shown correspond to the fundamental echo $\bar{N} = 1$. The estimated temperature of the atomic gas was found by fitting Equation (47) to the data. The signals shown in Figure 17a are the largest that could be obtained in the short pulse limit with the laser power and detuning used. In contrast to the signal obtained from the interferometer in Cahn et al. (1997) (also shown in Figure 17a for a similar number of atoms), the lattice interferometer signal reaches a maximum at the echo time ($\Delta t = 0$) and with a maximal signal size more than a factor of four larger, demonstrating an improved signal-to-noise ratio and higher contrast of the atomic density modulation. We ascribe this to the fact that in this interferometer the signal is an echo of a density modulation of the atoms, whereas in Cahn et al. (1997) it is a velocity (or phase) modulation that with time evolves into a density modulation, but also partially dephases because of the thermal velocity spread of the atoms. By laser cooling the atoms into the optical lattice, we avoid the huge loss of

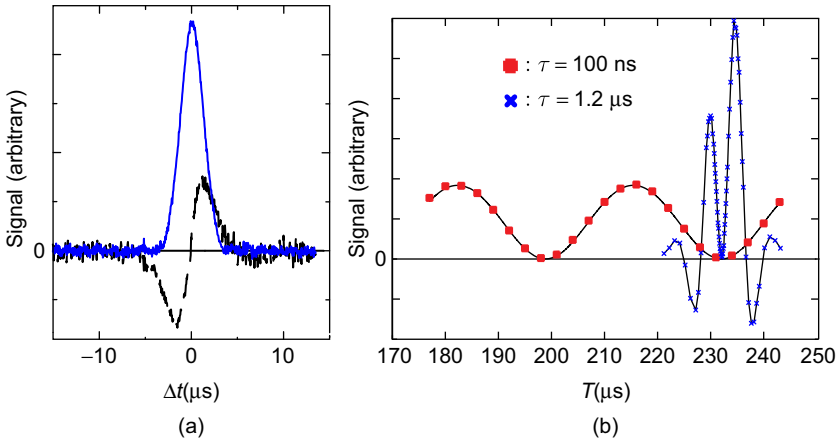

Figure 17 (a) Solid curve: signal from lattice interferometer for $\tau = 350\,\text{ns}$ and $T = 81\,\mu\text{s}$. Dashed curve: the maximum signal we could obtain from the interferometer described in Cahn et al. (1997). (b) Peak signal as a function of pulse separation T for small-area pulses $\tau = 100\,\text{ns}$ (squares). Peak signal theoretically expected from Equation (47) (corresponding solid curve). Crosses connected by a solid line: the measured peak signal for $\tau = 1.2\,\mu\text{s}$, too long to satisfy the Raman–Nath condition. The longer pulse yields sharper features in the signal.

atoms, associated with using an optical mask—the atom-optics analog of an absorption grating in light optics (Turlapov et al., 2005)—for generation of the atomic density modulation. Note that the revival of the density modulation shows that the atomic state continues to carry the information of its lattice preparation, despite its density distribution shortly after release being indistinguishable from a thermal cloud.

Equation (47) also shows that the peak signal at the echo time varies periodically as a function of T with period given by the Talbot time $\tau_T = 2\tau_q = 2\pi/\omega_q$. This interferometer can therefore be used to measure the Talbot time (or equivalently, the recoil frequency), which, together with other well-known constants, constitutes a measurement of the fine structure constant, α (see Section 2). Figure 17b shows the analytical prediction of Equation (47) together with the experimental measurements of the peak signal as a function of T for a pulse length of 100 ns. In the analytical prediction we use $\chi = 2.0\,\text{MHz}$ determined in a separate measurement of the value of τ that yields the first maximum in the signal for $T = 81\,\mu\text{s}$. The overall amplitude of the analytical result was adjusted to fit the data. By comparing the size of the echo signal for $\bar{N} = 1, 2$, and 3, we can use Equation (47) to extract the degree of localization, σ, of the atoms in the lattice. We find that $\sigma = 55\,\text{nm}$, or about 1/7th the 390-nm period of the lattice potential. This could be reduced by using a BEC released from an optical lattice.

Sharp features in the interferometric signal as a function of T (or equivalently higher frequency components in the signal) improves the precision with which the Talbot time and recoil frequency can be determined (Cataliotti et al., 2001). Equation (47) indicates that if one increases u, more oscillations and sharper features occur in each period when T is scanned, thus increasing the sensitivity of the interferometer. The depth of the lattice potential $\hbar\chi$, and thereby u, can be increased by increasing the power in the lattice beams, but these results were obtained using the maximum laser power available. Increasing τ will also increase u, but this will eventually lead to a breakdown of the Raman–Nath condition, and Equation (47) will no longer apply. When the Raman–Nath condition is violated, the signal is still periodic in T, however, with period τ_T independent of pulse duration. Thus, the recoil frequency can be determined simply from this period. It is therefore of interest to know what happens when the pulse length is increased beyond the Raman–Nath limit. Figure 17b shows the signal as a function of T for a pulse duration of $\tau = 1.2\,\mu$s, which is too long to satisfy the Raman–Nath condition. It is clear that the longer pulse yields sharper features in the signal as a function of T.

Figure 18 shows the echo signal as a function of both T and Δt for different pulse durations τ. Horizontal cross sections in this figure represent the signal as a function of Δt (as shown in Figure 17a), and vertical cross sections represent the signal as a function of T (as shown in Figure 17b). For $\tau = 1.2\,\mu$s (Figure 18c) we see a clear deviation from the results predicted by Equation (47), namely that the signal vanishes for T around $(n + 1/2)\tau_T/2$ with n an integer ($\sim$80 μs in Figure 18c), and that the signal is asymmetric around $n\tau_T/2$. However, the narrow "dark" fringe around $n\tau_T/2$ persists, enabling an accurate determination of τ_T. The experimental observation that the sharpest features of the echo signal are found for pulse durations between 1 and 2 μs is perhaps not surprising, since the optical lattice imparts maximum momentum into the atoms for durations around $\tau \sim \tau_{\rm osc}/4$, where $\tau_{\rm osc}$ is the oscillation period of an atom close to a potential minimum.

We use the sharp features described earlier to determine the Talbot time by taking data with high resolution in T for $\tau = 1.2\,\mu$s around $T = 65\,\mu$s and around $T = 455\,\mu$s—differing in T by $\sim$6 Talbot times (see Figure 18d). From this we obtain a value[1] of $h/M_{\rm Rb} = (4.6997 \pm 0.0003) \times 10^{-9}$ m^2/s^2, where $M_{\rm Rb}$ is the mass of a ^{85}Rb atom, in agreement with the value of $h/M_{\rm Rb} = 4.6994 \times 10^{-9}$ m^2/s^2 deduced from Audi et al. (2003). Our "large" uncertainty arises from the determination of the angle between the beams, a problem that can be overcome by using counter

[1]The uncertainties are one standard deviation combined systematic and statistical.

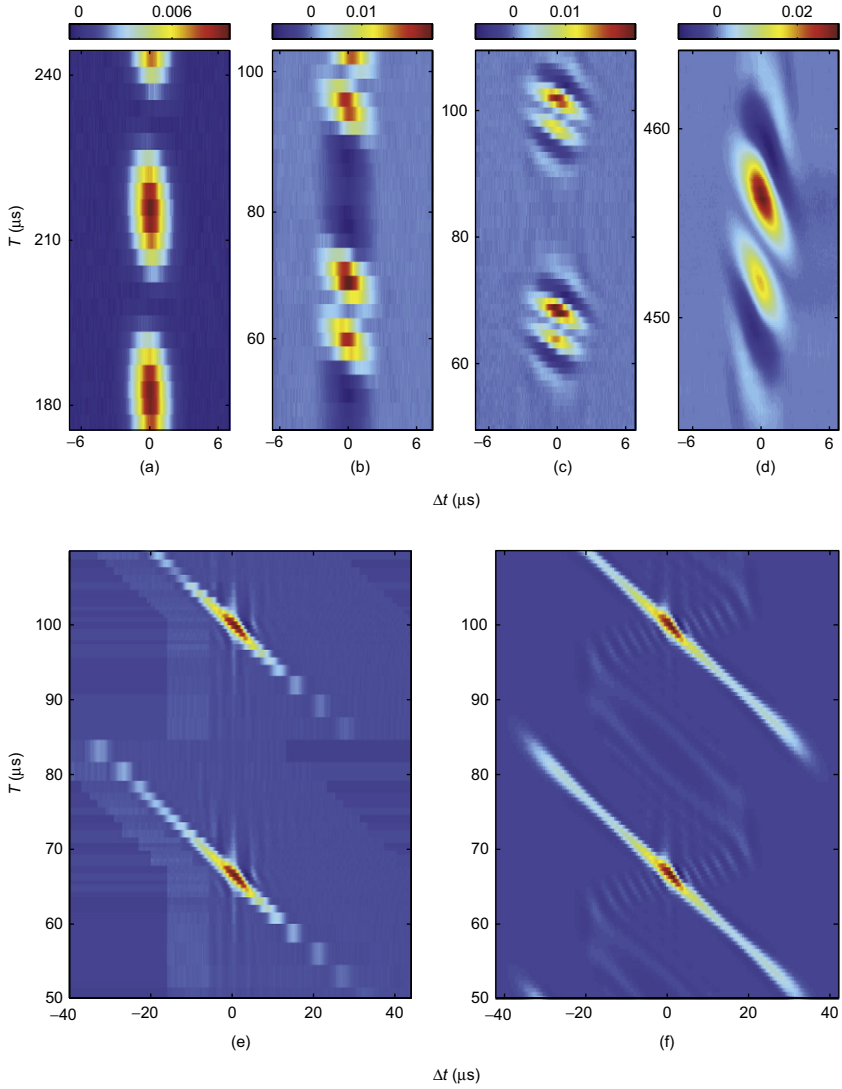

Figure 18 Echo signal as a function of Δt and time of the lattice pulse T (the echo time is $t_1 = 2T + \tau$). Figure 17b is a vertical cross section at the echo time ($\Delta t = 0$) and Figure 17a is a horizontal cross section of the data in this figure. (a), (b), (c): Experimental data for pulse durations $\tau = 100$ ns, 600 ns, and 1.2 μs, respectively. For $\tau = 1.2\,\mu$s, the signal vanishes for all T around 80 μs. (d) High-resolution experimental data for $\tau = 1.2\,\mu$s. (e) Experimental data for $\tau = 3.5\,\mu$s. Features as a function of T are no longer as sharp as for $\tau = 1.2\,\mu$s. We observe a coherent signal for times that differ greatly from the echo time. (f) Numerical calculation of the expected signal for the parameters of (e).

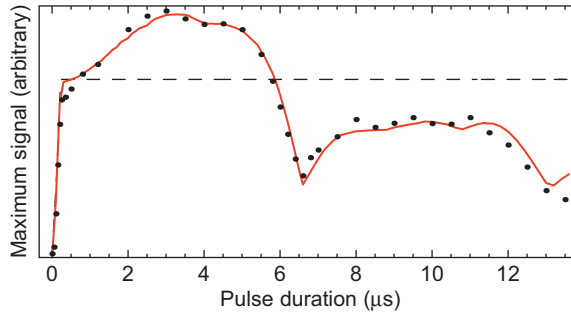

Figure 19 Maximum signal as a function of pulse duration. Dots are the data, and the solid curve is a numerical calculation multiplied by an exponential decay to accommodate for decoherence due to photon scattering. The dashed line is the maximum signal expected from Equation (47) and does not show oscillations. We see that violating the Raman–Nath condition can increase the contrast of the atomic density modulation.

propagating beams and coupling between optical fibers (Cladé et al., 2006; Muller et al., 2008).

For $\tau = 3.5\,\mu$s (see Figure 18e), we observe the interesting phenomenon that a coherent signal for certain values of T is observed for times that differ from the echo time $(2T + \tau)$ by as much as 40 μs. This is more than 10 times the decoherence time of a few μs expected from the initial thermal spread of atoms. The nature of the signal also seems to indicate that its occurrence is not due to long coherence times, but rather because the dynamics of the atoms during the lattice pulse enables a coherent rephasing at this time. We note that this phenomenon occurs for pulse durations τ around $\tau_{\text{osc}}/2$. Figure 18f shows a 1D numerical calculation of the expected signal for the same parameters as the experimental results in Figure 18e. No photon scattering was included in the calculation.

To further investigate the dynamics of the atoms in the optical lattice we measured the maximum signal size for a given pulse duration τ by scanning the pulse separation T. Figure 19 shows a plot of this maximum signal as a function of τ. We observe that violating the Raman–Nath limit can improve the contrast of the atomic density modulation since pulse lengths from 1 to 5 μs yield a larger signal than predicted by Equation (47) (also shown in Figure 19). In contrast to the prediction of Equation (47), the signal shows damped oscillations with a period of around 6.6 μs. This period is consistent with τ_{osc} reflecting a partial revival of the initial state at this time. This effect has been observed previously using a BEC in an optical lattice (Ovchinnikov et al., 1999), and the fact that it is easily seen in our data indicates that this interferometer can be used as a sensitive probe of the quantum dynamics in diffracting structures, including classical

chaotic systems such as the δ-kicked rotor (Raizen, 1999). Figure 19 also shows a numerical calculation of the expected maximum signal as a function of τ. This calculation is based on the coherent interaction of the atoms with the laser field, but to account for decay of coherence due to photon scattering in the optical lattice, includes a multiplicative exponential decay as a function of τ, where the decay rate of 3.5×10^4 s^{-1} is found by fitting to the data. This decay rate is smaller than the average photon scattering rate of 9×10^4 s^{-1} calculated from our measured value of χ and the detuning of the light.

In summary we have described an atom interferometer that uses atoms, laser-cooled into an optical lattice, followed by an optical-lattice pulse. The technique is capable of producing atomic density modulations with a contrast significantly higher than the interferometer of Cahn et al. (1997). This increases the signal-to-noise ratio of the interferometric signal. We discussed how the interferometer performs when the pulse violates the Raman–Nath condition and found that a moderate violation can improve the sensitivity and increase the contrast of the atomic density modulation. For specific pulse lengths in the long-pulse regime, we observe a coherent signal at times that differ greatly from the echo time. We showed that the interferometric signal can be used as a probe of the dynamics of the atoms in the optical lattice. The technique also reveals the degree of localization of atoms in an optical lattice, and may therefore be employed in the study of superfluid to Mott-insulator quantum phase transition of BECs in optical lattices (Greiner et al., 2002; Spielman et al., 2007).

4. FREQUENCY-DOMAIN AI EXPERIMENTS

4.1 Frequency-Domain Measurements of Recoil

This section describes an atom interferometric frequency-domain measurement of ω_q (Weel & Kumarakrishnan, 2003) that uses the echo technique to generate a ground-state Ramsey fringe pattern. This work is based on the scheme proposed in Dubetsky and Berman (1997).

Figure 20 shows the pulsed-laser fields used to excite the laser-cooled sample. At $t = 0$, an excitation pulse consisting of two off-resonant, counter-propagating traveling waves with frequencies ω_1 and ω_2 is used to drive two-photon transitions in atoms prepared in a single hyperfine ground state. The sample is again excited at time $t = T$ by a second set of traveling-wave pulses with reversed k-vectors. As a result, the sample experiences an intensity modulation that is translated along two opposing directions. Reversing the directions of the second set of excitation pulses results in a cancelation of Doppler phases associated with momentum states differing by $\hbar q$ that interfere in the vicinity of the echo time $t =$

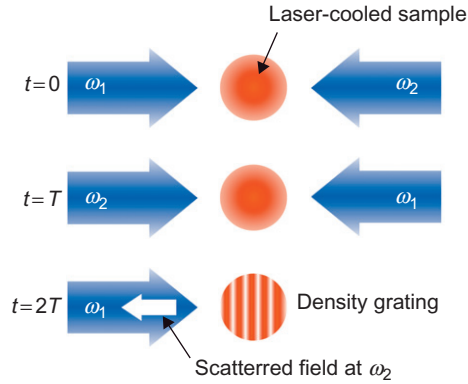

Figure 20 Schematic diagram of pulsed laser fields used in experiment.

$2T$. Here, $q = 2k$. The rephased density grating formed in the sample is detected by scattering an off-resonant traveling wave with frequency ω_1 and measuring the amplitude and phase of the scattered light at frequency ω_2. In this manner, it is possible to probe the oscillatory Ramsey phase $\phi = T\delta$ acquired by the grating, which depends on the frequency difference $\delta = \omega_1 - \omega_2$. In comparison, other Ramsey fringe experiments involving ground or excited states (Barger et al., 1979; Bergquist et al., 1977; Ruschewitz et al., 1998; Sengstock et al., 1993; Weiss et al., 1993) rely on similar excitation schemes and the detuning dependence of the population or coherence associated with an atomic level.

Using the treatment in (Dubetsky & Berman, 1997), the back-scattered electric field amplitude can be expressed as

$$S(\delta; T) = \exp(4iT\delta)J_2[2u_2 \sin(\omega_q T)], \tag{48}$$

where u_2 is the pulse area of the second excitation pulse. The complex exponential in Equation (48) makes it necessary to measure the phase of the signal in order to observe the effect of recoil.

In Ramsey fringe experiments using atomic beams (Bordé et al., 1984), the excitation zones are spatially separated. The time between interactions with the laser fields, T, differs for each velocity class associated with the longitudinal velocity distribution of the atomic source. As a consequence, the fringe pattern can be observed because the signal is averaged over the entire velocity distribution. In an experiment with a laser-cooled sample, the time separation between interactions with light are the same for all the atoms. Therefore, it is necessary to average the signal over T to obtain the Ramsey lineshape (Vasilenko et al., 1985).

4.2 Experimental Details

The experiment is carried out in a laser-cooled sample with a temperature of ~200 μK that contains ~10^8 Rb atoms. The traveling-wave pulses used for atom interferometry are tuned ~90 MHz above the $F = 3 \rightarrow F = 4'$ transition in ^{85}Rb, and controlled by AOMs. The AOMs are driven by oscillators which are phase locked to a commercially available rubidium frequency standard with a stability characterized by a 1-second Allan deviation of 2×10^{-11}. The oscillators operate near 250 MHz and the frequency difference, δ, can be adjusted to within 1 mHz. The time separation, T, between pulses can be controlled with an accuracy of 500 ps using delay generators with time bases slaved to the rubidium standard. Signal detection is accomplished using the balanced heterodyne detection system used in Cahn et al. (1997) and Weel and Kumarakrishnan (2003). The echo signal is observed on both channels of the detection system in the form of a beat note. These signals are mixed down to DC to obtain the in-phase and in-quadrature components from which the signal amplitude and phase can be determined.

4.3 Results and Discussion

By integrating the first half (before the zero crossing) of the dispersion-shaped echo envelope (shown in Fig. 3a) and subtracting the integral of the second half, it is possible to obtain an amplitude component. Figure 21a shows the amplitude as a function of δ for $T = 100$ μs. The amplitude exhibits an oscillatory dependence on δ given by $S_0 = \cos(T\delta)$ as seen from the fit in Figure 21a. For a fixed value of T, the average value of the oscillation frequency is determined from the in-phase and

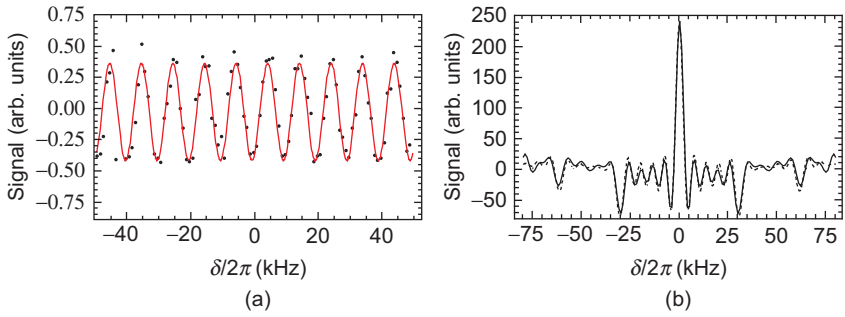

Figure 21 (a) Oscillation of a component of the echo signal as a function of detuning, δ, for $T = 100$ μs. Data are fitted to the form $\cos(T\delta)$ (solid line). The fit gives a period of 9.99 kHz, which is consistent with $T = 100$ μs. (b) Average of the signal over T—Ramsey fringe pattern. The solid line is data and the dashed line is a fit which yields $\omega_q = 97.0 \times 10^3$ s^{-1} and $u_2 = 1.8$.

in-quadrature components of the signal. The measurement is repeated for different time pulse separations, T. A linear fit of the measured period as a function of T gives a slope of 4.004 and an offset of 0.7 μs. The value of the slope is in agreement with Equation (48), which predicts a slope of 4.

The amplitudes of the oscillatory signals are weighted to compensate for the exponential decay of the echo amplitude versus T due to decoherence from scattered light and collisions. The Ramsey fringe pattern shown in Figure 21b is obtained by averaging a particular signal component over the range $T = 12 \rightarrow 164\,\mu s$ in steps of 4 μs.

The fringe pattern in Figure 21b shows peaks at $\pm 0.5\,\omega_q$ and $\pm\,\omega_q$, which is consistent with Equation (48). The value of ω_q is obtained by fitting the data to Equation (48) using a least squares fit with ω_q and u_2 as free parameters. The fit yields $\omega_q = 97.0 \times 10^3\ s^{-1}$, which is consistent with the expected value of the two-photon recoil frequency. Analysis of the residuals allows a determination of ω_q with a precision of $\sim 1/10^3$. The precision can be improved by measuring the frequency difference between widely separated recoil components that can be recorded by increasing the pulse area u_2. As in all Ramsey experiments, the range of detunings (~10 MHz) is determined by the excitation pulse bandwidth, and the width of the recoil peaks is expected to scale as $\sim 1/T$.

4.4 Frequency Synthesizer

A potential advantage of this measurement technique is that possible systematic uncertainties in the definition of T that can affect time-domain experiments are avoided, since the signal is averaged over T. In contrast to Ramsey experiments with excited states (Barger et al., 1979; Bergquist et al., 1977; Ruschewitz et al., 1998; Sengstock et al., 1993) that are limited by the radiative decay time, the precision that can be achieved if decoherence mechanisms are eliminated should be limited only by the transit time of ground-state atoms through the region of interaction. Since the experiment utilizes the same laser to generate excitation frequencies ω_1 and ω_2, variations in laser frequency are common to both beams and a laser with an ultra narrow linewidth is not required, as it is in atomic clock experiments (Barger et al., 1979; Bergquist et al., 1977; Ruschewitz et al., 1998; Sengstock et al., 1993). In comparison, an advantage of time-domain measurements is that they are insensitive to the effect of vibrations, since they do not rely on the phase of the scattered electric field.

If the transit time limit is achieved, as in time-domain experiments, the precision of frequency-domain measurements will depend on the precision and tunability of δ. The measurement in Weel and Kumarakrishnan (2003) relied on a RF synthesizer assembled from commercially available components to produce dual outputs (differing by δ) to drive the excitation AOMs. The synthesizer allows δ to be varied over ~10 MHz in steps

of 1 mHz while maintaining frequency stability with respect to a master reference oscillator. Additionally, a simple measurement and correction loop ensures that the outputs maintain a fixed phase relationship if δ is varied.

The block diagram of the synthesizer is shown in Figure 22. In this circuit, there are two phase-locked loops (PLLs) operating at 250 MHz and 238 MHz. These are fractional-divide-by-N PLLs, meaning that the reference and output frequencies are not necessarily related by an integer multiple. These devices are tunable only in steps of ~0.2 MHz, necessitating additional electronics for fine-tuning. To tune the output at 250 MHz + δ, a commercially available arbitrary waveform generator (AWG) tunable in steps as small as 1 mHz is incorporated. This device has a maximum output frequency of 30 MHz and is set to 12 MHz + δ. The choice of 12 MHz ensured that when the AWG's output is mixed with the PLL output at 238 MHz, a sum frequency near 250 MHz is obtained. A signal with frequency 250 MHz + δ is obtained by filtering out the difference frequency. Filtering is accomplished using a commercially fabricated narrow-band notch filter (FWHM 8 MHz) whose center frequency is 250 MHz. Both of the PLLs and the AWG are referenced to a rubidium clock operating at 10 MHz. This clock has excellent short-term stability, with a 1-second Allan deviation of 2×10^{-11}. Both the 250 MHz and 250 MHz + δ outputs are locked in phase to the stable Rb clock, and are therefore phase-locked to each other.

4.5 Measurements of Rotation

The frequency synthesizer developed for the recoil measurement is also suitable for a proof of concept measurement of rotation. If a closed-loop optical interferometer rotates about an axis perpendicular to its enclosed

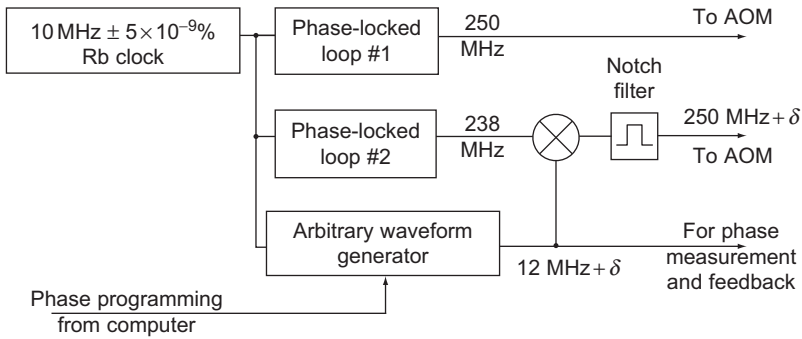

Figure 22 The block diagram for the synthesizer, where ⊗ is a RF mixer.

area, the path difference between counter-propagating waves due to rotation produces a phase shift $\Delta\phi_R = \Omega Ak/c$ (Sagnac effect). Here, Ω is the frequency of rotation, A is the area enclosed by the interferometer, k is the wave vector, and c is the speed of light. The Sagnac effect is the basis for the fibre ring gyroscope (Vali & Shorthill, 1976), a device commonly used in navigation. The obvious advantage of laser gyroscopes is that the enclosed area can be enhanced by sending the light on many round-trips, thereby improving the sensitivity.

For an AI, the corresponding phase shift is $\Delta\phi_R = \Omega AM/\hbar$, where M is the mass of the atom. Replacing light waves with matter waves can lead to a significant improvement in sensitivity. This is because, for the same enclosed area, the phase shift is $Mc/\hbar k \sim 10^{10}$ times greater for atoms in comparison with light. For atoms, the challenge is to produce a large enclosed area. Such atom gyroscopes should be able to detect rotations as small as 6×10^{-3} deg/h (Sleator et al., 1999). This is around three orders of magnitude smaller than the Earth's rate of rotation. Examples of AI-based measurements of rotation include a Raman interferometer measurement in a cesium atomic beam (Durfee et al., 2006; Gustavson et al., 1997a) and a BEC experiment in which the rotational phase shift is enhanced by circulating the sample in an elongated trap (Burke & Sackett, 2009). Another approach involves confining the atoms within a linear magnetic guide and moving this guide back and forth while diffracting the atoms, thereby enhancing the enclosed area through multiple circuits of the same small physical area (Wu et al., 2007).

If the Ramsey fringe experiment is carried out by launching a cloud of cold atoms across the zone of interaction in a direction such that $\boldsymbol{A} \cdot \boldsymbol{\Omega}$ is a maximum, the effect of the earth's rotation is expected to produce a shift in the position of the central fringe in Figure 21b. The area enclosed by the AI can be estimated as

$$A = \frac{\hbar q v T^2}{M}. \tag{49}$$

For typical operating parameters of $T \sim 10$ ms and an atom launch speed $v \sim 2.5$ m/s the area is 0.76 mm^2. Assuming that Ω is the vertical component of the Earth's rotation in Toronto, we obtain a fringe shift of 0.8 Hz. The expected width of the central fringe for these parameters is 20 Hz, which suggests that the fringe shift should be easily observable, since δ can be varied in subhertz steps.

Although this experiment is simple in concept, the fringe shift due to rotation is indistinguishable from the shift produced by gravitational acceleration. Therefore, it is critical to align the AI beams in a plane

perpendicular to the local gravitational field and to measure the angle of the beams with respect to the horizontal.

5. TIME-DOMAIN AI EXPERIMENTS—GRAVITY

5.1 Introduction

Atom interferometers based on cold atoms have enormous practical applications related to inertial sensing because of the extraordinary sensitivity to gravitational acceleration, g (Peters et al., 1999), gravity gradients, (McGuirk et al., 2002; Snadden et al., 1998), and rotation (Durfee et al., 2006; Gustavson et al., 1997b, 2000). Common applications include oil and mineral prospecting, seismic exploration and monitoring, and correction of tidal charts. Most of these developments have been realized using the well-known Raman interferometer (Kasevich & Chu, 1991) in which cold cesium atoms are manipulated in two hyperfine ground states using optical Raman transitions. Raman interferometers have also been used for precision measurements of the universal gravitational constant, G (Fixler et al., 2007; Lamporesi et al., 2008), and gravitational redshift (Müller et al., 2010). The technology based on this class of interferometers has become sufficiently advanced that it is being utilized for remote sensing using mobile payloads (Le Gouët et al., 2008; Young et al., 2007; Yu et al., 2006). Another independent technique for realizing precise measurements of gravity in a compact setup involves exploiting the properties of Bloch oscillations in an optical lattice (Poli et al., 2011).

Despite the advances of Raman interferometers, it is interesting to consider the potential for realizing precise measurements of gravitational acceleration using the single-state echo type interferometer used for recoil measurements as described in earlier sections. The AI is based on the configuration developed at NYU (Cahn et al., 1997; Weel et al., 2006). As in the case of cold-atom Raman interferometers, the timescale of the experiment is determined by the transit time of atoms through the region of interaction defined by the laser beams. A particular advantage of the echo AI is that only a single laser frequency is used and that no velocity selection is required. Transit-time-limited recoil experiments using this technique that are presented in this work indicate that state selection may not be required if magnetic gradients are adequately suppressed (Weel et al., 2006).

5.2 Theoretical Background

The AI involves excitation of the sample along the vertical by two standing-wave pulses separated by a time T as shown in Figure 23. This configuration is similar to that of the AI used in the time-domain

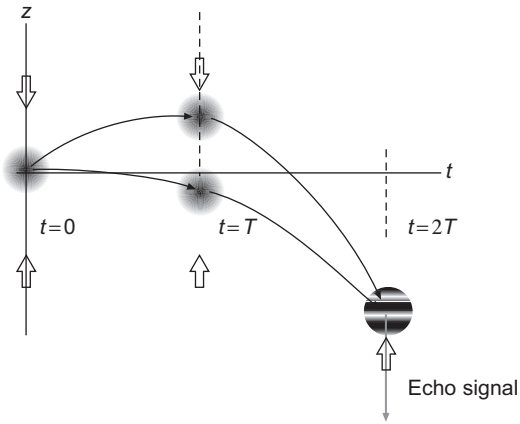

Figure 23 Curved trajectories of atomic wave packets due to gravity.

measurements of atomic recoil. The traveling-wave components of the standing-wave pulses are sufficiently blue detuned with respect to the excited state such that the effects of spontaneous emission during excitation can be ignored. The durations of the excitation pulses are sufficiently short, meeting the Raman–Nath criterion that the displacement of atoms is small compared to the standing-wave period during the interaction time. The first pulse at $t = 0$ diffracts atoms into a superposition of momentum states that differ by $n\hbar q$, where $q = 2k$ for counter-propagating beams and $\boldsymbol{k} = 2\pi/\lambda\hat{z}$ is the wavevector of the laser light. The $\lambda/2$ grating that is formed by atoms focused to the nodes of the standing wave potential is rephased by the second standing-wave pulse at $t = T$ in the vicinity of the echo time $t = 2T$. The determination of gravitational acceleration relies on measuring the contrast and phase of the grating by coherently back-scattering a traveling-wave read-out pulse from the sample.

Figure 23 shows a recoil diagram representing curved trajectories of a subset of momentum states that contribute to the signal. The read-out pulse detects the amplitude and phase of the matter wave interference in the vicinity of $2T$ only from trajectories that differ by $\hbar q$. It is possible to show that the gravitational phase shift is not related to the difference in path lengths between the arms of the interferometer. Rather, it is related to the energy of the atom that is affected by both recoil and gravity. Using the action principle, it can be shown that the phase accumulation due to gravity scales as gT^2. Thus, the measurement of gravity relies on the connection of the phase of the back-scattered light and the phase of the grating.

A calculation of the signal in the absence of spontaneous emission is discussed in Cahn et al. (1997). It can be shown that the back-scattered

electric field amplitude is proportional to the $\lambda/2$-periodic spatial component (q-Fourier harmonic) of the atomic density grating. The echo signal (scattered field amplitude) can be written as

$$E(\Delta t;T) \propto -\mathrm{e}^{-(\Delta t/\tau_{\mathrm{coh}})^2} J_1[2u_1 \sin(\omega_q \Delta t)] J_2\{2u_2 \sin[\omega_q (T+\Delta t)]\}, \tag{50}$$

where $J_n(x)$ is the nth-order Bessel function of the first kind, u_1 and u_2 are the pulse areas of the first and second standing-wave pulses, respectively, which define the atom-field coupling, $\omega_q = \hbar q^2/2M$ is the two-photon recoil frequency, and $\Delta t = t - 2T$ is the time relative to the echo time.

In the presence of gravity, the echo signal can be shown to be (Weel et al., 2006)

$$E_g(\Delta t;T) = E(\Delta t;T)\mathrm{e}^{i\phi_{\mathrm{g}}(\Delta t;T)}, \tag{51a}$$

$$\phi_{\mathrm{g}}(\Delta t;T) = -\frac{qg}{2}\left(2T^2 + 4T\Delta t + \Delta t^2\right), \tag{51b}$$

where ϕ_{g} is the phase of the atomic grating, which is accelerating downward because of gravity. This phase is imprinted on the light scattered by the atoms from the read-out pulse. It is useful to split the phase due to gravity into two components, $\phi_{\mathrm{g}} = \phi_{\mathrm{AI}} + \phi_{\mathrm{D}}$. The first term, $\phi_{\mathrm{AI}} = -qgT^2$, is referred to as the AI phase, since it depends solely on T and is proportional to the area of the interferometer. The second term, $\phi_{\mathrm{D}} = -qg(2T\Delta t + \Delta t^2/2)$, is called the Doppler phase, since it can be shown that $\phi_{\mathrm{D}} = qv(t)\Delta t$, where $v(t) = \partial(\phi_{\mathrm{D}}/q)/\partial\Delta t = -gt$ is the speed the atoms have gained in the presence of gravity.

Figure 24a is an illustration of the effect of the Doppler phase on the signal envelope at fixed T. The overall signal amplitude as a function of T in Figure 24b illustrates the modulation at the recoil period $\tau_q = \pi/\omega q$ and the increasing oscillation frequency due to the interferometer phase. The experiment relies on measuring the phase of the signal with respect to a frame of reference in which the atomic sample is falling in gravity. Such an inertial reference frame can be defined by an optical local oscillator (LO) with a frequency ω_{LO}. The back-scattered light from the sample due to the read-out pulse with a frequency ω_{AI} is detected in the form of a beat note at a frequency $\omega_{\mathrm{LO}} - \omega_{\mathrm{AI}}$ using a heterodyne technique (Cahn et al., 1997; Shim et al., 2002, 2005; Weel et al., 2006).

The electric field of the LO can be written as $E_{\mathrm{LO}}(z,t) = E_0\mathrm{e}^{i(kz-\omega_{\mathrm{LO}}t)}$, while the scattered electric field from the atoms has the form $E_{\mathrm{AI}}(z,t) = E(T;\Delta t)\mathrm{e}^{i(k(z+\Delta z)-\omega_{\mathrm{AI}}t)}$. The heterodyne signal produced by overlapping the two beams on a photodetector can be shown to be

$$I(t) \propto E_0 E(T;\Delta t)\cos[(\omega_{\mathrm{AI}} - \omega_{\mathrm{LO}})t + k\Delta z] \tag{52}$$

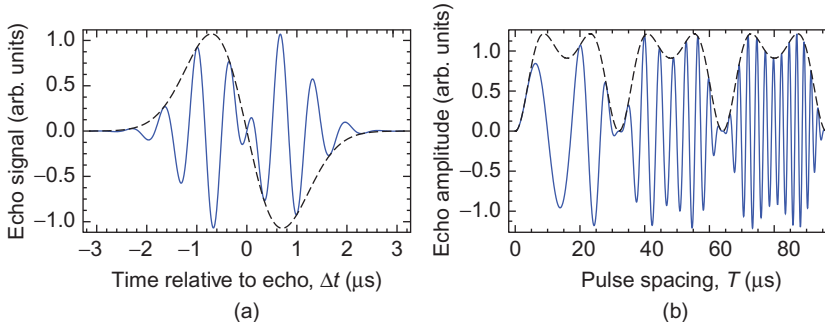

Figure 24 Illustrative plots representing the echo signal in Equation (51a) and the dependence of the AI phase as a function of T in Equation (51b). (a) Echo signal (shown as the dashed line) exhibits a dispersion shape in the absence of gravity. The echo signal in the presence of gravity (shown as the solid line) exhibits additional oscillations due to the Doppler phase in Equation (51b). (b) The amplitude of the echo signal as a function of T (dashed curve) is modulated at the recoil frequency, ω_q. The solid curve shows the in-phase component of the echo amplitude in the presence of gravity. A value of $g = 980$ m/s^2 has been used so that the changing frequency is evident over successive recoil periods. This represents the effect of the AI phase term in Equation (51b). In experiments involving laser-cooled rubidium atoms, the duration of the signal envelope is $\tau_{\text{coh}} \approx 2\,\mu$s, and the recoil period $\tau_q \approx 32\,\mu$s.

where $E(T; \Delta t)$ is given by Equation (50) and

$$\Delta z = -\frac{1}{2} g(2T)^2 + v_0(2T) + z_0. \tag{53}$$

Here, the grating displacement Δz is determined by g, a launch velocity v_0, and the initial position of the grating, z_0. The next section describes how the in-phase and in-quadrature components of the electric field are obtained from the signal intensity in Equation (52).

5.3 Experimental Setup

Figure 25a shows the experimental setup. Figure 25b illustrates the displacement Δz given by Equation (53). An acousto-optic modulator (AOM) is used to produce the excitation beams. The diffracted beam from the AOM passes through the atom cloud and is reflected by a corner cube retro-reflector to produce a standing wave. At the time of the read-out pulse, a mechanical shutter blocks the retro-reflection to produce a traveling wave. The undiffracted beam from the AOM is the LO, which is aligned through the same optical elements as the excitation beam and is physically separated from the atomic cloud. The back-scattered light from the sample and the LO are combined on a balanced heterodyne detector to produce a beat note at $\omega_{\text{RF}} = \omega_{\text{LO}} - \omega_{\text{AI}}$. The heterodyne signal is

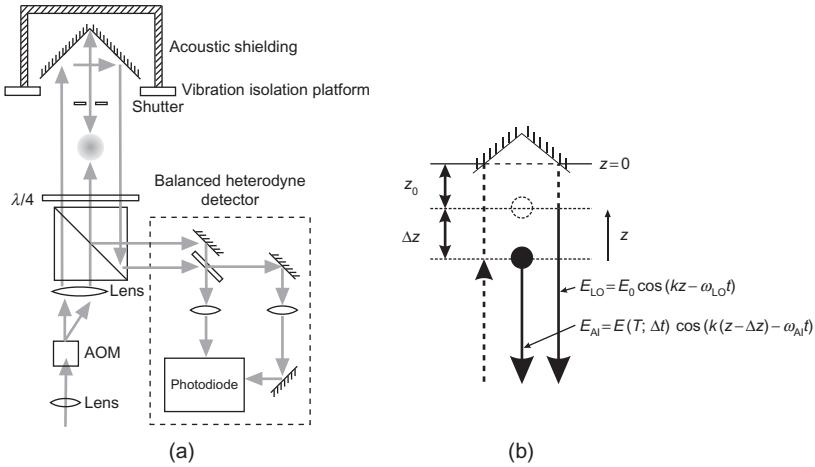

Figure 25 (a) Experimental setup. (b) Illustration of beam paths and cloud displacement in Equation (53). As T is increased, the atom cloud falls in gravity, changing the path difference between the back-scattered signal and the local oscillator.

mixed down to DC using the RF oscillator driving the AOM to generate the in-phase and in-quadrature components of the back-scattered electric field. The signal components are squared and integrated to obtain the in-phase and in-quadrature amplitudes. The total signal amplitude is equal to the individual component amplitudes combined in quadrature.

5.4 Measurement of g

Figure 26a shows the in-phase component of the scattered field in the vicinity of the echo for $T \sim 1.5$ ms. The signal envelope can be modeled by Equation (51a). At small values of T, the effect of gravity is not appreciable and the signal envelope resembles a dispersion shape. Figure 26b shows the echo signal shape for a larger pulse separation: $T \sim 11$ ms. The signal envelope is modulated by the Δt-dependent Doppler phase, $\phi_D = -qgt\Delta t$, due to the effect of gravity. It is interesting that g can be inferred from the echo signal shape by measuring the change in the Doppler frequency as a function of t, where t is the time relative to trap turn-off. Here, t can be changed by increasing the area of the interferometer (i.e., increasing T), or by holding T constant and varying the timing of the excitation pulses relative to trap turn-off. Figure 26c shows the in-phase and in-quadrature components of the signal as a function of T. The two signals can be used to measure the AI phase, $\phi_{AI} = -qgT^2$. Since the AI phase scales as T^2, while the Doppler frequency effectively scales as T, a measurement of ϕ_{AI} results in a more sensitive measurement of g.

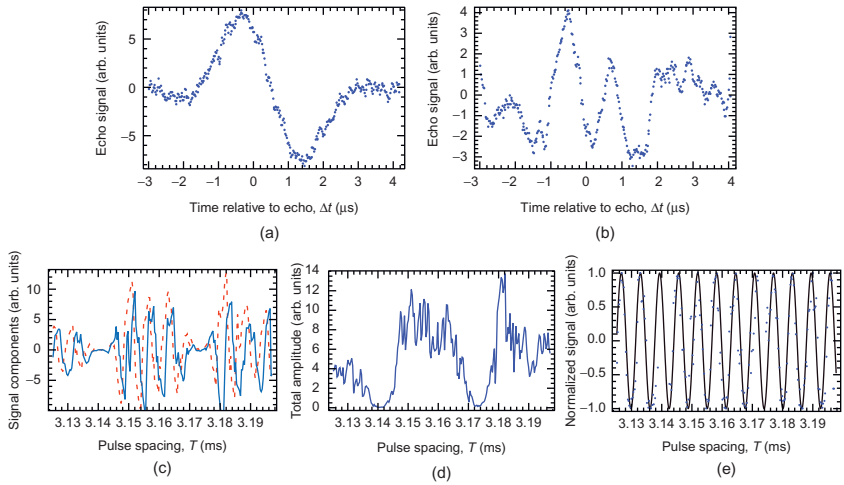

Figure 26 (a) Dispersion-shaped echo envelope at $T \sim 1.5$ ms. (b) Echo envelope modulated because of the effect of gravity at $T \sim 11$ ms. (c) In-phase (dashed) and in-quadrature (solid) components of the signal as a function of T obtained by averaging 32 repetitions. (d) Total signal amplitude (components combined in quadrature) as a function of T, showing modulation due to atomic recoil. (e) In-phase component of the signal as a function of T obtained by normalizing the total signal amplitude.

Figure 26d represents the total signal amplitude obtained from the signal components combined in quadrature. The shape of the signal, which is modeled by the square of Equation (50), exhibits recoil modulation at $2\omega_q$ given by $J_2^2[2u_2 \sin(\omega_q T)]$. Figure 26e shows ϕ_{AI} as a function of T. The AI phase has the functional form $\cos(-qgT^2 + qv_0T + \phi_0)$, where v_0 is the initial launch velocity v_0 of the atomic cloud and ϕ_0 is an arbitrary phase representing the initial position of the grating. The data in this figure were obtained by normalizing the in-phase component of the signal using the total signal amplitude. Similar data are obtained in a number of discrete windows over the timescale of the experiment ($2T \sim 20$ ms). A least-squares fit of the data across all observational windows yielded a measurement of g precise to 5 part per million (ppm).

Other work related to gravimetry that involves repeated reflections in a multipulse AI is discussed in Hughes et al. (2009).

5.5 Future Prospects

The preliminary measurement presented here relied on turning on an attenuated excitation beam during the time in which the atom trap is loaded, measuring the equipment phase and correcting the effect of vibrations by actively controlling the phase of the RF oscillator used

to drive the AOM. In this method, the feedback can be engaged during the period the atom trap is loaded, but not during the excitation pulses. As a result, the phase stability progressively deteriorates over the timescale of the measurement. The experimental timescale was limited by the magnetization of the stainless steel vacuum chamber. Several developments suggest that the precision in the determination of g can be improved significantly. Atomic recoil experiments using this AI have achieved transit-time limited timescales of $2T \sim 70$ ms in a nonmagnetizable glass vacuum chamber in which magnetic gradients were suppressed using external canceling coils. Additionally, the experimental setup shown in Figure 25a has been modified to include a probe beam that continuously tracks the phase variations resulting in a hundredfold improvement in phase stability. If a transit time of 300 ms is achieved, a compact experiment can be realized using an atomic fountain. Under these conditions, it is anticipated that a competitive measurement of g—precise to better than ~1 part per billion (ppb)—is possible.

6. INTERNAL STATE LABELED INTERFEROMETER

6.1 Introduction

In this section, we describe the temporal evolution of magnetic sublevel coherences in laser-cooled samples under the influence of static magnetic fields. Previous work (Chan et al., 2008; Kumarakrishnan et al., 1998a,b) has shown that spatially periodic superposition states (coherence gratings) of magnetic sublevels within the same hyperfine ground-state manifold can be optically excited using two-photon transitions driven by appropriately polarized laser fields. For excitation by counter-propagating pulses, the grating period is $\lambda/2$, where λ is the wavelength of light. The decay time of the coherence due to Doppler dephasing occurs on a time scale of a few microseconds in which the displacement of a typical atom exceeds the grating period. For this geometry, the effect of atomic recoil is significant as in the standing-wave experiments described in earlier sections. In contrast to single-state interferometers, echo experiments involving magnetic sublevel coherences represent state-labeled interferometers in which the exchange of photons with the laser fields is associated with a precise change in internal state (Kasevich & Chu, 1991). For nearly copropagating small-angle excitation, recoil effects are not important and the spatial period can be $\sim 1000\,\lambda$. As a result, the decay time of the coherence can be several milliseconds. The relatively long coherence decay time and the ability to apply a uniform magnetic field across a compact laser-cooled sample can be exploited for precision measurements of magnetic interactions such as atomic g-factor ratios. Such a measurement relies on a determination of the Larmor frequency ω_L associated with the

evolution of a coherent superposition of magnetic levels in a static magnetic field. We use a magneto-optical trap (MOT) consisting of spatially overlapped samples of laser-cooled ^{85}Rb and ^{87}Rb isotopes. Our measurements suggest that a precision of better than 1 ppm is attainable. Such a measurement represents a sensitive test of the Zeeman Hamiltonian. In comparison, pioneering measurements (Cohen-Tannoudji & Kastler, 1966; Cohen-Tannoudji et al., 1969; White et al., 1968) used RF spectroscopy to ensure narrow linewidths and paraffin-coated vapor cells to prevent spin relaxation from wall collisions (that resulted in transit-time-limited signal decay) to achieve precisions of a few ppm.

We use coherent transient effects designated as magnetic grating free induction decay (MGFID) and magnetic grating echoes (MGE) that were originally predicted in Dubetsky and Berman (1994). A laser-cooled gas is excited using two simultaneous traveling-wave laser pulses applied at $t = 0$ with wave vectors $\boldsymbol{k}_1$ and $\boldsymbol{k}_2$ at a small angle ($\theta' \sim 10$ mrad), as shown in Figure 27a. The individual traveling waves pulses have orthogonal linear or circular polarizations so that it is possible to excite $\Delta m = 1$ or $\Delta m = 2$ coherences, respectively. The pulses are detuned from the excited state and resonant with the two-photon transition that couples two magnetic sublevels of the ground state as shown in Figure 27b. The timing diagram is shown in Figure 27c. The excitation creates a spatially periodic superposition (coherence grating) between the magnetic sublevels of the ground state. The grating, which has a period of $\sim \lambda/\theta'$, is probed by a read-out pulse along $\boldsymbol{k}_2$. The resulting MGFID signal is coherently scattered along $\boldsymbol{k}_1$ due to conservation of momentum. The grating dephases because of thermal motion of the atoms causing the MGFID to decay on a time scale of $\lambda/\theta' u$, where u is the most probable speed associated with the Maxwell–Boltzmann velocity distribution. The dephasing time of the MGFID can therefore be used to infer the temperature of the sample.

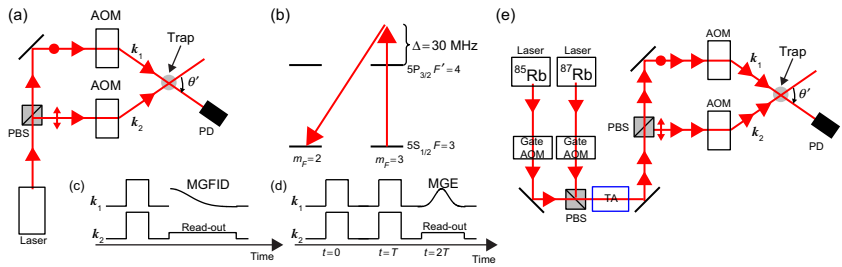

Figure 27 (a) Experimental schematic; $\theta' \sim 10$ mrad. PBS = Polarizing beam splitter, PD = photodetector, AOM = acousto-optic modulator. (b) Level diagram in ^{85}Rb showing two-photon excitation with orthogonal linear polarizations; Δ is the one-photon detuning. (c), (d) Timing diagram for the MGFID and MGE experiments respectively. (e) Experimental schematic for precision measurements.

The effect of Doppler dephasing can be eliminated by observing magnetic grating echo (MGE) signals. The MGE is observed using a second set of excitation pulses at $t = T$ to rephase the coherence grating as in Figure 27d. The second pulse modifies the time-dependent coefficients that describe the coherent superposition of magnetic sublevels so that the grating reforms at $t = 2T$. This effect is analogous to the reversal of the Doppler phases of individual atoms in a traditional two-pulse photon echo experiment (Rotberg et al., 2007). In the absence of decoherence due to collisions and background light, the MGE amplitude should decay on a time scale determined by the transit time of atoms through the laser beams as shown in Kumarakrishnan et al. (1998b).

The excitation and read-out pulses are derived using acousto-optic modulators (AOM) and intersect at a small angle in a sample of laser-cooled atoms as in Figure 27a. A single tapered amplifier (TA) is used to generate the trapping light for both ^{85}Rb and ^{87}Rb isotopes. Another TA is used to generate the excitation beams as in Figure 27e. In order to minimize the effect of time-varying magnetic fields, the ^{85}Rb and ^{87}Rb traps are spatially overlapped. This allows the MGFID signals from both isotopes to be recorded $\sim$1 ms apart. The trapping chamber is made of pyrex to minimize magnetized materials near the MOT and to avoid the effects of eddy currents. Magnetic field canceling coils suppress magnetic gradients to the level of 10^{-5} G/cm. The experiment also relies on active feedback to stabilize magnetic fields. In this manner, variations of static fields are limited to $\sim$10 μG and fluctuations in AC fields are reduced to $\sim$30 μG over the time scale of the measurement. At the start of the experiment, both ^{85}Rb and ^{87}Rb atoms are simultaneously loaded from background vapor into the dual isotope MOT. After turning off the magnetic field gradient of the MOT, both isotopes are cooled in an optical molasses for $\sim$10 ms to temperatures of $\sim$30 μK. The excitation pulses ($\sim$5 μs in duration) and read-out ($\sim$1 ms in duration) for each isotope are separately switched on in a random sequences. The signal is recorded by a gated photomultiplier tube or a balanced heterodyne detector that is turned off at the time of the excitation pulses.

The Doppler dephasing time can be measured by mapping out the MGFID using a short intense read-out pulse with a variable delay with respect to the excitation pulse in the absence of magnetic fields using a single isotope. Figure 28a shows the MGFID from a sample of laser-cooled ^{85}Rb atoms optically pumped into a single magnetic sublevel. The MGFID is fitted to a Gaussian form predicted by theory (Dubetsky & Berman, 1994) and consistent with previous observations (Kumarakrishnan et al., 1998a,b). The time constant of the decay, τ, and the angle between the excitation beams are used to extract the most probable speed (and temperature) associated with the Maxwell–Boltzmann distribution of the cloud along the direction $\boldsymbol{k}_1 - \boldsymbol{k}_2$. Figure 28b shows the radius of the sample along $\boldsymbol{k}_1 - \boldsymbol{k}_2$ measured using a CCD camera as a function of delay time

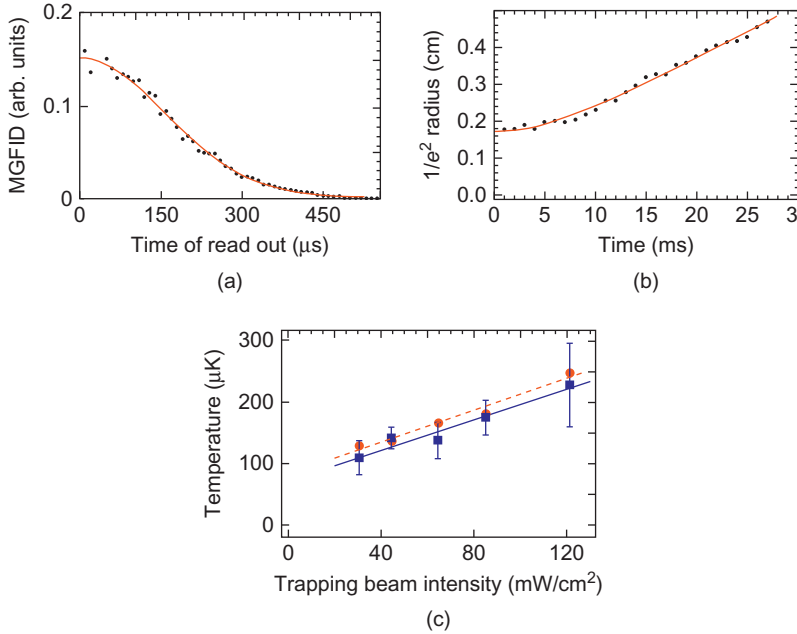

Figure 28 (a) Decay of the MGFID (circles) as a function of time for an angle $\theta' = 6.6$ mrad. The decay time extracted by fitting the data to the equation $Ae^{-(t/\tau)^2} + C$ (solid line) is $\tau = 221\,\mu$s. The most probable speed, given by $u = 2/(k\theta'\tau)$, is 0.17 m/s. The corresponding temperature is $\mathcal{T} = 149.2\,\mu$K. (b) Ballistic expansion of the cloud as a function of time (circles). u is extracted by fitting the cloud radius $R(t)$ to a hyperbola $R(t) = \sqrt{R_0^2 + (ut)^2}$ (solid line), where R_0 is the initial cloud radius. (c) Temperature of the cloud measured by the CCD camera (circles) and the temperature measured from the decay time of the MGFID (squares) as a function of total trap laser intensity. Linear fits are represented by a dashed line with $1.3I + 82.6\,\mu$K and a solid line with $1.2I + 73.3\,\mu$K. Here, I is the trapping laser intensity in mW/cm^2.

with respect to the turn off of the trapping lasers (Vorozcovs et al., 2005). The temperature is extracted by fitting the data to a hyperbola using the measured cloud size and the delay time. A comparison of the temperature measurements using these two techniques is shown in Figure 28c. The temperature was varied by changing the total trap laser intensity. It is clear that the temperature measurements show good agreement within experimental error.

6.2 Effect of a Uniform Magnetic Field on the MGFID

It is known that the Zeeman shift between magnetic sublevels causes temporal oscillations within the envelopes of these signals at multiples of ω_L (Kumarakrishnan et al., 1998a). Chan et al. (2008) presents an analytical

calculation that predicts the functional form of the Larmor oscillations in the the MGFID in arbitrary static magnetic fields for excitation pulses with both orthogonal linear and circular polarizations.

The theoretical treatment is based on a rotation matrix approach (Edmonds, 1996; Rochester & Budker, 2001; Shore, 1990) in which the effect of the magnetic field can be described as a time-dependent rotation of the atomic system about the quantization axis. The evolution of $\Delta m = 1$ and $\Delta m = 2$ coherences in a magnetic field resembles the evolution of dipole and quadrupole moments of the atom (effects termed alignment and orientation respectively) in an irreducible tensor basis. On the basis of the treatment in Rochester and Budker (2001), the probability of the atom being in a specific coherent superposition is defined by $\langle F\, m \mid \rho \mid F\, m' \rangle$, where F and m refer to the total angular momentum and magnetic quantum numbers of the ground state, respectively, and ρ is the atomic density matrix. To calculate the probability that an atom will be in a particular atomic state in the presence of a magnetic field, we apply the rotation operator to align the quantization axis as defined by the laser polarizations with the quantization axis as defined by the magnetic field. This involves rotating the atomic coordinate system through the Euler angles (α,β,γ) that describe rotations about each of the axes. The rotated density matrix is given by

$$\rho_{m\,m'}(\theta,\phi) = \left[D^{-1}(\phi,\theta,0)\rho D(\phi,\theta,0)\right]_{m\,m'}, \tag{54}$$

where

$$D(\alpha,\beta,\gamma) = \exp\left(i\gamma\hat{J}_z\right)\exp\left(i\beta\hat{J}_y\right)\exp\left(i\alpha\hat{J}_z\right). \tag{55}$$

In Equation (54), θ and ϕ represent the polar and azimuthal angles in the new coordinate system. The rotation generates a surface such that the distance from the origin to a point on the surface defined by (r, θ, ϕ) is proportional to the probability of finding the system in a particular state.

The rotation matrix in Equation (55) can be evaluated for the level structure of interest (specific angular momentum $\hat{\boldsymbol{J}}$). We apply the rotation operator D to the density matrix and evolve the system in time using the Hamiltonian for the magnetic interaction. The time-dependent atomic density matrix element $\rho_{m\,m'}(t)$ is then transformed into an irreducible tensor basis $\rho^K_Q(t)$ using the transformation

$$\rho^K_Q = \sum_{m,\,m'} (-1)^{F-m'} \left\langle F, m; F, -m' \,\middle|\, K, Q \right\rangle \rho_{m\,m'}, \tag{56}$$

where $\langle F, m; F, -m' \mid K, Q\rangle$ is a Clebsch–Gordan coefficient. It is particularly convenient to write the atomic density matrix in this basis, since the

coherence that is established by the laser pulses is proportional to the tensor elements ρ_Q^K. The inverse transformation allows us to predict the state of the system in the m basis and is given by

$$\rho_{mm'} = \sum_{K=0}^{2F} \sum_{Q=-K}^{K} (-1)^{F-m'} \langle F, m; F, -m' \mid K, Q \rangle \, \rho_Q^K. \tag{57}$$

Since the time dependence of the density matrix in Equation (54) is given by

$$\dot{\rho}_{m\,m'}(\theta, \phi, t) = -\frac{i}{\hbar} \left[\hat{H}, \rho(\theta, \phi, t) \right]_{m\,m'}. \tag{58}$$

where $\hat{H} = -g_J \mu_B \boldsymbol{B} \cdot \boldsymbol{J}$, the solution to Equation (58) is

$$\rho_{m\,m'}(\theta, \phi, t) = \left[\mathrm{e}^{-i\hat{H}t/\hbar} \rho(\theta, \phi, t = 0) \mathrm{e}^{i\hat{H}t/\hbar} \right]_{m\,m'}. \tag{59}$$

We calculate ρ_Q^K (defined by Equation (56)) as a function of time for the $F = 3$ manifold in ^{85}Rb for excitation by Lin⊥Lin and $\sigma^+\sigma^-$ pulses. The relevant tensor elements are ρ_1^1 and ρ_2^2, respectively. Correspondingly, the time dependence of the MGFID in a magnetic field is given by

$$\rho_1^1(t) \propto \cos(\omega_L t) + \sin(\eta) + i \cos(\eta) \sin(\omega_L t). \tag{60}$$

$$\rho_2^2(t) \propto \mathrm{e}^{-2i(\omega_L t + \eta)} \left[i \left(1 - \mathrm{e}^{-i\eta} \right) + \mathrm{e}^{i\omega_L t} + \mathrm{e}^{i(\omega_L t + \eta)} \right]^4. \tag{61}$$

Here, we use η to specify the angle between the magnetic field and the quantization axis of the atoms as defined by the laser polarizations. It is evident that the signals exhibit Larmor oscillations because of the magnetic field. The precision measurement of the g-factor ratio relies on a determination of the ratio of Larmor frequencies in two rubidium isotopes under such conditions. In order to compare predictions to experimental results, Equations (60) and (61) are multiplied by a Gaussian decay to model Doppler dephasing.

The temporal evolution of the coherences is illustrated in Figure 29 which shows the MGFID from laser-cooled ^{85}Rb atoms. The entire decay was recorded using a long weak read-out pulse. A heterodyne technique was used to determine the in-phase and quadrature components of the signal.

Figure 29 shows the signals for Lin⊥Lin and $\sigma^+\sigma^-$ excitation with the uniform magnetic field at an angle $\eta = \pi/4$ with respect to the quantization axis. For Lin⊥Lin excitation, the MGFID is proportional to the irreducible tensor element ρ_1^1 predicted by Equation (60). For $\sigma^+\sigma^-$ the

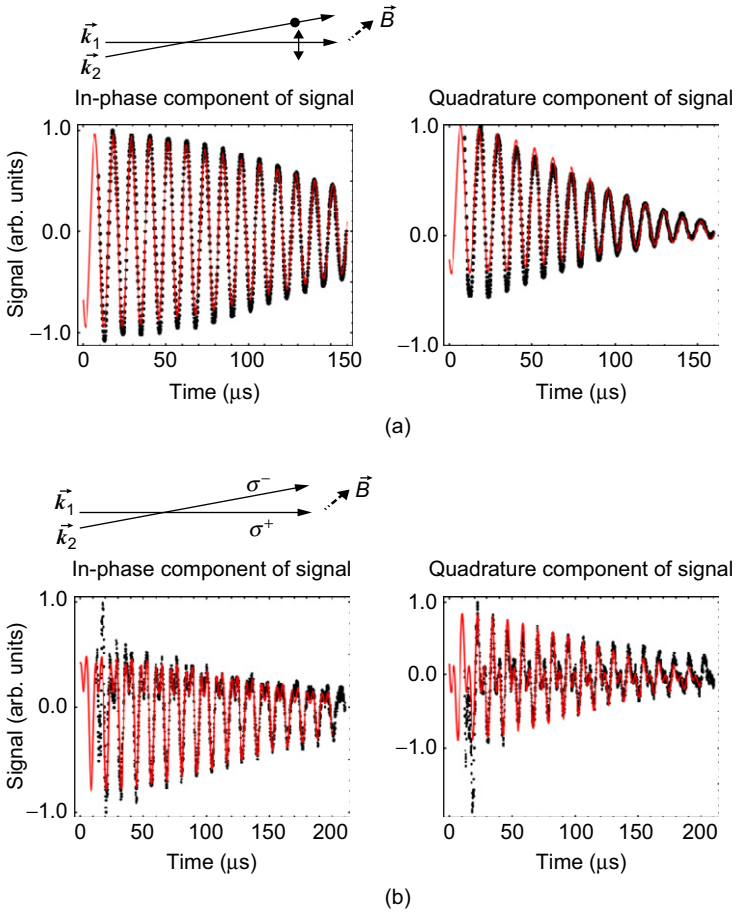

Figure 29 Evolution of the in-phase and quadrature parts of the MGFID in a sample of cold atoms. (a) The excitation pulses have orthogonal linear polarizations and the magnetic field is directed at an angle of $\pi/4$ with respect to the polarization of k_2. (b) The excitation pulses have opposite circular polarizations with the direction of the magnetic field at an angle of $\pi/4$ to the direction of k_1. In both cases the excitation pulse widths were 2 μs, and the detuning was 40 MHz. The data are shown as dots and the solid lines are fits based on Equations (60) and (61).

MGFID is given by ρ_2^2 predicted by Equation (61). Data shown in Figure 29 exhibits excellent agreement with the fits based on Equations (60) and (61). The overall signal shapes and oscillation frequency are consistent with predictions. It is also clear that Larmor oscillations can be recorded over the entire signal dephasing time.

Figure 30 shows an example of single-shot measurements of the MGFID signals from the dual species MOT for Lin⊥Lin excitation. To determine

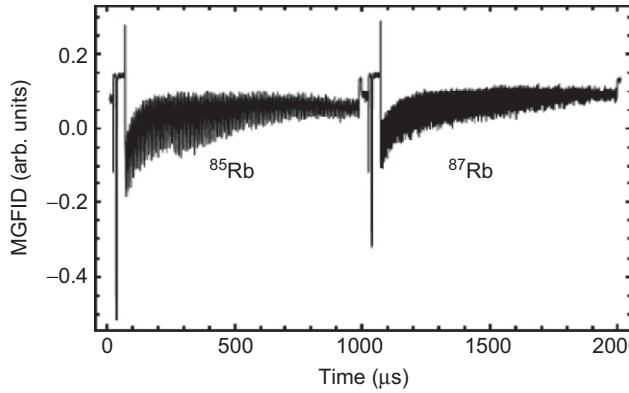

Figure 30 MGFID signals from a dual isotope MOT. The temporal separation of the signals is 1 ms.

the oscillation frequency, the data are fitted to a function based on Equation (60) with $\eta = 0$. This procedure can be used to extract the ratio of g-factors, which is taken to be the ratio of Larmor frequencies. The precision in the measured Larmor frequencies is 24 ppm and 16 ppm for ^{85}Rb and ^{87}Rb respectively. For a given set of experimental conditions (pulse power, duration, magnetic field, read-out pulse intensity, distribution of magnetic sublevel populations) the average value of the ratio is determined by averaging ∼100 repetitions. The major systemic effects that are being investigated include AC stark shifts associated with the read-out pulse, the Breit–Rabi correction due to the nonlinear variation of the Larmor frequency with magnetic field that causes the g-factor ratio to be dependent on the field, and magnetic sublevel population distributions that cause a variation in the Larmor frequencies of $\Delta m = 1$ coherences within the same ground-state manifold due to the Breit–Rabi effect.

6.3 Effect of a Uniform Magnetic Field on the MGE

The precision of the g-factor ratio can be improved by observing T dependent oscillations in the amplitude of the MGE signal. Such a measurement raises the exciting prospect of testing relativistic effects that have been predicted at the level of 100 ppb by Anthony and Sebastian (1994).

The rotation matrix approach described in Section 6.2 is clearly well suited to describing the MGFID in the tensor basis, since it gives analytical expressions for arbitrary magnetic field directions. In contrast, the evolution of the MGE is more complicated. It requires knowledge of the evolution of the magnetic sublevel populations and coherences during both excitation pulses as well as the evolution of the Doppler and Larmor

phases during the experiment. As a result, we use numerical simulations to model a system of rate equations (Berman, 1991; Berman et al., 1993) to describe the MGE and to understand this signal in a magnetic field.

An interesting prediction of the simulations is that the amplitude of the MGE envelope exhibits oscillations that depend on the Rabi frequencies of the excitation pulses and the magnetic field as a function of the time between excitation pulses. The amplitude of the MGE oscillates as a function of T with a characteristic frequency $\sqrt{(\chi^2/\Delta)^2 + \omega_L^2}$, where χ and Δ are the Rabi frequency and detuning of the excitation beams, respectively. This expression has the same form as the generalized Rabi frequency for a laser field interacting with a two-level atom (Allen & Eberly, 1987). The term χ^2/Δ characterizes the two-photon interaction and replaces the one-photon Rabi frequency. The two-photon detuning ω_L due to the Zeeman shifted magnetic sublevels levels replaces the one-photon detuning. Owing to the spatial variation in the Rabi frequency χ, the component of the MGE oscillation at frequency $\xi = \chi^2/\Delta$ averages out on a time scale of $\sim 1/\xi$ ($\sim$100 ns). As a result, it can be expected that the frequency of the T-dependent oscillations on suitably long time scales will be determined by ω_L. The results of simulations are consistent with expectations based on a derivation in the limit $\chi \ll \delta$, where δ is the two-photon detuning (Dubetsky & Berman, 1994). This treatment shows that the echo envelope oscillates as a function of T with frequency δ (which is analogous to ω_L). Since it should be possible to observe the MGE on a time scale comparable to the transit time of cold atoms through the region of interaction (several tens of milliseconds), it should be possible to use this signal to achieve a significant improvement in the precision with which the g-factor ratio can be determined. However, the time scale on which magnetic-field-induced oscillations in the amplitude of the echo envelope can be observed will be limited by the presence of magnetic field gradients. In the presence of a gradient, all the atoms that contribute to the signal have slightly different Larmor frequencies, depending on their spatial locations. As T increases, the oscillations from individual atoms get out of phase and cancel out as shown in Chan et al. (2008).

Figure 31 shows the amplitude of the MGE at $t = 2T$ as a function of T from laser-cooled ^{85}Rb atoms. These data were obtained using a short intense read-out pulse. To record MGE signals for small values of T, we used counter-propagating excitation pulses ($\boldsymbol{k}_1 \approx -\boldsymbol{k}_2$) so that durations of the MGFID and MGE envelopes are $\sim$1 μs. The data show that the effect of atomic recoil is significant for this geometry. The signal amplitude in Figure 31 shows the expected modulation at the atomic recoil frequency $\omega_q = \hbar q^2/2M$, where $\hbar \boldsymbol{q} = \hbar(\boldsymbol{k}_1 - \boldsymbol{k}_2)$ is the momentum transfer to the atoms from the laser fields and M is the atomic mass. The corresponding value of $\tau_q = \pi/\omega_q$ shown in Figure 31 is $\tau_q \sim 32$ μs. The Larmor

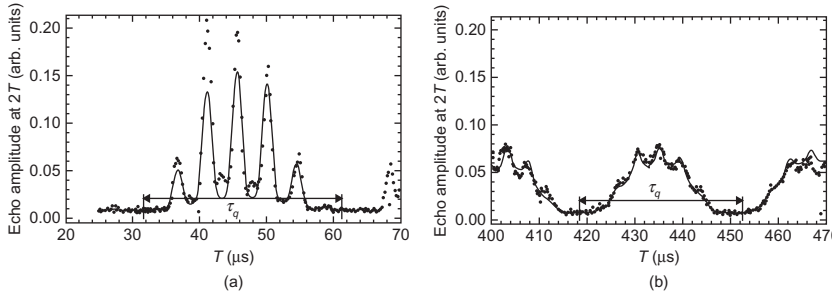

Figure 31 MGE signal intensity measured with a PMT (dots) using counter-propagating Lin⊥Lin excitation pulses in a laser-cooled sample. A magnetic field of $B \sim 0.25$ G is directed along the polarization direction of k_1. The first and second excitation pulses are 680 ns and 70 ns in duration, respectively. In addition to the T-dependent magnetic field oscillations, the signal is modulated at the atomic recoil frequency ($\omega_q = 96.95(4)$ rad/ms). The extracted value of ω_L from the fit (solid line) is consistent with the expected value.

frequency was determined to be $\omega_L = 110.395(15)$ kHz (∼100 ppm) from a fit based on Equation 26 in Beattie et al. (2008) with an additional $\cos^4(\omega_L T)$ term to account for the magnetic field oscillations. The value of ω_L was consistent with expectations based on the applied magnetic field. Both ω_q and ω_L were obtained from a single multiparameter fit to the data in Figure 31a and b.

Figure 31b shows that Larmor oscillations in the amplitude of the echo envelope cancel out for $T \sim 500\,\mu$s although the overall decay time of the signal is several milliseconds. This behavior is due to the presence of a magnetic field gradients of ∼0.05 G/cm due to the magnetized walls of a stainless steel vacuum chamber (Weel et al., 2006). Following the demonstration of transit-time-limited recoil experiments in the glass cell, we anticipate similar observations on time scales of ∼70 ms. As a result, it should be possible to utilize the MGE to improve the precision in the g-factor ratio measurements to ∼100 ppb. The main experimental challenge will be associated with the long-term stability of magnetic fields, since the time for acquiring a data set such as in Figure 31 is ∼1 hour.

7. COHERENT TRANSIENT EFFECTS

7.1 Introduction

In this section, we describe the suitability of the echo technique for precision measurements of radiative lifetimes of atomic excited states. The knowledge of atomic lifetimes is essential for a wide range of experiments in laser spectroscopy such as atom and ion trapping (Moehring

et al., 2006), trace gas analysis, and remote sensing. Precision measurements are also essential for testing quantum mechanical calculations of level structure (Blundell et al., 1991; Dzuba et al., 1989; Safronova et al., 2004).

Precision measurements of natural linewidths and atomic lifetimes have generally involved scanning a probe laser with a narrow linewidth or observing the decay of the atomic fluorescence using photon-counting techniques. The dominant systematic effects in these experiments are the contribution of laser linewidth and radiation trapping respectively. As a result, these experiments have required the development of sophisticated experimental setups. A prominent example is a measurement of the natural linewidth precise to ~0.25% in a sample of velocity-selected laser-cooled Na atoms (Oates et al., 1996). This experiment utilized a laser with a linewidth of only a few kilohertz. Such lasers are accessible to only a small number of groups. An alternative technique for measuring the atomic lifetime with comparable precision involves exciting a sample of trapped atoms with a laser pulse and observing the fluorescence decay. Such an experiment requires specialized expertise to develop electronics for photon counting (Simsarian et al., 1998). Examples of other independent techniques include photo-association spectroscopy (McAlexander et al., 1996) in cold atoms and fast atomic-beam experiments (Volz & Schmoranzer, 1996; Young et al., 1994).

The widely established two-pulse photon echo technique is particularly well suited for precision measurements of atomic lifetimes because it is insensitive to the effects of radiation trapping and laser linewidth and is widely accessible to a large number of experimental groups. Although photon echoes have been used extensively to measure relaxation rates in atomic and molecular species (Patel & Slusher, 1968), collisional rates (Flusber et al., 1978), diffractive collisions (Forber et al., 1990), atomic level structure (Chen et al., 1980), and lifetimes in solids and doped crystals (Becker et al., 1988; Macfarlane & Shelby, 1981), it does not appear to have been used for atomic lifetime measurements.

Spin echoes (Hahn, 1950b) and photon echoes (Abella et al., 1965) are well understood and have been studied extensively over the past 60 years. In a typical photon echo experiment involving dilute atomic gases, a laser pulse is applied at $t = 0$ to create a coherent superposition of ground and excited states (Allen & Eberly, 1987). Owing to Doppler broadening, the superposition dephases with time. At $t = T$ a second pulse is applied and rephases the superposition so that dipole radiation occurs at $t = 2T$ (photon echo). The decay of the echo signal as a function of T can be used to measure various relaxation effects. The basic properties of a two-level atom and its interaction with an external electric field are based on the treatment in (Allen & Eberly, 1987; Cohen-Tannoudji et al., 1997, 1998). This treatment can be used to describe coherent transient effects such

as free induction decay and photon echoes using the semiclassical Bloch vector model.

In a typical photon echo experiment involving an inhomogeneously broadened sample, a $\pi/2$ pulse applied at $t = 0$ will rotate the Bloch vector associated with the macroscopic dipole moment to the uv-plane. Following the pulse, the Bloch vectors associated with the individual atoms will precess freely around the w-axis. Owing to Doppler broadening, the precession occurs with different rates for different atoms resulting in rapid dephasing of the macroscopic dipole moment (FID). It is possible to reverse the dephasing process after some time $t = T$ using a π-pulse. This creates a rephased dipole moment resulting in an echo at time $t = 2T$. A schematic representation of the process of echo formation is shown in Figure 32.

For a Doppler-broadened gas, in the absence of collisional dephasing, the echo intensity depends only on radiative decay. This dependence is given by

$$I = I_0 \exp\left(-\frac{2T}{\tau}\right). \tag{62}$$

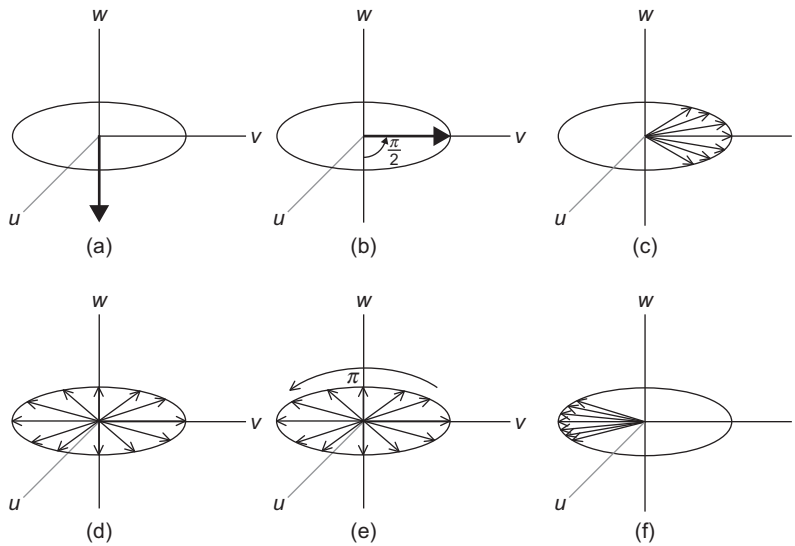

Figure 32 Bloch vector representation. (a) Macroscopic Bloch vector representing all atoms in the ground state. (b) Superposition state immediately after $\pi/2$-pulse. (c), (d) Bloch vector dephasing. (e) Inversion due to π-pulse. (f) Bloch vector rephasing (photon echo).

The laser linewidth and the temporal shape of the excitation pulses determine the velocity distribution that contributes to the echo formation. Although these factors affect the signal strength, they do not affect the decay time constant, τ. Similarly, the intensity, temporal shape of the excitation pulses and sample density affect the echo amplitude and pulse propagation but not the decay time constant. Spontaneous emission during the excitation pulses is also not expected to affect τ.

On the basis of Rotberg et al. (2007), we describe a measurement of the $5P_{3/2}$ excited state lifetime using two-pulse photon echoes in rubidium vapor. The measurement is precise to ~1% and agrees with the best measurement of atomic lifetime in Rb (Simsarian et al., 1998).

7.2 Experimental Setup and Results

The excited state lifetime is determined by measuring the exponential decay of the photon echo intensity as a function of the time T between the excitation pulses. The experiment relies on precisely timed and sufficiently short optical pulses generated from a CW laser using acousto-optic modulators (AOMs). The excitation pulses are on resonance with the $F = 3 \rightarrow F' = 4$ transition in ^{85}Rb or $F = 2 \rightarrow F' = 3$ transition in ^{87}Rb. The echo signal is detected using a heterodyne detection technique used in many experiments involving cold atoms. The signals are generated in a 7-cm-long vapor cell containing a natural abundance of rubidium isotopes (~72% of ^{85}Rb and ~28% of ^{87}Rb). The vapor density, which can be varied by heating the cell, is monitored by measuring the absorption of a probe laser scanned across the atomic resonance.

The experimental setup is shown in Figure 33. Short pulse generation was achieved by focusing and spatially filtering light into two AOMs operating at 260 MHz and 400 MHz. As a result, the resonant excitation pulses have temporal Gaussian profiles with a full width at half maximum (FWHM) of ~20 ns and an on/off ratio of $\sim 10^6 : 1$. The heterodyne detection technique involves use of a local oscillator (LO) derived from a separate 260 MHz AOM as shown in Figure 33. The echo signal is combined with the LO on a beam splitter and detected as a 400 MHz beat note using photodiodes. The echo decay time can be measured by varying T and recording the echo amplitude by averaging 128 repetitions as shown in Figure 34a. To acquire the background for each data point, the experiment is repeated with the first pulse turned off. The oscilloscope traces shown in Figure 34a are squared and integrated to obtain the echo intensity. The echo intensity is expected to show an exponential decay as a function of $2T$ (see Equation [62]). The measurement of the lifetime is achieved by fitting the signal as a function of $2T$ to this model, as shown in Figure 34b.

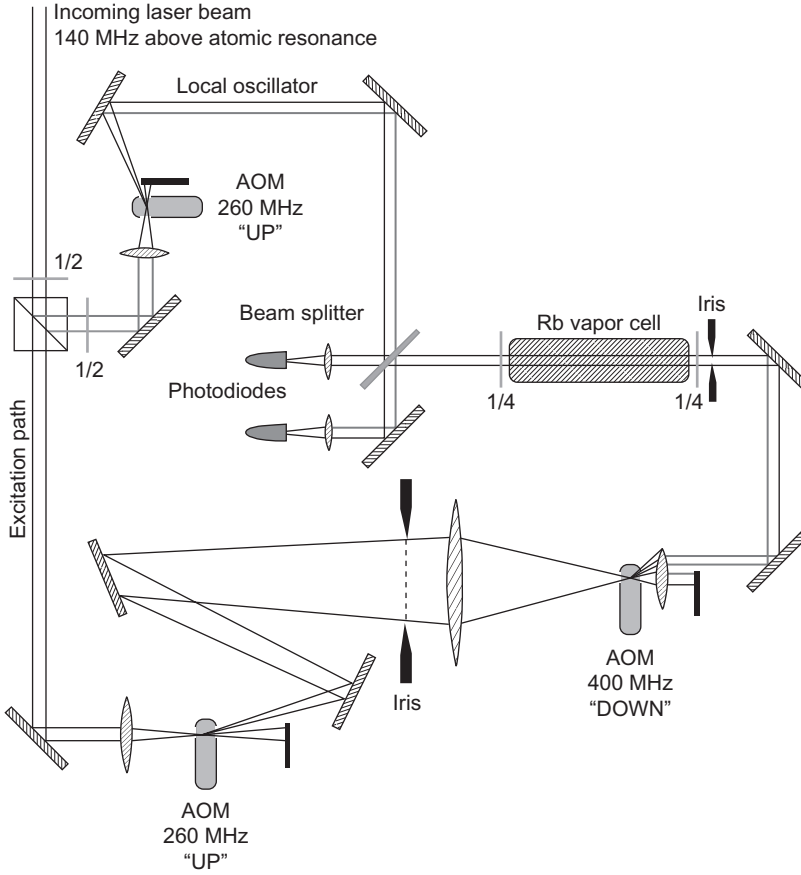

Figure 33 The optical layout. 1/2 and 1/4 represent $\lambda/2$ and $\lambda/4$ wave plates respectively.

7.3 Discussion

Systematic effects on the echo decay time constant were investigated by varying several parameters affecting the echo intensity. These include the intensity and durations of the excitation pulses, cell temperature, strength of a quantizing magnetic field, and the beam diameter of the excitation pulses. Other effects such as collisional dephasing and decoherence due to background light can be ruled out on the time scale of the experiment on the basis of experimental conditions. As shown in Rotberg et al. (2007), these parameters did not produce systematic effects on the measured echo decay time. The final value for the lifetime was determined on the basis of a double-blind study by averaging 67 equally weighted data sets distributed between both ^{85}Rb and ^{87}Rb isotopes. The distribution of

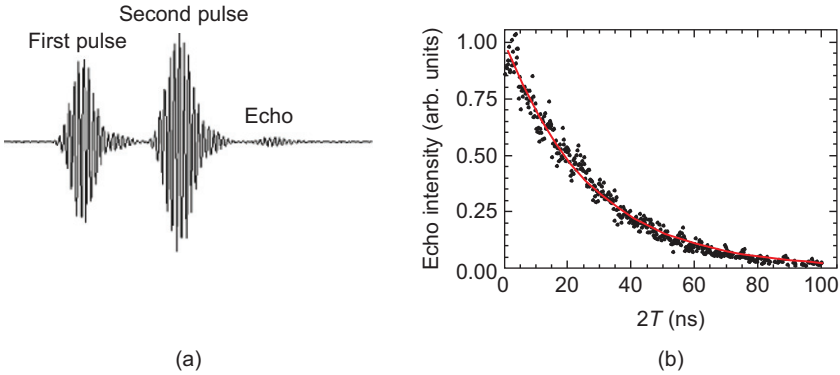

Figure 34 (a) Oscilloscope trace of excitation pulses and the photon echo using heterodyne detection. (b) Decay of the echo intensity as a function of $2T$. Data are fitted to an exponential function that results in a lifetime measurement of $\tau = 25.25 \pm 0.38$ ns.

points is a Gaussian with an average value $\tau = 26.47 \pm 0.30$ ns. The quoted error represents the standard deviation of the mean (1σ uncertainty). The measurement has a precision of 1.14% and is in agreement at the level of 1σ with the best measurement in rubidium (Simsarian et al., 1998) (26.20 ± 0.09 ns).

The theoretical prediction for the echo intensity as a function of the excitation pulse area is well understood in the absence of spontaneous emission (Allen & Eberly, 1987). Since the experiment involved pulse widths that are comparable to the lifetime and since the excitation beams have a finite spatial profile, the dependence of the signal intensity is expected to differ from that in the ideal case. The theory must be modified to include the effect of spontaneous emission and Gaussian pulse shapes (Allen & Eberly, 1987). The effect of the spatial profile can also be taken into account by assigning a Gaussian distribution of Rabi frequencies and averaging the response over the profile. Results based on numerical simulations (Rotberg et al., 2007) show that the maximum echo intensity is obtained when the ratio of the excitation pulse areas is ~1.2. In contrast, for the ideal case, the theory ignores the effect of spontaneous emission and the temporal and spatial profiles of the excitation beams so that this ratio is predicted to be 2.

In summary, the results suggest that improved measurements precise to ~0.25% are attainable through additional data acquisition and studies of systematic effects. Improvements are expected to include optical pumping into a single magnetic sublevel to achieve an increase in the signal-to-noise ratio and use of shorter excitation pulses to minimize the effects of spontaneous emission. The work can also be extended to the $5P_{1/2}$ transitions so that comparisons with previous measurements (such as in

Young et al. [1994]) are possible. The absence of systematic effects and the relative simplicity of this technique suggest that the photon echo technique may be well suited for precision measurements in atomic and ionic transitions that have relatively large oscillator strengths.

8. SUPERFLUORESCENCE IN COLD ATOMS

8.1 Introduction

Previously described experiments on single-state atom interferometers and magnetic sublevel coherences have relied on the coherent transient response of a sample of laser-cooled atoms for signal detection. It is well known that the radiation from a coherently driven sample containing N_{ex} excited atoms will exhibit an N_{ex}^2 enhancement in peak intensity in the far field. It is interesting that this well-known signature is shared by two distinct collective effects termed superfluorescence (SF) and superradiance (SR). In this section, we review observations of both effects in a sample of laser-cooled atoms (Paradis et al., 2008).

In SF, a sample of incoherently excited atoms can be locked in phase to produce coherent emission by spontaneously emitted photons emitted into preferred electromagnetic modes (Gross & Haroche, 1982). SF is characterized by a burst of radiation that has some of the features of radiation from a phased array of dipoles (Rehler & Eberly, 1971). For SR (Dicke, 1954), the direction of emission is defined by the initial phases of excitation pulses and phase-matching conditions (Schneble et al., 2003). In contrast, the shape of the sample defines the directions of SF emissions (Bonifacio & Lugiato, 1975).

The ideal conditions for SF can be achieved if the propagation time for light to travel through the sample, τ_e, satisfies the condition $\tau_e < \tau_r$, where $\tau_r = (N_{ex}\Gamma\mu)^{-1}$ is the dipole coupling time for the evolution of a macroscopic dipole moment (Bonifacio & Lugiato, 1975). Here, Γ is the rate of spontaneous emission for a single atom and μ is the diffraction solid angle at the SF wavelength, which defines the fraction of spontaneously emitted photons that are amplified. Under these conditions, spontaneously emitted photons from one end of the sample can influence the collective evolution of the entire sample. In this regime, the SF peak intensity scales as N_{ex}^2 and the pulse width scales as N_{ex}^{-1} to conserve energy. If $\tau_e > \tau_r$, the emission of the system can be regarded as the incoherent sum of coherent emissions from a number of subregions within the sample that evolve independently (Arecchi & Courtens, 1970; Gross & Haroche, 1982; Kumarakrishnan & Han, 1998; Kumarakrishnan et al., 2005).

SF is also characterized by a delay time with respect to the excitation pulse. Under conditions in which $\tau_e < \tau_r$, a fully quantum-mechanical model for SF initiation predicts that the delay time for SF with respect

to the excitation pulse is given by (Polder et al., 1979):

$$\tau_d = \frac{\tau_r}{4}\left[\ln\left(\sqrt{2\pi N_{ex}}\right)\right]^2. \quad (63)$$

Since τ_d is proportional to τ_r, it approximately scales as N_{ex}^{-1}.

The threshold number of atoms N_T required for SF is achieved when $\tau_r = T_2$, where T_2 is the dephasing time of the system. For a Doppler-broadened vapor $N_T \sim 10^{10}$ (Gibbs et al., 1977), whereas it is typically $\sim 10^5$ for the case of laser-cooled atoms because of the negligible effect of the Doppler broadened linewidth $\Gamma_D \lesssim 1$ MHz. Therefore, SF can become a dominant channel for relaxation and observations of SF from atom traps can be recorded with a high signal-to-noise ratio. Studies of SF scaling laws can serve as useful diagnostic tools for studying various dephasing processes, such as cold Rydberg atom interactions (Gross & Haroche, 1982). Another interesting aspect of working with atom traps is that it is relatively straightforward to change the shape of the sample and to observe the enhancement of SF along the preferred axes of the atomic cloud. Apart from realizing the threshold atom number, it is further necessary that $\tau_d < \tau_n$, where τ_n is the natural radiative decay time associated with the excited state. In some cases (Kumarakrishnan & Han, 1998), effects such as radiation trapping can extend the effective lifetime of the excited state permitting SF to evolve even from rapidly decaying atomic states.

SF has been extensively studied in atomic gases to understand its scaling laws (Gibbs et al., 1977), effects of pulse propagation (Skribanowitz et al., 1973), quantum fluctuations (Gross & Haroche, 1982; MacGillivray & Feld, 1985; Vrehen et al., 1982), and dephasing processes (Maki et al., 1989; Schuurmans, 1980). SF has also been studied as an amplifier of quantum noise, since peak heights, pulse widths, and delay times exhibit characteristic fluctuations because of the stochastic nature of SF initiation (Glauber & Haake, 1976; Haake et al., 1979; Raymer & Walmsley, 1990).

In recent studies (Paradis et al., 2008), we have observed SF from spherical and cigar-shaped clouds of laser-cooled Rubidium atoms. The atomic system is excited to the $5D_{5/2}$ level from the $5S_{1/2}$ ground state via two-photon excitation through the intermediate $5P_{3/2}$ level as shown in Figure 35. The evolution of the system from the $5D_{5/2}$ level through the $6P_{3/2}$ level to the $5S_{1/2}$ ground level is monitored by time-resolved measurements of the light emitted on the $6P \rightarrow 5S$ transition at 420 nm. The time delays for the 420-nm radiation scaled as $\sim N^{-1}$, where N is the atom number. However, the delays are much smaller than expectations for uncorrelated cascade fluorescence. Since N is significantly smaller than the threshold number for SF on the 420-nm transition and larger than the threshold number for the $5D \rightarrow 6P$ transition at 5.2 μm, our observations suggest that rapid de-excitation of the 5D to the 6P level via SF

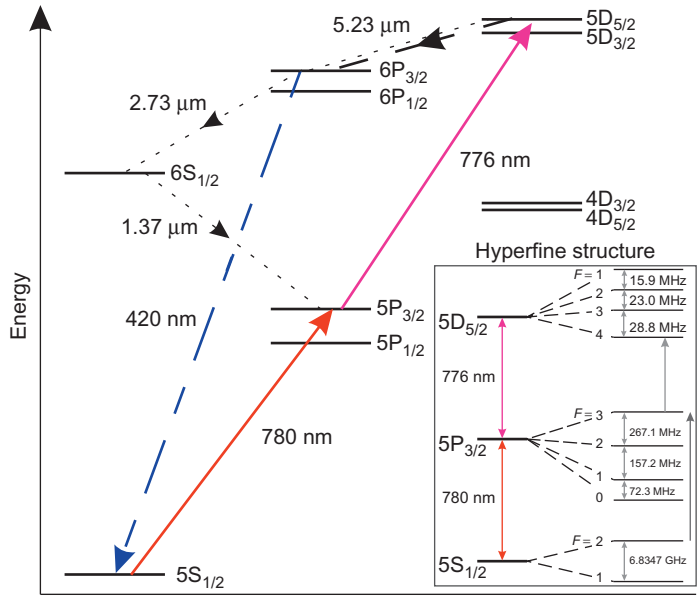

Figure 35 Rubidium 87 level diagram: the solid lines represent excitation pulses, and the dashed lines correspond to SF emissions pertaining to this work. The dotted lines represent the expected SF cascade for incoherent excitation. The radiative lifetimes of the $5D_{5/2} \rightarrow 6P_{3/2}$ and the $6P_{3/2} \rightarrow 5S_{1/2}$ transitions are 690 ns and 357 ns, respectively. The total radiative lifetimes of the $5D_{5/2}$ and $6P_{3/2}$ states are 241 ns and 109 ns, respectively. These lifetimes are based on Arimondo et al. (1977), Sansonetti (2006). The hyperfine structure of the 5D state shown in the inset was measured in Grove et al. (1995).

at 5.2 μm triggered SR-like emissions at 420 nm. This inference is supported by the observed time delays for the 420-nm emission that agree with SF time-delay estimates for the 5.2-μm transition. Pronounced variations in the directionality of of the 420-nm radiation were also observed by changing the shape of the sample. For spherical clouds, the emission is isotropic, whereas for cigar-shaped clouds, it is highly anisotropic. Along the long axis of cigar-shaped atom clouds, it is possible to observe both triggered emission and incoherent cascade fluorescence as temporally well-resolved peaks in the detected signal. The triggered emission is highly concentrated along a direction in between the directions of the two almost parallel excitation beams, which is a well-known characteristic of SR-like emission.

The experiment showed that the evolution of the system depended critically on whether the excitation is coherent or incoherent. As shown in Bowden and Sung (1978), avoiding coherent excitation imposes a particularly restrictive condition on pumping. If the rubidium system can be excited without any initial coherence between the 5S and 5D states, the

system can be expected to decay through a multistep SF cascade involving the 6P → 6S (2.7 μm) and 6S → 5P (1.3 μm) transitions shown in Figure 35. In contrast, if there is an initial coherence between the 5S and 5D states, the system is expected to decay through SF on the 5D → 6P (5.2 μm) transition and triggered SF on the 6P → 5S (420 nm) transition—a process referred to as "Yoked SF" (Brownell et al., 1995; Lvovsky & Hartmann, 1999; Lvovsky et al., 2002).

8.2 Experimental Details

A schematic of the experimental setup is shown in Figure 36. Light from an external-cavity diode laser (ECDL) is used for both the MOT beams on the $5S_{1/2}$, $F = 2 \rightarrow 5P_{3/2}$, $F = 3$ transition in ^{87}Rb and the first excitation beam for the SF experiment (~30 MHz above the MOT transition).

Another ECDL is used to produce ~50 mW of 776-nm light. Beams derived from the locked 780-nm laser and the 776-nm laser are counter propagated through a rubidium vapor cell at room temperature. The inherently Doppler-free two-photon transition resonances associated with the $5D_{5/2}$ hyperfine levels can be observed by measuring the absorption of 776-nm light in the cell. The 776-nm laser is stabilized by means of side-locking to the $5P_{3/2}$, $F = 3 \rightarrow 5D_{5/2}$, $F = 4$ absorption resonance. This laser also produces the light for the second excitation beam for the SF experiment, which is ~30 MHz below the $5P_{3/2}$, $F = 3 \rightarrow 5D_{5/2}$, $F = 4$ transition.

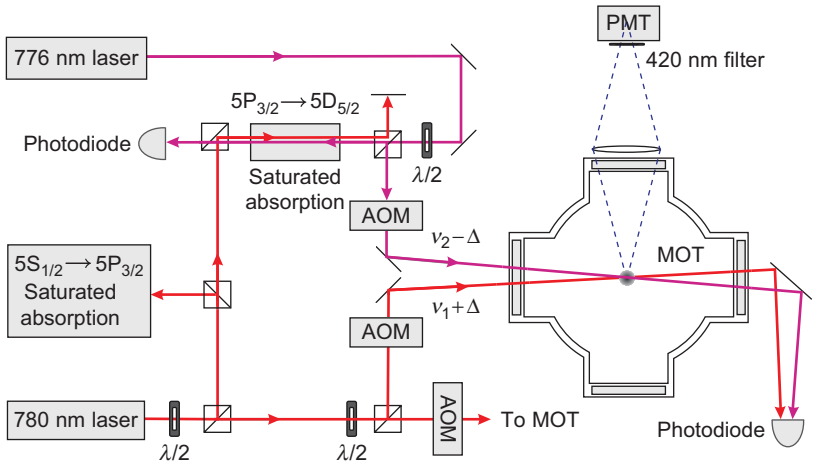

Figure 36 Diagram of experimental setup. SF emissions at 420 nm can be measured both perpendicular to and along the direction of the excitation pulses. (ν_1 denotes the frequency of the $5S_{1/2}$, $F = 2 \rightarrow 5P_{3/2}$, $F = 3$ transition, and ν_2, that of the $5P_{3/2}$, $F = 3 \rightarrow 5D_{5/2}$, $F = 4$ transition).

8.3 Results and Discussion

The ground-state atom number, N, was varied from $\sim 10^7$ to 10^9 by changing the loading time of the MOT. The observed emissions were found to be sensitive to the delay time between the two excitation pulses. One limiting case is when the lower-transition pulse peaks before the upper-transition pulse—referred to as sequential excitation. Another limiting case occurs when the upper-transition pulse peaks before the lower-transition pulse; this case is referred to as Stimulated Raman Adiabatic Passage (STIRAP) (Gaubatz et al., 1990). In both cases, a significant fraction of the ground-state population was transferred to the 5D state. We estimate a typical $5S \rightarrow 5D$ excitation efficiency of $\sim 50\%$ on the basis of the photon yield observed on the $6P \rightarrow 5S$ decay channel and on simulations of the excitation process.

We first describe time-resolved measurements of the 420-nm emission on the transition $6P_{3/2} \rightarrow 5S_{1/2}$ along the long axis of cigar-shaped atom clouds. Each curve in Figure 37 represents the emission intensity versus time for a distinct ground-state atom number, N. This atom number

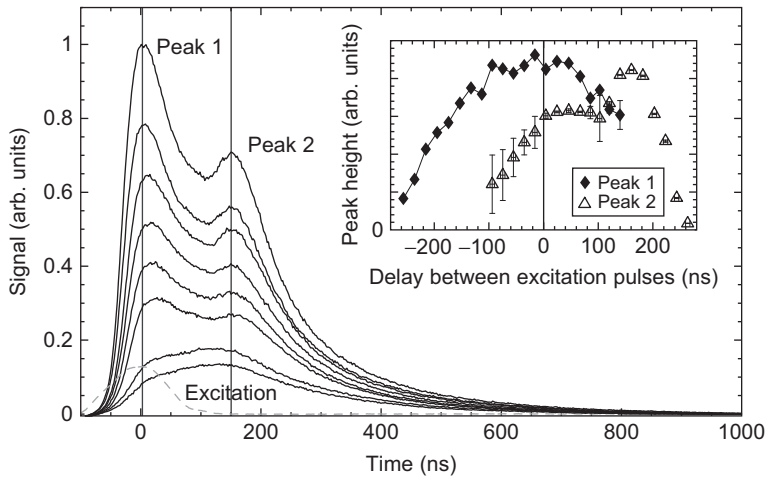

Figure 37 Time-resolved SF detected along the long axis of cigar-shaped atom clouds for various ground-state atom numbers, N. The excitation pulses are overlapped, and time $t = 0$ corresponds to the center of the excitation pulses. N increases from the bottom to the trop curve. The dashed curve indicates the time-dependence of the excitation pulses. The inset shows the height of the two maxima observed in the time-resolved emission signals (peak 1 and peak 2) for a fixed number of atoms, as a function of the delay time between the two excitation pulses. (Delay time < 0 corresponds to STIRAP excitation pulse ordering, while delay time > 0 corresponds to sequential excitation pulse ordering.)

is varied by changing the loading time of the MOT. The steady-state MOT fluorescence is monitored using a calibrated photodetector. N is determined from the measured photocurrent, the solid angle subtended by the detector, the total intensity of the MOT beams, and the detuning of the MOT beams from resonance. It is assumed that the MOT fluorescence is isotropic.

It is evident in Figure 37 that for a large N two time-resolved peaks occur. The time delay of the second peak (peak 2) remains unchanged. We interpret peak 2 as being due to cascade fluorescence. To support this interpretation, we have modeled the level system shown in Figure 35 using rate equations for atomic populations. In the simulation, a laser pulse with a Gaussian envelope (FWHM $\sim$200 ns) excites atoms from the 5S to the 5D level. The simulation shows that the 420-nm emission resulting from uncorrelated decay peaks at a delay time of $\sim$200 ns. This predicted delay of the cascade fluorescence peak matches peak 2 in Figure 37 reasonably well.

The first of the peaks in Figure 37 (peak 1) shows the essential characteristic of SF, namely a decreasing time delay with increasing N. In accordance with this interpretation, it is also observed that peak 1 increasingly dominates peak 2 as N increases. For large atom numbers, the peak 1 practically coincides in time with the excitation pulses, shown as a dashed line in Figure 37. This observation indicates that the 5D level is regeneratively pumped while the SF emission occurs (Gross et al., 1976).

The inset in Figure 37 shows the peak heights of the time-resolved emissions as a function of the delay between the excitation pulses for a fixed atom number ($N \approx 3 \times 10^8$). Negative pulse delays correspond to STIRAP excitation, where the 776-nm pulse precedes the 780-nm pulse, while positive pulse delays correspond to sequential excitation. The SF emission in peak 1 is dominant in the STIRAP regime and a large part of the sequential regime. The cascade fluorescence (peak 2) dominates for sequential excitation-pulse ordering with pulse delays larger than about +100 ns.

Estimates based on Equation (63), assuming the largest atom numbers available in our experiment, show that SF should occur on the $5D \rightarrow 6P$ transition, while conditions are below the SF threshold for the $6P \rightarrow 5S$ transition. Therefore, for the higher atom numbers (see Figure 37) SF on the $5D \rightarrow 6P$ transition is expected to rapidly populate the 6P level, leading to a rapid onset of 420-nm emission, as observed for peak 1. The 420-nm emission appears to be SF as well, as evidenced by the presence of two peaks in Figure 37, the short duration of the emission peak 1 (which is of the order, or less than the 6P lifetime), and the high directionality of the 420-nm emission for cigar-shaped clouds. As the conditions in our experiment are below threshold for SF on the $6P \rightarrow 5S$ transition, the

observed (apparently superfluorescent) emission on that transition must be attributed to triggered SF (Lvovsky & Hartmann, 1999; Lvovsky et al., 2002) that results from coherence between the 5S and 5D state amplitudes generated during excitation.

We now compare the time delays of the emission peaks observed for both cigar-shaped and spherical atom clouds. Figure 38 shows the time delays as a function of N for peak 1 (solid diamonds) and peak 2 (empty diamonds) for observation along the long axis of the cigar-shaped cloud. The delays are measured with respect to the peak of the excitation pulses (with 780-nm and 776-nm pulses temporally overlapped). A fit to the data for peak 1 (solid line) establishes that the SF emission exhibits the expected N^{-1} variation, with no fit offset. The dashed line shows the expected SF delay for 5.2-μm emission, for the same range of N, calculated using Equation (63) based on the measured trap parameters. Although the two curves are in excellent agreement, we note that there are systematic uncertainties with the measured trap parameters, at the level of ±10%. Nevertheless, it is clear that the predicted time delay for the 5.2 μm occurs on the same

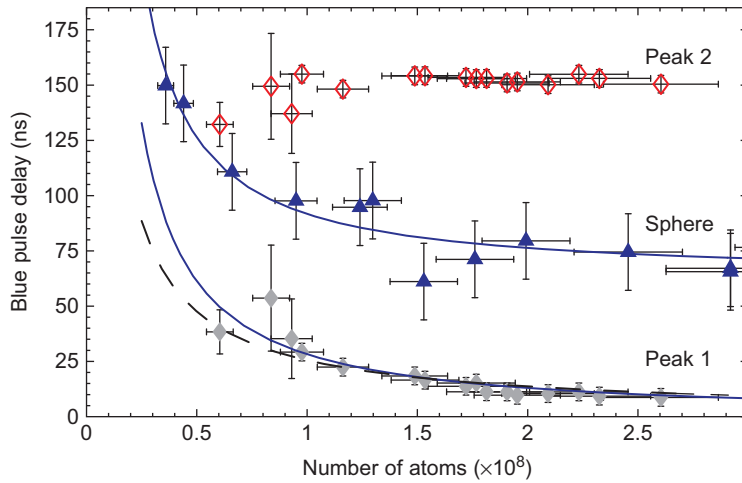

Figure 38 Delay time of SF versus number of atoms. The delays marked peak 1 (solid diamonds) and peak 2 (empty diamonds) correspond to temporally resolved peaks, as shown in Figure 37, measured along the long axis of the cigar-shaped cloud. Delays for the spherical trap are shown with triangles. For the case of the cigar and the sphere, the experimental data are fitted with functions of the type $aN^{-x} + b$ (with fit parameters a, b, and x), shown as solid lines. The fits show that the delays scale as the expected, with $x = (1.12 \pm 0.16)$ for the cigar and $x = (1.17 \pm 0.14)$ for the sphere, respectively. The offset b is zero for the cigar, and ∼70 ns for the sphere. The dashed line shows the predicted 5.2-μm delay, calculated on the basis of Equation (63) using measured cloud parameters. Numerical simulations for cascade fluorescence suggest that peak 2 should occur at 174 ns.

time scale as the 420-nm SF. This indicates that the 420-nm emission is triggered by the presence of the 5.2-μm emission, confirming the results in Lvovsky and Hartmann (1999). The data also show that there is no variation in the delay time for peak 2, consistent with expectations for cascade fluorescence. The discrepancy between the observed delay (∼150 ns) and the predicted delay for cascade fluorescence (174 ns for an excitation FWHM of 114 ns) can be attributed to the uncertainty in the degree of overlap between excitation pulses.

Similar data for the time delay of emission from the spherical trap (triangles) are also shown in Figure 38. A fit (solid line) establishes that the emission exhibits a N^{-1} dependence, indicating superfluorescent decay. The emission delay for the spherical cloud is considerably longer than for the case of the cigar-shaped cloud (peak 1). We attribute this difference to the fact that for the spherical cloud the value of μ and the atom density are lower than for the cigar-shaped cloud. For spherical atom clouds, we cannot resolve the SF emission from the cascade emission over the entire accessible range of N. The fact that for spherical clouds the SF and cascade emissions blend into one another may explain the fit offset of ∼70 ns for the case of the spherical cloud, apparent in Figure 38.

In future studies in cold atoms, it could be investigated if the expected SF cascade emissions at 5.2, 2.7, and 1.4 μm occur in the presence of incoherent excitation. Detection of time-resolved signals with adequate signal to noise ratio at these wavelengths would constitute the main experimental challenge. Applications of this work could extend to studies of dephasing processes, such as interatomic interactions, in cold atoms. Other applications could relate to Bose-condensed samples that typically have low atom numbers and verification of predicted statistical properties for spherical samples (Prasad & Glauber, 1985).

ACKNOWLEDGMENTS

We acknowledge Alexei Tonyushkin for useful comments on the manuscript.

Work at York University was supported by the institution and the Canada Foundation for Innovation, Ontario Innovation Trust, Natural Sciences and Engineering Research Council of Canada, and Ontario Centres of Excellence.

REFERENCES

Abella, I. D., Kurnit, N. A., & Hartmann, S. R. (1965). Photon echoes. *Physical Review*, *141*, 391.

Allen, L., & Eberly, J. H. (1987). *Optical resonance and two-level atoms*. New York: Dover.

Andersen, M. F., & Sleator, T. (2009). Lattice interferometer for laser-cooled atoms. *Physical Review Letters*, *103*, 070402.

Andrews, M. R., Townsend, C. G., Miesner, H. J., Durfee, D. S., Kurn, D. M., & Ketterle, W. (1997). Observation of interference between two bose condensates. *Science*, *275*, 637–641.
Anthony, J. M., & Sebastian, K. J. (1994). Relativistic corrections to the zeeman effect in hydrogenlike atoms and positronium. *Physical Review A*, *49*, 192.
Arecchi, F. T., & Courtens, E. (1970). Cooperative phenomena in resonant electromagnetic propagation. *Physical Review A*, *2*, 1730.
Arimondo, E., Inguscio, M., & Violino, P. (1977). Experimental determinations of the hyperfine structure in the alkali atoms. *Reviews of Modern Physics*, *49*, 31.
Audi, G., Wapstra, A. H., & Thibault, C. (2003). The ame2003 atomic mass evaluation (ii). tables, graphs and references. *Nuclear Physics A*, *729*, 337.
Bacon, A. M., Zhao, H. Z., Laverty, P. J., Wang, L. J., & Thomas, J. E. (1994). Photon-echo interferometry to measure collision-induced optical phase shifts. *Physical Review A*, *49*, 379–396.
Barger, R. L., Bergquist, J. C., English, T. C., & Glaze, D. J. (1979). Resolution of photon-recoil structure of the 6573-å calcium line in an atomic beam with optical ramsey fringes. *Applied Physics Letters*, *34*, 850.
Barrett, B., Yavin, I., Beattie, S., & Kumarakrishnan, A. (2010). Numerical simulation of a multi-level atom interferometer. *Physical Review A*, *82*, 023625.
Beattie, S., Barrett, B., Chan, I., Mok, C., Yavin, I., & Kumarakrishnan, A. (2009a). Atom interferometric studies of light scattering. *Physical Review A*, *80*, 013618.
Beattie, S., Barrett, B., Chan, I., Mok, C., Yavin, I., & Kumarakrishnan, A. (2009b). Technique for measuring atomic recoil frequency using coherence functions. *Physical Review A*, *79*, 021605(R).
Beattie, S., Barrett, B., Weel, M., Chan, I., Mok, C., Cahn, S. B., et al. (2008). Influence of spontaneous emission on a single-state atom interferometer. *Physical Review A*, *77*, 013610.
Becker, P. C., Fragnito, H. L., Cruz, C. H. B., Fork, R. L., Cunningham, J. E., Henry, J. E., et al. (1988). Femtosecond photon echoes from band-to-band transitions in gaas. *Physical Review Letters*, *61*, 1647.
Bergquist, J. C., Lee, S. A., & Hall, J. L. (1977). Saturated absorption with spatially separated laser fields: observation of optical "ramsey" fringes. *Physical Review Letters*, *38*, 159.
Berman, P. R. (1991). Nonlinear spectroscopy and laser cooling. *Physical Review A*, *43*, 1470.
Berman, P. R. (Ed.), (1997). *Atom interferometry*. San Diego: Academic Press.
Berman, P. R., & Malinovsky, V. S. (2011). *Principles of laser spectroscopy and quantum optics*. Princeton: Princeton University Press.
Berman, P. R., Rogers, G., & Dubetsky, B. (1993). Rate equations between electronic-state manifolds. *Physical Review A*, *48*, 1506.
Blundell, S. A., Johnson, W. R., & Sapirstein, J. (1991). Relativistic all-order calculations of energies and matrix elements in cesium. *Physical Review A*, *43*, 3407.
Bonifacio, R., & Lugiato, L. A. (1975). Cooperative radiation processes in two-level systems: superfluorescence. *Physical Review A*, *11*, 1507.
Bordé, C. J., Salomon, C., Avrillier, S., van Lerberghe, A., Bréant, A., Bassi, D., et al. (1984). Optical ramsey fringes with traveling waves. *Physical Review A*, *30*, 1836.
Bowden, C. M., & Sung, C. C. (1978). Cooperative behavior among three-level systems: transient effects of coherent optical pumping. *Physical Review A*, *18*, 1558.
Brownell, J. H., Lu, X., & Hartmann, S. R. (1995). Yoked superfluorescence. *Physical Review Letters*, *75*, 3265.
Burke, J. H. T., & Sackett, C. A. (2009). Scalable bose-einstein-condensate sagnac interferometer in a linear trap. *Physical Review A*, *80*, 061603.
Cadoret, M., de Mirandes, E., Cladé, P., Guellati-Khélifa, S., Schwob, C., Nez, F., et al. (2008). Combination of bloch oscillations with a ramsey-bordé interferometer: new determination of the fine structure constant. *Physical Review Letters*, *101*, 230801.
Cahn, S. B. (1997). Matter wave interference. Ph.D. thesis, Stony Brook, NY: State University of New York at Stony Brook 11794-3800.
Cahn, S. B., Kumarakrishnan, A., Shim, U., Sleator, T., Berman, P. R., & Dubetsky, B. (1997). Time-domain de broglie wave interferometry. *Physical Review Letters*, *79*, 784.
Campbell, G. K., Leanhardt, A. E., Mun, J., Boyd, M., Streed, E. W., Ketterle, W., et al. (2005). Photon recoil momentum in dispersive media. *Physical Review Letters*, *94*, 170403.

Cataliotti, F. S., Scheunemann, R., Hänsch, T. W., & Weitz, M. (2001). Superresolution of pulsed multiphoton raman transitions. *Physical Review Letters*, *87*, 113601.
Chan, I., Andreyuk, A., Beattie, S., Barrett, B., Mok, C., Weel, M., et al. (2008). Properties of magnetic sublevel coherences for precision measurements. *Physical Review A*, *78*, 033418.
Chapman, M. S., Hammond, T. D., Lenef, A., Schmiedmayer, J., Rubenstein, R. A., Smith, E., et al. (1995). Photon scattering from atoms in an atom interferometer: coherence lost and regained. *Physical Review Letters*, *75*, 3783.
Chen, Y. C., Chiang, K., & Hartmann, S. R. (1980). Spectroscopic and relaxation character of the $^3P_0$-$^3H_4$ transition in LaF_3:Pr^{3+} measured by photon echoes. *Physical Review B*, *21*, 40.
Chiow, S. W., Herrmann, S., Chu, S., & Müller, H. (2009). Noise-immune conjugate large-area atom interferometers. *Physical Review Letters*, *103*, 050402.
Cladé, P., de Mirandes, E., Cadoret, M., Guellati-Khélifa, S., Schwob, C., Nez, F., et al. (2006). Determination of the fine structure constant based on bloch oscillations of ultracold atoms in a vertical optical lattice. *Physical Review Letters*, *96*, 033001.
Cohen-Tannoudji, C., Dupont-Roc, J., & Grynberg, G. (1997). *Photons and atoms*. New York: Wiley-Interscience.
Cohen-Tannoudji, C., Dupont-Roc, J., & Grynberg, G. (1998). *Atom-photon interactions*. New York: Wiley-Interscience.
Cohen-Tannoudji, C., DuPont-Roc, J., Haroche, S., & Laloë, F. (1969). Detection of the static magnetic field produced by the oriented nuclei of optically pumped ^{3}He gas. *Physical Review Letters*, *22*, 758.
Cohen-Tannoudji, C., & Kastler, A. (1966). *Progress in optics* (Vol. V). Amsterdam: Elsevier.
Dicke, R. H. (1954). Coherence in spontaneous radiation processes. *Physical Review*, *93*, 99.
Dubetsky, B. (1997). (private communication).
Dubetsky, B., & Berman, P. R. (1994). Magnetic grating free induction decay and magnetic grating echo. *Laser Physics*, *4*, 1017.
Dubetsky, B., & Berman, P. R. (1997). Ground-state ramsey fringes. *Physical Review A*, *56*, R1091.
Dubetsky, B., & Kasevich, M. A. (2006). Atom interferometer as a selective sensor of rotation or gravity. *Physical Review A*, *74*, 023615.
Durfee, D. S., Shaham, Y. K., & Kasevich, M. A. (2006). Long-term stability of an area-reversible atom-interferometer sagnac gyroscope. *Physical Review Letters*, *97*, 240801.
Durr, S., Nonn, T., & Rempe, G. (1998). Origin of quantum-mechanical complementarity probed by a "which-way" experiment in an atom interferometer. *Nature*, *395*, 33–37.
Dzuba, V. A., Flambaum, V. V., Krafmakher, A. Y., & Sushkov, O. P. (1989). Summation of the high orders of perturbation theory in the correlation correction to the hyperfine structure and to the amplitudes of e1-transitions in the caesium atom. *Physical Letters A*, *142*, 373.
Edmonds, A. (1996). *Angular momentum in quantum mechanics*. San Diego: Princeton University Press.
Fixler, J. B., Foster, G. T., McGuirk, J. M., & Kasevich, M. A. (2007). Atom interferometer measurement of the newtonian constant of gravity. *Science*, *315*, 74.
Flusber, A., Mossberg, T., & Hartmann, S. R. (1978). Excited-state photon-echo relaxation in Na vapor. *Optics Communications*, *24*, 207.
Forber, R. A., Spinelli, L., Thomas, J. E., & Feld, M. S. (1990). Observation of quantum diffractive velocity-changing collisions by use of two-level heavy optical radiators. *Physical Review Letters*, *50*, 331.
Gaubatz, U., Rudecki, P., Schiemann, S., & Bergmann, K. (1990). Population transfer between molecular vibrational levels by stimulated raman scattering with partially overlapping laser fields. A new concept and experimental results. *The Journal of Chemical Physics*, *92*, 5363.
Gibbs, H. M., Vrehen, Q. H. F., & Hikspoors, H. M. J. (1977). Single-pulse superfluorescence in cesium. *Physical Review Letters*, *39*, 547.
Glauber, R. J., & Haake, F. (1976). Superradiant pulses and directed angular momentum states. *Physical Review A*, *13*, 357.
Greiner, M., Mandel, O., Esslinger, T., Hänsch, T. W., & Bloch, I. (2002). Quantum phase transition from a superfluid to a mott insulator in a gas of ultracold atoms. *Nature*, *415*, 39.

Gross, M., Fabrem, C., Pillet, P., & Haroche, S. (1976). Observation of near-infrared dicke superradiance on cascading transitions in atomic sodium. *Physical Review Letters*, *36*, 1035.
Gross, M., & Haroche, S. (1982). Superradiance: an essay on the theory of collective spontaneous emission. *Physics Reports*, *93*, 301.
Grove, T. T., Sanchez-Villicana, V., Duncan, B. C., Malecki, S., & Gould, P. L. (1995). Two-photon two-color diode laser spectroscopy of the Rb $5D_{5/2}$ state. *Physica Scripta*, *52*, 271.
Gupta, S., Dieckmann, K., Hadzibabic, Z., & Pritchard, D. E. (2002). Contrast interferometry using bose-einstein condensates to measure h/m and α. *Physical Review Letters*, *89*, 140401.
Gustavson, T. L., Bouyer, P., & Kasevich, M. A. (1997a). Precision rotation measurements with an atom interferometer gyroscope. *Physical Review Letters*, *78*, 2046.
Gustavson, T. L., Bouyer, P., & Kasevich, M. A. (1997b). Precision rotation measurements with an atom interferometer gyroscope. *Physical Review Letters*, *78*, 2046.
Gustavson, T. L., Landragin, A., & Kasevich, M. A. (2000). Rotation sensing with a dual atom-interferometer sagnac gyroscope. *Classical Quantum Gravity*, *17*, 2385.
Haake, F., King, H., Schröder, G., & Haas, J. (1979). Macroscopic quantum fluctuations in superfluorescence. *Physical Review Letters*, *42*, 1740.
Hackermüller, L., Hornberger, K., Brezger, B., Zeilinger, A., & Arndt, M. (2004). Decoherence of matter waves by thermal emission of radiation. *Nature*, *427*, 711–714.
Hagley, E. W., Deng, L., Kozuma, M., Trippenbach, M., Band, Y. B., Edwards, M., et al. (1999). Measurement of the coherence of a bose-einstein condensate. *Physical Review Letters*, *83*, 3112.
Hahn, E. L. (1950a). Spin echoes. *Physical Review*, *80*, 580.
Hahn, E. L. (1950b). Spin echoes. *Physical Review*, *80*, 580.
Hanneke, D., Fogwell, S., & Gabrielse, G. (2008). New measurement of the electron magnetic moment and the fine structure constant. *Physical Review Letters*, *100*, 120801.
Hughes, K. J., Burke, J. H. T., & Sackett, C. A. (2009). Suspension of atoms using optical pulses, and application to gravimetry. *Physical Review Letters*, *102*, 150403.
Kasevich, M., & Chu, S. (1991). Atomic interferometry using stimulated raman transitions. *Physical Review Letters*, *67*, 181.
Keith, D. W., Schattenburg, M. L., Smith, H. I., & Pritchard, D. E. (1988). Diffraction of atoms by a transmission grating. *Physical Review Letters*, *61*, 1580.
Kokorowski, D. A., Cronin, A. D., Roberts, T. D., & Pritchard, D. E. (2001). From single- to multiple-photon decoherence in an atom interferometer. *Physical Review Letters 86*, 2191.
Kumarakrishnan, A., Cahn, S. B., Shim, U., & Sleator, T. (1998a). Magnetic grating echoes from laser-cooled atoms. *Physical Review A*, *58*, R3387.
Kumarakrishnan, A., Chudasama, S., & Han, X. L. (2005). Collision-induced superfluorescence. *Journal of the Optical Society of America B*, *22*, 1538.
Kumarakrishnan, A., & Han, X. L. (1998). Superfluorescence from optically trapped calcium atoms. *Physical Review A*, *58*, 4153.
Kumarakrishnan, A., Shim, U., Cahn, S. B., & Sleator, T. (1998b). Ground-state grating echoes from rb vapor at room temperature. *Physical Review A*, *58*, 3868.
Lamporesi, G., Bertoldi, A., Cacciapuoti, L., Prevedelli, M., & Tino, G. M. (2008). Determination of the newtonian gravitational constant using atom interferometry. *Physical Review Letters*, *100*, 050801.
Le Gouët, J., Mehlstäubler, T. E., Kim, J., Merlet, S., Clairon, A., Landragin, A., et al. (2008). Limits to the sensitivity of a low noise compact atomic gravimeter. *Applied Physics B*, *92*, 133.
Lvovsky, A. I., Hartmann, S. R., & Moshary, F. (2002). Superfluorescence-stimulated photon echoes. *Physical Review Letters*, *89*, 263602.
Lvovsky, A. L., & Hartmann, S. R. (1999). Omnidirectional superfluorescence. *Physical Review Letters*, *82*, 4420.
Macfarlane, R. M., & Shelby, R. M. (1981). Sub-kilohertz optical linewidths of the $^7F_0 \leftrightarrow {}^5D_0$ transition in Y_2O_3: Eu^{3+}. *Optics Communications*, *39*, 169.
MacGillivray, J. C., & Feld, M. S. (1985). Coherent ringing in superfluorescence. *Physical Review Letters*, *54*, 677.
Maki, J. J., Malcuit, M. S., Raymer, M. G., Boyd, R. W., & Drummond, P. D. (1989). Influence of collisional dephasing processes on superfluorescence. *Physical Review A*, *40*, 5135.

Mandel, L. (1979). Distribution of atomic momentum in resonance fluorescence. *Journal of Optics (Paris)*, *10*, 51.
McAlexander, W. I., Abraham, E. R. I., & Hulet, R. G. (1996). Radiative lifetime of the 2p state of lithium. *Physical Review A*, *54*, R5.
McGuirk, J. M., Foster, G. T., Fixler, J. B., Snadden, M. J., & Kasevich, M. A. (2002). Sensitive absolute-gravity gradiometry using atom interferometry. *Physical Review A*, *65*, 033608.
Moehring, D. L., Blinov, B. B., Gidley, D. W., Kohn, R. N., Madsen, M. J., Sanderson, T. B., et al. (2006). Precision lifetime measurement of a single trapped ion with ultrafast laser pulses. *Physical Review A*, *73*, 023413.
Muller, H., Chiow, S. W., Herrmann, S., & Chu, S. (2008). Atom-interferometry tests of the isotropy of post-newtonian gravity. *Physical Review Letters*, *100*, 031101.
Müller, H., Peters, A., & Chu, S. (2010). A precision measurement of the gravitational redshift by the interference of matter waves. *Nature*, *463*, 926.
Oates, C. W., Vogel, K. R., & Hall, J. L. (1996). High precision linewidth measurement of laser-cooled atoms: resolution of the Na 3p $^2P_{3/2}$ lifetime discrepancy. *Physical Review Letters*, *76*, 2866.
Ovchinnikov, Y. B., Muller, J. H., Doery, M. R., Vredenbregt, E. J. D., Helmerson, K., Rolston, S. L., et al. (1999). Diffraction of a released bose-einstein condensate by a pulsed standing light wave. *Physical Review Letters*, *83*, 284.
Paradis, E., Barrett, B., Kumarakrishnan, A., Zhang, R., & Raithel, G. (2008). Observation of superfluorescent emissions from laser-cooled atoms. *Physical Review A*, *77*, 043419.
Patel, C. K. N., & Slusher, R. E. (1968). Photon echoes in gases. *Physical Review Letters*, *20*, 1087.
Peters, A., Chung, K. Y., & Chu, S. (1999). Measurement of gravitational acceleration by dropping atoms. *Nature*, *400*, 849.
Pfau, T., Spalter, S., Kurtsiefer, C., Ekstrom, C. R., & Mlynek, J. (1994). Loss of spatial coherence by a single spontaneous emission. *Physical Review Letters*, *73*, 1223.
Polder, D., Schuurmans, M. F. H., & Vrehen, Q. H. F. (1979). Superfluorescence: quantum-mechanical derivation of maxwell-bloch description with fluctuating field source. *Physical Review A*, *19*, 1192.
Poli, N., Wang, F., Tarallo, M. G., Alberti, A., Prevedelli, M., & Tino, G. M. (2011). Precision measurement of gravity with cold atoms in an optical lattice and comparison with a classical gravimeter. *Physical Review Letters*, *106*, 038501.
Prasad, S., & Glauber, R. J. (1985). Initiation of superfluorescence in a large sphere. *Physical Review A*, *31*, 1583.
Raizen, M. G. (1999). Quantum chaos with cold atoms. *Advances in Atomic, Molecular, and Optical Physics*, *41*, 43.
Raymer, M. G., & Walmsley, I. A. (1990). The quantum coherence properties of stimulated raman scattering. *Progress in Optics*, *28*, 181.
Rehler, N. E., & Eberly, J. H. (1971). Superradiance. *Physical Review A*, *3*, 1735.
Rochester, S. M., & Budker, D. (2001). Atomic polarization visualized. *American Journal of Physics*, *69*, 450.
Rotberg, E., Barrett, B., Beattie, S., Chudasama, S., Weel, M., Chan, I., et al. (2007). Measurement of excited state lifetime using two-pulse photon echoes in rubidium vapor. *Journal of the Optical Society of America B*, *24*, 671.
Ruschewitz, F., Peng, J. L., Hinderthür, H., Schaffrath, N., Sengstock, K., & Ertmer, W. (1998). Sub-kilohertz optical spectroscopy with a time domain atom interferometer. *Physical Review Letters*, *80*, 3173.
Safronova, M. S., Williams, C. J., & Clark, C. W. (2004). Relativistic many-body calculations of electric-dipole matrix elements, lifetimes and polarizabilities in rubidium. *Physical Review A*, *69*, 022509.
Sansonetti, J. E. (2006). Wavelengths, transition probabilities, and energy levels for the spectra of rubidium (rb i through rb xxxvii), volume = 35, pages = 301, note = from NIST Atomic Spectra Database (version 3.1.2), [Online]. Available: http://physics.nist.gov/asd3 [2007, May 7]. National Institute of Standards and Technology, Gaithersburg, MD. Journal of Physical Chemistry Ref. Data.

Schneble, D., Torii, Y., Boyd, M., Steed, E. W., Pritchard, D. E., & Ketterle, W. (2003). The onset of matter-wave amplification in a superradiant bose-einstein condensate. *Science*, *300*, 475.

Schuurmans, M. F. H. (1980). Superfluorescence and amplified spontaneous emission in an inhomogeneously broadened medium. *Optics Communications*, *34*, 185.

Sengstock, K., Sterr, U., Hennig, G., Bettermann, D., Müller, J., & Ertmer, W. (1993). Optical ramsey interferences on laser-cooled and trapped atoms, detected by electron shelving. *Optics Communications*, *103*, 73.

Shim, U., Cahn, S., Kumarakrishnan, A., Sleator, T., & Kim, J. (2002). Optical free induction decay in cold ^{85}Rb atoms. *Japanese Journal of Applied Physics*, 41, 3688.

Shim, U., Cahn, S. B., Kumarakrishnan, A., Sleator, T., & Kim, J. (2005). Optical nutation in cold ^{85}Rb atoms. *Japanese Journal of Applied Physics*, *44*, 168.

Shore, B. W. (1990). *The theory of coherent atomic excitation*. San Diego: Wiley.

Simsarian, J. E., Orozco, L. A., Sprouse, G. D., & Zhao, W. Z. (1998). Lifetime measurements of the 7p levels of atomic francium. *Physical Review A*, *57*, 2448.

Skribanowitz, N., Herman, I. P., MacGillivray, J. C., & Feld, M. S. (1973). Observation of dicke superradiance in optically pumped HF gas. *Physical Review Letters*, *30*, 309.

Sleator, T., Berman, P. R., & Dubetsky, B. (1999). High precision atom interferometry in a microgravity environment. arXiv physics/9905047v1 [physics.atom-ph].

Smiciklas, M., & Shiner, D. (2010). Determination of the fine structure constant using helium fine structure. *Physical Review Letters*, *105*, 123001.

Snadden, M. J., McGuirk, J. M., Bouyer, P., Haritos, K. G., & Kasevich, M. A. (1998). Measurement of the earth's gravity gradient with an atom interferometer-based gravity gradiometer. *Physical Review Letters*, *81*, 971.

Spielman, I. B., Phillips, W. D., & Porto, J. V. (2007). Mott-insulator transition in a two-dimensional atomic bose gas. *Physical Review Letters*, *98*, 080404.

Strekalov, D. V., Turlapov, A., Kumarakrishnan, A., & Sleator, T. (2002). Periodic structures generated in a cloud of cold atoms. *Physical Review A*, *66*, 023601.

Taylor, B. (1994). Determining the avogadro constant from electrical measurements. *Metrologia*, *31*, 181.

Thomas, J. E., & Wang, L. J. (1995). Precision position measurement of moving atoms. *Physics Reports*, *262*, 311.

Tonyushkin, A., & Prentiss, M. (2009). Selective manipulation of degenerate interferometer loops by an atom-optics kicked rotor. *Physical Review A*, *78*, 053625.

Tonyushkin, A., & Prentiss, M. G. (2010). Straight macroscopic magnetic guide for cold atom interferometer. *Journal of Applied Physics*, *108*, 094904.

Tonyushkin, A., Wu, S., & Prentiss, M. (2009a). Demonstration of a multipulse interferometer for quantum kicked-rotor studies. *Physical Review A*, *79*, 051402.

Tonyushkin, A., Wu, S., & Prentiss, M. (2009b). Demonstration of a multipulse interferometer for quantum kicked-rotor studies. *Physical Review A*, *79*, 051402(R).

Turlapov, A., Tonyushkin, A., & Sleator, T. (2005). Talbot-lau effect for atomic de broglie waves manipulated with light. *Physical Review A*, *71*, 043612.

Uys, H., Perreault, J. D., & Cronin, A. D. (2005). Matter-wave decoherence due to a gas environment in an atom interferometer. *Physical Review Letters*, *95*, 150403.

Vali, V., & Shorthill, R. W. (1976). Fiber ring interferometer. *Applied Optics*, *15*, 1099.

Vasilenko, L. S., Matveyenko, I. D., & Rubtsova, N. N. (1985). Study of narrow resonances of coherent radiation in time separated fields in SF_6. *Optics Communications*, *53*, 371.

Volz, U., & Schmoranzer, H. (1996). Precision lifetime measurements on alkali atoms and on helium by beam-gas-laser spectroscopy. *Physica Scripta*, *T65*, 48.

Vorozcovs, A., Weel, M., Beattie, S., Cauchi, S., & Kumarakrishnan, A. (2005). Measurements of temperature scaling laws in an optically dense magneto-optical trap. *Journal of the Optical Society of America B*, *22*, 943.

Vrehen, Q. H. F., Gibbs, H. M., & Bonifacio, R. (1982). *Dissipative systems in quantum optics*. Berlin: Springer-Verlag.

Watson, G. N. (1980). *A treatise on the theory of bessel functions*. Cambridge: Cambridge University Press.

Weel, M., Chan, I., Beattie, S., Kumarakrishnan, A., Gosset, D., & Yavin, I. (2006). Effect of a magnetic field gradient and gravitational acceleration on a time domain grating echo interferometer. *Physical Review A*, *73*, 063624.

Weel, M., & Kumarakrishnan, A. (2003). Observation of ground state ramsey fringes. *Physical Review A*, *67*, 061602(R).
Weiss, D. S., Young, B. C., & Chu, S. (1993). Precision measurement of the photon recoil of an atom using atomic interferometry. *Physical Review Letters*, *70*, 2706.
White, C. W., Hughes, W. M., Hayne, G. S., & Robinson, H. G. (1968). Determination of g-factor ratios for free Rb^{85} and Rb^{87} atoms. *Physical Review*, *174*, 23.
Wicht, A., Hensley, J. M., Sarajlic, E., & Chu, S. (2002). A preliminary measurement of the fine structure constant based on atom interferometry. *Physica Scripta*, *T102*, 82–88.
Wu, S., Su, E., & Prentiss, M. (2007). Demonstration of an area-enclosing guided-atom interferometer for rotation sensing. *Physical Review Letters*, *99*, 173201.
Wu, S., Su, E. J., & Prentiss, M. (2005). Time domain de broglie wave interferometry along a magnetic guide. *The European Physical Journal D*, *35*, 111.
Wu, S., Tonyushkin, A., & Prentiss, M. (2009). Observation of saturation of fidelity decay with an atom interferometer. *Physical Review Letters*, *103*, 034101.
Young, B., Bonomi, D. S., Patterson, T., Roller, F., Tran, T., Vitouchkine, A., et al. (2007). Atom optic inertial and gravitational sensors. In: Proceedings of the International Conference on Laser Science. Optical Society of America, p. LTuH1.
Young, L., Hill III, W. T., Sibener, S. J., Price, S. D., Tanner, C. E., Wieman, C. E., et al. (1994). Precision lifetime measurements of cs $6p\,^2P_{1/2}$ and $6p\,^2P_{3/2}$ levels by single-photon counting. *Physical Review A*, *50*, 2174.
Yu, N., Kohel, J. M., Kellogg, J. R., & Maleki, L. (2006). Development of an atom-interferometer gravity gradiometer for gravity measurement from space. *Applied Physics B*, *84*, 647.

This page intentionally left blank

CHAPTER 4

Interaction between Atomic Ensembles and Optical Resonators: Classical Description

Haruka Tanji-Suzuki[a,b], **Ian D. Leroux**[a], **Monika H. Schleier-Smith**[a], **Marko Cetina**[a], **Andrew T. Grier**[a], **Jonathan Simon**[b], and **Vladan Vuletić**[a]

[a]*Department of Physics, MIT-Harvard Center for Ultracold Atoms, and Research Laboratory of Electronics, Massachusetts Institute of Technology, Cambridge, MA 02139, USA*
[b]*Department of Physics, Harvard University, Cambridge, MA 02138, USA*

Contents

Advances in Atomic, Molecular, and Optical Physics, Volume 60, Copyright © 2011 Elsevier Inc.
ISSN 1049-250X, DOI: 10.1016/B978-0-12-385508-4.00004-8.

Abstract

Many effects in the interaction between atoms and a cavity that are usually described in quantum mechanical terms (cavity quantum electrodynamics, cavity QED) can be understood and quantitatively analyzed within a classical framework. We adopt such a classical picture of a radiating dipole oscillator to derive explicit expressions for the coupling of single atoms and atomic ensembles to Gaussian modes in free space and in an optical resonator. The cooperativity parameter of cavity QED is shown to play a central role and is given a geometrical interpretation. The classical analysis yields transparent, intuitive results that are useful for analyzing applications of cavity QED such as atom detection and counting, cavity cooling, cavity spin squeezing, cavity spin optomechanics, or phase transitions associated with the self-organization of the ensemble-light system.

1. INTRODUCTION

The interaction of atoms with a single electromagnetic mode is a problem of significant fundamental interest. The quantum mechanical system consisting of a single atom interacting with a single mode can be analyzed exactly in the rotating wave approximation for an arbitrary coupling constant. This famous Jaynes–Cummings model (Jaynes & Cummings, 1963) of cavity quantum electrodynamics (cavity QED) gives rise to many interesting effects such as Rabi oscillations with a single photon (vacuum Rabi oscillations), collapse and revival effects due to a dependence of the Rabi frequency on photon number, or optical nonlinearity at the single-photon level. Many of these effects have been observed in pioneering experiments

both in the microwave domain by Haroche and coworkers (Goy et al., 1983; Haroche & Raimond, 1985; Kaluzny et al., 1983) and Walther and coworkers (Meschede et al., 1985), and in the optical domain by Kimble (Birnbaum et al., 2005; Boozer et al., 2007; Kimble, 1998; McKeever et al., 2004b; Rempe et al., 1991; Thompson et al., 1992; Turchette et al., 1995), Rempe (Kuhn et al., 2002; Legero et al., 2004; Maunz et al., 2004; Nußmann et al., 2005b; Pinkse et al., 2000; Schuster et al., 2008; Wilk et al., 2007), and others (Brennecke et al., 2007; Colombe et al., 2007; Heinzen et al., 1987; Heinzen & Feld, 1987). Studies have concentrated on fundamental aspects of the system such as the vacuum Rabi splitting (Agarwal, 1984; Boca et al., 2004; Brennecke et al., 2007; Colombe et al., 2007; Kaluzny et al., 1983; Raizen et al., 1989; Thompson et al., 1992; Zhu et al., 1990), nonclassical light generation (Gupta et al., 2007; Kuhn et al., 2002; Legero et al., 2004; McKeever et al., 2004a; Schuster et al., 2008; Simon et al., 2007b; Thompson et al., 2006; Wilk et al., 2007), single-atom maser (Meschede et al., 1985) and laser operation (McKeever et al., 2003a), or superradiance in the case of many atoms (Kaluzny et al., 1983; Raimond et al., 1982). Significant effort has gone toward increasing the single-photon Rabi frequency $2g$ (also called the vacuum Rabi frequency), at which a single quantum of excitation is exchanged between the atom and the cavity, above the dissipation rates κ and Γ at which the photon is lost from the cavity or from the atom by emission into free space, respectively. In this so-called strong-coupling limit of cavity QED, namely $2g \gg (\kappa, \Gamma)$, the coherent, reversible light–atom interaction dominates over dissipative processes. This should enable full quantum mechanical control over the atoms and photons, e.g., in the form of quantum gates between two atoms (Pellizzari et al., 1995) or quantum networks (Cirac et al., 1997).

Besides being of fundamental interest, cavity QED enables an increasing number of applications related to atom detection (Bochmann et al., 2010; Gehr et al., 2010; Heine et al., 2009; Hope & Close, 2004, 2005; Kohnen et al., 2011; McKeever et al., 2004b; Poldy et al., 2008; Puppe et al., 2007; Teper et al., 2006; Terraciano et al., 2009; Trupke et al., 2007; Wilzbach et al., 2009) and manipulation—be it of the spatial degrees of freedom (Black et al., 2005a; Hood et al., 2000; Münstermann et al., 1999; Murch et al., 2008; Nußmann et al., 2005a) such as in cavity cooling (Boozer et al., 2006; Cirac et al., 1993, 1995; Domokos et al., 2001; Gangl & Ritsch, 1999, 2000; Hechenblaikner et al., 1998; Horak et al., 1997; Leibrandt et al., 2009; Lev et al., 2008; Maunz et al., 2004; McKeever et al., 2003b; Morigi et al., 2007; Mossberg et al., 1991; Murr, 2006; Nußmann et al., 2005b; Vuletić & Chu, 2000), feedback cooling (Fischer et al., 2002; Koch et al., 2010; Vuletić et al., 2007), self-organization and the superradiant phase transition (Baumann et al., 2010; Black et al., 2003, 2005a), or of the spin degrees of freedom such as in spin squeezing (Appel et al., 2009; Dantan et al., 2003a,b; Genes et al., 2003; Kuzmich et al., 1997, 1998, 2000; Leroux et al.,

2010a,b; Schleier-Smith et al., 2010a,b), spin optomechanics (Brahms & Stamper-Kurn, 2010), preparation of nonclassical atomic states (Mekhov et al., 2007; Mekhov & Ritsch, 2009a,b; Simon et al., 2007a), or cavity-based quantum memories for light (Black et al., 2005b; Simon et al., 2007a,b; Tanji et al., 2009; Thompson et al., 2006).

Many of the above applications make use of atomic ensembles rather than single atoms, in which case the complete quantum description of the ensemble–cavity interaction is nontrivial as it in general involves a very large Hilbert space (Baragiola et al., 2010). (Under assumptions of symmetry, exact solutions are possible in a much smaller Hilbert space, see Tavis and Cummings 1968.) On the other hand, many of these applications operate via coherent (Rayleigh) scattering, whereas incoherent spontaneous emission (Cohen-Tannoudji et al., 1998; Mollow, 1969) is either negligible or an undesired process whose effect can be estimated by means other than solving the problem exactly. In such circumstances, the full quantum description may not be necessary, and a simpler classical picture may yield the correct results and provide a complementary or more intuitive understanding. An example of this is cavity cooling, where the full quantum mechanical description yields complex dynamics (Horak et al., 1997; Zippilli & Morigi, 2005), but in the relevant limit of interest for applications (large light-atom detuning and low saturation of the atomic transition), a classical model yields simple and correct results that can be understood in terms of cavity-enhanced coherent scattering (Vuletić & Chu, 2000; Vuletić et al., 2001).

Furthermore, it has become increasingly clear that features which were originally assigned a quantum mechanical origin, such as the vacuum Rabi splitting (Agarwal, 1984; Cohen-Tannoudji et al., 1998), can be in fact described within a classical framework, and arise simply from a combination of linear atomic absorption and dispersion (Dowling, 1993; Zhu et al., 1990). This is not surprising as in the limit of low saturation the atom can be modeled as a harmonic oscillator, and the classical theory of coupled harmonic oscillators (a cavity mode and a weakly driven atom) gives the same mode structure as the quantum-mechanical treatment. It can then be advantageous to use the classical theory—within its limits of applicability—to describe, and develop an intuition for, more complex problems involving atomic ensembles.

The classical description also leads to some results that are of course contained in the quantum theory, but that are not necessarily obvious within that formalism. For instance, the quantum description in terms of a vacuum Rabi frequency (that perhaps should be more appropriately called single-photon Rabi frequency) that scales inversely with the square root of the mode volume (Cohen-Tannoudji et al., 1998) may lead one to believe that strong-coupling and coherent atom–light interaction require

a small cavity volume. However, the classical description immediately reveals that the mode area plays a more fundamental role than the mode volume. As discussed below, this feature is captured in the so-called cooperativity parameter $\eta = 4g^2/(\kappa\Gamma)$ of cavity QED (Kimble, 1998), that, as we shall show, is a geometric parameter that characterizes the absorptive, emissive, or dispersive coupling of an atom to the cavity mode.

In this work, we will analyze the atom–cavity interaction from the classical point of view and derive analytical formulas that remain valid quantum mechanically. We shall see that in this description the dimensionless cooperativity parameter η governs all aspects of the atom–cavity interaction. A strong-coupling limit can be defined by the condition $\eta > 1$, corresponding to a situation where we can no longer assume the atomic dipole to be driven by the unperturbed incident field, but have to self-consistently include the field emitted by the atom, and circulating in the cavity, into the total driving field. Thus for $\eta > 1$, the backaction of the cavity field generated by the oscillating atomic dipole on that same dipole is not negligible. This leads, among other effects, to the interesting result known from a quantum mechanical analysis (Alsing et al., 1992) that the emission by the atom into free space can be substantially modified by a cavity, even if the cavity subtends only a small solid angle.

For equal cavity and atomic line widths, $\kappa = \Gamma$, the thus defined classical strong-coupling condition $\eta > 1$ is equivalent to the standard strong-coupling condition $2g > (\kappa, \Gamma)$ of cavity QED, but it is less stringent than the latter for $\kappa > \Gamma$ or $\kappa < \Gamma$. (The classical strong-coupling condition $\eta > 1$ corresponds to the single-photon Rabi frequency $2g$ being larger than the geometric mean of the atomic and cavity line widths.) In general, the system can be parameterized in terms of two dimensionless parameters, namely the ratios g/κ and g/Γ in the cavity QED description, or, in the classical description, the cooperativity parameter η, and the line width ratio κ/Γ. The cavity QED strong-coupling condition $2g > (\kappa, \Gamma)$ corresponds to a normal-mode splitting that is much larger than the line widths of the normal modes. In contrast, the less stringent classical condition $\eta > 1$ also includes situations where the normal modes overlap within their line widths, but destructive interference between them arises in a manner that is closely related to electromagnetically induced transparency (Harris, 1989, 1997; Litvak & Tokman, 2002).

In most cases, the coherent emission into the cavity will be associated with the desired "signal" process, whereas the emission into free space constitutes a "noise" process that leads to atomic decoherence, motional heating, etc. To understand the fundamental limitations to processes like cavity cooling, spin squeezing, spin optomechanics, or phase transitions due to self-organization, we must therefore quantify both the emission into the cavity mode of interest, and into all other (free-space) modes.

In the following, we will usually express the results as power ratios that can be given simple physical or geometrical interpretations.

In the following, we always consider two different scenarios: in the "scattering" or "driven-atom" setup, radiation is coupled into the mode of interest $\mathcal{M}$ via the atom that is driven by an external field incident from the side. In the "absorption/dispersion" or "driven-mode" setup, the mode of interest $\mathcal{M}$ is excited directly, and the atom modifies the field in $\mathcal{M}$ via forward scattering, while also emitting radiation into all other modes. We will analyze both scenarios for $\mathcal{M}$ being either a free-space mode or a cavity mode.

2. INTERACTION BETWEEN A SINGLE ATOM AND A FREE-SPACE MODE

In the following, we analyze the interaction of a single atom, described as a point-like classical dipole oscillator, with a single transverse electromagnetic mode in free space. We will consider a Gaussian TEM_{00} mode with a waist w that is at least somewhat larger than an optical wavelength λ, such that the paraxial approximation for the propagation of Gaussian beams (Kogelnik & Li, 1966; Siegman, 1986) remains valid. The classical-oscillator description of the atom agrees with the quantum mechanical treatment in the limit where the saturation of the atomic transition is negligible, be it due to low beam intensity, or large detuning of the light from atomic resonances (Cohen-Tannoudji et al., 1998; Mollow, 1969). The assumption that the atom is point-like, i.e., that it can be localized to a small fraction of an optical wavelength implies that the atom's kinetic temperature is well above the recoil limit.

The electric-field component $\tilde{\mathbf{E}}(t) = \frac{1}{2}\hat{\mathbf{e}}Ee^{-i\omega t} + c.c.$ of a linearly polarized light field oscillating at frequency $\omega = ck$ induces a proportional atomic dipole moment $\tilde{\mathbf{p}} = \frac{1}{2}\hat{\mathbf{e}}pe^{-i\omega t} + c.c.$ that is oscillating at the same frequency. Here, $\hat{\mathbf{e}}$ is the unit polarization vector, and $p = \alpha E$ is the amplitude of the induced dipole moment. The complex polarizability α is given by (see, e.g., Grimm et al., 2000; Milonni et al., 2008)

$$\alpha = 6\pi\varepsilon_0 c^3 \frac{\Gamma/\omega_0^2}{\omega_0^2 - \omega^2 - i(\omega^3/\omega_0^2)\Gamma}. \tag{1}$$

Here, $\omega_0 = ck_0 = 2\pi c/\lambda_0$ denotes the atomic resonance frequency and Γ is the line width of the atomic transition. Equation (1) is valid both classically and quantum mechanically. In the classical description, the oscillating electron is damped due to the emission of radiation. In the quantum mechanical description, $\Gamma = k_0^3|\mu|^2/(3\pi\epsilon_0\hbar)$ is the spontaneous population decay rate of the atomic excited state, given in terms of the dipole

matrix element $\mu \equiv \langle e|\mu|g\rangle$ between a ground state $|g\rangle$ and an excited state $|e\rangle$. Due to the validity of Equation (1) in both the classical and quantum domains, the classical results we will derive below agree with the semiclassical results derived from quantum theory in the limit of low saturation of the atomic transition.

The polarizability α obeys the relation

$$|\alpha|^2 = \frac{6\pi\varepsilon_0}{k^3}\mathrm{Im}(\alpha), \tag{2}$$

which will be useful in relating the total scattered power, proportional to $|\alpha|^2$, to the absorption, given by the out-of-phase component of the forward-scattered field that is proportional to $\mathrm{Im}(\alpha)$ (see Section 2.2). Equation (2) ensures that the optical theorem is satisfied, i.e., that the rate at which energy is absorbed from the incident mode by the atom equals the power scattered into other field modes (Berman et al., 2006).

The oscillating dipole emits a radiation field whose amplitude at large distance $R \gg \lambda$ from the atom is given by (Jackson, 1998)

$$E_{\mathrm{rad}}(R,\theta) = \frac{k^2 \sin\theta}{4\pi\varepsilon_0}\frac{\mathrm{e}^{ikR}}{R}\alpha E, \tag{3}$$

where θ is the angle between the polarization $\hat{\mathbf{e}}$ of the driving field and the direction of observation.

A fraction of the radiated power can be collected in some mode of interest. The field radiated into the same mode as the driving field can interfere with the latter, resulting in attenuation of the driving field, i.e., absorption, and a phase shift of the total field, i.e., dispersion. In the following sections, we derive simple expressions for these quantities, and interpret them geometrically.

2.1 Scattering into a Free-Space Mode: Emission

We consider a traveling-wave TEM_{00} Gaussian mode $\mathcal{M}$ of wave number $k = 2\pi/\lambda = \omega/c$, waist w, and Rayleigh range $z_R = \pi w^2/\lambda$. The atom is located on the axis of that mode at the waist, as shown in Figure 1, and driven by an external field with amplitude E propagating in some other direction. The driving field polarization is assumed to be linear and perpendicular to the direction of propagation of the mode $\mathcal{M}$. We would like to know what fraction of the total power scattered by the driven atom is emitted into $\mathcal{M}$. This question can be answered by decomposing the dipole emission pattern into Hermite-Gaussian modes in a tangential plane located at distance $z = R \gg z_R$ in the far field (see Figure 1).

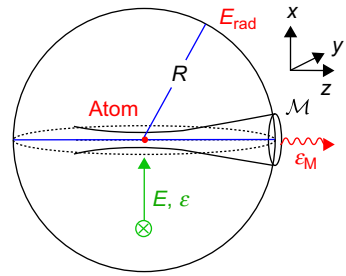

Figure 1 Scattering of radiation by a weakly driven atom. The incident field $\mathcal{E}$ polarized perpendicular to the TEM_{00} mode of interest $\mathcal{M}$ and drives an atomic dipole oscillator that emits an electromagnetic field which is given by E_{rad} at large distance R from the atom. For the analysis, we choose R much larger than the Rayleigh range z_R of $\mathcal{M}$.

The normalized mode function $e_{\mathcal{M}}(\rho, z)$ can be found in Siegman (1986); in the tangential plane at $z \gg z_R$, it is approximately

$$e_{\mathcal{M}}(\rho, z) \approx \left(\frac{2}{\pi \tilde{w}^2}\right)^{1/2} \exp\left(-\frac{\rho^2}{\tilde{w}^2} + ikz + ik\frac{\rho^2}{2z} - i\frac{\pi}{2}\right). \tag{4}$$

Here, the first term in the exponent accounts for the intensity profile of the expanding Gaussian beam with waist $\tilde{w}(z) = w\sqrt{1 + (z/z_R)^2} \approx wz/z_R$, the second and third term describe the beam wave fronts, and the last term is the Gouy phase shift of $\pi/2$ at $z \gg z_R$.

In general, the electric field amplitude $E_{\mathcal{M}}(\rho, z)$ in mode $\mathcal{M}$ at position (ρ, z) can be written as $E_{\mathcal{M}}(\rho, z) = e_{\mathcal{M}}(\rho, z)\mathcal{E}_{\mathcal{M}}/\sqrt{\varepsilon_0 c}$ in terms of a position-independent quantity $\mathcal{E}_{\mathcal{M}}$ that we will refer to as the mode amplitude. $\mathcal{E}_{\mathcal{M}}$ is related to the total power $P_{\mathcal{M}}$ in mode $\mathcal{M}$ via $P_{\mathcal{M}} = |\mathcal{E}_{\mathcal{M}}|^2/2$, and to the electric field amplitude at the waist $E_{\mathcal{M}}(0, 0)$ via $\mathcal{E}_{\mathcal{M}} = E_{\mathcal{M}}(0, 0)\sqrt{\varepsilon_0 cA}$, where $A = \pi w^2/2$ is the effective mode area. In the following, it will be useful to similarly formally define a mode amplitude for the field E driving the atom as $\mathcal{E} = \sqrt{\varepsilon_0 cA}E$, even if the driving field is in some arbitrary mode. As the induced dipole depends only on the electric field E at the atom's position, all atomic absorption and emission can be expressed in terms of the rescaled quantity $\mathcal{E}$.

The mode $\mathcal{M}$ with $w \gg \lambda$ subtends only a small far-field angle $\lambda/(\pi w) \ll 1$ (Siegman, 1986), such that the spatial dependence of the emitted dipole field E_{rad} [Equation (3)], over the region occupied by $\mathcal{M}$ can be approximated as $\sin\theta \approx 1$ and $e^{ikR}/R \approx e^{ikz + ik\rho^2/(2z)}/z$. Then the mode amplitude $\mathcal{E}_{\mathcal{M}}$ arising from the radiated field can be calculated easily as the projection $\mathcal{E}_{\mathcal{M}} = \sqrt{\varepsilon_0 c}\int e^*_{\mathcal{M}} E_{rad} 2\pi\rho d\rho$ in the plane at $z \gg z_R$. This yields the

simple result

$$\mathcal{E}_{\mathcal{M}} = i\beta\mathcal{E} \tag{5}$$

in terms of a dimensionless parameter

$$\beta = \frac{k}{\pi w^2}\frac{\alpha}{\varepsilon_0} \tag{6}$$

that characterizes the coupling of the incident field $\mathcal{E}$ to mode $\mathcal{M}$ via the atom with polarizability α at the drive frequency ck. From Equation (2), it follows that β obeys the optical-theorem relation

$$|\beta|^2 = \frac{6}{k^2 w^2}\mathrm{Im}(\beta) = \eta_{\mathrm{fs}}\mathrm{Im}(\beta), \tag{7}$$

where we have defined another dimensionless parameter, which we will call the single-atom cooperativity in free space

$$\eta_{\mathrm{fs}} = \frac{6}{k^2 w^2}. \tag{8}$$

The total scattered power into all directions $P_{4\pi}$ can be calculated by integrating the intensity $I_{\mathrm{rad}} = \varepsilon_0 c|E_{\mathrm{rad}}|^2/2$ of the radiated field [Equation (3)] over the surface of the sphere of radius R. Using Equations (5)–(7), the total emitted power can be expressed as

$$P_{4\pi} = \frac{ck^4}{12\pi\varepsilon_0}|\alpha E|^2 = \mathrm{Im}(\beta)|\mathcal{E}|^2 = \frac{1}{\eta_{\mathrm{fs}}}|\mathcal{E}_{\mathcal{M}}|^2. \tag{9}$$

The power emitted into both directions of mode $\mathcal{M}$ is $2P_{\mathcal{M}} = |\mathcal{E}_{\mathcal{M}}|^2$, and hence the cooperativity η_{fs} is equal to the ratio of (bidirectional) emission into mode $\mathcal{M}$ and free-space emission $P_{4\pi}$,

$$\frac{2P_{\mathcal{M}}}{P_{4\pi}} = \eta_{\mathrm{fs}}, \tag{10}$$

independent of the light frequency or the value of the atomic polarizability. The free-space cooperativity η_{fs} is a purely geometric quantity and can be interpreted as the effective solid angle $\Delta\Omega = 4/(k^2w^2)$ subtended bidirectionally by the mode of interest. An additional factor 3/2 accounts for the directionality of the dipole emission pattern and would be absent if the atomic dipole was driven by unpolarized light. Equation (10) is correct to lowest order in $(kw)^{-2} \ll 1$, and thus valid as long as the mode of interest is not focussed too strongly, i.e., $w \gtrsim \lambda$.

2.2 Scattering from a Free-Space Mode: Absorption

We consider the same mode $\mathcal{M}$ as in the previous Section 2.1, but now take the light to be incident in that mode with power $P_{\text{in}} = |\mathcal{E}|^2/2$, as shown in Figure 2. The power $P_{4\pi}$ scattered by the atom located at the mode waist on the mode axis, as given by Equation (9), by virtue of energy conservation must equal the power P_{abs} absorbed from the driving field. Then the fractional attenuation can be expressed as

$$\frac{P_{\text{abs}}}{P_{\text{in}}} = \frac{P_{4\pi}}{P_{\text{in}}} = \text{Im}(2\beta). \tag{11}$$

Within the rotating wave approximation (RWA), $\Delta \equiv \omega - \omega_0 \ll \omega_0$, the mode-coupling parameter β in terms of the light-atom detuning Δ takes the simple form

$$\beta_{\text{RWA}} = \eta_{\text{fs}} \left(\mathcal{L}_d(\Delta) + i\mathcal{L}_a(\Delta)\right), \tag{12}$$

where $\mathcal{L}_a(\Delta) = \Gamma^2/(\Gamma^2 + 4\Delta^2)$ and $\mathcal{L}_d(\Delta) = -2\Delta\Gamma/(\Gamma^2 + 4\Delta^2)$ are the Lorentzian absorptive and dispersive lineshapes, respectively. Then the fractional attenuation can be written as

$$\left(\frac{P_{4\pi}}{P_{\text{in}}}\right)_{\text{RWA}} = 2\eta_{\text{fs}}\mathcal{L}_a(\Delta). \tag{13}$$

On resonance ($\Delta = 0$), the beam attenuation (single-atom optical depth) equals twice the free-space cooperativity η_{fs}. These results are valid for $w \gtrsim \lambda$, i.e., for $\eta_{\text{fs}} \lesssim 6/(2\pi)^2 \approx 0.2$. Comparison of Equations (10) and (13) reveals that the same geometric parameter η_{fs} governs the fractional emission by the atom into a particular mode, and the resonant fractional absorption from a mode of the same geometry.

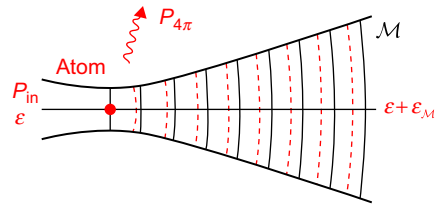

Figure 2 Absorption by an atom placed at the center of a TEM_{00} mode $\mathcal{M}$. The absorption can be calculated from the power $P_{4\pi}$ radiated into free space, or from the field $\mathcal{E}_{\mathcal{M}}$ emitted by the atom in the forward direction that interferes with the incident field $\mathcal{E}$. The solid and dashed lines indicate the wave fronts of a A Gaussian beam and spherical wave, respectively.

The atomic scattering cross section σ is defined as the ratio of scattered power $P_{4\pi}$ and incident intensity $I_{\text{in}} = P_{\text{in}}/A$,

$$\sigma = \frac{P_{4\pi}}{I_{\text{in}}} = \text{Im}(2\beta)A. \tag{14}$$

In the RWA, the scattering cross section according to Equation (12) is given by

$$\sigma = \frac{6\pi}{k_0^2}\mathcal{L}_a(\Delta). \tag{15}$$

The resonant absorption, and hence the cooperativity $\eta_{\text{fs}} = 6/(k^2w^2) \approx 6/(k_0^2w^2)$, can thus also be understood in terms of the ratio of the resonant scattering cross section $\sigma_0 = 6\pi/k_0^2$ and the effective beam area $A = \pi w^2/2$, i.e., $\eta_{\text{fs}} \approx \sigma_0/(2A)$.

It is instructive to derive the atomic absorption from the requirement that the power reduction in the forward direction must arise from the destructive interference between the incident field $\mathcal{E}$ and the field $\mathcal{E}_{\mathcal{M}} = i\beta\mathcal{E}$ [Equation (5)] forward-scattered by the atom into the same mode $\mathcal{M}$. The total mode amplitude in the forward direction is $\mathcal{E} + \mathcal{E}_{\mathcal{M}}$, and the fractional absorption can be calculated as

$$\frac{P_{\text{abs}}}{P_{\text{in}}} = \frac{|\mathcal{E}|^2 - |\mathcal{E} + \mathcal{E}_{\mathcal{M}}|^2}{|\mathcal{E}|^2} \approx -\frac{\mathcal{E}\mathcal{E}_{\mathcal{M}}^* + \mathcal{E}^*\mathcal{E}_{\mathcal{M}}}{|\mathcal{E}|^2} = \text{Im}(2\beta), \tag{16}$$

in agreement with the derivation based on the radiated power $P_{4\pi}$ [Equation (11)]. In Equation (16), we have neglected the term $|\mathcal{E}_{\mathcal{M}}|^2$ that is smaller by a factor $(kw)^{-2} \ll 1$.

Note that the polarizability α on resonance is purely imaginary. Therefore, from the expression for the radiated field E_{rad} [Equation (3)], it would appear that the forward-scattered field on resonance is $\pi/2$ out of phase with the incident field, and thus cannot cancel the latter. However, we must keep in mind that the field E_{rad} in Equation (3) is a radial wave, whereas the input field is a Gaussian mode. To understand the implication of this, we can decompose the radial wave into Gaussian modes, or equivalently, consider the relative phase in the far field, where both modes are approximately spherical waves, and therefore interfere directly. In the far field $z \gg z_R$, there is a $\pi/2$ Gouy phase shift of the input field (relative to the driving field at the waist) (Kogelnik & Li, 1966; Siegman, 1986), as obvious from the mode function, Equation (4), and indicated by the wave fronts in Figure 2. This additional phase shift of $\pi/2$ ensures that, on atomic resonance, the forward-scattered field interferes destructively with the input field. The above derivation represents a version of the optical

theorem that states that the total scattered power $P_{4\pi}$ is proportional to the imaginary part of the forward-scattering amplitude (see, e.g., Berman et al., 2006; Jackson, 1998).

2.3 Phase Shift of a Free-Space Mode: Dispersion

In general, the driving field in mode $\mathcal{M}$ not only is attenuated, but also experiences a phase shift in the presence of the atom. This phase shift, corresponding to the atomic index of refraction, can be simply understood as arising from the interference of the out-of-phase component of the field $\mathcal{E}_{\mathcal{M}}$ forward-scattered by the atom with the incident field $\mathcal{E}$ in the same mode (Feynman et al., 1977). Writing the field amplitude in the forward direction using Equation (5) as $\mathcal{E} + \mathcal{E}_{\mathcal{M}} = (1 + i\beta)\mathcal{E} \approx e^{i\beta}\mathcal{E}$, we see that the atom-induced phase shift of the light is

$$\phi = \mathrm{Re}(\beta). \tag{17}$$

In the RWA, the atom-induced phase shift of the incident mode for $\Delta \gg \Gamma$ can be written as

$$\phi_{\mathrm{RWA}} = \eta_{\mathrm{fs}}\mathcal{L}_d(\Delta) \approx -\eta_{\mathrm{fs}}\frac{\Gamma}{2\Delta}. \tag{18}$$

At large detuning $\Delta \gg \Gamma$ from atomic resonance, the real part of the polarizability exceeds the imaginary part by a factor Δ/Γ, so the dispersion dominates the absorption [Equation (12)]. We see that the effect of the atom's index of refraction on the Gaussian mode also scales with the cooperativity η_{fs}.

3. INTERACTION BETWEEN AN ATOMIC ENSEMBLE AND A FREE-SPACE MODE

3.1 Absorption and Dispersion by an Ensemble

For an ensemble of N atoms located on the mode axis, the total absorption cross section equals N times the single-atom cross section, Equation (14), producing Beer's law of exponential attenuation

$$\frac{P_{\mathrm{in}} - P_{\mathrm{abs}}}{P_{\mathrm{in}}} = e^{-\mathrm{Im}(2N\beta)}. \tag{19}$$

The exponential absorption arises as each layer of atoms is driven by a total field that consists of the incident field on the previous layer and the forward scattered field by that previous layer (Feynman et al., 1977). If the

laser is tuned to atomic resonance,

$$\left(\frac{P_{\text{in}} - P_{\text{abs}}}{P_{\text{in}}}\right)_{\omega=\omega_0} = \mathrm{e}^{-2N\eta_{\text{fs}}}, \tag{20}$$

i.e., the resonant ensemble optical depth equals twice the collective cooperativity $N\eta_{\text{fs}}$.

Similarly, the phase shift induced by the ensemble on the light field is just N times the single-atom phase shift $\phi_N = N\phi = \text{Re}(N\beta)$ [see Equation (17)] and at large detuning Δ from atomic resonance, but within the RWA, $\Gamma \ll \Delta \ll \omega_0$, can be written as

$$(\phi_N)_{\text{RWA}} = N\eta_{\text{fs}}\mathcal{L}_d(\Delta) \approx -N\eta_{\text{fs}}\frac{\Gamma}{2\Delta}. \tag{21}$$

Comparing the absorption and dispersion by a single atom to that by an atomic ensemble, we see that the single-atom cooperativity η_{fs}, Equation (8), for the former is replaced by the collective cooperativity $N\eta_{\text{fs}}$ for the latter. The fact that the phase shift experienced by the light at a fixed light-atom detuning is proportional to the atom number and a geometric parameter can be used for dispersive measurements of the atom number or the atomic state (Hope & Close, 2004, 2005; Lodewyck et al., 2009), and for measurement-induced spin squeezing in free space (Appel et al., 2009; Kuzmich et al., 1998).

Neither the absorption nor the dispersion depend (with interferometric sensitivity) on the distribution of atoms although both effects rely on a definite phase relationship between the incident field and the forward-scattered field by the atoms. The reason is the cancelation of the phases of the incident and scattered fields in the forward direction: an atom at position $z_1 > 0$ experiences a drive field whose phase is delayed by kz_1 relative to an atom at $z = 0$, but the phase of the field emitted forward is advanced by the same amount. Therefore, the contributions of all atoms are phase-matched in the forward direction, producing maximum interference, independent of the distribution of atoms along the beam. As we shall now see, this is no longer the case when we consider the scattering into a direction other than the direction of the incident beam: the scattered power in any given direction is strongly influenced by the atomic distribution due to interatomic interference.

3.2 Scattering into a Free-Space Mode by an Ensemble: Cooperative Effects from Spatial Ordering

In the geometry of Figure 1 for scattering from a driving beam into mode $\mathcal{M}$, we assume that the single atom is replaced by N atoms that, for simplicity, are located at positions $\mathbf{r}_j$ sufficiently close to the mode axis

such that they all couple to $\mathcal{M}$ with the same magnitude. We also assume that the scattered field $\mathcal{E}_{\mathcal{M}N}$ in mode $\mathcal{M}$ is small compared with the incident field so that we can take the induced dipoles to be proportional to the incident field $\mathcal{E}$ alone, whose magnitude is assumed to be the same for all atoms (i.e., the sample is optically thin along the incident beam). The phase of the contribution from any atom to the mode amplitude $\mathcal{E}_{\mathcal{M}}$ of the radiated field depends on the atom's position, and we can use Equation (5) to write

$$\mathcal{E}_{\mathcal{M}N} = iNF\beta\mathcal{E} \tag{22}$$

in terms of a collective coupling parameter

$$F = \frac{1}{N}\sum_{j=1}^{N} \mathrm{e}^{i(\mathbf{k}-\mathbf{k}_{\mathcal{M}})\cdot\mathbf{r}_j} \equiv \{\mathrm{e}^{i(\mathbf{k}-\mathbf{k}_{\mathcal{M}})\cdot\mathbf{r}}\}. \tag{23}$$

Here, $\mathbf{k}$ and $\mathbf{k}_{\mathcal{M}}$ are the wave vectors of the incident field and mode $\mathcal{M}$, respectively, and $\{\}$ denotes the average atomic coupling for the given fixed atomic distribution as defined by Equation (23). The power $P_{\mathcal{M}N} = |\mathcal{E}_{\mathcal{M}N}|^2/2$ scattered by the ensemble (unidirectionally) into mode $\mathcal{M}$ relative to the power scattered by a single atom into free space $P_{4\pi} = \mathrm{Im}(\beta)|\mathcal{E}|^2$ [Equation (9)] is then given by

$$\frac{P_{\mathcal{M}N}}{P_{4\pi}} = \frac{1}{2}|F|^2N^2\eta_{\mathrm{fs}}. \tag{24}$$

(Compared with Equation (10), the additional factor $\frac{1}{2}$ appears here because we consider only one direction of $\mathcal{M}$, as in general the factor F will be different for the two directions of propagation.) Due to the phase factors in F, the emission into $\mathcal{M}$ by the ensemble depends on the spatial ordering of the atoms that determines the extent of interference between the fields coherently scattered by different atoms. In particular, $|F|^2$ can take on any value between 0 and 1. The lowest value $|F|^2 = 0$ corresponds to perfect destructive interference between the contributions by different atoms and is, e.g., attained for a perfectly ordered ensemble that contains an integer number $n \geq 2$ of atoms per wavelength. The highest possible value $|F|^2 = 1$ is attained for a periodic lattice of atoms with reciprocal lattice vector $\mathbf{k} - \mathbf{k}_{\mathcal{M}}$ such that the fields emitted by all atoms into $\mathcal{M}$ interfere constructively. This situation corresponds to Bragg scattering and interestingly can arise in a self-organizing manner due to light forces on the atoms generated by the interference pattern between the incident and the scattered fields (Baumann et al., 2010; Black et al., 2003, 2005a; Domokos & Ritsch, 2002; Zippilli et al., 2004). In this situation, the power emitted

into $\mathcal{M}$ scales as N^2, similar to the situation encountered in superradiance (Dicke, 1954).

Finally, in the common situation of a gaseous ensemble, corresponding to a random distribution of atoms, $\langle F \rangle = 0$ and $\langle |F|^2 \rangle = 1/N$, i.e., the phase of the emitted light field is completely random when an ensemble average over different atomic distributions is performed, and the ensemble-averaged emitted power is proportional to the atom number N. The fact that, for a random distribution of atoms, the emitted power in any given direction is (on average) proportional to the atom number also explains why the usual picture of each atom emitting power independently is valid for gaseous samples, even though in the low-saturation limit all emitted light is coherent, and thus the fields from different atoms interfere. However, we have also seen that the absence of interatomic interference (on average) is just a special, although common, case occurring for disordered ensembles, and that for ordered ensembles both superradiant (emitted power scales as N^2) and subradiant (little emitted power) coherent Rayleigh scattering into a given mode is possible.

We have already noted in Section 3.1 that the absorption from a mode does not depend on the atomic distribution, whereas the emission into a particular mode does. Since the absorbed power must equal the total scattered power by virtue of energy conservation, it follows that cooperative effects in scattering from an (ordered) distribution of atoms correspond merely to a directional redistribution between different free-space modes, and that the total power emitted into free space does not change. In particular, it is not possible to change the scattering cross section per atom by ordering the ensemble. It should be kept in mind, however, that in this argument and in the derivation of the formulas of this section we have assumed that the scattered field in mode $\mathcal{M}$ is much smaller than the driving field ($|\mathcal{E}_{\mathcal{M}N}|^2 \ll |\mathcal{E}|^2$), so that we could ignore the backaction of $\mathcal{E}_{\mathcal{M}N}$ on the atomic dipoles and assume that they are driven by the incident field $\mathcal{E}$ alone. When analyzing the interaction with a cavity mode in the following section, we will drop this restriction, with interesting consequences.

4. INTERACTION BETWEEN A SINGLE ATOM AND A CAVITY MODE

Based on the quantitative understanding of atomic emission into and absorption from a single Gaussian mode in free space, we can now analyze the classical interaction between a single atom and a single mode of an optical resonator. In the microwave domain, the cavity can partly or completely surround the atom, modifying strongly the total emitted power $P_{4\pi}$ (Haroche & Raimond, 1985; Kleppner, 1981). In contrast, the active modes of an optical resonator typically subtend only a very small solid

angle. Since we are concerned with optical transitions, we will assume as in the previous section that the solid angle subtended by the cavity mode is small. One might naïvely expect that in this case the scattering into free space is not affected by the cavity, but as we will see, a cavity supporting a strongly coupled mode can reduce the atomic emission into all free-space modes by acting back on the induced dipole $p = \alpha E$, which depends on the total field E experienced by the atom. This situation arising in a two-level atom driven by two fields is akin to electromagnetically induced transparency (EIT) (Harris, 1997, 1989) occurring in a three-level atom driven by two fields.

We assume that the atom is at rest and ignore light forces and the photon recoil. A stationary atom that is continuously and weakly driven can be treated as a classical dipole since it simply scatters the incoming narrowband radiation elastically without changing the radiation frequency (coherent or elastic Rayleigh scattering) (Cohen-Tannoudji et al., 1998; Mollow, 1969). The driven atom inside the optical resonator can then be treated as a monochromatic source of radiation at the frequency $\omega = ck$ of the driving light.

4.1 Attenuation of a Cavity Mode: Cavity-Enhanced Absorption

We consider a standing-wave resonator of length L with two identical, lossless, partially transmitting mirrors (Figure 3) with amplitude reflection and transmission coefficients r and iq, respectively (r, q real, $r^2 + q^2 = 1$), and $q^2 \ll 1$. The resonator supports a TEM_{00} mode with waist size w (mode $\mathcal{M}$), and the atom is located on the mode axis near the waist at an antinode. $\mathcal{E}_{in} = \sqrt{\varepsilon_0 c A} E_{in}$ is the mode amplitude incident onto the cavity, and $\mathcal{E}_c$ is the mode amplitude of the traveling intracavity field. The mode amplitude leaking into the cavity through the input mirror is $iq\mathcal{E}_{in}$, and the atom at the antinode, driven by a field $\mathcal{E} = 2\mathcal{E}_c$, coherently scatters a field $2\mathcal{E}_{\mathcal{M}} = 4i\beta\mathcal{E}_c$ [see Equation (5)] into the resonator that adds to $\mathcal{E}_c$.

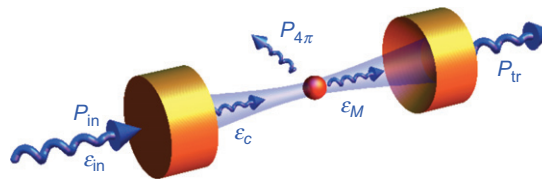

Figure 3 Transmission through an optical standing-wave resonator containing an atom. An incident field $\mathcal{E}_{in}$ produces a steady-state intracavity field with traveling mode amplitude $\mathcal{E}_c$. The atom at an antinode driven by the field $2\mathcal{E}_c$ contributes a field $2\mathcal{E}_{\mathcal{M}}$ per round trip. The transmitted power is P_{tr}, the power scattered by the atom into free space is $P_{4\pi}$.

(The factor of 2 here arises from simultaneous scattering into both cavity directions by the atom at an antinode.) The traveling field $\mathcal{E}_c$ thus experiences reflection at the cavity mirrors, as well as input coupling and atomic source terms, $iq\mathcal{E}_{in}$ and $2\mathcal{E}_{\mathcal{M}}$, respectively, per round trip. The steady-state amplitude $\mathcal{E}_c$ can be determined from the condition that the field after one round trip be unchanged:

$$\mathcal{E}_c = r^2 \mathrm{e}^{2ikL}\mathcal{E}_c + iq\mathcal{E}_{in} + 2\mathcal{E}_{\mathcal{M}}, \tag{25}$$

where e^{2ikL} accounts for the round-trip phase experienced by the circulating light of frequency $\omega = ck$. For not too large detuning $\delta \equiv \omega - \omega_c \ll \pi c/L$ from cavity resonance ω_c, we can approximate $r^2\mathrm{e}^{2ikL} \approx 1 - q^2 + 2iq^2\delta/\kappa$, where $\kappa = q^2c/L$ is the resonator line width (decay rate constant of the energy, see, e.g., Siegman, 1986). AQ:1

Solving for the cavity field, we find

$$\mathcal{E}_c = \frac{i\mathcal{E}_{in}}{q}\left[1 - i\frac{2\delta}{\kappa} - i\frac{4\beta}{q^2}\right]^{-1}. \tag{26}$$

The ratio of transmitted power $P_{tr} = q^2|\mathcal{E}_c|^2/2$ to incident power $P_{\mathrm{in}} = |\mathcal{E}_{in}|^2/2$ is then

$$\frac{P_{tr}}{P_{\mathrm{in}}} = \left[\left(1 + \frac{\mathrm{Im}(4\beta)}{q^2}\right)^2 + \left(\frac{2\delta}{\kappa} + \frac{\mathrm{Re}(4\beta)}{q^2}\right)^2\right]^{-1}. \tag{27}$$

Here, $\beta = k\alpha/(\pi w^2\varepsilon_0)$, Equation (6), containing the atomic polarizability α, is evaluated at the frequency $\omega = ck$ of the incident light. The atom can change the transmission through the cavity not only via absorption $\propto \mathrm{Im}(\beta) \propto \mathrm{Im}(\alpha)$, but also by shifting the cavity resonance via $\mathrm{Re}(\beta) \propto \mathrm{Re}(\alpha)$, i.e., via the atom's index of refraction that introduces a phase shift of the light (see Section 2.3). Both absorptive and dispersive effects can be used for single-atom detection by means of an optical resonator (Bochmann et al., 2010; Gehr et al., 2010; Heine et al., 2009; Hope & Close, 2004, 2005; McKeever et al., 2004b; Poldy et al., 2008; Puppe et al., 2007; Teper et al., 2006; Trupke et al., 2007).

The power $P_{4\pi}$ emitted by the atom into free space is given by Equation (9), with $\mathcal{E}_{\mathcal{M}} = 2i\beta\mathcal{E}_c$. The ratio of emitted to incident power P_{in} can be written as

$$\frac{P_{4\pi}}{P_{\mathrm{in}}} = \frac{\mathrm{Im}(8\beta)}{q^2}\left[\left(1 + \frac{\mathrm{Im}(4\beta)}{q^2}\right)^2 + \left(\frac{2\delta}{\kappa} + \frac{\mathrm{Re}(4\beta)}{q^2}\right)^2\right]^{-1}. \tag{28}$$

In the RWA, the coupling factor β takes the simple form of Equation (12), and we can write

$$\left(\frac{4\beta}{q^2}\right)_{\mathrm{RWA}} = \eta\left(\mathcal{L}_a(\Delta) + i\mathcal{L}_a(\Delta)\right), \tag{29}$$

where we have defined a cavity cooperativity parameter (also called the Purcell factor [Motsch et al., 2010; Purcell, 1946])

$$\eta = \frac{4\eta_{\mathrm{fs}}}{q^2} = \frac{24}{q^2k^2w^2} = \frac{24\mathcal{F}/\pi}{k^2w^2}. \tag{30}$$

Here, $\mathcal{F} = \pi c/(L\kappa) = \pi/q^2$ is the cavity finesse, and $\mathcal{L}_a(\Delta) = \Gamma^2/(\Gamma^2 + 4\Delta^2)$ and $\mathcal{L}_d(\Delta) = -2\Delta\Gamma/(\Gamma^2 + 4\Delta^2)$ are the Lorentzian absorptive and dispersive lineshapes, respectively. The cavity cooperativity can be understood as the free-space cooperativity η_{fs} augmented by the average number of photon round trips $\mathcal{F}/\pi$ inside the cavity, with an additional factor of four accounting for the four times larger intensity at an antinode of a standing wave compared with a traveling mode. Note that the above-defined cooperativity parameter η is twice as large as the cooperativity parameter C_1 most widely used in cavity QED, see, e.g., Horak et al. (2003).

Equation (29) can be substituted into Equation (27) and (28) to write explicit expressions in the RWA for the resonator transmission and free-space emission as a function of cavity cooperativity η, detuning between the incident light and the cavity resonance $\delta = \omega - \omega_c$, and detuning between the incident light and the atomic resonance $\Delta = \omega - \omega_0$:

$$\left(\frac{P_{tr}}{P_{\mathrm{in}}}\right)_{\mathrm{RWA}} = \frac{1}{\left[1 + \eta\mathcal{L}_a(\Delta)\right]^2 + \left[\frac{2\delta}{\kappa} + \eta\mathcal{L}_d(\Delta)\right]^2} \tag{31}$$

and

$$\left(\frac{P_{4\pi}}{P_{\mathrm{in}}}\right)_{\mathrm{RWA}} = \frac{2\eta\mathcal{L}_a(\Delta)}{\left[1 + \eta\mathcal{L}_a(\Delta)\right]^2 + \left[\frac{2\delta}{\kappa} + \eta\mathcal{L}_d(\Delta)\right]^2}. \tag{32}$$

Similar expressions were already derived by Zhu et al. (1990) with a classical formalism as used here, and they agree with the quantum mechanical formulas in the low-saturation limit. Atomic absorption, spectrally characterized by the absorptive Lorentzian $\mathcal{L}_a(\Delta)$ and scaled by the cavity cooperativity parameter η, reduces the intracavity power and the transmission, whereas Lorentzian atomic dispersion $\eta\mathcal{L}_d(\Delta)$ shifts the cavity resonance. In the expression for the free-space emission, Equation (32), the absorptive Lorentzian appears also in the numerator since for a given

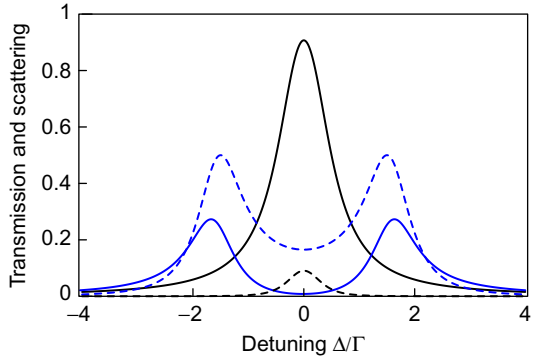

Figure 4 Transmission through the cavity (solid) and free-space scattering (dashed) for a resonant atom-cavity system ($\omega_c = \omega_0$) vs. detuning $\Delta = \delta$ in units of $\kappa = \Gamma$ for a weakly coupled system ($\eta = 0.05$, thin black lines) and for a strongly coupled system ($\eta = 10$, thick grey (blue) lines). Both transmission and scattering are normalized to the power incident on the cavity. The strongly coupled system exhibits vacuum Rabi splitting, i.e., the normal-mode splitting exceeds the normal-mode widths.

intracavity power the atomic free-space emission scales in the same way as the absorption.

The transmission and scattering into free space are plotted as a function of incident frequency ω for fixed cavity frequency in a few representative cases in Figures 4 and 5. For $\eta < 1$ (weak-coupling limit), the atomic absorption broadens the line width and reduces the transmission, whereas the atomic dispersion induces a cavity shift. In the weak-coupling limit, the two eigenmodes of the system, one atom-like, the other cavity-like, maintain their character, each with a little admixture of the other mode. In the opposite strong-coupling limit $\eta > 1$, the two modes are strongly mixed when the cavity resonance coincides with the atomic resonance. Both cavity transmission and atomic emission into free space show a normal-mode splitting, given by $2g = \sqrt{\eta\Gamma\kappa}$, that in the quantum description for $2g > (\Gamma, \kappa)$ is interpreted as the vacuum (or single-photon) Rabi splitting of cavity QED (Cohen-Tannoudji et al., 1998; Kimble, 1998).

In the classical picture, the single-photon Rabi splitting or normal-mode splitting for a resonant atom-cavity system ($\omega_c = \omega_0$, i.e., $\delta = \Delta$) and similar cavity and atomic line widths ($\kappa \sim \Gamma$) can be understood as follows (Figure 4): On resonance for $\eta > 1$, the atomic absorption spoils the cavity finesse, and the intracavity and transmitted power are low. As the laser is detuned away from resonance, the atomic absorption is reduced and the transmission increases until the cavity loss due to atomic emission no longer limits the remaining constructive interference arising from multiple round trips of the light in the detuned cavity. (The round-trip phase also includes the atomic contribution that has the opposite

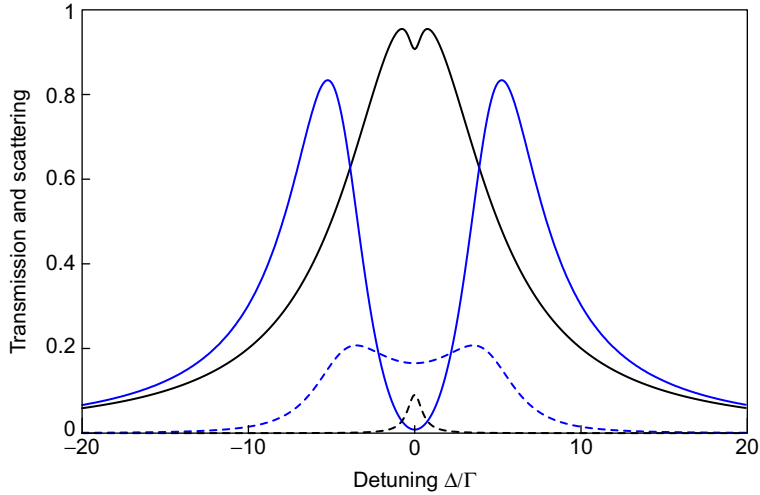

Figure 5 Transmission through the cavity (solid) and free-space scattering (dashed) for a resonant atom-cavity system ($\omega_c = \omega_0$) vs. detuning $\Delta = \delta$ in units of Γ for $\kappa = 10\Gamma$ for a weakly coupled system ($\eta = 0.05$, thin black lines) and for a strongly coupled system ($\eta = 10$, thick grey (blue) lines). Both transmission and scattering are normalized to the power incident on the cavity. In this situation, there is no standard Rabi splitting as the cavity width is larger than the normal-mode splitting, but the transmission drops sharply near $\Delta = 0$, akin to the situation in EIT.

sign as the cavity contribution and tends to decrease the total round-trip phase, and increase the intracavity power.) Further detuning $|\delta|$ then again decreases the intracavity power as the increasing round-trip phase shift decreases the constructive interference inside the cavity. The combination of atomic absorption and dispersion results in two transmission peaks that are symmetric about $\delta = 0$.

If the atomic line width is much narrower that the cavity line width ($\Gamma \ll \kappa$), then the atomic absorption affects the cavity transmission only in a narrow region near atomic resonance (Figure 5). The transmission is substantially reduced for $\eta > 1$, but if the cooperativity parameter is not too large ($\eta < \kappa/\Gamma$) the normal-mode splitting is less than the cavity line width, and there is no standard Rabi splitting. Rather, there is a dip in the transmission and in the free-space scattering.

The ratio of atomic free-space scattering to cavity transmission is given by the simple expression

$$\left(\frac{P_{4\pi}}{P_{tr}}\right)_{\text{RWA}} = 2\eta\mathcal{L}_a(\Delta), \tag{33}$$

and independent of the atom-cavity detuning $\delta - \Delta$. For a resonant system ($\delta = \Delta = 0$), the transmission and free-space scattering are given by

$$\left(\frac{P_{tr}}{P_{\text{in}}}\right)_{\Delta=\delta=0} = \frac{1}{(1+\eta)^2}, \tag{34}$$

and

$$\left(\frac{P_{4\pi}}{P_{\text{in}}}\right)_{\Delta=\delta=0} = \frac{2\eta}{(1+\eta)^2}. \tag{35}$$

Comparison of Equation (35) with the corresponding free-space Equation (11) shows that in the weak-coupling limit $\eta < 1$ the quantity $2\eta = 8\mathcal{F}\eta_{\text{fs}}/\pi$ can be interpreted as the cavity-aided optical depth. In the strong-coupling limit $\eta \gg 1$, both the transmission and the free-space scattering decrease with coupling strength η, but the transmission decreases faster than the free-space scattering. This is closely related to EIT (Harris, 1989, 1997) where the population of the state or mode driven by the probe field (here the resonator, in EIT the atomic excited state) is more suppressed than that of the indirectly driven state or mode (here the free-space modes, in EIT the second atomic ground state).

Equation (34) also shows that in a cavity the transmitted power decreases only quadratically, rather than exponentially, with optical depth $2\eta > 1$. The reason is that the enhanced absorption resulting in $\eta = (4\mathcal{F}/\pi)\eta_{\text{fs}}$ is due to multiple round trips inside the cavity: as the atomic absorption per round trip increases, the cavity finesse and the number of round trips decrease, which acts to convert the exponential absorption into a polynomial one. (The single-pass optical depth is $2\eta_{\text{fs}} = 12/(k^2w^2) < 1$.)

4.2 Frequency Shift of a Cavity Mode: Dispersion

In the limit of sufficiently large detuning from atomic resonance, such that the cavity finesse is not spoiled by atomic absorption ($\eta\mathcal{L}_a(\Delta) < 1$), the dominant effect of the atom on the resonator is a shift of the cavity resonance frequency by atomic dispersion, since the real part of the atomic polarizability falls off more slowly with detuning than the imaginary part. From Equation (31), it follows that the atom-induced cavity resonance shift $\delta\omega_c$, in units of the cavity line width κ, in the RWA is given by

$$\left(\frac{\delta\omega_c}{\kappa}\right)_{\text{RWA}} = -\frac{\eta}{2}\mathcal{L}_d(\Delta) \approx \eta\frac{\Gamma}{4\Delta}, \tag{36}$$

which is proportional to the cavity cooperativity parameter η. The atom-induced cavity shift can be used for atom detection or atomic-state detection (Bochmann et al., 2010; Gehr et al., 2010; Heine et al., 2009; Hope & Close, 2004, 2005; McKeever et al., 2004b; Poldy et al., 2008; Puppe et al., 2007; Teper et al., 2006; Terraciano et al., 2009; Trupke et al., 2007), or, in the case of an atomic ensemble, for generating cavity-mediated infinite-range atomic-state-dependent interactions between atoms enabling spin squeezing (Leroux et al., 2010a,b; Schleier-Smith et al., 2010a).

4.3 Scattering into a Cavity Mode: Cavity-Enhanced Emission

We now consider the scattering of radiation by an atom into a resonator of the same geometry and parameters as in Section 4.1. The atomic dipole is driven by a mode amplitude $\mathcal{E}_{in}$ of frequency $\omega = ck$ from the side, and emits monochromatic radiation of the same frequency into the resonator (Figure 6). In particular, the atom at an antinode contributes a mode amplitude $2\mathcal{E}_{\mathcal{M}}$ per round trip to the mode amplitude $\mathcal{E}_c$ of the circulating field inside the cavity. In steady state, $\mathcal{E}_c$ can be determined from the condition that the field after one round trip, experiencing reflection at the mirrors as well as the atomic source term, be unchanged (Siegman, 1986):

$$\mathcal{E}_c = r^2 \mathrm{e}^{2ikL} \mathcal{E}_c + 2\mathcal{E}_{\mathcal{M}}, \tag{37}$$

which, under the same conditions as in Section 4.1 [not too high mirror transmission $q^2 \ll 1$ and not too large detuning from cavity resonance $\delta \ll c/(2L)$], has a solution of the form

$$\mathcal{E}_c = \frac{2\mathcal{E}_{\mathcal{M}}}{q^2} \frac{1}{1 - 2i\delta/\kappa}. \tag{38}$$

The power emitted by the atom into the cavity is determined by the field leaking through both cavity mirrors, $P_c = q^2 |\mathcal{E}_c|^2$. The power emitted

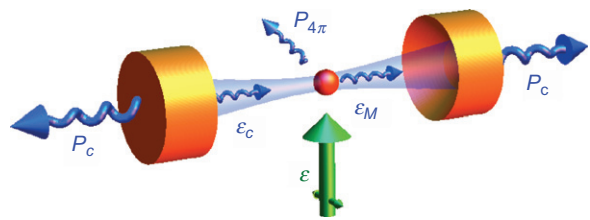

Figure 6 An atom driven by an incident field $\mathcal{E}$ scattering monochromatic radiation into an optical standing-wave resonator. The traveling mode amplitude is $\mathcal{E}_c$, the atom at an antinode adds a mode amplitude $2\mathcal{E}_{\mathcal{M}}$ per round trip. The power leaving the cavity in both directions is P_c, the power scattered by the atom into free space is $P_{4\pi}$.

into free space is $P_{4\pi} = |\mathcal{E}_{\mathcal{M}}|^2/\eta_{\text{fs}}$ [Equation (9)] and using Equation (30) the ratio of cavity-to-free-space emission can be simply written as

$$\frac{P_c}{P_{4\pi}} = \eta \frac{\kappa^2}{\kappa^2 + 4\delta^2}. \tag{39}$$

Compared with the emission into the same free-space mode given by Equation (10), the resonant cavity ($\delta = 0$) enhances the emission by a factor $4/q^2 = 4\mathcal{F}/\pi$. This factor arises from the constructive interference between the images of the atomic dipole formed by the cavity mirrors, or equivalently, from the constructive interference of the atomic emission on successive round trips of the light during the lifetime of the cavity. This frequency-dependent enhancement of coherent scattering that persists even at large detuning from atomic resonance, as observed by Motsch et al. (2010), is the principle behind cavity cooling (Horak et al., 1997; Leibrandt et al., 2009; Lev et al., 2008; Maunz et al., 2004; Morigi et al., 2007; Mossberg et al., 1991; Nußmann et al., 2005b; Vuletić et al., 2001; Vuletić & Chu, 2000; Zippilli & Morigi, 2005).

Note the formal similarity between the result for cavity emission by the driven atom [Equation (39)] and free-space emission when the cavity is driven [Equation (33)]: apart from the factor of 2 difference between absorption and scattering (compare also Equations (10) and (13) for scattering and absorption in free space), the roles of the cavity field and the atomic emission are interchanged in the two cases, and so are the corresponding Lorentzian factors.

Although the ratio between cavity (P_c) and free-space ($P_{4\pi}$) emission is independent of atomic parameters and detuning relative to atomic resonance, the individual terms P_c and $P_{4\pi}$ depend on the atomic polarizability at the frequency of the driving light. To obtain a solution that remains valid in the limit of strong light-atom coupling (large cooperativity $\eta > 1$), we need to take self-consistently into account that the atomic dipole ($\propto \mathcal{E}_{\mathcal{M}}$) is driven not only by the external field $\mathcal{E}_{in}$ but also by the field $\mathcal{E}_c$ of the same frequency circulating inside the cavity. An atom at an antinode experiences a total field $\mathcal{E} = \mathcal{E}_{in} + 2\mathcal{E}_c$, and we write Equation (5) as

$$\mathcal{E}_{\mathcal{M}} = i\beta\,(\mathcal{E}_{in} + 2\mathcal{E}_c). \tag{40}$$

Substituting $\mathcal{E}_{\mathcal{M}}$ into the steady-state condition for the cavity field $\mathcal{E}_c$, Equation (37), and solving for $\mathcal{E}_c$, we find

$$\mathcal{E}_c = \frac{2i\beta\mathcal{E}_{in}}{q^2} \frac{1}{1 - i\frac{2\delta}{\kappa} - i\frac{4\beta}{q^2}}. \tag{41}$$

We can now also find the atomic source term $\mathcal{E}_{\mathcal{M}}$ (driven by both incident and cavity fields) by substituting $\mathcal{E}_c$ into Equation (40) for the

atomic dipole,

$$\mathcal{E}_{\mathcal{M}} = i\beta\mathcal{E}_{in}\frac{1 - i\frac{2\delta}{\kappa}}{1 - i\frac{2\delta}{\kappa} - i\frac{4\beta}{q^2}}. \tag{42}$$

The bidirectional cavity emission rate $P_c = q^2|\mathcal{E}_c|^2$, relative to the power emitted into free space in the absence of the cavity $P_{4\pi}^{(0)} = |\beta\mathcal{E}_{in}|^2/\eta_{\mathrm{fs}}$, Equation (9), is then

$$\frac{P_c}{P_{4\pi}^{(0)}} = \frac{\eta}{\left(1 + \frac{\mathrm{Im}(4\beta)}{q^2}\right)^2 + \left(\frac{2\delta}{\kappa} + \frac{\mathrm{Re}(4\beta)}{q^2}\right)^2}. \tag{43}$$

The emission into free space $P_{4\pi} = |\mathcal{E}_{\mathcal{M}}|^2/\eta_{\mathrm{fs}}$ is similarly modified by the presence of the cavity from its value $P_{4\pi}^{(0)}$ in the absence of the cavity:

$$\frac{P_{4\pi}}{P_{4\pi}^{(0)}} = \frac{1 + \left(\frac{2\delta}{\kappa}\right)^2}{\left(1 + \frac{4\mathrm{Im}(\beta)}{q^2}\right)^2 + \left(\frac{2\delta}{\kappa} + \frac{4\mathrm{Re}(\beta)}{q^2}\right)^2}. \tag{44}$$

It is highly interesting to see that power emitted into free space can be enhanced or reduced by a cavity that subtends only a tiny solid angle, as has been first noted by Alsing et al. (1992) using a quantum mechanical description. The modification of free-space emission is not a saturation effect of the atom, as we have explicitly constructed a classical model that does not include atomic saturation. Rather, it is the backaction of the cavity field driving the atomic dipole in antiphase with the incident field, which reduces the magnitude of the dipole, and thus the amount of emission into free space.

On atomic and cavity resonance ($\delta = \Delta = 0$), the emission into the cavity and into free space are given by the simple expressions

$$\left(\frac{P_c}{P_{4\pi}^{(0)}}\right)_{\delta=\Delta=0} = \frac{\eta}{(1+\eta)^2} \tag{45}$$

and

$$\left(\frac{P_{4\pi}}{P_{4\pi}^{(0)}}\right)_{\delta=\Delta=0} = \frac{1}{(1+\eta)^2}, \tag{46}$$

respectively. Note again the complementarity between these formulas and Equations (34) and (35) for the driven cavity. Although we are considering

here only a two-level atom, these formulas are closely related to electromagnetically induced transparency in a three-level system (Harris, 1989, 1997) as both the incident light and the light inside the cavity couple to the atomic excited state (Field, 1993; Rice & Brecha, 1996). The intracavity field builds up π out of phase with the driving field at the location of the atom, and acts to reduce the emission by the atom, both into the cavity and into free space (Alsing et al., 1992; Heinzen et al., 1987; Zippilli et al., 2004). In the limit of strong coupling $\eta \gg 1$, the intracavity electric field experienced by the atom, $2\mathcal{E}_c \approx -\mathcal{E}_{in}$ is independent of the atomic or cavity properties, and builds up to be (almost) equal in value to the driving field at the position of the atom. This reduces the atomic emission into free space by $(1+\eta)^2$, and the dominant emission process is into the cavity. A cavity with perfectly reflecting mirrors ($\eta \to \infty$) would cancel all resonant free-space emission, even when it subtends only a small solid angle $\Delta\Omega \ll 1$ (Alsing et al., 1992).

In the RWA, we can substitute Equation (29) to write explicit expressions for the cavity and free-space scattering as a function of laser frequency:

$$\frac{P_c}{P_{4\pi}^{(0)}} = \frac{\eta}{\left[1+\eta\mathcal{L}_a(\Delta)\right]^2 + \left[\frac{2\delta}{\kappa} + \eta\mathcal{L}_d(\Delta)\right]^2} \tag{47}$$

and

$$\frac{P_{4\pi}}{P_{4\pi}^{(0)}} = \frac{1+\left(\frac{2\delta}{\kappa}\right)^2}{\left[1+\eta\mathcal{L}_a(\Delta)\right]^2 + \left[\frac{2\delta}{\kappa} + \eta\mathcal{L}_d(\Delta)\right]^2}. \tag{48}$$

Both quantities are plotted in Figure 7 vs. detuning of the incident laser when the cavity resonance is chosen to coincide with the atomic resonance (i.e., $\omega_c = \omega_0$, $\Delta = \delta$). For strong atom-cavity coupling, $\eta \gg 1$, both cavity and free-space emission display two maxima split by $2g = \sqrt{\eta\Gamma\kappa}$, i.e., the system shows the normal-mode splitting usually associated with the vacuum Rabi splitting of cavity QED (Cohen-Tannoudji et al., 1998). We see that this feature appears in linear dispersion theory also when the coupled atom-cavity system is not probed via transmission through the cavity (Section 4.1), but via excitation of the atom.

It is interesting to consider the transmission of the beam from the side, $T = 1 - (P_{4\pi} + P_c)/P_{\text{in}}$, which can be calculated from Equations (47) and (48) and $P_{\text{in}} = |\mathcal{E}_{in}|^2/2$. The side-beam transmission, displayed in Figure 8, for $\kappa < \Gamma$ and $\eta \geq 1$ shows a cavity-induced transmission window within the atomic absorption line. The physical mechanism is the same as in EIT

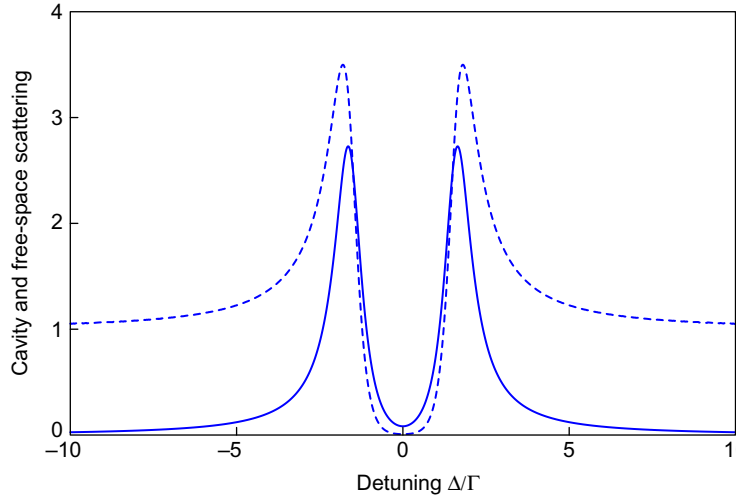

Figure 7 Scattering rate into the cavity $P_c/P_{4\pi}^{(0)}$ (solid line) and into free space $P_{4\pi}/P_{4\pi}^{(0)}$ (dashed line) for a cavity resonant with the atomic transition ($\omega_c = \omega_0$) vs. probe laser detuning $\delta = \Delta$ in units of $\Gamma = \kappa$. The displayed curves are for cooperativity parameter $\eta = 10$. Note the suppression of free-space scattering (and cavity scattering) on resonance, and the enhancement of free-space and cavity scattering off resonance. The strong modification of free-space scattering by a cavity subtending only a very small solid angle arises from the interference between the cavity field and the incident field at the atom's position.

(Harris, 1989, 1997), where the strongly coupled cavity mode replaces the usual classical coupling beam (Field, 1993; Rice & Brecha, 1996).

In summary, we find that the cooperativity parameter η governs the strength of the atom–cavity interaction: the fractional scattering into a resonant cavity, the reduction in cavity transmission, and the dispersive shift of the cavity resonance frequency are all determined by the dimensionless factor η. This factor is the product of the resonant single-pass absorption of the light, as given by the ratio of atomic cross section and beam area, and the average number of photon round trips in the optical resonator, as determined by the cavity finesse $\mathcal{F}$. Since the latter depends only on mirror properties, we find that all resonators with the same mirror reflectivity and the same waist size produce the same strength of atom–light interaction, independent of the length of the cavity. In other words, the atom–light interaction, at least in aspects that can be described classically, depends on mode *area*, rather than mode *volume*. Any volume-dependent effects enter through the ratio κ/Γ of cavity-to-atomic line width, but the classical strong-coupling condition $\eta > 1$ is determined by the mode area and the cavity finesse alone.

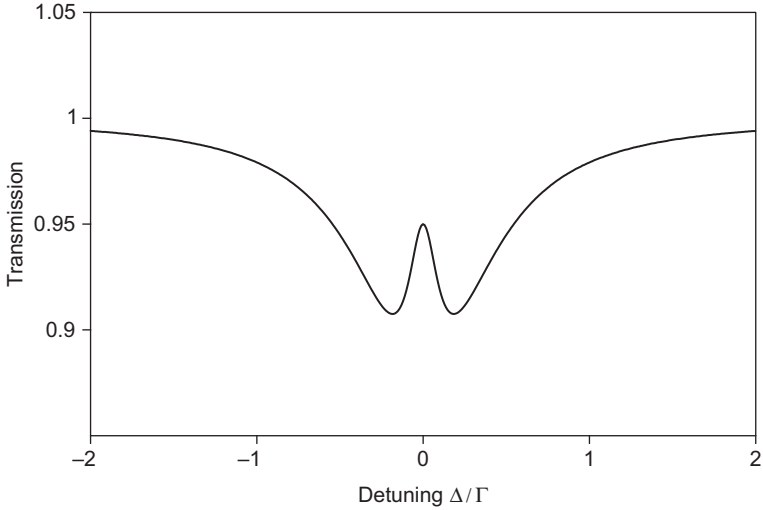

Figure 8 Transmission of the side beam in the "scattering scenario" of Figure 6 in the presence of the cavity for a resonant atom-cavity system ($\omega_0 = \omega_c$) as a function of detuning Δ of the side beam in units of Γ. The cavity line width is chosen much narrower than the atomic line width, $\kappa = \Gamma/10$, and the absorption of the side beam in the absence of the cavity is chosen to be 10%. The origin of the resonant transmission peak is the same as in EIT, with the strongly coupled cavity ($\eta = 1$) replacing the coupling laser in standard EIT.

5. INTERACTION BETWEEN AN ATOMIC ENSEMBLE AND A CAVITY MODE

5.1 Absorption and Dispersion by an Ensemble in a Cavity Mode

As in the free space case, Section 3.2, we consider N atoms located at positions $\mathbf{r}_j$ sufficiently close to the cavity axis such that the radial variation of the coupling may be ignored (see Figure 3). The cavity is driven by an incident field. An atom at an antinode experiences a cavity mode amplitude $2\mathcal{E}_c$ (see Section 4.1), and hence the atomic source term is

$$2\mathcal{E}_{\mathcal{M}} = 4i\beta NH\mathcal{E}_c \tag{49}$$

with the collective coupling parameter

$$H = \frac{1}{N}\sum_{j=1}^{N} \cos^2 kz_j \equiv \{\cos^2 kz\}. \tag{50}$$

With the cavity oriented along the z-axis, the cavity field at position z_j driving the dipole is proportional to $\cos kz_j$, and so is the field emitted by the atom into the cavity mode for a given dipole, hence the $\cos^2 kz_j$ dependence. As in Section 3.2, the curly brackets denote the average for a given and fixed atom distribution. Solving the steady-state condition for the cavity field, Equation (25), with the atomic source term $2\mathcal{E}_{\mathcal{M}}$ from Equation (49), we find for the ratio of transmitted to incident power

$$\frac{P_{tr}}{P_{\text{in}}} = \left[\left(1 + \frac{\text{Im}(4NH\beta)}{q^2}\right)^2 + \left(\frac{2\delta}{\kappa} + \frac{\text{Re}(4NH\beta)}{q^2}\right)^2\right]^{-1}. \tag{51}$$

Since the summands in H are all positive quantities, the result depends only weakly on the ordering of the atoms. A perfectly ordered ensemble with all atoms at antinodes has $H = 1$, while a random distribution of atoms along the cavity standing wave has $\langle H\rangle = \frac{1}{2}$ when averaged over different atomic spatial distributions.

For the total scattering into all free-space modes, there is effectively no interference between different atoms (see Section 3.2), and the total emitted power is obtained by adding the emitted power of all atoms, Equation (9). This yields $P_{4\pi N} = \text{Im}(4\beta)|\mathcal{E}_c|^2 NH$, and

$$\frac{P_{4\pi N}}{P_{\text{in}}} = NH\frac{\text{Im}(8\beta)}{q^2}\left[\left(1 + \frac{\text{Im}(4NH\beta)}{q^2}\right)^2 + \left(\frac{2\delta}{\kappa} + \frac{\text{Re}(4NH\beta)}{q^2}\right)^2\right]^{-1}. \tag{52}$$

In the RWA, we can write for the transmission and free-space scattering

$$\left(\frac{P_{tr}}{P_{\text{in}}}\right)_{\text{RWA}} = \frac{1}{[1 + HN\eta\mathcal{L}_a(\Delta)]^2 + \left[\frac{2\delta}{\kappa} + HN\eta\mathcal{L}_d(\Delta)\right]^2} \tag{53}$$

and

$$\left(\frac{P_{4\pi}}{P_{\text{in}}}\right)_{\text{RWA}} = \frac{2HN\eta\mathcal{L}_a(\Delta)}{[1 + HN\eta\mathcal{L}_a(\Delta)]^2 + \left[\frac{2\delta}{\kappa} + HN\eta\mathcal{L}_d(\Delta)\right]^2}. \tag{54}$$

Comparison of these equations to Equations (31) and (32) shows that for the ensemble the single-atom cooperativity η is replaced by the collective cooperativity $N\eta$, with a proportionality factor between 0 and 1, given by $H = \{\cos^2 kz\}$, that depends on the atomic distribution relative to the cavity standing wave. Similarly, the cavity shift at large detuning from atomic resonance in the RWA, $\omega_0 \gg \Delta \gg \Gamma$, is given by

$$\left(\frac{\delta\omega_c}{\kappa}\right)_{\text{RWA}} = -\frac{1}{2}HN\eta\mathcal{L}_d(\Delta) \approx HN\eta\frac{\Gamma}{4\Delta}. \tag{55}$$

Since $H = \{\cos^2 kz\}$ depends only weakly on the atomic distribution as it varies from a disordered $\left(\langle H\rangle = \frac{1}{2}\right)$ to a superradiant $(H = 1)$ situation, one does not expect the atomic trajectories to influence each other severely (Domokos et al., 2001). The situation is very different if the system is excited from the side, i.e., if the cavity mode is excited via the atomic scattering, as discussed in the next section.

5.2 Scattering by an Ensemble into a Cavity Mode

We consider an ensemble of N atoms at positions $\mathbf{r}_j$ in a cavity oriented along z, as in the previous Section 5.1, but now being driven with a beam from the side traveling along x, as in Figure 6. The ensemble is assumed to be optically thin for the incident field so that all atoms experience the same incident-field magnitude. As each atom is driven both by the incident field (E_{in}) and the cavity mode ($2\mathcal{E}_c$ at an antinode), the atomic source term is

$$2\mathcal{E}_{\mathcal{M}} = 2i\beta N\left(G\mathcal{E}_{in} + 2H\mathcal{E}_c\right) \tag{56}$$

with the collective coupling parameter $H = \{\cos^2 kz\}$ along the cavity given by Equation (50), and the collective coupling parameter for the incident beam being

$$G = \frac{1}{N}\sum_{j=1}^{N} \mathrm{e}^{ikx_j}\cos kz_j \equiv \{\mathrm{e}^{ikx}\cos kz\}. \tag{57}$$

Using the same procedure as in Section 4.3, i.e., inserting the expression for $\mathcal{E}_{\mathcal{M}}$ into the steady-state condition for the cavity field, Equation (37), and solving for $\mathcal{E}_c$, we now have

$$\mathcal{E}_c = \frac{2i\beta NG\mathcal{E}_{in}}{q^2}\frac{1}{1 - i\frac{2\delta}{\kappa} - i\frac{4NH\beta}{q^2}}. \tag{58}$$

This yields for the power scattered into the cavity relative to the power $P_{4\pi}^{(0)}$ scattered by a single atom into free space in the absence of the cavity

$$\frac{P_{cN}}{P_{4\pi}^{(0)}} = \frac{|G|^2N^2\eta}{\left(1 + \frac{\mathrm{Im}(4NH\beta)}{q^2}\right)^2 + \left(\frac{2\delta}{\kappa} + \frac{\mathrm{Re}(4NH\beta)}{q^2}\right)^2}. \tag{59}$$

In the RWA, we can use Equation (12) to write for the scattering into the cavity

$$\frac{P_{cN}}{P_{4\pi}^{(0)}} = \frac{|G|^2N^2\eta}{\left[1 + HN\eta\mathcal{L}_a(\Delta)\right]^2 + \left[\frac{2\delta}{\kappa} + HN\eta\mathcal{L}_d(\Delta)\right]^2}. \tag{60}$$

The atomic distribution along the cavity axis as quantified by $H = \{\cos^2 kz\}$ determines the absorption and dispersion of the resonator, whereas the distribution with respect to both the incident beam and the cavity as quantified by $G = \{e^{ikx} \cos kz\}$ determines the scattering into the resonator. If the atomic detuning Δ is large enough that the absorption can be ignored ($HN\eta\mathcal{L}_a(\Delta) < 1$), then the scattering into the cavity can have super- or subradiant features similar to those discussed for the free-space case in Section 3.2. In particular, for an average over randomly ordered ensembles, we have $\langle|G|^2\rangle = \frac{1}{2N}$, i.e., the scattering into the cavity is proportional to the atom number, whereas for a perfectly ordered ensemble $G = 1$, i.e., the emission into the resonator is superradiant and scales as N^2.

The light field emitted into the cavity can interfere with the incident field to form an optical lattice that is sufficiently strong to influence the motion and spatial distribution of a laser-cooled atomic gas. In this case, self-organization can set in suddenly as a phase transition above a certain incident pumping threshold (Domokos & Ritsch, 2002; Fernández-Vidal et al., 2010; Keeling et al., 2010; Nagy et al., 2010), as observed both for a cold thermal ensemble (Black et al., 2003) and for a Bose–Einstein condensate (Baumann et al., 2010).

6. QUANTUM MECHANICAL EXPRESSION FOR THE COOPERATIVITY PARAMETER

Having concluded our purely classical treatment of atom–cavity interactions, we now show that our definition of the cooperativity parameter is equivalent to the standard cavity QED definition in terms of the quantum mechanical vacuum Rabi frequency $2g$ (Cohen-Tannoudji et al., 1998; Haroche & Raimond, 2006; Kimble, 1998). There, g is given by the atom's dipole coupling $g = \mu E_v/\hbar$ to the RMS vacuum field E_v at an antinode of a cavity mode at the atomic transition frequency $\omega_0 = ck_0$. The vacuum energy in this mode is

$$\frac{1}{2}\hbar\omega_0 = \epsilon_0 E_v^2 V, \tag{61}$$

where $V = \int \exp(-2\rho^2/w^2)\sin^2(k_0 z)2\pi\rho d\rho dz = \pi w^2 L/4$ represents the mode volume. Thus,

$$g = \mu\sqrt{\frac{\omega_0}{2\epsilon_0\hbar V}}. \tag{62}$$

We have already suggested a relation between the vacuum Rabi frequency $2g$ and the normal-mode splitting

$$2g_{\mathrm{cl}} = \sqrt{\eta\kappa\Gamma} \tag{63}$$

appearing in the cavity transmission and atomic emission spectra derived in Section 4.1. That this classically derived normal-mode splitting is indeed identical to the vacuum Rabi frequency in cavity QED can be verified by substituting into Equation (63) the cooperativity $\eta = 24\mathcal{F}/(\pi k_0^2 w^2)$ from Equation (30), the cavity line width $\kappa = \pi c/(L\mathcal{F})$, and the atomic excited-state line width $\Gamma = k_0^3|\mu|^2/(3\pi\epsilon_0\hbar)$. One obtains

$$g_{\mathrm{cl}} = \mu\sqrt{\frac{2\omega_0}{\epsilon_0\hbar\pi w^2 L}} = g. \tag{64}$$

Rearranging Equation (63) thus gives the standard quantum mechanical expression (Kimble, 1998) for the cooperativity parameter as an interaction-to-decay ratio:

$$\eta = \frac{4g^2}{\kappa\Gamma}. \tag{65}$$

Note that this expression can also readily be interpreted as the cavity-to-free-space scattering ratio; in particular, for $\eta < 1$, the rate at which an excited atom emits into the cavity is given by Fermi's Golden Rule as $4g^2/\kappa$.

7. CONCLUSION

We have shown that a variety of fundamental features of the atom–cavity interaction can be described in classical terms, and that the dimensionless cooperativity parameter η that scales with the beam area, rather than the beam volume, plays a central role in the classical description. The weak and strong-coupling regime can be distinguished by the condition $\eta \lessgtr 1$, which quantum mechanically corresponds to a single-photon Rabi frequency that is small or large compared with the geometric mean of the atomic and cavity line widths. In the strong-coupling regime even an optical resonator mode that subtends a small solid angle can increase or substantially decrease the emission into free space by the atom, due to the backaction of the cavity field on the atomic dipole.

The classical model is valid at low saturation of atomic transitions, be it due to low beam intensity or large detuning from atomic resonances. The limit of low saturation of the atomic transition exists even if a single

cavity photon saturates the atomic transition, i.e., for $2g > \Gamma$ or critical photon number less than one in cavity QED terms. In this case, a weak coherent state with less than the critical photon number on average needs to be used to avoid atomic saturation. Then the classical description used here will remain valid.

Most applications of the atom–cavity interaction rely on the narrow-band coherent scattering by the atom that can be correctly described in classical terms. The classical model is easily extended to include the interaction of an atomic ensemble and a cavity mode. In this case, the collective cooperativity parameter depends strongly on the ordering of the ensemble.

It is particularly noteworthy that even the strong-coupling regime of cavity QED, giving rise to a normal-mode or "vacuum Rabi splitting" (Zhu et al., 1990) can be described in classical terms. One may even ask with Dowling (1993) "How much more classical can you get?", a viewpoint that we cannot completely disagree with.

ACKNOWLEDGEMENTS

Over the past years, several colleagues have contributed to a deeper, simpler, and more intuitive understanding of the interaction between atoms and cavities, among them Adam Black, Hilton Chan, Yu-ju Lin, Igor Teper, and James Thompson. Dan Stamper-Kurn was the first to point out to one of us (V.V.) that the cavity-to-free-space scattering ratio introduced in the context of cavity cooling (Vuletić & Chu, 2000) is the same as the cooperativity parameter in cavity QED. We also acknowledge inspiring discussions with Isaac Chuang, Tilman Esslinger, Mikhail Lukin, Jakob Reichel, and Helmut Ritsch. We thank Paul Berman for critical reading of the manuscript and discussions.

We gratefully acknowledge support by the NSF, DARPA, and ARO.

REFERENCES

Agarwal, G. S. (1984). Vacuum-field Rabi splittings in microwave absorption by Rydberg atoms in a cavity. *Physical Review Letters*, *53*, 1732–1734.

Alsing, P. M., Cardimona, D. A., & Carmichael, H. J. (1992). Suppression of fluorescence in a lossless cavity. *Physical Review A*, *45*, 1793–1803.

Appel, J., Windpassinger, P. J., Oblak, D., Hoff, U. B., Kjærgaard, N., & Polzik, E. S. (2009). Mesoscopic atomic entanglement for precision measurements beyond the standard quantum limit. *Proceedings of the National Academy of Sciences*, *106*(27), 10960–10965.

Baragiola, B. Q., Chase, B. A., & Geremia, JM (2010). Collective uncertainty in partially polarized and partially decohered spin-$\frac{1}{2}$ systems. *Physical Review A*, *81*, 032104.

Baumann, K., Guerlin, C., Brennecke, F., & Esslinger, T. (2010). Dicke quantum phase transition with a superfluid gas in an optical cavity. *Nature*, *464*, 1301–1306.

Berman, P. R., Boyd, R. W., & Milonni, P. W. (2006). Polarizability and the optical theorem for a two-level atom with radiative broadening. *Physical Review A*, *74*, 053816.

Birnbaum, K. M., Boca, A., Miller, R., Boozer, A. D., Northup, T. E., & Kimble, H. J. (2005). Photon blockade in an optical cavity with one trapped atom. *Nature*, *436*, 87.

Black, A. T., Chan, H. W., & Vuletić, V. (2003). Observation of collective friction forces due to spatial self-organization of atoms: from Rayleigh to Bragg scattering. *Physical Review Letters*, *91*, 203001.

Black, A. T., Thompson, J. K., & Vuletić, V. (2005a). Collective light forces on atoms in resonators. *Journal of Physics B: Atomic, Molecular and Optical Physics*, *38*, S605–S615.

Black, A. T., Thompson, J. K., & Vuletić, V. (2005b). On-demand superradiant conversion of atomic spin gratings into single photons with high efficiency. *Physical Review Letters*, *95*, 133601.

Boca, A., Miller, R., Birnbaum, K. M., Boozer, A. D., McKeever, J., & Kimble, H. J. (2004). Observation of the vacuum Rabi spectrum for one trapped atom. *Physical Review Letters*, *93*, 233603.

Bochmann, J., Mücke, M., Guhl, C., Ritter, S., Rempe, G., & Moehring, D. L. (2010). Lossless state detection of single neutral atoms. *Physical Review Letters*, *104*, 203601.

Boozer, A. D., Boca, A., Miller, R., Northup, T. E., & Kimble, H. J. (2006). Cooling to the ground state of axial motion for one atom strongly coupled to an optical cavity. *Physical Review Letters*, *97*, 083602.

Boozer, A. D., Boca, A., Miller, R., Northup, T. E., & Kimble, H. J. (2007). Reversible state transfer between light and a single trapped atom. *Physical Review Letters*, *98*, 193601.

Brahms, N., & Stamper-Kurn, D. M. (2010). Spin optodynamics analog of cavity optomechanics. *Physical Review A*, *82*, 041804(R).

Brennecke, F., Donner, T., Ritter, S., Bourdel, T., Köhl, M., & Esslinger, T. (2007). Cavity QED with a Bose-Einstein condensate. *Nature*, *450*, 268–271.

Cirac, J. I., Lewenstein, M., & Zoller, P. (1995). Laser cooling a trapped atom in a cavity: Bad-cavity limit. *Physical Review A*, *51*, 1650.

Cirac, J. I., Parkins, A. S., Blatt, R., & Zoller, P. (1993). Cooling of a trapped ion coupled strongly to a quantized cavity mode. *Optics Communications*, *97*, 353.

Cirac, J. I., Zoller, P., Kimble, H. J., & Mabuchi, H. (1997). Quantum state transfer and entanglement distribution among distant nodes in a quantum network. *Physical Review Letters*, *78*, 3221.

Cohen-Tannoudji, C., Dupont-Roc, J., & Grynberg, G. (1998). *Atom-Photon Interactions: Basic Processes and Applications*. New York, NY: John Wiley & Sons, Inc.

Colombe, Y., Steinmetz, T., Dubois, G., Linke, F., Hunger, D., & Reichel, J. (2007). Strong atom-field coupling for Bose-Einstein condensates in an optical cavity on a chip. *Nature*, *450*, 272.

Dantan, A., Pinard, M., & Berman, P. (2003a). EIT-assisted atomic squeezing. *The European Physical Journal D - Atomic, Molecular, Optical and Plasma Physics*, *27*, 193–199.

Dantan, A., Pinard, M., Josse, V., Nayak, N., & Berman, P. R. (2003b). Atomic spin squeezing in a Λ system. *Physical Review A*, *67*, 045801.

Dicke, R. H. (1954). Coherence in spontaneous radiation processes. *Physical Review*, *93*, 99.

Domokos, P., Horak, P., & Ritsch, H. (2001). Semiclassical theory of cavity-assisted atom cooling. *Journal of Physics B: Atomic, Molecular and Optical Physics*, *34*, 187.

Domokos, P., & Ritsch, H. (2002). Collective cooling and self-organization of atoms in a cavity. *Physical Review Letters*, *89*, 253003.

Dowling, J. P. (1993). Spontaneous emission in cavities: how much more classical can you get? *Foundations of Physics*, *23*, 895.

Fernández-Vidal, S., De Chiara, G., Larson, J., & Morigi, G. (2010). Quantum ground state of self-organized atomic crystals in optical resonators. *Physical Review A*, *81*, 043407.

Feynman, R. P., Leighton, R. B., & Sands, M. (1977). *The Feynman Lectures on Physics* (Vol. 1). Reading, MA: Addison Wesley.

Field, J. E. (1993). Vacuum-Rabi-splitting-induced transparency. *Physical Review A*, *47*, 5064–5067.

Fischer, T., Maunz, P., Pinkse, P. W. H., Puppe, T., & Rempe, G. (2002). Feedback on the motion of a single atom in an optical cavity. *Physical Review Letters*, *88*, 163002.

Gangl, M., & Ritsch, H. (1999). Collective dynamical cooling of neutral particles in a high-Q optical cavity. *Physical Review A*, *61*, 011402(R).

Gangl, M., & Ritsch, H. (2000). Cold atoms in a high-Q ring cavity. *Physical Review A*, *61*, 043405.
Gehr, R., Volz, J., Dubois, G., Steinmetz, T., Colombe, Y., Lev, B. L., et al. (2010). Cavity-based single atom preparation and high-fidelity hyperfine state readout. *Physical Review Letters*, *104*, 203602.
Genes, C., Berman, P. R., & Rojo, A. G. (2003). Spin squeezing via atom-cavity field coupling. *Physical Review A*, *68*, 043809.
Goy, P., Raimond, J. M., Gross, M., & Haroche, S. (1983). Observation of cavity-enhanced single-atom spontaneous emission. *Physical Review Letters*, *50*, 1903.
Grimm, R., Weidemuller, M., & Ovchinnikov, Y. (2000). Optical dipole traps for neutral atoms. *Advances in Atomic, Molecular, and Optical Physics*, *42*, 95–170.
Gupta, S., Moore, K. L., Murch, K. W., & Stamper-Kurn, D. M. (2007). Cavity nonlinear optics at low photon numbers from collective atomic motion. *Physical Review Letters*, *99*, 213601.
Haroche, S., & Raimond, J. M. (1985). Radiative properties of Rydberg states in resonant cavities. *Advances in Atomic and Molecular Physics*, *20*, 347.
Haroche, S., & Raimond, J.-M. (2006). *Exploring the Quantum: Atoms, Cavities, and Photons (Oxford Graduate Texts)*. New York: Oxford University Press.
Harris, S. (1997). Electromagnetically induced transparency. *Physics Today*, *50*(7), 36–42.
Harris, S. E. (1989). Lasers without inversion: Interference of lifetime-broadened resonances. *Physical Review Letters*, *62*, 1033–1036.
Hechenblaikner, G., Gangl, M., Horak, P., & Ritsch, H. (1998). Cooling an atom in a weakly driven high-Q cavity. *Physical Review A*, *58*, 3030.
Heine, D., Wilzbach, M., Raub, T., Hessmo, B., & Schmiedmayer, J. (2009). Integrated atom detector: Single atoms and photon statistics. *Physical Review A*, *79*, 021804(R).
Heinzen, D. J., Childs, J. J., Thomas, J. E., & Feld, M. S. (1987). Enhanced and inhibited visible spontaneous emission by atoms in a confocal resonator. *Physical Review Letters*, *58*, 1320.
Heinzen, D. J., & Feld, M. S. (1987). Vacuum radiative level shift and spontaneous-emission linewidth of an atom in an optical resonator. *Physical Review Letters*, *59*, 2623.
Hood, C. J., Lynn, T. W., Doherty, A. C., Parkins, A. S., & Kimble, H. J. (2000). The atom-cavity microscope: single atoms bound in orbit by single photons. *Science*, *287*, 1447.
Hope, J. J., & Close, J. D. (2004). Limit to minimally destructive optical detection of atoms. *Physical Review Letters*, *93*, 180402.
Hope, J. J., & Close, J. D. (2005). General limit to nondestructive optical detection of atoms. *Physical Review A*, *71*, 043822.
Horak, P., Hechenblaikner, G., Gheri, K. M., Stecher, H., & Ritsch, H. (1997). Cavity-induced atom cooling in the strong coupling regime. *Physical Review Letters*, *79*, 4974.
Horak, P., Klappauf, B. G., Haase, A., Folman, R., Schmiedmayer, J., Domokos, P., et al. (2003). Possibility of single-atom detection on a chip. *Physical Review A*, *67*, 043806.
Jackson, J. D. (1998). *Classical Electrodynamics*. Hoboken, NJ: John Wiley & Sons, Inc.
Jaynes, E. T., & Cummings, F. W. (1963). Comparison of quantum and semiclassical radiation theories with application to the beam maser. *Proceedings of the IEEE*, *51*, 89–109.
Kaluzny, Y., Goy, P., Gross, M., Raimond, J. M., & Haroche, S. (1983). Observation of self-induced Rabi oscillations in two-level atoms excited inside a resonant cavity: The ringing regime of superradiance. *Physical Review Letters*, *51*, 1175.
Keeling, J., Bhaseen, M. J., & Simons, B. D. (2010). Collective dynamics of Bose-Einstein condensates in optical cavities. *Physical Review Letters*, *105*, 043001.
Kimble, H. J. (1998). Strong interactions of single atoms and photons in cavity QED. *Physica Scripta, , T76*, 127–137.
Kleppner, D. (1981). Inhibited spontaneous emission. *Physical Review Letters*, *47*, 233.
Koch, M., Sames, C., Kubanek, A., Apel, M., Balbach, M., Ourjoumtsev, A., et al. (2010). Feedback cooling of a single neutral atom. *Physical Review Letters*, *105*, 173003.
Kogelnik, H., & Li, T. (1966). Laser beams and resonators. *Applied Optics*, *5*, 1550.
Kohnen, M., Succo, M., Petrov, P. G., Nyman, R. A., Trupke, M., & Hinds, E. A. (2011). An array of integrated atom-photon junctions. *Nature Photonics*, *5*, 35–38.
Kuhn, A., Hennrich, M., & Rempe, G. (2002). Deterministic single-photon source for distributed quantum networking. *Physical Review Letters*, *89*, 067901.
Kuzmich, A., Bigelow, N. P., & Mandel, L. (1998). Atomic quantum non-demolition measurements and squeezing. *Europhysics Letters*, *42*(5), 481–486.

Kuzmich, A., Mandel, L., & Bigelow, N. P. (2000). Generation of spin squeezing via continuous quantum nondemolition measurement. *Physical Review Letters*, *85*, 1594.
Kuzmich, A., Mølmer, K., & Polzik, E. S. (1997). Spin squeezing in an ensemble of atoms illuminated with squeezed light. *Physical Review Letters*, *79*, 4782–4785.
Legero, T., Wilk, T., Hennrich, M., Rempe, G., & Kuhn, A. (2004). Quantum beat of two single photons. *Physical Review Letters*, *93*, 070503.
Leibrandt, D. R., Labaziewicz, J., Vuletić, V., & Chuang, I. L. (2009). Cavity sideband cooling of a single trapped ion. *Physical Review Letters*, *103*, 103001.
Leroux, I. D., Schleier-Smith, M. H., & Vuletić, V. (2010a). Implementation of cavity squeezing of a collective atomic spin. *Physical Review Letters*, *104*, 073602.
Leroux, I. D., Schleier-Smith, M. H., & Vuletić, V. (2010b). Orientation-dependent entanglement lifetime in a squeezed atomic clock. *Physical Review Letters*, *104*, 250801.
Lev, B. L., Vukics, A., Hudson, E. R., Sawyer, B. C., Domokos, P., Ritsch, H., et al. (2008). Prospects for the cavity-assisted laser cooling of molecules. *Physical Review A*, *77*, 023402.
Litvak, A. G., & Tokman, M. D. (2002). Electromagnetically induced transparency in ensembles of classical oscillators. *Physical Review Letters*, *88*, 095003.
Lodewyck, J., Westergaard, P. G., & Lemonde, P. (2009). Nondestructive measurement of the transition probability in a Sr optical lattice clock. *Physical Review A*, *79*, 061401(R).
Maunz, P., Puppe, T., Schuster, I., Syassen, N., Pinkse, P. W. H., & Rempe, G. (2004). Cavity cooling of a single atom. *Nature*, *428*, 50.
McKeever, J., Boca, A., Boozer, A. D., Buck, J. R., & Kimble, H. J. (2003a). Experimental realization of a one-atom laser in the regime of strong coupling. *Nature*, *425*, 268–271.
McKeever, J., Boca, A., Boozer, A. D., Miller, R., Buck, J. R., Kuzmich, A., et al. (2004a). Deterministic generation of single photons from one atom trapped in a cavity. *Science, 303*, 1992.
McKeever, J., Buck, J. R., Boozer, A. D., & Kimble, H. J. (2004b). Determination of the number of atoms trapped in an optical cavity. *Physical Review Letters*, *93*, 143601.
McKeever, J., Buck, J. R., Boozer, A. D., Kuzmich, A., Nägerl, H.-C., Stamper-Kurn, D. M., et al. (2003b). State-insensitive cooling and trapping of single atoms in an optical cavity. *Physical Review Letters*, *90*, 133602.
Mekhov, I. B., Maschler, C., & Ritsch, H. (2007). Cavity-enhanced light scattering in optical lattices to probe atomic quantum statistics. *Physical Review Letters*, *98*, 100402.
Mekhov, I. B., & Ritsch, H. (2009a). Quantum nondemolition measurements and state preparation in quantum gases by light detection. *Physical Review Letters*, *102*, 020403.
Mekhov, I. B., & Ritsch, H. (2009b). Quantum optics with quantum gases: Controlled state reduction by designed light scattering. *Physical Review A*, *80*, 013604.
Meschede, D., Walther, H., & Müller, G. (1985). One-atom maser. *Physical Review Letters*, *54*, 551.
Milonni, P. W., Loudon, R., Berman, P. R., & Barnett, S. M. (2008). Linear polarizabilities of two- and three-level atoms. *Physical Review A*, *77*, 043835.
Mollow, B. R. (1969). Power spectrum of light scattered by two-level systems. *Physical Review*, *188*, 1969–1975.
Morigi, G., Pinkse, P. W. H., Kowalewski, M., & de Vivie-Riedle, R. (2007). Cavity cooling of internal molecular motion. *Physical Review Letters*, *99*, 073001.
Mossberg, T. W., Lewenstein, M., & Gauthier, D. J. (1991). Trapping and cooling of atoms in a vacuum perturbed in a frequency-dependent manner. *Physical Review Letters*, *67*, 1723.
Motsch, M., Zeppenfeld, M., Pinkse, P. W. H., & Rempe, G. (2010). Cavity-enhanced Rayleigh scattering. *New Journal of Physics*, *12*(6), 063022.
Münstermann, P., Fischer, T., Maunz, P., Pinkse, P. W. H., & Rempe, G. (1999). Dynamics of single-atom motion observed in a high-finesse cavity. *Physical Review Letters*, *82*, 3791.
Murch, K. W., Moore, K. L., Gupta, S., & Stamper-Kurn, D. M. (2008). Observation of quantum-measurement backaction with an ultracold atomic gas. *Nature Physics, 4*, 561–564.
Murr, K. (2006). Large velocity capture range and low temperatures with cavities. *Physical Review Letters*, *96*, 253001.
Nagy, D., Kónya, G., Szirmai, G., & Domokos, P. (2010). Dicke-model phase transition in the quantum motion of a Bose-Einstein condensate in an optical cavity. *Physical Review Letters*, *104*, 130401.

Nußmann, S., Hijlkema, M., Weber, B., Rohde, F., Rempe, G., & Kuhn, A. (2005a). Submicron positioning of single atoms in a microcavity. *Physical Review Letters 95*, 173602.
Nußmann, S., Murr, K., Hijlkema, M., Weber, B., Kuhn, A., & Rempe, G. (2005b). Vacuum-stimulated cooling of single atoms in three dimensions. *Nature Physics, 1*, 122.
Pellizzari, T., Gardiner, S. A., Cirac, J. I., & Zoller, P. (1995). Decoherence, continuous observation, and quantum computing: a cavity QED model. *Physical Review Letters 75*, 3788.
Pinkse, P. W. H., Fischer, T., Maunz, P., & Rempe, G. (2000). Trapping an atom with single photons. *Nature*, *404*, 365.
Poldy, R., Buchler, B. C., & Close, J. D. (2008). Single-atom detection with optical cavities. *Physical Review A*, *78*, 013640.
Puppe, T., Schuster, I., Grothe, A., Kubanek, A., Murr, K., Pinkse, P. W. H., et al. (2007). Trapping and observing single atoms in a blue-detuned intracavity dipole trap. *Physical Review Letters*, *99*, 013002.
Purcell, E. M. (1946). Spontaneous emission probabilities at radio frequencies. *Physical Review*, *69*, 681.
Raimond, J. M., Goy, P., Gross, M., Fabre, C., & Haroche, S. (1982). Statistics of millimeter-wave photons emitted by a Rydberg-atom maser: An experimental study of fluctuations in single-mode superradiance. *Physical Review Letters*, *49*, 1924–1927.
Raizen, M. G., Thompson, R. J., Brecha, R. J., Kimble, H. J., & Carmichael, H. J. (1989). Normal-mode splitting and linewidth averaging for two-state atoms in an optical cavity. *Physical Review Letters*, *63*, 240–243.
Rempe, G., Thompson, R. J., Brecha, R. J., Lee, W. D., & Kimble, H. J. (1991). Optical bistability and photon statistics in cavity quantum electrodynamics. *Physical Review Letters*, *67*, 1727.
Rice, P. R., & Brecha, R. J. (1996). Cavity induced transparency. *Optics Communications*, *126*, 230.
Schleier-Smith, M. H., Leroux, I. D., & Vuletić, V. (2010a). Squeezing the collective spin of a dilute atomic ensemble by cavity feedback. *Physical Review A*, *81*(2), 021804(R).
Schleier-Smith, M. H., Leroux, I. D., & Vuletić, V. (2010b). States of an ensemble of two-level atoms with reduced quantum uncertainty. *Physical Review Letters*, *104*, 073604.
Schuster, I., Kubanek, A., Fuhrmanek, A., Puppe, T., Pinkse, P. W. H., Murr, K., et al. (2008). Nonlinear spectroscopy of photons bound to one atom. *Nature Physics, 4*, 382–385.
Siegman, A. E. (1986). *Lasers*. Sausalito, CA: University Science Books.
Simon, J., Tanji, H., Ghosh, S., & Vuletić, V. (2007a). Single-photon bus connecting spin-wave quantum memories. *Nature Physics, 3*, 765.
Simon, J., Tanji, H., Thompson, J. K., & Vuletić, V. (2007b). Interfacing collective atomic excitations and single photons. *Physical Review Letters*, *98*, 183601.
Tanji, H., Ghosh, S., Simon, J., Bloom, B., & Vuletić, V. (2009). Heralded single-magnon quantum memory for photon polarization states. *Physical Review Letters*, *103*, 043601.
Tavis, M., & Cummings, F. W. (1968). Exact solution for an *N*-molecule—radiation-field Hamiltonian. *Physical Review*, *170*, 379–384.
Teper, I., Lin, Y.-J., & Vuletić, V. (2006). Resonator-aided single-atom detection on a microfabricated chip. *Physical Review Letters*, *97*, 023002.
Terraciano, M. L., Olson Knell, R., Norris, D. G., Jing, J., Fernández, A., & Orozco, L. A. (2009). Photon burst detection of single atoms in an optical cavity. *Nature Physics, 5*, 480–484.
Thompson, R. J., Rempe, G., & Kimble, H. J. (1992). Observation of normal-mode splitting for an atom in an optical cavity. *Physical Review Letters*, *68*, 1132.
Thompson, J. K., Simon, J., Loh, H.-Q., & Vuletić, V. (2006). A high-brightness source of narrowband, identical-photon pairs. *Science, 313*, 74.
Trupke, M., Goldwin, J., Darquié, B., Dutier, G., Eriksson, S., Ashmore, J., et al. (2007). Atom detection and photon production in a scalable, open, optical microcavity. *Physical Review Letters*, *99*, 063601.
Turchette, Q. A., Hood, C. J., Lange, W., Mabuchi, H., & Kimble, H. J. (1995). Measurement of conditional phase shifts for quantum logic. *Physical Review Letters*, *75*, 4710–4713.
Vuletić, V., Chan, H. W., & Black, A. T. (2001). Three-dimensional cavity Doppler cooling and cavity sideband cooling by coherent scattering. *Physical Review A, 64*(3), 033405.
Vuletić, V., & Chu, S. (2000). Laser cooling of atoms, ions, or molecules by coherent scattering. *Physical Review Letters*, *84*, 3787.

Vuletić, V., Thompson, J. K., Black, A. T., & Simon, J. (2007). External-feedback laser cooling of molecular gases. *Physical Review A*, *75*, 051405(R).

Wilk, T., Webster, S. C., Kuhn, A., & Rempe, G. (2007). Single-atom single-photon quantum interface. *Science, 317*, 488–490.

Wilzbach, M., Heine, D., Groth, S., Liu, X., Raub, T., Hessmo, B., et al. (2009). Simple integrated single-atom detector. *Optics Letters*, *34*, 259–261.

Zhu, Y., Gauthier, D. J., Morin, S. E., Wu, Q., Carmichael, H. J., & Mossberg, T. W. (1990). Vacuum Rabi splitting as a feature of linear-dispersion theory: Analysis and experimental observations. *Physical Review Letters*, *64*, 2499.

Zippilli, S., & Morigi, G. (2005). Cooling trapped atoms in optical resonators. *Physical Review Letters*, *95*, 143001.

Zippilli, S., Morigi, G., & Ritsch, H. (2004). Suppression of Bragg scattering by collective interference of spatially ordered atoms with a high-Q cavity mode. *Physical Review Letters*, *93*, 123002.

This page intentionally left blank

CHAPTER 5

The First Atomic and Molecular Experiments at the Linac Coherent Light Source X-Ray Free Electron Laser

Philip H. Bucksbaum[a,c], **Ryan Coffee**[b,c], and **Nora Berrah**[d]

[a]*PULSE Institute and Departments of Physics, Applied Physics, and Photon Science, Stanford University, Stanford, CA 94305, USA*
[b]*Linac Coherent Light Source*
[c]*SLAC National Accelerator Laboratory, Menlo Park, CA 94025, USA*
[d]*Western Michigan University Physics Department, Kalamazoo, MI 49008, USA*

Contents

Advances in Atomic, Molecular, and Optical Physics, Volume 60, Copyright © 2011 Elsevier Inc.
ISSN 1049-250X, DOI: 10.1016/B978-0-12-385508-4.00005-X.

Abstract The Stanford Linac Coherent Light Source (LCLS) located at the SLAC National Accelerator Laboratory in Menlo Park, California, began operation in the Fall of 2009. The LCLS is a true x-ray laser, approximately one billion times brighter than any previous laboratory source of x-ray radiation. Here we review some of the first atomic, molecular, and optical experiments that probe the fundamental interactions of such uniquely bright and short x-ray pulses with atoms and molecules, summarize some of the theory leading up to these experiments and conclude with some ideas on future avenues of investigation.

1. INTRODUCTION

This review describes some of the research that has been initiated in atomic physics at new "fourth generation" x-ray light sources. The first

such light source capable of operating in the kilovolt x-ray range is the Stanford Linac Coherent Light Source (LCLS) at the SLAC National Accelerator Laboratory on the grounds of Stanford University in Menlo Park, CA. The LCLS began operations in the Fall of 2009 and is currently producing radiation wavelengths between 22 Å and 1.2 Å. The pulse duration can be adjusted between approximately 10 fs and more than 500 fs, and the pulse energies are in the range of hundreds of microjoules to millijoules. This beam intensity is greater than typical synchrotrons by more than nine orders of magnitude.

This extraordinary increase in available x-ray pulse intensity and ultrashort pulse duration creates new opportunities in atomic and molecular physics. This review provides an overview of atomic physics in this new physical regime and contains a discussion of some of the preliminary results of the first year of investigation of atoms and molecules at the LCLS. The organization of the review is as follows: The first section introduces the x-ray laser source, and some of the technical advances and limitations that determine the regime of the first experimental investigations. This is followed by a description of the basic physics of atoms and molecules interacting with ultrashort pulse intense x-ray laser radiation. The bulk of the review is a consolidated description of the first experiments. The emphasis is on those research results that have already been published, which both describe new physics and also give a good indication of the strengths and challenges of laser research at LCLS.

1.1 X-Ray Laser Interactions with Atoms

The widespread availability of third-generation synchrotron x-ray sources has led to substantial advances in our understanding of structure and dynamics in atomic, molecular, and cluster systems. X-rays can resolve features at the sub-Ångstrom level (Hendrickson, 1991), with element-specific sensitivity (Hoener et al., 2010a; Pešić et al., 2007; Prümper et al., 2008; Rolles et al., 2008; Schöffler et al., 2008).

X-ray resonant absorption processes in atoms and molecules are considerably weaker than those in the visible and ultraviolet parts of the spectrum. Typically the cross sections scale as the wavelength squared or worse. Furthermore, the optics, particularly in the vacuum ultraviolet and soft x-ray spectrum are relatively inefficient. Nonetheless, spectroscopy in this region has flourished because of the high brightness and complete tunability of modern synchrotron light sources, which can be as high as 10^{24} $\gamma/\mathrm{s}/\mathrm{mm}^2/\mathrm{mr}^2/0.1\%$ bandwidth. When coupled to high throughput crystal monochrometers, these sources have tunability and frequency stability in the range of $\delta\omega/\omega \approx 10^{-5}$ or better.

Spectroscopic studies have also been enabled by the rapid advance of detection for atomic and molecular fragments. Momentum and energy detecting instruments permit some or all of the products of photoabsorption to be measured with high precision. These include the reaction microscope (Dörner et al., 2000; Schöffler et al., 2008; Ullrich et al., 1997), VMI detectors coupled with high-resolution electron time of flight spectrometers (Prümper et al., 2008; Rolles et al., 2008), and high-efficiency magnetic bottles (Eland et al., 2010; Lablanquie et al., 2011), which all have allowed detailed information to be obtained regarding single-photon ionization processes.

X-ray pulses from synchrotron light sources have important limitations in the study of transient phenomena, or nonlinear high field atomic and molecular physics. Synchrotron pulses typically last for tens of picoseconds and are therefore too long to observe the time-evolution of transient processes such as dissociation, isomerization, or faster electronic processes such as Auger relaxation. They are also unable to capture the transient structures within molecules during chemical reactions or in strongly driven molecules.

Subpicosecond dynamics can be observed using femtosecond lasers, which cover wavelength regimes ranging from the infrared (IR) to the extreme ultraviolet (EUV). This has led to a revolution in time-resolved studies of physical and chemical processes (Corkum et al., 2009; Krausz & Ivanov, 2009; McFarland et al., 2008). Laboratory-based laser sources provide sufficient time resolution to follow atomic motion during the course of molecular vibration, dissociation, and reaction. Unfortunately, the long wavelengths of these sources do not allow for direct imaging of the motion of individual atoms. As a result, there has been tremendous interest in "fourth generation" accelerator-based free electron lasers (FEL's), which offer an unprecedented combination of spatial and temporal resolution.

A soft x-ray free electron laser called FLASH has been operating since 2005 at the *Deutsches Elektronen-Synchrotron* (DESY), an electron accelerator research laboratory in Hamburg, Germany. The FLASH FEL is tunable from 25 eV to 200 eV in the first harmonic, and could reach 780 eV at the fifth harmonic (Ackermann et al., 2007; Gutt et al., 2009). A review of the atomic and molecular achievements using the vacuum ultraviolet (VUV) FEL can be found in Berrah et al. (2010). The Linac Coherent Light Source (LCLS) at the SLAC National Accelerator Laboratory has demonstrated in April 2009 lasing between 800 eV and 8000 eV, making it the world's first hard x-ray FEL (Emma et al., 2010; Feldhaus et al., 2005). In October of 2009, the first atomic and molecular experiments focused on nonlinear investigations in atoms (Young et al., 2010), molecules (Cryan et al., 2010; Fang et al., 2010; Hoener, 2010b), and clusters.

2. OPTICAL PROPERTIES OF X-RAYS FROM ELECTRON ACCELERATORS

The physics of strong-field laser–atom interactions has not been pursued in the short wavelength regime, largely because strong x-ray fields have not been available until now. Coherent x-ray narrow band light sources based on atomic transitions have been produced in laser-driven plasmas, but their focused output is well outside the fluence necessary to saturate a core-level process in an atom, and their wavelengths are typically in the vacuum ultraviolet regime on the order of 100 eV or less (Benware et al., 1999; Daido, 2002; Dunn et al., 2000). Sources based on high harmonic radiation are also far too weak to drive strong field processes, although their extremely short time structure has been useful in studies of ultrafast processes in atoms and molecules (Krausz & Ivanov, 2009; Lewenstein et al., 1994; McFarland et al., 2008).

The 1990s saw the construction and commissioning of the "third generation" x-ray synchrotron light sources, which made use for the first time of coherent synchrotron radiators using permanent magnet undulators. These are periodic magnet arrays (typically 1–3 cm periods) through which electrons execute periodic transverse oscillations. The word "coherence" refers to the fact that the radiated fields from successive oscillations add coherently in the forward direction, thereby yielding pulse energies on axis that scale as the square of the number of periods. Yet these are not sources of coherent *laser* radiation, for at least two reasons. First, the number of photons emitted by a single electron while traversing an undulator is typically much less than one. Second, there is no mechanism in a synchrotron undulator to ensure that different electrons radiate in phase. In fact, typically they do not, so the light field has the longitudinal characteristics of a fully incoherent source. Another way of saying this is that the number of photons per mode in the electromagnetic field is much less than one.

The transition from undulator radiation to free electron laser radiation is based on the build up of a coherent field in the undulator structure. The details of this are described in an excellent review by Huang and Kim (2007). Here we will present a simple qualitative description of the properties of the radiation, which is central for understanding the physics of the laser–atom interaction.

2.1 Free Electron Laser Radiation

As electrons pass through a long undulator, they are accompanied by their own radiation field. Because the electrons are ultrarelativistic, their synchrotron radiation field does not outrun them, but rather each electron can

experience the forces resulting from fields radiated by all of the electrons. In fact, the synchrotron radiation does move slightly faster than the electrons along the undulator axis for two reasons: First, the electron velocities are slightly slower than the vacuum speed of light, but this difference is extremely small (the percentage below c is $1/2\gamma^2$, which is less than a part per *billion* at LCLS). A larger source of slippage at LCLS is that the electrons do not travel along a straight path like the radiation, but rather are forced to wiggle by the magnetic fields of the undulator. The total slippage λ_l per undulator period λ_u is the sum of these two effects

$$\lambda_l = \frac{\lambda_u}{2\gamma^2}\left(1 + \frac{K_0^2}{2}\right), \tag{1}$$

where K_0/γ is the maximum angle of deviation of the wiggling electron. The synchrotron fields are periodic of course, and this slippage creates the opportunity for a resonance between the oscillation of the electron in the field, and its oscillation because of the undulator, which works as follows: If the synchrotron field exerts a transverse force on an electron that is in the same direction as the force due to the undulator magnet at some point in the wiggle oscillation, then those forces will be in the same direction on the next cycle as well. The electron will have slipped exactly one radiation cycle during its wiggle cycle, when the synchrotron radiation is in resonance. This is shown graphically in Figure 1.

The presence of a resonance increases the coupling between the electron kinetic energy and the synchrotron field because the synchrotron field and the magnetic field forces are coherently adding. This also creates a tendency for the electrons to become bunched because a slightly higher energy electron will make smaller excursions in the magnetic field, which will cause it to fall out of resonance, and therefore lose energy, and therefore come back into resonance. On every field cycle, there is a region with the optimal position relative to the field phase to attract electrons with the optimal energy, so that the electrons form local density maxima known as

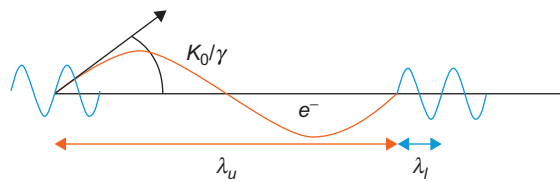

Figure 1 The resonance condition for a free electron laser is that the difference between the electron progress in one undulator cycle and the synchrotron radiation propagation over the same time interval is equal to one wavelength of the synchrotron radiation.

microbunches. The electrons in these microbunches oscillate together, and therefore radiate coherently. This is the laser action. Free electron lasers were first developed in the 1970s and 1980s in infrared or optical resonator cavities, where a standing wave electromagnetic field inside the resonator controlled the microbunching process.

In the 1980s, work by Pellegrini and others established that FEL's with sufficiently high gain do not require the electromagnetic resonator structure because spontaneous density and field fluctuations could feed on each other to lead to self-organization of microbunches, a process known as "Self-Amplified Spontaneous Emission," or SASE (Murphy & Pellegrini, 1985). The SASE concept does away with the need for optical elements, and thereby it permits extension of FEL's to the vacuum ultraviolet and x-ray spectral range where mirrors are poor or nonexistent. A SASE-based FEL also requires relatively dense electron bunches because the radiation only passes through the gain structure a single time. Compression techniques to increase the electron peak current are therefore required, and these were also developed at relativistic electron linear accelerators in the past decade.

The result is a laser with good transverse coherence but the poor longitudinal coherence that is characteristic of a chaotic source, with little control over the detailed spectral or temporal shape of the laser pulse. This is reminiscent of the early days of Q-switched, solid-state lasers, where it was first noted that such temporal properties can enhance nonlinear light scattering and other strong field processes (Rohringer & Santra, 2007a). The SASE-generated lasing process saturates when the microbunched electrons lose enough energy to the laser field to fall out of resonance. In practice, relativistic electron accelerators can produce laser peak powers in the 1–100 GW range, which can be focused to micron or submicron spot sizes, resulting in peak intensities in excess of 10^{18} W/cm^2. This places the x-ray FEL in the class of the most intense laser sources available.

The first SASE-based VUV FEL was built at DESY in 2005, and the first hard x-ray FEL was commissioned at SLAC in 2009. As of this writing, these are the only two VUV or x-ray SASE FELs in operation, but several more are in planning or under construction, at DESY (XFEL), Japan, Switzerland, Italy, and elsewhere. The current performance parameters of the two sources in operation are shown in the Table 1.

2.2 The SLAC Injector and Linac

The Stanford Linear Accelerator that powers LCLS is able to deliver electron beams with approximately 1000 times higher phase-space density than those available at synchrotron storage rings. To to this, both the electron injector and the beam conditioning along the accelerator have been specially modified. The accelerator is the last third of a 3-km radio

Table 1 FLASH and LCLS operating parameters.

Parameter	FLASH	LCLS
Wavelength range (nm)	6.8–47	0.15–2.4
Pulse energy (μJ)	10–100	150–4000
Pulse duration (fs [FWHM])	10–70	<5–200
Spectral width (% [FWHM])	∼1	∼1
Peak brilliance (γ/s/mr^2/mm^2/0.1%bw)	10^{29-30}	10^{30-32}

Source: FLASH (2011); Iverson (2011).

frequency linear accelerator originally built in the 1960s for high-energy physics. The basic accelerator structure is changed little from the original design, which is based on copper cavities operating in the S-band (2856 MHz). The following three elements have been added to this:

- A laser-driven copper photocathode now produces up to 500 pC of electrons with under 1 mm-mr of emittance. These are produced in a side-arm to the linac placed at the 2/3 point, 2 km from the original electron source. The laser is frequency-tripled Ti:Sapphire operating at 266 nm, and synchronized to the pulse rf accelerator.
- Two bunch compressors have been added to the accelerating structure to compress the longitudinal phase space of the electrons and thereby create the necessary high peak brightness. The principle of operation of an ultrarelativistic electron bunch compressor is analogous to an ultrafast optical pulse compressor. The electron bunch receives a longitudinal energy dispersion, or chirp, across its length longitudinally, primarily because of acceleration off the electric field crest of a traveling electromagnetic wave. The compressor is a series of dipole magnets that create a chicane in the beam path. Higher momentum electrons take a shorter path through the chicane and therefore catch up to lower momentum electrons, so if the beam is originally chirped so that the higher momentum electrons are behind, then the result is bunch compression.

2.3 Coherence Properties of the Light

The transverse coherence properties of the free electron laser are extremely important for determining the ultimate focal properties of the beam, and its use for coherent scattering or diffractive imaging. These have been simulated extensively (Barty et al., 2009; Saldin et al., 2008). Deviations from diffraction limited performance come from both the electron beam laser light generation process and from the downstream optics. The degree of transverse coherence of the beam emerging from the LCLS undulators can

be as high as 90%, and is generally expected to be poorer for higher peak current and for shorter wavelength, but generally on the order of 60% or better (Ding & Huang, 2010).

The longitudinal coherence is very far from an ideal, transform-limited pulse. The coherence length of the LCLS is equal to the cooperation length of the radiating electron bunch. For soft x-rays, $\nu \in [0.2, 2]$ keV, the coherence time can be as long as 1 fs or so. Therefore, it may be possible to make use of the finite coherence for processes such as resonant excitation.

3. PHOTOEXCITATION AND PHOTOIONIZATION

The proper interpretation of scientific results using these sources requires an understanding of the interplay between field intensity and field frequency in photoionization and photoexcitation. This subject starts with the simple results of Fermi's Golden Rule for lowest order perturbation theory, from which we derive that the single-photon absorption rate W for any process is directly proportional to the photon intensity I, and may be written as the product of the photon flux $I/\hbar\omega$ and the cross section σ:

$$W^{(1)} = \sigma I/\hbar\omega. \tag{2}$$

If the photon energy is insufficient to permit ionization by one photon, the photoionization process may still proceed through second-order perturbation theory, and Fermi's Golden Rule then shows that the rate is quadratic in I, expressed by a second-order cross section $\sigma^{(2)}$:

$$\sigma^{(2)} = W/(I/\hbar\omega)^2 \propto \left| \sum \frac{\langle \varepsilon \cdot \mathbf{r} \rangle_{fn} \langle \varepsilon \cdot \mathbf{r} \rangle_{ni}}{\omega_{ni} - \omega} \right|, \tag{3}$$

where $\langle \varepsilon \cdot \mathbf{r} \rangle_{ab}$ is the dipole coupling matrix element between energy levels a and b, where a and b represent the initial state (i), final state (f), or any intermediate state (n). The energy splitting between two levels a and b is denoted by ω_{ab}. The frequency and polarization of the coupling laser is represented by ω and ϵ, respectively.

The magnitude of $\sigma^{(2)}$ can be estimated by noting that the energy denominator in the second-order perturbation expression above is essentially the uncertainty principle times the interval that the molecule can exist in a virtual state following absorption of the first photon and prior to absorbing the second. We can therefore write the second-order transition rate as the product of two one-photon absorption rates multiplied by this virtual state lifetime:

$$W^{(2)} \sim \sigma_{in}(I/\hbar\omega)1/(\Delta\omega)\sigma_{nf}(I/\hbar\omega). \tag{4}$$

This emphasizes the relationship of nonlinear absorption to the linear process, and can be extended to higher orders in perturbation theory (Lambropoulos & Tang, 1987). This picture cannot extend to very high intensities because each order depends on a higher power of the intensity so ultimately perturbation theory must break down. This breakdown will happen at intensities where higher order processes proceed faster than lower order processes, and a quick examination of the simple estimates given above shows that this occurs when the single photon cross section times the flux exceeds the laser frequency. For valence photoionization by optical lasers, this catastrophe occurs at intensities on the order of 10^{13} W/cm^2, which corresponds to fields on the order of 1V/Å. We now turn to a discussion of this regime.

3.1 Field Ionization

A linearly polarized electromagnetic field intensity of 1.9×10^{16} W/cm^2 has a peak electric field F_0 of one atomic unit, i.e., $F_0 = 5.14 \times 10^9$ V/cm. (Here and henceforth, we adopt the usual definition of atomic units, with $\hbar = m_e = |e| = 1$). The peak electric field of an optical pulse is a relevant physical quantity for the process of photoemission when the electromagnetic frequency is small compared with the resonant frequencies of the quantum system under study. In this case, the slowly varying optical cycle superposes with the static Coulomb field of the nucleus creating a depressed local weak spot, or "tunnel" in the potential energy function experienced by a bound electron. This leads to field ionization for an electron with binding energy E when the field strength is on the order of $E^2/4$ atomic units (Gallagher, 1994). An atomic unit of field is therefore sufficient to dc-field ionize any neutral atom, and fields that are an order of magnitude weaker (two orders of magnitude weaker intensity) are sufficient to ionize most ground-state atoms in the periodic table.

The tunnel ionization probability associated with the field-induced ionization described in the preceding paragraph should increase like a step function as the field increases to its critical threshold value, except for two effects. First, the electromagnetic field is only above the ionization barrier during a portion of a cycle, and the tunnel in the potential occupies only a small volume of the atom. Therefore, even a classical electron should have some probability to survive a field above the critical threshold if it fails to find and traverse the tunnel during this time. The second effect of significance is quantum tunneling, which permits some electron amplitude to leave the atom when the field is below threshold, and it also permits some reflection from the tunnel opening even when the field is above the threshold.

3.2 ADK and the Keldysh Parameter

The proper treatment of low-frequency strong-field ionization requires quantum mechanics, and it has been done in the WKB approximation by Ammosov, Delone, and Krainov (the ADK formula) (Ammosov et al., 1986). According to ADK, the instantaneous ionization rate can be expressed as the time-varying electron probability current $J(t)$ passing through the tunnel formed by the strong field. It is exponential in the field magnitude F, and also dependent on the magnitude of the electron binding energy $|E|$:

$$J(t) = 4(2|E|)^{5/2}\frac{1}{F(t)}\exp\left[-\frac{2}{3F(t)}(2|E|)^{3/2}\right]. \tag{5}$$

The ADK result shows how to extend the concept of a *transition rate* into the regime where perturbation theory is no longer valid. The crossover point from the multiphoton picture to the field ionization picture is when the ADK ionization probability integrated over one cycle becomes significant. We define a strong field parameter γ as (Reiss, 2010).

$$\gamma_{\mathrm{K}} = \frac{(\text{ionization lifetime})}{(\text{wave period of the applied field})}. \tag{6}$$

When $\gamma_{\mathrm{K}} \leq 1$ the system is best described by the ideas of strong field tunnel ionization. The multiphoton regime is most appropriate for $\gamma_{\mathrm{K}} > 1$.

In the low-frequency regime where ADK is valid, γ_{K} is called the "Keldysh parameter" (Keldysh, 1965):

$$\gamma_{\mathrm{K}} = \sqrt{|E|/2U_{\mathrm{p}}}, \tag{7}$$

where U_{p} is the cycle-averaged kinetic energy of an electron driven by the laser field, which is called the "ponderomotive potential":

$$U_{\mathrm{p}} = \frac{e^2F^2}{4m\omega^2}. \tag{8}$$

The Keldysh formula in Equation (7) exceeds its domain of validity when the source field frequency can no longer be considered small compared with the internal electron dynamics of an atom or molecule. The notion of an electron wave function evolving adiabatically on a slowly changing distorted Coulomb potential is no longer reasonable when the laser frequency exceeds the dynamical timescale set by the spacing between bound states, and this picture must breakdown altogether when the photon energy exceeds the binding energy. The numerator in γ_{K} in Equation (7) is then no longer a tunneling time, but the γ_{K} parameter is still a useful concept.

3.3 Floquet Formalism

Another way to treat the evolution of a quantum system under the influence of a strong field is the Floquet or "dressed state" approach. Floquet analysis is a method for finding the solution to a Schrödinger-type differential equation that contains an explicit time-periodic driving term, such as the interaction term containing a laser oscillating electric field. The essential idea is to directly include the external optical field in the Hamiltonian and diagonalize in the interaction picture to find the so-called field dressed states (see ref. Friedrich, 1994; Meystre & Sargent III, 1990). The eigenstates are actually time-varying admixtures of field-free stationary states, but these admixtures are periodic at the optical cycle period T. Scalar products in this dressed Hilbert space are evaluated over an optical cycle, $\phi_1 \cdot \phi_2 = \frac{1}{T}\int_0^T \langle \phi_1(t)|\phi_2(t)\rangle \, \mathrm{d}t$.

Although this Floquet formalism is general to fields of any strength, the idea of diagonalizing the interaction Hamiltonian is particularly well suited for cases where the transition probability grows to near unity. It does not assume that the driving term is weak or low frequency, and therefore the validity of Floquet analysis can extend to strong field x-rays.

3.4 KFR and Volkov States

One way to apply dressed state ideas in the limit of photon energies that are much greater than the electron binding energy is to suppose that the strong x-ray field couples the initial bound state of the atom or molecule to a state that is high enough in the continuum to be free from the influence of the Coulomb binding field, and only influenced by the strong x-ray laser field itself. This is a form of dressed state calculation that has also been used for low-frequency fields, called the "KFR approximation" (Faisal, 1973; Keldysh, 1965; Reiss, 1980). The dressed electron in the final state is called a "Volkov state" (Wolkow, 1935; Yudin et al., 2007):

$$\psi_V(\mathbf{r}, t) = (2\pi)^{-3/2} \exp\left[i\mathbf{p}\cdot\mathbf{r} - \frac{i}{2}\int^t \left[\mathbf{p} + \mathbf{A}_\mathrm{L}(t)\right]^2 \mathrm{d}t \right]. \tag{9}$$

Here we use the standard atomic units, and $\mathbf{A}_\mathrm{L}$ is the oscillating electromagnetic vector potential of the laser field.

The spectrum of ψ_V consists of a superposition of the main photopeak at the kinetic energy $\mathbf{p}^2/2$ together with photopeaks separated by $\pm n\hbar\omega$, with amplitudes given by the Bessel Function coefficients in the Fourier decomposition of Equation (9) (Reiss, 1980). The relative magnitude of these peaks scales as the ratio of the ponderomotive energy U_p to the photon energy $\hbar\omega$.

The probability for photoionization by a strong field x-ray can then be approximated by the laser-induced coupling between the initial state of

the atom or molecule, whose wave function is expressed in the absence of a field, and the final ion state times a field-dressed Volkov state of the outgoing electron. This is the essence of the KFR approximation, and it has been described for both long and short wavelengths in various ways by many authors, often referred to as the "Coulomb-Volkov *ansatz*" (Cavaliere et al., 1980; Yudin et al., 2007). The validity of this approximation is expected to survive to shorter wavelengths so long as the dipole approximation remains valid, which should be the case for all but the hardest x-rays at LCLS. But as Figure 2 shows, strong field effects will diminish at shorter wavelengths because of the unfavorable scaling of the ratio of the ponderomotive potential to the relevant energy scale of the bound system.

Under these low-frequency strong-field conditions, the interaction Hamiltonian mixes field-free states significantly. The dipole polarizability of an atom or molecule is a measure of this mixing of electronic states. Those states with the highest oscillator strength, i.e., highest dipole-coupling matrix elements, will mix more strongly. These are spatial integrals, and scale with the size of the orbital. The compact low-n core orbitals

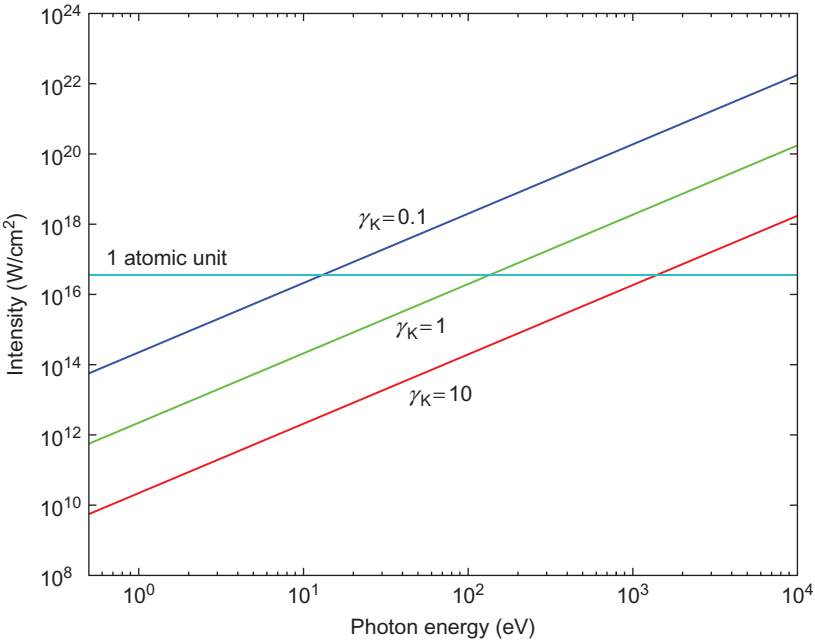

Figure 2 Value of the Keldysh parameter γ_K, which is the ratio of the ionization lifetime to the laser cycle period, against laser intensity and photon energy, for atomic hydrogen. The tunneling regime is generally described as the region with $\gamma_K < 1$.

in a multielectron atom levels must therefore play a relatively minor role in the low-frequency polarization response of a material.

3.5 Ionization Saturation and Multiple Ionization

Although traditional strong field effects are suppressed by wavelength, there are new strong field processes that are unique to the short wavelength regime of x-rays because of the inverted *order* of photoionization for x-rays: the more deeply bound electrons have much higher photoionization cross sections, once they are above the energy threshold to ionize. We therefore examine next the phenomenon of multiple electron ionization, saturation, and relaxation.

The simple process of one-photon absorption as described by Equation (2) is perfectly adequate to describe all photoabsorption processes at synchrotrons, and is the starting point for any consideration of multielectron strong-field effects at x-ray lasers. However, the following two points bear mentioning: First, this formula does not consider any effect resulting from the finite temporal coherence time of the source; and second, this assumes that the initial state of the system is not depleted by the process, i.e., this is a weak-field result.

The depletion phenomenon can be included in a simple rate equation model if the coherence time is sufficiently short. The result is that the ionization probability P goes to unity according to an exponential

$$P = 1 - \exp\left(\sigma^{(1)}\mathfrak{F}\right), \tag{10}$$

where the fluence $\mathfrak{F}$ is number of photons per unit area in the laser pulse

$$\mathfrak{F} = \int I(t)\mathrm{d}t/\hbar\omega. \tag{11}$$

Typical cross sections for the photoionization of light atoms such as nitrogen by kilovolt x-rays are on the order of megabarns, or 10^{-18} cm^2. The LCLS can routinely supply a fluence of a millijoule of kilovolt x-rays focused to 10 μm^2, on the order of 10^{20} photons/cm^2. As a consequence, single x-ray photoabsorption processes are strongly saturated at LCLS. In fact, a core level can be depleted in only a few femtoseconds, which can be significantly shorter than the nonradiative Auger-driven repopulation of the core electron.

Coherence is the other property missing from the single-photon absorption formula described by Equation (2). In coherent fields, the phase of the electromagnetic field is well-defined over a significant interval, so that ground and excited quantum states coupled by the oscillating field can develop a definite relative phase. This appears as nonzero off-diagonal

elements of the density matrix describing the system. These coherences allow population to oscillate between coupled electronic states. If they are well controlled, they can lead to formation of coherent superposition states, partial or total inversion of the population known as Rabi flopping, as well as more complex phenomena such as electromagnetically induced transparency or slow light (Hau et al., 1999; Kash et al., 1999; Rabi et al., 1939).

A source based on the SASE process is not well controlled, but rather is inherently chaotic in nature (Bonifacio et al., 1994; Rohringer & Santra, 2007b; Saldin et al., 2000). However, there is a finite coherence length based on the cooperation length of the radiating electron bunch. Simulations show that the LCLS can exhibit coherence lengths that are on the order of 1–2 fs, which can be an appreciable fraction of the overall pulse duration. As shown in the simple estimate above, the intensity required to transfer 100% of the population of a core state into an unoccupied bound or continuum state, and to do it within one coherence time of the LCLS pulse is well within reach in the focused LCLS beam. Therefore, some phenomena requiring coherence are expected.

Simple estimates such as Equation (10) show that any new x-ray physics with large population transfers will require an interaction cross section of $\sigma \gtrsim 0.3$ Mb. Figure 3 shows the atoms that satisfy this criterion for LCLS, which are the second-row elements B–Ne with absorption edges below 1 keV. All of the first experiments in the AMO program at LCLS have concentrated on atoms in this row, particularly on nitrogen and neon.

3.6 *P*, *A*, and *V*-Type Processes

A number of sequential ionization processes occur and compete with each other in ionization using intense x-ray radiation. These can be classified into three main types: Core-level photoionization (*P*); Auger relaxation (*A*), in which a photoexcited core vacancy is filled by a valence electron due to electrostatic forces within the atom, while another valence electron is ejected to conserve total energy; and valence photoionization *V*. *P* and *V* are distinct because of the large difference in their energies: *V* processes are usually not followed by an *A*-type emission of a further electron, but *P* processes almost always are followed by *A*. During the intense interaction with the focused LCLS beam, these processes follow closely upon each other in sequence, and their order is determined by the x-ray laser wavelength and its intensity. This is shown diagrammatically in Figure 4.

Other processes beyond the simple sequences described above can also contribute to the ion yield spectra. For example, Auger relaxation can occasionally produce two continuum electrons, a process known as

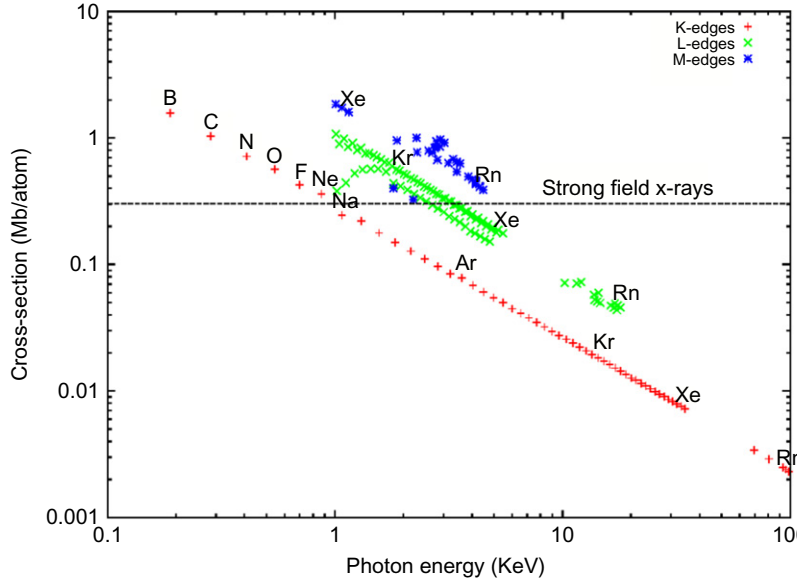

Figure 3 Photoabsorption cross sections in megabarns per atom for various elements. The noted "strong-field" regime simply marks the condition that absorption is saturated for an x-ray source of intensity three photons per femtosecond per megabarn as is typical for the LCLS. *K*-shell absorption (+) follows closely to the $1/\nu$ trend and cross into the strong-field regime below 1 keV. The *L*-shell (x) an *M*-shells (*) extend into the strong-field regime up to about 5 keV.

"shake-off"; or it may produce a continuum and excited valence electron, known as "shake-up." One could term shake-off a PAA process. It produces a triply ionized fragment, as do the sequential valence processes VPA or PAV.

Finally, there are some processes that are particularly related to the high intensity of the laser beam. One example is nonlinear absorption, in which two photons contribute together to produce a single electron. Through this means it is possible to ionize high charge states of Ne even when their binding energy exceeds the photon energy. Nonlinear two-photon absorption is an example of a coherent strong-field process that is expected to be extremely weak at LCLS (see discussion in Section 4.2).

A second intensity-dependent process is rapid sequential photoionization without Auger relaxation, i.e., a PP process. This could be expected to relax through a single Auger electron (PPA) or more than one (PPAA). There are several electron energy signatures of PP at LCLS, which will be discussed more fully in Section 5 of this review.

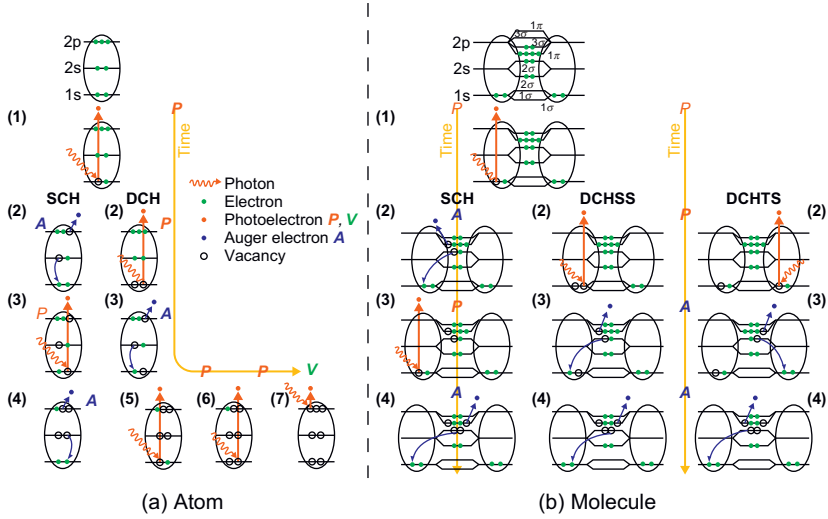

Figure 4 Diagram of the photoabsorption (P) and Auger (A) decay pathways for SCH and DCH states in (a) atomic N (left side) and (b) N_2 (right side). The ellipses represent atoms.

4. LAYOUT OF LCLS EXPERIMENTAL HALLS

The experimental LCLS layout is shown in Figure 5. LCLS has six experimental regions, or "hutches." Each region is specialized for a particular x-ray technique. Two are "soft x-ray" (500–2000 eV), and four are hard x-ray regions. The first experimental laboratory commissioned at LCLS was the AMO area, which was one of the soft x-ray areas that contains a general chamber built by the LCLS project for gas phase measurements. This chamber was commissioned and used during the initial experiments that will be described in this review. The design of the chamber was the responsibility of a commissioning team led by LCLS physicist John Bozek, who received broad input from the AMO research community (Bozek, 2009).

4.1 The AMO Instrument

The AMO instrument is designed to deliver the highest fluence possible for multiple ionization of gas phase targets, including targets that have been excited by an ultrafast laser pulse in advance of the x-rays. The chamber has been designed to focus the x-ray beams to intensities exceeding 10^{18} W/cm^2. The design is modular to allow some flexibility in the placement of the focus and the arrangement of instruments around it.

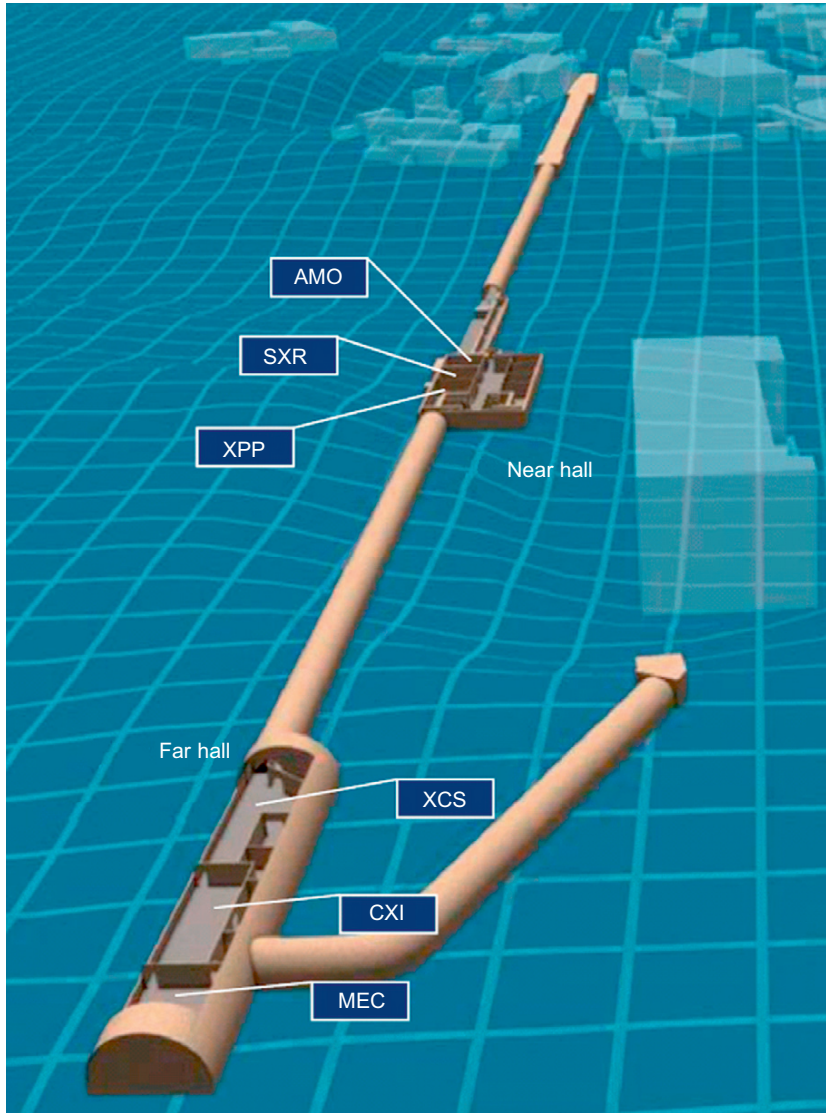

Figure 5 Layout of the underground experimental halls at LCLS. The soft x-ray AMO hall is the furthest upstream, at the upstream end of the structure. Figure by Greg Stewart – SLAC National Accelerator Laboratory. LCLS (2010).

There are three main sections in the AMO chamber (see Figure 6): a mirror housing to enclose the focusing optics; a high field chamber surrounded by time-of-flight type particle detectors; and a diagnostic chamber. The entire system is kept under vacuum to reduce as much as possible attenuation of the soft x-ray beam by background gas. Differential

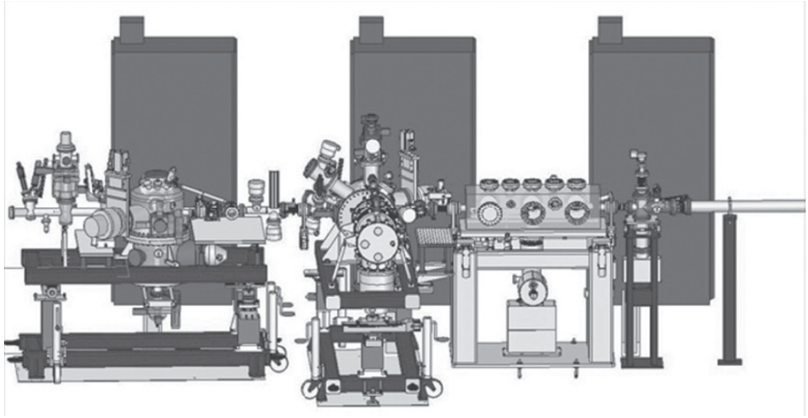

Figure 6 Assembled AMO instrument for LCLS. The x-rays enter from the right. The chambers from right to left are the mirror housing, the high field physics chamber, and the diagnostics chamber. From Bozek (2009), with the kind permission of the European Physical Journal.

pumping allows the mirror chamber to be kept free from target gases used in the other two chamber. Carbon-containing gases are particularly damaging to the optics because the x-ray beam can create reactive organic species which can then stick to the mirrors.

4.1.1 X-Ray Focusing Optics

The focusing optics for high intensity soft x-rays are particularly challenging. Because all materials are strongly absorbing in this wavelength range, the only possibilities are diffractive optics such as free-standing zone plates, or grazing incidence optics that take advantage of the relatively high reflectivity for soft x-rays at near-grazing angles below a critical angle. Zone plates cannot be used at LCLS because they damage too easily in the LCLS beam. Instead, two grazing incidence dynamically bent cylindrical mirrors are placed in a Kirkpatrick-Baez (K–B) configuration as shown in Figure 7 (Kirkpatrick & Baez, 1948). The mirrors are made out of crystalline silicon with a coating of B_4C. The K–B mirrors maintain a nominal grazing incidence angle of 30 mrad. The pair is designed to produce a 1 μm focal spot in the center of the high-field interaction chamber located about a meter from the mirror. For a 1-nm wavelength, this is a diffraction-limited focus for a 1-mm spot size on the mirror. This focus can be moved to the diagnostics chamber by changing the amount of the bend in the mirrors, and therefore their focal lengths. This design is intended to withstand damage under the full illumination of LCLS. The damage threshold has been tested with LCLS beams and found to be on the order

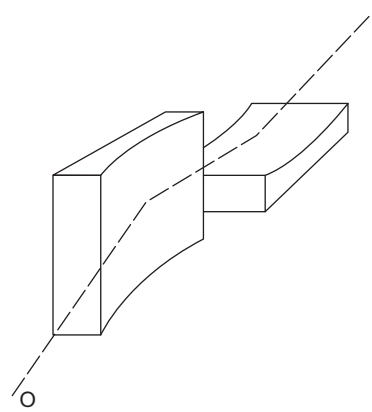

Figure 7 The Kirkpatrick-Baez mirror configuration used in the AMO instrument has two grazing incidence cylindrical mirrors with a common focus. From Kirkpatrick and Baez (1948).

of the fluence required to melt the mirror, which is approximately 2 J/cm^2 (Hau-Riege et al., 2009, 2010).

4.1.2 High Field Physics Region

The focus of the K–B optic is in the center of the main section of the AMO instrument. Atomic and molecular gases may be introduced to the focal region with an injection system consisting of a pulsed valve source and a skimmer. A well-defined molecular beam geometry is highly desirable, to limit ionization of gas by the x-ray beam away from the focus. The background gas in the chamber must kept in the range of $1–10 \times 10^{-10}$ torr as well, also to reduce the charged particles from x-ray interactions with the background gas. There is a significant difference in the need for high vacuum compared with strong-field laser-molecule experiments, where the high nonlinearity of the process generally ensures that no interactions take place away from the focus.

The main measurement tools in this section of the AMO chamber are charged particle detectors of the time-of-flight type. Ion spectrometers can measure momentum, energy, and charge to analyze the different types of x-ray-induced photofragmentation. The earliest experiments that are described in this review used the simplest type of ion spectrometer, an integrating time-of-flight device that can be used either in a Wiley-McLaren type configuration to measure the charge/mass of ions, or with a narrow slit, where the time-of-arrival also records the z-component of the momentum. The latter mode is useful for dissociation of aligned diatomic gases, as described further below.

Another type of ion spectrometer that has been used in this chamber is a velocity-map imager, which records the position of the ions away from the axis of the extraction field, and thus measures the transverse momentum. If this is combined with time-of-flight, then full 3D imaging of the vector momentum is possible.

The focal region is also surrounded by five high-resolution electron time-of-flight spectrometers (ETOFs), which are optimized for the study of photoelectrons and Auger electrons originating at the focus. The spectrometers each have multiple electrostatic retarding plates and biased flight tubes to decelerate electrons to maintain good energy resolution and high transmission. They are designedto measure electron energies up to several kiloelectron volt, with relatively flat acceptance of more than 20 eV, and a small opening angle ($\approx 2.7^{o}$) (Hemmers et al., 1998). The five ETOFs are positioned around the interaction region as shown in Figure 8 and Table 2.

4.1.3 Diagnostics Chamber

Downstream from the high field physics section of the AMO chamber is the diagnostics section. This chamber is designed to hold a variety of diagnostic tools to provide information about the x-ray spectrum, pulse

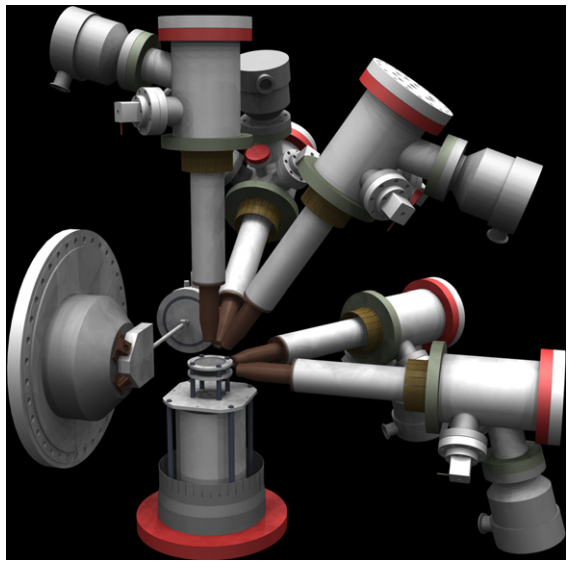

Figure 8 The five electron time-of-flight spectrometers are shown from a vantage point approximately upstream of the interaction region. Three spectrometers are in the polarization plane. Two are at forward "magic" angles (see Table 2). Greg Stewart – SLAC National Accelerator Laboratory. LCLS (2010).

Table 2 Angular orientation of the five ETOF spectrometers in the high field physics AMO chamber.

	$\theta(^\circ)$	$\phi(^\circ)$	Comment
1	90	90	Perpendicular to ϵ
2	54.7	90	Magic angle
3	0	90	Along ϵ
4	35.3	0	Out of the polarization plane
5	0	35.3	Magic angle

Here, $\theta = 0$ is the direction of polarization, which is horizontal and taken as the z-axis for these purposes. $\phi = 0$ is along the k-vector of the x-ray laser beam. ETOFs 2 and 5 are at magic angles, i.e., angles where the $L = 2$, $M = 0$ electron continuum vanishes. ETOFs 4 and 5 are out of the polarization plane.

energy, and timing. In addition, the K–B optics can be refocused into this chamber, producing a slightly larger (3–5 μm) beam waist.

Single-shot diagnostics are required at LCLS because the x-ray laser beam has significant pulse-to-pulse fluctuations in pulse energy, central photon energy, and bandwidth, and needs to be measured on each x-ray laser pulse. Among the instruments that can be accommodated in this chamber are beam profile diagnostics, beam energy monitors, and a magnetic bottle electron spectrometer.

4.1.4 Optical Lasers and the AMO Instrument

Both sections of the AMO instrument are also accessible to optical laser radiation for use in ultrafast pump-probe experiments. The optical beam and x-ray beams are brought into collinear propagation alignment in order to preserve the best possible pump-probe timing. This is accomplished by sending the x-rays through a small hole in a 45°-turning mirror at one or the other end of vacuum chamber.

Some of the initial experiments were designed in part to help establish the methods for relative timing between the optical laser and the x-ray laser, and these will be described later in this review. The laser is based on an 800-nm Ti:Sapphire chirped pulse amplifier (CPA), followed by a flexible suite of wavelength conversion options. The ultrafast optical laser radiation is too intense to propagate in the air for long distances, so the light is maintained in a chirped, long-pulse state while it is transported from the laser hall to the radiation hutch just below it. Grating compressors and wavelength conversion is then performed on optical tables in the AMO radiation hutch.

The optical lasers available for experiments at LCLS are capable of producing several millijoules per pulse at the repetition rate of LCLS

at 800 nm, or less pulse energy at wavelengths from the midinfrared to the midultraviolet. The laser light can also be split into multiple beams for interferometry, wave packet applications, autocorrelations, or optical gating applications.

4.2 Capabilities for Pump-Probe Experiments at LCLS

The opportunities for ultrafast science utilizing the short pulses from LCLS require excellent synchronization between the x-ray FEL and an external laser. Femtosecond precision between two independent modelocked laser sources that have no common optical source presents a significant challenge even in the best of cases, but here the situation is complicated by the large scale of the accelerator-driven x-ray laser, and the many sources of technical noise associated with its operation.

The AMO end station hosted the first experiments that required this synchronization in fall 2009. The pump pulse in these experiments was used for impulsive stimulated raman scattering of N_2, in order to create a coherent rotational wave packet that could exhibit rotational alignment. The probe was the LCLS beam, which ionized the molecule, leading to dissociation that could be analyzed in the angle-resolved ion time-of-flight (ITOF) spectrometer (Glownia et al., 2010).

The Stanford Linear Accelerator must carefully synchronize the phase of its RF cavities by means of a reference timing clock, and this can be used to lock a harmonic of the Kerr-Lens modelocked oscillator at the front end of the pump laser system. Because these are both narrowband frequencies in the 0.5-GHz range, locking to the picosecond scale is not difficult, and this takes care of thermal drifts that are inevitable in a machine that stretches over kilometers. However, the LCLS pulse durations and the relevant physical timescales are at the level of tens of femtoseconds, not picoseconds. Therefore, a number of technical improvements were made in this feedback system to drive the synchronization jitter down to the level of a few hundred femtoseconds (Wilcox et al., 2009).

There are significant sources of jitter in the arrival time of the electrons relative to their own RF acceleration field, due to the acceleration process itself. For example, energy jitter in the electron bunch translates to timing jitter because of the magnetic chicanes used to compress the bunch. A more direct approach at synchronization correlates the research pump laser pulse with the field of the electrons as they arrive at the end of the LCLS undulator chain. This has been done at SLAC in the past by means of single-shot electro-optic sampling (Cavalieri et al., 2005). Here an electro-optic material such as ZnSe is placed in the vicinity of the electron bunch, so that the enormous Coulomb fields accompanying the passage of the bunch can produce a transient disturbance in the material index of refraction. The ultrafast

laser pulse can image the passage of this index disturbance, and the image is directly related to the time of arrival, length, strength, and shape of the electrons that produced it. This is not a feedback method, but rather a sampling technique, where the single-shot timing information is recorded so that the data can be re-sorted according to the timing on each shot.

LCLS used a similar sampling method based on single-shot measurements of the bunch arrival time in two S-band (2.8-GHz) RF cavities at the end of the undulator that record the passage of the electrons. This system can then be used in postprocessing the data to re-sort it by relative time of arrival (Figure 9). Residual jitter of ~100 fs RMS has been demonstrated as shown in the first transient molecular alignment experiments (Glownia et al., 2010). The synchronization hardware appears to be capable of ultimate timing jitter on the order of 50 fs.

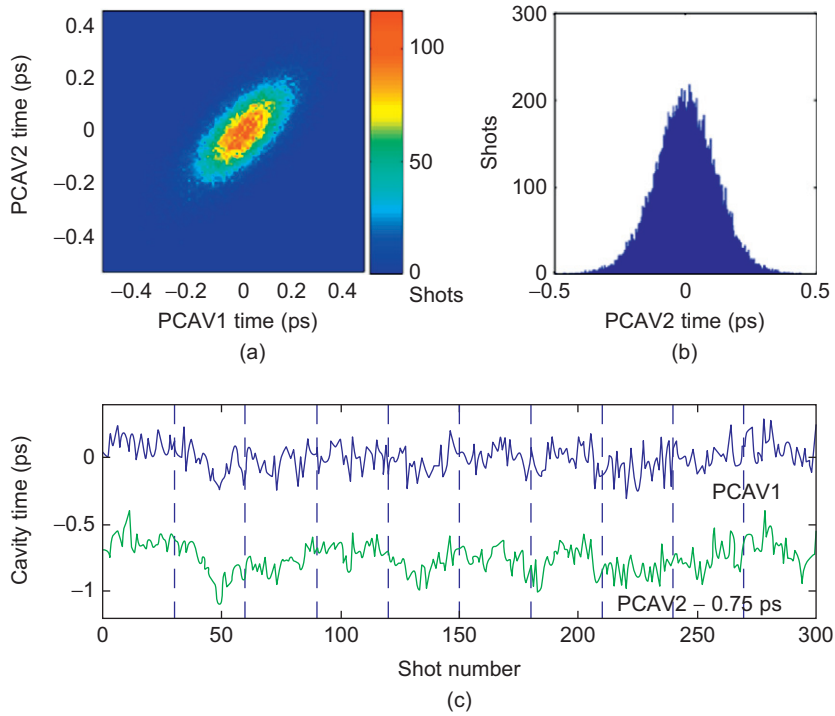

Figure 9 Two RF cavities independently recorded the time of arrival of the electron bunch to the LCLS undulators. This figure shows their correlation over 300 LCLS laser shots. The data are displayed (a) as a 2D correlation, (b) as a time-of-arrival histogram, and (c) as a time series. From Glownia et al. (2010).

4.3 CFEL ASG Multipurpose, CAMP Instrument

A European collaboration led by DESY and Max Planck Society has also designed and built a chamber called Chamber for Atomic and Molecular Physics (CAMP) that was transported to LCLS for use in some of the first gas phase experiments. Its main differences are an injector for small particles, and a soft x-ray camera for light scattering from gas phase and nanoscale objects. The CAMP detector is described in Epp et al. (2009) and Strüder et al. (2010).

5. INITIAL EXPERIMENTS ON X-RAY PHOTOIONIZATION

Several of the first AMO experiments at LCLS involved intense field photoionization. Understanding the interaction of atoms and molecules with intense ultrashort x-ray radiation is increasingly relevant to studies of structure and dynamics in biology, chemistry, and physics. Knowledge of this interaction is important in understanding a wide range of topics from biomolecular structure–function relationships (Bogan et al., 2008; Chapman et al., 2006; Marchesini et al., 2008; Neutze et al., 2000) to plasma production and inertial confinement fusion (Lindl et al., 2004) as well as possible means of producing warm dense matter at atomic densities (Dyer et al., 2008).

5.1 Neon Rapid Sequential Ionization

The first experiment performed at LCLS tested a new regime of intense x-ray interactions with atoms (Young et al., 2010). Neon gas was chosen for the initial studies. The ionization potential of the most deeply bound state of the atom, the ground state hydrogenic Ne^{9+} ion, is 1.36 keV (10^2 Rydbergs), so that it is possible to tune the LCLS to be able to single-photon ionize the atom down to the bare nucleus. The binding energy of the 1*s* orbital in the neutral atom is 870 eV, affording the opportunity to explore near-edge photoabsorption as well: At energies less than 870 eV, all initial photoionization is via the $n = 2$ valence shells; but at energies more than this 1s absorption edge, the core is responsible for nearly all of the ionization.

One of the main goals of the Ne experiment was to verify the ability of the focused LCLS beam to produce very high charge states of atoms, and this was accomplished. Fully stripped Ne could be observed when the photon energy exceeded the 100 Ry threshold energy. When the wavelength was changed, the ion spectra changed according to the simple picture given above. This established the LCLS as a reliable source of intense x-ray radiation for physics (see Figure 10).

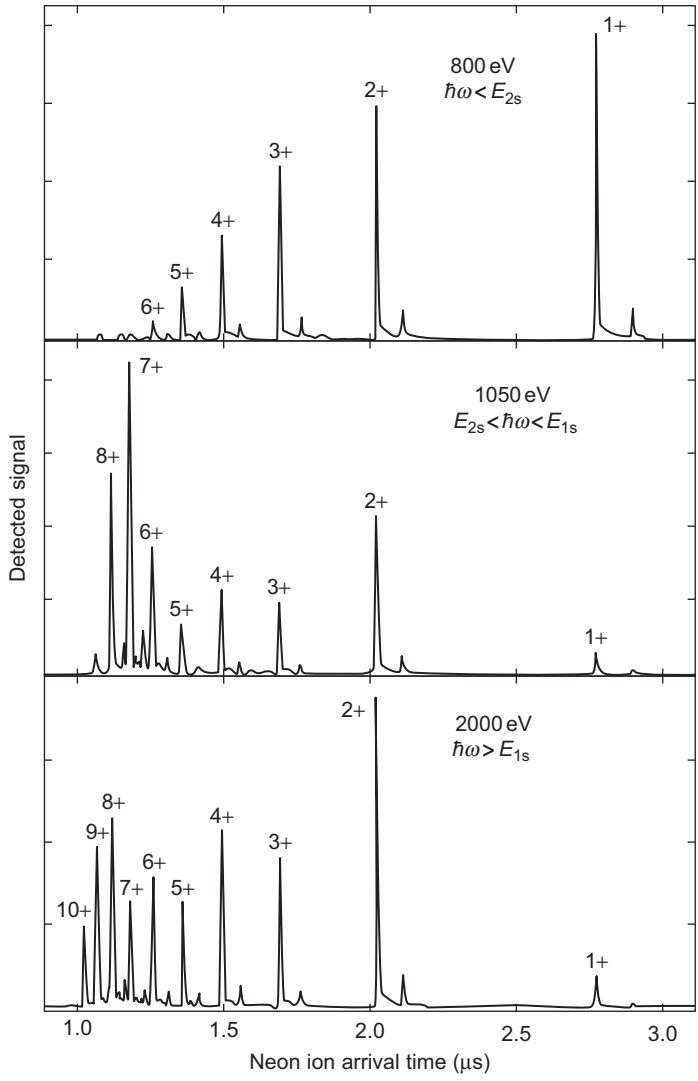

Figure 10 Ion time of flight spectra for Ne multiple photoionization at three LCLS photon energies. At 800 eV, only V-type photoionization is possible. At 1050 eV, the 1s shell cannot ionize. At 2000 eV, all electrons can be ionized, one photon at a time. Variations in the relative heights of peaks can be related to the PAPA process described in the text. From Young et al. (2010).

The neon experimental signature of PP processes was a distinct change in the apparent opacity of the Ne for 2-keV radiation when the pulse duration was varied but the fluence kept constant. For shorter pulse durations, the atoms absorbed less. Simulations show that this observation is

consistent with a decrease in photoabsorption for atoms that have lost both of their core electrons and have not yet acquired more from Auger relaxation from the valence shell. Essentially, the neon becomes a more transparent medium when there are no core electrons to contribute to the absorption cross section.

For example, atomic Ne has a ground state configuration with 10 electrons $1s^2 2s^2 2p^6$. The outer valence 2p shell consists of six equivalent p-electrons. An inner valence 2s shell has two electrons; and the core has two 1s electrons with an ionization threshold energy of 870 eV. For photon energies less than 870 eV, only *V*-type ionization is possible, and multiple ionization occurs by means of sequential *V*-type events, only terminating when the ionization potential of the most weakly bound electron in the ion becomes greater than the photon energy. At energies around 1 keV, well above the core photoabsorption edge, the dominant process is P followed closely by A, so that most x-ray absorption events produce a double ion. Further ionization events continue this PA process until the binding energy excludes them. For 1050 eV photons, which was one of the energies used by Young et al., this occurs after PAPAPA production of Ne^{6+}. After that, only valence ionization can occur, and this terminates as well, at Ne^{8+}, at which point the entire $n = 2$ shell is empty.

5.2 Nonsequential Multiphoton Processes

The one-photon threshold for the ionization of this helium-like Ne ion is 1196 eV. Further ionization of the ground state $1s^2$ configuration of Ne^{8+} at lower photon energy can only proceed by direct two-photon processes, and so they provided the first critical test of a coherence-driven process at LCLS. The starting point for understanding this nonlinear mechanism is the two-photon cross section Equation (3). This has a calculated value of $\sigma^2 = 10^{-56}$ cm^4s (Novikov & Hopersky, 2001), which is close to the simple estimate of Equation (4) (Lambropoulos & Tang, 1987). This should be visible in a tightly focused LCLS beam.

The signature of multiphoton ionization is the appearance of the photoionized daughter ion, in this case Ne^{9+}. There is, however, a significant background which comes from excited states of Ne^{8+} that must be present because of the complex sequential processes described above. Some of the same qualities that make neon ideal for studying multiple core vacancies, lead to backgrounds that cannot be easily distinguished from the nonsequential process.

Nonlinear absorption was studied in neon by comparing Ne^{9+} production rates at 1110 and 1225 eV, less than and more than the one-photon edge (Doumy et al., 2011). The lower photon energy was chosen to be more than the energy needed to ionize Ne^{6+} with one photon because the PA process from this parent is the main mechanism to produce the Ne^{8+}

initial state needed in this study. One way of rejecting background processes that also produce the Ne^{9+} final state ion is to study the dependence on incident intensity of the ratio of Ne^{9+} to Ne^{8+}, where we expect the nonsequential direct two-photon ionization to yield a quadratic dependence in intensity at 1110 eV, but the same ratio should increase linearly with intensity at 1225 eV.

Unfortunately, there are some background processes that produce Ne^{9+} and also have the same quadratic dependence of the ratio of Ne^{9+} to Ne^{8+} on x-ray intensity. For example, the PVV process in $Ne^{6+} \rightarrow Ne^{9+}$ has the same intensity dependence as the desired PAP process. Therefore, it is difficult to extract the nonsequential signal without some modeling. This analysis was performed by Doumy et al. (2011), and the result is that the direct two-photon process is clearly observed, but the estimated nonlinear cross section is two to three orders of magnitude higher than expected. There are technical uncertainties to the nonlinear cross section measurement, such as the length and temporal shape of the LCLS beam, but the largest contribution to the discrepancy is believed to be the nonlinear cross section (Doumy et al., 2011).

5.3 Intense X-Ray Induced Ionization, Dissociation, and Frustrated Absorption in Molecular Nitrogen

The interaction of intense x-rays with matter is dominated by core-shell excitation, and in particular by the competition between Auger relaxation and multiple inner-shell ionization events that become feasible at extreme x-ray intensities. These x-ray–matter interactions complement investigations carried out in the EUV regime, such as the N_2 multiple-ionization through few-photon inner-valence ionization studied at the FLASH facility (Jiang et al., 2009). Figure 4 illustrates concepts that have been proposed to describe the creation of highly charged atomic and molecular states by ultraintense, femtosecond x-ray pulses at photon energies above the core shell ionization threshold (409.9 eV). For atomic nitrogen, N, charge states up to N^{4+} may be created by two sequential inner shell photoionization (P) events followed by Auger (A) relaxation, PAPA, shown in Figure 4a. Following single-core hole (SCH) production, the ratio of the core hole lifetime and the incident photon flux determines whether double-core holes (DCH), PPAA, are produced, or if Auger decay refills the SCH before a second core vacancy is generated.

With increasing charge, Auger decay becomes slower because of the smaller number of valence electrons, and the highest charge states are predominantly created by a sequence of inner shell and valence shell ionization events. To illustrate the different types of molecular DCH states, the core electron population in N_2 is sketched in Figure 4b as if electrons would occupy separate atomic orbitals. For molecular DCH states, a PPAA

sequence leads to N_2^{4+}. For atoms, PA cycles are associated with SCHs and PPAA cycles with DCHs. A SCH N^{5+} state cannot Auger-decay (however may decay by slow fluorescence). Therefore, N^{6+} and N^{7+} are formed by continued sequential photon absorption.

There are two different types of molecular DCH states (Cederbaum et al., 1986): one corresponding to the removal of two core electrons from the same atom and the other corresponding to the removal of one electron from each of the two atoms. With increasing molecular charge state, dissociation is expected to compete with electronic relaxation, and the ionization dynamics will transition from molecular to atomic behavior. With photon energies 600–700 eV above the K edge of N_2 and pulse durations longer than the Auger-decay lifetimes, all pathways illustrated in Figure 4 are possible resulting in charge states up to N^{7+} as shown in Figure 11.

5.3.1 The Effect of Pulse Duration: Frustrated Absorption

The interest in single-pulse imaging for structure determination has raised questions about radiation damage and the ability to extract information before the sample is degraded or destroyed. Initial calculations and

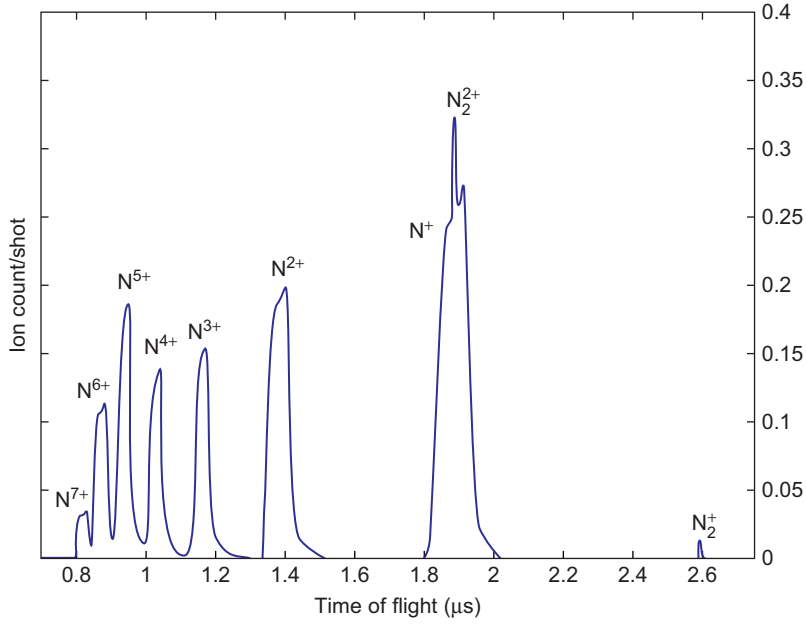

Figure 11 Ion time of flight spectrum recorded at 1-keV photon energy, 280-fs pulse duration, and fluence of 7×10^4 photon $- Å^{-2}$ (1×10^4 photon $- Å^{-2}$) corrected for photon beam losses. The central spike on top of the N_2^+ feature in the mass spectrum corresponds to stable N_2^{2+} ions.

experiments have focused on the idea of "inertial delay" of the Coulomb explosion during scattering from a pulse that is significantly shorter than the disassembly timescale for the object (Bogan et al., 2008; Chapman et al., 2006; Marchesini et al., 2008; Neutze et al., 2000). Another contribution to inertial delay in the case of sub-10 fs x-ray pulses is frustrated absorption. The effective total photoionization cross section is reduced by frustration, so that and Coulomb-repulsion effects that distort molecular samples during exposure to an imaging light pulse are reduced.

Figure 12 shows ion time of flight spectra for three different pulse durations (~7, 80, and 280 fs) at similar pulse energies (0.26 mJ, reading at LCLS beam monitor). As a reference to show where the different charge states are expected at higher intensities, the ion time of flight spectrum for 2.2 mJ, 280 fs pulses is given (light gray curve). Over the range of parameters investigated, longer pulses generally result in the observation of the highest charge states (dashed curve), whereas shorter pulses lead almost exclusively to lower charge states. The spectra in Figure 12

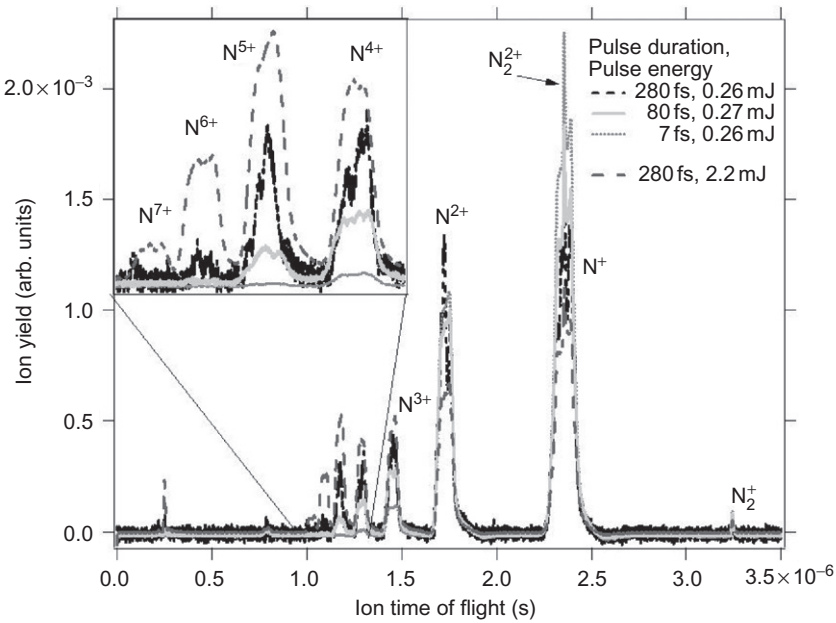

Figure 12 Ion time-of-flight mass spectra of N_2 recorded at 1100 eV at three different pulse durations and similar pulse energy (~0.26mJ, LCLS beam monitor). The inset shows the region of highly charged ions up to N^{7+}. The curve recorded at 280 fs, 2.2 mJ (energy measured by the LCLS beam monitor) serves as a reference for the positions of the different charge states. The spectra are normalized to their respective total ion yields. From Hoener et al. (2010a).

are normalized to the integrated total ion yield. Highly charged N^{5+} and N^{6+} ions are clearly observed for 80 and 280 fs pulse lengths. In contrast, the ~7 fs spectrum shows only charge states up to N^{4+}. Furthermore, the intensity of the N^{3+}, N^{4+}, and N^{5+} peaks decreases monotonically from 280 to 7 fs pulse duration. This indicates that molecular N_2 and its fragments cannot absorb photons as efficiently for short pulses as for longer pulses.

The effect shown in Figure 12 can be explained by frustrated absorption after the removal of the K-shell electrons with the short pulse. The finite Auger relaxation time determines how fast the K-shell can be replenished with electrons, and thereby limits the number of photons that can be absorbed in a given time interval. This leads to a reduction of multiple ionization events with an increasing peak power and, therefore, a suppression of the production of higher charge states for short pulses.

The interpretation of the measurements within the concept of frustrated absorption is supported by a theoretical description. The model describing the interaction of intense x-rays with nitrogen molecules consists of a parameterized rate equation model which include interatomic valence electron dynamics accounting for the delocalized nature of valence electrons (Hoener et al., 2010a). Rate equation models have previously been applied to describe intense x-ray-induced photoionization dynamics of independent atoms (Rohringer & Santra, 2007c). Figures 13a–d show the measured charge state distributions for four different x-ray pulse durations along with the results of the parameterized rate equation model. To illustrate the importance of molecular valence charge dynamics in the description of the observed effects, the results of an isolated atom based rate equation model for a pulse energy of 49 μJ have been included as dashed lines in (a)–(d).

Suppressed photon absorption at high peak intensities has been observed before in the regimes of optical and infrared light (Lewis et al., 1941) as well as soft x-ray (Nagler et al., 2009) and x-ray radiation (Young et al., 2010). However, a microscopic picture of femtosecond time resolved charge formation and frustrated absorption in molecules that includes the decisive x-ray-induced chemical dynamics has never been reported.

5.3.2 Creation of Double-Core Holes in N_2 by Nonlinear X-Ray Ionization

Conventional x-ray light sources enable access to electronic states with a single-core hole (SCH), however because of fluence limitations, the absorption of more than a single photon is unlikely. Thus, the observed interaction is dominated by linear, single-photon absorption processes.

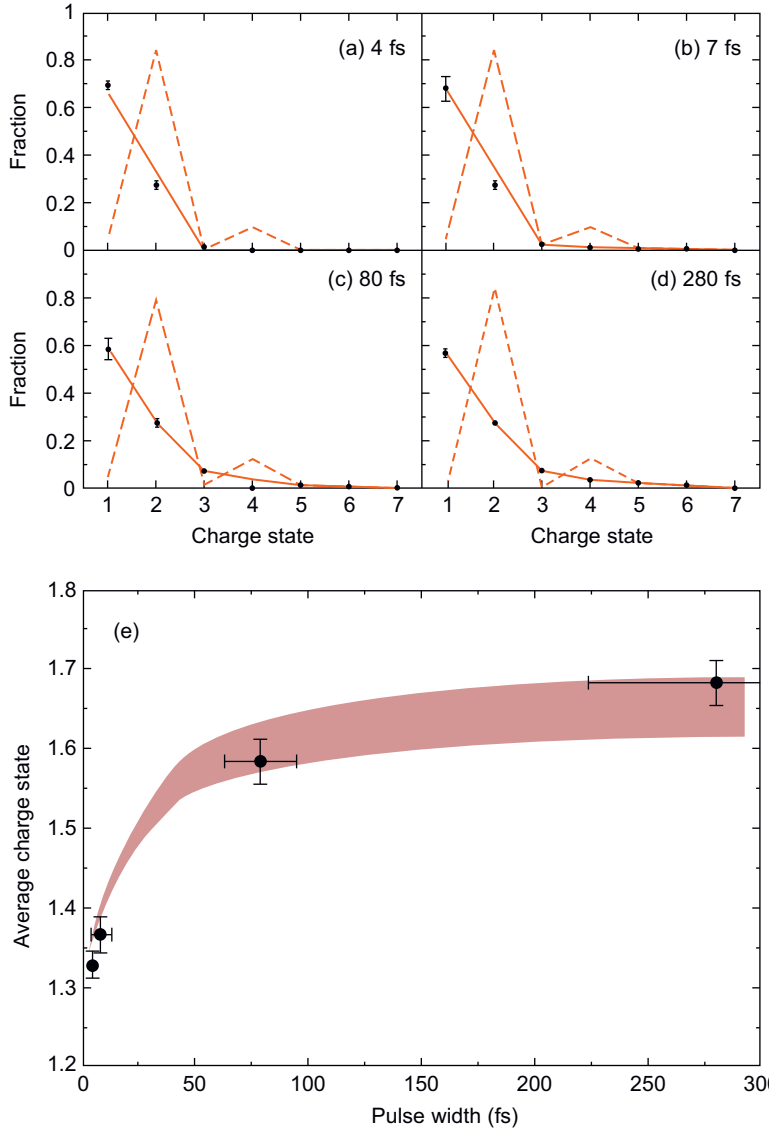

Figure 13 (a)–(d) Charge state distributions and (e) average charge states of N^{n+} ions generated in the photoionization and relaxation of N_2 molecules. The band indicates the variation of the model calculations for pulse energies between 44 μJ (17% of nominal 0.26 mJ) and 55 μJ (21% of nominal 0.26 mJ). From Hoener et al. (2010a).

Single-photon absorption of short wavelengths can also lead to the production of double-core holes (DCH) through electron correlation, but these processes have a very low yield (Eland et al., 2010; Southworth et al., 2003).

Calculations show that DCH spectroscopy can provide a richer and more sensitive technique than inner-shell photoemission spectroscopy, amplifying and rendering observable subtle differences between similar chemical systems (Cederbaum et al., 1986). Multiple atomic sites in a molecule introduce multiple possibilities for DCH locations, i.e., double-core holes with both vacancies on a single site (SSDCH) and double-core holes with a single vacancy on two different sites (TSDCH). The presence and location of the first hole affects the energy to produce the second hole, as well as the decay mechanisms and fragmentation patterns of the resulting DCH states. The different types of DCH states are expected to exhibit unique spectroscopic signatures. Furthermore, these states can show unique energetic shifts which can provide new information on the chemical environment of the core holes (Santra et al., 2009b; Tashiro et al., 2010).

DCH formation by multiple photon absorption has only become possible because of the unprecedented x-ray photon flux of the LCLS that allows sequential absorption to compete with Auger decay creating a second inner shell vacancy before the first one has been refilled (Cryan et al., 2010; Fang et al., 2010). For N_2, the Auger lifetime for a single-core hole is 6.4 fs (Kempgens et al., 1996). The production and decay of these states were characterized by using photoelectron spectroscopy and Auger electron spectroscopy. The experimental results are interpreted with the help of ab-initio Green's function calculations of the energies of the DCH states and of the Auger decay energies. These results will serve not only as a basis for understanding double- and multiple-core hole states in more complex molecules, but also for producing selective configurations with single- or double-core holes on specific atoms, ultimately controlling how these states decay and how the molecule fragment. A new technique based on the x-ray two-photon photoelectron spectroscopy (XTPPS) of such SSDCH and TSDCH states has recently been proposed (Santra et al., 2009b), and the present observations also provide the first experimental results for the method.

Figure 15 shows photoelectron spectra recorded at 1000 and 1100 eV energies using an electron time-of-flight (ETOF) spectrometer aligned along the polarization axis of the x-ray beam. The 1000-eV spectrum has been shifted to higher energies by 100 eV to allow for direct comparison with the 1100-eV spectrum. The two spectra show rich, but very similar structure. The observed structures correspond to the following:

1. Photoelectrons from single core-shell ionization of N_2, N_2^+, and N_2^{2+}, where the initial state electron vacancies are located in the valence shells. These SCH energies are indicated by the dot-dashed lines.
2. Photoelectrons from core-shell ionization of atomic N^{m+} (initial state with m valence holes). These SCH energies are indicated by the dashed lines.

3. Photoelectrons from core-shell ionization of atomic $N^{m+}(1s)$, with a single-core hole and the remaining holes in the valence shells. The processes responsible for these photoelectrons result in DCH production. These multiple state calculated energies are shown by the dotted lines.
4. Photoelectrons from core-shell ionization of $N_2^+(1s)$ with a single hole in the 1s orbital of one N atom, and the second electron ejected from the same atom, i.e., the SSDCH process. This energy is indicated by the purple solid line. Also shown is the TSDCH where the second electron is ejected from the other N atom. This energy is indicated by the solid line.

5.4 Molecular TSDCH States

Two-site double-core hole formation is a uniquely molecular phenomenon. The spectrum of the second electron ionized in this process is expected to be shifted in energy because of the coulomb potential of the first core hole. For example, the two atoms of a diatomic molecule have four possible core electrons to draw from. If the x-ray pulse ionizes the first and then does not have the required 70 eV or so to free the second electron from that core, one electron from the partner atom can be ionized. This electron will experience the added Coulomb potential from the first vacancy, but at a distance of the internuclear separation, $\sim$2 Bohr. We therefore expect to see a molecule-specific ionization channel with an absorption edge that is about 1/2 Hartree more deeply bound, or about 13 eV.

The detection and assignment of electrons associated with the production of the TSDCH states require an improved energy resolution, which is achieved by increasing the retardation voltage in the photoelectron spectrometer to 480 V. Figure 14 shows a photoelectron spectrum recorded using x-ray pulses of 1000-eV photon energy, 280-fs pulse duration, and a fluence at the focus of 10^4 photons $Å^{-2}$ per pulse. The spectrum is analyzed (Fang et al., 2010) by considering the contributions from single-photon shake-up/off (SUO) processes (Kaneyasu et al., 2008; Svensson et al., 1992) convolved with the experimental energy resolution of the current study. The dashed lines and longest shaded area in Figure 14 indicate the shape and the range of uncertainty of the SUO contributions, respectively, based on the uncertainties in assigning exact peak areas in the spectrum (Svensson et al., 1992). Note that in the single-photon ionization regime, SUO processes would generate the only contributions to the photoelectron spectrum in the kinetic energy range between 400 and 580 eV. Therefore, all photoelectron signal shown in Figure 14 that is not contained in the main photoline at 590 eV or the SUO contributions, is because of multiple photon processes that are enabled by the LCLS. In order to

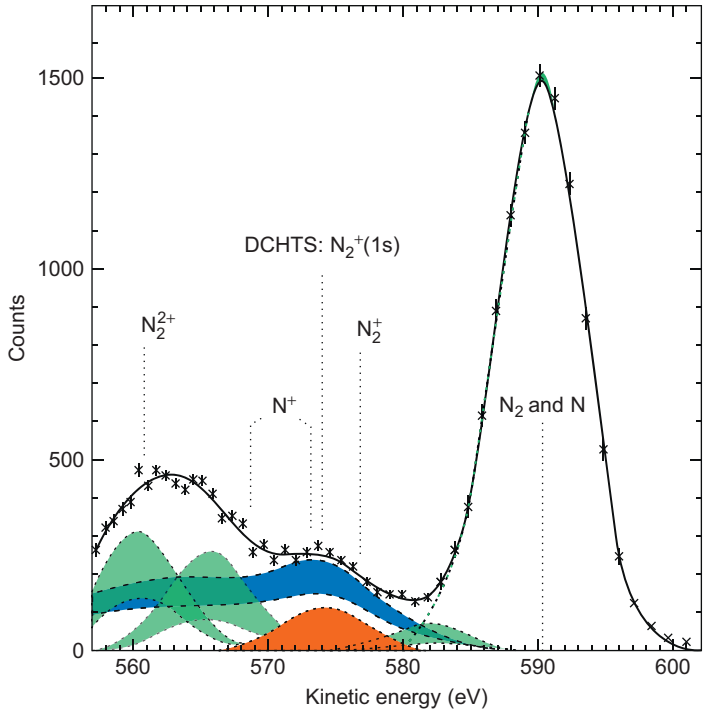

Figure 14 Photoelectron spectrum (crosses with error bars) recorded at 1-keV photon energy, 280-fs pulse duration the same fluence as in Figure 3, and 480 V spectrometer retardation voltage. The shaded areas mark the correlated uncertainties for various spectral components as described in the text. The constant sum of all components is marked by the solid black line. Calculated line positions are marked by vertical dashed lines. The shaded Gaussian area centered at 574 eV is the upper limit estimate of TSDCH contributions. From Fang et al. (2010).

disentangle the major contributions generated by multiple photon ionization, a nonlinear least-squares fit is performed based on five spectral components with identical peak shapes and independent amplitudes and center energies (shaded areas with gaussian shapes). The common peak shape is derived by a description of the well-defined main photoline by a Gaussian function, which gives a good approximation of the light-source- and apparatus-induced line broadening effects (Fang et al., 2010).

Considering the finite precision of the calculations ($\sim$1–2 eV) and the finite energy resolution of the measurements, the agreement of the experimentally derived peak positions with the theoretical expectations is mostly very good (Fang et al., 2010). In particular, one spectral component is consistently found exactly at the position of the expected TSDCH photoline (574 eV). Unfortunately, this spectral region is also marked by

the strongest SUO contributions. Additionally, the N1s-1 photoline from inner shell ionization of excited $N^+(1s^22s^12p^3)$ fragments coincides with the TSDCH photoline within the theoretical and experimental uncertainties. As indicated by the grey area, the estimate of the total multiple photon ionization signal at 574 eV varies between zero and 8% of the main photoline intensity. Given the uncertainty in the contributions from overlapping spectral components, we resort to give an upper bound for the TSDCH signal instead of an absolute value as described in Fang 2010. The analysis leads to an upper bound for TSDCH contributions in the photoelectron spectrum of 4% relative to the intensity of the N_2(1s-1) main photoline.

The most intense peak in Figure 15 corresponds to SCH production in N_2. Photoelectron lines are also clearly observed for a sequence of ionization events in higher charge states of both N_2 and N. The ionization events

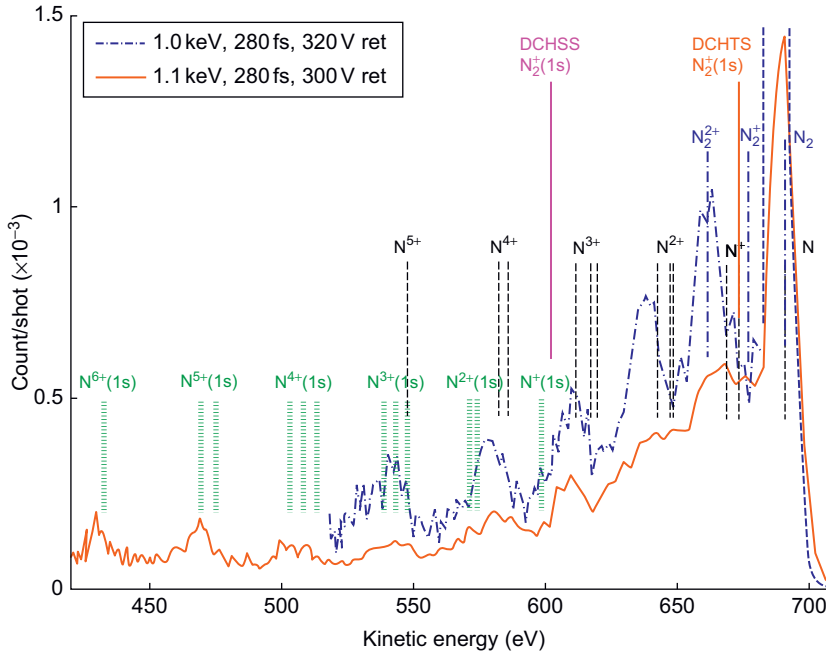

Figure 15 Photoelectron spectra recorded at 1.1 and 1.0 keV. The electron energies in the 1-keV spectrum have been shifted by 100 eV to higher kinetic energies. Vertical markers indicate the calculated photoelectron line positions for various molecular and atomic states of nitrogen: molecular SCH (dash-dotted lines), atomic SCH (dash lines), atomic DCH (dotted lines), and molecular SSDCH (thin solid line), and TSDCH (thick solid line). Marker labels indicate the initial states. The superscripts indicate the charge of the initial states being ionized. Annotation (1s) indicates that one of the initial charges is because of a core hole. From Fang et al. (2010).

leading to high charge states of atomic N are apparent and are consistent with the mass spectra shown in Figure 11. In particular, peaks corresponding to process 2 and 3 in atomic N are readily identified in Figure 15. Although all processes are produced by Auger decay and fragmentation of N_2 and molecular ions, process 3 involves sequential ionization faster than Auger decay. For the higher charge states, the reduced number of valence electrons increases the Auger lifetime, and thus increases the probability of producing atomic DCH states. The peak identification is particularly clear for $N^{4+}(1s)$, $N^{5+}(1s)$, and $N^{6+}(1s)$ ionization because no other photoelectrons are expected at energies less than $\sim$550 eV, and the observed peaks are in good agreement with the predicted line positions.

5.5 Molecular SSDCH States

Figure 15 clearly shows a substantial peak at the expected position of the molecular SSDCH photoelectron peak. However, this energy is also close to the calculated position of a peak that results from core-ionization of a triply valence-ionized nitrogen atom, and the two processes cannot be distinguished from the photoelectron data. In contrast, the decay of the molecular SSDCH state arising from neutral N_2 is expected to produce an Auger electron with kinetic energies several tens of electron volt above the main Auger peaks. Figure 16 shows the corresponding Auger spectra for N_2, where the solid curves are the experimental data and the dashed curves are our theoretical results. The experimental spectra were collected along axes perpendicular to the polarization axis to minimize contributions from direct photoionization as opposed to Auger peaks. Figure 16 shows the Auger electron spectrum, extending from 330 to 450 eV, along with a synchrotron-based spectrum and our calculated normal (nonresonant) N_2 Auger spectrum. In the region 360–370 eV the normal Auger spectrum, resulting from decay of the main SCH state of N_2 (Agren, 1981; Liegener, 1983), dominates, as demonstrated by the agreement between the experimental and theoretical spectra. Between 370 and 390 eV, weak features (satellites) are seen corresponding to Auger decay from excited (shake-up) SCH states. Above 400 eV, no Auger electrons of N_2 have been observed with conventional x-ray sources. However, the spectrum shows two new Auger peaks with energies about 50–80 eV above the main SCH Auger peaks. These high-energy Auger peaks at energies of 413 and 442 eV are called Auger hypersatellites (Southworth et al., 2003), and they are resulting from the decay of SSDCH states (Cryan et al., 2010; Fang et al., 2010). Our calculation shown in Figure 16 (shaded region at 400 and 410 eV) predicts peaks at about 410 eV, which are produced from the Auger decay of the main SSDCH state of N_2^{2+}. The prediction agrees very well with the observed peak position considering the expected

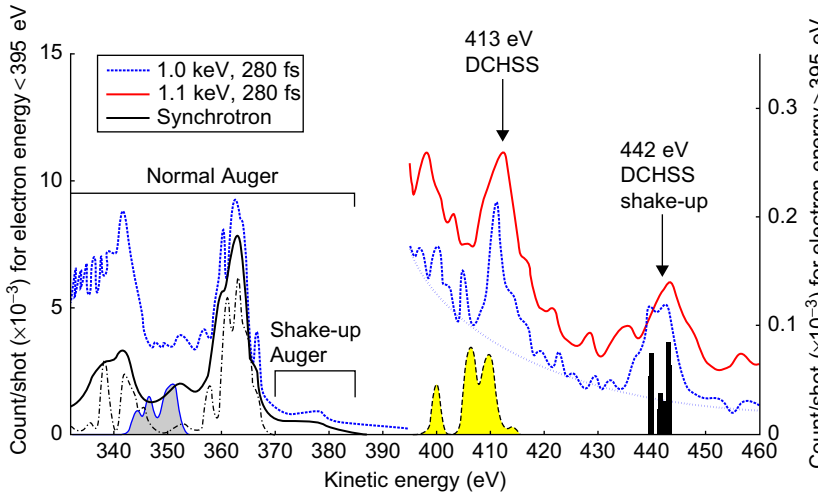

Figure 16 Auger spectra from LCLS, synchrotron experiments, and from theoretical calculations. Thick solid curves: Auger spectra recorded at 1.0 and 1.1 keV, pulse duration of 280 fs and same fluence as in Figure 15. The 1.1-keV spectrum is offset vertically up for clarity. Solid curve: Auger spectrum recorded with synchrotron source (Fang et al., 2010). Calculated Auger spectra of various initial states (heavy dashed line scaled), including SCH (dashed line), TSDCH (dotted line-shaded area), SSDCH (dotted-dashed line; shaded curve). Stems at about 440 eV indicate predicted energies of SSDCH shake-up Auger electrons. Dotted curve under SSDCH and its shake up: spline fit to background from Fang et al. (2010).

underestimate in theory of 2–4 eV because of partially unaccounted electron relaxation in the final states (Schulte et al., 1996). We estimate the SSDCH signal intensity to be 1% of the main Auger peak signal between 355 and 370 eV (5 eV).

Although Auger decay calculations of SSDCH shake-up states have not been performed explicitly, the energy splitting between the SSDCH main Auger peak and the SSDCH shake-up Auger peaks can be estimated by the energy difference between the calculated SSDCH photoline and the SSDCH shake-up photoline (Fang et al., 2010). The predicted energies of the SSDCH shake-up Auger electrons are indicated by black stem lines in Figure 16. The good agreement of the calculated positions with the peak at 442 eV suggests that this peak corresponds to Auger decay of the SSDCH shake-up states. Furthermore, the structures at 413 and 442 eV were observed at several pulse durations ranging from 280 to 80 fs, demonstrating reproducibility of the Auger hypersatellites. SSDCH with single-photon absorption has been measured very successfully using synchrotron radiations with high-detection efficiency magnetic bottles (Eland et al., 2010; Lablanquie et al., 2011).

6. FIRST OPTICAL-PUMP, X-RAY PROBE EXPERIMENTS

6.1 Dissociation of the Nitrogen Molecular Dication

The first pump-probe experiments at LCLS examined the interaction of x-rays with molecular nitrogen. The first experiment that was sensitive to the pump-probe timing synchronization was strong-field dissociation of an x-ray-prepared dication (doubly ionized) state in diatomic nitrogen (Glownia et al., 2010).

A substantial amount of the initial *K*-shell photoionization relaxes by Auger electron emission that finally leaves the doubly charged molecular dication in a quasi-bound electronic state. These quasibound states can tunnel through the barrier into the Coulombic repulsive outer part of the potential curve. This tunneling time can be as long nanoseconds to many milliseconds. An 800-nm laser pulse can effectively dissociate these states, producing two singly charged atomic fragments. This system is of interest for strong-field physics because it exhibits many characteristic strong-field phenomena such as field-dressing and bond softening (Coffee et al., 2006; Zavriyev et al., 1990). Here, however, the emphasis in this first experiment was on the timing information that could be provided by the laser-induced fragmentation of the molecular parent.

The setup is shown in Figure 17. The LCLS was tuned in the range of 1 keV and focused into nitrogen gas, where it efficiently produced the metastable doubly ionized molecular state through the process of core ionization and Auger relaxation (the PA process which has been discussed above.) The dication could be differentiated from other process by its time of arrival in the ITOF placed just below the interaction region. The LCLS 800-nm Ti:Sapphire laser was then focused into the interaction region in order to dissociate the dication. The depletion of the dication peak in the ITOF was then monitored as a function of pump-probe delay. A strong depletion signal of 10%–20% was observed when the laser arrived after the x-rays. Postprocessing was performed to re-sort the data to account for the jitter recorded in the electron RF arrival cavities discussed in Section 4.2. A synchronization of ~100-fs RMS was observed.

6.2 Transient Alignment Experiments

A diatomic molecules experiences transient impulsive Raman scattering from an intense 800-nm laser pulse. This excites it into a coherent state of rotation, following which it will evolve into a state of field-free transient alignment. Probes incident at the instant of alignment do not suffer the problem of orientational averaging because the apparatus viewing the aligned molecules is briefly in the molecular coordinate frame. Impulsive molecular alignment is a well-known technique for optical experiments

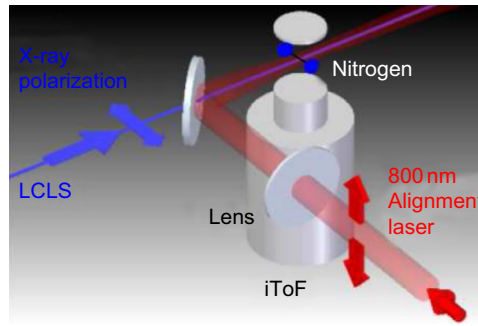

Figure 17 Pump-probe experimental setup for the nitrogen experiments. The optical laser was introduced parallel to the x-ray beam by means of a laser-turning mirror with a hole for the x-rays. From Glownia et al. (2010).

(Cryan et al., 2009; Stapelfeldt & Seideman, 2003). The alignment is nearly perfectly periodic in nitrogen at a period inversely proportional to the rotational constant because the rotational eigenvalues are almost perfectly quadratic in energy. Transient alignment methods have never been utilized before now at an x-ray source because of the need for short pulses and subpicosecond synchronization.

X-ray irradiation of the aligned molecules leads to photoabsorption followed by Auger decay, just as for an ordinary molecular beam. Some of the doubly ionized products of this process will dissociate immediately, producing two singly ionized atomic fragments with significant dissociation momentum. A few will remain as molecular dications, just as in timing experiments described above in Section 4.2. Many of the molecules and the fragment atoms can continue to absorb x-rays, through processes such as PAPA, as well as exotic multiple core vacancy processes such as PPA.

All of these processes can be seen to occur in an angle-selective ITOF whose entrance slit is placed just below the interaction region, as shown in Figure 17. The data as a function of pump-probe delay are shown for the two mass peak manifolds corresponding to the molecular and the atomic dications (Figure 18). The transient alignment and antialignment feature are clearly visible, as well as the periodic alignment revivals.

6.3 Angle Resolved Auger Analysis

Auger analysis of states produced in the PPA process has not been possible before LCLS, and these "hollow atom" states are new test beds for studies of correlation. There is a possibility to use transient double-core hole processes to study chemical dynamics as well (Santra et al., 2009b; Tashiro

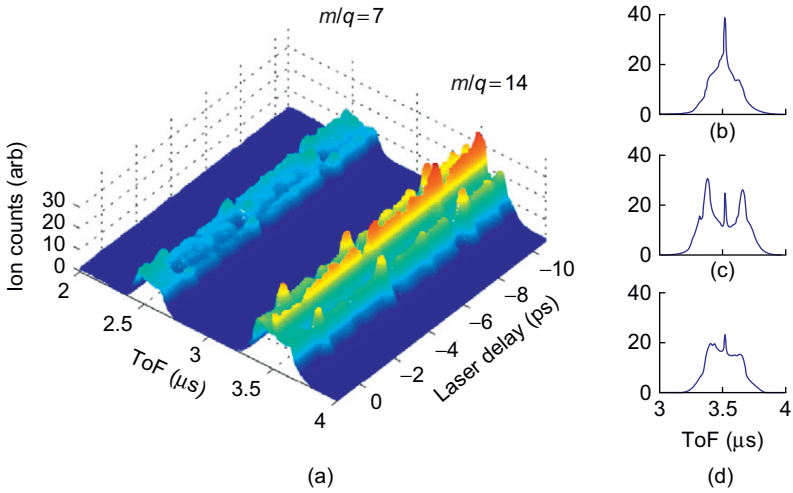

Figure 18 Angle-resolved ion time-of-flight spectra plotted as a function of the pump-probe delay for impulsively excited rotational wave packets in N_2, with ions measured along the polarization axis. (a) The spectrum near the peaks corresponding to the molecular dication N_2^{2+} and the atomic dication N^{2+}. The periodic rotational alignment revivals are clearly visible. (b)–(d) show the detailed time-of-flight spectrum of the molecular dication spectrum for three laser-x-ray delays: In (b), the delay is t = –8.5 ps. This corresponds to an alignment perpendicular to the spectrometer axis so that dissociating fragments do not enter the spectrometer. In (c), the molecules are aligned with the ITOF axis, and enter it, resulting in an ITOF spectrum that has peaks corresponding to the dissociation momentum of the x-ray-induced fragmentation. In (d), the x-rays precede the optical pulse, so no alignment occurs. From Glownia et al. (2010).

et al., 2010). Electron spectroscopy experiments were performed at a point of maximum alignment of nitrogen molecules following impulsive excitation. The Auger spectra showed the distinct signature of electrons coming from the PPA process involving two core vacancies on a single nitrogen ion (the SSDCH state discussed above in Section 5.5.) The line shape in the SSDCH region of the Auger spectrum shows similar features to the regular single vacancy Auger spectrum (the PA process), but shifted to higher energy because of the reduced screening of the nucleus (Figure 19). A calculation shows that much of the asymmetry in the SSDCH spectrum shown in Figure 19a is because of the effect of two-site interference caused by the two equivalent nitrogen atoms that can act as a source of the signal.

7. FUTURE PROSPECTS

Ultrafast core vacancy-driven dynamics may be a rich area for future studies at x-ray-free electron lasers such as LCLS. The formation of a core

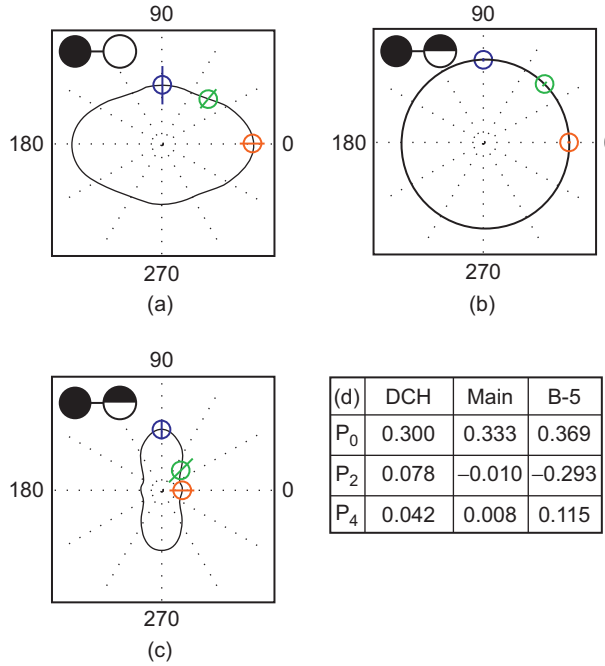

(d)	DCH	Main	B-5
P_0	0.300	0.333	0.369
P_2	0.078	–0.010	–0.293
P_4	0.042	0.008	0.115

Figure 19 Angle resolved single-site double-core hole Auger spectra for nitrogen molecules aligned horizontally in the picture. Angular distributions of the SSDCH feature (a) are compared to (b) the angular distribution from the total single vacancy Auger spectrum, and (c) the angular distribution of the most prominent peak in the single vacancy Auger spectrum at 360 eV. Panel (d) are fitting coefficients to Legendre polynomials. From Cryan et al. (2010).

vacancy in only a few femtoseconds may be viewed as sudden creation of a charge disturbance that is quite localized. The resulting coulomb-driven electron relaxation can lead to the breaking or forming of new bonds. A particularly rich area for study may be hydrogen migration driven by photoexcitation.

The dynamics of core hole relaxation has been studied in early LCLS experiments. We briefly describe some of the motivations for these kinds of investigations, as well as the instrumentation required to extract transient structural information. The basic experiment involves excitation of the target molecule by a laser, either through ultrafast resonant excitation or strong-field coupling. Subsequent evolution of the system could lead to isomerization, ionization, photofragmentation, or even the extreme Coulomb explosion following multiple electron ejection. In any case, the transient nuclear motion can be probed in several ways using x-rays.

Atom-selective core ionization is one of the most revealing techniques. Here the x-rays are tuned just near an absorption edge for atoms of a particular type in a molecule. For example, in methyl alcohol one could selectively probe the vicinity of the oxygen atom by using radiation in the vicinity of the O K-edge. This energy is accessible at LCLS.

The femtosecond pulse durations of LCLS permit the study of transient processes such as isomerization and photofragmentation. The x-rays can be used to probe shifting energy levels, in analogy to optical pump-probe spectroscopy. Here the advantage of the x-rays is that they probe local structure in the vicinity of an atomic core. Ultrafast x-ray pulses can also induce molecular rearrangement, which can be probed by strong lasers.

Resonant excitation has some limitations in the case of multiple atoms of the same species. Even though different chemical environments will lead to edge shifts on the order of electron volt, the LCLS cannot generally differentiate between these atoms without the aid of a monochromator, which reduces the laser pulse energy substantially. In addition, many of the most interesting chemical changes involve carbon atoms in small organic molecules, and these wavelengths, on the order of 284 eV, cannot be reached by LCLS. Therefore, nonresonant detection must be used.

Another technique is momentum analysis of photofragments. As an example, consider the fragmentation of two similar ring molecules, 1,3-cyclohexadiene and 1,4-cyclohexadiene. These ring molecules are C_6H_8 isomers consisting of a benzene ring with two additional hydrogen atoms. The only difference between them is the relative placement of the extra hydrogens, which leads to the formation of double bonds in the 1,3 or 1,4 positions, respectively. K-shell photoionization with the relatively high energy of LCLS cannot discriminate one of these bonds vs. another. However, the different absorption channels can be detected by their different photofragment momenta. Such analysis techniques make use of position-sensitive time-of-flight detectors, known as velocity-map imaging.

7.1 Coherence Effects

One prospect of interest is electromagnetically induced transparency in the x-ray regime (Glover et al., 2010). Originally proposed as a potential scheme for cleaning the chaotic fluctuations of typical FEL pulses, this scheme is also interesting from a fundamental physics point of view. The quintessential indicator of EIT is the narrowing of a traditionally broad absorption line, accompanied by an Autler-Townes splitting of the resonance. In the soft x-ray regime for instance, the linewidths are typically of the order of tenths of electron volts. Excited state linewidths however

are of order few electron volts owing to their rapid relaxation. One could therefore imagine a lambda system with a core-excited upper state that is for instance in a shape resonance in the continuum that can then be coupled strongly to the ground-state. Such a system could be driven into EIT if the ground-state stability could effectively be made to narrow the shape resonance width and then split the resonance through Autler-Townes splitting. This would suppress the absorption of the x-rays by driving coherence in the electronic system.

A straightforward application of time domain spectroscopy is to measure the x-ray pulse duration or, alternatively, the relaxation rate of core excitations. To first order, the photoabsorption cross section is proportional to the number of electrons available for absorption. Reducing the number of electrons in a shell simply reduces the absorption cross section proportionately. This saturation effect may be used to autocorrelate an ultrafast x-ray beam in a split and delay arrangement, which would also be a direct way to measure the core refilling when the x-ray pulses are shorter than the lifetime of the vacancy.

One could use two x-ray pulses of different frequency in the high-fluence regime of Equation (10) to investigate core-hole relaxation for specific channels directly in the time domain. In the sequential regime (PAPA), when the core-excitation relaxes, either by fluorescence or Auger decay, a new vacancy will open in the valence shell. If we assume a KL1L1 relaxation, we would expect the $[2s\sigma^{-2}]$ excitation to persist for many hundreds of picoseconds. Because the relaxation refilled the core level, the overall absorption cross section returns although the edge is shifted by the now doubly charged Coulomb field. Below the edge, however, the inner-valence vacancy can accept a resonant excitation from the core for a subsequent x-ray pulse. Unfortunately, the newly born resonance will lie some tens of electron volt lower in energy than the original absorption edge. Furthermore, the valence states will feel a reduced screening, yet the filled core will feel nearly the same binding as the neutral. The only way to observe this phenomenon is either by optically preparing it (Glover et al., 2010) or using a two-color x-ray scheme. With the two-color x-ray scheme, one could in principle measure specific lifetimes for the different Auger and fluorescence decay channels.

7.2 Improved DCH Electron Spectroscopy

The sequential formation of a double-core hole is of particular interest in physical chemistry; the double-core hole is effectively a chemical shift amplifier. When the double-core hole is distributed among different sites in a molecule, the resulting photoelectron and Auger spectra are much more sensitive to the valence binding environment than are the more traditional single core-hole excitations (Cederbaum et al., 1986, 1987; Santra

et al., 2009a). The enhanced sensitivity for the two-hole system arises from the screening of the hole–hole interaction by the valence electron density that fills the volume between the two sites. To first order, the two half vacant cores undergo a $1/R^3$ dipole–dipole interaction that is more or less quenched by the induced polarization of the valence shell. The quenching is therefore a strong function of the occupied number of valence bonding versus antibonding orbitals. This system relaxes on a timscale short compared with typical nuclear motion. It could therefore be used as a time-stop measurement of the dynamically changing valence during a photo-triggered chemical reaction (Cryan et al., 2010; Fang et al., 2010; Santra et al., 2009a).

The analysis of the photo- and Auger-electron spectra presented here and explained in detail in Fang et al. (2010) shows a very encouraging agreement between the theoretically predicted and the experimentally determined positions of DCH features. In particular, the hypersatellite spectrum allows for a clear identification of SSDCH contributions in good agreement with theory. However, it is also evident that a clear identification of double-core hole states that comprise core vacancies on more than one atom is rather challenging. The two major limiting factors are the spectral overlap with SCH features in both the photoelectron and the Auger-electron spectrum and the available power densities in the interaction region of the LCLS AMO end station (Bozek, 2009). The improvement of the latter, in addition to measuring the SCH contribution by defocusing the FEL beam, allowed in a recent investigation in the fall of 2010 a much clearer distinction of TSDCH contributions. There are more recent measurements of SSDCH and TSDCH in $N_2, CO, CO_2,$ and N_2O and the data is being compared with new ab initio calculations (Tarantelli, 2006).

7.3 Large Molecular Dynamics/Clusters

Photoionization of larger molecules such as H_2S and SF_6 have also been carried out with a pulse duration of 280 fs and nominal pulse energy of 2 mJ. Complete Coulomb explosion was observed leading to a high charged state distribution of the S and F fragments. Furthermore, van der Waal clusters photoionization experiments were conducted as a function of pulse duration and pulse intensity leading to surprising results compared with ionization with IR lasers or VUV FELs. This work is presently being analyzed.

7.4 Resonance Phenomena Using the SXR Beam Line

The soft x-ray (SXR) beam line is a second experimental area that has been commissioned following the first experiments described in this review. It affords the opportunity to tune the LCLS wavelength through resonances

thanks to the use of its monochromator, with a resolving power on the order of 5000, which access energies between 500 and 2000 eV. Several important K- and L-edges are covered for resonant excitation of the second- and third-row elements. This beam line, which was successfully commissioned in the fall of 2010, has already been used for various experiments such as laser pump-x-ray probe investigations in the gas–liquid and solid phase which are poised to provide new physical and chemical understanding. In particular, one of the use of the SXR beam line is to observe electrons in controlled correlated motion in various states of matter. The science that can be performed at the SXR beam line covers widespread fields such as catalysis, magnetism, correlated materials, clusters, and biological structure.

All techniques used on the SXR beam line are single shot, pump probe, and resonant excitation compatible. The range of methods includes single-shot x-ray absorption spectroscopy, resonant coherent imaging, x-ray diffraction (from solids), x-ray emission spectroscopy (on solids, surfaces, warm dense plasma), liquid jet x-ray science, resonant inelastic x-ray scattering, photo-electron spectroscopy (on surfaces), coherent x-ray scattering (transmission or reflection), materials damage thresholds studies, and electron beam ion studies.

7.5 Second-Generation Instrument: LAMP

A second-generation end-station, significantly advancing the present state-of-the-art instrumentation and allowing for structural dynamics experiments across a wide range of science areas is being constructed by a collaboration among LCLS, Max Planck Society Advanced Study Group (ASG), and Western Michigan University for the LCLS. This instrumentation consists of three essential parts:

1. A two mirror "x-ray split and delay" (XRSD) to enable x-ray-pump-x-ray-probe experiments.
2. An OPA (optical parametric amplifier stage) laser providing intense, ultrashort laser pulses over a wide range of wavelengths for two-color pump-probe experiments together with the required optics.
3. A multipurpose end-station supporting experiments ranging from AMO to chemistry, warm dense matter (WDM), surface physics, and biological and inorganic particle imaging.

In its overall design, the end-station is inspired by the Center for Free Electron Lasers (CFEL) Multi-Purpose, CAMP instrument (Strüder et al., 2010), but offers significant additional capabilities, as briefly outlined below.

Some of the future scientific directions that will be enabled by LAMP include (1) photoelectron holography to "make a molecular movie," (2) a

new class of multiparameter experiments in gas, liquid, and solid matter, exploring ultrafast dynamics in highly excited matter, and (3) high-resolution spectrometers that will help to disentangle the formation and decay of molecular two-side double-core hole states (TSDCH) using a magnetic bottle detector in order to measure the TSDCH in various molecules. Visions of the science that will be enabled by x-ray-pump-x-ray-probe measurements might be extrapolated from first results of similar VUV-VUV pump-probe experiments at the FLASH and the SCSS facilities. Among them are the ultrafast tracing of molecular wave-packets in D_2^+ which delivered, for the first time, information on the internuclear distance dependence of VUV photoionization cross sections (Jiang et al., 2010b) and on the isomerization dynamics of $[C_2H_2]^+$ cations (Jiang et al., 2010a). Studies demonstrate time resolutions on the order of the coherence lengths of the radiation (Pfeifer et al., 2010), pointing to the fascinating possibility to achieve subfemtosecond time resolution with the LAMP split-mirror unit at LCLS. In addition to providing a direct measurement of the longitudinal coherence length, information on the transverse coherence of the LCLS beam can be achieved as well. The ability to follow electronic wave packet dynamics in molecules with the goal to perform precision spectroscopy experiments in the time domain through Fourier analysis of the time-dependent wave-packet motion is also being explored.

ACKNOWLEDGMENTS

This work was supported by the U.S. Department of Energy Office of Basic Energy Sciences for the PULSE Institute at SLAC and by the Chemical Sciences, Geosciences, and Biosciences Division of BES under contracts DE-FG02-92ER14299. We thank the LCLS staff for providing an excellent x-ray laser source, mechanical and electrical support of the AMO instrument data transport support.

REFERENCES

Ackermann, W., Asova, G., Ayvazyan, V., Azima, A., Baboi, N., Bahr, J., et al. (2007). Operation of a free-electron laser from the extreme ultraviolet to the water window. *Nature Photonics*, *1*(6), 336–342.

Agren, H. (1981). On the interpretation of molecular valence auger spectra. *The Journal of Chemical Physics*, *75*(3), 1267–1283.

Ammosov, M. V., Delone, N. B., & Krainov, V. P. (1986). Tunnel ionization of complex atoms and atomic ions in a varying electromagnetic-field. *Zhurnal Eksperimentalnoi I Teoreticheskoi Fiziki*, *91*(6), 2008–2013.

Barty, A., Soufli, R., McCarville, T., Baker, S. L., Pivovaroff, M. J., Stefan, P., et al. (2009). Predicting the coherent x-ray wavefront focal properties at the linac coherent light source (LCLS) X-ray free electron laser. *Optics Express*, *17*(18), 15508–15519.

Benware, B. R., Ozols, A., Rocca, J. J., Artioukov, I. A., Kondratenko, V. V., & Vinogradov, A. V. (1999). Focusing of a tabletop soft-x-ray laser beam and laser ablation. *Optics Letters*, *24*(23), 1714–1716.

Berrah, N., Bozek, J., Costello, J. T., Dsterer, S., Fang, L., Feldhaus, J., et al. (2010). Non-linear processes in the interaction of atoms and molecules with intense EUV and X-ray fields from sase free electron lasers (FELs). *Journal of Modern Optics*, *57*(12), 1015–1040.

Bogan, M. J., Benner, W. H., Boutet, S., Rohner, U., Frank, M., Barty, A., et al. (2008). Single particle X-ray diffractive imaging. *Nano Letters*, *8*(1), 310–316.

Bonifacio, R., De Salvo, L., Pierini, P., Piovella, N., & Pellegrini, C. (1994). Spectrum, temporal structure, and fluctuations in a high-gain free-electron laser starting from noise. *Physical Review Letters*, *73*, 70–73.

Bozek, J. D. (2009). Amo instrumentation for the LCLS x-ray FEL. *The European Physical Journal - Special Topics*, *169*, 129–132.

Cavaliere, P., Ferrante, G., & Leone, C. (1980). Particle-atom ionising collisions in the presence of a laser radiation field. *Journal of Physics B: Atomic and Molecular Physics*, *13*(22), 4495–4507.

Cavalieri, A. L., Fritz, D. M., Lee, S. H., Bucksbaum, P. H., Reis, D. A., Rudati, J., et al. (2005). Clocking femtosecond x rays. *Physical Review Letters*, *94*(11), 114801.

Cederbaum, L., Tarantelli, F., Sgamellotti, A., & Schirmer, J. (1986). On double vacancies in the core. *The Journal of Chemical Physics*, *85*, 6513–6523.

Cederbaum, L., Tarantelli, F., Sgamellotti, A., & Schirmer, J. (1987). Double vacancies in the core of benzene. *The Journal of Chemical Physics*, *86*, 2168–2175.

Chapman, H. N., Barty, A., Bogan, M. J., Boutet, S., Frank, M., Hau-Riege, S. P., et al. (2006). Femtosecond diffractive imaging with a soft-x-ray free-electron laser. *Nature Physics*, *2*(12), 839–843.

Coffee, R. N., Fang, L., & Gibson, G. N. (2006). Light-induced potentials ignite dissociation of N_2^{2+}. *Physical Review A*, *73*, 043417.

Corkum, P., Silvestri, S., Nelson, K. A., Riedle, E., & Schoenlein, R. W. (Eds.), (2009). *Ultrafast Phenomena XVI (Proceedings of the 16th International Conference on Ultrafast Phenomena)*. Palazzo dei Congressi Stresa, Italy, June 9-13, 2008, Springer *Series in Chemical Physics*, 92, p. 667.

Cryan, J. P., Bucksbaum, P. H., & Coffee, R. N. (2009). Field-free alignment in repetitively kicked nitrogen gas. *Physical Review A*, *80*, 063412.

Cryan, J. P., Glownia, J. M., Andreasson, J., Belkacem, A., Berrah, N., Blaga, C. I., et al. (2010). Auger electron angular distribution of double core-hole states in the molecular reference frame. *Physical Review Letters*, *105*(8), 083004.

Daido, H. (2002). Review of soft x-ray laser researches and developments. *Reports on Progress in Physics*, *65*(10), 1513.

Ding, Y., & Huang, Z. (2010). Transverse-coherence properties of the FEL at the LCLS. Menlo Park, CA: SLAC publication SLAC-PUB-14235.

Dörner, R., Mergel, V., Jagutzki, O., Spielberger, L., Ullrich, J., Moshammer, R., et al. (2000). Cold target recoil ion momentum spectroscopy: a 'momentum microscope' to view atomic collision dynamics. *Physics Reports*, *330*(2–3), 95–192.

Doumy, G., Roedig, C., Son, S.-K., Blaga, C. I., DiChiara, A. D., Santra, R., et al. (2011). Nonlinear atomic response to intense ultrashort x rays. *Physical Review Letters*, *106*(8), 083002.

Dunn, J., Li, Y., Osterheld, A. L., Nilsen, J., Hunter, J. R., & Shlyaptsev, V. N. (2000). Gain saturation regime for laser-driven tabletop, transient ni-like ion x-ray lasers. *Physical Review Letters*, *84*(21), 4834–4837.

Dyer, G. M., Bernstein, A. C., Cho, B. I., Osterholz, J., Grigsby, W., Dalton, A., et al. (2008). Equation-of-state measurement of dense plasmas heated with fast protons. *Physical Review Letters*, *101*(1), 015002.

Eland, J. H. D., Tashiro, M., Linusson, P., Ehara, M., Ueda, K., & Feifel, R. (2010). Double core hole creation and subsequent auger decay in NH_3 and CH_4 molecules. *Physical Review Letters*, *105*(21), 213005.

Emma, P., Akre, R., Arthur, J., Bionta, R., Bostedt, C., Bozek, J., et al. (2010). First lasing and operation of an angstrom-wavelength free-electron laser. *Nature Photonics*, *4*(9), 641–647.

Epp, S. W., Graafsma, H., Hartmann, R., Hirsemann, H., Kahnel, K. U., Rolles, D., et al. (2009). Camp: A new endstation for simultaneous detection of photons and charged particles in free electron lasers experiments. *Journal of Physics: Conference Series*, *194*(14), 142017.
Faisal, F. H. M. (1973). Multiple absorption of laser photons by atoms. *Journal of Physics B: Atomic and Molecular Physics*, *6*(4), L89.
Fang, L., Hoener, M., Gessner, O., Tarantelli, F., Pratt, S. T., Kornilov, O., et al. (2010). Double core hole production in N2: Beating the auger clock. *Physical Review Letters*, *105*, 083005.
Feldhaus, J., Arthur, J., & Hastings, J. B. (2005). X-ray free-electron lasers. *Journal of Physics B: Atomic, Molecular and Optical Physics*, *38*(9), S799.
FLASH, (2011). Free-electron laser flash. http://flash.desy.de/
Friedrich, H. (1994). *Theoretical atomic physics* (2nd ed.). Berlin: Springer-Verlag, Ch. 3.4.3 - Atoms in an oscillating electric field, pp. 189–192.
Gallagher, T. (1994). *Rydberg atoms*. Cambridge: Cambridge Press, Ch. 7.
Glover, T. E., et al. (2010). Controlling x-rays with light. *Nature Physics*, *6*, 69.
Glownia, J. M., Cryan, J., Andreasson, J., Belkacem, A., Berrah, N., Blaga, C. I., et al. (2010). Time-resolved pump-probe experiments at the LCLS. *Optics Express*, *18*(17), 17620–17630.
Gutt, C., Stadler, L.-M., Streit-Nierobisch, S., Mancuso, A. P., Schropp, A., Pfau, B., et al. (2009). Resonant magnetic scattering with soft x-ray pulses from a free-electron laser operating at 1.59 nm. *Physical Review B*, *79*(21), 212406.
Hau, L. V., Harris, S. E., Dutton, Z., & Behroozi, C. H. (1999). Light speed reduction to 17 metres per second in an ultracold atomic gas. *Nature*, *397*(6720), 594–598.
Hau-Riege, S. P., London, R. A., Bionta, R. M., Ryutov, D., Soufli, R., Bajt, S., et al. (2009). Wavelength dependence of the damage threshold of inorganic materials under extreme-ultraviolet free-electron-laser irradiation. *Applied Physics Letters*, *95*(11), 111104.
Hau-Riege, S. P., London, R. A., Graf, A., Baker, S. L., Soufli, R., Sobierajski, R., et al. (2010). Interaction of short x-ray pulses with low-z x-ray optics materials at the LCLS free-electron laser. *Optics Express*, *18*(23), 23933–23938.
Hemmers, O., Whitfield, S. B., Glans, P., Wang, H., Lindle, D. W., Wehlitz, R., et al. (1998). High-resolution electron time-of-flight apparatus for the soft x-ray region. *Review of Scientific Instruments*, *69*(11), 3809–3817.
Hendrickson, W. (1991). Determination of macromolecular structures from anomalous diffraction of synchrotron radiation. *Science*, *254*(5028), 51–58.
Hoener, M., Rolles, D., Aguilar, A., Bilodeau, R. C., Esteves, D., Velasco, P. O., et al. (2010a). Site-selective ionization and relaxation dynamics in heterogeneous nanosystems. *Physical Review A*, *81*(2), 021201.
Hoener, M., et al. (2010b). Ultraintense x-ray induced ionization, dissociation, and frustrated absorption in molecular nitrogen. *Physical Review Letters*, *104*, 253002.
Huang, Z., & Kim, K.-J. (2007). Review of x-ray free-electron laser theory. *Physical Review Special Topics-Accelerators Beams*, *10*(3), 034801.
Iverson, R. (2011). Lcls parameters. https://slacportal.slac.stanford.edu/sites/lclscore_public/Accelerator_Physics_Published_Documents/LCLS-parameters.pdf
Jiang, Y. H., Pfeifer, T., Rudenko, A., Herrwerth, O., Foucar, L., Kurka, M., et al. (2010a). Temporal coherence effects in multiple ionization of N_2 via XUV pump-probe autocorrelation. *Physical Review A*, *82*(4), 041403.
Jiang, Y. H., Rudenko, A., Kurka, M., Kühnel, K. U., Ergler, T., Foucar, L., et al. (2009). Few-photon multiple ionization of N_2 by extreme ultraviolet free-electron laser radiation. *Physical Review Letters*, *102*(12), 123002.
Jiang, Y. H., Rudenko, A., Pérez-Torres, J. F., Herrwerth, O., Foucar, L., Kurka, M., et al. (2010b). Investigating two-photon double ionization of D_2 by XUV-pump–XUV-probe experiments. *Physical Review A*, *81*(5), 051402.
Kaneyasu, T., Hikosaka, Y., Shigemasa, E., Lablanquie, P., Penent, F., & Ito, K. (2008). Auger decays of 1s shake-up and shake-off states in N2 molecules. *Journal of Physics B: Atomic, Molecular and Optical Physics*, *41*(13), 135101.
Kash, M. M., Sautenkov, V. A., Zibrov, A. S., Hollberg, L., Welch, G. R., Lukin, M. D., et al. (1999). Ultraslow group velocity and enhanced nonlinear optical effects in a coherently driven hot atomic gas. *Physical Review Letters*, *82*(26), 5229–5232.
Keldysh, L. V. (1965). Ionization in the field of a strong electromagnetic wave. *Soviet Physics JETP*, *20*, 1307–1314.

Kempgens, B., KivimÃki, A., Neeb, M., Kppe, H. M., Bradshaw, A. M., & Feldhaus, J. (1996). A high-resolution n 1s photoionization study of the n_2 molecule in the near-threshold region. *Journal of Physics B: Atomic, Molecular and Optical Physics*, *29*(22), 5389–5402.

Kirkpatrick, P., & Baez, A. V. (1948). Formation of optical images by x-rays. *Journal of the Optical Society of America*, *38*(9), 766–773.

Krausz, F., & Ivanov, M. (2009). Attosecond physics. *Reviews of Modern Physics*, *81*(1), 163–234.

Lablanquie, P., Penent, F., Palaudoux, J., Andric, L., Selles, P., Carniato, S., et al. (2011). Properties of hollow molecules probed by single-photon double ionization. *Physical Review Letters*, *106*(6), 063003.

Lambropoulos, P., & Tang, X. (1987). Multiple excitation and ionization of atoms by strong lasers. *Journal of the Optical Society of America B*, *4*(5), 821–832.

LCLS, (2010). http://lcls.slac.stanford.edu.

Lewenstein, M., Balcou, P., Ivanov, M. Y., L'Huillier, A., & Corkum, P. B. (1994). Theory of high-harmonic generation by low-frequency laser fields. *Physical Review A*, *49*(3), 2117–2132.

Lewis, G., Lipkin, D., & Magel, T. (1941). Reversible photochemical processes in rigid media. a study of the phosphorescent state. *Journal of the American Chemical Society*, *63*(11), 3005–3018.

Liegener, C. M. (1983). Calculations on the auger spectrum of N2. *Journal of Physics B: Atomic and Molecular Physics*, *16*(23), 4281.

Lindl, J., Amendt, P., Berger, R., Glendinning, S., Glenzer, S., Haan, S., et al. (2004). The physics basis for ignition using indirect-drive targets on the national ignition facility. *Physics of Plasmas*, *11*(2), 339–491.

Marchesini, S., Boutet, S., Sakdinawat, A. E., Bogan, M. J., Bajt, S., Barty, A., et al. (2008). Massively parallel x-ray holography. *Nature Photonics*, *2*(9), 560–563.

McFarland, B. K., Farrell, J. P., Bucksbaum, P. H., & Guhr, M. (2008). High harmonic generation from multiple orbitals in N2. *Science*, *322*(5905), 1232–1235.

Meystre, P., & Sargent, M. III (1990). *Elements of quantum optics*. Berlin: Springer-Verlag, Ch. 13 – Interaction Between Atoms and Quantized Fields, pp. 336–360.

Murphy, J., & Pellegrini, C. (1985). Free electron lasers for the XUV spectral region. *Nuclear Instruments and Methods in Physics Research Section A: Accelerators, Spectrometers, Detectors and Associated Equipment*, *237*(1–2), 159–167.

Nagler, B. et al. (2009). Turning solid aluminium transparent by intense soft x-ray photoionization. *Nature Physics*, *5*(9), 693–696.

Neutze, R., Wouts, R., van der Spoel, D., Weckert, E., & Hajdu, J. (2000). Potential for biomolecular imaging with femtosecond x-ray pulses. *Nature*, *406*(6797), 752–757.

Novikov, S. A., & Hopersky, A. N. (2001). Two-photon excitation-ionization of the 1s shell of highly charged positive atomic ions. *Journal of Physics B: Atomic, Molecular and Optical Physics*, *34*(23), 4857–4864.

Pešić, Z., Rolles, D., Perri, M., Bilodeau, R. C., Ackerman, G. D., Rude, B. S., et al. (2007). Velocity map ion imaging applied to studies of molecular fragmentation with synchrotron radiation. *Journal of Electron Spectroscopy and Related Phenomena*, *155*, 155–159.

Pfeifer, T., Jiang, Y., Düsterer, S., Moshammer, R., & Ullrich, J. (2010). Partial-coherence method to model experimental free-electron laser pulse statistics. *Optics Letters*, *35*(20), 3441–3443.

Prümper, G., Fukuzawa, H., Rolles, D., Sakai, K., Prince, K. C., Harries, J. R., et al. (2008). Is CO carbon *KVV* auger electron emission affected by the photoelectron. *Physical Review Letters*, *101*(23), 233202.

Rabi, I. I., Millman, S., Kusch, P., & Zacharias, J. R. (1939). The molecular beam resonance method for measuring nuclear magnetic moments. the magnetic moments of ${}_3li^6$, ${}_3li^7$ and ${}_9f^{19}$. *Physical Review*, *55*(6), 526–535.

Reiss, H. R. (1980). Effect of an intense electromagnetic field on a weakly bound system. *Physical Review A*, *22*(5), 1786–1813.

Reiss, H. R. (2010). Unsuitability of the Keldysh parameter for laser fields. *Physical Review A*, *82*(2), 023418.

Rohringer, N., & Santra, R. (2007a). X-ray nonlinear optical processes using a self-amplified spontaneous emission free-electron laser. *Physical Review A*, *76*(3), 033416.
Rohringer, N., & Santra, R. (2007b). X-ray nonlinear optical processes using a self-amplified spontaneous emission free-electron laser. *Physical Review A*, *76*, 033416.
Rohringer, N., & Santra, R. (2007c). X-ray nonlinear optical processes using a self-amplified spontaneous emission free-electron laser. *Physical Review A*, *76*(3), 033416.
Rolles, D., Prümper, G., Fukuzawa, H., Liu, X.-J., Pešić, Z. D., Fink, R. F., et al. (2008). Molecular-frame angular distributions of resonant $co : c(1s)$ auger electrons. *Physical Review Letters*, *101*(26), 263002.
Saldin, E., Schneidmiller, E., & Yurkov, M. (2000). *The physics of free electron lasers*. Berlin: Springer-Verlag.
Saldin, E., Schneidmiller, E., & Yurkov, M. (2008). Coherence properties of the radiation from x-ray free electron laser. *Optics Communications*, *281*(5), 1179–1188.
Santra, R., Kryzhevoi, N., & Cederbaum, L. (2009a). X-ray two-photon photoelectron spectroscopy: A theoretical study of inner-shell spectra of the organic para-aminophenol molecule. *Physical Review Letters*, *103*, 013002.
Santra, R., Kryzhevoi, N. V., & Cederbaum, L. S. (2009b). X-ray two-photon photoelectron spectroscopy: A theoretical study of inner-shell spectra of the organic para-aminophenol molecule. *Physical Review Letters*, *103*(1), 013002.
Schöffler, M. S., Titze, J., Petridis, N., Jahnke, T., Cole, K., Schmidt, L. P. H., et al. (2008). Ultrafast probing of core hole localization in N2. *Science*, *320*(5878), 920–923.
Schulte, H. D., Cederbaum, L. S., & Tarantelli, F. (1996). Core-valence doubly ionized states: General aspects, examples, production mechanisms. *The Journal of Chemical Physics*, *105*(24), 11108–11133.
Southworth, S. H., Kanter, E. P., Krässig, B., Young, L., Armen, G. B., Levin, J. C., et al. (2003). Double k-shell photoionization of neon. *Physical Review A*, *67*(6), 062712.
Stapelfeldt, H., & Seideman, T. (2003). Colloquium: Aligning molecules with strong laser pulses. *Reviews of Modern Physics*, *75*, 543–557.
Strüder, L., Epp, S., Rolles, D., Hartmann, R., Holl, P., Lutz, G., et al. (2010). Large-format, high-speed, x-ray pnccds combined with electron and ion imaging spectrometers in a multipurpose chamber for experiments at 4th generation light sources. *Nuclear Instruments and Methods in Physics Research Section A: Accelerators, Spectrometers, Detectors and Associated Equipment*, *614*(3), 483–496.
Svensson, S., de Brito, A. N., Keane, M. P., Correia, N., Karlsson, L., Liegener, C. M., et al. (1992). The n 1s core electron shake-up and the shake-up auger satellite spectrum of the N2 molecule. *Journal of Physics B: Atomic, Molecular and Optical Physics*, *25*(1), 135–144.
Tarantelli, F. (2006). The calculation of molecular double ionization spectra by green's functions. *Chemical Physics*, *329*(1–3), 11–21.
Tashiro, M., Ehara, M., Fukuzawa, H., Ueda, K., Buth, C., Kryzhevoi, N. V., et al. (2010). Molecular double core hole electron spectroscopy for chemical analysis. *The Journal of Chemical Physics*, *132*(18), 184302.
Ullrich, J., Moshammer, R., Drner, R., Jagutzki, O., Mergel, V., Schmidt-Bcking, H., et al. (1997). Recoil-ion momentum spectroscopy. *Journal of Physics B: Atomic, Molecular and Optical Physics*, *30*(13), 2917.
Wilcox, R., Byrd, J. M., Doolittle, L., Huang, G., & Staples, J. W. (2009). Stable transmission of radio frequency signals on fiber links using interferometric delay sensing. *Optics Letters*, *34*(20), 3050–3052.
Wolkow, D. M. (1935). ber eine klasse von lsungen der diracschen gleichung. *Zeitschrift fr Physik A Hadrons and Nuclei*, *94*, 250–260.
Young, L., Kanter, E. P., Krssig, B., Li, Y., March, A. M., Pratt, S. T., et al. (2010). Femtosecond electronic response of atoms to ultra-intense x-rays. *Nature*, *466*(7302), 56–61.
Yudin, G. L., Patchkovskii, S., Corkum, P. B., & Bandrauk, A. D. (2007). Attosecond photoelectron interference in the separable coulomb-volkov continuum. *Journal of Physics B: Atomic, Molecular, and Optical Physics*, *40*(5), F93–F103.
Zavriyev, A., Bucksbaum, P. H., Muller, H. G., & Schumacher, D. W. (1990). Ionization and dissociation of H_2 in intense laser fields at 1.064 μm, 532 nm, and 355 nm. *Physical Review A*, *42*(9), 5500–5510.

This page intentionally left blank

CHAPTER 6

Generation and Applications of *n*-Qubit Hyperentangled Photon States

Giuseppe Vallone[a,b,d] and **Paolo Mataloni**[b,c]

[a]*Museo Storico della Fisica e Centro Studi e Ricerche "Enrico Fermi", Via Panisperna 89/A, Compendio del Viminale, I-00184 Roma, Italy*
[b]*Dipartimento di Fisica, Università Sapienza di Roma, I-00185 Roma, Italy*
[c]*Istituto Nazionale di Ottica (INO-CNR), Largo E. Fermi 6, I-50125 Florence, Italy*
[d]*Department of Information Engineering, University of Padova, I-35131 Padova, Italy*

Contents

Advances in Atomic, Molecular, and Optical Physics, Volume 60, Copyright © 2011 Elsevier Inc.
ISSN 1049-250X, DOI: 10.1016/B978-0-12-385508-4.00006-1.

Abstract In recent years, a number of theoretical and experimental demonstrations regarding the use of photonic entangled states based on many qubits, spanning a large size Hilbert space has been provided. The entanglement of two particles in more than one degree of freedom, namely *hyperentanglement*, is a useful technique which allows to take full advantage of the possibilities offered by quantum mechanics. Compared to multiphoton entangled states, hyperentangled states offer important advantages as far as purity and generation/detection rate are concerned. The present work is intended to survey the most relevant examples of hyperentangled multiqubit photon states aimed at the verification of fundamental tests of quantum mechanics and the realization of important quantum information protocols.

1. INTRODUCTION

The most distinctive feature of quantum physics is the possibility of entangling different qubits. First recognized by Erwin Schroedinger as "the characteristic trait of quantum mechanics," quantum entanglement represents the key resource for modern quantum information. It derives from "subtle" nonlocal correlations between the parts of a quantum system and combines three basic structural elements of quantum theory, i.e., the superposition principle, the quantum non-separability property, and the exponential scaling of the state space with the number of partitions. This unique resource can be used to perform computational and cryptographic tasks otherwise impossible with classical systems. An entangled state shared by two or more separated parties is a valuable resource for fundamental quantum communication protocols, such as quantum teleportation, which is probably the most spectacular demonstration of quantum entanglement. Another important aspect of entangled states is represented by the possibility of performing fundamental tests of quantum nonlocality.

Quantum optics represents an excellent experimental test bench for various novel concepts introduced within the framework of quantum information theory. Quantum states of photons, generally produced by the spontaneous parametric down-conversion (SPDC) process, may be easily and accurately manipulated using linear and nonlinear optical devices and measured by efficient single-photon detectors. Photonic qubits represent the typical carrier of quantum information and can be distributed over long distances, either in freespace or in low-loss optical fibers.

In the typical conditions of SPDC (see Section 3) activated by a continuous wave laser pump beam, no more than one photon pair is generated time by time. This corresponds to operate with qubits belonging to a 2×2

Hilbert space. On the other hand, many quantum information tasks and fundamental tests of quantum mechanics, such as the simulation of properties of quantum systems, the realization of quantum algorithms with increasing complexity, or the investigation of the quantum world at a mesoscopic level, deal with a large number of qubits. In order to take full advantage of the possibilities offered by quantum mechanics, more qubits must be added to quantum states. For example, the larger the number of qubits, the stronger the violation of Bell inequalities and the computational power of a quantum processor.

Two approaches may be followed to increase the number of qubits. The first one consists of increasing the number of entangled particles (Kiesel et al., 2005; Leibfried et al., 2005; Lu et al., 2007; Prevedel et al., 2007; Sackett et al., 2000; Walther et al., 2005a,b; Zhao et al., 2003). In this way, multiqubit entangled states are created by distributing the qubits between the particles so that each particle carries one qubit. This is the way by which four-qubit graph states with atoms (Sackett et al., 2000) and photons (Kiesel et al., 2005; Prevedel et al., 2007; Walther et al., 2005a,b; Zhao et al., 2003), and six-qubit graph states with atoms (Leibfried et al., 2005) and photons (Lu et al., 2007) were realized.

A second strategy consists of encoding more than one qubit in each particle, by exploiting different degrees of freedom (DOFs) of the photon (Barbieri et al., 2005; Barreiro et al., 2005; Chen et al., 2007; Gao et al., 2010a; Vallone et al., 2008a, 2007). This has been used to create two-photon four- and six-qubit graph states (Ceccarelli et al., 2009a; Chen et al., 2007; Gao et al., 2010b; Vallone et al., 2008a, 2007) and up to five-photon ten-qubit graph states (Gao et al., 2010a). The entanglement of two particles in different DOFs corresponds to so-called hyperentangled (HE) state (Kwiat, 1997).

2. HYPERENTANGLEMENT

Two systems A and B are **entangled** if the (pure) state of the total system $|\psi\rangle_{AB}$ is not **separable**, i.e., if it cannot be written as a product of two states belonging to A and B:

$$|\psi\rangle_{AB} \neq |\chi\rangle_A \otimes |\varphi\rangle_B \tag{1}$$

In case of mixed states ρ_{AB} of the composite system $A \otimes B$, the previous relation generalizes to $\rho_{AB} \neq \sum_k p_k \rho_k^A \otimes \rho_k^B$, where p_k are probabilities and ρ_k^A's (ρ_k^B's) are generic density matrix of the system A (B).

Quantum entanglement has no classical analogue. This unique resource can be used to perform tasks that are impossible with classical systems. An entangled state shared by two or more separated parties is a key

element in many quantum information (QI) protocols, such as quantum computing (Raussendorf & Briegel, 2001), quantum cryptography (Ekert, 1991), quantum dense coding (Bennett & Wiesner, 1992), and quantum teleportation (Bennett et al., 1993). The latter protocol was realized by two different optical approaches in Roma and Innsbruck (Boschi et al., 1998; Bouwmeester et al., 1997). By using entangled states, we can deeply investigate the nonlocal properties of the quantum world as first pointed out by Einstein et al. (1935) and successively by Bell (1964).

The simplest examples of entangled states are given by the so-called "Bell states":

$$\left|\Phi^{\pm}\right\rangle = \frac{1}{\sqrt{2}}(|0\rangle_A |0\rangle_B \pm |1\rangle_A |1\rangle_B), \qquad \left|\Psi^{\pm}\right\rangle = \frac{1}{\sqrt{2}}(|0\rangle_A |1\rangle_B \pm |1\rangle_A |0\rangle_B) \quad (2)$$

representing an entangled basis for a two-qubit system.

In the framework of quantum optics, two-photon Bell states have been realized by different approaches. The two qubits may be encoded in a particular DOF of the particles, such as polarization (Kwiat et al., 1995), momentum based on linear (Rarity & Tapster, 1990), orbital (Mair et al., 2001), or transverse (Langford et al., 2004) spatial modes, energy-time (Franson, 1989), and time-bin (Brendel et al., 1999).

As mentioned earlier, by entangling two particles in different DOFs, it is possible to generate hyperentangled states. A more formal definition of HE state is the following. Let us consider two photons A and B and n independent DOFs $\{a_j\}$ and $\{b_j\}$, with $j = 1, \ldots n$. Each DOF spans a 2-dimensional Hilbert space (i.e., it is equivalent to a qubit) with basis $\{|0\rangle_{a_j}, |1\rangle_{a_j}\}$ ($\{|0\rangle_{b_j}, |1\rangle_{b_j}\}$) for particle A (B). In this way, each particle encodes exactly n qubits. A state $|\varphi\rangle$ is *separable in the hyperentangled sense* if it satisfies the following condition:

$$\exists j \text{ such that } |\varphi\rangle = |\varphi_1\rangle_{a_j \mathcal{I}} |\varphi_2\rangle_{b_j \mathcal{J}} \quad (3)$$

where $\{\mathcal{I}, \mathcal{J}\}$ represents a generic bi-partition of the set $\mathcal{T}_j \equiv \{a_1, b_1, \ldots, a_n, b_n\} \backslash \{a_j, b_j\}$, so that $\mathcal{I} \cup \mathcal{J} = \mathcal{T}_j$ and $\mathcal{I} \cap \mathcal{J} = \emptyset$.

Definition: A (mixed) state is **hyperentangled** in n degrees of freedom if it is separately entangled in each of them and cannot be written as a mixture of states satisfying Equation (3).

In order to experimentally detect hyperentanglement, we can develop the same method used for entanglement that corresponds to measure a *(hyper-)entanglement witness*. A witness W is a hermitian operator whose expectation value is nonnegative for any separable state, whereas it is negative for an entangled state (Horodecki et al., 1996; Terhal, 2000). By measuring a negative value of $\langle W \rangle$, the presence of entanglement is demonstrated by only few local measurements. The method can be generalized for HE states (Vallone et al., 2008c). It consists in verifying the presence

of entanglement for each DOF and in measuring a hyperentanglement witness which is positive for any state that can be written as a mixture of states satisfying Equation (3) and is negative for some hyperentangled states.

3. HYPERENTANGLED/MULTIDOF PHOTON STATES: EXPERIMENTAL REALIZATIONS

The techniques commonly used to generate entangled photons exploit the spontaneous parametric down-conversion process, as mentioned.

When an intense pump laser beam (p) shines a nonlinear birefringent crystal, pairs of photons, referred as idler (i) and signal (s), are probabilistically generated from the crystal. The probability of emitting pairs of photons is maximized when the following conditions are satisfied:

$$\text{phase-matching: } \vec{k}_p = \vec{k}_i + \vec{k}_s, \qquad \text{energy matching: } \omega_p = \omega_i + \omega_s. \tag{4}$$

Phase-matching is usually obtained by exploiting the birefringence of the nonlinear crystal. More precisely, a SPDC two-photon state may be expressed as (Kolenderski et al., 2009)

$$\mathcal{N} \int \mathrm{d}^2\mathbf{k}_s \mathrm{d}^2\mathbf{k}_i \mathrm{d}\omega_s \mathrm{d}\omega_s A_p(\mathbf{k}_s + \mathbf{k}_i, \omega_s + \omega_i) \mathrm{sinc}\left(\frac{\Delta k_z L}{2}\right) |\mathbf{k}_s, \omega_s\rangle \, |\mathbf{k}_i, \omega_i\rangle \,. \tag{5}$$

In the previous equations, $\mathbf{k}_i$ and $\mathbf{k}_s$ are the transverse momentum coordinates, $|\mathbf{k}, \omega\rangle = a^\dagger(\mathbf{k}, \omega)\,|0\rangle$, $A_p(\mathbf{k}, \omega)$ is the pump profile in the momentum–frequency space, $\mathcal{N}$ is normalization constant, and L is the crystal length. Δk_z represents the (longitudinal) phase mismatch $\Delta k_z(\mathbf{k}_i, \mathbf{k}_s, \omega_i, \omega_s) = k_{pz}(\mathbf{k}_i + \mathbf{k}_s, \omega_i + \omega_s) - k_{sz}(\mathbf{k}_s, \omega_s) - k_{iz}(\mathbf{k}_i, \omega_i)$. The longitudinal component of momentum is given by $k_z(\mathbf{k}, \omega) = \sqrt{\left[\frac{n(\omega)\omega}{c}\right]^2 - \mathbf{k}^2}$. In usual conditions, the pump wavefunction is assumed to be a Gaussian function $A_p(\mathbf{k}, \omega) = C_0 e^{-\frac{w_0^2}{4}\mathbf{k}_p^2} e^{-\frac{\tau_p^2}{4}(\omega - \omega_p)^2}$, with τ_p and w_0, respectively, representing the coherence time and the beam waist of the pump laser beam. The phase-matching condition is satisfied when $\Delta k_z = 0$. Two kinds of phase-matching are commonly adopted, depending on the extraordinary (e) or ordinary (o) polarization of the pump and of the SPDC photons:

$$\text{Type-I: } e \to o + o, \qquad \text{Type-II: } e \to e + o. \tag{6}$$

In the first case, assuming degenerate generated photons, $\omega_i = \omega_s$, the phase-matching is satisfied for all the wavevectors $\vec{k}_i$ and $\vec{k}_s$ belonging to the external surface of a single emission cone. With Type-II phase-matching, the two degenerate photons are emitted over two different, mutually crossing, emission cones, see Figures 1 and 2.

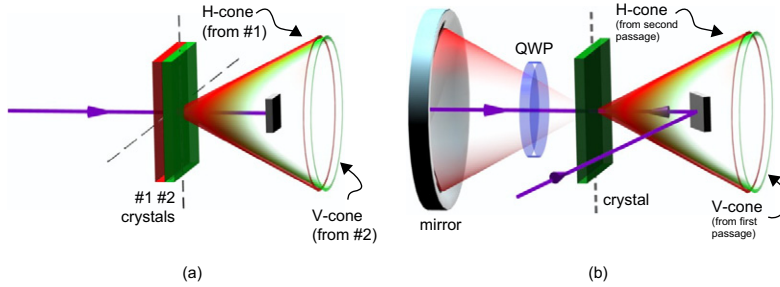

Figure 1 Type-I polarization entanglement sources of degenerate photons. (a) "Kwiat's" source consists of two nonlinear crystals with orthogonal optical axes shined by a 45° linearly polarized ($|H\rangle + |V\rangle$) laser beam. The first (second) crystal generates the state $|HH\rangle$ ($|VV\rangle$). (b) In the "Roma" source a vertically ($|V\rangle$) polarized UV laser beam passes two times through a Type-I nonlinear crystal with vertical optical axis. A quarter wave plate QWP transforms the $|HH\rangle$ SPDC photons into $|VV\rangle$. The spherical mirror reflects both the pump beam and the SPDC photons.

3.1 Entanglement in a Single Degree of Freedom

Polarization entanglement - Let us now describe the polarization entanglement based on Type-I phase-matching. Typically, two main setups are used in experiments with Type-I phase-matching, the "Kwiat's" source (Kwiat et al., 1999) and the "Roma" source (Barbieri et al., 2004; Cinelli et al., 2005a, 2004; Giorgi et al., 2003). The former uses two identical crystals with orthogonal optical axes and a single passage of the laser beam through the crystals. The latter uses a single crystal and a double passage of the laser beam after reflection on a spherical mirror. Both sources typically generate the polarization entangled state $|\Phi^{\pm}\rangle$ with $|0\rangle \rightarrow |H\rangle$ and $|1\rangle \rightarrow |V\rangle$ (see Figure 1 for details). With Type-II phase-matching, two orthogonally polarized photons are emitted over two different cones. The $|\Psi^{\pm}\rangle$ state can be generated (Kwiat et al., 1995) along the two directions in which the two cones intersect (see Figure 2).

3.1.1 Path-Position Entanglement

Let us consider a Type-I crystal and a Gaussian pump profile with a long value of τ_p. By assuming monochromatic SPDC photons (satisfying $\omega_i + \omega_s = \omega_p$), the two-photon state may be written as

$$|\Psi\rangle \propto \int \mathrm{d}^2\mathbf{k}_s \mathrm{d}^2\mathbf{k}_i e^{-\frac{w_0^2}{4}(\mathbf{k}_s+\mathbf{k}_i)^2} \mathrm{sinc}\left(\frac{\Delta k_z L}{2}\right) |\mathbf{k}_s\rangle\, |\mathbf{k}_i\rangle\,. \tag{7}$$

This wavefunction shows that the two correlated photons are emitted over opposite directions of the cone surface. The different events corresponding to different emission directions are coherent because of the transverse

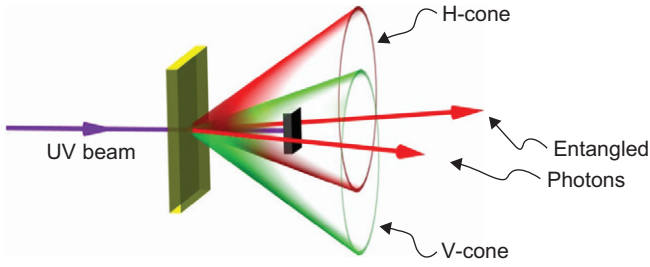

Figure 2 Type-II source. The nonlinear crystal is excited by a vertically polarized UV laser beam. The intersections of the two cones identify the directions on which the polarization entangled degenerate photons are generated.

coherence of the pump profile. By selecting different pairs of correlated emission modes with single mode fibers (Rossi et al., 2009; Żukowski et al., 1997) or a holed mask (Cinelli et al., 2005b), it is possible to generate path (or linear momentum) entanglement. By Fourier transforming the two-photon state, it is possible to measure their transverse spatial correlation. By a different scheme, each photon is forced to pass through two slits that correspond to two orthogonal states (Neves et al., 2005). Transverse spatial correlations are controlled by manipulating the pump laser beam. By making the biphotons to pass only through symmetrically opposite slits, entangled states are generated.

3.1.2 Energy-Time Entanglement

A further available photon DOF is given by the conjugate variables energy and time. Let us define $|\omega\rangle = a_\omega^\dagger |0\rangle$ and consider only two definite spatial modes (as done by selecting the radiation with two single mode fibers) and a Gaussian pump profile. In the limit of perfect phase-matching and assuming constant refractive indices $n_o(\omega) \sim n_o(\omega_0)$, the (normalized) SPDC two-photon state is expressed as (here we set the emission time $t_0 = 0$):

$$|\Psi\rangle = \sqrt{\frac{\tau_p T}{\pi}} \int \mathrm{d}\omega_s \mathrm{d}\omega_i \, e^{-\frac{T^2}{4}(\omega_s-\omega_i)^2} e^{-\frac{\tau_p^2}{4}(\omega_s+\omega_i-\omega_p)^2} |\omega_s\rangle \, |\omega_i\rangle \tag{8}$$

with $T = \frac{n_o(\omega_0)\bar{w}\theta}{c}$, $\bar{w}$ related to the beam waist of the pump and the selected photons and θ corresponding to the emission angle (Kolenderski et al., 2009). By defining $|t\rangle = \frac{1}{\sqrt{2\pi}} \int \mathrm{d}\omega e^{-i\omega t} |\omega\rangle$ the SPDC state may be expressed as

$$|\Psi\rangle = \sqrt{\frac{1}{\pi T \tau_p}} \int \mathrm{d}t_1 \mathrm{d}t_2 \, e^{-\frac{(t_1-t_2)^2}{4T^2}} e^{-\frac{(t_1+t_2)^2}{4\tau_p^2}} e^{i\omega_0(t_1+t_2)} |t_1\rangle \, |t_2\rangle \tag{9}$$

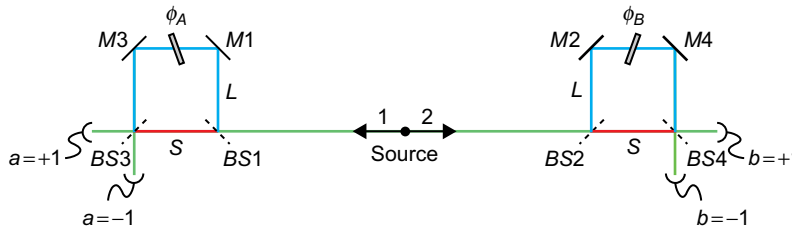

Figure 3 Experimental scheme for the measurement of energy-time entanglement. Short and long paths are labeled as *S* and *L*, respectively.

For $T \neq \tau_p$, the SPDC state is entangled in energy (or time). When $\tau_p \gg T$, frequency anticorrelations and emission time correlations are observed: in this case, the photons are emitted at the same time, and emission events occurring at different times are coherent within τ_p. A scheme invented by Franson (Franson, 1989) enables the measurement of energy-time entanglement (see Figure 3). For each photon, it consists of an unbalanced Mach–Zehnder interferometer with a short (S) and a long (L) arm. If $c\tau_p \gg L - S$, interference is observed when the two photons are detected in coincidence since it is not possible to determine if they followed both the short or the long paths. When used for nonlocality experiments, the Franson's scheme suffers from additional loopholes, that may be removed by using a modified version of the setup (Cabello et al., 2009; Lima et al., 2010).

3.1.3 OAM-Angle Entanglement

Besides spin, photons possess a further angular momentum, called orbital angular momentum (OAM). In the paraxial approximation, photons described by a mode function expressed by a Laguerre-Gaussian mode $|\ell, p\rangle$ are eigenstates of the OAM operator with eigenvalues $\ell\hbar$ ($\ell = 0, \pm 1, \pm 2, \ldots$) (Allen et al., 1992). The integer quantum number p is related to the radial profile of the beam and the integer ℓ, referred to as the topological winding number, describes the helical structure of the wave front around a wave front singularity. The two-photon SPDC state may be expressed as (Torres et al., 2003a)

$$|\Psi\rangle = \sum_{\ell_s, p_s} \sum_{\ell_s, p_s} C^{\ell_s, \ell_i}_{p_s, p_i} \left|\ell_s, p_s\right\rangle \left|\ell_i, p_i\right\rangle, \tag{10}$$

enlightening the possible entanglement in the OAM degree of freedom. By using the relationship between OAM and its conjugate variable, angular position (Barnett & Pegg, 1990), it is possible to observe entanglement in the angular domain (Jha et al., 2010).

Under collinear phase-matching conditions, when the pump beam is a $|\ell_0, p_0\rangle$ mode, the two-photon state at the output of the nonlinear crystal contains only terms such that $\ell_s + \ell_i = \ell_0$. In many OAM applications, one considers only modes with $p_i = p_s = 0$. In this subspace, when the pump beam is a Gaussian TEM_{00} beam, the two-photon state is expressed as (Di Lorenzo Pires et al., 2010)

$$|\Psi\rangle = \sum_{\ell=-\infty}^{+\infty} \sqrt{P_\ell}\, |\ell\rangle_s\, |-\ell\rangle_i \tag{11}$$

where P_l represents the probability of creating a signal photon with orbital angular momentum ℓ and an idler photon with $-\ell$. The state of Equation (11) represents an OAM entangled state. It is worth stressing that the OAM space is infinite dimensional. In typical QI experiments, qubits are encoded into subspaces of the whole Hilbert space (Nagali et al., 2009a; Torres et al., 2003b; Vaziri et al., 2003). To manipulate the OAM degree of freedom, several optical tools, such as computer-generated holograms (Mair et al., 2001), Dove's prisms, cylindrical lenses, spiral plates (Oemrawsingh et al., 2004), and q-plates (Nagali et al., 2009b), may be exploited.

3.2 Hyperentanglement in Different Degrees of Freedom

The above described techniques may be combined to generate photon states that are entangled in more than one DOF, so-called hyperentangled states. The first proposal of energy-momentum-polarization HE state with a Type-II phase-matching was given in 1997 (Kwiat, 1997). The first experimental realizations of HE states were provided in 2005 (Barbieri et al., 2005; Barreiro et al., 2005; Cinelli et al., 2005a; Yang et al., 2005). In the following, we will describe the different kinds of hyperentangled states so far realized.

3.2.1 Polarization-Momentum Hyperentanglement

By using the "Roma" source of polarization entanglement, the extension to path entanglement is straightforward: the two polarization entangled photons (labeled as A and B) are emitted over two symmetric directions belonging to the external surface of the degenerate cone. By selecting with a holed mask two pairs of correlated modes, due to the spatial coherence property of the source, the photons are also entangled in path (see Figure 4a). Precisely, if $|r\rangle$ and $|\ell\rangle$ represent the two modes in which each photon can be emitted, the hyperentangled state may be written as:

$$\frac{1}{\sqrt{2}}\left(|H\rangle_A|V\rangle_B + |V\rangle_A|H\rangle_B\right) \otimes \frac{1}{\sqrt{2}}\left(|r\rangle_A|\ell\rangle_B + |\ell\rangle_A|r\rangle_B\right). \tag{12}$$

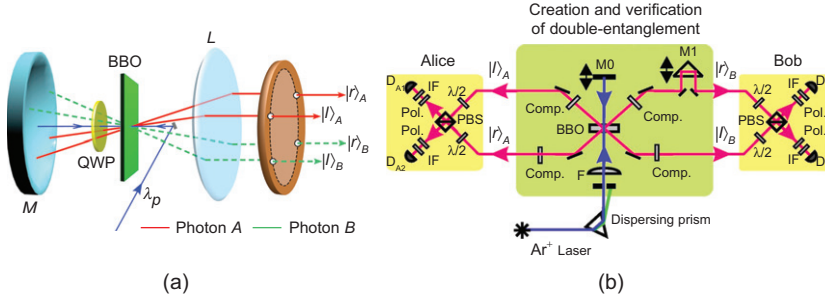

Figure 4 Two schemes for the generation of polarization-momentum hyperentangled state. The figure of scheme b is reprinted with permission from Yang et al. (2005). Copyright 2005 of the American Physical Society.

This state encodes four qubits into two photons (Barbieri et al., 2005; Cinelli et al., 2005a). With a larger number of optical paths, more qubits may be added to the state. Precisely, with four pairs of modes, a six-qubit two-photon hyperentangled state can be generated (Vallone et al., 2009). In order to demonstrate that the prepared state is a genuine hyperentangled state, a hyperentanglement witness was measured (Vallone et al., 2009). A generalization of the above described scheme including energy-time has been proposed for the preparation of six-qubit polarization-momentum-time entanglement (Ceccarelli et al., 2009b).

An alternative approach to realize polarization-momentum hyperentanglement exploits a double passage of pump beam in a Type-II nonlinear crystal (Simon & Pan, 2002; Yang et al., 2005). The Type-II phase-matching allows to create polarization entanglement. The two possible emissions (forward or backward) generate momentum entanglement. The $|r\rangle$ and $|\ell\rangle$ modes are identified with the two possible directions in which each photon can be emitted (see Figure 4b)).

3.2.2 Polarization-OAM-Time

Using the "Kwiat's" source of polarization entanglement and operating with a long pump coherence time, the following polarization-OAM-time hyperentangled state was generated (Barreiro et al., 2005):

$$\underbrace{(|HH\rangle + |VV\rangle)}_{\text{polarization}} \otimes \underbrace{(|-1,+1\rangle + \alpha\,|0,0\rangle + |+1,-1\rangle)}_{\text{OAM}} \otimes \underbrace{(|SS\rangle + |LL\rangle)}_{\text{time}}. \quad (13)$$

In the previous equation, $|\pm 1\rangle$ and $|0\rangle$ represent the OAM eigenstates and α describes the OAM spatial-mode balance prescribed by the source and selected via the mode-matching conditions. Figure 5 shows the experimental setup to generate and measure the quantum state. It is worth

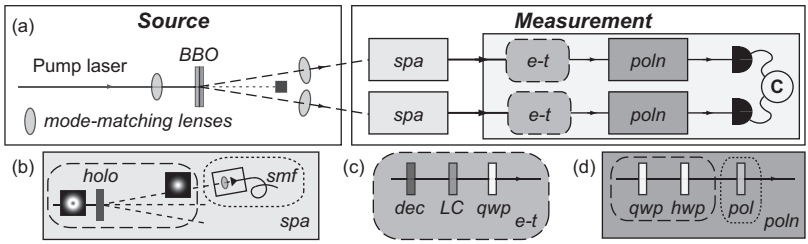

Figure 5 Source of polarization-OAM-time hyperentanglement. Figure reprinted with permission from Barreiro et al. (2005). Copyright 2005 of the American Physical Society.

noting that the measurement apparatus in the figure does not allow to observe simultaneously polarization and energy entanglement.

Similar schemes were adopted for the generation of polarization-OAM (Barreiro et al., 2008) or polarization-time (Schuck et al., 2006) hyperentangled states.

3.3 MultiDOF States and Hybrid Entanglement

The use of different DOFs opens the possibility to create general multiqubit states, here named multiDOF states. These states involve more that one degree of freedom, and in general, they are not hyperentangled in the sense of the definition given in Section 2. The difference between hyperentangled (HE) and general multiDOF state is based on the different amount of entanglement between the particles, maximized in HE states. As a simple example, by using a polarization entangled photon pair and entangling the path DOF with the polarization of a single photon, a three-qubit entangled state is generated, but the entanglement between the two particles is not increased. On the contrary, with HE states, the amount of entanglement between the two particles grows with the number of independent DOFs added to the state.

Another term, so-called *hybrid entanglement*, is also used in the literature to refer to a two-qubit entanglement between two different degrees of freedom of two particles (Barreiro et al., 2010; Ma et al., 2009; Nagali & Sciarrino, 2010; Neves et al., 2009).

Different experiments were performed with multiDOF states. By using polarization and OAM of a single photon, mutually unbiased bases of ququarts were generated (Nagali et al., 2010). A 10-qubit entangled state was created by entangling the path with the polarization of five photons initially into a GHZ polarization state, see Figure 6 (Gao et al., 2010a). The multiDOF approach was essential in the teleportation experiment performed in Rome in 1998 (Boschi et al., 1998). The used resource for

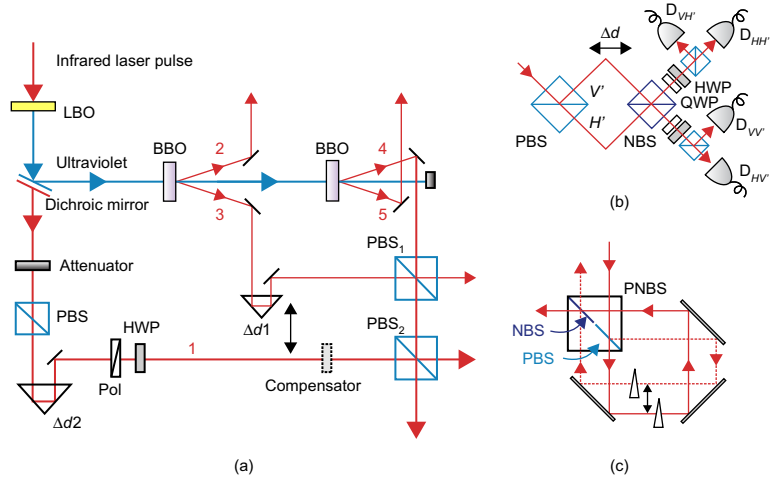

Figure 6 Scheme used for the generation and the measurement of the five-photon 10-qubit entangled state. Figure reprinted with permission from Gao et al. (2010a). Copyright 2010 of MacMillan.

teleporting an unknown qubit was represented by a hybrid entangled state of two photons: qubit 1 was encoded in the polarization of particle A and qubit 2 in the path DOF of particle B, whereas the unknown qubit 3 was encoded in the particle B polarization. Qubit 3 was teleported into the polarization of particle A by a Bell measurement performed between qubits 2 and 3.

4. HYPERENTANGLEMENT FOR QUANTUM INFORMATION

4.1 Quantum Nonlocality Tests

Hyperentanglement allows to generalize the Greenberger–Horne–Zeilinger (GHZ) theorem (Greenberger et al., 1989) with only two entangled particles. The GHZ theorem, sometimes referred as "Bell's theorem without inequalities" or "All-Versus-Nothing (AVN)" proof of Bell's theorem, shows a contradiction between quantum mechanics (QM) and local realistic theories even for definite predictions. The quantum nonlocality can thus, in principle, be manifested in a single run of a certain measurement. Although the GHZ argument requires at least three particles and, consequently, three spacelike separated observers, with hyperentanglement an AVN nonlocality proof may be derived with only two photons (Chen et al., 2003). The contradiction between QM and local realistic theories arises from perfect correlations. On the other hand, in a real experiment, perfect correlations and ideal measurement devices are practically impossible. To face this difficulty, it is possible to introduce a

Bell–Mermin inequality. Hence, an operator $\mathcal{O}$, whose expectation value on the hyperentangled state of Equation (12) is $\langle \mathcal{O} \rangle = 9$, is defined. However, local hidden variable (LHV) theories predict an upper bound on the observed values of $\mathcal{O}$, $\langle \mathcal{O} \rangle_{LHV} \leq 7$, which is in contradiction with quantum mechanical predictions. The experimental realizations of Cinelli et al. (2005b); Yang et al. (2005) show that, under the fair sampling assumption, the inequality is violated. Stronger AVN inequalities can be found with four (Cabello, 2005; Vallone et al., 2007) and six qubits (Ceccarelli et al., 2009a) encoded in two photons.

Hyperentanglement is also crucial to demonstrate the Mermin's growing-with-size quantum nonlocality effect, predicting that the ratio between the quantum prediction and the classical bound grows as in the case of n-qubit systems prepared in Greenberger–Horne–Zeilinger (GHZ) states (Mermin, 1990). Under some assumptions, hyperentanglement allows us to replace $2n$ two-level systems by two 2^n-level systems. This significatively reduces the decoherence problems, simplifies the task of achieving spacelike separation between measurements, and dramatically increases the efficiency in detecting photons. By using the state given in Equation (12), it was demonstrated that the violation of the Bell inequalities grows exponentially with the number of the internal degrees of freedom (Barbieri et al., 2006; Cabello, 2006).

One of the main limitations of the nonlocality tests performed with photons is represented by the so-called "detection loophole": if the particle detection efficiency is lower than a certain threshold level, the undetected events can be exploited by a local model to reproduce the quantum predictions (Pearle, 1970; Santos, 1992). For two-qubit Bell inequalities, the threshold detection efficiency is 82.8% for two particles in a maximally entangled state and can be lowered down to 66.7% by using partially entangled states (Eberhard, 1993). Qudits (i.e., d-level systems with $d > 2$) or hyperentangled states offer a significant advantage over qubits in view of closing the detection loophole. It has been recently shown that, by using hyperentanglement with two DOFs, a threshold efficiency level of 61.8% can be tolerated (Vértesi et al., 2010). Massar (2002) has also demonstrated that, by increasing the dimension of the entangled state, lower bounds decreasing exponentially with the dimension of the Hilbert space can be obtained.

4.2 Bell State Analysis and Dense Coding

Bell state analysis, i.e., the complete and deterministic discrimination between the four orthogonal and maximally entangled "Bell states" of Equation (2), are central in many quantum information applications and processing, such as quantum dense coding (Bennett & Wiesner, 1992); (Mattle et al., 1996), teleportation (Bennett et al., 1993; Boschi et al., 1998; Bouwmeester et al., 1997), entanglement swapping (Bennett et al., 1993;

Jennewein et al., 2001; Pan et al., 1998; Sciarrino et al., 2002), cryptography (Ekert, 1992; Gisin et al., 2002), quantum fingerprinting (Buhrman et al., 2001; Horn et al., 2005), and direct characterization of quantum dynamics (Mohseni & Lidar, 2006). However, it is not possible to completely and deterministically discriminate between the four states using only linear operations and classical communication. Moreover, the optimal probability of success in these cases is only 50% (Calsamiglia, 2002; Calsamiglia & Ltkenhaus, 2000; Ghosh et al., 2001; Lütkenhaus et al., 1999; Mattle et al., 1996; Ursin et al., 2004; Vaidman & Yoran, 1999; van Houwelingen et al., 2006).

By working in a larger Hilbert space, i.e., by employing hyperentangled states, a complete analysis of Bell states with only linear optical elements can be achieved (Barbieri et al., 2007; Kwiat & Weinfurter, 1998; Schuck et al., 2006; Walborn et al., 2003). The method adopting polarization-path hyperentanglement is explained as follows. Let us consider the four hyperentangled states of the form $|\Xi\rangle = |\Pi\rangle_\pi \otimes |\psi^+\rangle_{\mathbf{k}}$, where $|\Pi\rangle_\pi$ is one of the four polarization Bell states of Equation (2) and $|\psi^+\rangle = \frac{1}{\sqrt{2}}(|r\ell\rangle + |\ell r\rangle)$. For a given momentum state $|\psi^+\rangle$, the discrimination of the four hyperentangled states is equivalent to distinguish among the four Bell polarization states. The method is based on the following equations:

$$\begin{aligned} |\Phi^\pm\rangle|\psi^+\rangle &= \frac{1}{2}[\pm|\sigma^+\rangle_A|\tau^\pm\rangle_B \mp |\sigma^-\rangle_A|\tau^\mp\rangle_B + |\tau^+\rangle_A|\sigma^\pm\rangle_B - |\tau^-\rangle_A|\sigma^\mp\rangle_B], \\ |\Psi^\pm\rangle|\psi^+\rangle &= \frac{1}{2}[\pm|\sigma^+\rangle_A|\sigma^\pm\rangle_B \mp |\sigma^-\rangle_A|\sigma^\mp\rangle_B + |\tau^+\rangle_A|\tau^\pm\rangle_B - |\tau^-\rangle_A|\tau^\mp\rangle_B], \end{aligned} \tag{14}$$

which allows to express the four possible states $|\Pi\rangle_\pi\,|\psi^+\rangle_{\mathbf{k}}$ in terms of the single-photon Bell basis $|\sigma^\pm\rangle = \frac{1}{\sqrt{2}}[|H\rangle|\ell\rangle \pm |V\rangle|r\rangle]$, $|\tau^\pm\rangle = \frac{1}{\sqrt{2}}[|V\rangle|\ell\rangle \pm |H\rangle|r\rangle]$. Each product state on the r.h.s. of Equation (14) identifies unambiguously one of the states $|\Xi\rangle$. To distinguish among the four Bell polarization states, it is sufficient to measure each particle into the single-photon Bell states. The experimental probabilities corresponding to joint single-photon Bell state detections are shown in Figure 7. Projection into

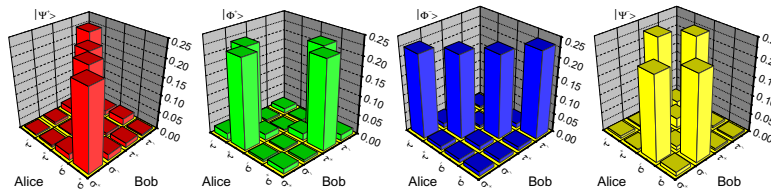

Figure 7 Experimental probabilities showing the complete Bell state analysis of the polarization states $|\Phi^\pm\rangle$ and $|\Psi^\pm\rangle$. Relative errors are typically 2% for the maxima and 5% for the other terms. Figure reprinted with permission from Barbieri et al. (2007). Copyright 2007 of the American Physical Society.

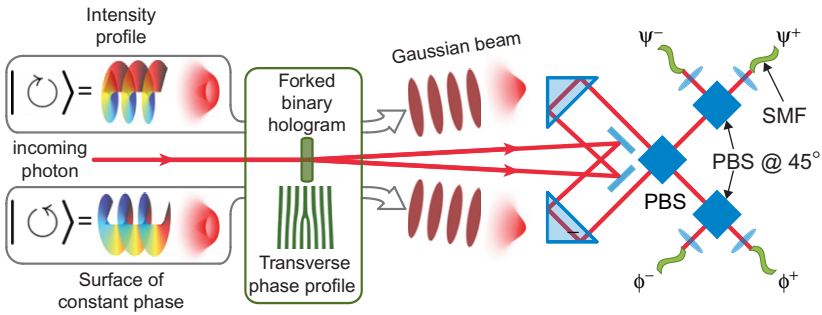

Figure 8 Experimental setup used to generate polarization-OAM hyperentangled states able to implement the dense-coding protocol breaking the conventional linear-optic limits . Figure reprinted with permission from Barreiro et al. (2008). Copyright 2008 of MacMillan.

$|\tau^{\pm}\rangle$ and $|\sigma^{\pm}\rangle$ is achieved by implementing a controlled-Not (CNOT) gate between the polarization and the momentum of each particle that transforms them into separable states. By using a half wave plate (with the optical axis oriented at 45° with respect to vertical direction) on the $|\ell\rangle$ mode, Barbieri et al. (2007) were able to implement a CNOT gate with momentum and polarization playing the role of control and target, respectively. The role of polarization and momentum is exchanged using a PBS to implement the CNOT (Walborn et al., 2003). A similar scheme with polarization-time HE state was implemented by Schuck et al. (2006).

Bell state analysis is crucial for dense coding (Bennett & Wiesner, 1992), one of the fundamental QI protocols. It works as follows: two observers, Alice and Bob, share an entangled pair and each observer possesses a particle. One observer, say Bob, can encode a two-bit message by applying one of four unitary operations on his particle, which he then transmits to Alice. Alice decodes the message by performing a Bell state analysis. Since a deterministic discrimination of all four Bell states with linear optics is not possible, Bob can only send to Alice three of four bits, reducing the attainable capacity from 2 to $\log_2 3 \simeq 1.585$ bits. As explained, entanglement in an extra-degree of freedom enables the complete and deterministic discrimination of all Bell states. Using a polarization-OAM hyperentangled state, a dense-coding experiment breaking the conventional linear-optics threshold was reported (Barreiro et al., 2008) (see Figure 8).

4.3 Quantum Computing

Hyperentanglement or, in general, the possibility of encoding more qubits in different DOFs of the same particle is a useful tool for quantum computation (QC). The realization of multiqubit states can be achieved

with relevant advantages in terms of generation rate and state fidelity, compared with multiphoton states. Indeed, by increasing the number of qubits encoded in different DOFs of the same particle, the overall detection efficiency, and hence the repetition rate of detection is constant, since it scales as η^N (N being the number of photons and η the detector quantum efficiency). Furthermore, an entangled state built on a larger number of particles is in principle more affected by decoherence because of the increased difficulty of making photons indistinguishable. However, it is worth to remember that increasing the number n of involved DOFs implies an exponential requirement of resources. For instance, 2^n modes must be exploited to encode n qubits into a photon. However, according to the current optical technology, working with few DOFs (such as $n = 2, 3, 4$) offers still more advantages than working with a corresponding number of photons, because of the higher repetition rate and state generation and detection efficiency. On a medium-term timescale, a hybrid approach to QC (i.e., multiDOF and multiphoton states) may represent a convenient solution to overcome the structural limitations in generation and detection of quantum photon states.

Several quantum algorithms have been realized by exploiting multi-DOF states in the one-way framework of QC. Cluster states are particular quantum states associated to a graph with N vertex and L links. A qubit in the state $|+\rangle = \frac{1}{\sqrt{2}}(|0\rangle + |1\rangle)$ is associated to each vertex while a Controlled-Z (CZ_{ij}) gate: $|0\rangle_i \langle 0| 1\!1_j + |1\rangle_i \langle 1| (\sigma_z)_j$ is associated to each link. Cluster states represent the basic resource for the realization of a quantum computer operating in the one-way model. In the standard QC approach, any quantum algorithm can be realized by a sequence of single-qubit rotations and two-qubit gates on the physical qubits. Deterministic one-way QC is based on the initial preparation of the physical qubits in a cluster state, followed by a temporally ordered pattern of single-qubit measurements and feed-forward operations. In this way, nonunitary measurements on the physical qubits correspond to unitary gates on the logical qubits.

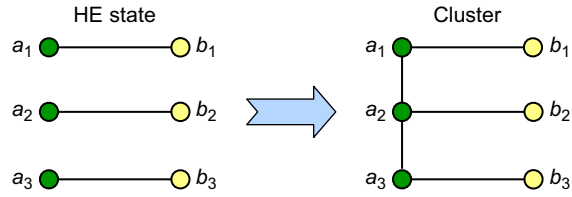

Figure 9 On the left of the arrow is the graph corresponding to a six-qubit hyperentangled state and on the right a possible transformation into a more general cluster state. a_i (b_i) are DOFs of particle A (B).

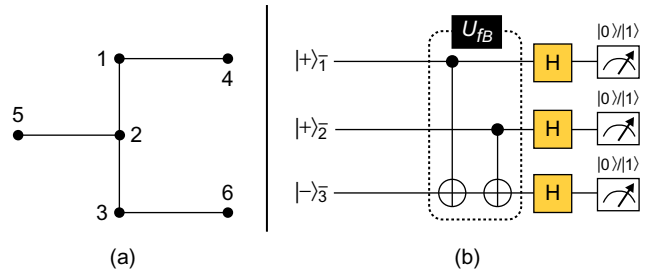

Figure 10 (a) Graph corresponding to the cluster state used to perform the Deutsch–Jozsa algorithm. By measuring qubits 5, 1, and 3, it is possible to implement the algorithm shown in b. The output of the algorithm is encoded in qubits 2, 4, and 6.

In the framework of cluster states, hyperentangled states correspond to a graph with pairwise connected vertices (see Figure 9). By applying suitable CZ operations between qubits belonging to the same particle, a HE state can be transformed into a more general cluster state. For example, with path $\{|\ell\rangle, |r\rangle\}$ and polarization $\{|H\rangle, |V\rangle\}$ qubits, in Vallone et al. (2007), the CZ gate has been implemented by using a half wave plate with vertical optical axis on photon mode $|r\rangle$. With two-photon four-qubit cluster states built from polarization-path HE states, the Grover algorithm and a CZ gate (Chen et al., 2007), a generic single qubit rotation with active feed-forward (Vallone et al., 2008a), a CNOT gate and the Deutsch algorithm (Vallone et al., 2008b,c) were implemented.

More complex algorithms have been realized with six-qubit cluster states. A CNOT gate with more general input qubits was implemented by Gao et al. (2010b); Vallone et al. (2010b). Moreover, Vallone et al. (2010a) presented an all-optical implementation of the Deutsch–Jozsa (DJ) algorithm for $n = 2$ bits (see Figure 10). The DJ algorithm allows to discriminate in one run if a boolean n-bit function f is constant or balanced (i.e., it takes the value 0 on half inputs and the value 1 on the remaining halves). Classically, $2^{n-1} + 1$ runs of the algorithm are necessary to deterministically solve the problem. At variance with the simple case $n = 1$, the DJ algorithm allows to take advantage of the exponential growing of the computational speed-up for increasing values of n. The correct output is identified at a frequency of almost 1 kHz without feed-forward, a result that overcomes by several orders of magnitude what is usually achieved with a six-photon cluster state created by SPDC.

HE states can be also useful for quantum simulation. By a two-photon polarization-path hyperentangled state, a simulation of decoherence on a fou-qubit (phased) Dicke state was realized (Chiuri et al., 2010). Precisely, it was possible to model the following decoherence channel $\rho \to \sum_{j=1}^{4} B_j \rho B_j^{\dagger}$ where $B_1 = (1 - q_2)11$, $B_2 = \sqrt{q_2(1 - q_2)}Y_1Y_2$,

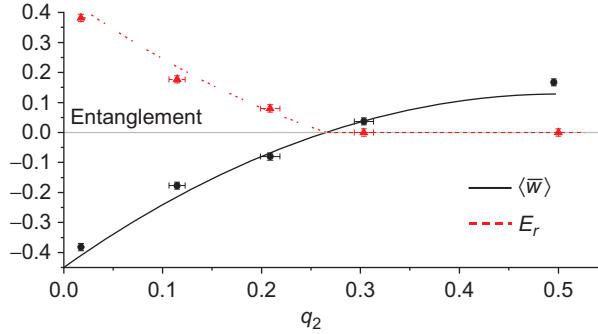

Figure 11 Experimental values of the witness $\overline{\mathcal{W}}$ and the bound on E_r as a function of q_2. Continuous (black) and dotted (red) lines represent the predicted curves.

$B_3 = \sqrt{q_2(1-q_2)}Y_3Y_4$, and $B_4 = q_2Y_1Y_2Y_3Y_4$ and the parameter q_2 represents the amount of noise introduced in a controlled way into the state. A symmetric four-qubit Dicke state with two excitations is the equally weighted superposition of all permutations of 4-qubit product states with two logical 1's and two logical 0's. A witness operator $\overline{\mathcal{W}}$ for different values of q_2 was measured, and the corresponding results are shown in Figure 11. The continuous black curve corresponds to the expected behavior for the generated state. It is also possible to provide a lower bound on the *random robustness* of entanglement E_r (Eisert et al., 2007), $E_r(\rho) \geq |\langle\overline{\mathcal{W}}\rangle_{exp}|$. The bounds on E_r for different values of q_2 are also shown in Figure 11.

Wilde and Uskov (2009) proposed a linear-optical implementation of quantum error-correcting code by using hyperentanglement. The code is able to correct "bit-flip" errors.

4.4 Purification

The entanglement purification protocol (Bennett et al., 1996) allows to generate (almost) maximally entangled pairs from a larger number of less perfectly entangled pairs using only local operations and classical communication. It is essential in the case of two particles transmitted through a noisy channel and then affected by decoherence. Therefore, simple and precise implementations of entanglement purification is fundamental for many QI applications.

By using polarization-path hyperentangled photon, it is possible to purify the polarization entanglement (Simon & Pan, 2002; Cialdi et al., 2010; Sheng et al., 2008; Sheng & Deng, 2010). The first scheme, proposed in Simon and Pan (2002) and realized in Pan et al. (2003), is shown in Figure 12. For a single photon pair, the idea is the following: by using on each side of the CNOT operations, implemented by PBSs between

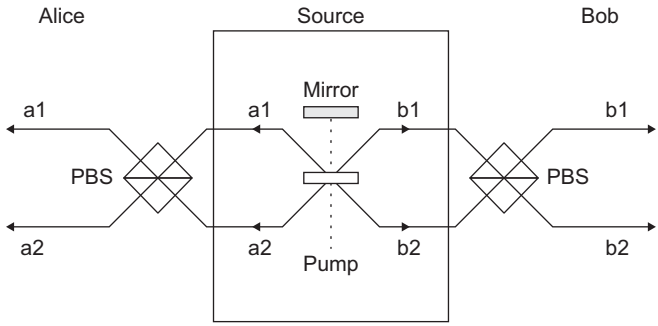

Figure 12 Proposed scheme for the realization of hyperentanglement assisted polarization purification protocol. Figure reprinted with permission from Simon and Pan (2002). Copyright 2002 of the American Physical Society.

path and polarization qubits, it is possible to purify the polarization entanglement by exploiting the path entanglement. Precisely, when the two photons are detected on modes $a1$ and $b1$, all the bit-flip errors in polarization are purified. The protocol works also in the case of four photon generation (i.e., when the pump beam peak intensity is sufficiently large). In this case, the spin-flip purification succeeds when one photon is detected in each of the four spatial modes behind the PBSs.

5. CONCLUSIONS

Hyperentangled photon states built on multiple degrees of freedom are a useful resource in quantum information and computation and for advanced fundamental tests of quantum mechanics. In this work, we have presented an overview of the main properties and some of the most important examples of application of such states. The advantages derived from the use of hyperentangled states mainly reside on the possibility of engineering and detecting at a relatively high rate multiqubit entangled states that are more pure than multiphoton states. The hyperentangled states based on two photons realized till now encode a maximum of six qubits. Multiqubit photon states spanning a larger size Hilbert space may be obtainable in the near future by adding to the previous ones a larger number of resources and, possibly, using at the same time a larger number of photons.

In this work, we have seen that the generation of multidegree of freedom hyperentangled photon states is affected by the non-scalability issue when the number of DOFs becomes large ($\geq$5). However, according to the current technology based on spontaneous parametric down-conversion and avalanche photodetectors of limited quantum efficiency, the hyperentanglement opens the path to new objectives more ambitious

than those achievable with multiphoton states. In order to increase the number of involved photons or DOFs, it is necessary to build complex interferometers. The actual technology adopted to achieve this goal, based on bulk optics, suffers from several limitations, such as large physical size and low phase stability of the optical setup. The emerging strategy allowing to overcome these limitations is currently represented by the integrated waveguide technology (Marshall et al., 2009; Politi et al., 2008; Sansoni et al., 2010; Smith et al., 2009).

REFERENCES

Allen, L., Beijersbergen, M. W., Spreeuw, R. J. C., & Woerdman, J. P. (1992). Orbital angular momentum of light and the transformation of Laguerre-Gaussian laser modes. *Physical Review A*, *45*(11), 8185–8189.

Barbieri, M., Cinelli, C., Mataloni, P., & De Martini, F. (2005). Polarization-momentum hyperentangled states: realization and characterization. *Physical Review A*, *72*(5), 052110.

Barbieri, M., De Martini, F., Di Nepi, G., & Mataloni, P. (2004). Generation and characterization of Werner states and maximally entangled mixed states by a universal source of entanglement. *Physical Review Letters*, *92*(17), 177901.

Barbieri, M., De Martini, F., Mataloni, P., Vallone, G., & Cabello, A. (2006). Enhancing the violation of the Einstein–Podolsky–Rosen local realism by quantum hyperentanglement. *Physical Review Letters*, *97*(14), 140407.

Barbieri, M., Vallone, G., Mataloni, P., & De Martini, F. (2007). Complete and deterministic discrimination of polarization Bell states assisted by momentum entanglement. *Physical Review A*, *75*(4), 042317.

Barnett, S. M., & Pegg, D. T. (1990). Quantum theory of rotation angles. *Physical Review A*, *41*(7), 3427–3435.

Barreiro, J. T., Langford, N. K., Peters, N. A., & Kwiat, P. G. (2005). Generation of hyperentangled photon pairs. *Physical Review Letters*, *95*(26), 260501.

Barreiro, J. T., Wei, T.-C., & Kwiat, P. G. (2008). Beating the channel capacity limit for linear photonic superdense coding. *Nature Physics*, *4*, 282–286.

Barreiro, J. T., Wei, T.-C., & Kwiat, P. G. (2010). Remote preparation of single-photon "hybrid" entangled and vector-polarization states. *Physical Review Letters*, *105*(3), 030407.

Bell, J. S. (1964). On the Einstein–Podolsky–Rosen paradox. *Physics, 1*(3), 195–200.

Bennett, C. H., Brassard, G., Crépeau, C., Jozsa, R., Peres, A., & Wootters, W. K. (1993). Teleporting an unknown quantum state via dual classical and Einstein–Podolsky–Rosen channels. *Physical Review Letters*, *70*(13), 1895–1899.

Bennett, C. H., Brassard, G., Popescu, S., Schumacher, B., Smolin, J. A., & Wootters, W. K. (1996). Purification of noisy entanglement and faithful teleportation via noisy channels. *Physical Review Letters*, *76*, 722.

Bennett, C. H., & Wiesner, S. J. (1992). Communication via one- and two-particle operators on Einstein–Podolsky–Rosen states. *Physical Review Letters*, *69*(20), 2881–2884.

Boschi, D., Branca, S., De Martini, F., Hardy, L., & Popescu, S. (1998). Experimental realization of teleporting an unknown pure quantum state via dual classical and Einstein–Podolsky-Rosen channels. *Physical Review Letters*, *80*(6), 1121–1125.

Bouwmeester, D., Pan, J.-W., Mattle, K., Eibl, M., Weinfurter, H., & Zeilinger, A. (1997). Experimental quantum teleportation. *Nature (London), 390*, 575.

Brendel, J., Gisin, N., Tittel, W., & Zbinden, H. (1999). Pulsed energy-time entangled twin-photon source for quantum communication. *Physical Review Letters*, *82*(12), 2594–2597.

Buhrman, H., Cleve, R., Watrous, J., & de Wolf, R. (2001). Quantum fingerprinting. *Physical Review Letters*, *87*(16), 167902.

Cabello, A. (2005). Stronger two-observer all-versus-nothing violation of local realism. *Physical Review Letters*, *95*(21), 210401.

Cabello, A. (2006). Bipartite Bell inequalities for hyperentangled states. *Physical Review Letters*, *97*(14), 140406.

Cabello, A., Rossi, A., Vallone, G., De Martini, F., & Mataloni, P. (2009). Proposed Bell experiment with genuine energy-time entanglement. *Physical Review Letters*, *102*(4), 040401.

Calsamiglia, J. (2002). Generalized measurements by linear elements. *Physical Review A*, *65*(3), 030301.

Calsamiglia, J., & Ltkenhaus, N. (2000). Maximum efficiency of a linear-optical Bell-state analyzer. *Applied Physics B: Lasers and Optics*, *72*(1), 67–71.

Ceccarelli, R., Vallone, G., De Martini, F., Mataloni, P., & Cabello, A. (2009a). Experimental entanglement and nonlocality of a two-photon six-qubit cluster state. *Physical Review Letters*, *103*, 160401.

Ceccarelli, R., Vallone, G., Martini, F. D., & Mataloni, P. (2009b). An optical scheme for the generation and analysis of a two photon six-qubit linear cluster state. *Advanced Science Letters*, *2*, 455–458.

Chen, K., Li, C.-M., Zhang, Q., Chen, Y.-A., Goebel, A., Chen, S., et al. (2007). Experimental realization of one-way quantum computing with two-photon four-qubit cluster states. *Physical Review Letters*, *99*, 120503.

Chen, Z.-B., Pan, J.-W., Zhang, Y.-D., Brukner, C., & Zeilinger, A. (2003). All-versus-nothing violation of local realism for two entangled photons. *Physical Review Letters*, *90*(16), 160408.

Chiuri, A., Vallone, G., Bruno, N., Macchiavello, C., Bruß, D., & Mataloni, P. (2010). Hyperentangled mixed phased Dicke states: optical design and detection. *Physical Review Letters*, *105*(25), 250501.

Cialdi, S., Brivio, D., & Paris, M. G. A. (2010). Demonstration of a programmable source of two-photon multiqubit entangled states. *Physical Review A*, *81*(4), 042322.

Cinelli, C., Barbieri, M., De Martini, F., & Mataloni, P. (2005a). Realization of hyperentangled two-photon states. *Laser Physics*, *15*, 124.

Cinelli, C., Barbieri, M., Perris, R., Mataloni, P., & De Martini, F. (2005b). All-versus-nothing nonlocality test of quantum mechanics by two-photon hyperentanglement. *Physical Review Letters*, *95*(24), 240405.

Cinelli, C., Di Nepi, G., De Martini, F., Barbieri, M., & Mataloni, P. (2004). Parametric source of two-photon states with a tunable degree of entanglement and mixing: experimental preparation of Werner states and maximally entangled mixed states. *Physical Review A*, *70*, 022321.

Di Lorenzo Pires, H., Florijn, H. C. B., & van Exter, M. P. (2010). Measurement of the spiral spectrum of entangled two-photon states. *Physical Review Letters*, *104*(2), 020505.

Eberhard, P. H. (1993). Background level and counter efficiencies required for a loophole-free Einstein–Podolsky–Rosen experiment. *Physical Review A*, *47*, R747.

Einstein, A., Podolsky, B., & Rosen, N. (1935). Can quantum-mechanical description of physical reality be considered complete? *Physical Review*, *47*, 777–780.

Eisert, J., Brandao, F. G. S. L., & Audenaert, K. M. R. (2007). Quantitative entanglement witnesses. *New Journal of Physics*, *9*(3), 46.

Ekert, A. K. (1991). Quantum cryptography based on Bell's theorem. *Physical Review Letters*, *67*(6), 661–663.

Ekert, A. (1992). Beating the code breakers. *Nature*, *358*, 14–15.

Franson, J. D. (1989). Bell inequality for position and time. *Physical Review Letters*, *62*, 2205.

Gao, W.-B., Lu, C.-Y., Yao, X.-C., Xu, P., Ghne, O., Goebel, A., et al. (2010a). Experimental demonstration of a hyper-entangled ten-qubit Schrödinger cat state. *Nature Physics*, *6*, 331–335, preprint.

Gao, W.-B., Xu, P., Yao, X.-C., Gühne, O., Cabello, A., Lu, C.-Y., et al. (2010b). Experimental realization of a Controlled-NOT gate with four-photon six-qubit cluster states. *Physical Review Letters*, *104*(2), 020501.

Ghosh, S., Kar, G., Roy, A., Sen(De), A., & Sen, U. (2001). Distinguishability of Bell states. *Physical Review Letters*, *87*(27), 277902.

Giorgi, G., Di Nepi, G., Mataloni, P., & De Martini, F. (2003). A high brightness parametric source of entangled photon states. *Laser Physics*, *13*, 350.

Gisin, N., Ribordy, G., Tittel, W., & Zbinden, H. (2002). Quantum cryptography. *Reviews of Modern Physics*, *74*(1), 145–195.

Greenberger, D. M., Horne, M. A., & Zeilinger, A. (1989). Going beyond Bell's theorem. In M. Kafatos (Ed.), *Bell's Theorem, Quantum Theory, and Conceptions of the Universe* (p. 69.). Dordrecht, Holland: Kluwer Academic.

Horn, R. T., Babichev, S. A., Marzlin, K.-P., Lvovsky, A. I., & Sanders, B. C. (2005). Single-qubit optical quantum fingerprinting. *Physical Review Letters*, *95*(15), 150502.

Horodecki, M., Horodecki, P., & Horodecki, R. (1996). Separability of mixed states: necessary and sufficient conditions. *Physics Letters A*, *223*, 1.

Jennewein, T., Weihs, G., Pan, J.-W., & Zeilinger, A. (2001). Experimental nonlocality proof of quantum teleportation and entanglement swapping. *Physical Review Letters*, *88*(1), 017903.

Jha, A. K., Leach, J., Jack, B., Franke-Arnold, S., Barnett, S. M., Boyd, R. W., et al. (2010). Angular two-photon interference and angular two-qubit states. *Physical Review Letters*, *104*(1), 010501.

Kiesel, N., Schmid, C., Weber, U., Tóth, G., Gühne, O., Ursin, R., et al. (2005). Experimental analysis of a four-qubit photon cluster state. *Physical Review Letters*, *95*(21), 210502.

Kolenderski, P., Wasilewski, W., & Banaszek, K. (2009). Modeling and optimization of photon pair sources based on spontaneous parametric down-conversion. *Physical Review A (Atomic, Molecular, and Optical Physics)*, *80*(1), 013811.

Kwiat, P. G. (1997). Hyper-entangled states. *Journal of Modern Optics*, *44*, 2173–2184.

Kwiat, P. G., Mattle, K., Weinfurter, H., Zeilinger, A., Sergienko, A. V., & Shih, Y. (1995). New high-intensity source of polarization-entangled photon pairs. *Physical Review Letters*, *75*(24), 4337–4341.

Kwiat, P. G., Waks, E., White, A. G., Appelbaum, I., & Eberhard, P. H. (1999). Ultrabright source of polarization-entangled photons. *Physical Review A*, *60*(2), R773–R776.

Kwiat, P. G., & Weinfurter, H. (1998). Embedded Bell-state analysis. *Physical Review A*, *58*, R2623–R2626.

Langford, N. K., Dalton, R. B., Harvey, M. D., O'Brien, J. L., Pryde, G. J., Gilchrist, A., et al. (2004). Measuring entangled qutrits and their use for quantum bit commitment. *Physical Review Letters*, *93*(5), 053601.

Leibfried, D., Knill, E., Seidelin, S., Britton, J., Blakestad, R. B., Chiaverini, J., et al. (2005). Creation of a six-atom 'Schrodinger cat' state. *Nature, 438*, 639–642.

Lima, G., Vallone, G., Chiuri, A., Cabello, A., & Mataloni, P. (2010). Experimental Bell-inequality violation without the postselection loophole. *Physical Review A*, *81*(4), 040101(R).

Lu, C.-Y., Zhou, X.-Q., Gühne, O., Gao, W.-B., Zhang, J., Yuan, Z.-S., et al. (2007). Experimental entanglement of six photons in graph states. *Nature Physics*, *3*, 91.

Lütkenhaus, N., Calsamiglia, J., & Suominen, K.-A. (1999). Bell measurements for teleportation. *Physical Review A*, *59*(5), 3295–3300.

Ma, X.-s., Qarry, A., Kofler, J., Jennewein, T., & Zeilinger, A. (2009). Experimental violation of a Bell inequality with two different degrees of freedom of entangled particle pairs. *Physical Review A*, *79*(4), 042101.

Mair, A., Vaziri, A., Weihs, G., & Zeilinger, A. (2001). Entanglement of the orbital angular momentum states of photons. *Nature (London), 412*, 313–316.

Marshall, G. D., Politi, A., Matthews, J. C. F., Dekker, P., Ams, M., Withford, M. J., et al. (2009). Laser written waveguide photonic quantum circuits. *Optics Express, 17*(15), 12546–12554.

Massar, S. (2002). Nonlocality, closing the detection loophole, and communication complexity. *Physical Review A*, *65*(3), 032121.

Mattle, K., Weinfurter, H., Kwiat, P. G., & Zeilinger, A. (1996). Dense coding in experimental quantum communication. *Physical Review Letters*, *76*(25), 4656–4659.

Mermin, N. D. (1990). Extreme quantum entanglement in a superposition of macroscopically distinct states. *Physical Review Letters*, *65*(15), 1838.

Mohseni, M., & Lidar, D. A. (2006). Direct characterization of quantum dynamics. *Physical Review Letters*, *97*(17), 170501.

Nagali, E., Sansoni, L., Marrucci, L., Santamato, E., & Sciarrino, F. (2010). Experimental generation and characterization of single-photon hybrid ququarts based on polarization and orbital angular momentum encoding. *Physical Review A*, *81*(5), 052317.

Nagali, E., Sansoni, L., Sciarrino, F., De Martini, F., Marrucci, L., Piccirillo, B., et al. (2009a). Optimal quantum cloning of orbital angular momentum photon qubits through Hong-Ou-Mandel coalescence, *3*(12), 720–723.

Nagali, E., & Sciarrino, F. (2010). Generation of hybrid polarization-orbital angular momentum entangled states. *Optics Express, 18*, 18243.
Nagali, E., Sciarrino, F., De Martini, F., Marrucci, L., Piccirillo, B., Karimi, E., et al. (2009b). Quantum information transfer from spin to orbital angular momentum of photons. *Physical Review Letters*, *103*(1), 013601.
Neves, L., Lima, G., Aguirre Gomez, J. G., Monken, C. H., Saavedra, C., & Padua, S. (2005). Generation of entangled states of qudits using twin photons. *Physical Review Letters*, *94*, 100501.
Neves, L., Lima, G., Delgado, A., & Saavedra, C. (2009). Hybrid photonic entanglement: realization, characterization, and applications. *Physical Review A*, *80*(4), 042322.
Oemrawsingh, S. S. R., Aiello, A., Eliel, E. R., Nienhuis, G., & Woerdman, J. P. (2004). How to observe high-dimensional two-photon entanglement with only two detectors. *Physical Review Letters*, *92*(21), 217901.
Pan, J.-W., Bouwmeester, D., Weinfurter, H., & Zeilinger, A. (1998). Experimental entanglement swapping: entangling photons that never interacted. *Physical Review Letters*, *80*(18), 3891–3894.
Pan, J.-W., Gasparoni, S., Ursin, R., Weihs, G., & Zeilinger, A. (2003). Experimental entanglement purification of arbitrary unknown states. *Nature, 423*(6938), 417–422.
Pearle, P. M. (1970). Hidden-variable example based upon data rejection. *Physical ReviewD, 2*, 1418.
Politi, A., Cryan, M. J., Rarity, J. G., Yu, S., & O'Brien, J. L. (2008). Silica-on-silicon waveguide quantum circuits. *Science, 320*(5876), 646–649.
Prevedel, R., Walther, P., Tiefenbacher, F., Böhi, P., Kaltenbaek, R., Jennewein, T., et al. (2007). High-speed linear optics quantum computing using active feed-forward. *Nature (London), 445*, 65.
Rarity, J. G., & Tapster, P. R. (1990). Experimental violation of Bell's inequality based on phase and momentum. *Physical Review Letters*, *64*, 24952498.
Raussendorf, R., & Briegel, H. J. (2001). A one-way quantum computer. *Physical Review Letters*, *86*(22), 5188.
Rossi, A., Vallone, G., Chiuri, A., De Martini, F., & Mataloni, P. (2009). Multipath entanglement of two photons. *Physical Review Letters*, *102*, 153902.
Sackett, C. A., Kielpinski, D., King, B. E., Langer, C., Meyer, V., Myatt, C. J., et al. (2000). Experimental entanglement of four particles. *Nature, 404*, 256–259.
Sansoni, L., Sciarrino, F., Vallone, G., Mataloni, P., Crespi, A., Ramponi, R., et al. (2010). Polarization entangled state measurement on a chip. *Physical Review Letters*, *105*(20), 200503.
Santos, E. (1992). Critical analysis of the empirical tests of local hidden-variable theories. *Physical Review A*, *46*, 3646.
Schuck, C., Huber, G., Kurtsiefer, C., & Weinfurter, H. (2006). Complete deterministic linear optics Bell state analysis. *Physical Review Letters*, *96*(19), 190501.
Sciarrino, F., Lombardi, E., Milani, G., & De Martini, F. (2002). Delayed-choice entanglement swapping with vacuum–one-photon quantum states. *Physical Review A*, *66*(2), 024309.
Sheng, Y.-B., & Deng, F.-G. (2010). Deterministic entanglement purification and complete nonlocal Bell-state analysis with hyperentanglement. *Physical Review A*, *81*(3), 032307.
Sheng, Y.-B., Deng, F.-G., & Zhou, H.-Y. (2008). Efficient polarization-entanglement purification based on parametric down-conversion sources with cross-Kerr nonlinearity. *Physical Review A*, *77*(4), 042308.
Simon, C., & Pan, J.-W. (2002). Polarization entanglement purification using spatial entanglement. *Physical Review Letters, 89*(25), 257901.
Smith, B. J., Kundys, D., Thomas-Peter, N., Smith, P. G. R., & Walmsley, I. A. (2009). Phase-controlled integrated photonic quantum circuits. *Optics Express, 17*(16), 13516–13525.
Terhal, B. M. (2000). Bell inequalities and the separability criterion. *Physics Letters A*, *271*(5–6), 319–326.
Torres, J. P., Alexandrescu, A., & Torner, L. (2003a). Quantum spiral bandwidth of entangled two-photon states. *Physical Review A*, *68*(5), 050301.
Torres, J. P., Deyanova, Y., Torner, L., & Molina-Terriza, G. (2003b). Preparation of engineered two-photon entangled states for multidimensional quantum information. *Physical Review A*, *67*(5), 052313.

Ursin, R., Jennewein, T., Aspelmeyer, M., Kaltenbaek, R., Lindenthal, M., Walther, P., et al. (2004). Quantum teleportation across the Danube. *Nature, 430*, 849–849.
Vaidman, L., & Yoran, N. (1999). Methods for reliable teleportation. *Physical Review A*, *59*(1), 116–125.
Vallone, G., Ceccarelli, R., De Martini, F., & Mataloni, P. (2009). Hyperentanglement of two photons in three degrees of freedom. *Physical Review A*, *79*(3), 030301(R).
Vallone, G., Donati, G., Bruno, N., Chiuri, A., & Mataloni, P. (2010a). Experimental realization of the Deutsch–Jozsa algorithm with a six-qubit cluster state. *Physical Review A*, *81*, 050302(R).
Vallone, G., Donati, G., Ceccarelli, R., & Mataloni, P. (2010b). Six-qubit two-photon hyperentangled cluster states: characterization and application to quantum computation. *Physical Review A*, *81*, 052301.
Vallone, G., Pomarico, E., De Martini, F., & Mataloni, P. (2008a). Active one-way quantum computation with two-photon four-qubit cluster states. *Physical Review Letters*, *100*(16), 160502.
Vallone, G., Pomarico, E., De Martini, F., & Mataloni, P. (2008b). One-way quantum computation via manipulation of polarization and momentum qubits in two-photon cluster states. *Laser Physics Letters*, *5*, 398–403.
Vallone, G., Pomarico, E., De Martini, F., & Mataloni, P. (2008c). One-way quantum computation with two-photon multi-qubit cluster state. *Physical Review A*, *78*, 042335.
Vallone, G., Pomarico, E., Mataloni, P., De Martini, F., & Berardi, V. (2007). Realization and characterization of a two-photon four-qubit linear cluster state. *Physical Review Letters*, *98*(18), 180502.
van Houwelingen, J. A. W., Brunner, N., Beveratos, A., Zbinden, H., & Gisin, N. (2006). Quantum teleportation with a three-Bell-state analyzer. *Physical Review Letters*, *96*(13), 130502.
Vaziri, A., Pan, J.-W., Jennewein, T., Weihs, G., & Zeilinger, A. (2003). Concentration of higher dimensional entanglement: qutrits of photon orbital angular momentum. *Physical Review Letters*, *91*(22), 227902.
Vértesi, T., Pironio, S., & Brunner, N. (2010). Closing the detection loophole in Bell experiments using qudits. *Physical Review Letters*, *104*(6), 060401.
Walborn, S. P., Pádua, S., & Monken, C. H. (2003). Hyperentanglement-assisted Bell-state analysis. *Physical Review A*, *68*, 042313.
Walther, P., Aspelmeyer, M., Resch, K. J., & Zeilinger, A. (2005a). Experimental violation of a cluster state Bell inequality. *Physical Review Letters*, *95*, 020403.
Walther, P., Resch, K. J., Rudolph, T., Schenck, E., Weinfurter, H., Vedral, V., et al. (2005b). Experimental one-way quantum computing. *Nature (London), 434*, 169.
Wilde, M. M., & Uskov, D. B. (2009). Linear-optical hyperentanglement-assisted quantum error-correcting code. *Physical Review A*, *79*, 022305.
Yang, T., Zhang, Q., Zhang, J., Yin, J., Zhao, Z., Zukowski, M., et al. (2005). All-versus-nothing violation of local realism by two-photon, four-dimensional entanglement. *Physical Review Letters*, *95*(24), 240406.
Zhao, Z., Yang, T., Chen, Y.-A., Zhang, A.-N., Żukowski, M., & Pan, J.-W. (2003). Experimental violation of local realism by four-photon Greenberger–Horne–Zeilinger entanglement. *Physical Review Letters*, *91*, 180401.
Żukowski, M., Zeilinger, A., & Horne, M. A. (1997). Realizable higher-dimensional two-particle entanglements via multiport beam splitters. *Physical Review A*, *55*(4), 2564–2579.

CHAPTER 7

A Pseudoclassical Method for the Atom-Optics Kicked Rotor: from Theory to Experiment and Back

Mark Sadgrove[a] and **Sandro Wimberger**[b]

[a]*Institute for Laser Science, The University of Electro-communication, 1-5-1 Chofugaoka, Chofu, Japan*
[b]*Institut für Theoretische Physik, Universität Heidelberg, Philosophenweg 19, 69120 Heidelberg, Germany*

Contents

Advances in Atomic, Molecular, and Optical Physics, Volume 60, Copyright © 2011 Elsevier Inc.
ISSN 1049-250X, DOI: 10.1016/B978-0-12-385508-4.00007-3.

Abstract We review the concept and applications of a semiclassical (ϵ-classical or pseudoclassical) approximation to the resonant dynamics of an atom "kicked" by a pulsed, periodic potential. This powerful method allows us to derive analytical results in the deep quantum limit of the kicked rotor. Additionally, classical phase space portraits may be used to represent the dynamics even though the system is fundamentally quantum mechanical. The technique has been successfully adapted for systems including noise and decoherence, as well as systems for which the initial state is a trivial quantum superposition (leading to directed transport at quantum resonance). For almost a decade, theoretical investigations and experimental investigations have been proceeding hand-in-hand in this field, which has been stimulated regularly by experimental progress in controlling driven dynamical systems. Here, we review both theoretical and experimental advances, which in turn may inspire future applications of the presented pseudoclassical method.

NOTATION

M	atomic mass
k_L	laser wave vector
T	laser pulse period
ω_{rec}	recoil angular frequency
p	atomic momentum in $2\hbar k_L$ units
β	rescaled atomic quasi-momentum
τ	kicking period in dimensionless units
t	total number of kicks and kick total time in units of τ
k	kicking strength in dimensionless units
ϵ	detuning from resonance value
	$\tilde{k} \equiv \lvert\epsilon\rvert k$
	$\omega = \sqrt{\tilde{k}}$

1. INTRODUCTION

1.1 The Quantum Kicked Rotor

The kicked rotor is a model system in the study of chaos. It is physically embodied by a "Gedankenexperiment" in which a rigid pendulum

is subject to periodic, sharp pulses from gravity (referred to as momentum "kicks") and evolves freely between those pulses. Its formal classical description is known as the *standard map* (Chirikov, 1979), and it is arguably the simplest Hamiltonian system in which to study the onset of chaotic dynamics (Lichtenberg & Lieberman, 1992).

Given its status as a paradigm system, it is natural that studies of the *quantum* dynamics of chaotic systems (vulgo *quantum chaos*) have focused heavily on the quantized standard map or, equivalently, the quantum kicked rotor (QKR). It became apparent in early numerical studies of the QKR that quantization of the system produced two particularly notable divergences from the classical dynamics of the standard map. Most well known is the appearance of *dynamical localization* (DL) in the generic quantum dynamics, that is, the freezing of diffusive energy growth after a characteristic quantum break time (Casati et al., 1979; Fishman, 1993; Izrailev, 1990). It was later demonstrated that the quantized standard map could be mapped onto a disordered tight-binding model in solid-state physics, demonstrating a link between the DL effect in the QKR and spatial Anderson localization in disordered solids (Fishman et al., 1982). Recently, this analogy between the QKR and solid-state systems was used to demonstrate a dynamical analog of the famous metal-insulator transition using cold atoms (Chabé et al., 2008; Lemarié et al., 2010).

Aside from the celebrated phenomenon of DL, the quantization of the standard map produces another notable qualitative difference between the classical and quantum dynamics. Quantization of the rotor momentum introduces a natural time scale to the system which is absent in the usual standard map. As the strength of the kicks is increased in the classical picture, chaos results and finally all invariant tori in phase space are completely destroyed by this strong perturbation of the pendulum dynamics. Among other things, this global chaos prevents the possibility of resonant driving by the kicks. However, in the quantum system, even in this chaotic limit, momentum quantization guarantees that the kick frequency remains an independent parameter along with the kick strength. This allows for resonant driving of discrete quantized states at certain kick periods, realizing the so-called *quantum resonances* (QRs) of the QKR (Dana & Dorofeev, 2006; Guarneri, 2009; Izrailev & Shepelyansky, 1979, 1980; Izrailev, 1990; Tian & Altland, 2010). In the present review, we will concern ourselves with the properties of the most prominent QRs (the so-called principal QRs) and, more precisely, with the dynamics of ensembles of cold atoms in the close vicinity of those resonances.

For a system rich enough to encompass dynamics analogous to Anderson-localization (Anderson, 1958; Lee & Ramakrishnan, 1985), it is not surprising that analytical results predicting the behavior of the QKR are few and far between. Kick-to-kick correlations remain analytically tractable only for small times (Daley & Parkins, 2002; Shepelyansky, 1987), and DL itself has only recently been rigorously demonstrated to exist for

the QKR (Bourgain, 2002; Jitomirskaya, 2002). Although numerical simulations of the system are relatively easy to perform, they usually provide little insight. In this review, we will detail one of the few approaches to the QKR that simplifies understanding and generates true physical insight about the system, in this case in the vicinity of the principal QRs. The so-called ϵ-classical method that we study accomplishes this insight by taking advantage of the fundamental periodicities of the quantum system to produce a *pseudoclassical* model for the near-resonant dynamics. The first insight this allows is that due to the pseudoclassical phase space description, we can simply illustrate the dynamics of the system near to the QRs. The second insight, which stems from these phase space portraits, is the existence of closed form analytical *scaling functions*. The derivation of these scaling functions marks one of the few analytical and, at the same time, experimentally useful results available for the QKR. Furthermore, the simplest of these scaling functions (in the absence of noise and external perturbations) is given as a function of a single parameter which combines time, detuning from resonance and strength of the kicks, providing a unified understanding of the effect of parameter changes on the quantum dynamics.

Since the original derivation of the ϵ-classical standard map (Fishman et al., 2002; Wimberger et al., 2004), it has been adapted to provide analytical theories for the QKR with decoherence (Wimberger et al., 2003), amplitude fluctuations (Sadgrove et al., 2008), for highly nonclassical initial states (Sadgrove & Wimberger, 2009) (as in the directed diffusion experiments discussed in Section 3.4), and also for the stability of wave packets with respect to deterministic variations of the kick strength (via fidelity) (Abb et al., 2009). In each case, as we will discuss, understanding comes from first examining the ϵ-classical phase space and its changes when varying parameters, and then adapting the theory to take account of those changes.

1.2 The Atom-Optics Realization of the Quantum Kicked Rotor

Aside from the addition of elegant analytical results to the canon of quantum chaos, the principle interest of the pseudoclassical method which we review here is that it was developed in response to and alongside experiments. Indeed, the initial development of the theory in refs. (Fishman et al., 2002; Wimberger et al., 2003, 2004) was in response to experimentally observed phenomena (d'Arcy et al., 2001; Oberthaler et al., 1999). It is therefore necessary to give a brief account of the experimental setup in which observations of the kicked rotor typically take place (Raizen, 1999).

The QKR was first realized experimentally using cold noninteracting sodium atoms exposed to a pulsed, optical standing wave (with spatial

period π/k_L, k_L being the wave vector of the laser creating the potential), far detuned from the nearest atomic transition (Latka & West, 1995; Moore et al., 1995). Before this publication, DL had been studied in the context of driven Rydberg atoms (Arndt et al., 1991; Bayfield et al., 1989; Casati et al., 1988; Galvez et al., 1988; Krug et al., 2003) and atoms in a modulated standing-wave potential (Moore et al., 1994). However, in Moore et al. (1995), the realization of effective $\delta-$like pulses (i.e., pulses much shorter than the pulsing period T) created a very good experimental realization of the standard map. This realization became known as the *atom-optics kicked rotor* (AOKR). Although the atom-optics setting swaps angular for linear momentum, it still makes the unique aspects of the QKR more clear. The atomic system may be represented by the following scaled Hamiltonian (Graham et al., 1992)

$$H(t') = \frac{p^2}{2} + k\cos(z)\sum_{j=0}^{t-1}\delta(t' - j\tau), \tag{1}$$

where p is the atomic momentum in units of $2\hbar k_L$, z is the atomic position scaled by $2k_L = 4\pi/\lambda$, t' is time. t is an integer which counts the total number of kicks, and in units of the kicking period τ it represents the total time. The scaled kicking period τ is defined by $\tau = 8\omega_{\text{rec}}T$, where $\omega_{\text{rec}} = E_{\text{rec}}/\hbar = \hbar k_L^2/2M$ is the angular recoil frequency for atoms of mass M and E_{rec} the recoil energy. The kicking strength k is proportional to the optical standing-wave intensity. An important time scale when studying QRs is defined by the Talbot time $T_T = \pi\hbar/(2E_{\text{rec}})$, since QRs can be seen to arise from nothing other than the Talbot effect (Deng et al., 1999; Dubetsky & Berman, 1997; Lepers et al., 2008; Talbot, 1836) (albeit in the time domain) for atomic matter waves diffracted from the "grating" induced by the flashed periodic potential. We will motivate this analogy further in Section 2.1. The state evolution of an atom from one kick to immediately after the next kick is determined by the unitary one-cycle Floquet operator (Wimberger et al., 2003):

$$\hat{\mathcal{U}}_{\beta,k} = \mathrm{e}^{-ik\cos(\hat{\theta})}\,\mathrm{e}^{-i\frac{\tau}{2}(\hat{\mathcal{N}}+\beta)^2}, \tag{2}$$

where $\theta \equiv z \bmod 2\pi$. The Floquet operator of Equation (2) differs from the Floquet operator of the original model of the QKR by the phase β, which represents the rescaled quasi-momentum of the atom moving along a line in contrast to a rotor which would move on a circle. By translational invariance of the potential, quasi-momentum is conserved for all times and, therefore, it acts just as a continuous index defined by the fractional part of the real momentum p (Wimberger et al., 2003). $\hat{\mathcal{N}}$ then corresponds to the integer part of p and can be interpreted as an angular momentum

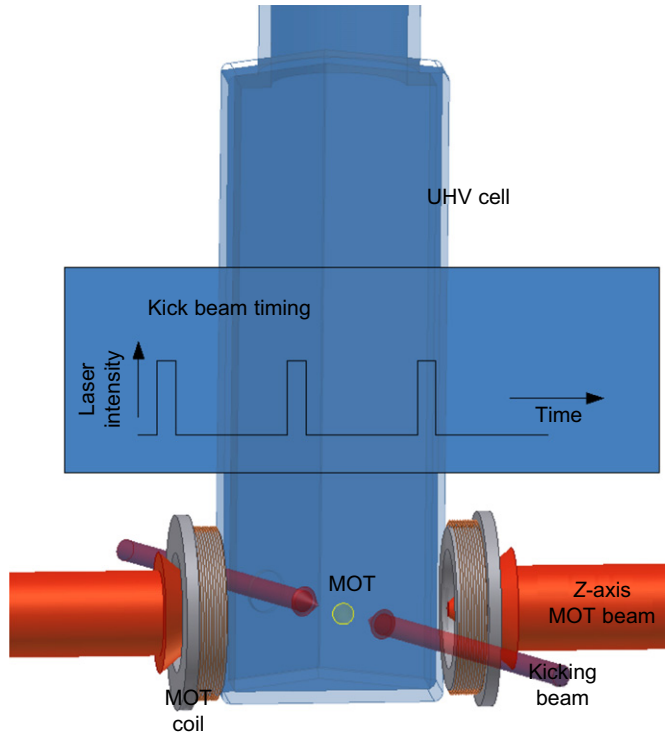

Figure 1 Diagram of the most basic experimental configuration of the atom-optics kicked rotor. Thin arrows represent counter-propagating, co-polarized laser beams which intersect with a sample of cold atoms which are released from a magneto-optical trap (MOT). (Note that only two of the six MOT beams are shown in this diagram). The kicking laser beams are periodically gated to create a pulsed potential with a form controlled precisely by the experimenter.

operator in the $\theta-$representation, $\hat{\mathcal{N}} = -i\mathrm{d}/\mathrm{d}\theta$, with periodic boundary conditions.

As shown schematically in Figure 1, all AOKR experiments using cold atoms follow roughly the same common sequence, first realized in (Moore et al., 1995): (1) a sample of atoms is laser cooled in a magneto-optical trap (MOT), (2) the cooled atomic sample is released from the trap (all optical and magnetic fields are turned off), (3) the released atoms are subject to a number of periodic pulses ("kicks") from an optical standing wave which intersects with the sample, and (4) the kicked atoms are allowed to expand for some milliseconds before being exposed to near-resonant light and having the consequent fluorescence distribution imaged on a charge coupled device (CCD) camera. This recipe gives access to the atoms' momentum distribution after t kicks, as shown in Figure 2. The

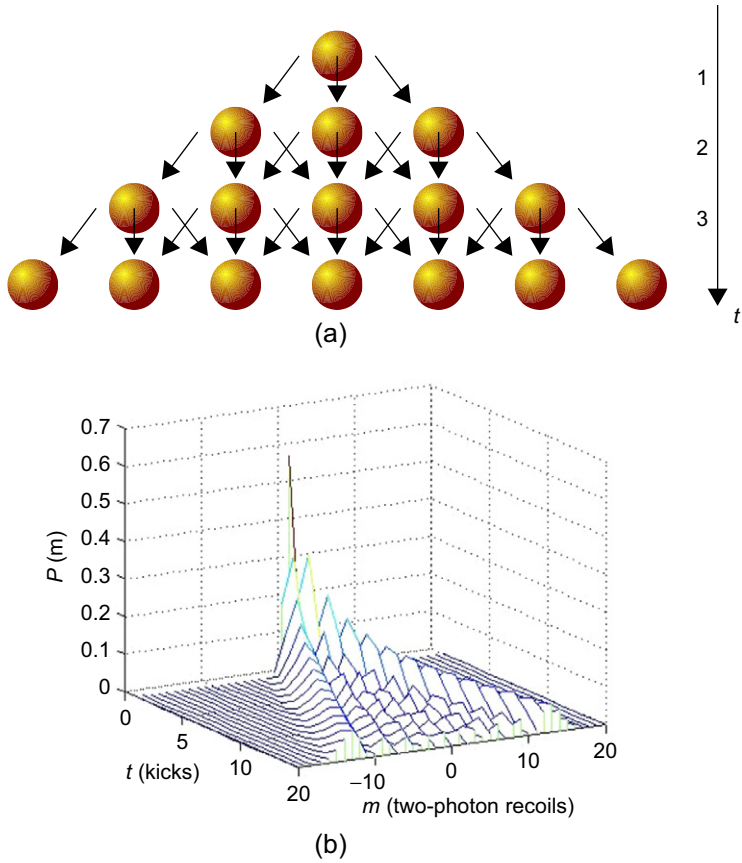

Figure 2 (a) Schematic depiction of the atom diffraction over a few kicks from the intersected optical standing wave, following just first order diffraction into momentum eigenstates separated by $2\hbar k$ (from an initial zero momentum eigenstate). Each ball represents a momentum eigenstate with value m in units of $2\hbar k$. The importance of interference effects (whenever two lines intersect in the diagram) becomes clear, and the difficulty of making analytical predictions in the general case is thus apparent. (b) Shows the predicted momentum distribution over 15 successive kicks for an atom starting from an initial zero momentum state and kicked at QR.

mean energy of the atomic ensemble may be inferred by calculating the second moment of the momentum distribution. Since the first realization of the AOKR in (Moore et al., 1995), however, a number of variations on steps (1–3) in the experiment have been implemented including the use of a diluted Bose–Einstein condensate (BEC) as the initial state (Currivan et al., 2009; Duffy et al., 2004b; Ryu et al., 2006), kicking of trapped samples (Duffy et al., 2004a), and nonperiodic kicking fields (Jones et al., 2007;

Monteiro et al., 2002), among other innovations as we will discuss now briefly.

One of the earliest variations on the AOKR experiment was the addition of noise in various forms to observe decoherence effects. In Ammann et al. (1998), a controllable, nonzero spontaneous emission rate was introduced leading to the destruction of DL. Experiments with a randomly fluctuating standing-wave amplitude (Klappauf et al., 1998; Milner et al., 2000) or temporal period between kicks (Oskay et al., 2003; Sadgrove et al., 2004) demonstrated similar decoherence effects, seen in the changing lineshape of atomic momentum distributions. However, when the effects of spontaneous emission were tested at QR in (d'Arcy et al., 2001), it was found that rather than destroying the quantum energy resonances, the addition of spontaneous emission *enhanced* their visibility. This unusual result, similar to behavior noticed in other investigations (Daley et al., 2002), was explained in (d'Arcy et al., 2004), and also in (Wimberger et al., 2003) using ϵ-classical theory as we will explain in detail in Section 3.3.1. The unusual response of the QR peaks to noise was confirmed in (Sadgrove et al., 2004), where the robustness of the QR peak structure in the presence of amplitude fluctuations was demonstrated and explained in terms of ϵ-classical stability of the near-resonant dynamics. More recently, the stability of the resonance behavior has been quantified more rigorously in experiments where *fidelity* of quantum states was measured directly (Tonyushkin et al., 2009; Wu et al., 2009).

Another fruitful variation on the kicked rotor is the kicked *accelerator*, where the standing wave is oriented in the vertical direction. This allows so-called accelerator modes to emerge—narrow momentum classes of atoms which gain energy in a resonant fashion from the pulsed standing wave (Oberthaler et al., 1999). These accelerator modes and their stability (Schlunk et al., 2003a) inspired the first ϵ-classical treatment of kicked atoms in (Fishman et al., 2002), and investigations of this rich system have also extended to higher order accelerator modes (Guarneri & Rebuzzini, 2008; Ramareddy et al., 2010), accelerator mode decay (Sheinman et al., 2006), and to study so-called Arnol'd Tongues (Guarneri et al., 2006). At this point, however, we note that the present review is concerned only with the "horizontal kicking" system as used in the original kicked rotor experiments (Moore et al., 1995). The behavior found when the kicks are administered in the vertical direction and acceleration due to gravity is nonnegligible is an interesting topic worthy of review in its own right.

Perhaps the single greatest experimental advance in the investigation of kicked atoms involved, the use of atoms sourced from a degenerate quantum gas rather than a thermal MOT source. The first such experiments using a dilute BEC (for which atom–atom interactions can be neglected [Wimberger et al., 2005a]) subject to standing-wave pulses were performed at NIST in Gaithersburg in a strictly atom-optics setting

(Deng et al., 1999). Both atom diffraction into discrete orders and the time-domain Talbot effect were demonstrated in these early studies. Other investigations probed QR and the opposite regime of anti-resonance (at which the system oscillates between states instead of absorbing energy [Izrailev, 1990]) more carefully using a BEC (Duffy et al., 2004b) and also investigated the kicking of a BEC in situ with the magnetic trap still on (Duffy et al., 2004a). BEC studies of the AOKR, along with nondegenerate ultra-cold samples (Kanem et al., 2007), also finally allowed such central predictions about QR as ballistic energy growth and some fractional resonances to be successfully demonstrated in the laboratory (Ryu et al., 2006).

In Figure 3, manifestations of QR behavior are shown in two different atom-optics settings. Figure 3a and b shows raw absorption images of a dilute BEC subject to anti-resonant (half-Talbot time) and resonant (Talbot-time) kicking, respectively. When the time between pulses equals half of the Talbot time, we see oscillations in the atomic energy from one kick to the next (seen here as alternate expansion and contraction of the atomic momentum distribution), whereas when the period matches the Talbot time, ballistic growth is seen and the momentum distribution expands with each kick. Figure 3c shows mean energies for a kicked atomic ensemble for which the initial momentum distribution is much larger than $2\hbar k$. In this case, individual momentum orders are not resolvable and the effect of resonant kicking on the atomic momentum distribution is more subtle. However, a strong signature of QR is still seen in the mean energies at integer or half integer multiples of the Talbot time. It is interesting to note that these energy peaks are indistinguishable between the anti-resonant and resonant cases, due to the fact that the broad quasi-momentum distribution allows resonant transport in both cases. In both of the experimental situations shown in Figure 3, ultra-cold atoms were kicked by standing-wave pulses which satisfied the *Raman–Nath* condition (Nath, 1936), which, physically speaking, requires that the pulse time is short compared with the time it takes for atoms to traverse a single period of the standing wave. Outside the Raman–Nath regime, momentum transfer to atoms is curtailed (Bharucha et al., 1999; Blümel et al., 1986; Vant et al., 1999), the extreme case being an optical lattice in which the standing wave is always on and the atoms do not absorb energy as from a flashed lattice. We also note in passing that the half-Talbot time effect was recently used to demonstrate fidelity decay in cold atoms perturbed by standing-wave kicks (Wu et al., 2009). We will have more to say on the topic of fidelity later in this review (see Section 3.5).

Still further intriguing variations on the basic AOKR experiment are possible when deviations from strict periodicity of the kicking are introduced. Double kicks were first used to probe the dynamics of atoms in the presence of classical phase space structures (Vant et al., 1999), but

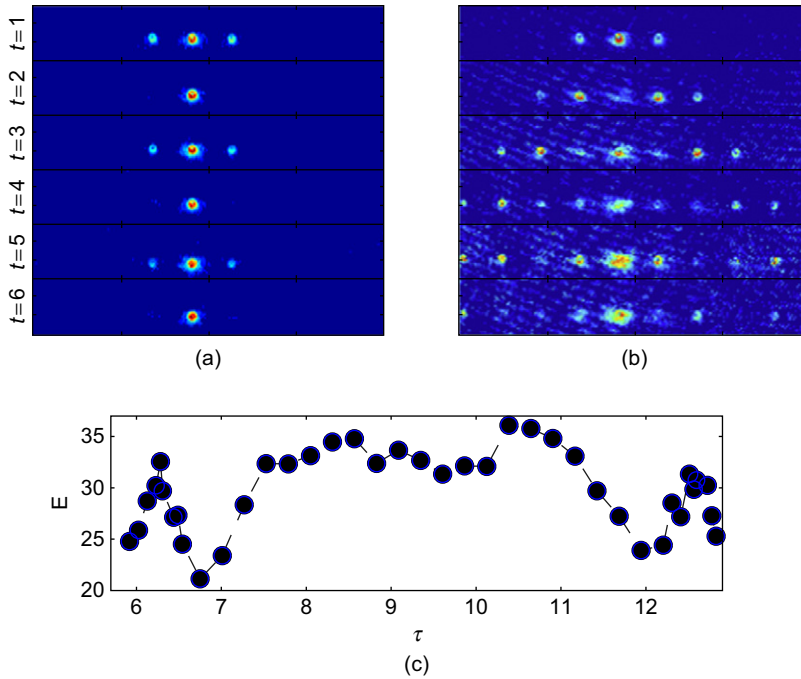

Figure 3 Manifestations of QR phenomena in cold atom experiments. (a) ($\tau \approx 2\pi$) and (b) ($\tau \approx 4\pi$) show absorption images for a kicked Bose–Einstein condensate demonstrating the clearly distinguishable cases of anti-resonance and resonance, respectively. This behavior is seen for an atomic ensemble with an initial momentum width $\sigma \ll 2\hbar k_L$. The absorption images reproduce the atomic momentum distribution after t kicks, schematically introduced in Figure 2a. At anti-resonance, atoms oscillate between 0 and nonzero energy from kick-to-kick. At resonance, the atoms gain energy quadratically as the kick number increases. (c) Shows the case for atoms where $\sigma \gg 2\hbar k_L$. In this case, we see peaks in the mean energy (on the y-axis) near the resonance *and* anti-resonance values at $\tau = 4\pi$ and 2π, respectively in (c).

the introduction of multiple kicking frequencies yielded more surprising results in (Lemarié et al., 2010). In these experiments, resonances were found depending on the ratio between two kicking frequencies. These resonances were further shown to possess a *sub-Fourier* nature, suggesting possible applications to signal processing. The QRs were later shown to possess a similar sub-Fourier narrowing of the mean energy with time, as will be discussed below in Section 3.1. Interestingly, an analysis of the fidelity overlap of two states kicked with slightly different periods shows such a sub-Fourier scaling, which is yet another manifestation of the stability of QR motion useful for applications (see the recent papers [McDowall et al., 2009; Talukdar et al., 2010]).

Finally, at the intersection between nonperiodic driving and studies performed with a BEC, investigations of directed transport have recently taken place. The goal to create a Hamiltonian ratchet (Flach et al., 2000; Hänggi & Marchesoni, 2009; Schanz et al., 2001) using a variant of the kicked rotor system was first investigated using thermal atoms (Jones et al., 2007; Monteiro et al., 2002) but a more surprising variation on ratchet motion was found using a BEC prepared in an initial superposition of momentum eigenstates and subjected to kicking at QR (Dana et al., 2008; Gong & Brumer, 2006; Lundh & Wallin, 2005; Sadgrove et al., 2007). It is also interesting to note that in the first true "ratchet" for cold atoms, achieved using an approximate saw-tooth potential combined with modulation of the standing wave, a significant current was only observed when the modulation frequency was close to QR (Salger et al., 2009).

Historically, the motivation to study the QKR experimentally was to observe DL, thus demonstrating the restriction on chaotic motion expected in quantum systems arising from a stabilizing interference effect. However, as the AOKR was extended to different initial conditions and driving fields, the QRs have become more compelling phenomena of study, due to the possible applications to precision measurements, atomic transport, and stable quantum behavior that they represent (Madroñero et al., 2006). Thus, we believe it is timely to review the tools provided by the pseudoclassical description of the quasi-resonant regime embodied by the ϵ-classical theory of QR. For reasons of compactness, we restrict our overview to the principal QRs of the QKR and mainly, but not exclusively, discuss our own research work on the topic.

2. THE PSEUDOCLASSICAL METHOD FOR NEARLY RESONANT QUANTUM MOTION

This section introduces the theoretical concepts of the pseudoclassical method which has proven very useful for the description of experiments and applications such as those detailed in the following Section 3. We start out with a short review of the dynamical regimes of the QKR, in particular, the QR regime at which the rotor maximally absorbs energy from the kicking field, essentially because of a revival of its wave function in momentum space in-between two kicks. The reported pseudoclassical method (see Section 2.3) allows us to characterize the QKR and its experimental realization by kicked cold or ultra-cold noninteracting atoms (see Section 1) in the vicinity of these QRs.

2.1 Dynamical Localization and Quantum Resonances

As mentioned in the introduction, the QKR—at first glance a system seemingly too simple to be of practical use—became famous because it

reproduces in a clear way the predictions made by P. W. Anderson on the transport of single-particles wave packets across disordered samples (Anderson, 1958; Lee & Ramakrishnan, 1985). Although the original idea of Anderson—recently verified in an ingenious experiment by Billy et al. (2008)—describes transport in real space, the QKR realizes the same situation in momentum space (Fishman, 1993; Fishman et al., 1982). Kicking the system with periods such that $\tau/4\pi$ is sufficiently far from a rational number leads to what is known as "dynamical localization" (DL) of a spreading wave packet, stressing its dynamical origin.[1] DL, as a purely quantum effect, suppresses the classically expected diffusion in systems such as the QKR which have a classically chaotic counterpart. It is a ubiquitous effect which also occurs in other periodically driven quantum chaotic systems, such as microwave driven hydrogen or alkali Rydberg states of electronic wave packets (Casati et al., 1988; Wimberger & Buchleitner, 2001) (for which DL was indeed observed for the very first time in the laboratory [Arndt et al., 1991; Bayfield et al., 1989; Galvez et al., 1988]). Although for driven Rydberg states the effect of localization manifests itself only indirectly in the measurable ionization yield, the experimental realization of the QKR allowed the observation of localized momentum space wave functions in situ along with the extraction of the average energy of the kicked atoms (Bharucha et al., 1999; Moore et al., 1995) (i.e., the second moment of the wave packet in momentum space) long before its real space analog could be directly observed (Billy et al., 2008). Since we aim to describe the motion close to QR for the QKR, here we provide only an intuitive description of DL: for $\tau/4\pi$ irrational, the phases of the free part of the QKR evolution in momentum representation, i.e., from $\exp(-\mathrm{i}\tau n^2/2)$ (see Equation [2] for $\beta = 0$), in-between two kicks are essentially randomly distributed between the different momentum classes. Even if deterministically defined, these phases have a pseudo-random character, which is discussed, e.g., in (Brenner & Fishman, 1992). This pseudo-randomness plays the same role as the spatial disorder in the real-space Anderson problem, and it essentially leads to a destructive interference in the temporal evolution of the QKR hindering the spread of the wave packet in momentum space (after some transient time which is known as the "break time" [Shepelyansky, 1987]).

The above mentioned phases $\exp(-\mathrm{i}\tau n^2/2)$ allow us to understand the origin of quantum resonant motion as well. QRs occur for rational values of $\tau/4\pi$ leading to a complete (i.e., for all momenta n) or partial (i.e., for a subset of momenta) phase revivals in-between two successive kicks.

[1]The notion dynamic or dynamical localization is unfortunately also used in different contexts, one example being the suppression of tunneling by a periodic driving force (Dunlap & Kenkre, 1986), for experimental realizations of this effect see, e.g., (Kierig et al., 2008; Lignier et al., 2007).

Those revivals are analogous to the Talbot effect or the fractional Talbot effect, respectively, of interfering light or matter waves diffracted and recombined at a series of gratings, see, e.g., (Dubetsky & Berman, 1997; Talbot, 1836) for a discussion of this constructive interference effect. In the following, we concentrate on the *principal QRs of the QKR* at which a complete revival happens, i.e., $\exp(-\mathrm{i}\,\tau n^2/2) \equiv 1$ for all $n \in \mathbb{Z}$, or for real atoms moving along a line, $\exp(-\mathrm{i}\,\tau(n+\beta)^2/2) \equiv 1$, which occurs at $\tau = 2\pi\ell$ (ℓ a positive integer) and $\beta = 1/2 + j/\ell \bmod(1), j = 0, \ell, \ldots, \ell - 1$ (Wimberger et al., 2003).

2.2 Exact Results at Quantum Resonance

The existence of QRs in the QKR was noticed by Izrailev and Shepelyansky (1979, 1980) shortly after the discovery of DL. They obtained the exact quasi-momentum spectrum for some major resonances. This spectrum must be continuous to support unlimited ballistic growth with the number of kicks t for the mean energy of the QKR, i.e., $E(t) = E(t=0) + \alpha t + \gamma t^2$, for appropriate values of the α and γ constants (Guarneri, 2009; Izrailev, 1990). For the principal QR at $\tau = 4\pi$ and $\beta = 0$, one can immediately see from Equation (2) that the spectrum is given by $e(\theta) = k\cos(\theta)$ for $\theta \in [0, 2\pi)$. Hence it is a continuous function of the θ angle variable of the rotor. Nevertheless, exact results at QR have been rare until recently (Guarneri, 2009; Izrailev, 1990; Tian & Altland, 2010), not least because the resonances were regarded as a rather peculiar property of the QKR. Inspired by experiments by d'Arcy et al. (2001), new theoretical as well as experimental progress has been made over the last decade. As a background for the pseudoclassical theory introduced in the next subsection, we review briefly some aspects of this theoretical progress at exact QR for $\delta-$kicked noninteracting atoms having a flat uniform distribution $f(\beta)$ of quasi-momenta $\beta \in [0, 1)$. As derived in detail in (Wimberger et al., 2003), the average energy of such an atomic ensemble at $\tau = 2\pi\ell$ ($\ell \in \mathbb{N}$) increases linearly with the number of kicks t

$$\langle E(n_0, \beta, t)\rangle_{n_0,\beta} \sim \langle E(\beta, t=0)\rangle_{n_0,\beta} + \frac{k^2 t}{4}, \tag{3}$$

where n_0 are the integer parts of the atomic momenta at time $t = 0$. For the momentum distribution of the kicked ensemble, we have the asymptotic result valid at large $t \to \infty$ and for $n \gg n_0$

$$P(n) \sim \frac{4k}{\pi^3 n^2}. \tag{4}$$

In essence, the contribution of many nonresonant rotors or nonresonant values of β and very few resonant ones (see end of previous subsection)

averages to a linear increase of the mean energy. This continued increase of the energy means that higher and higher momentum classes become populated with increasing time. This builds up the algebraic distribution of momenta (which, at finite t, shows a time-dependent cutoff momentum $n_{\mathrm{cut}} \approx \pi kt/2$ up to which Equation (4) faithfully describes the actual distribution [Wimberger et al., 2003]).

The experimental possibility of adding noise to the system (Ammann et al., 1998; d'Arcy et al., 2001, 2004; Klappauf et al., 1998; Milner et al., 2000; Oskay et al., 2003; Sadgrove et al., 2004) inspired a number of theoretical treatments yielding exact results, which typically are rare for noisy dynamical systems. Here, we quickly review two interesting cases of noise which will be extended later on in Sections 3.3.2 and 3.3.1 for values of τ not exactly but close to QR condition. The first of these results at exact QR describes the effect of amplitude noise in the kick pulse on the dynamical evolution of the atoms (Brouard & Plata, 2003; Sadgrove et al., 2008). It predicts a linear increase of the average energy of an atomic ensemble under the same assumptions as made above (now averaged over the ensemble and over many noise realizations):

$$\langle E(n_0, \beta, t)\rangle_{n_0,\beta,\delta k} \sim \langle E(\beta, t = 0)\rangle_{n_0,\beta} + \frac{k^2 t}{4}\left(1 + \frac{L^2}{12}\right), \tag{5}$$

where the actual kick strength is $k + \delta k$, with δk uniformly distributed in $[-L/2, L/2]$. The second term on the right side of the equation is now corrected with respect to Equation (3) by the standard deviation of the noise $L^2/12$. Since the conditions for QRs do not depend on the kick strength but just on τ and β, this case of amplitude noise is still fairly simple to analyze.

More work is needed to extend the above Equations (3) and (4) to a perturbation arising from spontaneous emission acting on the kicked atoms. For the specific realization of such an experiment at Oxford by d'Arcy et al. (2001, 2004), spontaneous emission was induced in a very controlled way by an additional light field independently of the kicking laser. It was then shown in Wimberger et al. (2003) that this kind of spontaneous emission acts as additional kicks (with random distributions of kick strengths) on the atoms, which occur in-between successive $\delta-$kicks of the original model. The result is that the average energy of an ensemble (averaged over many realizations of the random spontaneous emission events) again increases linearly in time. The momentum distribution approaches a Gaussian form with zero mean and a standard deviation $k^2 t/2 + Dt$ (as long as the initial – at $t = 0$ – momentum distribution of the atoms is symmetric around zero), where D is now the diffusion constant given by the mean square momentum change per period τ due to spontaneous emission. These results are based on exact proofs to be found in Wimberger et al. (2003), but one may intuitively understand them as

describing a diffusive process in momentum space driven by the random kicks from spontaneous emission.

2.3 Pseudoclassical Theory for Principal Quantum Resonances

This subsection presents the essentials of the pseudoclassical theory which has proven very powerful for describing the QKR and its experimental realizations in the vicinity of the QRs. This method allows us to extend our theoretical understanding to a regime for which direct quantum calculations would be extremely difficult in general. The pseudoclassical approach is inspired by a rescaling usually done for the standard semiclassical limit of the QKR. The latter is obtained by *simultaneously* letting the kick period $\tau \to 0$ and the kick strength $k \to \infty$ but keeping their product $K_s \equiv \tau k$ fixed. Fixing the "stochasticity parameter" K_s fixes also the classical phase space structure described by the standard map, the classical correspondence of the QKR:

$$I_{t+1} = I_t + K_s \sin(\theta_{t+1}), \quad \theta_{t+1} = \theta_t + I_t \mod(2\pi). \tag{6}$$

Here, the momentum I is rescaled with respect to the physical momentum p viz. $I = \tau p$, just as the kick strength above. In the standard semiclassical limit, the quantum version of the rotor now has less and less time for free phase evolutions while the kicks dominate more and more over these phases, c.f. the Floquet operator in Equation (2). Nevertheless, the classical phase space is not at all affected since K_s is kept constant, and it can either describe regular (for sufficiently small $K_s \ll 1$), chaotic (for $K_s \gtrsim 5$), or mixed regular-chaotic motion (for intermediate values of K_s).

The same idea of rescaling variables can now be applied for kick periods which are not at all small, i.e., far away from the standard classical limit, but for $\tau = 2\pi\ell + \epsilon$ ($\ell \in \mathbb{N}$ and ϵ small) in the vicinity of the QR condition on τ. The crucial difference to the scaling for the standard semiclassical limit is that the scaling factor is not directly τ but $\epsilon = \tau - 2\pi\ell$, the detuning from the exact resonant value (Hogg & Huberman, 1983). As we will see below, this gives a pseudoclassical map which is always integrable in the limit $\epsilon \to 0$, even if the system has a completely chaotic classical analog in the unscaled coordinates p and θ. Rescaling $I \equiv |\epsilon|N$ (for $p = N + \beta$) and $\tilde{k} \equiv |\epsilon|k$, we can rewrite the Floquet operator of the quantum map, c.f. Equation (2), in the following way:

$$\hat{\mathcal{U}}_{\beta,k}(t) = \mathrm{e}^{-\frac{\mathrm{i}}{|\epsilon|}\tilde{k}\cos(\hat{\theta})}\, \mathrm{e}^{-\frac{\mathrm{i}}{|\epsilon|}\hat{\mathcal{H}}_\beta}, \tag{7}$$

with

$$\hat{\mathcal{H}}_\beta(\hat{I}, t) = \frac{1}{2}\mathrm{sign}(\epsilon)\hat{I}^2 + \hat{I}(\pi\ell + \tau\beta). \tag{8}$$

To arrive at Equation (7), we have just rewritten the free evolution part of the Floquet operator for the $\beta-$rotor given in Equation (2) as follows:

$$e^{-i\frac{\tau}{2}(n+\beta)^2} = e^{-i\pi\ell n^2} e^{-i\frac{\epsilon}{2}n^2} e^{-i\tau n\beta} e^{-i\frac{\tau}{2}\beta^2} = e^{-i\pi\ell\frac{I}{|\epsilon|}} e^{-i\,\mathrm{sign}(\epsilon)\frac{I^2}{2|\epsilon|}} e^{-i\tau\beta\frac{I}{|\epsilon|}} e^{-i\frac{\tau}{2}\beta^2}, \qquad (9)$$

using the identity $\exp(-i\pi\ell n^2) = \exp(-i\pi\ell n)$ and where the last factor does not depend on I and may be omitted.

If $|\epsilon|$ is now regarded as the Planck constant, then Equation (7) formally defines just the quantized version of either of the following classical maps:

$$I_{t+1} = I_t + \tilde{k}\sin(\theta_{t+1}), \quad \theta_{t+1} = \theta_t \pm I_t + \pi\ell + \tau\beta \mod(2\pi), \qquad (10)$$

where $\pm$ has to be chosen according to the sign of ϵ. We stress that "classical" here is not related to the $\tau \to 0$ limit but to the limit $\epsilon \to 0$ instead. The small$-|\epsilon|$ asymptotics of the quantum $\beta-$rotor is thus equivalent to a quasi-classical approximation based on the "classical" dynamics given by Equation (10), that has been dubbed *ϵ-classical* in (Fishman et al., 2002; Wimberger et al., 2003). Changing variables to $J = \pm I + \pi\ell + \tau\beta$, $\vartheta = \theta + \pi(1 - \mathrm{sign}(\epsilon))/2$ turns the maps in Equation (10) into a single standard map (c.f. Equation [6]), known as the ϵ-classical standard map (ϵSM), independent of the value of β:

$$J_{t+1} = J_t + \tilde{k}\sin(\vartheta_{t+1}), \quad \vartheta_{t+1} = \vartheta_t + J_t. \qquad (11)$$

As we have already noted above, the semiclassical limit of the ϵSM is quite different from the one for the usual standard map of Equation (6). Equation (11) *always* describes a completely integrable system for $\epsilon \to 0$, since the effective kick strength $\tilde{k} \propto \epsilon$ also tends to zero in this limit.

To get a feeling for how powerful the method just introduced actually is, we compare in Figure 4 the average energies of an ensemble of rotors as a function of τ in a neighbourhood of the QR at $\tau = 2\pi$. All data are obtained from numerical simulations of the quantum map, Equation (2), and the ϵ-classical map, Equation (10), respectively, for the same initial ensemble of momenta and quasi-momenta. For any given particle in the initial ensemble, the map in Equation (10), with β equal to the quasi-momentum of the particle, was used to compute a set of trajectories started at $I = n_0|\epsilon|$ with uniformly distributed $\theta_0 \in [0, 2\pi)$. The final energies $\epsilon^{-2}I_t^2/2$ at $t = 30$ of the individual trajectories were averaged over θ_0, β, n_0 with the appropriate weights. This is equivalent to using the ϵSM in all cases, with different initial ensembles $J_0 = \mathrm{const} = \pm n_0|\epsilon| + \pi\ell + \tau\beta$.

The main qualitative features emerging of Figure 4 are: (1) on a larger scale along the τ axis, the curves are shaped in the form of a basin with a high, narrow spike in the centre, closely flanked by a much

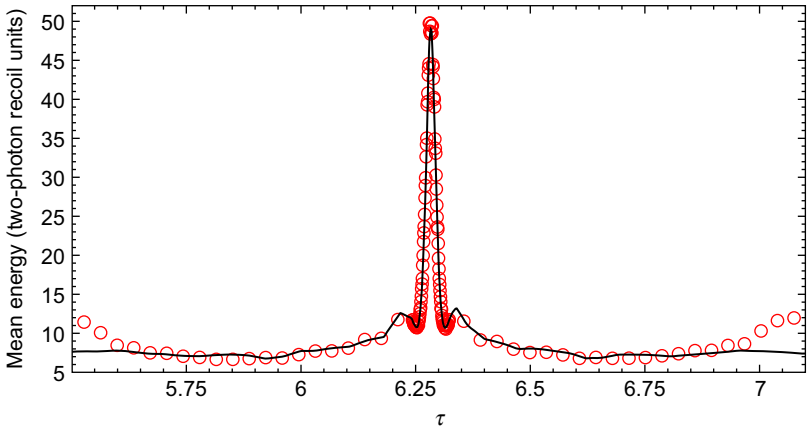

Figure 4 Atomic mean energy vs. τ, after $t = 30$ kicks, for $k = 0.8\pi$ near the QR at $\tau = 2\pi$. Quantum data (solid lines) are compared with ϵ-classical results (circles) for the same initial momentum distribution.

smaller peak on either side. (2) Quantum and ϵ-classical curves agree very well at small $|\epsilon|$, in particular the structure of the spike is the same. Their behavior at large $|\epsilon|$, i.e., for $\tau \gtrsim 6.6$ and $\tau \lesssim 6$ is qualitatively similar but quantitatively different. This overall behavior may be explained in ϵ-classical terms, and an approximate scaling law for the t, k, ϵ dependence of the average energy close to the QRs can be obtained, as shown in the Section 3.1. The ϵ-classical standard map is different from the map obtained in the classical limit proper $\tau \propto \hbar \to 0$. In particular, if $\tau k > 1$, then the classical and the ϵ-classical dynamics are at sharp variance whenever $\tilde{k} < 1$. In the former, unbounded diffusion occurs, whereas in the latter, the dynamics is quasi-integrable instead. In this quasi-integrable system, the ϵ-classical trajectories remain trapped forever in-between impenetrable phase space barriers, which survive small perturbations according to the Kolmogorov–Arnold–Moser (KAM) theorem (Lichtenberg & Lieberman, 1992). It is exactly the change occurring in the ϵ-classical phase space (see Figure 5) as τ is varied at constant k that accounts for the energy vs. τ dependence at fixed time (Figure 4).

In the following, we show that the introduced ϵ-classical technique allows us to fully recover the exact quantum result for the average energy reviewed above, see Equation (3), at exact QR. We assume for simplicity an initially flat distribution of $p_0 \in [0, 1)$; then $I_0 = 0$, and $J_0 = \pi\ell + \tau\beta_0$ with β_0 uniformly distributed in $[0, 1)$ and $n_0 = 0$. Without loss of generality we only consider $\ell = 1$. Hence if $|\epsilon| \ll 1$, then J_0 is practically uniformly distributed over one period (in action) $(\pi, 3\pi)$ of the ϵSM. Since

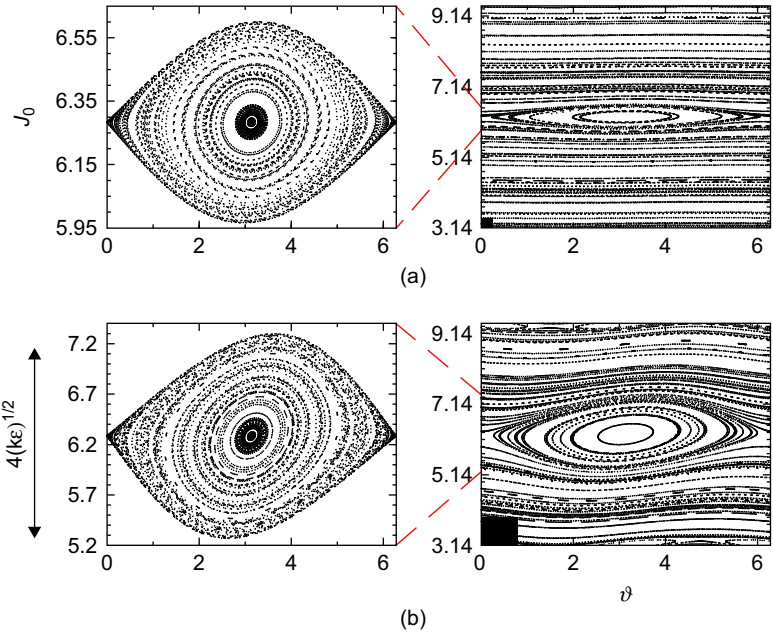

Figure 5 Poincaré surfaces of section for the standard map of Equation (11), and $k = 0.8\pi$, $\epsilon = 0.01$ (a), $\epsilon = 0.1$ (b). As ϵ increases, the invariant curves (right panels) become more and more distorted, with a primary resonance island (left panels) having a width of $\delta J_{\text{res}} \approx 4(\tilde{k})^{1/2}$. The black boxes in the right panels represent the Planck cell of area $2\pi|\epsilon|$.

$J_t = \pm I_t + \pi + \tau\beta$, and $I_0 = 0$, the mean energy of the rotor after a total number of kicks t is:

$$\langle E_{t,\epsilon}\rangle = \epsilon^{-2}\langle I_t^2\rangle/2 = \frac{\langle(\delta J_t)^2\rangle}{2\epsilon^2}, \quad \text{with} \quad \delta J_t = J_t - J_0. \tag{12}$$

The exact QR at $\epsilon = 0$ corresponds to the integrable limit of the ϵSM, where $\delta J_t = 0$. However, $\langle E_{t,\epsilon}\rangle$ is scaled by ϵ^{-2}, so to compute it at $\epsilon = 0$ one has to compute δJ_t at first order in ϵ. This is done by substituting the 0-th ϵ-order of the second part of Equation (11), i.e., $\vartheta_t \simeq \vartheta_0$, into the first part of Equation (11). This leads to

$$\delta J_t = |\epsilon| k \sum_{s=0}^{t-1} \sin(\theta_0 + J_0 s) + r(\epsilon, t), \tag{13}$$

where $r(\epsilon, t) = O(\epsilon)$ as $\epsilon \to 0$ at any fixed t. The energy at time t is found from Equation (13) by taking squares, averaging over θ_0, J_0, dividing by

$2|\epsilon|^2$, and finally letting $\epsilon \to 0$:

$$\langle E_{t,\epsilon}\rangle = \frac{1}{8\pi^2}\int_0^{2\pi} \mathrm{d}\theta_0 \int_\pi^{3\pi} \mathrm{d}J_0\ \frac{(\delta J_t)^2}{\epsilon^2} \quad \stackrel{\epsilon\to 0}{\longrightarrow}$$

$$\frac{k^2}{8\pi^2}\int_0^{2\pi} \mathrm{d}\theta_0 \int_\pi^{3\pi} \mathrm{d}J_0 \left(\sum_{s=0}^{t-1} \sin(\theta_0 + J_0 s)\right)^2 = \frac{k^2}{8\pi}\int_\pi^{3\pi} \mathrm{d}J_0\ \frac{\sin^2(J_0 t/2)}{\sin^2(J_0/2)}. \tag{14}$$

With the help of $\int_0^{2\pi} dx\ \sin^2(tx)/\sin^2(x) = 2\pi t$, this yields:

$$\langle E_{t,0}\rangle = \langle E(\beta, t=0)\rangle_\beta + \frac{k^2}{4}t, \tag{15}$$

where we have added in the first term on the right hand side the small contribution of the initial quasi-momenta in energies which we had neglected so far. Equation (15) reproduces the quantum behavior at exact QR, given by Equation (3) of Section 2.2.

The integral over J_0 in Equation (14) collects contributions from all the invariant curves $J_0 = \text{const}$ of the ϵSM at $\epsilon = 0$. Of these, the one at $J_0 = 2\pi$ leads to quadratic energy growth because it consists of (period 1) fixed points (Lichtenberg & Lieberman, 1992). This is called a classical nonlinear resonance and it can be seen clearly in Figure 5. It is responsible for the linear growth of energy in Equation (15), because the main contribution to the integral in Equation (14) comes from a small interval $\sim 2\pi/t$ of actions around $J_0 = 2\pi$. Note that $J_0 = 2\pi$ corresponds to $\beta_0 = 1/2$, the resonant value of quasi-momentum at the QR at $\tau = 2\pi$. It is hence seen that the ϵ- or pseudoclassical approximation explains the *quantum* resonances of the QKR in terms of the principal *classical* resonance of a quasi-integrable standard map.

Before we come to actual applications of the pseudoclassical method, we briefly discuss its range of validity. The ϵ-quasi-classical approximation is exact at all times for $\epsilon = 0$, as shown above. At nonzero ϵ, it is valid when the number of kicks t is not too large, and in the long run it is spoiled by quantum, non-ϵ-classical effects. At $|\epsilon| < |\epsilon|_{cr,}$ the ϵ-classical motion is bounded by KAM curves, so the main quantum mechanism leading to non-ϵ-classical behavior is tunnelling across the regular regions. Estimating the related time scales is not at all easy, because the 2π-periodicity in action of the ϵ-classical phase space may enhance tunnelling, and even result in delocalization, depending on the degree of commensuration between 2π and the "Planck constant" $|\epsilon|$. For instance, if $|\epsilon|/2\pi$ is rational, then the quantum motion will be ballistic at some stage asymptotically in time (it would just realize a high-order QR). In order that such

a resonance with $|\epsilon| = 4\pi s/q$ exists at $|\epsilon|$ less than some $|\epsilon_0|$, it is necessary that the order q of the QR obeys $q > 4\pi/|\epsilon_0|$. It will show up after a time roughly estimated by $|\epsilon|$ times the inverse bandwidth of the continuous quasi-energy spectrum at this QR (Guarneri, 2009). The bandwidth is estimated to decrease faster than exponentially at large q (Guarneri, 2009; Izrailev, 1990), so one may infer that the time of validity of the ϵ-quasi-classical approximation is at least exponentially increasing with $1/|\epsilon|$ as the exact resonance at $\epsilon = 0$ is approached. At $|\epsilon| > |\epsilon|_{cr,}$ the ϵ-classical motion is unbounded, and the difference between ϵ-classical and quantum energy curves vs. τ is basically set by various quantum localization effects, including localization by cantori close to the $|\epsilon|_{cr}$ (Fishman et al., 1987; Grempel et al., 1984). As a consequence, if t is large enough, then the ϵ-classical curve lies higher than the quantum one (see Figure 4 at the very right and left).

3. APPLICATION OF THE PSEUDOCLASSICAL METHOD

3.1 Scaling Functions for Mean Energy of the AKOR

Having reviewed the fundamentals of the ϵ-classical method, we now turn to one of the most useful corollaries of the theory. By approximating the near-resonant quantum dynamics of the AOKR with a classical standard map of small kicking strength, the ϵ-classical model allows a *pendulum approximation* (Lichtenberg & Lieberman, 1992) to the dynamics to be made. It turns out that the near-resonant quantum dynamics can be captured by a single parameter description, so long as appropriate scaling of the momentum or energy is made—a fact which has been confirmed experimentally (Wimberger et al., 2005b). We now derive this so-called *scaling law* with emphasis on a heuristic explanation which arises from inspection of the ϵ-classical phase space (see Figure 6).

We start by considering the difference in the phase space for on-resonant and off-resonant kicked rotors. Figure 6b shows the on-resonant ($\epsilon = 0$) phase space—a continuum of flat "orbits" which give rise to the maximum energy at quantum resonance. In contrast, away from resonance ($|\epsilon| > 0$) a nonlinear resonance island disturbs the phase space as shown in Figure 6a. Inspecting the change in the phase space structure as $|\epsilon|$ is increased suggests the following relation between the off-resonant energy $E_{\epsilon,t}$ and the on-resonant energy $\langle E_{\epsilon=0,t}\rangle = k^2 t/4$:

$$\langle E_{\epsilon,t}\rangle \approx \frac{k^2 t}{4} - \Phi(t) + \langle E_t\rangle_{\text{res}}, \tag{16}$$

where the term $\Phi(t)$ corresponds to the energy associated with the *shaded* region in Figure 6b. (Note that we neglect any initial energy of the atoms

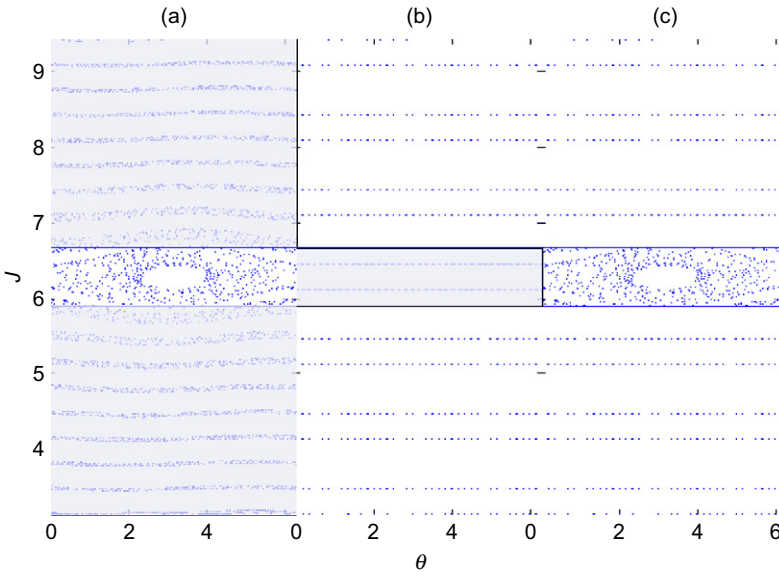

Figure 6 A depiction of the construction of the ϵ-classical scaling function in phase space. In (a), the entire phase space is shown as generated by iterating the ϵSM of Equation (11). The regions outside the influence of the central nonlinear resonance are shaded grey. The dynamics in the unshaded region where the dynamical resonance is seen are well modeled by the function G introduced in Equation (18) which calculates the mean energy due of the analogous pendulum trajectories. On the other hand, (b) shows the "flat" phase space when the rotor is perfectly on resonance and the mean energy is simply $(k^2/4)t$ as given by Equation (15). The shaded region in (b) shows the area which will be affected by the nonlinear resonance for the parameters used in (a). The energy in this shaded region is represented by the Φ function introduced in Equation (16). The figure (c) shows an approximation to the true phase space (a) found by taking (b), subtracting the shaded region and adding in the unshaded region (i.e., the resonance portion) of (a). This is the graphical equivalent of Equation (16), which is used to derive the scaling function.

in the above treatment; initial momentum does not change the periodic structure of the phase space, and the relevant energy can simply be added on to the final result, or subtracted from experimental and simulation results before comparison with theory). Off-resonance, this region is destroyed by the phase space island and so the $\Phi(t)$ term must be subtracted from the resonant energy and replaced with a term which gives the energy in the portion of phase space disturbed by the island. This term is $\langle E_t \rangle_{\text{res}}$—the energy associated with the resonance island itself in Figure 6a. In fact, the approximation in Equation (16) can be seen as corresponding to the approximation of the off-resonant phase space as shown in Figure 6a by adding the unshaded portions of Figure 6b and 6a to give Figure 6c.

We can extract analytic expressions for $\Phi(t)$ and $\langle E_t \rangle_{\rm res}$ from considerations of the portion of the entire phase space cell the island occupies and the solutions to the pendulum equations of motion. The latter solutions describe *continuous* time motion induced by the pendulum Hamiltonian

$$H_{\rm res} = \frac{1}{2}(J')^2 + \tilde{k}\cos(\vartheta), \tag{17}$$

in the canonical variable J' and ϑ of Equation (11), where J' measures the deviation from the island centre. The resonance width of the principal nonlinear island $\delta J_{\rm res} \approx 4\sqrt{\tilde{k}}$ is estimated by the separation (in action) between the separatrices of the pendulum motion (Lichtenberg & Lieberman, 1992). The period of the small pendulum oscillations is $2\pi t_{\rm res}$ where $t_{\rm res} = \tilde{k}^{-1/2}$ (Lichtenberg & Lieberman, 1992), so $t_{\rm res}$ defines a characteristic time scale for the elliptic motion in the resonant zone. One may altogether remove $|\epsilon|$ from Hamilton's equations as induced by Equation (17), by scaling momentum and time by factors $\tilde{k}^{-1/2} = 4/\delta J_{\rm res}$, $\tilde{k}^{1/2} = 1/t_{\rm res}$, respectively. Therefore,

$$\langle (\delta J_t)^2 \rangle = \langle (J'_t - J'_0)^2 \rangle \sim \tilde{k} G\left(t\sqrt{\tilde{k}}\right), \tag{18}$$

for an ensemble of orbits started inside the resonant zone, where $G(.)$ is a parameter-free function, whose explicit expression involves elliptic integrals. $G(.)$ represents the average energy contribution from trajectories in the primary island of the ϵSM. Hence, this function results from averaging over nonlinear pendulum motions with a continuum of different periods, so it saturates to a constant value when its argument $\gg 1$. At small values ($\ll 1$) of the argument, it behaves quadratically. This behavior is illustrated in Figure 7 below, where G is plotted vs. the scaled variable $x \equiv t/t_{\rm res}$. The contribution to the total energy is then obtained on multiplying Equation (18) by $|\epsilon|^{-2}\delta J_{\rm res}/(4\pi)$, because only a fraction $\sim \delta J_{.\rm res}/(2\pi)$ of the initial ensemble is trapped in the resonant zone. As a result,

$$\langle E_{t,\epsilon} \rangle_{\rm res} \sim \frac{\delta J_{\rm res}}{2\pi} \frac{\langle (\delta J_t)^2 \rangle}{2\epsilon^2} \sim \frac{k^2}{\pi\sqrt{\tilde{k}}} G\left(t\sqrt{\tilde{k}}\right). \tag{19}$$

Furthermore, if we divide through by the peak energy $k^2 t/4$ (c.f. Equations [3] and [15]), it turns out the right hand side of Equation (16) can be written solely as a function of the scaled time variable x, as we expect given the scaling property of the pendulum. The scaling function we finally arrive at is

$$\frac{\langle E_{\epsilon,t} \rangle}{\langle E_{t,0} \rangle} \approx H(x) \equiv 1 - \Phi_0(x) + \frac{4}{\pi x} G(x). \tag{20}$$

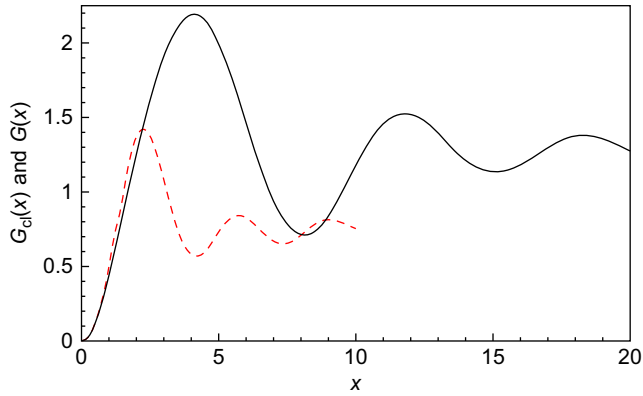

Figure 7 $G(x)$ used in Equation (20) (solid line) is shown along with G_{cl} from Equation (26) (dashed line). The differences between the two scaling functions arise due to the different initial conditions in phase space in the classical and ϵ-classical limits.

Explicit expressions for $\Phi_0(x)$ and $G(x)$ may be found in refs. (Sadgrove, 2005; Sadgrove et al., 2005; Wimberger, 2004; Wimberger et al., 2003) together with methods for calculating these functions.

To gain an appreciation for the convenience of the scaling function formulation from an experimental point of view, consider the experimental data shown in Figure 8 (Wimberger et al., 2005b). In the left panel, simulation energies are shown, and in the right panel experimental energies were measured for three different kick numbers. Both simulations and experimental results make clear that the peaks have different widths and even different structures, with side peaks flanking the main quantum resonance being visible in the case of 15 kicks. Nonetheless, the three different experimental data sets, when scaled by the peak energy, all collapse onto a single curve as shown in Figure 9[2].

Considering that comparison of experimental data with theory typically requires the estimation of the theoretical parameter k along with time-consuming quantum simulations, for all values of t and ϵ used in the experiment, the scaling function can immediately be seen to be a huge boon for experimentalists, who now need only compare data with a single analytical function of one variable.

[2]Because of imperfect experimental detection, the wings of momentum distributions where resonant atoms are concentrated are inevitably underestimated in measurements, leading to deviation from the exact theory for very small $|\epsilon|$. When comparing with the scaling function, we typically suppress these points as in Wimberger et al. (2005b).

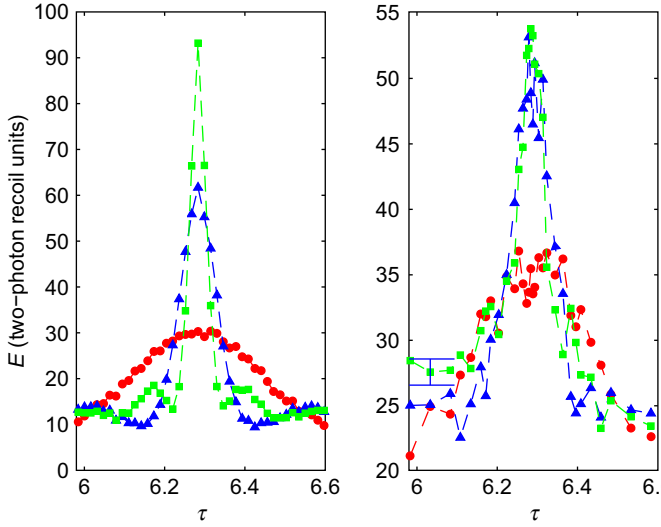

Figure 8 ϵ-classical simulation energies (left panel) and experimental results (right panel) demonstrating the change in the QR peaks as the total number of kicks is increased from 5 (circles), 10 (triangles) to 15 (squares) for similar values of kicking strength. Note both the narrowing of the peak and the appearance of small peaks to the side of the main resonance. In the right panel, we show a representative error bar which gives the standard error of the mean over five experimental runs. (Adapted figure from Wimberger et al. (2005b).)

3.2 Comparison of Near-Resonant Method with the Standard Semiclassical Limit

We now consider an intuitive question regarding the ϵ-classical standard map: since it describes the pseudoclassical limit near exact quantum resonance so well, can it also describe dynamics in the standard semiclassical limit, that is, when $\epsilon = \tau \to 0$?. As might be expected, the answer is indeed "yes". However, there are some interesting differences between the dynamics in the ϵ-classical and standard semiclassical limit.

To investigate the regime of vanishing τ, we can use the ϵ-classical standard map as derived in Section 2 with $\ell = 0$ (i.e., choosing the "zeroth" quantum resonance) and setting $\epsilon = \tau$. The appropriate map is then again given by Equation (11), but now with $\tilde{k} = k\tau = K_s$. Plotting the phase space of the map of Equation (11) for various values of $\epsilon = \tau$, as done in Figure 10, immediately reveals differences with the standard ϵ-classical phase space. In particular, we note that all trajectories are now contained within the central phase space island. This means that in calculating the off-resonant energy, only the kinetic energy from the pendulum approximation to the motion within the island needs to be considered and not

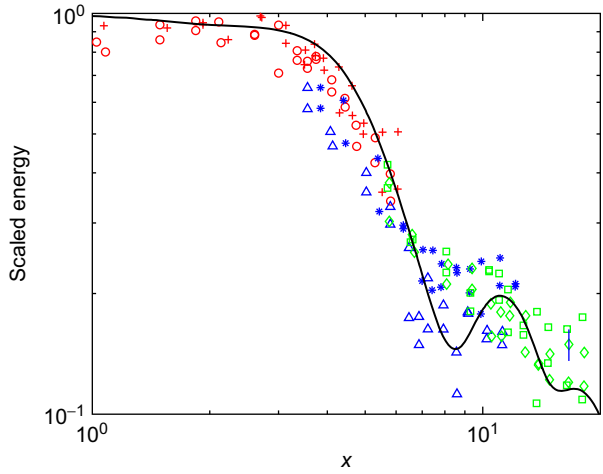

Figure 9 Experimental (discrete points) and analytical results (solid) for the scaled data near the first and second QRs. The plus, star, and diamond symbols show points taken near the first primary QR at $\tau = 2\pi$ for 5, 10, and 15 kicks, respectively. Circles, triangles, and squares show data near $\tau = 4\pi$ for the same respective kick numbers as the $\tau = 2\pi$ case. Note again the representative error bar as explained in Figure 8. (Adapted figure from Wimberger et al. (2005b).)

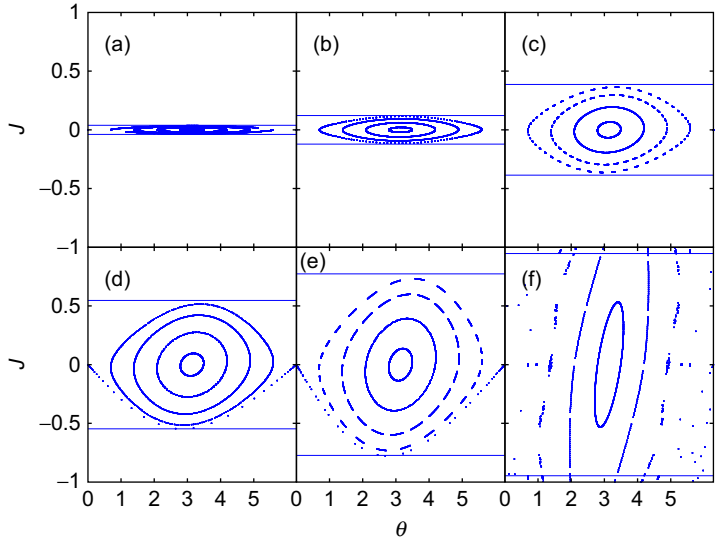

Figure 10 Phase space diagrams for the ϵSM with $\ell = 0$ and $\tau = \epsilon =$ (a) 0.0001, (b) 0.001, (c) 0.01, (d) 0.02 (e) 0.04, and (f) 0.06. The solid horizontal lines show the resonance width $\pm 2\sqrt{\tau k}$ in each case.

that due to the regular phase space outside the island. We proceed to find a version of the scaling function as follows: scaling momentum by $1/t_{\rm res} = 1/\sqrt{\tau k}$ as before, the mean energy due to the nonlinear resonance island may be written as

$$\langle E_t \rangle_{\rm res,cl} = \frac{\langle (J_t' - J_0')^2 \rangle}{2\tau^2} = k \frac{G_{\rm cl}(t\sqrt{\tau k})}{2\tau}, \tag{21}$$

where the subscript "cl" denotes "classical" and the $G_{\rm cl}$ function depends weakly on the ratio of τ and k. As $\tau \to 0$, $G_{\rm cl}$ tends to

$$G_{{\rm cl},\tau=0}(x) = \frac{1}{2\pi} \int_0^{2\pi} {\rm d}\vartheta_0 J'(x, \vartheta_0, J_0' = 0)^2, \tag{22}$$

for $x = t\sqrt{\tau k}$.

In the limits of small and "large τ", two interesting results can be derived for the mean energy (Sadgrove et al., 2005). First, as shown in Figure 7, as $\tau \to 0$, $G_{\rm cl}(x) \approx x^2/2$ and thus the energy in this limit is

$$\langle E_{t,\tau\to 0} \rangle = \frac{k^2 t^2}{4}, \tag{23}$$

that is, the energy grows *quadratically* with the number of kicks t. Such ballistic energy growth occurs in this case just as it does for quantum resonance for an ideal kicked rotor in an initial momentum eigenstate. This growth is much faster than the linear increase predicted for the quantum resonance peaks for the same broad initial momentum distribution. From Figure 7, it may be seen that ballistic growth occurs only for $x \lesssim 1$ which implies that

$$t_{\rm ball.} \lesssim \frac{1}{\sqrt{\tau k}} = t_{\rm res}, \tag{24}$$

which shows that ballistic energy growth may occur so long as t is less than the characteristic resonance period of the pendulum approximation.

Additionally, for large τ, Figure 7 shows that $G_{\rm cl}(x)$ saturates to a value $\alpha \approx 0.75$. Thus, the mean energy is

$$\langle E_{t,\tau \gg 0} \rangle \simeq \frac{k}{2\tau} \alpha. \tag{25}$$

This result implies that, after gaining energy in the first kick, the kicked rotor ensemble ceases to absorb energy from subsequent kicks—energy

growth is frozen. This result is as one would expect in the presence of DL except here we have a completely classical explanation for the frozen energy growth (Sadgrove et al., 2005).

Finally, ignoring the small τ dependence of the $G_{\rm cl}$ function, a scaling function for the $\tau \to 0$ resonance may be written as for the quantum resonance peaks:

$$\frac{\langle E_{t,\tau}\rangle}{\langle E_{t,\tau=0}\rangle} \approx R(x) \equiv \frac{2G_{\rm cl}(x)}{x^2}. \tag{26}$$

Figure 11 shows experimental data (discrete points) and theory for the standard ϵ-classical and the $\tau \to 0$ limit cases (Wimberger et al., 2005b). The experimental data for the two different limits clearly lie on different curves and in particular are in good agreement with their respective theoretical scaling functions.

Once again, we would like to emphasize that extending the scaling function to a new domain is not an inconsequential theoretical exercise; rather it can reveal new physics "hiding" in the opaque quantum formulation, such as the ballistic and frozen growth regimes seen in the semiclassical limit.

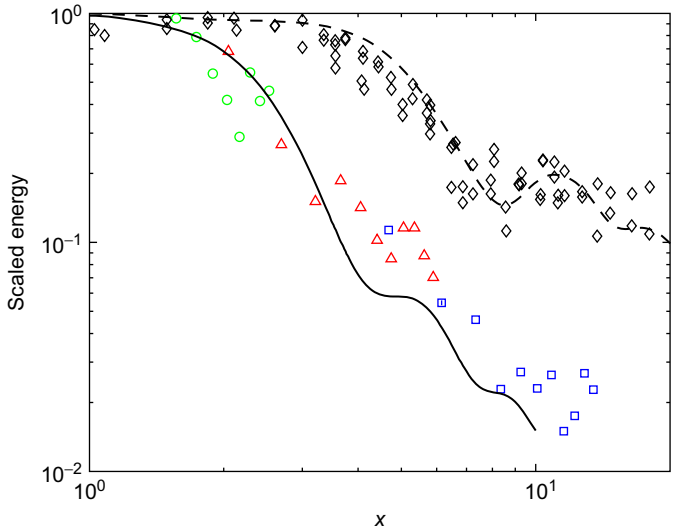

Figure 11 Experimental (symbols) and analytical results (solid line) for the scaled data near the semiclassical limit. The data shown is for 5 kicks (circles), 10 kicks (triangles), and 15 kicks (squares). Experimental data (diamonds) and theory (dashed line) for the first primary quantum resonance are reproduced from Figure 9 for comparison. (Adapted figure from Wimberger et al. (2005b).)

3.3 Noise and Decoherence

Surprisingly, the pseudoclassical description and the scaling of the mean energy introduced in Section 3.1 works in the presence of perturbations of the quantum evolution as well. In the following, we show this for two special cases where noise acts on the kicking strength (amplitude noise) and, even more interestingly, mainly on the phase evolution of the free rotational parts of the Floquet operator (i.e., on the second factor on the right hand side of Equation [2]). We start out with the latter in the next subsection.

3.3.1 Spontaneous Emission

Early experiments which perturbed the phase evolution of kicked cold atoms in a controlled manner used a kicking beam closer to resonance with the internal atomic transition of the atoms. This enhanced the spontaneous emission (SE) rate of the atoms, leading to random momentum kicks in additional to the conservative part of the potential (Ammann et al., 1998; Daley et al., 2002). Better control on the impact of SE is obtained by separating both effects, the kicks, and the SE events. This was implemented at Oxford some time ago, using a second laser (again closer to resonance than the kick laser) to induce SE events after each kick and in a short time interval compared with the kicking period (d'Arcy et al., 2001, 2004). Such SE events not only lead to a dephasing of the unperturbed quantum evolution of the kicked particle, but also to a heating of its centre of mass motion (since they correspond to additional kicks). Both can be taken into account in an amended version of the classical mapping describing the evolution close to quantum resonance (i.e., small ϵ). The amended mapping is given by

$$\begin{aligned} I_{t+1} &= I_t + |\epsilon|\delta_{t+1} + \tilde{k}\sin(\theta_{t+1}), \\ \theta_{t+1} &= \theta_t \pm I_t + \pi\ell + 2\pi\ell\eta_t, \\ \eta_{t+1} &= \eta_t + \delta_{t+1} \quad \text{with} \quad \eta_0 = \frac{\tau\beta}{2\pi\ell}. \end{aligned} \tag{27}$$

β is the initial quasi-momentum which is effectively shifted by the SE events (see third equation). Also the momenta I_t (corresponding to the ϵ-rescaled integer parts of momentum in the original physical system) are affected which is taken into account by the term $|\epsilon|\delta_{t+1}$ in the first equation. The δ_t describe the sum of momentum changes arising from SE up to the number of kicks t and they are independent random variables, whose distribution is determined by the statistics of SE. Numerical simulations using Equation (27) are shown in Figure 12, and the results are found to

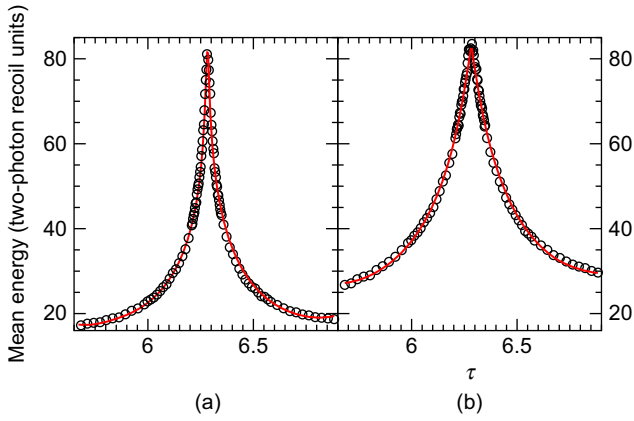

Figure 12 Mean energies of the same initial ensemble of atoms as shown in Figure 4 as a function of the kicking period τ scanned over the quantum resonance at $\tau = 2\pi$; for $k = 0.8\pi$ and in the presence of SE. Results of full quantum calculations (circles) and of ϵ-classical ones using the map of Equation (27) (solid lines) are compared for different SE rates (a) $n_{\mathrm{SE}} \approx 0.1, t = 50$ and (b) $n_{\mathrm{SE}} \approx 0.2, t = 50$. We note the asymmetry of the peaks which is best visible for larger n_{SE}. Its origin has not yet been discussed in the literature but it certainly lies in the asymmetry of the initial ensemble in the pseudoclassical phase space with respect to the sign of ϵ, which enters into the term $\tau\beta$ of the mappings of Equations (10) and (27).

match the true quantum evolution very well at small $|\epsilon|$. Under the substitution $J_t = \pm I_t + \pi\ell + 2\pi\ell\eta_t$, the map of Equation (27) reduces to a noisy pseudoclassical standard map, which differs from Equation (11) by a random shift $\tau\delta_t$ of the action J at each step. The scaling law of Equation (20) shows that the only relevant time scale for the evolution of the quantum motion sufficiently near to $\tau = 2\pi\ell$ ($\ell \in \mathbb{N}$) is given by $t_{\mathrm{res}} = 1/\sqrt{\tilde{k}}$. The noisy time evolution brings an additional time scale into play that characterises the strength of the noise. In the following, we indeed find an equivalent of the scaling law of Equation (20) in the presence of SE, which is based on the two time scales t_{res} and t_c, where t_c is the mean waiting time between two SE events. Then, the structure of the resonance peak in the mean energy in the presence of SE may be analytically studied, using essentially the same ideas developed above in Section 3.1.

Let us assume an initially uniform quasi-momentum distribution. At any SE event, the distribution of the ensemble in the phase space of the pseudoclassical standard map is reshuffled by the random action change. Under the assumption of homogeneous distribution of single SEs in an interval of integer length (in units of two photon recoils), the resulting distribution of $J \bmod (2\pi)$ is approximately homogeneous over the unit cell of the map of Equation (11). Such randomization may be assumed to wash

out correlations between the past and the subsequent random dynamics. Hence, the scaling of Equation (20) may be used to write the energy after a number of kicks t as

$$\langle E_{t,\epsilon} \rangle \sim \frac{k^2}{4} \left\langle \sum_{j=0}^{N_{t-1}} \Delta_j \, H(\Delta_j / t_{\rm res}) \right\rangle + \frac{1}{2} D n_{\rm SE} t, \tag{28}$$

where $\langle . \rangle$ stands for the average over all realizations of the times of SE events and N_{t-1} is is the number of SE events up to a number of kicks $t-1$. $n_{\rm SE}$ is the average number of SE per period, and $D = {n_{\rm SE}}^{-1} \langle \delta_t^2 \rangle$ is the mean square momentum imparted by a single SE. For an individual realization, Equation (28) states that the energy is given by the sum of the SE-free scaling function H of the evolutions over time intervals Δ_j. The SE resets the evolution after each event at times Δ_j, apart from the momentum shift contained in the second term in Equation (28). If t_c is sufficiently large compared with 1, one may replace the random process of SE events by a continuous time Poisson process with the characteristic time $t_c = 1/n_{\rm SE}$ (Wimberger et al., 2003). This process has delays Δ distributed with density $t_c^{-1} \exp(-\Delta/t_c)$. Its statistic reduces to that of the unit Poisson process (with $t_c = 1$) by just rescaling all times by the factor $1/t_c$. This reasoning allows the following approximation

$$\left\langle \sum_{j=0}^{N_{t-1}} \Delta_j \, H(\Delta_j / t_{\rm res}) \right\rangle \approx 4 t_c Q(t/t_c, t_c/t_{\rm res}), \tag{29}$$

where

$$Q(u,v) \equiv \frac{1}{4} \left\langle \sum_{j=0}^{N_u^1} \Delta_j^1 \, H(\Delta_j^1 v) \right\rangle. \tag{30}$$

The superscript 1 specifies that the average is now over the realizations of the unit Poisson process: each realization has a continuous time interval $[0,u]$ divided in subintervals Δ_j^1 by a random number N_u^1 of Poisson events. We are hence led to the following scaling law:

$$\langle E_{t,\epsilon} \rangle \sim D' \frac{t}{2t_c} + k^2 t_c Q\left(\frac{t}{t_c}, \frac{t_c}{t_{\rm res}} \right) \tag{31}$$

or, equivalently introducing $u = t/t_c$, $v = t_c/t_{\rm res}$,

$$\frac{2\langle E_{t,\epsilon} \rangle - D' t/t_c}{2k^2 t_c} \sim Q(u,v). \tag{32}$$

The scaling function $Q(u, v)$ may be explicitly written in terms of the function $H(x)$. This is shown in detail in appendix D of Wimberger et al. (2003) and it gives:

$$4Q(u,v) = uH(uv)\mathrm{e}^{-u} + \int_0^u \mathrm{d}x\ \mathrm{e}^{-x} xH(xv)(2+u-x). \tag{33}$$

Limiting behaviors of the scaling function $Q(u, v)$ immediately follow from this equation, or from Equation (30) itself. On one hand, for $u = t/t_c \gg 1$, the right-hand side in Equation (30) is a sum of a large number $\sim t/t_c$ of terms. In that limit, such terms are weakly correlated and can be averaged independently which gives

$$u \gg 1 \ : \quad Q(u,v) \sim \frac{1}{4} u \int_0^\infty \mathrm{d}x\ H(vx) x e^{-x}. \tag{34}$$

On the other hand, for $t/t_c \ll 1$, the sum reduces to the single term $j = 0$, with $\Delta_0^1 = t/t_c$; hence

$$u \ll 1 \ : \quad Q(u,v) \sim \frac{1}{4} uH(uv). \tag{35}$$

In particular, Equation (35) shows that Equation (31) coincides with Equation (20) in the SE-free limit $t_c \to \infty$. In the opposite limit, Equation (34) shows that, if k is fixed, then the width in ϵ of the resonant peak will not shrink any more with time when $t \gg t_c$, and its width thereafter scales like $(t_c^2 k)^{-1}$. The spike is therefore erased (i.e., it is absorbed in the background) in the strong noise limit $t_c \sim 1$. In the latter limit, the method developed above breaks down, because on average after each kick an SE event happens, which does not let the time evolution recover for some time interval. The result is then a completely random motion which does not depend on the system specific dynamics, and hence not on the chosen value of the kicking period τ.

The spreading of the resonance peaks with increasing noise, as can be seen in Figure 12, explains why they are more stable and easier to observe experimentally than in the case without noise for broadly distributed initial momenta of the atoms (d'Arcy et al., 2001, 2004). An intuitive argument for the spreading of the resonance peaks is that for a fixed value of ϵ, due to SE there is an enhanced chance to find a quasi-momentum β, such that the free evolution part of the Floquet operator is approximately the identity. This is the condition for quantum resonant motion.

Numerical simulations in Figure 13 support the scaling law of Equation (31). Data were obtained in a similar manner to the case without SE;

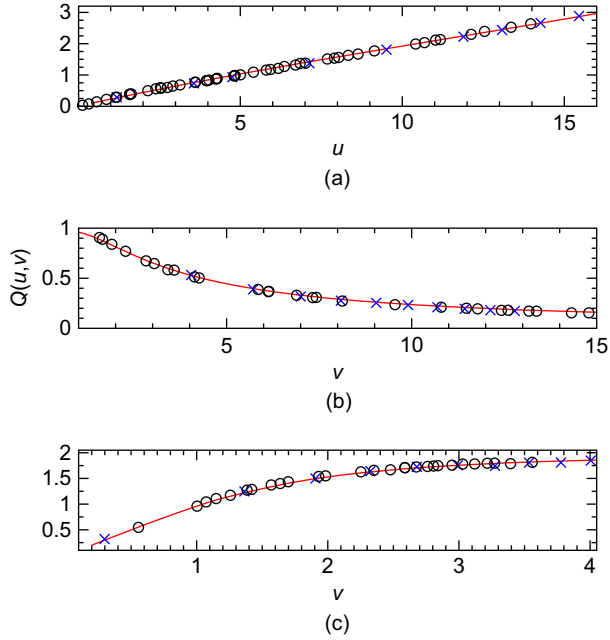

Figure 13 Demonstrating the scaling law of Equation (31) in a right neighbourhood of $\tau = 2\pi$. In (a), (b) the $Q(u, v)$ quantity on the left-hand side of Equation (32) is plotted vs. one of the parameters $u = t/t_c$ or $v = t_c/t_{\text{res}}$, whereas keeping the other fixed: (a) $v = 2$, (b) $u = 4$. In (c), the ratio $u/v = 4$ is fixed. Open circles correspond to different values of the parameters t, t_c, k, ϵ, randomly generated in the ranges $1 < t < 200$, $5 < t_c < 60$, $0.001 < \epsilon < 0.1$, $0.1 < k < 20$, with the constraints $0.001 < k\epsilon < 0.2$ and $t_c\sqrt{k\epsilon} = 2$ in (a), $t/t_c = 4$ in (b), $t = 4t_c^2\sqrt{k\epsilon}$ in (c). In each case, an ensemble of 2×10^6 ϵ-classical rotors was used, with a uniform distribution of initial momenta in $[0, 1)$ and a uniform distribution of initial θ in $[0, 2\pi)$. The random momentum shifts at each step of the ϵ-classical evolution of Equation (27) were generated from the uniform distribution in $[-1/2, 1/2]$. Crosses represent the results of quantum simulations for $k = 0.8\pi$, and $\epsilon = 0.01$ in (a), $\epsilon = 0.05$ in (c), and $t = 50$ and $t = 100$ in (b). The solid lines correspond to the theoretical prediction of Equation (33). (Adapted figure from Wimberger et al. (2003).)

however, one of the parameters u, v is varied, while keeping fixed either the other parameter or the ratio u/v. The theoretical scaling function $Q(u, v)$ was calculated numerically using in Equation (33) the function $H(x)$ introduced above in Section 3.1.

3.3.2 Amplitude Noise

Spontaneous emission is a dissipative noise process directly altering the momentum of individual atoms, and thus altering the otherwise coherent dynamics associated with the AOKR. But other types of noise

processes are also present in experimental implementations of the kicked rotor—particularly noise in the kicking parameters themselves. An example of some interest is caused by fluctuating laser power which gives rise to so-called *amplitude noise*—that is noise due to the strength of kicking fluctuating randomly.

To analyze the effects of this nondissipative noise, fluctuations are typically added in a controlled manner using a random number generator along with an optical attenuator to create a pulse amplitude with any desired noise distribution and noise strength. In studies up to now, it has been typical to use a uniform noise distribution and vary the noise from 0 to 200%—the latter indicating that pulses can vary in strength from 0 to twice the nominal kicking strength. Figure 14(a) depicts a kicked rotor experiment for which pulses with amplitude noise are applied.

The ϵ-classical method was co-opted for use in amplitude noise studies to explain the following puzzling observation: although in general, the amplitude noise was found to completely destroy the AOKR quantum correlations (Klappauf et al., 1998; Milner et al., 2000),

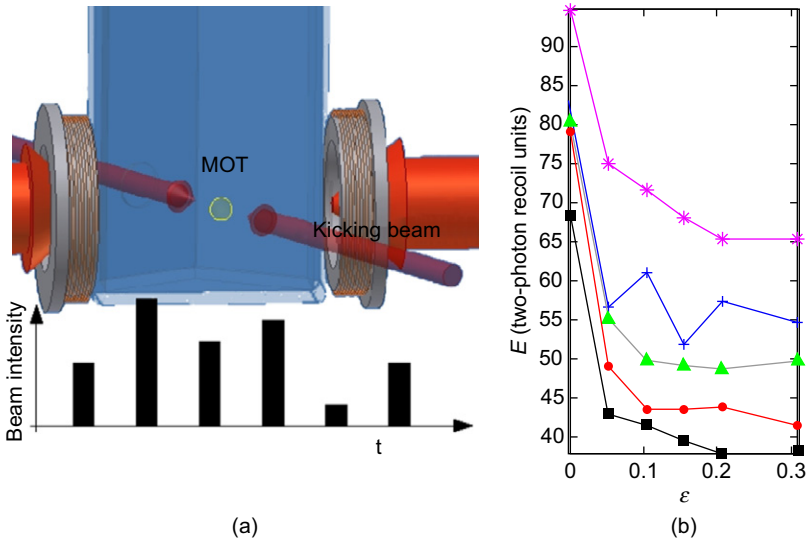

Figure 14 In (a) diagram illustrating the experimental setup used for amplitude noise experiments. The important difference in comparison with the system of Figure 1 is the time varying pulse amplitudes. In (b), experimental measurements for the E atomic mean kinetic energy (y-axis) vs. the ϵ detuning from quantum resonance (x-axis) demonstrating QR peaks broadened under the influence of amplitude noise. The noise level ranged from 0 (squares), 0.5 (circles), 1.0 (triangles), 1.5 (plus sign), and 2.0 (stars). (Adapted figure with permission from Sadgrove et al. (2008). Copyright 2008 of the American Physical Society.)

Sadgrove et al. (2004) demonstrated that in the vicinity of the quantum resonance, the peak structure is not destroyed even by maximum noise, as shown in Figure 14b. One intuitive interpretation of this phenomenon is to note that quantum resonance is dependent on the frequency of the applied pulses, and not their amplitude, and so the resonance condition itself is robust against amplitude fluctuations. This does not, however, explain why for a range of kicking frequencies which are merely *close* to quantum resonance, the effect of amplitude noise is minimal.

To explain the stability of the peak, we modify the ϵ-classical map as follows. Given a uniform noise level $L \in [0, 2]$, we introduce a stochastic parameter R_t which is drawn from $[-L/2, +L/2]$ for each pulse as labeled by the discrete time (i.e., the total number of kicks) t. We then simply multiply the kicking strength k by $(1 + R_t)$ to give uniform random fluctuations in the kicking strength about a mean of k. The modified ϵSM is then

$$J_{t+1} = J_t + \epsilon k\,(1 + R_t)\sin(\theta_{t+1}), \quad \theta_{t+1} = \theta_t + J_t. \tag{36}$$

From this map, we can immediately plot the phase space for various ϵ and look for answers regarding the stability of the quantum resonance in the changing phase space structure. Figure 15a shows the phase space away from resonance for a high level of noise—specifically for $L = 1.5$ (150% amplitude noise). The important thing to note is that even away from perfect quantum resonance ($\epsilon = 0$) the broad structure of the phase space is undamaged by noise, meaning that an energy peak is still present even at high noise levels.

We can formalize this intuition regarding the phase space and the associated stability of quantum correlations near resonance by seeking to extend the ϵ-classical scaling function to the amplitude noise case. Figure 15b shows the pendulum phase space which approximates the phase space in Figure 15a. The shaded gray area marks the region of the phase space around the separatrix which is most affected by the noise, as calculated by considering the fluctuations in k which directly determines the separatrix position (Sadgrove et al., 2008). Modification of trajectories near the separatrix has the largest effect on the near-resonant energy since stable librations may become higher energy rotation orbits if the separatrix becomes transparent. Applying this reasoning, an approximate scaling law for the AOKR quantum resonances in the presence of amplitude noise can be derived, specifically (Sadgrove et al., 2008):

$$\frac{\langle E_{t,\epsilon}\rangle}{\langle E_{t,0}\rangle} \approx 1 + \frac{L^2}{12} - [1 - L/(8\pi)]\Phi_0(x) + \frac{4}{\pi x}G(x)\,, \tag{37}$$

where the average is taken over the initial conditions in the pseudoclassical phase space.

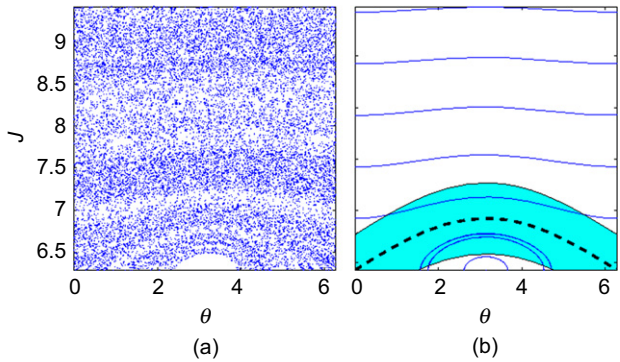

Figure 15 (a) The ϵ-classical phase space in the presence of amplitude noise. (Compared with Figure 6c). (b) Shows the pendulum phase space approximation to (a) with the area around the separatrix shaded. It is trajectories in this area (for a noise level $L = 1.5$ in [b]) which have the most effect on the energy when amplitude noise is added to the system. (Adapted figure with permission from Sadgrove et al. (2008). Copyright 2008 of the American Physical Society.)

In Figure 16, the modified scaling law is compared with experimental data (left column) and simulation results (right column) showing good agreement. Thus, with the addition of an additional parameter L, we find that the stability of the quantum resonances in the presence of amplitude noise may be characterized by a scaling law as in the noise-free case, and all of the usual benefits of a scaling law for data analysis and consolidation of experimental parameters are still available even in the noisy system.

3.4 Directed Transport at Quantum Resonance

This subsection and the following one present new theoretical results which have not all been tested experimentally yet. Specifically, in the present subsection, we consider a scaling function explanation for the results published in (Dana et al., 2008; Sadgrove et al., 2007), but we also use the pseudoclassical theory to predict new effects (Sadgrove & Wimberger, 2009).

Numerous reasons exist for studying directed transport due to non-biased forcing in quantum systems. These range from the motivation to explore fundamental physics (in particular thermodynamics which Feynman famously used as a motivator for the study of the ratchet and pawl system [Feynman, 1963]) to the more practical desire to find new ways to transport atoms and other quantum objects. Reviews of the broad area of ratchet dynamics are available (see, e.g., [Hänggi & Marchesoni, 2009; Reimann, 2002]). Here, we will restrict our discussion to cold atom ratchet systems and focus in particular on the "resonance ratchet" system

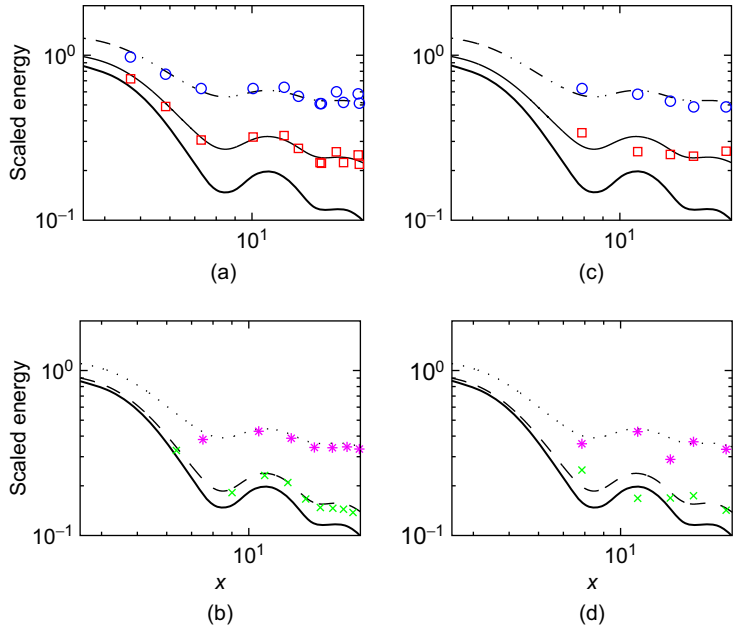

Figure 16 The ϵ-classical scaling function is compared with simulation data (a,b) and experimental data (c,d). In (a), simulation data for $L = 1$ (squares) and $L = 2$ (circles) are compared with the scaling functions (solid line, dash-dotted line) for the same respective noise values. (c) Experimental data, and scaling functions, using the same symbols for the same parameters as in (a). In (b), simulation data for $L = 0.5$ (crosses) and $L = 1.5$ (stars) are compared with the scaling functions (dashed line, dotted line) for the same respective noise values. In (d), experimental data and scaling functions with the same symbols corresponding to the same parameters as in (b). The scaling function in this case is augmented by additional terms dependent on the noise level L, although to a good approximation the energy contribution from the nonlinear resonance (the last term on the right hand side of Equation [37]) is not affected. Note that in all figures, the thick black line shows the standard (zero-noise) scaling function for comparison.

(Dana et al., 2008; Sadgrove et al., 2007) where ϵ-classical techniques may be used.

The resonance ratchet system, as realized in refs. (Dana et al., 2008; Sadgrove et al., 2007) uses ultra-cold atoms (so far sourced from a BEC) which are initially coherently split into two momentum components using a momentum conserving Bragg pulse. The quantum phase between the two components may be adjusted by allowing a free evolution period after the Bragg pulse. After this preparation phase, kicks are delivered to the atoms with period equal to the Talbot time. Figure 17 depicts the experimental setup used in Sadgrove et al. (2007), where a BEC was created on

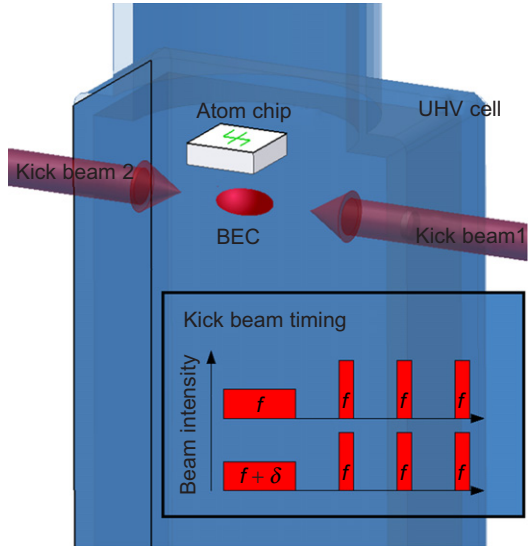

Figure 17 Depiction of the experimental system used to realize directed motion at QR. A BEC is created and split into two momentum components by an initial Bragg pulse, where counter-propagating beams have a frequency difference δ. After a phase evolution period, standard kicks (where both beams have frequency f) are applied giving rise to a momentum current.

an "atom chip" before being exposed to an optical standing wave giving rise to the ratchet effect.

Unlike the usual case for the kicked rotor, where atoms are always found to gain energy symmetrically about zero momentum, in the resonance ratchet configuration, the mean momentum of the atoms increases linearly with each kick with a direction and coefficient determined by the phase between the two initial momentum components. Figure 18 shows the ratchet behavior as a function of the number of pulses applied to the split condensate with both the raw data (left panel) and the measured mean momentum clearly showing a momentum current (right panel). With this brief background on the effect, we now turn to the ϵ-classical analysis of the resonance ratchet phenomenon, and show what additional light the method can shed on the conditions for and nature of the momentum current.

Because the ratchet effect takes place at or very near to quantum resonance, the system may be analyzed using an ϵ-classical treatment with a focus on the mean momentum of the atoms rather than their energy. There is, however, an important point to consider before diving into the analysis: how should we represent the initial momentum superposition state in the ϵ-classical formalism. Strictly, this is a problem without a

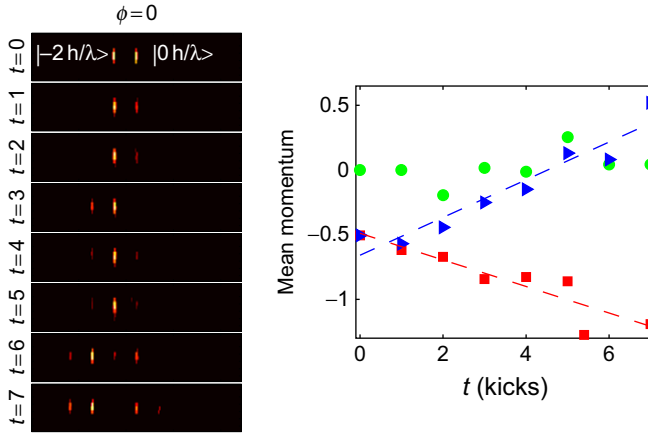

Figure 18 Left panel: absorption images for the momentum components of a Bose–Einstein condensate following a resonance ratchet experiment. In this case, the momentum components show a momentum current toward negative momentum. For each subpanel, the total number of kicks t is indicated on the y-axis. Initially, a coherent atomic superposition of the $p = 0$ and $p = -2\hbar k = -2h/\lambda$ momentum components was created using a Bragg pulse. In this initial absorption, image (at $t = 0$) that superposition appears as two "spots" with the momentum components labeled. The experimental data were taken at exact quantum resonance and with $\phi = 0$. The right panel shows experimentally measured mean momenta for the same experiment for two different phases 0 (triangles) and π (squares), which give opposite momentum currents. Dashed lines show linear fits to the data. The circles show measured mean momenta for a standard AOKR experiment (i.e., with no initial superposition). The results are for a kicking strength $k \approx 0.1$. (Adapted figure with permission from Sadgrove et al. (2007). Copyright 2007 of the American Physical Society.)

clear answer: the difference between quantum mechanics and classical mechanics arises precisely because of the existence of classically impermissible superpositions in the quantum theory, and the ϵ-classical theory which contains no operators and treats atoms as classical particles cannot accommodate the quantum initial state any better than a standard classical treatment could. For now, we delay discussion of this issue and simply present our method which produces useful ϵ-classical results in agreement with quantum simulations.

After the initial Bragg pulse, the atomic wave function is split into two momentum components. We can represent such an initial condition classically (i.e., non-coherently) by the distribution

$$P(p_0) = \frac{1}{2}(\delta_{p_0,0} + \delta_{p_0,1}). \tag{38}$$

where, as in Subsection 1.2, $\theta \equiv z \bmod 2\pi$. Fourier transforming the momentum space wave function gives the position space wave function. For the ϵ-classical atoms, we can choose the position space distribution to be the norm squared of this quantum wave function:

$$P(\theta) = |\psi(\theta)|^2 = \frac{1}{2\pi}(1 + \cos(\theta + \phi)). \tag{39}$$

Note that the role of the quantum phase is captured by adding the phase ϕ in the cosine term of Equation (39), physically signifying a phase difference between the (classical) atomic density distribution and the sinusoidal driving field.

Having made these choices, we now proceed as in Section 2.3, arriving at the on-resonance result (this time for momentum rather than energy) averaged over the initial conditions given in (Equations 39 and 38)

$$\langle p_{t,0} \rangle = \frac{kt}{2|\epsilon|} \cos(\phi). \tag{40}$$

This result agrees with the purely quantum expressions found in (Dana et al., 2008; Sadgrove et al., 2007). Furthermore, the result can also be modified to predict the effects of an arbitrary initial quasi-momentum, as explored experimentally in (Dana et al., 2008). The emergence of a momentum current is seen in the ϵ-classical phase space (see Figure 19) as an asymmetry in the trajectories at finite times.

Next, we consider a question which has not yet been experimentally investigated: what happens to the momentum current if the pulse rate moves off-resonance? Once again, we proceed as in Section 3.1, and with our new initial conditions. Intriguingly, we find that the off-resonant momentum scales just as the energy does as a function of the scaled time $x = t/t_{\text{res}}$.

Figure 20 shows the ϵ-classical scaling function for the momentum which is arrived at by dividing Equation (40) by $-kt\cos(\phi)$ to give a single parameter scaling law on the RHS:

$$\frac{\langle p_{t,\epsilon} \rangle}{-kt\sin(\phi)} \approx A(x)/x, \tag{41}$$

where $A(x)$ is a function derived from the average momentum over general solutions of the pendulum dynamics (Sadgrove & Wimberger, 2009). More explicitly, it is given by the expression

$$A(x) = \frac{1}{2\pi}\int_{-\pi}^{\pi} \mathrm{d}\theta_0 \, [\sin(\theta_0) \times J'(\theta_0, J'_0 = 0, x)]. \tag{42}$$

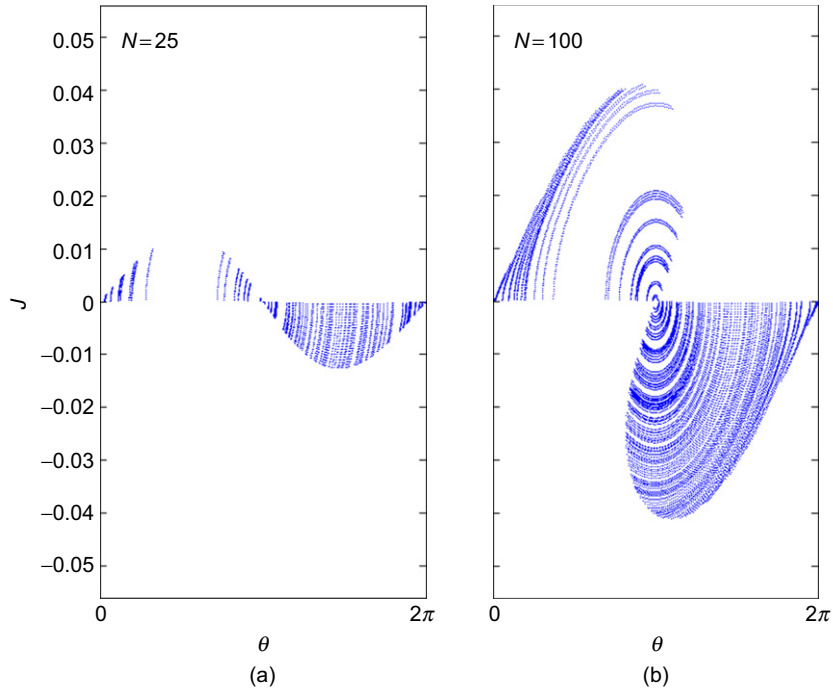

Figure 19 ϵ-classical phase space for the ratchet system at 25 and 100 kicks with $k = 1$ and $\epsilon = 5 \times 10^{-4}$. The asymmetry of the initial conditions, Eq. (39), in the phase space gives rise to the momentum current. (Adapted figure with permission from Sadgrove and Wimberger (2009). Copyright 2009 of the New Journal of Physics.)

The one parameter scaling may be seen to capture the full dynamics of the resonance ratchet system. Indeed, Equation (41) reveals a nontrivial feature of the off-resonant dynamics: current reversal (that is a negative mean momentum) is possible for certain parameter regimes *independent of the quantum phase* ϕ. This intriguing prediction has yet to be tested experimentally.

We now briefly return to the question of why replacing quantum superposition states with their associated classical probability distributions was a successful strategy here, when typically it would lead to a loss of the very quantum effects that are being modeled. One answer arises from a consideration of the role that momentum plays in ϵ-classical formalism. Say we start by setting the classical atomic position distribution to Equation (39), as above. The problem is that with no uncertainty principle in play, the fixing of the position space distribution does not constrain the momentum distribution in the ϵ-classical system, as it does in the quantum system (according to the Fourier transform). Thus, our choice of Equation (38) is

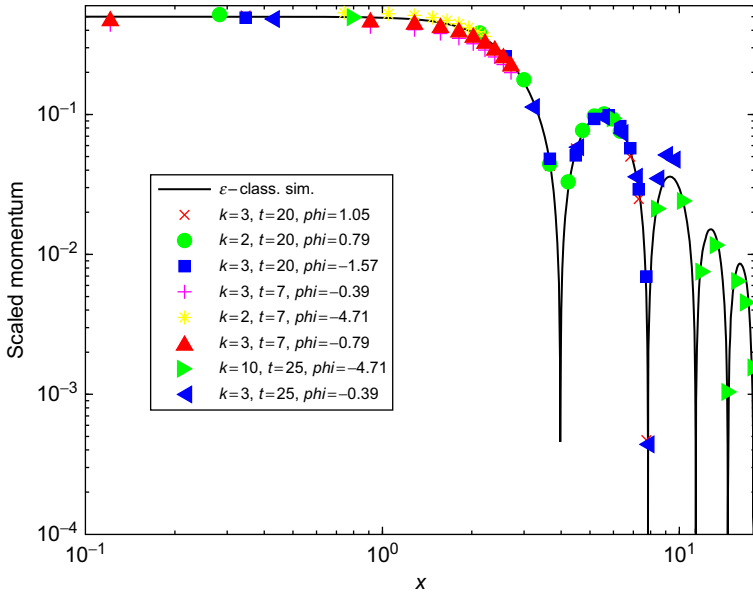

Figure 20 The absolute value of the ϵ-classical scaling function (solid line) from Equation (41). Here, we compare the theory with simulation results for a range of parameters (symbols) as indicated in the legend. (Adapted figure with permission from Sadgrove and Wimberger (2009). Copyright 2009 of the New Journal of Physics.)

rather arbitrary. However, when the quasi-momentum distribution is very narrow (or $\tau \to 0$) and, more importantly, when ϵ is small, the precise details of the momentum distribution are unimportant in the ϵ-classical model, as inspection of Equation (11) along with the definition of $I = |\epsilon|N$ shows. Thus, our choice of the classical analog to the quantum position distribution rewards us by successfully capturing position space correlations important to the ratchet dynamics, and the ϵ-classical formalism's indifference to the exact details of the momentum distribution mean that we do not have to pay any price for its ill-defined nature.

3.5 Fidelity as a Measure of Stability

In this section, we present a further tool to characterize the stability of the QR and near QR motion of the QKR, supporting our results in Sections 3.1–3.3.

Entanglement measures or witnesses have become modern tools of correlation analysis in multipartite quantum systems (Horodecki et al., 2009). For single-particle systems, some correlations can only build up during their temporal evolution, just like the kick-to-kick correlations for the QKR

(see Section 1.1). It is then the evolution of relative phases and the superposition principle which distinguish quantum from classical dynamics. Correlation functions may be used to monitor phase evolutions (Walls & Milburn, 2008). A related quantity which has gained much interest in the last decade is fidelity (Gorin et al., 2006), defined as the overlap of two wave functions subjected to slightly different temporal evolutions. The temporal evolution of this quantum fidelity crucially depends on evolving relative phases. For many-particle systems, fidelity can be viewed as a Hilbert space measure to study quantum phase transitions (Buonsante & Vezzani, 2007) or local and global spectral properties (Plötz et al., 2011). Fidelity was introduced originally as a measure for the stability of quantum motion with respect to changes in some control parameter of the Hamiltonian (Peres, 1984). In our case, this parameter will be the kicking strength. The predicted saturation of fidelity at exact QR (Wimberger & Buchleitner, 2006) reported in the following subsection has only recently been confirmed experimentally (Wu et al., 2009), whereas our predictions for finite detunings (Abb et al., 2009) of Subsection 3.6 still await experimental verification.

3.5.1 Fidelity at Exact Quantum Resonance

Using the kick-to-kick operator from Equation (2), the fidelity can be written (Wimberger, 2004; Wimberger & Buchleitner, 2006)

$$F(k_1,k_2,t) \;=\; \left|\int_0^1 \mathrm{d}\beta\;\rho(\beta)\langle\hat{\mathcal{U}}^{\,t}_{\beta,k_1}\Psi_\beta|\hat{\mathcal{U}}^{\,t}_{\beta,k_2}\Psi_\beta\rangle\right|^2, \tag{43}$$

where we note that the kick-to-kick operator is applied t times, and the kicking strengths k_1 and k_2 have distinct values, their difference giving the strength of the relative perturbation under the two time evolutions. The fidelity results from averaging the scalar product under the integral sign over β with the weight $\rho(\beta)$. Note that the rotor's fidelity is the squared modulus of this quantity, so the fidelity of Equation (43) of atomic evolution does not coincide with the β-average of the rotors' fidelities (Wimberger & Buchleitner, 2006). In good approximation of experiments, the initial rotor states Ψ_β can be taken to be plane waves. $\Psi_\beta(\theta) = (2\pi)^{-1/2}$ if only the zero momentum class is initially populated (which we will assume in the following discussion). For kicking periods at exact QR, i.e., $\tau = 2\pi\ell$ ($\ell \in \mathbb{N}$), the fidelity may be derived analytically to be $\left|\langle\hat{\mathcal{U}}^{\,t}_{\beta,k_1}\Psi_\beta|\hat{\mathcal{U}}^{\,t}_{\beta,k_2}\Psi_\beta\rangle\right|^2 = J_0^2(|W_t|\Delta k)$, where J_0 is the Bessel function of 1st kind and order 0, $\Delta k = k_2 - k_1$ and $|W_t| = |\sin(\pi t\ell(\beta - \frac{1}{2})\csc(\pi\ell(\beta - \frac{1}{2})|$ (Wimberger et al., 2003; Wimberger & Buchleitner, 2006). With $|W_t| = t$

for resonant quasi-momenta β and using the asymptotic expansion formula (9.2.1) from (Abramowitz & Stegun, 1972) for Bessel function J_0, one further arrives at $F_{\beta_{\rm res}}(t) \simeq \frac{2}{\pi\Delta k t}\cos^2\left(\Delta k t - \frac{\pi}{4}\right)$. This shows that the fidelity decay is very slow obeying a power law $\propto 1/t$ for the resonant β-states. For an ensemble of initial atoms representing a broad quasi-momentum distribution with $\rho(\beta) = 1$, an interesting freeze or saturation of fidelity occurs, typically already after a small number of kicks which immediately made this result accessible to experiments performed by the Harvard group (Wu et al., 2009):

$$F(k_1, k_2, t \to \infty) \to F^*(\Delta k) \equiv \frac{1}{(2\pi)^2}\left(\int_0^{2\pi} {\rm d}y\, J_0^2\left(\frac{\Delta k}{2\sin(y)}\right)\right)^2 . \qquad (44)$$

This result is strictly true only in the limit of a large number of kicks, but practically the saturation is reached after $t \sim \Delta k^{-1}$ kicks. This follows from the minima in the inset in Figure 21 which are found by differentiating the time-dependent fidelity with respect to Δk. Then, the first zero of the 1st order Bessel function $J_1(t\Delta k)$ at $t\Delta k \simeq 3.83$ is essentially responsible for the observed minima. Interestingly, $F^*(\Delta k)$ oscillates quasi-periodically rather than dropping monotonically as a function of the perturbation Δk, another feature which highlights the stability of the QR dynamics of the QKR. The aforementioned features are all illustrated in Figure 21 which also shows that strict saturation is destroyed by arbitrarily small detunings $\epsilon \equiv 2\pi\ell - \tau$ from resonance. However, the temporal decay of the fidelity depends continuously on ϵ and is again slow for small ϵ. This implies that the predicted saturation is an *experimentally robust* observable (Wu et al., 2009). In the following subsection, we will use the pseudoclassical approach of Section 2.3 to compute the long-time behavior of fidelity for near-resonant rotors.

3.6 Pseudoclassical Theory for Fidelity

We have seen above in Section 2.3 that the resonant rotor dynamics essentially corresponds to the pseudoclassical motion astride a nonlinear resonance island, provided ϵ is sufficiently small. We consider from now on only initial atomic states with a narrow distribution of momenta near $p = 0$. This means that we restrict ourselves to a portion of the pseudoclassical phase space that contains only the principal resonance island which is located at $J = 2\pi$ or $I = 0$ (assuming $\ell = 1$ for the rest of this subsection). At the centre of that island, we have a stable elliptic fixed point of the pseudoclassical standard map, and the motion around it can be locally

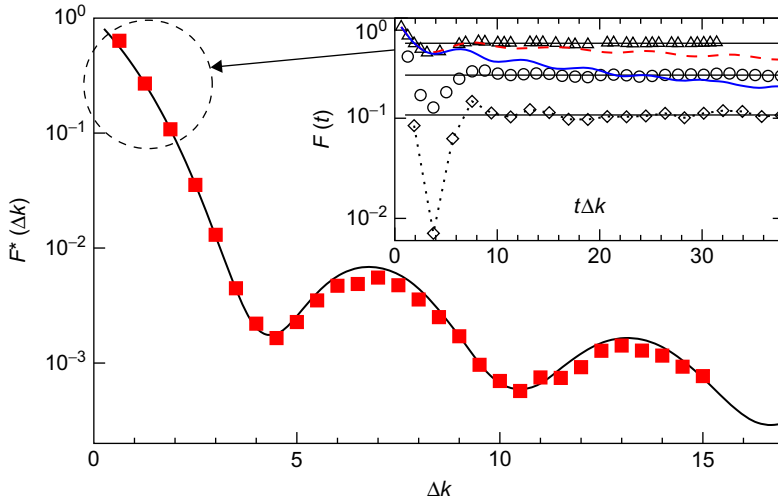

Figure 21 $F^*(\Delta k)$ from Equation (44) (solid line) compared with numerical data (red squares) obtained by evolving ensembles of 10^4 $\beta-$rotors with an initially uniform momentum distribution in $[0, 1)$, at $\tau = 2\pi$ and $t = 50$. Inset: numerically computed fidelity ($F(t) \equiv F(k_1, k_2, t)$) vs. $t\Delta k$ for $\tau = 2\pi$, $k_1 = 0.8\pi$, and fixed $\Delta k = 0.6283$ (triangles), 1.257 (circles), 1.885 (diamonds). The position of the minima corresponds to the time $3.83/\Delta k$. The fidelity saturates for times $t\Delta k \gtrsim 20$ at Δk-dependent, constant values, indicated by the thin horizontal lines. Data for finite detunings $\epsilon = 0.025$ (red dashed) and 0.1 (blue thick solid line) are shown for $\Delta k = 0.6283$. (Adapted figure from Wimberger and Buchleitner [2006]).

approximated by a simple harmonic oscillator Hamiltonian

$$H(I, \theta) = \frac{1}{2}(I + \bar{\beta})^2 + \frac{\omega^2}{2}\theta^2, \tag{45}$$

where $\omega \equiv \sqrt{\bar{k}}$, $\bar{\beta} \equiv \tau\beta - \pi \approx \tau(\beta - 0.5)$, and a shift of θ by π is understood. Using this approximation of the dynamics along the nonlinear resonance island, we can directly compute the fidelity using semiclassical wave functions of the form

$$\hat{\mathcal{U}}^t_{\beta,k}\Psi_\beta(\theta) \sim \frac{1}{\sqrt{2\pi}} \sum_s \left|\frac{\partial\theta}{\partial\theta'}\right|^{-1/2}_{\theta'=\theta'_s} \mathrm{e}^{\frac{i}{\epsilon}\Phi_s(\theta,t) - i\frac{\pi}{2}\nu_s}, \tag{46}$$

where we chose as initial state a zero momentum plane wave $\Psi_\beta(\theta) = (2\pi)^{-1/2}$ and $\epsilon > 0$ is assumed with no limitation of generality. The sum is over all trajectories (labeled by the index s) which start with $I = 0$ at $t = 0$ and reach position θ at after a number of kicks t. $\theta' = \theta'_s$ are their initial positions, and the function whose derivative is taken in the pre-factor

yields θ at time t as a function of position θ' at $t = 0$, given that the initial momentum $I' = 0$. Finally, the function $\Phi_s(\theta, t) = S(\theta, \theta'_s, t)$ is the action of the s-th trajectory and ν_s is the Morse-Maslov index (Haake, 2000; Schulman, 1981). Except at exact multiples of the period, there is one harmonic oscillator trajectory in the sum in Equation (46); moreover, Maslov indices do not depend on the trajectory in this case. Straightforward calculation of the action integral (Abb, 2009) yields $\theta'(\theta, t) = \sec(\omega t)\big(\theta - \bar{\beta}\omega^{-1}\sin(\omega t)\big)$ and $\Phi(\theta, t) = \bar{\beta}\theta\,\big(\sec(\omega t) - 1\big) - (\omega^{-1}\bar{\beta}^2 + \omega\theta^2)\tan(\omega t)/2$, giving

$$\langle \hat{\mathcal{U}}^{\,t}_{\beta,k_1}\Psi_\beta | \hat{\mathcal{U}}^{\,t}_{\beta,k_2}\Psi_\beta\rangle \;\sim\; \frac{e^{i\lambda(t)}}{2\pi\sqrt{|\cos(\omega_1 t)\cos(\omega_2 t)|}} \int_{-\pi}^{\pi} \mathrm{d}\theta\; e^{\frac{i}{2\epsilon}\{A(t)\theta^2 + C(t)\bar{\beta}^2 - 2\bar{\beta}\theta B(t)\}}, \tag{47}$$

where $\omega_{1,2} \equiv \sqrt{\tilde{k}_{1,2}}$. Additionally, we have defined $A(t) = \omega_2\tan(\omega_2 t) - \omega_1\tan(\omega_1 t)$, $B(t) = \sec(\omega_2 t) - \sec(\omega_1 t)$, and $C(t) = \omega_2^{-1}\tan(\omega_2 t) - \omega_1^{-1}\tan(\omega_1 t)$. $\lambda(t)$ is a phase factor accumulated by the Maslov indices which depends only on time, rendering it irrelevant to the computation of fidelity. We next insert Equation (47) in Equation (43) and choose for $\rho(\beta)$ a uniform distribution in some interval $\left[\frac{1}{2} - b, \frac{1}{2} + b\right)$, with $0 \le b \le 1/2$. It is necessary to assume that b is smaller than the halfwidth of the pseudoclassical resonant island, because the harmonic approximation we have started from is, of course, valid just inside the island. Then

$$F(k_1, k_2, t) \sim \frac{\left|\int_{-\pi}^{\pi} \mathrm{d}\theta\; \mathrm{e}^{-\frac{i}{2\epsilon}\Lambda_1(\theta,\epsilon,t)} \int_{-\tau b}^{\tau b} \mathrm{d}\bar{\beta}\; \mathrm{e}^{-\frac{i}{2\epsilon}\Lambda_2(\bar{\beta},\theta,\epsilon,t)}\right|^2}{16\pi^2 b^2 \tau^2 |\cos(\omega_1 t)\cos(\omega_2 t)|}, \tag{48}$$

where $\Lambda_1(\theta, \epsilon, t) = (A(t) - B^2(t)C(t)^{-1})\theta^2$ and $\Lambda_2(\bar{\beta}, \theta, \epsilon, t) = \big(\bar{\beta}\sqrt{C(t)} - B(t)C(t)^{-1/2}\theta\big)^2$. As $\Lambda_2 \sim \epsilon^{-1/2}$ in the limit when $\epsilon \to 0$ and $t\sqrt{\epsilon} \sim$const., the limits in the $\bar{\beta}$-integral in Equation (48) can be taken to $\pm\infty$ to yield $\int_{-\tau b}^{\tau b} \mathrm{d}\bar{\beta}\; e^{-\frac{i}{2\epsilon}\Lambda_2(\bar{\beta},\theta,\epsilon,t)} \sim (2\pi)^{1/2}\epsilon^{1/2}C(t)^{-1/2}e^{-i\pi/4}$. Due to this approximation, Equation (49) below is valid in the regime where ϵ is small compared with b^2. The remaining θ-integral is dealt with similarly, because the prefactor of θ^2 in Λ_1 is $\sim \epsilon^{-1/2}$. Thus finally

$$\begin{aligned} F(k_1, k_2, t) &\sim \frac{\epsilon^2}{16\pi^2 b^2 |C(t)A(t) - B(t)^2||\cos(\omega_1 t)\cos(\omega_2 t)|} \\ &= \frac{\epsilon^2\omega_1\omega_2}{8\pi^2 b^2 |4\omega_1\omega_2 - \omega_+^2\cos(\omega_- t) - \omega_-^2\cos(\omega_+ t)|}, \end{aligned} \tag{49}$$

where $\omega_\pm = \omega_1 \pm \omega_2$. Singularities of this expression are artifacts of the approximations used in evaluating the integrals in Equation (48), which indeed break down when the divisor in Equation (49) is small compared

with ϵ. However, they account for the "revivals" of the fidelity occurring periodically with the beating period $T_{12} = 2\pi/|\omega_-|$. For purely resonant rotors (here $\beta = 1/2$), the revivals occur with the period $T_{12}/2$. This can be seen by evaluating Equation (48) with just one, the purely resonant β, to arrive at

$$F(k_1, k_2, t) \equiv F_{\text{res}}(k_1, k_2, t) \sim \frac{\epsilon/(2\pi)}{|\omega_2 \cos(\omega_1 t)\sin(\omega_2 t) - \omega_1 \cos(\omega_2 t)\sin(\omega_1 t)|}, \tag{50}$$

which has singularities with the mentioned periodicity of $T_{12}/2$. This behavior of resonant rotors has a simple qualitative explanation. The stationary-phase trajectories of the two harmonic oscillators, which were started at $I = 0$, exactly return to $I = 0$ whenever time is a multiple of the half-period $T_{12}/2$, and so fully contribute to fidelity, in spite of their angles being different by π in the case of odd multiples. At $\beta \neq 0$ this symmetry is lost, which suppresses each second revival according to Equation (49).

Comparing numerical data (obtained by repeated application of the Floquet operator to the initial wave function) with the analytical predictions, we find fairly good agreement. We observe the expected peak structure of the revivals in Figure 22a and the loss of intermediate revival peaks at $T_{12}/2$ in Figure 22b. An experimental observation of these revivals is quite challenging since a good control over a narrow initial distribution of quasi-momenta and a stable experiment over a relatively large number of kicks are both required. The time scale on which the revivals occur is proportional to $\epsilon^{-1/2}$ and of crucial impact to experimental measurements. A conservation of coherence has been shown for up to 150 kicks (see e.g., ref. [Schlunk et al., 2003b]) with cold atoms, making an observation of the revivals for reasonable $\epsilon \lesssim 0.01$ possible. Earlier realizations of the QKR were implemented using cold atoms (Ammann et al., 1998; Bharucha et al., 1999; d'Arcy et al., 2001, 2004; Moore et al., 1995; Sadgrove et al., 2005) with broad distributions in quasi-momentum. Nowadays, much better control of quasi-momentum is provided by using BECs (see [Duffy et al., 2004b; Ramareddy et al., 2010; Ryu et al., 2006]), which allows for a restriction in β up to 0.2% of the Brillouin zone (as achieved, e.g., in [Ryu et al., 2006]). This would allow the verification of our results by reducing the intervals in quasi-momentum and thus retracing the revivals with period $T_{12}/2$ to the exactly resonant and the revivals with period T_{12} to the near-resonant rotors. There exists a second possibility to measure the transition from Equation (50) to Equation (49) with just cold atoms, since the $\bar{\beta}$ we use scales with the kicking period, i.e., $\bar{\beta} \approx \tau(\beta - 1/2)$. Due to this scaling, the limit $\tau \to 0$ (automatically implying also $\epsilon \to 0$, c.f. Section 3.2) permits a measurement of Equation (50), even with an ensemble of cold atoms whose quasi-momenta occupy the full

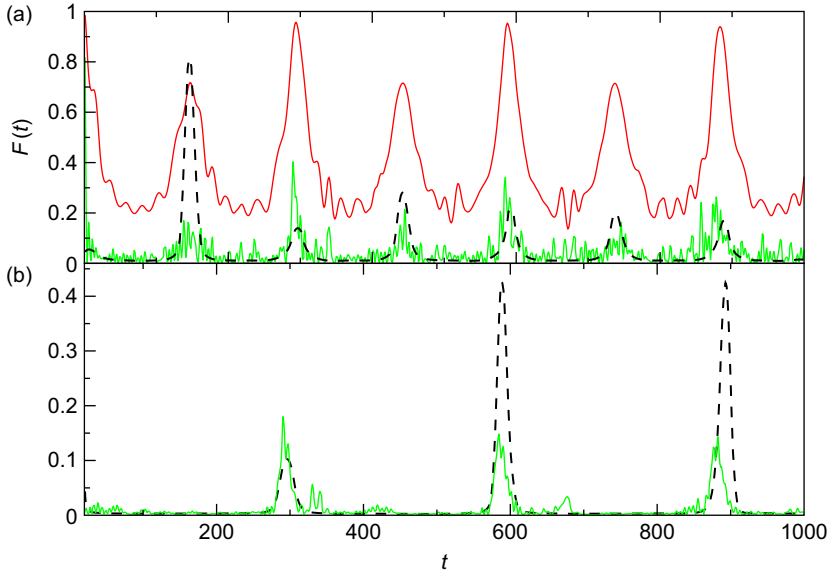

Figure 22 (a) Fidelity as predicted by Equation (50)—because of the singularities of the analytical formula the curve is folded with normalized Gaussians with a standard deviation of $t \approx 6$ kicks (dashed black line)—and numerical data for a single-resonant rotor (grey/green curve) and a coherent initial state built up for fixed resonant $\beta = 1/2$ and centred at the elliptic fixed point of the island (solid red/dark line), for $k_1 = 0.8\pi$, $k_2 = 0.6\pi$ and detuning $\epsilon = 0.01$ from $\tau - \epsilon = 2\pi$. The coherent state shows almost perfect revivals at T_{12} and slightly smaller ones at the intermediate peaks. (b) Same as in (a) for an ensemble of 5000 equidistantly chosen rotors (grey/green curve) with a width of $\Delta\beta = 0.05$ (or $\Delta\bar{\beta} \approx 0.31$) around the resonant value, covering half the width of the resonance island in the phase space induced by Equation (11) compared with the smoothed version of Equation (49) (dashed black line). The intermediate revival peaks observed in (a) disappear as predicted by Equation (49).

Brillouin zone. This subsection exclusively focused on the evolution of fidelity corresponding to librational motion within the nonlinear resonance island of the pseudoclassical phase space. Ongoing research is currently extending our understanding to nonresonant values of quasi-momentum corresponding to rotational orbits in phase space (Probst, 2010; 2011). It remains to combine these two classes of motion to provide a full account of the behavior seen in the inset of Figure 21 for finite ϵ.

4. CONCLUSIONS AND OUTLOOK

4.1 Review of the State of the Art

Although the principle aim of this review is to introduce the ϵ-classical method to a wider audience, we would also like to think that it serves

to illustrate the way that physics progresses in a microcosm. The interplay between theory and experiment in this particular field has driven the method well beyond the tasks for which it was originally conceived. At times, the desire to verify new details turned up by the theory has been the driving force of investigations. Just as often, the observation of new phenomena, or the modification of an experiment has motivated the extension of the theory.

Below, we recap the uses to which the ϵ-classical theory has so far been put in list form:

1. **Analysis of quantum accelerator modes.** Although outside the scope of this review, we note that these studies marked the invention of the ϵ-classical map (Fishman et al., 2002).
2. **Reduction of near-resonant quantum dynamics to a one-parameter scaling law.** The quantum kicked rotor until very recently remained a theoretically opaque system in that quantum correlations between kicks could only be evaluated precisely up to $N \sim 5$ and the exact behavior was sensitive to three principle parameters—kick strength, kick number, and the period of the kicks. The application of a pendulum approximation to the ϵ-classical approximation allowed the entire problem to be reduced to a one parameter scaling function for the dynamics near to resonance.

   New features predicted and measured by the scaling law. The ϵ-classical scaling law for dynamics of the AOKR near QR predicted some features which had not been noticed before in experimental or numerical studies. In particular, side peaks around the quantum resonance where predicted and measured, and anomalous behavior including frozen and ballistic energy growth near the actual semiclassical limit were predicted and observed experimentally. The observation of these effects also served to demonstrate that quantum resonance peaks exhibit sub-Fourier narrowing with respect to the applied pulse train—a phenomenon predicted clearly by the scaling law for the resonances.
3. **Modelling of the effect of spontaneous emission near quantum resonance.** The study of spontaneous emission in the kicked rotor near quantum resonance showed that the effect on the dynamics of a decoherence process could be captured using a quasi-classical model.
4. **Explanation of stability of QR against large amplitude fluctuations.** The puzzle of why amplitude fluctuations destroy some quantum coherent effects (notably dynamical localization) but leave near-resonant dynamics largely unchanged was solved by modifying the ϵ-classical map to include amplitude fluctuations. However, such fluctuations have little effect on the phase space, explaining why the quantum resonance peaks are robust.

5. **Scaling law in the presence of amplitude fluctuations.** An explanation of the stability of the QR peaks in the presence of amplitude noise was finally given in terms of a scaling law. By observing that the noise changed the phase space predominantly around the separatrix, an approximate scaling law was derived, extending analytical results to the system in the presence of a common source of decoherence.
6. **Scaling law for directed transport experiments (quantum resonance ratchets).** Choosing the appropriate classical initial conditions allows the pseudoclassical method to be extended to the case where the initial state is a quantum superposition of momentum states. Once again, extending the scaling law to this variant of the kicked rotor predicts new dynamics such as current reversal for slight detunings from exact QR.
7. **Fidelity of kicked rotors described pseudoclassically.** Although the concept of fidelity is inherently quantum mechanical, the pseudoclassical method was once again extended to describing the evolution of the phase sensitive fidelity in the AOKR near QR.

4.2 Future Perspectives for the Pseudoclassical Method

The state of the art in AOKR experiments is arguably represented by experiments on atoms with very narrow initial momentum distributions (typically sourced from a BEC) and indeed for the last two topics listed above, a BEC would be necessary to fully test the new phenomena suggested by the theory. We note that, of course, there are topics outside of quantum resonance where studies of the kicked rotor are being extended and even thermal atoms still allow the measurement of very interesting new results (such as the metal-insulator transition reported in Chabé et al. [2008]). Such studies are outside the scope of the present review.

However, we tend to believe that the quantum resonance phenomenon in the AOKR provides the most fertile ground for new applications of cold atoms in time-dependent optical lattices. It is interesting to note, for example, that the momentum current in the first "atom motor" (i.e., Hamiltonian quantum ratchet) experiment was sharply peaked around quantum resonance (Salger et al., 2009). Additionally, the extension of the pseudoclassical method to quantum fidelity and the fact that the Talbot effect has been used to perform factorization (Bigourd et al., 2008; Mack et al., 2002) suggests that the ϵ-classical method might be applicable in quantum information settings.

Slightly more prosaically, it should be noted that the extension of the ϵ-classical theory to fractional quantum resonances still represents a challenge (c.f. results in this direction for the accelerator modes in the amended QKR [Guarneri & Rebuzzini, 2008]), even though the fractional resonances have been measured carefully in both ultra-cold by

Ryu et al. (2006) and cold atom settings by Kanem et al. (2007). That this task represents more of a challenge than extending the theory to some of the interesting variants of the AOKR explored above, serves as a reminder that the derivation of analytical results in the AOKR system is still not a trivial task in general.

Qualitatively, new directions of research would include the effects of either atom–atom interactions (Monteiro et al., 2009; Rebuzzini et al., 2005, 2007; Wimberger et al., 2005a) or the dissipative opening of kicked atomic systems (Benenti et al., 2001; Carlo et al., 2006; Facchini et al., 2007; Romanelli, 2009; Schomerus & Tworzydło, 2004; Tomadin et al., 2006). For instance, the stability of QR motion with respect to typical values of a mean-field nonlinearity arising from atom–atom interactions in a BEC was numerically predicted in Wimberger et al. (2005a) and experimentally tested in Ryu et al. (2006), yet an extension to near-resonant motion is desirable, in particular by analytical means. New ideas based on the pseudoclassical method may allow us to take into account such complications in a more or less rigorous way.

ACKNOWLEDGMENTS

The work reported in this review was supported by the Alexander von Humboldt Foundation, the Heidelberg Centre for Quantum Dynamics, the Excellence Initiative by the German Research Foundation (DFG) through the Heidelberg Graduate School of Fundamental Physics (Grant No. GSC 129/1), the Frontier Innovation Fonds and the Global Networks Mobility Measures of the University of Heidelberg. We are indebted to Ken'ichi Nakagawa and the staff of the Institute for Laser Science for their support and hospitality. S.W. is grateful to the Heidelberg Academy of Sciences and Humanities for the Academy Award 2010 and to the Hengstberger Foundation for support by the Klaus-Georg and Sigrid Hengstberger Prize 2009. Finally, we would like to warmly thank our collaborators, Andreas Buchleitner, Italo Guarneri, Shmuel Fishman, Scott Parkins, Rainer Leonhardt, Terry Mullins, Andrew Hilliard, Roberto Artuso, Michael d'Arcy, Gil Summy, Riccardo Mannella, Andrea Tomadin, Angelo Facchini, Martina Abb, Benedikt Probst, Torben Schell and Remy Dubertrand, for their help in pushing forward research based on the AOKR system.

REFERENCES

Abb, M. (2009). Fidelity for kicked atoms at nearly resonant driving. Master's thesis, University of Heidelberg.

Abb, M., Guarneri, I., & Wimberger, S. (2009). Pseudoclassical theory for fidelity of nearly resonant quantum rotors. *Physical Review E*, *80*(3), 035206.

Abramowitz, M., & Stegun, I. A. (1972). *Handbook of mathematical functions*. New York: Dover.

Ammann, H., Gray, R., Shvarchuck, I., & Christensen, N. (1998). Quantum delta-kicked rotor: experimental observation of decoherence. *Physical Review Letters*, *80*(19), 4111–4115.

Anderson, P. W. (1958). Absence of diffusion in certain random lattices. *Physical Review*, *109*(5), 1492–1505.

Arndt, M., Buchleitner, A., Mantegna, R. N., & Walther, H. (1991). Experimental study of quantum and classical limits in microwave ionization of rubidium Rydberg atoms. *Physical Review Letters*, *67*(18), 2435–2438.

Bayfield, J. E., Casati, G., Guarneri, I., & Sokol, D. W. (1989). Localization of classically chaotic diffusion for hydrogen atoms in microwave fields. *Physical Review Letters*, *63*(4), 364–367.

Benenti, G., Casati, G., Guarneri, I., & Terraneo, M. (2001). Quantum fractal fluctuations. *Physical Review Letters*, *87*(1), 014101.

Bharucha, C. F., Robinson, J. C., Moore, F. L., Sundaram, B., Niu, Q., & Raizen, M. G. (1999). Dynamical localization of ultracold sodium atoms. *Physical Review E*, *60*(4), 3881–3895.

Bigourd, D., Chatel, B., Schleich, W. P., & Girard, B. (2008). Factorization of numbers with the temporal Talbot effect: optical implementation by a sequence of shaped ultrashort pulses. *Physical Review Letters*, *100*(3), 030202.

Billy, J., Josse, V., Zuo, Z., Bernard, A., Hambrecht, B., Lugan, P., et al. (2008). Direct observation of Anderson localization of matter waves in a controlled disorder. *Nature*, *453*, 891.

Blümel, R., Fishman, S., & Smilansky, U. (1986). Excitation of molecular rotation by periodic microwave pulses – a testing ground for Anderson localization. *The Journal of Chemical Physics*, *84*, 2604.

Bourgain, J. (2002). Estimates on Green's functions, localization and the quantum kicked rotor model. *Annals of Mathematics*, *156*, 249.

Brenner, N., & Fishman, S. (1992). Pseudo-randomness and localization. *Nonlinearity*, *5*(1), 211.

Brouard, S., & Plata, J. (2003). Quantum-kicked rotor: the effect of amplitude noise on the quantum resonances. *Journal of Physics A: Mathematical and General*, *36*(13), 3745.

Buonsante, P., & Vezzani, A. (2007). Ground-state fidelity and bipartite entanglement in the Bose-Hubbard model. *Physical Review Letters*, *98*(11), 110601.

Carlo, G. G., Benenti, G., Casati, G., Wimberger, S., Morsch, O., Mannella, R., et al. (2006). Chaotic ratchet dynamics with cold atoms in a pair of pulsed optical lattices. *Physical Review A*, *74*(3), 033617.

Casati, G., Chirikov, B., Ford, J., & Izrailev, F. (1979). Stochastic behavior of a quantum pendulum under periodic perturbation. In G. Casati, J. Ford, (Eds.), *Stochastic behavior in classical and quantum hamiltonian systems* (p. 334). Berlin: Springer.

Casati, G., Guarneri, I., & Shepelyansky, D. (1988). Hydrogen atom in monochromatic field: chaos and dynamical photonic localization. *IEEE Journal of Quantum Electronics*, *24*, 1420.

Chabé, J., Lemarié, G., Grémaud, B., Delande, D., Szriftgiser, P., & Garreau, J. C. (2008). Experimental observation of the Anderson metal-insulator transition with atomic matter waves. *Physical Review Letters*, *101*, 255702.

Chirikov, B. V. (1979). A universal instability of many-dimensional oscillator systems. *Physics Reports*, *52*(5), 263–379.

Currivan, J.-A., Ullah, A., & Hoogerland, M. D. (2009). The initial velocity dependence of the quantum resonance in the delta-kicked rotor. *Europhysics Letters*, *85*, 3005.

Daley, A. J., Parkins, A., Leonhardt, R., & Tan, S. M. (2002). Diffusion resonances in action space for an atom optics kicked rotor with decoherence. *Physical Review E*, *65*, 035201(R).

Daley, A. J., & Parkins, A. S. (2002). Early time diffusion for the quantum kicked rotor with narrow initial momentum distributions. *Physical Review E*, *66*(5), 056210.

Dana, I., & Dorofeev, D. L. (2006). Fluctuations and transients in quantum-resonant evolution. *Physical Review E*, *74*(4), 045201.

Dana, I., Ramareddy, V., Talukdar, I., & Summy, G. S. (2008). Experimental realization of quantum-resonance ratchets at arbitrary quasimomenta. *Physical Review Letters*, *100*(2), 024103.

d'Arcy, M. B., Godun, R. M., Oberthaler, M. K., Cassettari, D., & Summy, G. S. (2001). Quantum enhancement of momentum diffusion in the delta-kicked rotor. *Physical Review Letters*, *87*(7), 074102.

d'Arcy, M. B., Godun, R. M., Summy, G. S., Guarneri, I., Wimberger, S., Fishman, S., et al. (2004). Decoherence as a probe of coherent quantum dynamics. *Physical Review E*, *69*(2), 027201.

Deng, L., Hagley, E. W., Denschlag, J., Simsarian, J. E., Edwards, M., Clark, C. W., et al. (1999). Temporal, matter-wave-dispersion Talbot effect. *Physical Review Letters*, *83*(26), 5407–5411.
Dubetsky, B., & Berman, P. R. (1997). Atomic interferometry. *Advances in Atomic and Molecular Physics*, *37*(suppl. 3), 407.
Duffy, G. J., Mellish, A. S., Challis, K. J., & Wilson, A. C. (2004a). Nonlinear atom-optical δ-kicked harmonic oscillator using a Bose-Einstein condensate. *Physical Review A*, *70*(4), 041602.
Duffy, G. J., Parkins, S., Müller, T., Sadgrove, M., Leonhardt, R., & Wilson, A. C. (2004b). Experimental investigation of early-time diffusion in the quantum kicked rotor using a Bose-Einstein condensate. *Physical Review E*, *70*(5), 056206.
Dunlap, D. H., & Kenkre, V. M. (1986). Dynamic localization of a charged particle moving under the influence of an electric field. *Physical Review B*, *34*(6), 3625–3633.
Facchini, A., Wimberger, S., & Tomadin, A. (2007). Multifractal fluctuations in the survival probability of an open quantum system. *Physica A: Statistical Mechanics and its Applications*, *376*, 266–274.
Feynman, R. P. (1963). *The Feynman lectures on physics* (Vol. 1). Addison-Wesley: Reading. MA, ch. 46.
Fishman, S. (1993). Quantum localization. In G. Casati, I. Guarneri, U. Smilansky, (Eds.), *Quantum chaos: Proceedings of the International School of Physics Enrico Fermi: Cource CXIX* (pp. 187–219). Amsterdam: North Holland.
Fishman, S., Grempel, D. R., & Prange, R. E. (1982). Chaos, quantum recurrences, and Anderson localization. *Physical Review Letters*, *49*(8), 509–512.
Fishman, S., Grempel, D. R., & Prange, R. E. (1987). Temporal crossover from classical to quantal behavior near dynamical critical points. *Physical Review A*, *36*(1), 289–305.
Fishman, S., Guarneri, I., & Rebuzzini, L. (2002). Stable quantum resonances in atom optics. *Physical Review Letters*, *89*(8), 084101.
Flach, S., Yevtushenko, O., & Zolotaryuk, Y. (2000). Directed current due to broken time-space symmetry. *Physical Review Letters*, *84*, 2358.
Galvez, E. J., Sauer, B. E., Moorman, L., Koch, P. M., & Richards, D. (1988). Microwave ionization of H atoms: breakdown of classical dynamics for high frequencies. *Physical Review Letters*, *61*(18), 2011–2014.
Gong, J., & Brumer, P. (2006). Generic quantum ratchet accelerator with full classical chaos. *Physical Review Letters*, *97*(24), 240602.
Gorin, T., Prosen, T., Seligman, T. H., & Znidaric, M. (2006). Dynamics of Loschmidt echoes and fidelity decay. *Physics Reports*, *435*(2–5), 33–156.
Graham, R., Schlautmann, M., & Zoller, P. (1992). Dynamical localization of atomic-beam deflection by a modulated standing light wave. *Physical Review A*, *45*(1), R19–R22.
Grempel, D. R., Fishman, S., & Prange, R. E. (1984). Finite-planck's-constant scaling at stochastic transitions of dynamical systems. *Physical Review Letters*, *53*(13), 1212–1215.
Guarneri, I. (2009). On the spectrum of the resonant quantum kicked rotor. *Annales Henri Poincare*, *10*, 1097.
Guarneri, I., & Rebuzzini, L. (2008). Quantum accelerator modes near higher-order resonances. *Physical Review Letters*, *100*(23), 234103.
Guarneri, I., Rebuzzini, L., & Fishman, S. (2006). Arnol'd tongues and quantum accelerator modes. *Nonlinearity*, *19*(5), 1141.
Haake, F. (2000). *Quantum signatures of chaos*. Berlin: Springer.
Hänggi, P., & Marchesoni, F. (2009). Artificial brownian motors: controlling transport on the nanoscale. *Reviews of Modern Physics*, *81*(1), 387–442.
Hogg, T., & Huberman, B. (1983). Quantum dynamics and nonintegrability. *Physical Review A*, *28*, 22–31.
Horodecki, R., Horodecki, P., Horodecki, M., & Horodecki, K. (2009). Quantum entanglement. *Reviews of Modern Physics*, *81*(2), 865–942.
Izrailev, F., & Shepelyansky, D. (1979). Quantum resonance for a rotator in a nonlinear periodic field. *Soviet Physics Doklady*, *24*, 996.
Izrailev, F., & Shepelyansky, D. (1980). Quantum resonance for a rotator in a nonlinear periodic field. *Theoretical and Mathematical Physics*, *43*, 353.
Izrailev, F. M. (1990). Simple models of quantum chaos: spectrum and eigenfunctions. *Physics Reports*, *196*(5–6), 299–392.

Jitomirskaya, S. (2002). Non-perturbative localization. *Proceedings of the ICM*, *3*, 445, arXiv:math-ph/0304044.
Jones, P. H., Goonasekera, M., Meacher, D. R., Jonckheere, T., & Monteiro, T. S. (2007). Directed motion for delta-kicked atoms with broken symmetries: comparison between theory and experiment. *Physical Review Letters*, *98*(7), 073002.
Kanem, J. F., Maneshi, S., Partlow, M., Spanner, M., & Steinberg, A. M. (2007). Observation of high-order quantum resonances in the kicked rotor. *Physical Review Letters*, *98*(8), 083004.
Kierig, E., Schnorrberger, U., Schietinger, A., Tomkovic, J., & Oberthaler, M. K. (2008). Single-particle tunneling in strongly driven double-well potentials. *Physical Review Letters*, *100*(19), 190405.
Klappauf, B. G., Oskay, W. H., Steck, D. A., & Raizen, M. G. (1998). Observation of noise and dissipation effects on dynamical localization. *Physical Review Letters*, *81*(6), 1203–1206.
Krug, A., Wimberger, S., & Buchleitner, A. (2003). Decay, interference, and chaos: how simple atoms mimic disorder. *The European Physical Journal D*, *26*, 21.
Latka, M., & West, B. (1995). Nature of quantum localization in atomic momentum transfer experiments. *Physical Review Letters*, *75*, 4202.
Lee, P. A., & Ramakrishnan, T. V. (1985). Disordered electronic systems. *Reviews of Modern Physics*, *57*(2), 287–337.
Lemarié, G., Lignier, H., Delande, D., Szriftgiser, P., & Garreau, J. C. (2010). Critical state of the Anderson transition: between a metal and an insulator. *Physical Review Letters*, *105*, 090601.
Lepers, M., Zehnlé, V., & Garreau, J. C. (2008). Kicked-rotor quantum resonances in position space. *Physical Review A*, *77*(4), 043628.
Lichtenberg, A., & Lieberman, M. (1992). *Regular and chaotic dynamics*. Berlin: Springer.
Lignier, H., Sias, C., Ciampini, D., Singh, Y., Zenesini, A., Morsch, O., et al. (2007). Dynamical control of matter-wave tunneling in periodic potentials. *Physical Review Letters*, *99*(22), 220403.
Lundh, E., & Wallin, M. (2005). Ratchet effect for cold atoms in an optical lattice. *Physical Review Letters*, *94*(11), 110603.
Mack, H., Bienert, M., Haug, F., Straub, F. S., Freyberger, M., & Schleich, W. P. (2002). Wave packet dynamics and factorization of numbers. *Physica Status Solidi B*, *233*, 408.
Madroñero, J., Ponomarev, A., Carvalho, A., Wimberger, S., Viviescas, C., Kolovsky, A., et al. (2006). Quantum chaos, transport, and control in quantum optics. *Advances in Atomic, Molecular, and Optical Physics*, *53*, 33.
McDowall, P., Hilliard, A., McGovern, M., Grünzweig, T., & Andersen, M. F. (2009). A fidelity treatment of near-resonant states in the atom-optics kicked rotor. *New Journal of Physics*, *11*(12), 123021.
Milner, V., Steck, D. A., Oskay, W. H., & Raizen, M. G. (2000). Recovery of classically chaotic behavior in a noise-driven quantum system. *Physical Review E*, *61*(6), 7223–7226.
Monteiro, T. S., Dando, P. A., Hutchings, N. A. C., & Isherwood, M. R. (2002). Proposal for a chaotic ratchet using cold atoms in optical lattices. *Physical Review Letters*, *89*(19), 194102.
Monteiro, T. S., Rançon, A., & Ruostekoski, J. (2009). Nonlinear resonances in δ-kicked Bose-Einstein condensates. *Physical Review Letters*, *102*(1), 014102.
Moore, F. L., Robinson, J. C., Bharucha, C., Williams, P. E., & Raizen, M. G. (1994). Observation of dynamical localization in atomic momentum transfer: a new testing ground for quantum chaos. *Physical Review Letters*, *73*(22), 2974–2977.
Moore, F. L., Robinson, J. C., Bharucha, C. F., Sundaram, B., & Raizen, M. G. (1995). Atom optics realization of the quantum δ-kicked rotor. *Physical Review Letters*, *75*(25), 4598–4601.
Nath, N. S. N. (1936). The diffraction of light by high-frequency sound waves: generalized theory. *Proceedings of the Indian Academy of Sciences*, *4*, 222.
Oberthaler, M. K., Godun, R. M., d'Arcy, M. B., Summy, G. S., & Burnett, K. (1999). Observation of quantum accelerator modes. *Physical Review Letters*, *83*(22), 4447–4451.
Oskay, W. H., Steck, D. A., & Raizen, M. G. (2003). Timing noise effects on dynamical localization. *Chaos, Solitons and Fractals*, *16*(3), 409–416.
Peres, A. (1984). Stability of quantum motion in chaotic and regular systems. *Physical Review A*, *30*(4), 1610–1615.
Plötz, P., Lubasch, M., & Wimberger, S. (2011). Detection of avoided crossings by fidelity. *Physica A: Statistical Mechanics and its Applications*, *390*, 1363–1369.

Probst, B. (2010). The pendulum approximation for fidelity in quantum kicked rotor systems. Master's thesis, University of Heidelberg.
Probst, B., Dubertrand, R., & Wimberger, S. (2011). Fidelity of the near resonant quantum kicked rotor. *Journal of Physics A*, in press.
Raizen, M. (1999). Quantum chaos with ultra-cold atoms. *Advances in Atomic and Molecular Physics*, *41*, 43.
Ramareddy, V., Behinaein, G., Talukdar, I., Ahmadi, P., & Summy, G. S. (2010). High-order resonances of the quantum-kicked accelerator. *Europhysics Letters*, *89*(3), 33001.
Rebuzzini, L., Wimberger, S., & Artuso, R. (2005). Delocalized and resonant quantum transport in nonlinear generalizations of the kicked rotor model. *Physical Review E*, *71*(3), 036220.
Rebuzzini, L., Artuso, R., Fishman, S., & Guarneri, I. (2007). Effects of atomic interactions on quantum accelerator modes. *Physical Review A*, *76*(3), 031603.
Reimann, P. (2002). Brownian motors: noisy transport far from equilibrium. *Physics Reports*, *361*(2–4), 57–265.
Romanelli, A. (2009). Decoherence without classicality in the resonant quantum kicked rotor. *Physical Review A*, *80*, 022102.
Ryu, C., Andersen, M. F., Vaziri, A., d'Arcy, M. B., Grossman, J. M., Helmerson, K., et al. (2006). High-order quantum resonances observed in a periodically kicked Bose-Einstein condensate. *Physical Review Letters*, *96*(16), 160403.
Sadgrove, M. (2005). Resonant quantum transport for kicked atoms. Ph.D. thesis, University of Auckland.
Sadgrove, M., Hilliard, A., Mullins, T., Parkins, S., & Leonhardt, R. (2004). Observation of robust quantum resonance peaks in an atom optics kicked rotor with amplitude noise. *Physical Review E*, *70*(3), 036217.
Sadgrove, M., Horikoshi, M., Sekimura, T., & Nakagawa, K. (2007). Rectified momentum transport for a kicked Bose-Einstein condensate. *Physical Review Letters*, *99*(4), 043002.
Sadgrove, M., & Wimberger, S. (2009). Pseudo-classical theory for directed transport at quantum resonance. *New Journal of Physics*, *11*(8), 083027.
Sadgrove, M., Wimberger, S., Parkins, S., & Leonhardt, R. (2005). Ballistic and localized transport for the atom optics kicked rotor in the limit of a vanishing kicking period. *Physical Review Letters*, *94*(17), 174103.
Sadgrove, M., Wimberger, S., Parkins, S., & Leonhardt, R. (2008). Scaling law and stability for a noisy quantum system. *Physical Review E*, *78*(2), 025206.
Salger, T., Kling, S., Hecking, T., Geckeler, C., Morales-Molina, L., & Weitz, M. (2009). Directed transport of atoms in a hamiltonian quantum ratchet. *Science*, *326*(5957), 1241–1243.
Schanz, H., Otto, M.-F., Ketzmerick, R., & Dittrich, T. (2001). Classical and quantum hamiltonian ratchets. *Physical Review Letters*, *87*(7), 070601.
Schlunk, S., d'Arcy, M. B., Gardiner, S. A., Cassettari, D., Godun, R. M., & Summy, G. S. (2003a). Signatures of quantum stability in a classically chaotic system. *Physical Review Letters*, *90*(5), 054101.
Schlunk, S., d'Arcy, M. B., Gardiner, S. A., & Summy, G. S. (2003b). Experimental observation of high-order quantum accelerator modes. *Physical Review Letters*, *90*(12), 124102.
Schomerus, H., & Tworzydło, J. (2004). Quantum-to-classical crossover of quasibound states in open quantum systems. *Physical Review Letters*, *93*(15), 154102.
Schulman, L. S. (1981). *Techniques and applications of path integration*. New York: Wiley.
Sheinman, M., Fishman, S., Guarneri, I., & Rebuzzini, L. (2006). Decay of quantum accelerator modes. *Physical Review A*, *73*(5), 052110.
Shepelyansky, D. (1987). Localization of diffusive excitation in multi-level systems. *Physica D*, *28*, 103.
Talbot, H. F. (1836). Facts relating to optical science. *Philosophical Magazine*, *9*, 401.
Talukdar, I., Shrestha, R., & Summy, G. S. (2010). Sub-Fourier characteristics of a δ-kicked-rotor resonance. *Physical Review Letters*, *105*(5), 054103.
Tian, C., & Altland, A. (2010). Theory of localization and resonance phenomena in the quantum kicked rotor. *New Journal of Physics*, *12*(4), 043043.
Tomadin, A., Mannella, R., & Wimberger, S. (2006). Can quantum fractal fluctuations be observed in an atom-optics kicked rotor experiment? *Journal of Physics A: Mathematical and General*, *39*(10), 2477.

Tonyushkin, A., Wu, S., & Prentiss, M. (2009). Demonstration of a multipulse interferometer for quantum kicked-rotor studies. *Physical Review A*, *79*(5), 051402.
Vant, K., Ball, G., Ammann, H., & Christensen, N. (1999). Experimental evidence for the role of cantori as barriers in a quantum system. *Physical Review E*, *59*(3), 2846–2852.
Walls, D. F., & Milburn, G. J. (2008). *Quantum optics*. Berlin: Springer.
Wimberger, S. (2004). Chaos and localisation: Quantum transport in periodically driven atomic systems. Ph.D. thesis, Ludwig-Maximilians-Universität Munich and Università degli Studi dell'Insubria, http://edoc.ub.uni-muenchen.de/archive/00001687.
Wimberger, S., & Buchleitner, A. (2001). Signatures of Anderson localization in the ionization rates of periodically driven Rydberg states. *Journal of Physics A: Mathematical and General*, *34*(36), 7181.
Wimberger, S., & Buchleitner, A. (2006). Saturation of fidelity in the atom-optics kicked rotor. *Journal of Physics B: Atomic, Molecular and Optical Physics*, *39*(7), L145.
Wimberger, S., Guarneri, I., & Fishman, S. (2003). Quantum resonances and decoherence for -kicked atoms. *Nonlinearity*, *16*(4), 1381.
Wimberger, S., Guarneri, I., & Fishman, S. (2004). Classical scaling theory of quantum resonances. *Physical Review Letters*, *92*(8), 084102.
Wimberger, S., Mannella, R., Morsch, O., & Arimondo, E. (2005a). Resonant nonlinear quantum transport for a periodically kicked bose condensate. *Physical Review Letters*, *94*(13), 130404.
Wimberger, S., Sadgrove, M., Parkins, S., & Leonhardt, R. (2005b). Experimental verification of a one-parameter scaling law for the quantum and "classical" resonances of the atom-optics kicked rotor. *Physical Review A*, *71*(5), 053404.
Wu, S., Tonyushkin, A., & Prentiss, M. G. (2009). Observation of saturation of fidelity decay with an atom interferometer. *Physical Review Letters*, *103*(3), 034101.

This page intentionally left blank

CHAPTER 8

Principles and Applications of Attosecond Technology

Francesca Calegari, Federico Ferrari, Matteo Lucchini, Matteo Negro, Caterina Vozzi, Salvatore Stagira, Giuseppe Sansone, and **Mauro Nisoli**

Politecnico di Milano, Department of Physics, Istituto di Fotonica e Nanotecnologie, IFN-CNR, Piazza Leonardo da Vinci 32, 20133 Milano, Italy

Contents

Advances in Atomic, Molecular, and Optical Physics, Volume 60, Copyright © 2011 Elsevier Inc.
ISSN 1049-250X, DOI: 10.1016/B978-0-12-385508-4.00008-5.

Abstract

Recent progress in attosecond technology has determined an increasing interest in the application of attosecond pulses in atomic, molecular, and solid state-physics. Novel techniques have been introduced for the generation of subfemtosecond pulses and for their applications. We report on recent advances in attosecond science, with particular emphasis on the generation and use of isolated attosecond pulses, produced by using the process of high-order harmonic generation in gases. Several techniques have been proposed and partly implemented for the confinement of the harmonic generation process to a single event: in this article, we analyze various temporal gating techniques. Various schemes for attosecond measurements have been proposed and experimentally demonstrated in the last decade; here, we review important applications of isolated attosecond pulses.

1. INTRODUCTION

After a decade from the first experimental demonstration of the generation of attosecond pulses (Hentschel et al., 2001; Paul et al., 2001), the attosecond research area has shown exciting experimental and theoretical developments (Krausz & Ivanov, 2009; Nisoli & Sansone, 2009). Novel experimental methods have been introduced for the measurement and application of attosecond pulses. The attosecond technology is now well developed, and attosecond techniques are common in a number of laboratories around the world. This is particularly true in the case of trains of attosecond pulses, produced by high-order harmonic generation (HHG) in noble gases (Macklin et al., 1993); (L'Huillier & Balcou, 1993) exposed to intense (peak intensity $I \sim 10^{13} - 10^{15}$ W/cm^2) ultrashort light pulses. As a result of the physical processes at the basis of harmonic generation, bursts of extreme ultraviolet (XUV) pulses are emitted with subfemtosecond duration every half optical cycle of the fundamental radiation, as first theoretically proposed in 1992 (Farkas & Tóth, 1992). The attosecond metrology with trains of attosecond pulses has achieved relevant results: particularly important is the observation of nonlinear effects in the attosecond regime (Midorikawa et al., 2008). In 2003, by using the process of two-photon absorption in atoms, Tzallas et al. demonstrated the first autocorrelation measurement of a train of attosecond pulses (Tzallas et al., 2003); Coulomb explosion of diatomic molecules by two-photon double ionization has been used for the measurement of the interferometric autocorrelation of an attosecond pulse train (Nabekawa et al., 2006; Shimizu et al., 2007). Trains of attosecond pulses have been used in various experiments. In particular, in 2006, they have been used, in combination with a novel interferometric method, for the determination of the phase variation

of electronic wave packets in momentum space (Remetter et al., 2006); in 2008, an attosecond quantum stroboscope method has been proposed and experimentally demonstrated capable of capturing electron motion on an attosecond time scale (Mauritsson et al., 2008). A number of experimental and theoretical works have been published, based on the use of trains of attosecond pulses.

The generation and the applications of isolated attosecond pulses present peculiar characteristics. From the point of view of laser technology, the confinement of the XUV generation process to a single event requires the use of femtosecond driving pulses with controlled electric field. This is not required in the case of trains of attosecond pulses, thus relaxing the requirements on laser characteristics. The stabilization of the carrier-envelope phase (CEP) of laser pulses after amplification was experimentally demonstrated in 2003 (Baltuška et al., 2003). Since the first demonstration of the generation of isolated subfemtosecond pulses, various techniques have been proposed and partly implemented for the production of such pulses. In particular, a number of temporal gating schemes have been used, which will be discussed in this chapter. Since the first application of isolated subfemtosecond pulses in the investigation of the ultrafast dynamics of Auger electrons (Drescher et al., 2002), impressive results have been obtained.

The aim of this study is to present recent advances in the field of attosecond science in the case of isolated attosecond pulses. Section 2 reviews the methods proposed so far for the generation of isolated attosecond pulses. Particular emphases will be devoted to the temporal gating schemes. Section 3 briefly discusses numerical methods developed for the investigation of the physical processes at the basis of attosecond pulse generation. Finally, Section 4 reviews the main applications of isolated attosecond pulses to atomic, molecular, and solid-state physics.

2. SCHEMES FOR GENERATION OF ISOLATED ATTOSECOND PULSES

There are currently two methods for the generation of isolated attosecond pulses. The first approach is based on bandpass filtering of the highest energy region of the XUV emission obtained by HHG in gases (Christov et al., 1997; Hentschel et al., 2001). Indeed, this portion of the XUV spectrum can only be emitted near the peak intensity of the laser field, and thus the corresponding XUV light is naturally confined within one-half of the laser oscillation period. This generation scheme requires the use of intense sub-5-fs driving pulses, with stabilized carrier-envelope phase (CEP) and linear polarization. Depending on the CEP value of the driving field, it is possible to generate a single pulse or a couple of pulses. Isolated

attosecond pulses with a temporal duration down to 80 as have been generated by using this approach (Goulielmakis et al., 2008), employing sub-4-fs driving pulses obtained by using the hollow-fiber compression technique (Nisoli et al., 1996, 1997).

An alternative way for the production of isolated attosecond pulses is to apply a temporal gate on the harmonic generation process. With such a method, the XUV generation is confined within a temporal window, which can be shorter than half an optical cycle of the driving field. Several approaches have been proposed and implemented to perform such temporal confinement of the XUV emission. One method (polarization gating, PG) relies on the strong sensitivity of the HHG process and on the ellipticity of the fundamental field. Indeed, if the polarization of the driving pulse is temporally modulated from circular to linear and back to circular, the XUV emission is limited during the temporal window where the driving field is linearly polarized. By applying such a method, which requires CEP-stabilized few-cycle pulses, isolated attosecond pulses with a duration down to 130 as were generated (Sansone et al., 2006).

In order to relax the constraint on the short temporal duration of the driving field, Chang (2007) proposed to add a second harmonic field to the PG field resulting in a double optical gating (DOG) scheme . Indeed, if the second harmonic is intense enough, one half cycles of the driving field are suppressed, and thus the time interval between two consecutive attosecond pulses is increased, with two main consequences: neutral atom population depletion is reduced and a wider temporal gate can be applied. This allows to generate isolated attosecond pulses by using multiple-cycle laser pulses.

In 2009, it was experimentally demonstrated (Abel et al., 2009; Thomann et al., 2009) that laser-induced ionization can be used to create a temporal gate on the harmonic generation process (ionization gating, IG). Indeed, it has been shown that, under proper conditions, plasma density rapidly increases on the leading edge of the laser driving field, therefore creating a phase mismatch responsible for the suppression of HHG for all later half cycles. Such IG allows one to confine the harmonic emission on the leading edge of the driving field. However, the temporal gate is not narrow enough to select an isolated attosecond pulse, and additional bandpass filtering is required. Recently, a novel approach based on the combined action of complete population depletion and spatial filtering of the XUV beam has been proposed to obtain an efficient temporal gating on the harmonic generation process. Isolated attosecond pulses having a temporal duration of 155 as and a pulse energy on target of 2.1 nJ have been generated by using such a method (Ferrari et al., 2010).

Exploiting all the earlier mentioned techniques, the generation of isolated attosecond pulses has been successfully obtained below 100 eV. Since the maximum photon energy emitted in the HHG process scales as the

square of the driving wavelength, parametric sources operating in the infrared (IR) have been proposed as a way to extend the attosecond pulse production from the XUV to the soft-X region (Shan & Chang, 2001). In this contest, it has been demonstrated that by properly combining an IR parametric source with a Ti:Sapphire source in a two-color scheme, it is possible to create a temporal gate on the harmonic generation process that results in a supercontinuous emission extending up to 200 eV (Calegari et al., 2009).

Since the spectral filtering technique has been already well analyzed in several review papers (Agostini & DiMauro, 2004; Corkum & Krausz, 2007; Scrinzi et al., 2006), in the following, we will focus on the earlier listed temporal gating methods.

2.1 Polarization Gating

It is well known that HHG allows one to produce a train of attosecond pulses separated by one half of the fundamental period. This physical process has been already depicted in several studies, and it can be easily described in a semiclassical picture, in which an electron is first tunnel ionized by the laser electric field, then it is accelerated in the continuum, and finally it recombines with the parent ion by emitting an XUV photon (Corkum, 1993; Krause et al., 1992a). As mentioned in the previous section, the polarization gating method allows one to generate isolated attosecond pulses by properly manipulating the ellipticity of the driving field. Indeed, an elliptically polarized field gives rise to a transverse displacement in the trajectory of the ionized electron. If this displacement exceeds an amount that can be compensated for by the initial transverse momentum distribution of the electron, the electron never rencounters the parent ion again, and harmonic production is no more possible. In a full quantum mechanical picture, the spreading of the recolliding electron wave packet increases with the ellipticity of the electric field, thus reducing the superposition with the ground state wave function and therefore the probability of recombination. Thus, if a driving field with time-dependent polarization state, characterized by a short temporal window of linear polarization, is used to drive the harmonic generation process, the XUV emission can be confined during the temporal window of linear polarization, and isolated attosecond pulses can thus be obtained, as first proposed in 1994 (Corkum et al., 1994). The proposed PG scheme was based on the use of two orthogonallypolarized light pulses, with slightly different carrier frequencies, ω_1 and ω_2, such that $\Delta\omega/\omega \ll 1$, where $\Delta\omega = \omega_2 - \omega_1$ and $\omega = (\omega_1 + \omega_2)/2$. The resulting field is characterized by a time-dependent ellipticity, ε:

$$\varepsilon = \tan(\Delta\omega\, t/2), \tag{1}$$

and it is linearly polarized at time, $t = n\pi/\Delta\omega$, where n is an integer number. This synthesized field, combined with a suitable filtering of the low-order harmonics, allows one to obtain efficient harmonic generation only in a single half cycle of the laser field. A second implementation of the PG scheme was proposed by Altucci et al. (1998): in this case, the temporal gate was achieved by sending a positively chirped laser pulse in a birefringent quartz plate. A single gate at the maximum of the electric field or two gates symmetric with respect to the central part of the pulse could be obtained.

One of the major limitations of the earlier listed schemes is represented by the fixed duration of the gate. To overcome this limitation, a different approach, based on a Michelson interferometer and three quarter-wave plates, was implemented (Kovačev et al., 2003). The Michelson interferometer and two quarter-wave plates (one for each arm of the interferometer) are used to create two delayed pulses having orthogonal linear polarizations. At the output of the interferometer, the linear polarizations are transformed into right and left circular polarizations respectively by the third quarter-wave plate. The superposition of these two delayed and circularlypolarized components results in a polarization that varies from circular to linear and back to circular, thus generating a gate whose duration can be arbitarily set by changing the temporal delay δ between the two replica. A similar approach for PG was introduced in 2003 based on a simple linear setup, which allows one to eliminate residual fluctuations due to the interferometric configuration (Tcherbakoff et al., 2003). The experimental setup is schematically reported in Figure 1: a first quartz plate creates two delayed replica of the incoming pulse with perpendicular polarizations propagating along the ordinary and the extraordinary axes of the plate. In this configuration, the temporal delay δ between the two components depends on the thickness of the plate. If the polarization of the incoming pulse forms an angle of $\alpha = 45^\circ$ with the axis of the plate, the total output pulse is linearly polarized on the leading and

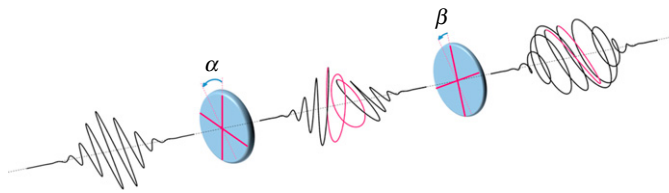

Figure 1 Scheme of collinear polarization gating based on two birefringent plates. The first plate transforms the linearly polarized input pulse into a pulse that is polarized on the leading and trailing edges and is circularly polarized in the center. An additional quarter wave plate allows one to obtain a final output polarization which changes from circular to linear and back to circular.

trailing edges, and it is circularly polarized in the center. An additional zero-order quarter-wave plate, having the axis at $\beta = 0^\circ$ with respect to the polarization direction of the incident beam, allows one to obtain an output polarization which changes from circular to linear and back to circular. The width of the temporal gate τ_g (defined as the temporal interval in which the ellipticity is smaller than 13%) is imposed by the delay δ, the angle β, and the input pulse duration τ according to the following expression:

$$\tau_g = \frac{\varepsilon_{th}}{\ln 2 |\cos(2\beta)|} \frac{\tau^2}{\delta}, \tag{2}$$

where ε_{th} is the threshold (13%) ellipticity. This equation clearly indicates that the narrowest gate (required for the isolation of single attosecond pulses) can be obtained either by reducing the pulse duration τ or by increasing the temporal delay δ. However, for large delays, the efficiency of the process is strongly reduced due to the appearance of a dip in the temporal intensity profile in correspondence of the linear polarization. A good compromise can be obtained for $\delta \simeq \tau$, since in this case, the synthesized pulse exhibits an almost flat top intensity profile. In this condition, pulses having a duration shorter than 7 fs are required to obtain isolated attosecond pulses.

By applying such a PG scheme, in combination with 5-fs driving pulses with stable CEP, the generation of isolated attosecond pulses at 36 eV photon energy has been demonstrated by Sansone et al. (2006). In this experiment, the first quartz plate was 181 μm thick, thus splitting the incoming linearly polarized pulse into two orthogonally polarized pulses separated by $\delta = 5.8$ fs. A CEP value of the driving field that determines the emission of an attosecond pulse at the center of the gate ($\varepsilon \simeq 0$) was selected. The complete temporal characterization of the isolated attosecond pulses was performed by frequency-resolved optical gating for complete reconstruction of attosecond bursts (FROG CRAB) (Mairesse & Quéré, 2005). This method is an extension to the attosecond domain of the well known FROG technique (Trebino et al., 1997) used for the temporal characterization of femtosecond pulses. The basic idea of the measurement is the following: the attosecond pulse ionizes a gas, thus generating an attosecond electron pulse, which is a replica of the optical pulse. The conversion of the XUV pulse into an electron wave packet is obtained in the presence of a streaking IR pulse, whose electric field acts as an ultrafast phase modulator on the generated electron wave packet. In this way, a time-nonstationary filter, which is required to achieve the temporal characterization of the ultrashort pulse, is realized. The evolution of the photoionization spectra as a function of the delay between the attosecond and the IR pulses allows one to retrieve the temporal intensity profile and phase of the XUV pulses,

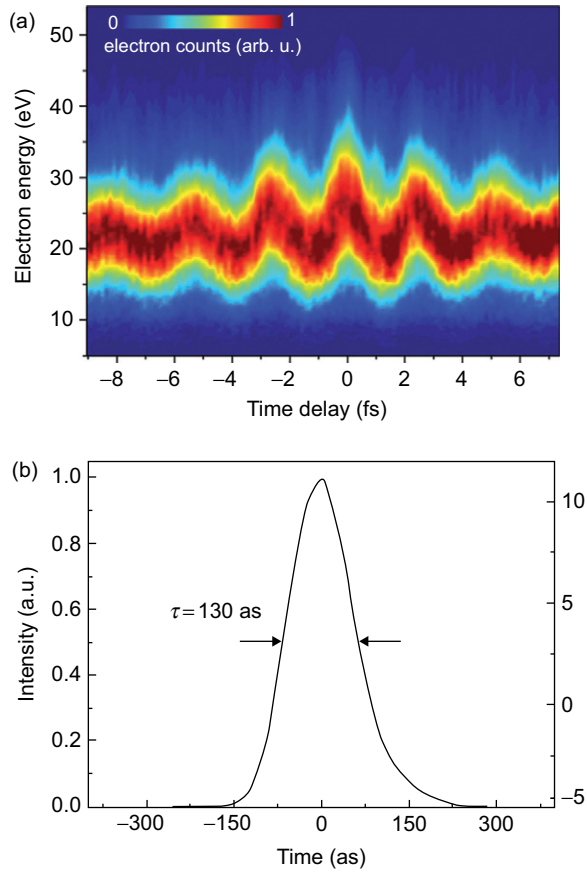

Figure 2 (a) Experimental FROG CRAB trace; isolated attosecond pulses were generated by phase-stabilized 5-fs pulses with modulated polarization state. (b) Reconstructed temporal intensity profile of the attosecond pulses obtained from the FROG CRAB trace. Figure adapted from Sansone et al. (2006).

as well as the electric field of the IR pulse. Figure 2a shows the acquired FROG CRAB trace; Figure 2b displays the retrieved temporal intensity profile of the XUV pulse, obtained by using the principal component generalized projections algorithm (PCGPA) (Kane, 1999). The reconstructed pulse has a duration (FWHM) of 130 as, close to the Fourier limit, thus indicating that the 300-nm-thick Al filter used in the experimental setup allows to compensate for the intrinsic chirp (atto chirp).

A different PG scheme suitable for multicycle driving pulses has been recently implemented by Altucci et al. (2010). Such a scheme is based on the combined action of PG and group-delay dispersion (GDD). The key idea is to produce a time window of nearly linear polarization at

the maximum possible laser intensity before population depletion occurs. This is achieved by sending 15-fs driving pulses into a Michelson interferometer having one arm equipped with both a half-wave plate and a variable amount of glass. The plate rotates the polarization of one of the two replica of 90°, whereas the glass provides the amount of GDD necessary to chirp the pulse to a final duration of about 35 fs. Two single-shot harmonic spectra generated in kripton by the synthesized field for temporal delays between the short and the chirped pulse of 15 fs (solid black line) and 15.5 fs (dashed red line), respectively, are reported in Figure 3. As it can be seen from this figure, for a delay of 15 fs (with the short pulse ahead in time), the recollision is confined within the gate, and one can observe the emission of a continuum spectrum. On the other hand, upon changing the delay of just 0.5 fs, more than one recollision events are selected, thus giving rise to a modulated spectrum.

Finally, it is worth mentioning a completely different approach for tailoring the polarization of the driving field, which has been recently demonstrated by Negro et al. (2010). The idea is to achieve a polarization shaping by birefringence effects in an aligned molecular gas. This approach requires a first IR pulse (pump) undergoing optical filamentation in a molecular gas, and a second, delayed visible pulse (driver), linearly polarized at 45° with respect to the pump polarization, propagating through the aligned medium. The refractive index modulation induced by the impulsive molecular alignment results in a time-dependent modulation of the polarization of the driver pulse. In this case, the alignment was induced in N_2, and a strong suppression of the harmonic signal was measured in correspondence to the maximum and minimum of the rotational

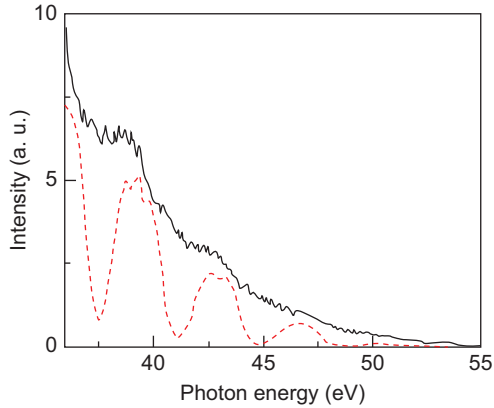

Figure 3 Single-shot harmonic spectra generated in krypton for delays of 15 fs (solid curve) and 15.5 fs (dashed curve), respectively, between the short and long driving pulse (short pulse ahead). Figure adapted from Altucci et al. (2010).

revival where the driver is elliptically polarized. With this approach, the temporal modulation of the polarization state depends on the duration of the rotational revival, and thus using lighter molecules (H_2 and D_2) would allow in principle to induce a polarization that varies from circular to linear and back to circular along the driver pulse.

2.2 Double Optical Gating

As discussed earlier, to keep a high efficiency in the XUV generation process, conventional PG requires the use of driving pulses shorter than ~7 fs. In order to relax the requirements on pulse duration of high-intensity pulses, several approaches have been proposed for the generation of isolated attosecond pulses in the case of multiple-optical-cycle driving pulses. Mauritsson et al. (2006) demonstrated that by adding a second harmonic field to a linearly polarized fundamental field, it was possible to halve the number of recollision events during the HHG process. The use of a two-color gating in the case of multiple-cycle driving field gives rise to the generation of a train of attosecond pulses spaced by one period of the fundamental field. In order to isolate a single pulse, additional cut-off filtering is required, thus leading to the reduction of the available bandwidth.

The combination of two-color gating and PG techniques (double optical gating, DOG) allows one to avoid cut-off filtering, thus opening the possibility to produce broadband attosecond pulses with multiple-cycle laser sources (Chang, 2007). The added second harmonic field in the DOG scheme also reduces population depletion caused by the leading edge of the driving field. The collinear configuration of DOG requires two quartz plates and a β-barium borate (BBO) crystal: the first quartz plate creates two delayed replica of the incoming pulse with perpendicular polarizations as in a conventional PG setup. The optical axis of the second quartz plate and the BBO are aligned and form an angle of 45° with respect to the axis of the first plate. They work together as a quarter-wave plate to create a polarization which varies from circular to linear and back to circular. In contrast to PG, the first plate thickness is set to obtain a polarization gate with a duration of one full optical period of the fundamental field. As a result, the longest pulse duration, which can be used for generating single attosecond pulses with DOG, is almost two times larger compared with the one used by conventional PG. By applying DOG to 8-fs pulses with 0.85 mJ energy at 790 nm carrier wavelength, the efficient generation of continuous XUV spectra in argon and neon have been successfully demonstrated by Mashiko et al. (2008). Pulses as short as 107 as have been obtained by Mashiko et al. (2009) using such a method.

In 2009, the same group extended the DOG method to longer driving pulses by introducing a similar approach, dubbed generalized double

optical gating (GDOG) (Feng et al., 2009). The idea is to create a driving field having a polarization which varies from elliptical to linear and back to elliptical with an ellipticity, ε. It is possible to demonstrate that in these conditions the width of the temporal gate τ_g is given by:

$$\tau_g = \varepsilon \frac{\varepsilon_{th}}{\ln 2} \frac{\tau^2}{\delta}, \tag{3}$$

where ε_{th} is the threshold ellipticity, δ is the delay, and τ is the input pulse duration. The advantage of using GDOG instead of DOG for long driving pulses can be easily understood by calculating the intensity profile of the output driving field in the two cases. Figure 4 shows the calculated driving (dashed red line) and gating (solid blue line) fields, as well as the ellipticity (dotted green line) in DOG (top panel) and GDOG (bottom panel) cases for an input pulse duration of 20 fs (Feng et al., 2009). As can be seen from this figure, in order to have a gate width corresponding to one optical cycle, DOG (ε = 1) requires a delay δ = 48 fs, whereas the same τ_g can be achieved with GDOG (ε = 0.5) by halving the time delay. As a result, the field strength before the gate is lower for GDOG than for DOG, thus allowing a strong reduction of population depletion even for very long laser pulses. The GDOG experimental setup is similar to the DOG one: it requires again two quartz plates and a BBO crystal. In addition, a fused

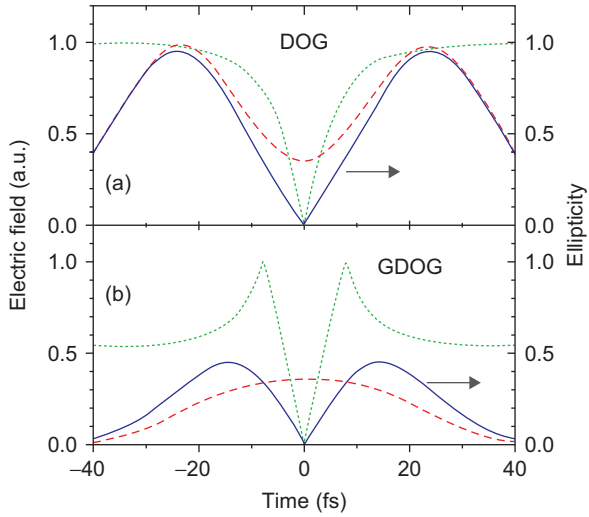

Figure 4 Comparison of laser field components for polarization gating in DOG (a) and GDOG (b). The driving field and gating field are plotted as dashed red and solid blue lines, respectively; the ellipticity is plotted as dotted green line. Figure adapted from Feng et al. (2009).

silica Brewster window is placed in between the two plates in order to create the desired ellipticity by rejecting half of the driving pulse. By applying the GDOG method, isolated attosecond pulses having a temporal duration of 148 as have been generated and completely characterized for the first time by driving the process with 28-fs pulses coming directly from the CPA laser system (Feng et al., 2009).

2.3 Temporal Gating by Sub-Cycle Ionization Dynamics

The role of ionization in the generation of attosecond pulses was theoretically studied in several works (Cao et al., 2006; Gaarde et al., 2008; Kim et al., 2004), and experimentally investigated in the case of 8-fs (Pfeifer et al., 2007) and 15-fs (Thomann et al., 2009) driving pulses. In the work of Pfeifer *et al.*, (2007) it has been demonstrated that plasma generation, due to strong ionization, is responsible for the propagation of induced mechanisms such as phase mismatch and defocusing, which inhibit the harmonic generation process at a certain time during the leading edge of the driving pulse, even for a relatively low level of population depletion (5%–10%) of the ground state. Indeed, in the presence of high-intensity driving pulses, ionization reaches a critical level at which the negative dispersion due to free electrons cannot be compensated for by the positive dispersion of the remaining neutral gas, therefore phase matching of the harmonic emission is no longer possible. Since this rapid loss of phase matching confines the HHG process to the leading edge of the driving field, the method was dubbed ionization gating (IG). As already mentioned, IG does not allow to isolate a single recollision event, and additional spectral filtering is required. In this experiment, the XUV emission obtained by HHG in neon at a gas pressure of 75 torr was filtered by a multilayer Mo/Si mirror having a reflectivity band centered at 93 eV with 4 eV bandwidth (FWHM). This split mirror was used also to induce a variable temporal delay between the attosecond pulse and the streaking field in order to perform the temporal characterization of the XUV pulses. For a proper value of the CEP of the driving field, isolated pulses having a temporal duration of 430 as have been obtained with this method (Abel et al., 2009).

In a similar experiment performed by Thomann et al. (2009), the role of IG was studied in presence of a multiple-cycle CEP-unstable driving field. In this case, the harmonic radiation was generated by focusing the laser pulses into a 150-μm-diameter, 3.5-cm-long hollow-core waveguide filled with argon at a gas pressure of 10 torr. Also in this experiment, IG was combined to spectral filtering by a Mo/Si multilayer mirror centered at 47 eV with 13-eV bandwidth (FWHM). The temporal characterization of the attosecond pulses was obtained by reconstructing the FROG CRAB traces with both a PCGPA and direct simulations extended to a 2π

detection scheme and CEP- unstabilized pulses. Both reconstruction methods retrieved a near-transform limited isolated XUV burst with 200-as duration.

More recently, it has been demonstrated by Ferrari et al. (2010) that the combined action of subcycle ionization dynamics during the HHG process and efficient spatial filtering in the XUV beamline allows one to efficiently generate isolated attosecond pulses with energy up to 2.1 nJ on target. This result indicates a pulse energy enhancement from one to three orders of magnitude compared with the generating methods demonstrated so far. The key elements of this technique are as follows: (1) the use of CEP-stable few-optical-cycle driving pulses, with linear polarization and peak intensity beyond the saturation intensity of the gas used for HHG, (2) the optimization of the interaction geometry in terms of gas pressure, position, and thickness of the gas cell, and (3) the presence of a 200-μm-diameter pinhole used for spatial filtering of the XUV radiation. In particular, the XUV emission was produced by focusing CEP-stable 5-fs pulses into a 2.5-mm-thick cell filled with xenon at static pressure (2.5–3 Torr), and a laser peak intensity $I \simeq 2.3 \times 10^{15}$ W/cm^2. As can be seen in Figure 5, the generated XUV spectra display an evolution from a continuous behavior to a modulated one upon changing the CEP value

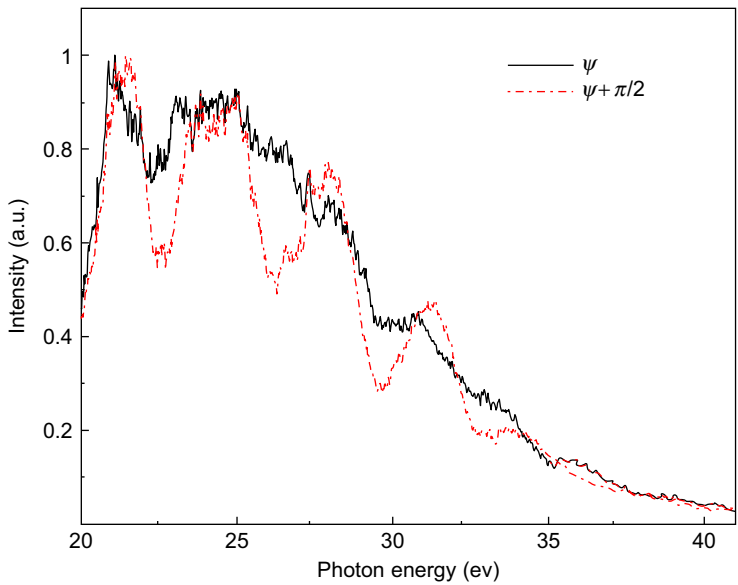

Figure 5 Normalized XUV spectra generated in a 2.5-mm-thick xenon cell by 5-fs pulses in the case of two different CEP values. The spectra were measured after the aluminum filter was used to block the fundamental radiation and the low-order harmonics. Figure adapted from Ferrari et al. (2010).

of the driving field by $\pi/2$. The energy of the XUV pulses in the case of continuous spectra was 2.1 nJ, after a 100-nm-thick aluminum filter was used to block the fundamental radiation and the low-order harmonics. The XUV pulses were temporally characterized by using the FROG CRAB technique: pulses as short as 155 as were measured.

The physical mechanisms at the basis of this temporal gating are related to the subcycle ionization dynamics in the generating medium. Indeed, the fast depletion of the neutral atom population induced by such an intense and ultrashort driver leads to the confinement of the generation process to a single contribution in the very beginning of the laser pulse. A theoretical calculation based on the Ammosov, Delone, and Krainov (ADK) theory (Ammosov et al., 1986), clearly indicates a strong dependence of the temporal evolution of the ionization rate on the CEP value of the driving field. This dependence strongly affects the shape of the temporal gate, thus leading to the production of isolated attosecond pulses or a couple of attosecond bursts depending on the CEP value. Unlike the IG method, in this case, the spatio-temporal reshaping of the driving pulses is weak, also considering multiple ionization of the generating medium, as a consequence of the very low pressure used in the experiment. Moreover, spectral filtering is not required, since the temporal gate created by the subcycle ionization dynamics is narrow enough to isolate a single attosecond pulse.

2.4 Heterodyne Mixing of IR and Visible Pulses

High-energy laser systems operating in the spectral region between 1.5 and 3 μm have been suggested for the generation of isolated attosecond pulses with photon energies exceeding 100 eV. Indeed, the maximum photon energy achievable in the HHG process is given by $h\nu = I_p + 3.17U_p$, where I_p is the ionization potential of the neutral atom and U_p is the ponderomotive energy, which turns out to be proportional to $\lambda_0^2 I$, where λ_0 is the wavelength of the driving field and I is the excitation intensity. For this reason, parametric sources operating in the IR (Vozzi et al., 2007) have been developed to extend the harmonic emission up to kiloelectron volt energies (Popmintchev et al., 2008; Takahashi et al., 2008). However, the main drawback of using longer wavelength is the reduction of the harmonic yield expected to decrease as λ^{-6} (Colosimo et al., 2008; Shiner et al., 2009). A first approach to gate the harmonic emission driven by a parametric source was experimentally investigated by Vozzi et al. (2007), and it is based on the combination of a few-cycle IR field ($I \sim 2 \times 10^{14}$ W/cm^2) and a weak multicycle 800-nm field ($I \sim 3 \times 10^{13}$ W/cm^2). The idea at the basis of this temporal gate was first theoretically proposed by Merdji and coworkers (Merdji et al., 2007): the generation of isolated attosecond pulses can be achieved by a multiple-cycle two-color field having one

component at frequency ω_0 and the other one at a frequency ω_1 slightly detuned from the second harmonic. Exploiting the tunability of the IR parametric source, the HHG process was studied both in a combination of 1.6-μm + 800-nm pulses and 1.5-μm + 800-nm pulses. Adding the 800-nm component to the 1.6-μm driving pulse allowed only for field symmetry breaking, which corresponds to the appearance of even harmonics in the XUV spectrum. A completely different situation was obtained when the 800-nm component was added to the 1.5-μm driving pulse: in this case, the acquired spectra showed a clear even and odd harmonic structures for some shots and a broad continuum for some other shots (Vozzi et al., 2009). This behavior was attributed to the CEP-unstabilized Ti:Sapphire source used in the experiment. The broad continuous spectrum generated in argon, extending up to 100 eV, is a strong indication of the presence of an isolated attosecond pulse. Nevertheless, in this method, the role of the 800-nm field is limited to a gentle perturbation of the strong IR driving pulse, which dominates the generation process, thus keeping a low conversion efficiency.

To overcome this limitation, an alternative approach was proposed, based on a proper mixing of intense IR and visible (VIS) few-cycle laser pulses (Calegari et al., 2009). In this case, the role of the IR pulse is to significantly extend the harmonic emission to higher photon energies, whereas the intense VIS pulse improves the conversion efficiency of the process. The IR and the VIS sources were developed starting from an amplified Ti:sapphire laser system (60-fs pulse duration, 800-nm central wavelength, 10-Hz repetition rate, and 10-mJ pulse energy). The IR parametric source generated up to 1.6-mJ CEP-stable pulses, with a nearly transform limited duration of 18 fs at 1.45-μm carrier wavelength. The 800-nm, 13-fs, and 0.8-mJ VIS pulses originated from optical filamentation of a fraction of the Ti:sapphire beam. The IR and the VIS beams were collinearly recombined, and the polarizations of the two beams were set parallel by a broadband half-wave plate. The peak intensities of IR and VIS pulses at the focus were estimated to be $I_{IR} = 2 \times 10^{14}$ W/cm^2 and $I_{VIS} = 8.5 \times 10^{14}$ W/cm^2. Left panel of Figure 6 shows the harmonic spectrum generated in argon acquired (by averaging over 30 laser shots) as a function of the delay between the two-color pulses. As can be seen from this figure, at zero delay, the harmonic emission is dramatically extended, and the harmonic spectrum becomes continuous, whereas when the two pulses do not overlap in time, the harmonic spectrum is dominated by the VIS component. Right panel of the same figure shows the comparison between the typical high-order harmonic spectra generated by the strong VIS pulse (dashed curve) and the synthesized two-color pulse at zero delay (solid curve). The harmonic emission driven by the VIS pulse is limited to 100 eV, since at the peak intensity, I_{VIS}, the medium is almost fully ionized. On the other hand, by driving the process with the two-color field, the XUV spectrum

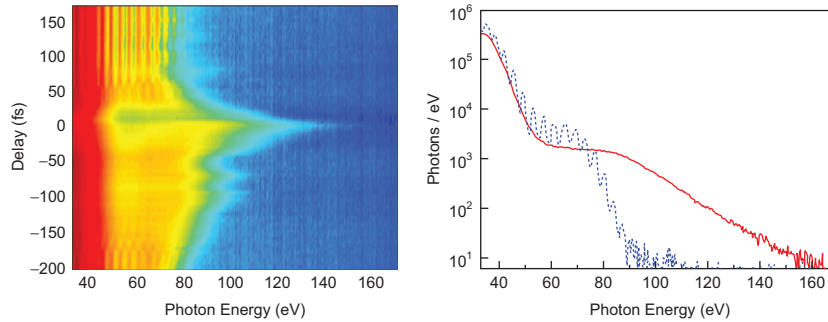

Figure 6 Left panel: sequence of harmonic spectra generated in argon as a function of the delay between the two-color pulses (logarithmic color map). Right panel: high-order harmonic spectra(number of photons) generated in argon by VIS pulses (dashed curve) and two-color pulses at zero delay (solid curve). Figure adapted from Calegari et al. (2009).

is extended up to 160 eV, and the harmonic peaks merge to a continuum as a result of the temporal gating. It is worth mentioning that the continuous emission was measured also for some single shot spectra, since the VIS pulses were CEP unstable. By performing the same measurement in neon, it was possible to obtain at synchronization a broad and continuous emission extending up to 200 eV. This was the first demonstration of the possibility to efficiently produce attosecond pulses at high energies exploiting the heterodyne mixing of intense and few-cycle IR and visible pulses.

In a recent work, Takahashi and coworkers investigated the possibility of generating isolated attosecond pulses from a multiple-cycle two-color laser field, obtained by mixing an 800-nm, 30-fs pulse with a 1300-nm, 40-fs pulse (Takahashi et al., 2010). The idea is to combine long driving pulses in order to relax the constraint on the CEP stabilization of the source. Moreover, the synthesized field significantly reduces the ionization probability in the multiple-cycle region, thus allowing to efficiently generate intense attosecond pulses from the neutral medium. Top panel of Figure 7 shows the acquired single-shot XUV 2D-spectrum generated at synchronization, and the corresponding 1D-spectrum is reported in the bottom panel of the same figure. As can be seen from this figure, a dense harmonic structure appears in the plateau region, whereas a continuum XUV spectrum can be observed in the cut-off region (33rd to 45th order). Thus, in this case the two-color gate is not narrow enough to isolate a single attosecond pulse, and additional spectral filtering is required. To evaluate the role of CEP, they simultaneously measured the harmonic spectrum and corresponding CEP for each laser shot using a nonlinear interferometer, which records the interference fringes between the pump

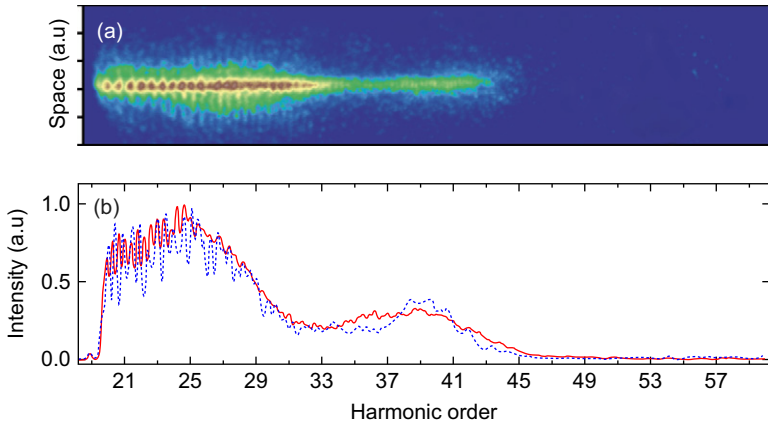

Figure 7 Top panel: 2D single-shot harmonic image driven by the two-color field. Bottom panel: single-shot 1D harmonic spectrum driven by the two-color field. Figure adapted from Takahashi et al. (2010).

pulse spectrally broadened by white light generation in a sapphire plate and the second harmonic of the idler pulse near 1 μm. The experimental results indicate that a continuous cut off emission can be obtained for all the CEP values, although the intensity of the cutoff is affected by the CEP drift. Such a scheme reduces the requirements for the pump laser system, thus opening new perspectives for the generation of isolated attosecond pulses exploiting TW-class, high-power laser systems.

3. NUMERICAL METHODS FOR THE INVESTIGATION OF THE HARMONIC GENERATION PROCESS

In order to analyze the physical processes leading to the generation of attosecond pulses, various numerical methods have been used. In this section, we will review in particular the nonadiabatic saddle-point method and a three-dimensional numerical propagation model. Physical insights in the strong-field process at the basis of HHG can be obtained with an intuitive classical model, the socalled three-step model (Corkum, 1993; Kulander et al., 1993). During the interaction between a strong IR driving field and the generating medium, the electric field can bend the bonding potential of atoms in such a way that tunnel ionization can occur. The electron sent in the continuum is then accelerated by the external field and acquires a large kinetic energy. Since the IR field changes its sign during its oscillations, it is possible that the the electron is driven back to the parent ion. During the recollision with the parent ion, the acquired energy can be released in the form of a high-energy photon. The various

harmonic frequencies correspond to different field-driven *electron trajectories* resulting in different kinetic energies at the recollision time. The saddle point method analyzes the generated XUV radiation in terms of *complex trajectories*, in space and time, followed by the electron from the ionization instant until the recombination with the parent ion. The three-step model is the classical limit of the saddle-point model; indeed, the real part of such quantum paths largely agrees with the classical electron trajectories. The imaginary part is related to the quantum origin of the electron by tunnel ionization. In general, we do not need to consider a great number of such quantum paths to describe the properties of the HHG process. The most relevant paths are those characterized by a single recollision event and an electron travel time in the continuum shorter than one-half or one optical period of the driving electric field. These are the socalled *short* and *long* quantum paths, respectively.

3.1 Saddle-Point Approximation

Following the first quantum idea of the "atomic antenna" (Kuchiev, 1987) and the three-step model, it is possible to obtain a more convenient semiclassical picture. As pointed out in Lewenstein et al. (1994), the component of the $\mathbf{x}(t)$ nonlinear time-dependent dipole moment along one direction defined by the unit vector $\mathbf{n}$ can be written as

$$x_{\mathbf{n}}(t) = i \int_0^t \mathrm{d}t' \int \mathrm{d}^3\mathbf{p}\, \mathbf{n}\cdot\mathbf{d}^*(\mathbf{p}-\mathbf{A}(t)) \times \mathbf{E}(t')\cdot\mathbf{d}(\mathbf{p}-\mathbf{A}(t'))\exp[-iS(\mathbf{p},t,t')] + \text{c.c}, \tag{4}$$

where $\mathbf{E}(t)$ and $\mathbf{A}(t)$ are the electric field and the vector potential of the driving field, respectively; $\mathbf{p} = \mathbf{v} + \mathbf{A}(t)$ is the canonical momentum and $\mathbf{d}(\mathbf{v})$ is the atomic dipole matrix for bound-free transition. In Equation (4), we can recognize the three steps of the classical model. Indeed, the term $\mathbf{E}(t')\cdot\mathbf{d}(\mathbf{p}-\mathbf{A}(t'))$ in the integral expresses the probability amplitude for an electron to make the transition to the continuum at the time t' with the canonical momentum $\mathbf{p}$. The quantity

$$S(\mathbf{p},t,t') = \int_{t'}^{t} \mathrm{d}t'' \left(\frac{[\mathbf{p}-\mathbf{A}(t'')]^2}{2} + I_p \right) \tag{5}$$

is called quasi-classical action, and the term $\exp[-iS(\mathbf{p},t,t')]$ represents the phase factor acquired by the electron wave function in its propagation

in the continuum until the time t. At that time, the electron can recollide with the parent ion with an amplitude probability given by $\mathbf{d}^*(\mathbf{p} - \mathbf{A}(t))$. If we analyze the time dependence of the quantities in Equation (4), it is possible to observe that, when the time $\tau = t - t'$ spent by the electron in the continuum is of the order of one period of the laser field, the semi-classical action varies faster than the other terms. Therefore, the major contribution to the integration over the momentum space comes from the *stationary points* of the semi-classical action. According to this discussion, we can perform the integral over $\mathbf{p}$ using the saddle-point approximation (SPA), thus obtaining the integral of Lewenstein et al. (1995):

$$\mathbf{x}(t) = i \int_0^\infty \mathrm{d}\tau \left(\frac{\pi}{\varepsilon + i\tau/2}\right)^{3/2} \mathbf{d}^*\left(\mathbf{p}_{st}(t,\tau) - \mathbf{A}_x(t)\right) \times \mathbf{E}(t-\tau)\cdot \mathbf{d}(\mathbf{p}_{st}(t,\tau) - \mathbf{A}_x(t-\tau)) \exp\left[-iS_{st}(t,\tau)\right] + \text{c.c}, \tag{6}$$

where ε is a positive regularization constant and S_{st} is defined as

$$S_{st}(t,\tau) = \frac{1}{2}\int_{t-\tau}^{t} \mathrm{d}t'' \left(\mathbf{p}_{st} - \mathbf{A}(t'')\right)^2, \tag{7}$$

where $\mathbf{p}_{st}$ is the stationary value of the momentum. Since the harmonic emission rate is related to the Fourier transform of the atomic dipole moment $\mathbf{x}(\omega)$, in order to evaluate it, we have to calculate a double integral in the (t,τ) space. Following the previous considerations, it is possible to apply the SPA to the two-dimensional integral, thus obtaining complex saddle-point solutions $(\mathbf{p}_{st}, t_{st}, \tau_{st})$, which allow one to write the Fourier transform of the dipole moment as a coherent superposition of the contribution of complex quantum paths:

$$\mathbf{x}(\omega) = \sum_{st} |\mathbf{x}_{st}(\omega)|\, \mathrm{e}^{i\Phi_{st}(\omega)} = = \sum_{st} \frac{i2\pi}{\sqrt{\det(S'')}} \left[\frac{\pi}{\varepsilon + i\tau_{st}/2}\right]^{3/2} \mathbf{d}^*[\mathbf{p}_{st} - \mathbf{A}(t_{st})] \times \mathbf{E}(t_{st} - \tau_{st})\cdot \mathbf{d}[\mathbf{p}_{st} - \mathbf{A}(t_{st} - \tau_{st})] \exp[-iS(\mathbf{p}_{st}, t_{st}, \tau_{st}) + i\omega t_{st}], \tag{8}$$

where the term $\det(S'')$ is the determinant of the matrix of the second time derivative of the phase Θ with respect to t and t' evaluated in correspondence of the saddle-point solutions.

According to Milošević and Becker (2002), for each photon energy ω, the most relevant saddle-point solutions can be grouped into few classes depending on the time spent by the electron in the continuum. In particular, we can take into account only the contribution coming from the so called short and long trajectories characterized by $\mathrm{Re}(\tau_{st}) < T_0$ (T_0 being the optical period of the driving field). For this reason, Equation (8) can be further approximated as

$$\mathbf{x}(\omega) = \sum_{s \in short} |\mathbf{x}_s(\omega)|\, \mathrm{e}^{i\Phi_s(\omega)} + \sum_{s \in long} |\mathbf{x}_s(\omega)|\, \mathrm{e}^{i\Phi_s(\omega)}. \tag{9}$$

Long and short trajectories can be grouped in couples having the same cutoff energy, $\omega^{(c)}$ identified by

$$\mathrm{Im}\{\Phi_{short}(\omega^{(c)})\} = \mathrm{Im}\{\Phi_{long}(\omega^{(c)})\}. \tag{10}$$

The saddle-points solutions of the short and long path coalesce in correspondence of the cutoff spectral region. In this region, the imaginary part of action became positive for the short quantum paths. This leads to an unphysical solution in which their contribution to the harmonic emission rate diverges and has to be discarded. In order to avoid the discontinuities introduced by simply removing the unphysical solution, it is possible to implement the uniform approximation, which takes into account simultaneously the solutions associated to the short and long paths (Figueira de Morisson Faria et al., 2002).

3.1.1 Nonadiabatic Saddle Point Approximation

When few-optical-cycle driving pulses are used for HHG, it is required to use a *nonadiabatic* generalization of the SPA, in which the full electric field of the light pulse is used to calculate the dipole moment (Sansone et al., 2004a). Upon considering a linearly polarized driving field,

$$E(t) = E_0 \cos^2(t/\bar{t}) \cos(\omega_0 t + \psi), \tag{11}$$

where ω_0 is the fundamental angular frequency; ψ is the CEP; $\bar{t}$ is related to the driving pulse duration T ($T = 2\bar{t} \arccos(2^{-1/4})$), it is possible to calculate the contribution of each electron quantum path. Figure 8 shows the harmonic emission rate produced by an increasing number of trajectories. Upon using the nonadiabatic SPA, it is possible to calculate all the physical quantities related to the generated trajectory such as: tunnelling time, electron birth position and time, initial velocity of tunnelled electrons, canonical momentum, recombination rate and time, harmonic energy and phase. Upon considering the contribution of the short electron

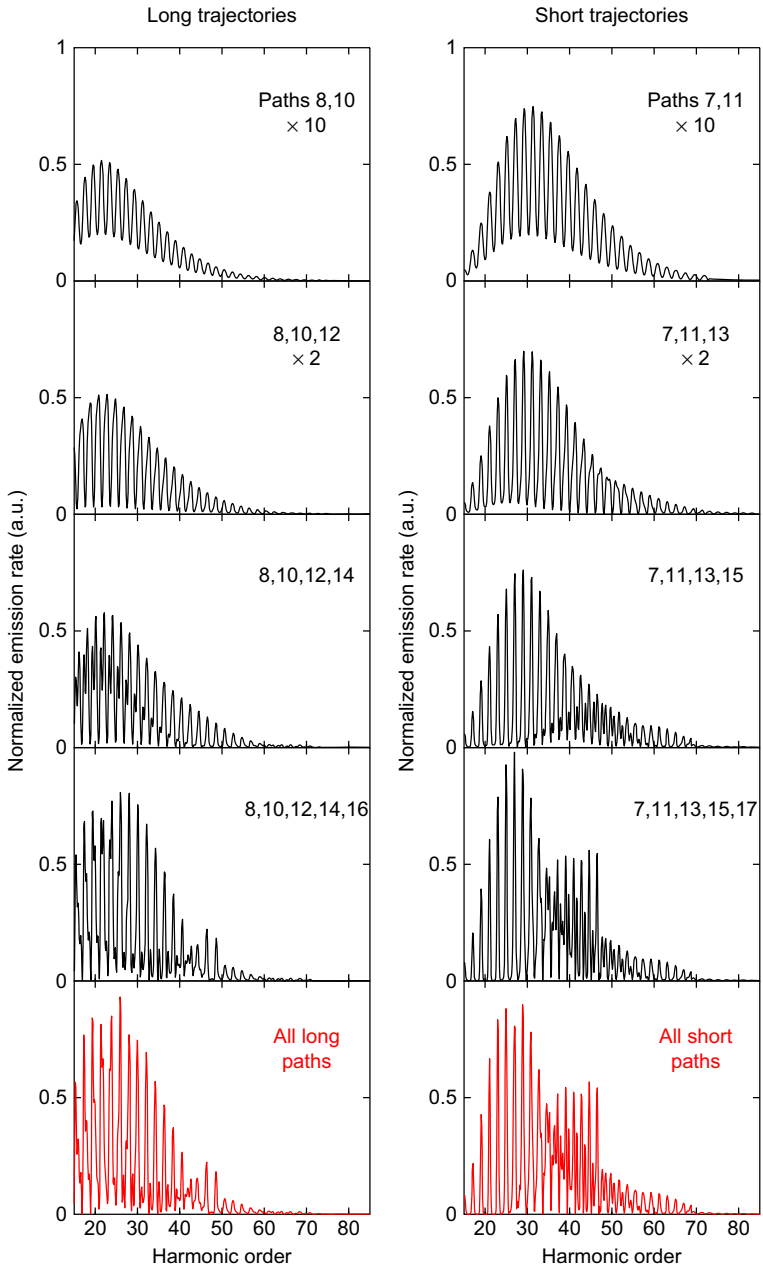

Figure 8 Harmonic emission rates produced by coherent superposition of an increasing number of long (left) and short (right) electron quantum paths for a 6-fs driving field with 7×10^{14} W/cm^2 peak intensity and $\psi = \pi/2$ in neon gas.

trajectories in the case of few-optical-cycle driving pulses (nonadiabatic regime), shown in Figure 8 (right panel), the calculated XUV spectrum is not a discrete spectrum made of odd harmonics of the fundamental radiation. Indeed, three distinct regions can be identified, in good qualitative agreement with the experimental results of Baltuška et al. (2003) and Nisoli et al. (2003). In the lower plateau region, the spectrum is characterized by well resolved odd harmonic peaks. In the upper plateau region, irregular peaks are present. Finally, the cutoff region is characterized by resolved peaks, which do not necessarily correspond to harmonics of the fundamental beam. The position of the spectral peaks is determined by the condition of constructive interference while summing in Equation (9). With the nonadiabatic SPA method, it is possible to calculate the phase difference between two quantum paths, thus explaining the spectral structures of the XUV spectrum (Sansone et al., 2004a). The same analysis can be performed considering the contribution of the long trajectories. In this case, shown in Figure 8 (left panel), the condition for constructive interference does not correspond to the generation of odd harmonics of the fundamental radiation even for the lower plateau region.

Another advantage of the SPA is that it is an ideal tool for the investigation of the effects of the CEP on the XUV emission rate for both the complete spectrum and a particular collection of trajectories. If we address again separately the long and short quantum paths, it is clear that they should display a different behavior with respect to the CEP variation (Sansone et al., 2004b).

Indeed, since the electron final energy is strongly determined by the electric field experienced during its motion in the continuum, as a consequence of the longer time spent by the electron in the continuum, the long quantum paths are more sensitive to even small changes in the laser field induced by different CEPs with respect to the short quantum paths. This is clearly shown in Figure 9, which displays the emission rates calculated for long and short paths as a function of the CEP of the driving pulses. The only part of the short-path spectrum that is affected by the CEP is the cutoff region, since the recollision times are longer at higher energies.

In order to calculate the HHG spectral and temporal characteristics as a function of the driving field laser intensity, the ground-state depletion cannot be neglected in the high-intensity regime. It is possible to add the ground-state depletion effect in the SPA upon introducing a suitable weight function in Equation (9). Since we know the ionization time $\mathrm{Re}\{t'_s\}$ for every electrons of each quantum path, we can obtain the total emission rate by multiplying the single-trajectory emission rate for the fraction of neutral atoms still present at time $\mathrm{Re}\{t'_s\}$. This fraction can be

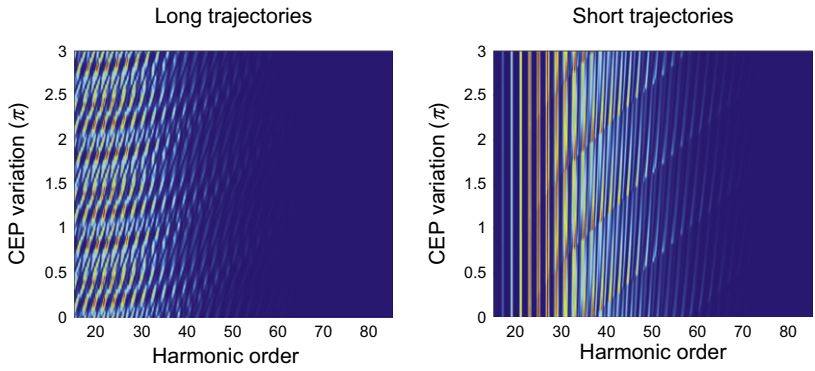

Figure 9 Emission rates calculated for long and short paths as a function of the CEP. Same parameters as in Figure 8.

evaluated using the theory of Ammosov et al. (1986) to calculate the ionization rate $w(t)$. The sum in Equation (9) can be then written as follows (Sansone et al., 2006):

$$\mathbf{x}(\omega) = \sum_{s\in short} |\mathbf{x}_s(\omega)|\, e^{i\Phi_s(\omega)} \exp\left\{-\int_{-\infty}^{Re(t_s')} w(t'')dt''\right\} + \\ + \sum_{s\in long} |\mathbf{x}_s(\omega)|\, e^{i\Phi_s(\omega)} \exp\left\{-\int_{-\infty}^{Re(t_s')} w(t'')dt''\right\}, \quad (12)$$

If the intensity of the driving field is high enough, the number of neutral atoms changes quickly during the interaction, and the total emission rate is deeply modified. This is shown in Figure 10, which displays the calculated emission rate in xenon in the case of a 5-fs driving pulse with 2.5×10^{15} W/cm^2 peak intensity and CEP $\psi = 0.6\pi$. The pulse parameters used in the calculation correspond to the experimental parameters used by Ferrari et al. (2010) for the demonstration of the temporal gating technique based on subcycle ionization dynamics, discussed in Section 2.3. As shown in Figure 10, the selection of a single electron trajectory is possible by taking advantage of the fast depletion of the ground state. It is worth noting that with such a fast dynamics of the ground-state population, the nature of the generated radiation shows a strong dependence on the CEP variation. In particular, by changing the value of the phase $\pi/2$, it is possible to select two short trajectories instead of one (which correspond to two distinct attosecond pulses), thus obtaining a generated radiation characterized by a discrete spectrum.

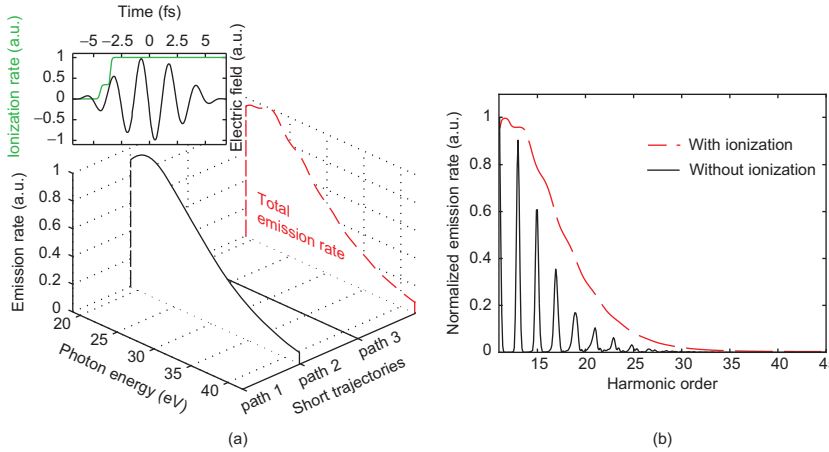

Figure 10 Calculated emission rate for a 5-fs IR driving pulse with 2.5×10^{15} W/cm^2 peak intensity and CEP $\psi = 0.6\pi$ in xenon gas. Panel (a) shows the fast varying ionization rate that explains the selection of a single quantum path (figure adapted from Ferrari et al. [2010]). Panel (b) shows the comparison between the normalized HHG spectra calculated with or without the ADK term (dashed and solid curves, respectively).

The SPA model can be used also in the case of driving fields with a time-dependent polarization state (e.g., as in the polarization gating technique). In this case, the driving field has to be treated as a superposition of two orthogonal linearly polarized waves. As discussed in Section 2, the electron trajectories are affected by both fields and so they are no longer monodimensional, but they belong to a two-dimensional space (Sansone, 2009). When the ellipticity is too strong, the complex trajectory does not return to the parent ion, and so there is no HH emission. Figure 11 shows the ionization and recombination times calculated for the driving field used in the polarization gating technique. It is possible to notice that the relevant complex trajectories are those generated inside the gate, where the driving field is linearly polarized.

3.2 Nonadiabatic Three-Dimensional Propagation Model

The nonadiabatic saddle-point approach discussed in the last subsection allows one to obtain interesting physical insights in the harmonic generation process. In order to calculate the spatial and spectral characteristics of the XUV radiation emitted by a macroscopic gas target irradiated by an ultrashort driving pulse, it is particularly important to use a nonadiabatic three-dimensional (3D) numerical propagation model (Priori et al., 2000). Indeed, the harmonic generation process is crucially affected by the spatial properties of the driving electric field (Gaarde et al., 2008).

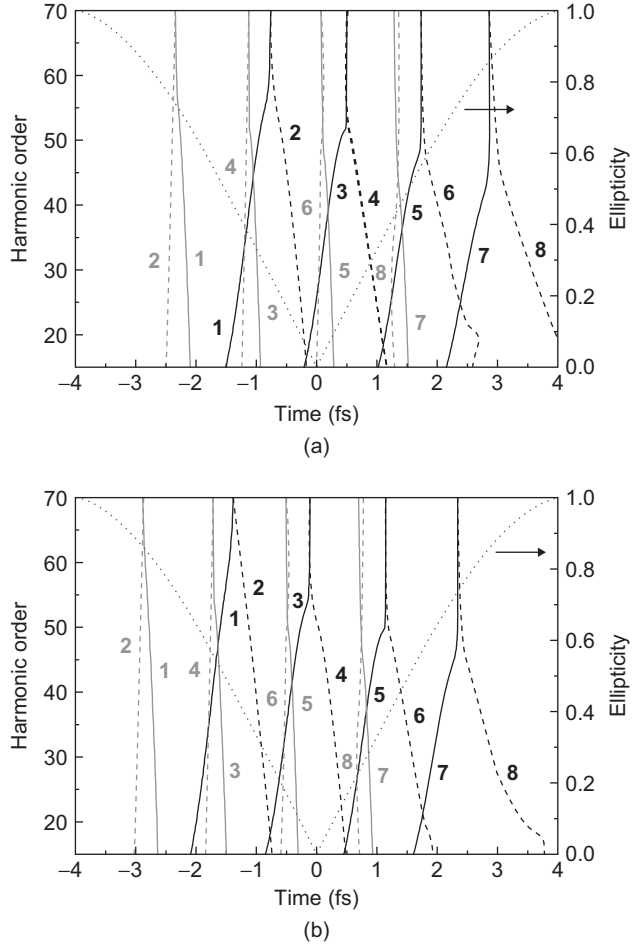

Figure 11 Real part of the ionization time t'_{st} (grey curves) and of the recombination time t_{st} (black curves) for the short (solid curves) and long (dashed curves) paths calculated for (a) $\psi = 0$ and (b) $\psi = \pi/2$. The absolute value of the ellipticity is given by the dotted curve. The short and long paths are indicated by odd and even numbers, respectively. Figure adapted from Sansone (2009).

In order to describe the propagation of the radiation through the nonlinear medium, it is necessary to solve the Maxwell wave equation. Assuming a radial symmetry, we can write

$$\nabla^2 E(r_\perp, z, t) - \frac{1}{c^2}\frac{\partial^2}{\partial t^2} E(r_\perp, z, t) = \frac{1}{\varepsilon_0 c^2}\frac{\partial^2}{\partial t^2} P(r_\perp, z, t), \tag{13}$$

where $E(r_\perp, z, t)$ is the total time and position-dependent electric field, and $P(r_\perp, z, t)$ is the polarization field. For relatively long IR pulses, it is

possible to solve Equation (13) within an adiabatic approximation, assuming that the atomic response is determined by the instantaneous laser intensity (Antoine et al., 1997; L'Huillier et al., 1992). As already discussed in the previous subsection, this approximation cannot be applied in the case of few-optical-cycle driving pulses. In such a case, it is better to use a nonadiabatic approach (Kan et al., 1995; Tempea et al., 1999).

In a coordinate frame moving at the group velocity v_g of the pulse ($z = z'$ and $t' = t - z/c$) and applying the slowly evolving wave approximation (SEWA) (Brabec & Krausz, 2000), we obtain

$$\nabla_\perp^2 E(t') - \frac{2}{v_g}\frac{\partial^2}{\partial z' \partial t'} E(t') + \left(\frac{1}{v_g^2} - \frac{1}{c^2}\right)\frac{\partial^2}{\partial t'^2} E(t') = \frac{1}{\varepsilon_0 c^2}\frac{\partial^2}{\partial t'^2} P(t'). \tag{14}$$

Hereafter, for simplicity, we do not write the explicit spatial dependence of the field and polarization. Equation (13) can be solved directly in the time and space domain (Haworth et al., 2007) or in the frequency domain after Fourier transforming with respect to t' (Priori et al., 2000):

$$\nabla_\perp^2 \tilde{E}(\omega) + \frac{2i\omega}{v_g}\frac{\partial \tilde{E}(\omega)}{\partial z'} + \left[\frac{\omega^2}{c^2} - \frac{\omega^2}{v_g^2}\right]\tilde{E}(\omega) = -\frac{\omega^2}{\varepsilon_0 c^2}\tilde{P}(\omega). \tag{15}$$

Since the generated XUV radiation is usually much weaker than the driving pulse, it is possible to assume that we can solve the propagation equation separately for the two fields. Furthermore, due to the short propagation lengths and moderate medium densities, we can neglect all linear dispersion and absorption effects for the driving field $\tilde{E}_l(\omega)$. If we denote the source terms for the driving field and the generated field with $\tilde{P}_{\text{ion}}(\omega)$ and $\tilde{P}_{\text{dip}}(\omega)$ respectively, we obtain

$$\nabla_\perp^2 \tilde{E}_l(\omega) + \frac{2i\omega}{c}\frac{\partial \tilde{E}_l(\omega)}{\partial z'} = -\frac{\omega^2}{\varepsilon_0 c^2}\tilde{P}_{\text{ion}}(\omega), \tag{16}$$

$$\nabla_\perp^2 \tilde{E}_h(\omega) + \frac{2i\omega}{c}\frac{\partial \tilde{E}_h(\omega)}{\partial z'} + \frac{i\omega}{c}\tilde{\alpha}(\omega)\tilde{E}_h(\omega) = -\frac{\omega^2}{\varepsilon_0 c^2}\tilde{P}_{\text{dip}}(\omega), \tag{17}$$

where $\tilde{\alpha}(\omega)$ is the frequency dependent absorption coefficient for the generated field $\tilde{E}_h(\omega)$. The source term for the driving field is mainly due to the loss of energy spent to move the free electrons in the laser field and the energy used to ionize the medium, this last term being in general small in the HHG process and negligible. As pointed out in Rae and Burnett (1992), the source term can be calculated from the time-dependent current density

$J(t) = \partial P_{\text{ion}}(t)/\partial t$. Following the above mentioned discussion, the current density may be written as a sum of two terms (Geissler et al., 1999):

$$J(t) = J_{pl}(t) + J_{abs}(t) = \frac{e^2}{m}\int_{-\infty}^{t} \mathrm{d}t'' n_e(t'')E(t'') + I_p\left(\frac{\partial_t n_e(t)}{E(t)}\right), \tag{18}$$

where I_p is the ionization potential of the atom in the nonlinear medium and $n_e(t)$ is the free-electron density, to be calculated with the ADK theory or with a numerical integration of the time-dependent Schrödinger equation (TDSE) in the single-active-electron approximation (Schafer & Kulander, 1997). The ADK theory can be also used with a corrective factor in order to obtain a better agreement with the TDSE solution (Gaarde et al., 2006). The source term for the generated field is calculated from the time-dependent nonlinear polarization, which is supposed to be proportional to the single-atom dipole moment $x(t)$ and to the density of neutral atoms n_{atom}.

$$\tilde{P}_{\text{dip}}(\omega) = \mathcal{F}\{n_{\text{atom}}(t)x(t)\}, \tag{19}$$

where $\mathcal{F}$ denotes a Fourier transform.

Of course, the most accurate way to obtain $x(t)$ is to solve the TDSE for the atom-laser field interaction (Christov et al., 1997; Krause et al., 1992b); however, such an approach is too time consuming. For this reason, it is preferred to use an analytical model based on the approximate solution of the Schrödinger equation as the Lewenstein integral of Equation (6). The SPA model is not usually used to evaluate the dipole moment inside the dipole source term because it needs to know the values of the driving field for complex times. Even if this is not a severe requirement if one knows the analytical form of the driving field, it does not fit with the numerical definition of the electric field inside a propagation code. Recently, a new approach has been proposed by Tosa et al. (2009) and by Kovács and Toşa (2010) to overcome the problem and to allow one to solve the saddle-point equations with an arbitrary numerical field, thus making possible its integration in a propagation model .

4. APPLICATIONS OF ISOLATED ATTOSECOND PULSES

So far, measurements with attosecond temporal resolution have been performed by using an isolated attosecond pulse as pump and an infrared femtosecond pulse as probe, or vice versa. Attosecond pump-probe experiments present characteristics completely different with respect to the well-established and used femtosecond pump-probe method, where the

probe pulse measures the changes of the optical properties of the sample (i.e., absorption or reflection coefficients) induced by the pump pulse. Novel experimental techniques to initiate and probe electron dynamics on an attosecond temporal scale are required. Due to the high photon energy of the attosecond pulses (ranging from a few tens to a few hundreds of electron volt), the excitation of the sample almost inevitably leads to valence or core photoelectron emission, followed by a rearrangement of the electronic system. Depending on the system, such electron rearrangement can be in the form of Auger decay, population of excited ionic states by shake-up processes, charge transfer and migration in large molecules, etc. So far, the electron dynamics initiated by an isolated attosecond pulse has been measured by using the electric field of a phase-stabilized few-cycle IR pulse (Krausz & Ivanov, 2009). The schemes for attosecond measurements proposed and experimentally demonstrated in the case of isolated pulses are the following:

1. Streaking spectroscopy, based on XUV ionization followed by acceleration of the ionized electron in a strong IR field: such a scheme has been used by Hentschel et al. (2001) for the temporal characterization of XUV pulses and for the investigation of the ultrafast dynamics in atoms by Drescher et al. (2002) and solids by Cavalieri et al. (2007).
2. Ion-charge-state chronoscopy, based on the use of the subcycle time dependence of strong-field ionization rates to measure electron dynamics in bound states of atoms (Xe and Ne) (Uiberacker et al., 2007).
3. Attosecond transient absorption spectroscopy, recently implemented by Goulielmakis et al. (2010) and by Wang et al. (2010) for the measurement of valence electron motion in krypton ions.
4. Attosecond electron interferometry, based on the measurement of a time-dependent interference between the ionization of bound electronic wave packet and a reference wave packet, and used by Mauritsson et al. (2010) to measure electron wave packets generated in He after excitation by isolated attosecond pulses .
5. Measurement of a time-dependent asymmetry in dissociative ionization, recently introduced by Sansone et al. (2010) in order to study the electron localization process in molecules after attosecond excitation.

In the following, we will briefly review the main results obtained using such attosecond measurement methods.

4.1 Attosecond Streaking Spectroscopy

In 2002, just one year after the first experimental demonstration of the generation of isolated attosecond pulses by Hentschel et al. (2001), Drescher et al. (2002) reported on the real-time observation of Auger decay in krypton: 0.9-fs soft x-ray pulses were used for excitation of krypton atoms and sub-7-fs IR pulses for probing electron emission. The attosecond pump

pulses, with a central photon energy of 97 eV, lead to photoemission of valence electrons, from the 4*s* and 4*p* subshells, and of core electrons from the 3*d* subshell. Upon measuring the evolution of the kinetic energy of such photoelectrons in the presence of the IR streaking pulse, it is possible to characterize the temporal evolution of the attosecond pump pulses, according to the streak-camera approach for attosecond metrology. In Drescher et al. (2002), the kinetic energy spectra of the 4*s* and 4*p* photoelectrons were not periodically modulated by the vector potential of the streaking pulse, since the CEP of the driving pulses was not stabilized and the duration of the XUV pulses used to excite the Kr atoms was comparable to half of the optical cycle of the streaking field. The photoemission of a core electron, with corresponding generation of a core hole, is followed by an ultrafast rearrangements of the electronic system. The core hole is filled by an outer-shell electron: the excess energy is released in the form of an XUV fluorescence photon, or it is transferred by electrostatic force to a second Auger electron, which can subsequently escape from the atom. Upon measuring the evolution of the kinetic energy of such Auger electron as a function of the delay between pump and probe pulses, it is possible to characterize the temporal evolution of the core hole and the Auger ultrafast dynamics. Indeed, the streaking spectrograms of the Auger electron emission calculated by Yakovlev and Scrinzi (as reported in the Supplementary Information of Drescher et al. (2002)) show peculiar characteristics as a function of the decay time of the core hole. Within the strong field approximation, the spectrum of the Auger electrons can be calculated by using the quantum mechanical model of laser dressed single x-ray photoionization reported by Kitzler et al. (2002), considering that the generation of free electrons is not due to dipole transitions induced by the streaking electric field $\mathbf{E}(t) = -\partial_t \mathbf{A}(t)$ (in atomic units), but by an Auger process. In such a case, the electron spectrum can be calculated as

$$b(\mathbf{p}) \propto i \int_{t_0}^{\infty} \exp\left[-i \int_{t'}^{\infty} \frac{1}{2}(\mathbf{p} - \mathbf{A}(t''))^2 \mathrm{d}t'' + iW_{kin}t' \right] \sqrt{\rho(t')}\chi(\mathbf{p} - \mathbf{A}(t'))\, \mathrm{d}t', \tag{20}$$

where $\mathbf{p}$ is the electron momentum, $b(\mathbf{p})$ is the momentum space wave function of the free electron, $\rho(t)$ is the population of the Auger state, and χ is the continuum wave function. The evolution of the Auger electron emission as a function of the delay between XUV and streaking pulses calculated by using Equation (20) is shown in Figure 12.

In the case of a core-hole decay time, τ_h, shorter than one half the optical period of the streaking pulse ($T_L = 2.5$ fs) (see Figure 12a), the Auger electron maps out the oscillation of the streaking field. From the corresponding streaking spectrogram, it is possible to retrieve the lifetime of the core hole. For core-hole decay times of the order of T_L or longer

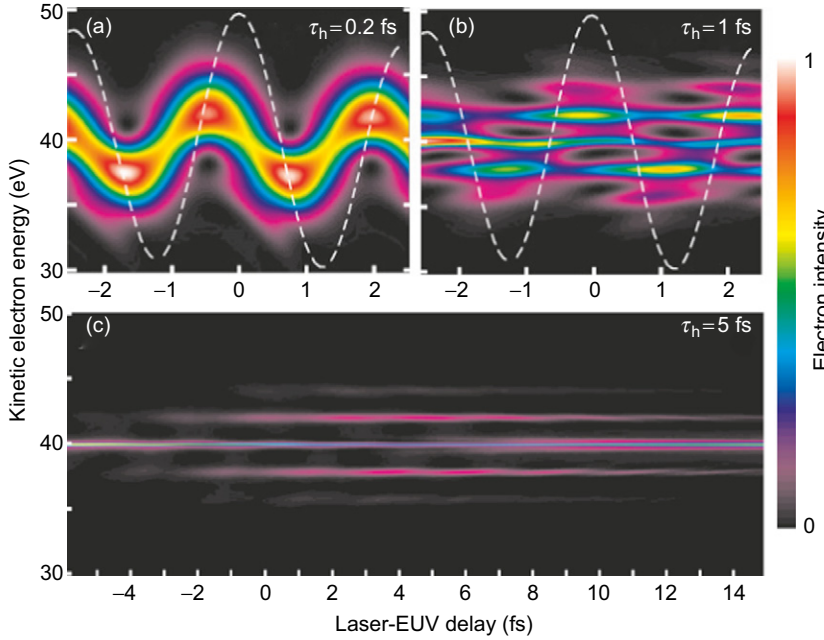

Figure 12 Calculated streaking spectrograms of Auger electron emission for various core-hole decay times, (a) $\tau_h = 0.2$ fs, (b) $\tau_h = 1$ fs, (c) $\tau_h = 5$ fs. Duration of the pump pulse: $\tau_X = 500$ as, at $\hbar\omega_X = 100$ eV; duration and peak intensity of the streaking pulse, at $\hbar\omega_L \approx 1.6$ eV: $\tau_L = 5$ fs (FWHM) and $I_p = 5 \times 10^{11}$ W/cm^2, respectively. Figure adapted from Drescher et al. (2002).

than T_L, the spectrogram of the Auger electron exhibits the generation of sidebands spaced by the photon energy, $\hbar\omega_L$, of the streaking pulse. In this case, the dynamics of the Auger electrons is revealed by the evolution of the area of the sidebands as a function of the delay between the XUV and the IR pulses. The measured evolution of the electron spectra following excitation reported in Drescher et al. (2002) showed the presence of sidebands spaced by $\hbar\omega_L \approx 1.6$ eV, thus indicating a core-hole decay time comparable to or longer than T_L. Indeed, a decay time $\tau_h \approx 7.9$ fs was extracted from the experimental data.

The streaking spectroscopy has been also extended to condensed matter systems: photoelectron emission from single-crystal tungsten, induced by isolated attosecond pulses, has been probed by the electric field of a 5-fs light pulse, showing a 100-as delay between the emission of photoelectrons that originate from localized 4*f* states of the metal, and those that are freed from delocalized conduction-band states (Cavalieri et al., 2007).

4.2 Ion-Charge-State Chronoscopy

The second attosecond technique, which has been proposed and experimentally demonstrated by Uiberacker et al. (2007) to investigate electron dynamics with subfemtosecond temporal resolution, is based on XUV excitation of bound states followed by ionization by intense IR field. The photoexcitation of an atom by XUV attosecond pulses is usually accompanied by the transition of an outer shell electron to an unoccupied state by a shake-up process. Such shake-up state can be ionized by an IR pulse, with controlled electric field. Upon measuring the number of ions generated during this process, it is possible to probe, with subfemtosecond resolution, the population of the shake-up states. At the same time, it is possible to investigate the process of strong-field ionization. In the experiment reported in Uiberacker et al. (2007), neon atoms were ionized by isolated 250-as pulses (with a photon energy of 95 eV) in the presence of a strong IR pulse ($\tau_L = 5$ fs) with controlled electric field. A fraction of such photoionization processes leads to the excitation of Ne^+ ions to excited states (shake-up process), which can be further ionized by the IR field (with intensity $I = (7 \pm 1) \times 10^{13}$ W/cm^2), thus increasing the Ne^{2+} population. The Ne^{2+} ion yield as a function of the delay between the attosecond pump pulse and the IR probe pulse shows a subcycle evolution, with consecutive steps separated by half the optical cycle of the probe strong field, thus providing a strong evidence of the crucial role of optical field ionization as the main cause of the depletion of the excited valence states. This experimental observation is particularly important since, as first theoretically pointed out in Yudin and Ivanov (2001), it demonstrates that light-field-induced tunnelling plays a central role in the ionization process in a broad excitation intensity region, where multiphoton ionization was predicted to be the dominant ionization mechanisms. Indeed, the Keldysh parameter $\gamma = \sqrt{I_p/2U_p}$ (where I_p is the ionization potential and U_p is the ponderomotive potential) was of the order of three, assuming the laser parameters used in the experiment, and the nonadiabatic tunnelling theory of Yudin and Ivanov (2001) predicts that at these values of γ, the ionization rate still presents a clear subcycle temporal evolution. The attosecond real-time observation of electron tunnelling in atoms is an important example of the use of attosecond methods for the investigation of basic electronic processes and for an experimental test of theoretical models.

4.3 Attosecond Transient Absorption Spectroscopy

Femtosecond transient absorption spectroscopy in the XUV spectral region was reported in the last few years by Loh et al. (2007) and

Loh and Leone (2008), based on a high-order harmonic generation source. Such a technique was implemented to investigate the dissociative ionization of CH_2Br_2 induced by 800-nm strong-field irradiation (Loh et al., 2007) and to investigate the strong-field ionization of xenon induced by 800-nm excitation, in order to resolve the complete quantum state distribution of the resulting Xe^+ ions (Loh & Leone, 2008). More recently, the same experimental method has been used with isolated attosecond pulses by Goulielmakis et al. (2010) and Wang et al. (2010). In the former case, krypton ions were generated by using sub-4-fs light pulses with controlled electric field, resulting in the generation of a broadband valence electron wave packet (or hole), characterized by a high degree of coherence. The IR pump pulse determines the emission of electrons from the $4p$ subshell and leaves the ions in a coherent superposition of $4p_{3/2}^{-1}$ and $4p_{1/2}^{-1}$ states. Isolated attosecond pulses were used to probe the temporal evolution of such electron wave packet. In particular, single-photon XUV absorption promotes the ions from the $4p_{3/2}^{-1}$ and $4p_{1/2}^{-1}$ states to the core-excited $3d_{3/2}^{-1}$ state. It turned out that the ensemble-averaged hole density distributions in the $4p$ subshell of Kr^+ is characterized by a periodic oscillation, with a period $T = 6.3 \pm 0.1$ fs (Goulielmakis et al., 2010), in excellent agreement with the value calculated on the basis of the energy separation, $\Delta E = 0.67$ eV, between the $4p_{3/2}^{-1}$ and $4p_{1/2}^{-1}$ states.

Wang et al. (2010) used the attosecond transient absorption spectroscopy technique to investigate the autoionization process of Fano (1961) in argon. In this case, $3s3p^6np\ ^1P$ autoionizing states were populated by isolated attosecond pulses. In the presence of a strong 750-nm pulse, the autoionization peak broadens and the central energies of the autoionizing peaks are shifted, as a consequence of additional coupling between the autoionizing states and Ar^{*+} ($3s3p^6\epsilon l$) continuum states.

4.4 Attosecond Electron Interferometry

In 2010, Mauritsson *et al.* reported on a novel interferometric pump-probe technique for the characterization of attosecond electron wave packets that uses a free wave packet as a reference to measure a bound wave packet (Mauritsson et al., 2010). The method was experimentally demonstrated by measuring an attosecond wave packet in helium, prepared using an isolated 350-as pulse with a central energy in the vicinity of the ionization threshold. The portion of the XUV spectrum below the ionization potential of He can excite one electron from the initial bound state $|i\rangle$ to the bound $|np\rangle$ state by single-photon absorption. According to the theoretical model reported by Choi et al. (2010), such a transition can be described by the transition probability amplitude $M_{n,i}^{(X)} = a_n\ e^{i\phi_n}$. At the same time the spectral components above the ionization threshold can determine a transition to an ionized state with photoelectron

momentum $\mathbf{p}$, with a corresponding transition probability amplitude $M^{(X)}_{\mathbf{p},i} = a_{\mathbf{p}}\, e^{i\phi_{\mathbf{p}}}$. In the same way, the probability amplitude for transitions induced by the IR pulse from the bound $|np\rangle$ state to an ionized state with photoelectron momentum $\mathbf{p}$ can be written as $M^{(L)}_{\mathbf{p},n} = b_{\mathbf{p},n}\, e^{i\phi_{\mathbf{p},n}}$. The total ionization probability density, which is a function of the delay τ between the XUV and IR pulses, is therefore given by the following expression:

$$|M_{\mathbf{p},i}|^2 = a_{\mathbf{p}}^2 + \sum_n b_{\mathbf{p},n}^2\, a_n^2 + 2\sum_n a_{\mathbf{p}}\, b_{\mathbf{p},n}\, a_n \cos[\phi_{\mathbf{p},n} - (E_{\mathbf{p}} - E_n)\tau] + 2\sum_{n<m} b_{\mathbf{p},n}\, b_{\mathbf{p},m}\, a_n\, a_m \cos[\phi_{m,n} - (E_m - E_n)\tau] \tag{21}$$

The phase $\phi_{\mathbf{p},n}$ contains the terms due to the Volkov phase and the dipole phases involved in transition from the ground state to the continuum $\mathbf{p}$ and in transition first from the ground state to the bound $|np\rangle$ state and then to the continuum $\mathbf{p}$. Similarly, the phase $\phi_{m,n}$ is related to the phase difference between the path from the ground state to the continuum $\mathbf{p}$, through the bound states $|mp\rangle$ and $|np\rangle$. E_n is the energy of the $|np\rangle$ state and $E_{\mathbf{p}}$ is the energy of the continuum states. The first and second terms on the right-hand side of Equation (21) correspond to direct ionization to the $\mathbf{p}$ states by the XUV and ionization by the combination of the IR and XUV field, respectively. The third term corresponds to an interference term between a direct ionization to the $\mathbf{p}$ state and ionization by the IR field of a bound state $|np\rangle$ excited by the XUV pulse. Finally, the fourth term corresponds to the interference between two bound states excited by the XUV ($|np\rangle$ and $|mp\rangle$) ionized by the IR field. The two interference patterns are characterized by a different evolution in the two-dimensional space (τ, $E_{\mathbf{p}}$). Indeed, the last interference term in Equation (21) indicates that the equiphase surfaces in the (τ, $E_{\mathbf{p}}$) plane can be written as

$$\cos[\phi_{m,n} - (E_m - E_n)\tau] = \mathrm{C}, \tag{22}$$

where C is a constant value, so that $\tau \propto \mathrm{C}/(E_m - E_n)$. Such equiphase surfaces do not depend on the continuum energy $E_{\mathbf{p}}$ and are represented by parallel lines in the (τ, $E_{\mathbf{p}}$) plane. The equiphase surfaces for the first interference term in Equation (21) can be obtained by the following expression:

$$\cos[\phi_{\mathbf{p},n} - (E_{\mathbf{p}} - E_n)\tau] = \mathrm{C}, \tag{23}$$

so that the equiphase surfaces are given by $\tau \propto \mathrm{C}/(E_{\mathbf{p}} - E_n)$ and are represented by hyperbolic curves in the (τ, $E_{\mathbf{p}}$) plane.

From the experimental point of view, a linearly polarized phase stabilized 5-fs IR laser pulse was divided into a central and annular part

using a mirror with a hole in the center. The polarization of the central part was modulated in time using two birefringent plates and was focused by a spherical mirror into a xenon gas cell with 3 mm length. The outgoing beam was frequency filtered using an aluminum filter (100 nm thickness) and was focused by a grazing incident toroidal mirror. The annular part (probe pulse), reflected by the drilled mirror, was delayed using a piezoelectric translation stage, and it was focused by means of a spherical mirror. The two pulses were recombined using a second drilled mirror, and they were focused into the active region of a velocity map imaging spectrometer (VMIS) (Eppink & Parker, 1997), which was used to record the photoelectron momentum distributions. The isolated attosecond pulses were characterized by a central frequency of 24 eV with a bandwidth exceeding 10 eV and excited helium from its ground state to a coherent superposition of bound and continuum states. Figure 13 shows the experimental photoelectron spectra in He as a function of delay between the XUV pump pulse and the IR probe pulse. The spectra were obtained by selecting a small collection angle along the polarization direction. In the region of temporal overlap a clear streaking pattern is observed. In the region where the attosecond pulse precedes the IR pulse, interference fringes are clearly observed in the low-energy region of the spectrum, up to about 2 eV. As expected from the earlier discussion, the interference fringes, defined as the curves of constant phase difference, are hyperboles, which become more closely spaced as the delay increases.

It is interesting to observe that the characterization of the angular distribution of the photo-electrons allows one to distinguish between

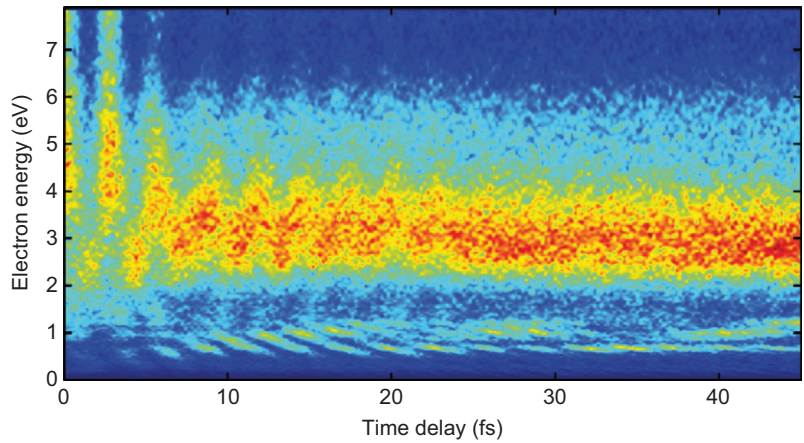

Figure 13 Photoelectron spectrum measured in helium as a function of the delay between the attosecond and the IR pulses. Figure adapted from Mauritsson et al. (2010).

the two interference terms of Equation (21). Indeed the two ionization channels are characterized by the absorption of a different number of photons: the direct channel involves the absorption of a single XUV photon, leading to the emission of an electron in a p ($l = 1$) state. On the other hand, the indirect channel requires the absorption of one XUV photon and one IR photon (or more, depending on the IR intensity), leading to the emission on an electron in an s ($l = 0$) or d state ($l = 2$). Applying a decomposition in Legendre polynomials of the measured angular distribution, the different contributions can be separated as shown in Mauritsson et al. (2010).

4.5 Time-Dependent Asymmetry in Molecular Dissociative Ionization

Sansone et al. (2010) reported on the first attosecond pump-probe measurement on molecules. Isolated attosecond pulses, with spectrum extending from 20 to 40 eV, were used to excite H_2 and D_2 molecules. The kinetic energy and angular distribution of H^+ and D^+ ionic fragments were measured as a function of the delay between the XUV pump and a 6-fs, IR pulse with stable CEP. The attosecond excitation leads to dissociative ionization of the molecule, following various pathways, which are strongly related to the photon energy and to the observation angle of the ionic fragment with respect to the laser polarization (Ito et al., 1996). The XUV photons with energy below 25 eV lead to direct dissociative ionization via the $^2\Sigma_g^+(1s\sigma_g)$ state, with the generation of ionic fragment with low kinetic energy (< 1 eV). A simplified scheme of the neutral and singly ionized potential energy curves of H_2, relevant for the discussion of the XUV-IR pump-probe measurement reported in this section, is shown in Figure 14. For photon energies between 25 and 36 eV, excitation of the doubly-excited $Q_1\ ^1\Sigma_u^+$ state becomes possible for molecules aligned along the polarization axis of the pump pulse. Autoionization of the Q_1 state to the $^2\Sigma_g^+(1s\sigma_g)$ state produces fragments with a kinetic energy in the range 0–10 eV (but preferentially between 2 and 7 eV) (Sanchez & Martín, 1997, 1998). The XUV spectral components above 30 eV can determine direct ionization to the repulsive $^2\Sigma_u^+(2p\sigma_u)$ state, with the generation of high-kinetic-energy fragments (5–10 eV). Above 31 eV, a perpendicular transition preferentially excites molecules that are orthogonally aligned to the laser polarization axis to the $Q_2^1\Pi_u$ doubly-excited states. These states autoionize to both the $^2\Sigma_g^+(1s\sigma_g)$ and the $^2\Sigma_u^+(2p\sigma_u)$ states, with the generation of fragments with kinetic energies of 1–5 eV and 5–8 eV, respectively (Ito et al., 1996).

Figure 15 shows the temporal evolution of the kinetic energy distribution of the D^+ ions after dissociative ionization induced by isolated attosecond pulses, as a function of the delay, τ, between the XUV pump and the IR probe pulse. At low kinetic energy ($E_k < 1$ eV), bond softening

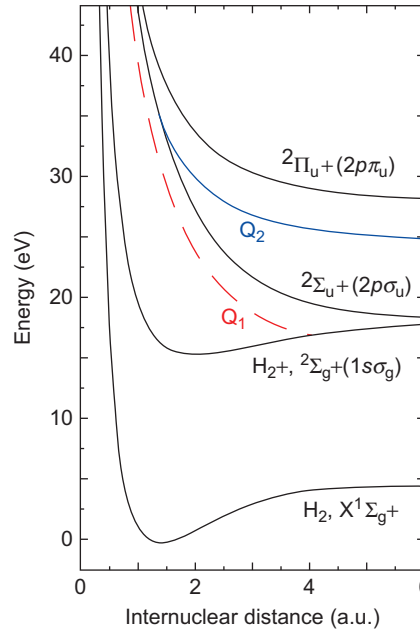

Figure 14 Simplified scheme of the potential energy curves of H_2 and H_2^+.

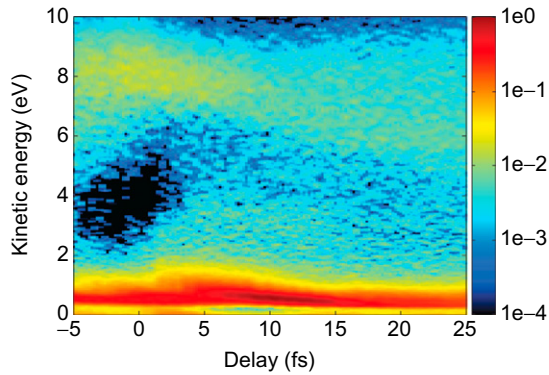

Figure 15 Experimental kinetic energy distributions of D^+ ions as a function of the delay between the attosecond pump pulses and the infrared probe pulses. Color scale represents fragment yield in arbitrary units. Figure adapted from Sansone et al. (2010).

(Bucksbaum et al., 1990) induced by the IR pulse is evident, with a maximum when the bound electron wave packet is at the outer turning point of the potential curve. The increase of the ion signal at kinetic energies around 8 eV for $\tau < 10$ fs can be associated with two effects:

(1) IR-induced photoionization of the $Q_1^1\Sigma_u^+$ doubly-excited state producing $2p\sigma_u$ states; (2) increase in the excitation cross-section of the $2p\sigma_u$ state caused by IR-induced mixing of the $2p\sigma_u$ and $1s\sigma_g$ states. Particularly interesting is the measured temporal evolution of the asymmetry parameter, reported in Figure 16, defined as:

$$A(E_k,\tau) = \frac{N_L(E_k,\tau) - N_R(E_k,\tau)}{N_L(E_k,\tau) + N_R(E_k,\tau)}, \tag{24}$$

where $N_L(E_k,\tau)$ and $N_R(E_k,\tau)$ are the numbers of ions arriving within 45° of the polarization axis on the left-hand and right-hand sides of the detector, respectively. Such a parameter is directly associated with the electron localization process after the photoionization process initiated by the attosecond excitation. The asymmetry parameter is characterized by a subcycle temporal evolution in the E_k kinetic energy range between 2 and 10 eV; moreover, the phase of the asymmetry oscillations depends on E_k. A left-right asymmetry is necessarily caused by a coherent superposition of gerade and ungerade states, and the relative phase between the two states leads to electron localization. In the case of H_2 (D_2), molecules the states involved in such coherent superposition are the two lowest electronic states, $^2\Sigma_g^+(1s\sigma_g)$ and $^2\Sigma_u^+(2p\sigma_u)$, of the molecular ion. The physical process leading to the localization dynamics has been investigated by Sanz-Vicario et al. (2006) by using a close-coupling method to solve the time-dependent Schrödinger equation for H_2, that includes the bound

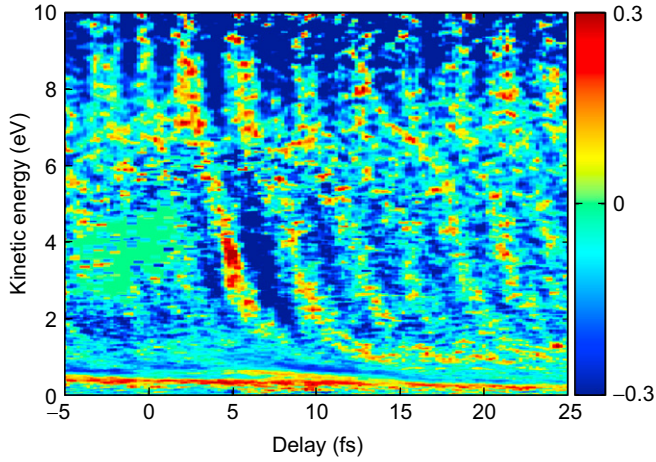

Figure 16 Asymmetry parameter (colour scale) for the formation of D^+ ions after attosecond excitation as a function of the fragment kinetic energy, E_k, and of the temporal delay between pump and probe pulses. Figure adapted from Sansone et al. (2010).

states, the $^2\Sigma_g^+(1s\sigma_g)$ and the $^2\Sigma_u^+(2p\sigma_u)$ ionization continua, and the doubly excited states. An important result of the numerical simulation is that the infrared probe pulse can cause an asymmetry either by changing the wave function of the continuum electron (hereafter called mechanism I), or by changing the wave function of the molecular ion (hereafter called mechanism II). In the first case, which is the predominant localization mechanism during the XUV-IR temporal overlapping period, the interaction of the IR pulse with the photoelectron generated by the XUV excitation leads to a redistribution of the electron angular momentum over various angular momentum states. At the same time, the autoionization of the Q_1 doubly-excited states determines the production of a dissociative wave packet on the $1s\sigma_g$ state with p-electron emission. Such two channels are completely indistinguishable, and therefore, they lead to quantum interference between the two states. In the case of mechanism II, the IR pulse determines a coupling between the $^2\Sigma_g^+(1s\sigma_g)$ and the $^2\Sigma_u^+(2p\sigma_u)$ states by population transfer and requires high intensity of the IR pulse during the dissociation of the molecule (Kling et al., 2006).

5. CONCLUSIONS

In this review, we have discussed recent progress in the field of attosecond science. Various schemes for the generation of isolated pulses have been proposed and implemented in the last years: we have concentrated our attention on different temporal gating methods. The applications of attosecond pulses reported so far in atomic, molecular, and solid-phase physics, have demonstrated that attosecond technology can offer unique tools for the investigation of ultrafast electronic processes on atomic scales.

ACKNOWLEDGMENTS

We acknowledge the contribution of various research groups, important for the development of the polarization gating technique and for the applications of isolated attosecond pulses in our laboratory. In particular, we acknowledge I. Sola, E. Mével and E. Constant (CELIA-Bordeaux, France), F. Kelkensberg, O. Ghafur, W. Siu and M.J.J. Vrakking (AMOLF-Amsterdam, The Netherlands), J. Mauritsson, T. Remetter, M. Swoboda, P. Johnsson and A. LHuillier (Lund Institute of Technology, Lund, Sweden), S. Zherebtsov, I. Znakovskaya and M.F. Kling (MPQ-Garching, Germany), K.J. Schafer (Louisiana State University, Baton Rouge, Louisiana, USA), F. Lépine (Université Lyon 1, Lyon, France), M.Yu. Ivanov (Imperial College-London, UK), J.F. Pérez-Torres, F Morales and F. Martín (Universidad Autonoma de Madrid, Spain), J.L. Sanz-Vicario (Universidad de Antioquia, Medellín, Colombia), C. Altucci and

R. Velotta (Federico II University, Naples, Italy), L. Poletto and P. Villoresi (University of Padova, Padova, Italy), E. Benedetti (Politecnico di Milano, Milano, Italy).

We acknowledge funding from the European Research Council under the European Community's Seventh Framework Programme (FP7/2007-2013)/ERC grant agreement n. 227355 - ELYCHE, from the Italian Ministry of Research (FIRB-IDEAS RBID08CRXK). Financial support by the Marie Curie Research Training Networks ATTOFEL (FP7-238362), and by the European Union within contract n. 228334 JRA-ALADIN (Laserlab Europe II) is also acknowledged.

REFERENCES

Abel, M. J., Pfeifer, T., Nagel, P. M., Boutu, W., Bell, M. J., Steiner, C. P., et al. (2009). Isolated attosecond pulses from ionization gating of high-harmonic emission. *Chemical Physics*, *366*, 9–14.

Agostini, P., & DiMauro, L. F. (2004). The physics of attosecond light pulses. *Reports on Progress in Physics*, *67*, 813–855.

Altucci, C., Delfin, C., Roos, L., Gaarde, M. B., L'Huillier, A., Mercer, I., et al. (1998). Frequency-resolved time-gated high-order harmonics. *Physical Review A*, *58*, 3934–3941.

Altucci, C., Velotta, R., Tosa, V., Villoresi, P., Frassetto, F., Poletto, L., et al. (2010). Interplay between group-delay-dispersion-induced polarization gating and ionization to generate isolated attosecond pulses from multicycle lasers. *Optics Letters*, *35*, 2798–2800.

Ammosov, M. V., Delone, N. B., & Krainov, V. P. (1986). Tunnel ionization of complex atoms and atomic ions by an alternating electromagnetic field. *Soviet Physics JETP, 64*, 1191–1194.

Antoine, P., Milošević, D. B., L'Huillier, A., Gaarde, M. B., Salières, P., & Lewenstein, M. (1997). Generation of attosecond pulses in macroscopic media. *Physical Review A*, *56*(6), 4960–4969.

Baltuška, A., Udem, T., Uiberacker, M., Hentschel, M., Goulielmakis, E., Gohle, C., et al. (2003). Attosecond control of electronic processes by intense light fields. *Nature, 421*, 611–615.

Brabec, T., & Krausz, F. (2000). Intense few-cycle laser fields: frontiers of nonlinear optics. *Reviews of Modern Physics*, *72*(2), 545–591.

Bucksbaum, P., Zavriyev, A., Muller, H., & Schumacher, D. (1990). Softening of H_2^+ molecular bond in intense laser fields. *Physical Review Letters*, *64*, 1883–1886.

Calegari, F., Vozzi, C., Negro, M., Sansone, G., Frassetto, F., Poletto, L., et al. (2009). Efficient continuum generation exceeding 200 eV by intense ultrashort two-color driver. *Optics Letters*, *34*, 3125–3127.

Cao, W., Lu, P., Lan, P., Wang, X., & Yang, G. (2006). Single-attosecond pulse generation with an intense multicycle driving pulse. *Physical Review A*, *74*, 063821.

Cavalieri, A., Muller, N., Uphues, T., Yakovlev, V., Baltuska, A., Horvath, B., et al. (2007). Attosecond spectroscopy in condensed matter. *Nature, 449*, 1029–1032.

Chang, Z. (2007). Controlling attosecond pulse generation with a double optical gating. *Physical Review A*, *76*, 051403.

Choi, N., Jiang, T., Morishita, T., Lee, M.-H., & Lin, C. (2010). Theory of probing attosecond electron wave packets via two-path interference of angle-resolved photoelectrons. *Physical Review A*, *82*, 013409.

Christov, I. P., Murnane, M. M., & Kapteyn, H. C. (1997). High-harmonic generation of attosecond pulses in the "single-cycle" regime. *Physical Review Letters*, *78*, 1251–1254.

Colosimo, P., Doumy, G., Blaga, C., Wheeler, J., Hauri, C., Catoire, F., et al. (2008). Scaling strong-field interactions towards the classical limit. *Nature Physics, 4*, 386–389.

Corkum, P. (1993). Plasma perspective on strong-field multiphoton ionization. *Physical Review Letters*, *71*, 1994–1997.

Corkum, P. B., Burnett, N. H., & Ivanov, M. Y. (1994). Subfemtosecond pulses. *Optics Letters*, *19*, 1870–1872.
Corkum, P. B., & Krausz, F. (2007). Attosecond science. *Nature Physics, 3*, 381–387.
Drescher, M., Hentschel, M., Kienberger, R., Uiberacker, M., Yakovlev, V., Scrinzi, A., et al. (2002). Time-resolved atomic inner-shell spectroscopy. *Nature, 419*, 803–807.
Eppink, A., & Parker, D. (1997). Velocity map imaging of ions and electrons using electrostatic lenses: application in photoelectron and photofragment ion imaging of molecular oxygen. *Review of Scientific Instruments*, *68*, 3477–3484.
Fano, U. (1961). Effects of configuration interaction on intensities and phase shifts. *Physical Review*, *124*, 1866–1878.
Farkas, G., & Tóth, C. (1992). Proposal for attosecond light pulse generation using laser induced multiple-harmonic conversion processes in rare gases. *Physics Letters A*, *168*, 447450.
Feng, X., Gilbertson, S., Mashiko, H., Wang, H., Khan, S. D., Chini, M., et al. (2009). Generation of isolated attosecond pulses with 20 to 28 femtosecond lasers. *Physical Review Letters*, *103*, 183901.
Ferrari, F., Calegari, F., Lucchini, M., Vozzi, C., Stagira, S., Sansone, G., et al. (2010). High-energy isolated attosecond pulses generated by above-saturation few-cycle fields. *Nature Photonics*, *4*, 875–879. doi:10.1038/nphoton.2010.250.
Figueira de Morisson Faria, C., Schomerus, H., & Becker, W. (2002). High-order above-threshold ionization: the uniform approximation and the effect of the binding potential. *Physical Review A*, *66*(4), 043413.
Gaarde, M. B., Murakami, M., & Kienberger, R. (2006). Spatial separation of large dynamical blueshift and harmonic generation. *Physical Review A*, *74*(5), 053401.
Gaarde, M., Tate, J., & Schafer, K. (2008). Macroscopic aspects of attosecond pulse generation. *Journal of Physics B: Atomic, Molecular and Optical Physics*, *41*, 132001.
Geissler, M., Tempea, G., Scrinzi, A., Schnürer, M., Krausz, F., & Brabec, T. (1999). Light propagation in field-ionizing media: extreme nonlinear optics. *Physical Review Letters*, *83*(15), 2930–2933.
Goulielmakis, E., Loh, Z., Wirth, A., Santra, R., Rohringer, N., Yakovlev, V., et al (2010). Real-time observation of valence electron motion. *Nature, 466*, 739–743.
Goulielmakis, E., Schultze, M., Hofstetter, M., Yakovlev, V. S., Gagnon, J., Uiberacker, M., et al. (2008). Single-cycle nonlinear optics. *Science, 320*, 1614–1617.
Haworth, C. A., Chipperfield, L. E., Robinson, J. S., Knight, P. L., Marangos, J. P., & Tisch, J. W. G. (2007). Half-cycle cutoffs in harmonic spectra and robust carrier-envelope phase retrieval. *Nature Physics, 3*(1), 52–57.
Hentschel, M., Kienberger, R., Spielmann, C., Reider, G., Milosevic, N., Brabec, T., et al. (2001). Attosecond metrology. *Nature, 414*, 509–513.
Ito, K., Hall, R., & Ukai, M. (1996). Dissociative photoionization of H_2 and D_2 in the energy region of 25-45 eV. *Journal of Chemical Physics*, *104*, 8449–8457.
Kan, C., Capjack, C. E., Rankin, R., & Burnett, N. H. (1995). Spectral and temporal structure in high harmonic emission from ionizing atomic gases. *Physical Review A, 52*(6), R4336–R4339.
Kane, D. (1999). Recent progress toward real-time measurement of ultrashort laser pulses. *IEEE Journal of Quantitative Electronics, 35*, 421–431.
Kim, K. T., Kim, C. M., Baik, M.-G., Umesh, G., & Nam, C. H. (2004). Single sub-50-attosecond pulse generation from chirp-compensated harmonic radiation using material dispersion. *Physical Review A*, *69*, 051805.
Kitzler, M., Milosevic, N., Scrinzi, A., Krausz, F., & Brabec, T. (2002). Quantum theory of attosecond XUV pulse measurement by laser dressed photoionization. *Physical Review Letters*, *88*, 173904.
Kling, M., Siedschlag, C., Verhoef, A., Khan, J., Schultze, M., Uphues, T., et al. (2006). Control of electron localization in molecular dissociation. *Science, 312*, 246–248.
Kovačev, M., Mairesse, Y., Priori, E., Merdji, H., Tcherbakoff, O., Monchicourt, P., et al. (2003). Temporal confinement of the harmonic emission through polarization gating. *European Physical Journal D*, *26*, 79–82.
Kovács, K., & Toşa, V. (2010). Quantum trajectories of electrons in arbitrary laser fields. *Journal of Modern Optics*, *57*(11), 977–983.

Krause, J., Schafer, K., & Kulander, K. (1992a). High-order harmonic generation from atoms and ions in the high intensity regime. *Physical Review Letters*, *68*, 3535–3538.
Krause, J. L., Schafer, K. J., & Kulander, K. C. (1992b). Calculation of photoemission from atoms subject to intense laser fields. *Physical Review A*, *45*(7), 4998–5010.
Krausz, F., & Ivanov, M. (2009). Attosecond physics. *Reviews of Modern Physics*, *81*(1), 163–234.
Kuchiev, M. Y. (1987). Atomic antenna. *Soviet Physics JETP, 45*, 404.
Kulander, K., Schafer, K., & Krause, K. L. (1993). Super intense laser-atom physics. *NATO Advanced Study Institute, Series B, 316*, 95.
Lewenstein, M., Balcou, P., Ivanov, M. Y., L'Huillier, A., & Corkum, P. B. (1994). Theory of high-harmonic generation by low-frequency laser fields. *Physical Review A*, *49*(3), 2117–2132.
Lewenstein, M., Salières, P., & L'Huillier, A. (1995). Phase of the atomic polarization in high-order harmonic generation. *Physical Review A*, *52*(6), 4747–4754.
L'Huillier, A., & Balcou, P. (1993). High-order harmonic generation in rare gases with a 1-ps 1053-nm laser. *Physical Review Letters*, *70*(6), 774–777.
L'Huillier, A., Balcou, P., Candel, S., Schafer, K. J., & Kulander, K. C. (1992). Calculations of high-order harmonic-generation processes in xenon at 1064 nm. *Physical Review A*, *46*(5), 2778–2790.
Loh, Z.-H., Khalil, M., Correa, R., Santra, R., Buth, C., & Leone, S. (2007). Quantum state resolved probing of strong-field-ionized xenon atoms using femtosecond high-order harmonic transient absorption spectroscopy. *Physical Review Letters*, *98*, 143601.
Loh, Z.-H., & Leone, S. (2008). Ultrafast strong-field dissociative ionization dynamics of CH_2Br_2 probed by femtosecond soft-X-ray transient absorption spectroscopy. *Journal of Chemical Physics*, *128*, 204302.
Macklin, J. J., Kmetec, J. D., & Gordon, C. L. (1993). High-order harmonic generation using intense femtosecond pulses. *Physical Review Letters*, *70*(6), 766–769.
Mairesse, Y., & Quéré, F. (2005). Frequency-resolved optical gating for complete reconstruction of attosecond bursts. *Physical Review A*, *71*, 011401.
Mashiko, H., Gilbertson, S., Chini, M., Feng, X., Yun, C., Wang, H., et al. (2009). Extreme ultraviolet supercontinua supporting pulse durations of less than one atomic unit of time. *Optics Letters*, *34*, 3337–3339.
Mashiko, H., Gilbertson, S., Li, C., Moon, E., & Chang, Z. (2008). Optimizing the photon flux of double optical gated high-order harmonic spectra. *Physical Review A*, *77*, 063423.
Mauritsson, J., Johnsson, P., Gustafsson, E., L'Huillier, A., Schafer, K. J., & Gaarde, M. B. (2006). Attosecond pulse trains generated using two color laser fields. *Physical Review Letters*, *97*, 013001.
Mauritsson, J., Johnsson, P., Mansten, E., Swoboda, M., Ruchon, T., LHuillier, A., et al. (2008). Coherent electron scattering captured by an attosecond quantum stroboscope. *Physical Review Letters*, *100*, 073003.
Mauritsson, J., Remetter, T., Swoboda, M., Klünder, K., L'Huillier, A., Schafer, K. J., et al. (2010). Attosecond electron spectroscopy using a novel interferometric pump-probe technique. *Physical Review Letters*, *105*(5), 053001.
Merdji, H., Auguste, T., Boutu, W., Caumes, J.-P., Carré, B., Pfeifer, T., et al. (2007). Isolated attosecond pulses using a detuned second-harmonic field. *Optics Letters*, *32*, 3134–3136.
Midorikawa, K., Nabekawa, Y., & Suda, A. (2008). XUV multiphoton processes with intense high-order harmonics. *Progress in Quantum Electronics*, *32*, 43–88.
Milošević, D. B., & Becker, W. (2002). Role of long quantum orbits in high-order harmonic generation. *Physical Review A*, *66*(6), 063417.
Nabekawa, Y., Shimizu, T., Okino, T., Furusawa, K., Hasegawa, H., Yamanouchi, K., et al. (2006). Interferometric autocorrelation of an attosecond pulse train in the single-cycle regime. *Physical Review Letters*, *97*, 153904.
Negro, M., Vozzi, C., Calegari, F., De Silvestri, S., & Stagira, S. (2010). Polarization pulse shaping induced by impulsive molecular alignment in optical filamentation and application to high-order harmonic generation. *Optics Letters*, *35*, 1350–1352.
Nisoli, M., De Silvestri, S., & Svelto, O. (1996). Generation of high energy 10 fs pulses by a new pulse compression technique. *Applied Physics Letters*, *68*, 2793–2795.
Nisoli, M., De Silvestri, S., Svelto, O., Szipöcs, R., Ferencz, K., Spielmann, C., et al. (1997). Compression of high energy laser pulses below 5 fs. *Optics Letters*, *22*, 522–524.

Nisoli, M., & Sansone, G. (2009). New frontiers in attosecond science. *Progress Quantum Electronics, 33*, 17–59.
Nisoli, M., Sansone, G., Stagira, S., De Silvestri, S., Vozzi, C., Pascolini, M., et al. (2003). Effects of carrier-envelope phase differences of few-optical-cycle light pulses in single-shot high-order-harmonic spectra. *Physical Review Letters*, *91*(21), 213905.
Paul, P., Toma, E., Breger, P., Mullot, G., Augé, F., Balcou, P., et al. (2001). Observation of a train of attosecond pulses from high harmonic generation. *Science, 292*, 1689–1692.
Pfeifer, T., Jullien, A., Abel, M. J., Nagel, P. M., Gallmann, L., Neumark, D. M., et al. (2007). Generating choerent broadband continuum soft-x-ray radiation by attosecond ionization gating. *Optics Express, 15*, 17120–17128.
Popmintchev, T., Chen, M.-C., Cohen, O., Grisham, M. E., Rocca, J. J., Murnane, M. M., et al. (2008). Extended phase matching of high harmonics driven by mid-infrared light. *Optics Letters*, *33*, 2128–2130.
Priori, E., Cerullo, G., Nisoli, M., Stagira, S., De Silvestri, S., Villoresi, P., et al. (2000). Nonadiabatic three-dimensional model of high-order harmonic generation in the few-optical-cycle regime. *Physical Review A*, *61*(6), 063801.
Rae, S. C., & Burnett, K. (1992). Detailed simulations of plasma-induced spectral blueshifting. *Physical Review A*, *46*(2), 1084–1090.
Remetter, T., Johnsson, P., Mauritsson, J., Varjú, K., Ni, Y., Lépine, F., et al. (2006). Attosecond electron wave packet interferometry. *Nature Physics, 2*, 323–326.
Sanchez, I., & Martín, F. (1997). Origin of unidentified structures in resonant dissociative photoionization of H_2. *Physical Review Letters*, *79*, 1654–1657.
Sanchez, I., & Martín, F. (1998). Resonant dissociative photoionization of H_2 and D_2. *Physical Review A*, *57*, 1006–1017.
Sansone, G. (2009). Quantum path analysis of isolated attosecond pulse generation by polarization gating. *Physical Review A*, *79*(5), 053410.
Sansone, G., Benedetti, E., Calegari, F., Vozzi, C., Avaldi, L., Flammini, R., et al. (2006). Isolated single-cycle attosecond pulses. *Science, 314*, 443–446.
Sansone, G., Kelkensberg, F., Pérez-Torres, J., Morales, F., Kling, M., Siu, W., et al. (2010). Electron localization following attosecond molecular photoionization. *Nature, 465*, 763–766.
Sansone, G., Vozzi, C., Stagira, S., & Nisoli, M. (2004a). Nonadiabatic quantum path analysis of high-order harmonic generation: role of the carrier-envelope phase on short and long paths. *Physical Review A*, *70*(1), 013411.
Sansone, G., Vozzi, C., Stagira, S., Pascolini, M., Poletto, L., Villoresi, P., et al. (2004b). Observation of carrier-envelope phase phenomena in the multi-optical-cycle regime. *Physical Review Letters*, *92*(11), 113904.
Sanz-Vicario, J., Bachau, H., & Martín, F. (2006). Time-dependent theoretical description of molecular autoionization produced by femtosecond XUV laser pulses. *Physical Review A*, *73*, 033410.
Schafer, K. J., & Kulander, K. C. (1997). High harmonic generation from ultrafast pump lasers. *Physical Review Letters*, *78*(4), 638–641.
Scrinzi, A., Ivanov, M. Y., Kienberger, R., & Villeneuve, D. M. (2006). Attosecond physics. *Journal of Physics B: Atomic, Molecular and Optical Physics*, *39*, R1.
Shan, B., & Chang, Z. (2001). Dramatic extension of the high-order harmonic cutoff by using a long-wavelength driving field. *Physical Review A*, *65*, 011804.
Shimizu, T., Okino, T., Furusawa, K., Hasegawa, H., Nabekawa, Y., Yamanouchi, K., et al. (2007). Observation and analysis of an interferometric autocorrelation trace of an attosecond pulse train. *Physical Review A*, *75*, 033817.
Shiner, A., Trallero-Herrero, C., Kajumba, N., Bandulet, H.-C., Comtois, D., Légaré, F., et al. (2009). Wavelength scaling of high harmonic generation efficiency. *Physical Review Letters*, *103*, 073902.
Takahashi, E. J., Kanai, T., Nabekawa, Y., & Midorikawa, K. (2008). 10 mj class femtosecond optical parametric amplifier for generating soft x-ray harmonics. *Applied Physics Letters*, *93*, 041111.
Takahashi, E. J., Lan, P., Mücke, O. D., Nabekawa, Y., & Midorikawa, K. (2010). Infrared two-color multicycle laser field synthesis for generating an intense attosecond pulse. *Physical Review Letters*, *104*, 233901.

Tcherbakoff, O., Mével, E., Descamps, D., Plumridge, J., & Constant, E. (2003). Time-gated high-order harmonic generation. *Physical Review A*, *68*, 043804.

Tempea, G., Geissler, M., & Brabec, T. (1999). Phase sensitivity of high-order harmonic generation with few-cycle laser pulses. *Journal of the Optical Society of America B*, *16*(4), 669–673.

Thomann, I., Bahabad, A., Liu, X., Trebino, R., Murnane, M. M., & Kapteyn, H. C. (2009). Characterizing isolated attosecond pulses from hollow-core waveguidesusing multi-cycle driving pulses. *Optics Express, 17*, 4611–4633.

Tosa, V., Kovacs, K., Altucci, C., & Velotta, R. (2009). Generating single attosecond pulse using multi-cycle lasers in a polarization gate. *Optics Express, 17*(20), 17700–17710.

Trebino, R., DeLong, K. W., Fittinghoff, D. N., Sweetser, J. N., Krumbugel, M. A., Richman, B. A., et al. (1997). Measuring ultrashort laser pulses in the time-frequency domain using frequency-resolved optical gating. *Review of Scientific Instruments 68*, 3277–3295.

Tzallas, P., Charalambidis, D., Papadogiannis, N., Witte, K., & Tsakiris, G. (2003). Direct observation of attosecond light bunching. *Nature, 426*, 267–271.

Uiberacker, M., Uphues, T., Schultze, M., Verhoef, A., Yakovlev, V., Kling, M., et al. (2007). Attosecond real-time observation of electron tunnelling in atoms. *Nature, 446*, 627–632.

Vozzi, C., Calegari, F., Benedetti, E., Gasilov, S., Sansone, G., Cerullo, G., et al. (2007). Millijoule-level phase-stabilized few-optical-cycle infrared parametric source. *Optics Letters*, *32*, 2957–2959.

Vozzi, C., Calegari, F., Frassetto, F., Poletto, L., Sansone, G., Villoresi, P., et al. (2009). Coherent continuum generation above 100 eV driven by an ir parametric source in a two-color scheme. *Physical Review A*, *79*, 033842.

Wang, H., Chini, M., Chen, S., Zhang, C.-H., He, F., Cheng, Y., et al. (2010). Attosecond time-resolved autoionization of argon. *Physical Review Letters*, *105*, 143002.

Yudin, G., & Ivanov, M. (2001). Nonadiabatic tunnel ionization: looking inside a laser cycle. *Physical Review A*, *64*, 013409.

This page intentionally left blank

CHAPTER 9

Accurate Evaluation of Parameters of Optical Lattice Clocks

Andrei Derevianko[a] and **Sergey G. Porsev**[a,b]

[a]*Department of Physics, University of Nevada, Reno, NV 89557, USA*

[b]*Petersburg Nuclear Physics Institute, Gatchina, Leningrad district, 188300, Russia*

Contents

Advances in Atomic, Molecular, and Optical Physics, Volume 60, Copyright © 2011 Elsevier Inc.
ISSN 1049-250X, DOI: 10.1016/B978-0-12-385508-4.00009-7.

Abstract We present a formalism for evaluating various atomic-structure parameters affecting performance and ultimate accuracy of the optical lattice-based atomic clocks. We evaluate a number of important properties such as the hyperfine-induced transition width of the clock transition, multipolar and vector dynamic polarizabilities, static polarizabilities, "magic" trapping wavelengths, hyperfine-induced g-factors, and blackbody radiation shifts. Accurate numerical calculations of these parameters are carried out for several divalent atoms presently under investigation. The numerical values are obtained with relativistic many-body techniques.

1. INTRODUCTION

Atomic clocks based on the ultranarrow $^3P_0 - {}^1S_0$ transition in divalent atoms may offer a new level of time-keeping accuracy and stability. In addition, they may facilitate tracking changes in fundamental constants over time, measuring gravitational red shifts, and timing pulsars. Compared with microwave atomic clocks, such as the present-day Cs frequency standard, the optical clocks have an advantage that optical transitions have a much higher frequency and potentially much higher resonance quality factors.

To motivate our theoretical work, below we briefly review the recent developments and main features of optical lattice clocks. Detailed reviews may be found in Derevianko and Katori (2011) and Lemonde (2009). In the Katori scheme (Katori, 2002), ultracold atoms are confined in an optical lattice, largely eliminating Doppler and recoil shifts. The lattice laser wavelength is selected in such a way that the dominant perturbation of the clock frequency, the induced AC Stark shifts, for both clock states exactly cancel. At this "magic" wavelength of the lattice laser, the clock frequency is relatively insensitive to laser polarization and power. Although other effects still perturb the clock frequency, estimates of Takamoto et al. (2005) and Porsev et al. (2004) indicate that the projected fractional uncertainty of such clocks may be as low as 10^{-18}. By comparison, a few 10^{-16} is the fractional uncertainty of the current Cs standard realizing the SI definition of the unit of time. Since millions of atoms are trapped and interrogated simultaneously, the optical lattice clocks have an exceptional stability.

There was a rapid progress in developing the lattice clocks over the past few years. The initial 2002 idea of Katori (2002) was followed in 2003 by a detailed theoretical proposal by Katori et al. (2003) for the Sr clock. For Sr, the magic wavelength was determined experimentally by Takamoto and Katori (2003), and finally, the Sr clock was demonstrated just a couple of years later in three different laboratories in Tokyo by

Takamoto et al. (2005, 2006), in Boulder by Ludlow et al. (2006), and in Paris by Le Targat et al. (2006). Recognizing this success, as early as 2006, the Sr optical lattice clock was adopted by the International Committee for Weights and Measures (CIPM) as one of the secondary representations of the second. The contender status of the lattice clocks was further solidified in 2008 when the international frequency comparison carried out in Boulder (Campbell et al., 2008), Paris (Baillard et al., 2008), and Tokyo (Hong et al., 2009) agreed with a fractional uncertainty of 6×10^{-16} that was only limited by the uncertainty of the Cs primary frequency standard. Similarly, a theoretical analysis of Yb clock performance was carried out in 2004 (Porsev et al., 2004); the Yb clock was demonstrated in 2006 (Barber et al., 2006) and the clock frequency was measured with the accuracy near that of the Cs standard in 2009 (Kohno et al., 2009; Lemke et al., 2009).

The advantages of the optical lattice clocks have motivated a number of recent proposals: the original Katori's scheme (Katori, 2002) with fermionic Sr isotopes has been extended to Mg (He et al., 2009), Ca (Riehle et al., 2003), Yb (Lemke et al., 2009; Porsev et al., 2004), and Hg (Hachisu et al., 2008) atoms and to bosonic isotopes (Barber et al., 2008; Hong et al., 2005; Malossi et al., 2005; Santra et al., 2005). In addition, various schemes of probing the highly forbidden $nsnp\,^3P_0 - ns^2\,^1S_0$ clock transition have been proposed as follows: three-photon transition, electromagnetically-induced transparency, and transition assisted by magnetic field (Hong et al., 2005; Santra et al., 2005; Taichenachev et al., 2006a).

The goal of this work is to present a rigorous theory for evaluating various atomic-structure parameters affecting performance and ultimate accuracy of the lattice-based atomic clocks. We start with an introduction to the correlation problem for divalent atoms in Section 2. In that section, we also describe a relativistic many-body code used in our calculations and demonstrate its capabilities by computing energies, dipole-matrix elements, hyperfine-structure constants, and static polarizabilities. We further evaluate parameters of the optical lattice clocks as follows: the magic wavelengths and multipolar polarizabilities (Section 3), hyperfine-induced natural width of the clock transitions (Section 4), vector polarizabilities (Section 5), hyperfine-induced electronic magnetic moments (g-factors, Section 6), blackbody radiation shifts (Section 7), and Rayleigh heating rates (Section 8). Numerical estimates are presented for a number of divalent atoms currently under investigation, with a particular emphasis on the ytterbium clock.

This review is partially based on our previous publications (Porsev et al., 2004), (Porsev & Derevianko, 2004, 2006b), (Derevianko et al., 2009; Hachisu et al., 2008), (Dzuba & Derevianko, 2010). In this review, we put an emphasis on developing a uniform relativistic formalism. We also present previously unpublished details of our derivations. Also,

we compile various atomic parameters for several atomic candidates for optical lattice clocks; the tables will be useful for design considerations and comparison of various clocks.

Unless specified otherwise, we use atomic units ($|e| = \hbar = m_e \equiv 1$) throughout this review. In these units, the speed of light is $c = 1/\alpha$, where $\alpha \approx 1/137$ is the fine-structure constant. We use the Gaussian electromagnetic units. Temperature is expressed in units of E_h/k_B, where E_h is the Hartree (atomic unit of energy) and k_B is the Boltzmann constant.

2. SOLVING THE ATOMIC MANY-BODY PROBLEM

The clockwork in optical lattice clocks takes advantage of the electronic structure of atoms with two valence electrons outside a closed-shell core. Such systems include group II atoms, such as magnesium, calcium, and strontium, or more complex divalent atoms, such as ytterbium and mercury atoms. A typical level structure of such atoms is shown in Figure 1. The clock transition is between the ground $ns^2\,{}^1S_0$ state and the $J = 0$ component of the lowest energy triplet state fine-structure manifold, $nsnp\,{}^3P_J$. In the following presentation, we will also require nuclear parameters for the stable isotopes; these are compiled in Table 1.

Most of the enumerated atoms are relatively heavy and the relativistic effects play an important role (for example, the nuclear charge of Hg is $Z = 80$). Moreover, certain properties, e.g., hyperfine-induced decay rates depend on the wave functions near the nucleus where the relativistic effects dominate. Because of this relativistic nature of the

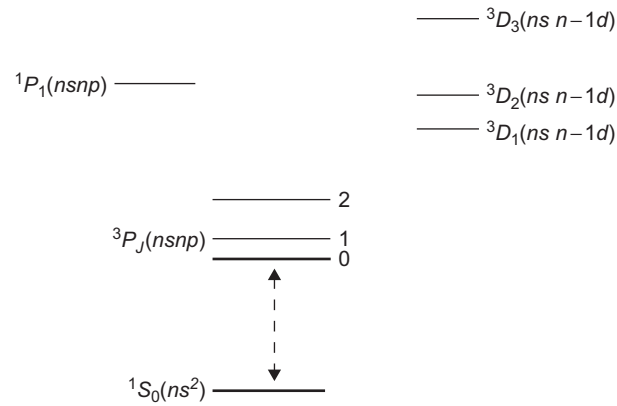

Figure 1 A diagram of the low-lying energy levels for Mg ($n = 3$), Ca ($n = 4$), Sr ($n = 5$), and Yb ($n = 6$). The relative position of the levels above the ^3P_J fine-structure manifold depends on the atom. This diagram reflects the Yb energy levels (the core-excited states are not shown). The clock transition is between the ground and the lowest-energy $^3P_0$ state.

Table 1 Nuclear parameters of the stable fermionic isotopes of Mg, Ca, Sr, and Yb. Here I are the nuclear spins and μ_I/μ_N are the nuclear magnetic moments expressed in units of the nuclear magneton μ_N.

Isotope	I	μ_I/μ_N
^{25}Mg	5/2	−0.85546
^{43}Ca	7/2	−1.31727
^{87}Sr	9/2	−1.09283
^{171}Yb	1/2	0.4919
^{173}Yb	5/2	−0.6776

problem, below we present a theoretical analysis that is uniformly based on the Dirac equation and ab initio relativistic methods of atomic structure. In most cases, we reduce the derived expressions to the more familiar nonrelativistic formulas.

In addition, an accurate description of the atomic structure of the heavy neutral divalent atoms requires treating the correlation problem. A variety of atomic-structure methods have been developed since the inception of quantum mechanics. One of such methods is the multiconfiguration Hartree–Fock method with relativistic effects included through the Breit-Pauli Hamiltonian (Froese Fischer et al., 2006). Another method for solving the electronic-structure problem for divalent atoms relies on the model potential approximation, see e.g., Santra et al. (2004). In this method, one starts by solving the one-electron eigenvalue problem for a singly charged alkaline-earth ion with a single valence electron. Next, using the solutions of the one-electron problem, one constructs two-electron basis functions and an effective two-electron Hamiltonian, which fully incorporates valence-electron correlation. In this way, the eigenenergies and eigenvectors of the two-electron valence shell can be obtained. Another approach (used in our work; see next section for details) is to employ a systematic formalism that combines advantages of both configuration interaction (CI) method and many-body perturbation theory (MBPT) (Dzuba et al., 1996). In the following, we refer to it as the CI + MBPT method. Relativistic effects are included exactly as the formalism starts from the Dirac Hamiltonian and employs relativistic bi-spinor wave functions. Resulting theoretical accuracy of the CI + MBPT calculations is an order of magnitude better than that of the conventional CI method.

2.1 CI + MBPT Method

Many-body perturbation theory provides a systematic prescription for solving the atomic many-body problem (Lindgren & Morrison, 1986).

Basically, the interaction between the electrons is treated as a perturbation and one applies a formalism similar to the textbook stationary perturbation theory. The MBPT produces excellent results for alkali-metal atoms, which have only one electron outside closed shells. Even for atoms as heavy as Cs (55 electrons), the modern ab initio many-body relativistic techniques demonstrate an accuracy of 0.1% for energy levels and a few 0.1% for hyperfine structure constants and lifetimes (Porsev et al., 2010).

One could easily see that bringing the MBPT techniques from univalent to divalent atoms requires substantial revision of the methods. Indeed, let us examine perturbative calculations of the ground state wave function of Be atom ($1s^2\,2s^2$ configuration). If we start our treatment from the Coulomb wave functions, the $2s$ and $2p$ orbitals have the same energies, and because of the degeneracy, we immediately acquire infinitely large terms in the perturbative expansion. Even if we start our analysis from the more accurate Hartree–Fock approximation, the levels remain nearly degenerate and the perturbative treatment breaks down.

These near-degenerate cases have to be treated essentially nonperturbatively using the configuration interaction or multiconfiguration Hartree–Fock methods. The accuracy of the CI is limited only by the completeness of the set of configurations used. For a many-electron atom, the number of possible configurations is enormous and one has to select only a small fraction of them (this subspace is usually referred to as the model space). In our treatment, the model space is limited to valence excitations. Contributions of remaining configurations (i.e., the ones involving excitations of core electrons) are treated within the MBPT. The convergence of the perturbative expansion involving the core-excited states is sufficiently rapid because of a relatively large energy gap between low-lying valence and core-excited states.

To summarize, the accuracy of the MBPT and the (restricted) CI methods is limited in two distinct sectors of the many-body problem. MBPT is not accurate in describing valence-valence interactions, whereas the CI fails to fully account for the core-valence and core-core correlations. For this reason, it is natural to combine the two methods in an attempt to reach higher accuracy for multivalent atoms. A general treatment of the correlation problem along these lines can be found, e.g., in the monograph on atomic MBPT (Lindgren & Morrison, 1986). In our case, we employ the CI + MBPT method as implemented by Dzuba et al. (1996). It was initially employed for accurate calculations of low-lying energy levels and then extended to calculations of various observables such as hyperfine structure constants, oscillator strengths, lifetimes, polarizabilities, and parity nonconserving amplitudes (Dzuba et al., 1998; Kozlov and Porsev, 1999a,b; Kozlov et al., 2001a,b; Porsev et al., 2001, 1999a,b).

A detailed description of the CI + MBPT method can be found in the papers cited earlier. Here we only briefly recapitulate its main features.

We consider Mg, Ca, Sr, and Yb as atoms with two valence electrons outside the closed-shell core. The strong repulsion between the two valence electrons is treated nonperturbatively using the configuration-interaction method. The core-valence and core-core correlations are taken into account with the help of the many-body perturbation theory.

The atomic spectrum is found from the equation for the valence electrons:

$$H_{\text{eff}}(E_n)|\Psi_n\rangle = E_n|\Psi_n\rangle, \tag{1}$$

where the effective Hamiltonian consists of two parts

$$H_{\text{eff}}(E) = H_{\text{FC}} + \Sigma(E).$$

Here H_{FC} is the Hamiltonian in the frozen core approximation and Σ is the energy-dependent correction, which takes into account virtual core excitations. Representative diagrams entering the operator Σ are shown in panels (b) and (c) of Figure 2. It is worth emphasizing that the underlying calculations are ab initio relativistic and are based on the Dirac equation and involve relativistic bi-spinors with large and small components of the electronic wave function.

At this stage, we are able to fully account for the second order of the perturbation theory and partially for the high-order corrections of the MBPT. The latter requires special discussion. The second-order corrections to the Hamiltonian include both one-electron (self-energy diagrams in panel (b) of Figure 2) and two-electron diagrams (see the screening diagrams in panel (c) of Figure 2). The latter are specific for atoms with several valence electrons. The number of the two-electron diagrams is very large and their calculation is exceedingly time-consuming. In higher orders, the calculation of two-electron diagrams becomes impractical: we rather account for the high orders of MBPT indirectly. One of such methods was suggested in Kozlov and Porsev (1999a), where it was shown that a proper choice of the optimum initial approximation for the effective Hamiltonian substantially improves the agreement between calculated and experimental spectra of a multielectron atom. In this approach, one introduces an empirical energy shift δ and makes a replacement in self-energy operator $\Sigma(E) \longrightarrow \Sigma(E-\delta)$. This leads to equation

$$H_{\text{eff}}(E_n - \delta)|\Psi_n\rangle = E_n|\Psi_n\rangle.$$

By solving this equation with different values of δ, we obtain parametric dependence of eigenenergies, $E_n(\delta)$. Choice $\delta = 0$ recovers the Brillouin–Wigner variant of MBPT, and the Rayleigh–Schrödinger flavor of MBPT corresponds to $\delta = E_n - E_n^{(0)}$, where $E_n^{(0)}$ is the zero-order energy

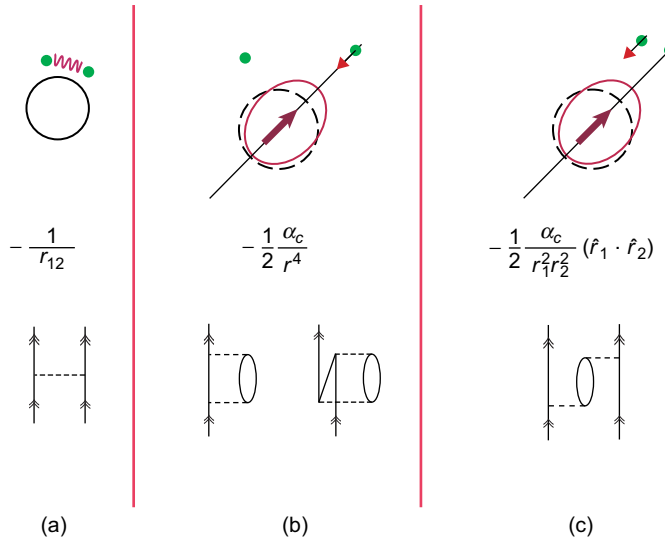

Figure 2 Major correlation effects for the divalent atoms. Panel (a): strong repulsion between the two valence electrons. Panel (b): self-induced (or self-energy) core-polarization attraction. Panel (c) cross-induced (or screening) core-polarization effect. We depict two valence electrons as dots above the closed shell core. Polarization of the core by the electrons is shown as deformation of the core with the heavy arrow showing the direction of the polarization. The induced dipole field causes attraction of either perturbing (panel (b)) or spectator (panel (c)) electron. The formulas below the sketches represent an approximation characteristic of model potential treatments, α_c being core polarizability and r_1 and r_2 being coordinates of the valence electrons. Their many-body analogs are represented by the Brueckner–Goldstone diagrams in the lower part of the figure.

of the level n. For few electron systems an intermediate value of δ is optimal. This optimal value can be found by fitting computed energy levels to experimental spectra.

As an example, in Table 2, we present numerical results for the low-lying energy levels of the atomic Sr. The results are tabulated for both pure two-electron CI and CI + MBPT method. As seen from the table, the two-electron binding energies are reproduced very well. Already at the CI stage, an agreement of the calculated and experimental energies is on the level of 5%. Additional incorporation of MBPT corrections allows us to improve the accuracy by approximately an order of magnitude, and the use of the optimal value of δ improves the accuracy further to ~0.1%–0.2%.

After the optimized effective Hamiltonian is constructed, we find wave functions of the ground and the low-lying excited states. With these wave functions, we may compute other observables such as hyperfine structure

Table 2 Two-electron binding energies E_{val} in atomic units and energy differences between a state and the ground state Δ in cm^{-1} for low-lying levels of Sr (Porsev et al., 2001).

		CI		CI + MBPT		Experiment (Moore, 1971)	
Configuration	Level	E_{val}	Δ	E_{val}	Δ	E_{val}	Δ
$5s^2$	$^1S_0$	0.586538	—	0.614409[1]	—	0.614601[2]	—
$5s4d$	$^3D_1$	0.497148	19619	0.532110	18063	0.531862	18159.1
$5s4d$	$^3D_2$	0.497077	19635	0.531809	18129	0.531590	18218.8
$5s4d$	$^3D_3$	0.496941	19664	0.531298	18242	0.531132	18319.3
$5s4d$	$^1D_2$	0.494339	20235	0.522311	20213	0.522792	20149.7
$5s6s$	$^3S_1$	0.460940	27566	0.481533	29162	0.482291	29038.8
$5s\,5p$	$^3P_0$	0.529636	12489	0.548754	14410	0.549366	14317.5
$5s5p$	$^3P_1$	0.528850	12662	0.547896	14598	0.548514	14504.4
$5s5p$	$^3P_2$	0.527213	13021	0.546079	14997	0.546718	14898.6
$5s5p$	$^1P_1$	0.491616	20833	0.515901	21621	0.515736	21698.5

[1]This value is obtained with $\delta = -0.3$ a.u.
[2]For the ground state, E_{val} = IP (Sr) + IP (Sr^+), where ionization potential (IP) for Sr = 45925.6 cm^{-1} and IP (Sr^+) = 88964.0 cm^{-1} (Moore, 1971).

constants, $E1$ transition amplitudes, and polarizabilities. For calculation of the matrix elements, we apply the technique of effective all-order ("dressed") operators. Technically, we employ the random-phase approximation (RPA). The RPA sequence of diagrams describes a shielding of externally applied field by the core electrons. We additionally incorporate the following smaller corrections: Brueckner corrections to core orbitals, subtraction and two-particle diagrams, structural radiation and normalization corrections. Detailed discussion of these corrections may be found elsewhere (Kozlov et al., 2001a).

To demonstrate the quality of the constructed wave functions and the accuracy of the effective-operator approach, we present in Tables 3 and 4 the calculated magnetic-dipole hyperfine structure constants A for the $^3P_{1,2}$ states and the reduced matrix elements $\langle ns^2\ ^1S_0||D||nsnp\ ^{3,1}P_1\rangle$ of the electric-dipole operator D for the transitions from the low-lying odd-parity $^{3,1}P_1$ states to the ground state (Porsev et al., 2001). As seen from Table 3, the differences between computed and experimental values for the constants A, even for heavy Yb, do not exceed 1%. For the heaviest and more computationally demanding Yb, the corrections to the effective hyperfine operator tend to cancel (Porsev et al., 1999a), and we simplify the calculations for Yb by using bare operators (no RPA "dressing").

The results presented in Table 4 illustrate an increasing importance of correlations when progressing from lighter to heavier atoms. For heavier atoms, MBPT corrections to matrix elements grow larger, and as

Table 3 Magnetic-dipole hyperfine structure constants A for the $nsnp\ ^3P_1$ and $nsnp\ ^3P_2$ states. The computed CI + MBPT values (Porsev & Derevianko, 2004) are compared with the experimental data.

		$A(^3P_1)$ (MHz)	$A(^3P_2)$ (MHz)
^{25}Mg	CI + MBPT	−146.1	−129.7
	Experiment	−144.977(5)[1]	−128.445(5)[1]
^{43}Ca	CI + MBPT	−199.2	−173.1
	Experiment	−198.890(1)[2]	−171.962(2)[3]
^{87}Sr	CI + MBPT	−258.7	−211.4
	Experiment	−260.083(5)[4]	−212.765(1)[4]
^{171}Yb	CI + MBPT	3964	2704
	Experiment	3957.97(47)[5]	2677.6[6]
^{173}Yb	CI + MBPT	−1092	−745
	Experiment	−1094.20(60)[5]	737.7[6]

[1]Lurio (1962), [2]Arnold et al. (1981), [3]Grundevik et al. (1979), [4]Heider and Brink (1977), [5]Clark et al. (1979), [6]Budick and Snir (1969).

Table 4 Reduced matrix elements for transitions from the low-lying $nsnp\ ^{3,1}P_1$ states to the ground $ns^2\ ^1S_0$ state are presented in atomic units. The computed values are compared with the experimental data.

	$\lvert\langle ns^2\ ^1S_0 \lvert\lvert D \rvert\rvert nsnp\ ^3P_1\rangle\rvert$		$\lvert\langle ns^2\ ^1S_0 \lvert\lvert D \rvert\rvert nsnp\ ^1P_1\rangle\rvert$	
	CI + MBPT	Experiment	CI + MBPT	Experiment
Mg	0.0064(7)[1]	0.0053(3)[2]	4.03(2)[1]	4.12(6)[3]
		0.0056(4)[4]		4.06(10)[5]
Ca	0.034(4)[1]	0.0357(4)[6]	4.91(7)[1]	4.905(22)[7]
		0.0352(10)[8]		
Sr	0.160(15)[1]	0.1555(16)[9]	5.28(9)[1]	5.249(2)[10]
Yb	0.54(8)[11]	0.549(4)[12]	4.4(8)[11]	4.148(2)[13]

[1]Porsev et al. (2001), [2]Godone and Novero (1992), [3]Smith and Gallagher (1966), [4]Kwong et al. (1982), [5]Lundin et al. (1973), [6]Husain and Roberts (1986), [7]Degenhardt et al. (2003), [8]Drozdowski et al. (1997), [9]Husain and Schifino (1984), [10]Yasuda et al. (2006), [11]Porsev et al. (1999b), [12]Bowers et al. (1999), [13]Takasu et al. (2004).

a result, the accuracy of calculations becomes worse. For example, for the $\langle ns^2\ ^1S_0||D||nsnp\ ^1P_1\rangle$ electric-dipole matrix element, the accuracy of the CI + MBPT method is 0.5% for Mg but only 18% for Yb. In the work of Savukov and Johnson (2002), a similar relativistic approach was used for calculating $E1$ transition amplitudes for divalent atoms, and the obtained results are in a fair agreement with our results (Porsev et al., 2001).

Poor accuracy for Yb is hardly surprising because we fully account for only the second order of the perturbation theory. For heavy atoms, higher orders of MBPT play a significant role. In case of Yb, the state $6s6p\ ^1P_1$ requires special attention. As noted in Porsev et al. (2001), the nearby $f^{13}5d6s^2$ core-excited state of the same symmetry lies only 3800 cm^{-1} above this state and their interaction is not negligible. The resulting admixture of the configuration $f^{13}5d6s^2$ to the $6s6p\ ^1P_1$ state is on the level of several percent, therby noticeably influencing the magnitude of the matrix element $\langle 6s^2\ ^1S_0||D||6s6p\ ^1P_1\rangle$ in Yb. This problem was discussed in detail in a recent paper by Dzuba and Derevianko (2010).

2.2 Sternheimer–Dalgarno–Lewis Method

A generic problem encountered in evaluating atomic properties relevant to lattice clocks is a computation of second-order sums over a complete set of atomic many-body states. One of such properties is the dynamic polarizability of atomic states entering Stark shift of atomic levels in the laser field. Directly determining the complete set of CI + MBPT many-body states needed for summations is impractical for divalent atoms. It is more convenient to lump contributions of the intermediate states into a single "perturbed" state. This method is conventionally referred to as the Sternheimer–Dalgarno–Lewis method (Dalgarno & Lewis, 1955; Sternheimer, 1950). Below we recapitulate the main features of this method, its implementation in the CI + MBPT framework, and illustrate the technique by computing static polarizabilities of divalent atoms. Computed static polarizabilities are relevant to evaluating blackbody radiation shifts, see Section 7.

We would like to evaluate a second-order sum $\mathcal{F}$ that depends on matrix elements of operators $\mathcal{A}$ and $\mathcal{B}$,

$$\mathcal{F} = \sum_k \frac{\langle\Psi_0|\mathcal{A}|\Psi_k\rangle\langle\Psi_k|\mathcal{B}|\Psi_0\rangle}{E_k - E_0}. \tag{2}$$

The states Ψ_k are the eigenfunctions of the atomic Hamiltonian, H, with energies E_k. Instead of direct summation over the intermediate states, one can find an intermediate-state "lumped" wave function $|\delta\Psi\rangle$ from an inhomogeneous equation

$$(H - E_0)|\delta\Psi\rangle = \sum_k |\Psi_k\rangle\langle\Psi_k|\mathcal{B}|\Psi_0\rangle = \mathcal{B}|\Psi_0\rangle. \tag{3}$$

With the computed $|\delta\Psi\rangle$, the quantity of interest, Equation (2), is obtained simply as

$$\mathcal{F} = \langle\Psi_0|\mathcal{A}|\delta\Psi\rangle. \tag{4}$$

This approach is generalized in a straightforward way to higher orders of the perturbation theory, i.e., when Equation (2) includes more than two operators and several summations over intermediate states.

To illustrate an application of the Sternheimer–Dalgarno–Lewis method in the CI + MBPT, in Table 5, we present our numerical results for the static scalar electric-dipole polarizabilities of the $ns^2\,{}^1S_0$ and $nsnp\,{}^3P_0$ clock states. Details of calculations may be found in Porsev and Derevianko (2006b) and Dzuba and Derevianko (2010). Here we only briefly describe the main points. In the framework of the CI + MBPT method, all electronic orbitals are separated into two groups: valence and core orbitals. Accordingly, intermediate states in Equation (2) can be separated into valence-excited states and core-excited states. The first group of states is generated when promoting valence electrons to other valence shells. As a result, the intermediate state remains in the model (CI) space of the effective Hamiltonian, Equation (1). The second group of states, in addition, involves real excitations from the core orbitals. These excitations necessarily live in the space complementary to the model space.

Static scalar electric-dipole polarizability of atomic state $|\Psi_0\rangle$ of the total angular momentum $J = 0$ may be expressed as

$$\alpha_0^{(E1)}(0) = 2\sum_k \frac{\langle\Psi_0|D_0|\Psi_k\rangle\langle\Psi_k|D_0|\Psi_0\rangle}{E_k - E_0}, \tag{5}$$

where D_0 is the z-component of the operator of the electric-dipole moment. Apparently, the polarizability may be computed with the help of Equations (2)–(4) with $\mathcal{A} = \mathcal{B} \equiv D_0$. For brevity in this subsection, we denote $\alpha \equiv \alpha_0^{(E1)}(0)$.

Following the approach suggested in Derevianko et al. (1999), we decompose the polarizability, Equation (5), into three parts

$$\alpha = \alpha_v + \alpha_c + \alpha_{cv}. \tag{6}$$

Table 5 Static electric-dipole polarizabilities (in a.u.) for the ground $^1S_0$ and the lowest-energy $^3P_0$ excited states of Mg, Ca, Sr, and Yb atoms. Theoretical uncertainties are indicated in parentheses.

	Mg[1]	Ca[1]	Sr[1]	Yb[2]
$\alpha_{^1S_0}$	71.3(7)	157.1(1.3)	197.2(2)	141(6)
$\alpha_{^3P_0}$	101.2(3)	290.3(1.5)	458.3(3.6)	302(14)

[1] Porsev and Derevianko (2006b), [2] Dzuba and Derevianko (2010).

Here α_v encapsulates contribution of intermediate states characterized by excitations of valence electrons within the model two-electron space, α_c involves core-excited intermediate states (i.e., states outside the model space), and α_{cv} is the so-called "Pauli-principle corrective term" related to details of computational scheme (see below).

The valence part, α_v, is the dominant contribution to the polarizability. Once the wave functions of the valence electrons $|\Psi_0\rangle$ are found from the eigenvalue equation, Equation (1), α_v are computed with the formally exact Sternheimer–Dalgarno–Lewis method implemented in the CI + MBPT framework. From Equation (3) we find

$$|\delta\Psi\rangle = \frac{1}{H_{\text{eff}} - E_0} \sum_k |\Psi_k\rangle\langle\Psi_k|D_0|\Psi_0\rangle = \frac{1}{H_{\text{eff}} - E_0} D_0|\Psi_0\rangle, \tag{7}$$

and finally, obtain the valence part of the polarizability,

$$\alpha_v = 2\,\langle\Psi_0|D_0|\delta\Psi\rangle. \tag{8}$$

The contribution of core-excited states to the polarizability, α_c, has to be added separately. Here we follow the approach of Derevianko et al. (1999) and use the relativistic random-phase approximation (Johnson, 1988) to determine the core polarizability as

$$\alpha_c = \sum_{\omega_\mu > 0} \frac{f_\mu}{\omega_\mu^2}. \tag{9}$$

Here the summation is over particle-hole excitations from the ground state of the atomic core; ω_μ are excitation energies and f_μ are the corresponding electric-dipole oscillator strengths. Accounting for core excitations is essential in our accurate calculations, especially for heavier atoms.

Finally, a small counter term α_{cv} is related to excitations of core electrons to occupied valence orbitals. Because we include the Pauli-principle-forbidden excitations in the calculations of core polarizabilities, we have to introduce this counter term.

Table 5 summarizes our numerical results for the static scalar electric polarizabilities. First, we discuss the results for the ground-state polarizabilities. Values for Mg, Ca, and Sr were obtained in Porsev and Derevianko (2006a). To estimate their uncertainties, we notice that the intermediate state $nsnp\,^1P_1$ contributes to the polarizability of the ground $ns^2\,^1S_0$ state at the level of 95%–97%. Taking this into account, we can single out this contribution to Equation (5) and rewrite α_v as the sum of two terms

$$\alpha_v = \alpha_v^p + \alpha_{v'}, \tag{10}$$

where

$$\alpha_v^p \equiv 2\,\frac{|\langle nsnp\,{}^1P_1|D_0|ns^2\,{}^1S_0\rangle|^2}{E_{^1P_1}-E_{^1S_0}}, \tag{11}$$

and $\alpha_{v'}$ includes all the other terms in Equation (5).

For calculating the dominant contribution α_v^p, we employ the most accurate literature values of the reduced matrix elements $\langle ns^2\,{}^1S_0||D||nsnp\,{}^1P_1\rangle$ tabulated in Porsev and Derevianko (2006a). For instance, for Sr, this matrix element was obtained from a high-precision measurement of the lifetime of the $5s5p\,{}^1P_1$ state (Yasuda et al., 2006): $|\langle 5s^2\,{}^1S_0||D||5s5p\,{}^1P_1\rangle| = 5.249(2)$ a.u. leading to the 0.1% uncertainty in $\alpha_v({}^1S_0)$. Contribution of the core corrections to the polarizability for this case ($\alpha_c + \alpha_{cv} = 5.4$ a.u. [Porsev & Derevianko, 2006a]) is less than 3%. Because the uncertainty of the latter can be roughly estimated as 1% (Porsev & Derevianko, 2002), the final uncertainty of the polarizability α is at the level of 0.1%. The uncertainties in the remaining polarizabilities were estimated as one half of the difference between two predictions obtained with $\delta = 0$ and with δ determined with the best fit to the experimental energies (thus mimicking omitted higher order many-body corrections).

The polarizabilities of the ${}^1S_0$ and ${}^3P_0$ states for Yb can be found with the very same technique as for Sr, but their calculation is more involved. In particular, accurate calculation of the ground-state polarizability have to account for contributions of the $(4f^{13}\,5d_{5/2}6s^2, J = 1)$ and $(6s6p\,{}^1P_1)$ states. The details of this evaluation can be found in Dzuba and Derevianko (2010). Finally, the uncertainties in the ground-state polarizabilities range from 0.1% for Sr to 4% for Yb.

For the ${}^3P_0$ states, the uncertainties range from 0.3% for Mg to 5% for Yb. Unlike the case of the ground state, the polarizability of the ${}^3P_0$ states is accumulated because of several transitions: the lowest energy ${}^3D_1$ states contribute only at the level of 50%–60%. Generally, the accuracy of the calculations becomes worse for heavier atoms. This follows the general trend of many-body calculations, where the correlations, and thus the omitted higher orders of perturbation theory, become increasingly important as the number of electrons grows. The results presented in Table 5 for the ground states of divalent atoms are in good agreement with other calculations (see, e.g., Mitroy & Bromley [2003]; Patil [2000]) and with experimental results of Degenhardt et al. (2003) and Lundin et al. (1973). Unfortunately, the existing experiments are not sufficiently accurate to test our predictions.

In this section, we briefly described the main features of the CI + MBPT method that couples the configuration interaction technique with the many-body perturbation theory. We presented the results of

calculations of different quantities (energies of the low-lying levels for Sr, hyperfine structure constants, and $E1$ transition amplitudes for divalent atoms) in the CI + MBPT framework. We also discussed evaluation of sums over a complete set of intermediate states using the Sternheimer–Dalgarno–Lewis method and random-phase approximation. We illustrated this technique by evaluating the static scalar electric-dipole polarizabilities of the clock states for Mg, Ca, Sr, and Yb. In general, we find that the CI + MBPT approach is capable of reliably and accurately predicting a wide variety of experimental observables, ranging from hyperfine constants to lifetimes and energies.

3. MAGIC WAVELENGTH

Armed with the accurate CI + MBPT atomic structure toolbox, in the following sections, we evaluate optical lattice clock–related parameters. In the optical lattice clocks, the atoms are confined to sites of an optical lattice (formed by a standing-wave laser field). We start off with analyzing the quantity central to the Stark-free spectroscopy: a specific choice of the wavelength of the lattice laser. At a certain, "magic", value of the wavelength, the laser-induced perturbations of both clock levels are identical and the atom responds spectroscopically as if it were placed in laser-free vacuum. The determination of the magic wavelength does not, fortunately, require magic: it involves computation of dynamic polarizabilities. Although usually knowing the dominant electric-dipole polarizability is sufficient, other (e.g., magnetic-dipole, electric-quadrupole, etc) polarizabilities may introduce additional corrections to the Stark shifts and affect values of the magic wavelength. Therefore, based on the Floquet approach and multipolar expansions, we derive in this section the general multipolar dynamic polarizabilities. Further, we illustrate the derived expressions by numerically determining the magic wavelength for ytterbium clock.

3.1 Second-Order Dynamic Response

In this section, we start with reviewing the formalism of quasi-energy states (Floquet formalism) and then apply it to deriving atomic properties relevant to the design of lattice clock. The Floquet formalism, as it applies to the atom-laser interaction, was reviewed, for example, by Manakov et al. (1986). One considers an interaction of a quantum system with a monochromatic perturbation

$$V(t) = v^{(-)}\mathrm{e}^{-i\omega t} + v^{(+)}\mathrm{e}^{+i\omega t}. \tag{12}$$

This perturbation drives a system characterized by the time-independent Hamiltonian H_0 and the "bare" eigenspectrum $\{\psi_a, E_a\}$, so that

$$H_0\psi_a = E_a\psi_a.$$

In the Floquet formalism, the entire Hamiltonian is replaced by

$$H \to H - i\frac{\partial}{\partial t},$$

and the inner product is extended to include the time-averaging over the period of the perturbation $T = 2\pi/\omega$,

$$\langle\langle\phi_i|\phi_k\rangle\rangle = \frac{1}{T}\int_0^T \langle\phi_i|\phi_k\rangle \mathrm{d}t, \tag{13}$$

$\langle\phi_i|\phi_k\rangle$ being the traditional inner product. In the lowest order, we deal with the "dressed" atomic states

$$\phi_{a,k} = \psi_a \mathrm{e}^{ik\omega t},\ k = 0, \pm1, \pm2, \ldots \tag{14}$$

$$E_{a,k} = E_a + k\omega, \tag{15}$$

where the functions $\phi_{a,k}$ satisfy the modified Schrodinger equation

$$\left(H_0 - i\frac{\partial}{\partial t}\right)\phi_{a,k} = E_{a,k}\phi_{a,k}.$$

Since the time derivative is already incorporated in the formalism, one may show that the expressions from the stationary perturbation theory may be employed to describe the response to the monochromatic $V(t)$. In the "upgraded" expressions, all the "bare" eigenfunctions and energies are replaced by their "dressed" counterparts and the inner products are extended according to the prescription (13). For example, the lowest order correction reads

$$E_a^{(1)} = \langle\langle\phi_{a,0}|V|\phi_{a,0}\rangle\rangle.$$

This correction vanishes for the electric-dipole interactions and the atomic states of definite parity. The second-order expression, however, is nonzero and will be of particular interest to us

$$E_a^{(2)} = \sum_{b,k} \frac{\langle\langle\phi_{a,0}|V|\phi_{b,k}\rangle\rangle\langle\langle\phi_{b,k}|V|\phi_{a,0}\rangle\rangle}{E_a - E_{b,k}}.$$

Explicit evaluation of the extended inner products limits the sums to single-photon transitions ($k = \pm 1$) leading to the familiar result

$$E_a^{(2)} = \sum_b \frac{\left|\langle\psi_a|v^{(+)}|\psi_b\rangle\right|^2}{E_a - (E_b - \omega)} + \sum_b \frac{\left|\langle\psi_a|v^{(-)}|\psi_b\rangle\right|^2}{E_a - (E_b + \omega)}. \tag{16}$$

Although the above second-order result can be recovered in the more traditional secular approximation (see, e.g., Section 7) of the time-dependent perturbation theory, the advantage of the Floquet formalism is that one could employ the higher order expressions from the less complicated time-*independent* perturbation theory and readily derive corresponding high-order corrections (such as hyperpolarizability) to the energy shift in the oscillating fields. We will employ this technique for deriving hyperfine-induced light shifts in Section 5.

As a familiar example, consider perturbation by a linearly polarized electric field

$$V(t) \equiv V_{E1}(t) = -D_z \mathcal{E}_0 \cos\omega t = -\frac{1}{2} D_z \mathcal{E}_0 \left(e^{i\omega t} + e^{-i\omega t}\right),$$

where D_z is the component of the atomic electric-dipole moment along the electric field. By comparing with Equation (12), we identify $v^{(+)} = v^{(-)} = -D_z\mathcal{E}_0/2$, and from Equation (16), we immediately recover the well-known result

$$E_a^{(2)} = -\frac{1}{4}\mathcal{E}_0^2\, \alpha_a^{E1}(\omega), \tag{17}$$

$$\alpha_a^{E1}(\omega) = 2\sum_b \frac{E_b - E_a}{(E_b - E_a)^2 - \omega^2} |\langle\psi_a|D_z|\psi_b\rangle|^2, \tag{18}$$

with $\alpha_a^{E1}(\omega)$ being the dynamic (a.c.) electric-dipole polarizability of the state a.

3.2 Dynamic Multipolar Polarizabilities

Here we apply the Floquet formalism to derive the expressions for the dynamic multipolar polarizabilities. We use the relativistic approach. Incidentally, compared with the nonrelativistic treatment, the relativistic formulation leads to more concise derivations, as the couplings are linear in the vector potential. An interaction of an electron with the electromagnetic field reads (to unclutter notation, here we consider only a single electron, the generalization for the many-electron case being straightforward)

$$V = \boldsymbol{\alpha} \cdot \mathbf{A}(\mathbf{r}, t) - \Phi(\mathbf{r}, t),$$

where A and Φ are the magnetic and electric potentials, respectively and $\boldsymbol{\alpha}$ represents a collection of the conventionally defined Dirac matrices (Bjorken & Drell, 1964). For an electromagnetic wave in the transverse gauge (where $\Phi \equiv 0$), the perturbation reduces to $V = (\boldsymbol{\alpha} \cdot \mathbf{A})$ with the vector potential

$$\mathbf{A} = \frac{1}{2}\hat{\boldsymbol{\varepsilon}} A_0 \mathrm{e}^{i(\mathbf{k}\cdot\mathbf{r})}\mathrm{e}^{-i\omega t} + c.c.,$$

where $\hat{\boldsymbol{\varepsilon}}$ is the polarization vector (this may include circular and linear polarizations) and $c.c.$ stands for the complex conjugate. The amplitude A_0 is related to the laser intensity I as $I = \frac{\omega^2}{8\pi c}|A_0|^2$ and the corresponding amplitude of the electric field $\mathcal{E}_0 = A_0\omega/c$. The wavevector k (in atomic units) is given by $k = \omega/c = \alpha\,\omega$. We identify,

$$v^{(-)} = \frac{1}{2}A_0\left(\boldsymbol{\alpha}\cdot\hat{\boldsymbol{\varepsilon}}\right)\mathrm{e}^{i(\mathbf{k}\cdot\mathbf{r})}, \quad v^{(+)} = \frac{1}{2}A_0\left(\boldsymbol{\alpha}\cdot\hat{\boldsymbol{\varepsilon}}^*\right)\mathrm{e}^{-i(\mathbf{k}\cdot\mathbf{r})}.$$

3.2.1 Multipolar Expansion

At this point, we focus on multipolar fields. We will use the outlined multipolar formalism in this section and later in Section 7. The reader is referred to Berestetskii et al. (1982); Johnson et al. (1995) for additional details.

We make use of the multipolar expansion of $\boldsymbol{\varepsilon}\mathrm{e}^{i(\mathbf{k}\cdot\mathbf{r})}$ in vector spherical harmonics $\mathbf{Y}^{(\lambda)}_{JM}$ (Varshalovich et al., 1988)

$$\boldsymbol{\varepsilon}\mathrm{e}^{i(\mathbf{k}\cdot\mathbf{r})} = 4\pi\sum_{JM\lambda} i^{J-\lambda}\left(\mathbf{Y}^{(\lambda)}_{JM}\left(\hat{\mathbf{k}}\right)\cdot\hat{\boldsymbol{\varepsilon}}\right)\mathbf{a}^{(\lambda)}_{JM}(\mathbf{r}), \tag{19}$$

where $\lambda = 0$ is for magnetic (MJ) and $\lambda = 1$ is for electric (EJ) 2^J-polar amplitudes. Explicit expressions for the expansion amplitudes $\mathbf{a}^{(\lambda)}_{JM}(\mathbf{r})$ in terms of the spherical Bessel functions can be found in Johnson et al. (1995). Since no expansion is made in powers of $\mathbf{k}\cdot\mathbf{r}$, the retardation is built in into the formalism from the onset. We may introduce a similar multipolar expansion for the coupling

$$t(\omega, r) = \left(\boldsymbol{\alpha}\cdot\hat{\boldsymbol{\varepsilon}}\right)\mathrm{e}^{i\mathbf{k}\cdot\mathbf{r}} = 4\pi\sum_{JM\lambda} i^{J-\lambda}\left(\mathbf{Y}^{(\lambda)}_{JM}\left(\hat{\mathbf{k}}\right)\cdot\hat{\boldsymbol{\varepsilon}}\right)\tau^{(\lambda)}_{JM}, \tag{20}$$

where the tensors $\tau^{(\lambda)}_{JM} = \left(\boldsymbol{\alpha}\cdot\mathbf{a}^{(\lambda)}_{JM}(\mathbf{r})\right)$.

The irreducible tensor operators $\tau_{JM}^{(\lambda)}$ of rank J may be related to the conventional multipolar operators $q_{JM}^{(\lambda)}$ as

$$\tau_{JM}^{(\lambda)} = i(-1)^{\lambda+1}\left(\frac{(2J+1)\,(J+1)}{4\pi J}\right)^{1/2}\frac{k^J}{(2J+1)\,!!}\,q_{JM}^{(\lambda)}.$$

Relativistic expressions with retardation for matrix elements of $q_{JM}^{(\lambda)}$ can be found in Johnson et al. (1995). Neglecting retardation effects, $q_{JM}^{(1)}$ become the conventional frequency-independent EJ moments (in the length gauge)

$$q_{JM}^{(1)} \approx r^J C_{JM}\left(\hat{\mathbf{r}}\right),$$

where $C_{JM}\left(\hat{\mathbf{r}}\right)$ are the normalized spherical harmonics. In the case of magnetic-dipole transitions in the nonrelativistic limit,

$$q_{1M}^{(0)} \approx -\frac{\alpha}{2}\left(\mathbf{L}+2\mathbf{S}\right)_M.$$

This expression is essentially the nonrelativistic atomic magnetic moment $\boldsymbol{\mu} = -\mu_B(\mathbf{L}+2\mathbf{S})$, with the Bohr magneton $\mu_B = |e|\hbar/(2m_e c)$ expressed in the Gaussian/atomic units. Further, the retardation brings correction on the order of $(\alpha\omega)^2$ to these expressions, and it may be safely discarded for transitions between low-lying states of neutral systems. For example, neglecting retardation, for the E1 tensor

$$\tau_{1M}^{(1)} \approx i\frac{k}{\sqrt{6\pi}}D_M,$$

where $D_M \equiv q_{1M}^{(1)}$ are the spherical components of the traditional electric-dipole operator.

Now we turn our attention to the effect of the multipolar fields on the second-order shift of the atomic energy level

$$E_a^{(2)} = \frac{1}{4}A_0^2\left\{\sum_b \frac{|\langle\psi_b|t\,(\omega,r)\,|\psi_a\rangle|^2}{E_a-(E_b-\omega)} + \sum_b \frac{|\langle\psi_a|t\,(\omega,r)\,|\psi_b\rangle|^2}{E_a-(E_b+\omega)}\right\}. \qquad (21)$$

The problem can be solved in general by substituting the expansion of Equation (20) in the above expression. Because of our particular emphasis on the lattice clocks, we limit our consideration to spherically symmetric ($J_a = 0$) atoms. Then only the rotationally invariant (scalar) component is of relevance.

Below we demonstrate that various multipoles contribute to the light-shift of Equation (16) incoherently; $E_a^{(2)}$ may be represented as a sum over individual multipolar contributions. Indeed, a typical summation in Equation (16) reduces to

$$|\langle\psi_b|t\,(\omega,r)\,|\psi_a\rangle|^2 = (4\pi)^2 \sum_{JM\lambda} \frac{1}{(2J+1)} \delta_{Jj_b}\delta_{MM_b} \left|\mathbf{Y}_{JM}^{(\lambda)}\left(\hat{\mathbf{k}}\right)\cdot\hat{\boldsymbol{\varepsilon}}\right|^2 \left|\langle\psi_b||\tau_J^{(\lambda)}||\psi_a\rangle\right|^2,$$

where we used the Wigner–Eckart theorem. To simplify this expression further, we choose the z-axis along the wavevector $\mathbf{k}$ and fix the linear polarization along the x-axis ($\hat{\boldsymbol{\varepsilon}} = \hat{\mathbf{e}}_x$). The result for the scalar polarizability would not depend on the polarization direction. Then for $\lambda = 0, 1$, we arrive at $\mathbf{Y}_{JM}^{(\lambda)}\left(\hat{\mathbf{e}}_z\right)\cdot\hat{\mathbf{e}}_x = \sqrt{\frac{2J+1}{16\pi}}\left(\delta_{M,-1} + (-1)^\lambda\,\delta_{M,+1}\right)$. The final result may be represented as a sum over multipolar a.c. polarizabilities,

$$E_a^{(2)}\,(J_a = 0) = \frac{\mathcal{E}_0^2}{4}\sum_{J\lambda}\alpha_a^{(J\lambda)}\,(\omega)\,, \tag{22}$$

each being defined as

$$\alpha_a^{(J\lambda)}\,(\omega) = \frac{J+1}{J}\,\frac{k^{2J-2}}{[(2J-1)!!]^2}\sum_b \frac{E_a - E_b}{(E_a-E_b)^2-\omega^2}\left|\langle\psi_b|q_{J0}^{(\lambda)}|\psi_a\rangle\right|^2. \tag{23}$$

In the lattice clocks, the frequency of the lattice laser is chosen in such a way that the a.c. Stark shifts of the two clock levels are exactly the same ("magic" frequency). To the leading order, the E1 polarizability overwhelms the a.c. Stark shift, Equation (22). Compared with the E1 contribution, the higher order multipole polarizabilities are suppressed by a factor of $(\alpha\omega)^{2J-2}$ for EJ and by a factor of $\alpha^2(\alpha\omega)^{2J-2}$ for MJ multipoles. Nevertheless, the higher order multipolar a.c. shifts may modify the value of the magic frequency. From the general formula, Equation (23), we immediately obtain for the magnetic-dipole polarizability,

$$\alpha_a^{(M1)}\,(\omega) = 2\sum_b \frac{E_a - E_b}{(E_a-E_b)^2-\omega^2}\left|\langle\psi_b|q_{10}^{(0)}|\psi_a\rangle\right|^2, \tag{24}$$

and for the electric-quadrupole a.c. polarizability,

$$\alpha_a^{(E2)}\,(\omega) = \frac{1}{6}\,(\alpha\,\omega)^2\sum_b \frac{E_a - E_b}{(E_a-E_b)^2-\omega^2}\left|\langle\psi_b|q_{20}^{(1)}|\psi_a\rangle\right|^2. \tag{25}$$

3.3 Ytterbium Magic Wavelength

Now we illustrate the developed formalism by presenting numerical results for Yb lattice clock (Porsev et al., 2004). First, we compute the $E1$ a.c. polarizabilities, Equation (18), with the CI + MBPT method, as described in Section 2. The results of the calculations for both $6s^2\ ^1S_0$ and $6s6p\ ^3P_0$ states are shown in Figure 3. According to our calculations, the two dynamic polarizabilities intersect at the "magic" wavelength $\lambda_m \approx 752$ nm. This result is in a good agreement with the experimental value 759.25(2) nm obtained recently in Barber et al. (2006). It is worth noting that at ω_m, the sum (18) for the ground state is dominated by the $6s6p\ ^1P_1$ state and for the $6\ ^3P_0$ level by the $6s7s\ ^3S_1$ state. We estimate that the computed scalar a.c. polarizabilities are a few percent accurate.

We verified that at the magic frequency, there are no resonant contributions for the next-order $E2$ and $M1$ polarizabilities, and we expect $\alpha^{(E2,M1)} \lesssim 10^{-6}\alpha^{(E1)}$, similar to the case of Sr (Katori et al., 2003). At the same time, we notice that the core-excited state $4f^{13}(^2F_{7/2})5d_{5/2}6s^2\ J = 5$ may become resonant with an excitation from the $6\ ^3P_0$ level. The relevant $M5$ polarizability is highly suppressed, and we anticipate that the magic frequency will be only slightly shifted by the presence of this state.

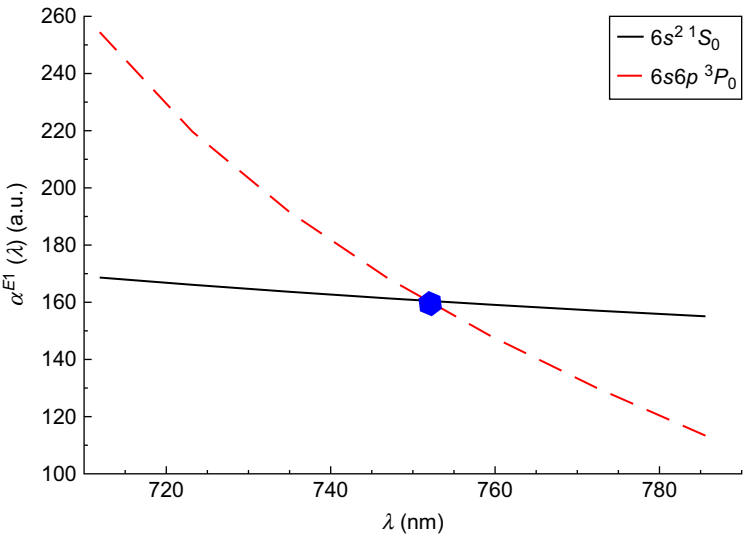

Figure 3 Electric-dipole a.c. polarizabilities for $6\ ^1S_0$ (solid line) and $6\ ^3P_0$ (dashed line) states of Yb. The polarizabilities are shown as a function of lattice laser wavelength λ. Crossing point of two polarizabilities yields the value of the magic wavelength.

Table 6 Magic wavelengths for the $^1S_0 - {}^3P_0$ clock transition in divalent atoms. The values of the magic wavelengths, λ_m, for Sr (Takamoto & Katori, 2003) and Yb (Barber et al., 2006) are experimental. The values for other atoms are the theoretical results (Derevianko et al., 2009).

atom	$\nu_{\rm clock}$ (Hz)	λ_m (nm)
Mg	6.55×10^{14}	466
Ca	4.54×10^{14}	739
Sr	4.29×10^{14}	813
Yb	5.18×10^{14}	759
Zn	9.69×10^{14}	416
Cd	9.03×10^{14}	419
Hg	11.3×10^{14}	362

Higher order correction to the a.c. Stark frequency shift arises because of terms quartic in the field strength $\mathcal{E}_0$. This fourth-order contribution is expressed in terms of the a.c. hyperpolarizability. The expression for hyperpolarizability (Manakov et al., 1986) has a complicated energy denominator structure exhibiting both single- and two-photon resonances. Although for the ground state there are no such resonances, for the $6\,{}^3P_0$, a two-photon resonance may occur for $6s8p\,{}^1P_1$ and $6s8p\,{}^3P_J$ intermediate states. We cannot predict if the two-photon resonances would occur, but the experiments (Barber et al., 2006) indicate that these are not an issue at least presently. For Sr (Katori et al., 2003), the hyperpolarizability shifts the energy levels by a few millihertz at a trapping laser intensity of 10 kW/cm^2.

3.4 Compilation of Magic Wavelengths

Calculations for other divalent atoms (Mg, Ca, Sr, Zn, Cd, and Hg) follow the same pattern as the Yb calculations of the previous section. These calculations were carried out in Derevianko et al. (2009). In Table 6, we compile these wavelengths.

4. HYPERFINE QUENCHING OF THE $^3P_0$ STATES

The lifetime of the $^3P_0$ state determines the natural width of the clock transition between the ground and the $^3P_0$ state. For all *bosonic* isotopes of divalent atoms, the nuclear spin I vanishes and these isotopes lack hyperfine structure. For bosonic isotopes, the $^3P_0$ state may decay only through very weak multiphoton transitions. However, for the *fermionic* isotopes, $I \neq 0$, a new radiative decay channel becomes available because of the

hyperfine interaction (HFI). The HFI admixes $J = 1$ atomic states, opening a fast E1 decay route. The resulting HFI-induced decays determine the lifetimes of the $^3P_0$ states and set the natural width of the clock transition.

Below we derive the hyperfine-induced decay rates for fermionic isotopes and compute the decay rates with the CI + MBPT method.

4.1 Derivation of Hyperfine Quenching Rates

In the presence of nuclear moments, the total electronic angular momentum J no longer remains a good quantum number. The atomic energy levels are characterized instead by the total angular momentum $\mathbf{F = J + I}$. We develop the formalism in terms of the hyperfine states $|\gamma(IJ)FM_F\rangle$. Here the angular momenta I and J are conventionally coupled to produce a state of definite total momentum F and its projection M_F, and γ encapsulates all other atomic quantum numbers. To the lowest order in the hyperfine interaction, $H_{\rm HFI}$, the correction to the hyperfine level $|\gamma(IJ)FM_F\rangle$ reads

$$|\gamma(IJ)FM_F\rangle^{(1)} = \sum_{\gamma' J'} |\gamma'(IJ')FM_F\rangle \frac{\langle\gamma'(IJ')FM_F|H_{\rm HFI}|\gamma(IJ)FM_F\rangle}{E(\gamma' J') - E(\gamma J)}, \qquad (26)$$

where $E(\gamma J)$ are the energies of atomic states.

In general, a nucleus may possess a number of magnetic and electric multipole moments. These moments couple to the internal atomic fields and give rise to the hyperfine structure. In this review, we are mainly concerned with the properties of the $J = 0$ clock states. For all the considered properties, only the magnetic-dipole moment of the nucleus, μ_I, is relevant (this comes from angular selection rules and more general analysis). The magnetic-dipole hyperfine Hamiltonian, $H_{\rm HFI}$, may be represented by a rotationally invariant expression

$$H_{\rm HFI} = \left(\mathcal{M}^{(1)} \cdot \mathcal{T}^{(1)}\right). \qquad (27)$$

Here $\mathcal{M}^{(1)}$ is the nuclear magnetic moment operator, with the nuclear moment defined as an expectation value of $\mathcal{M}^{(1)}$ in the stretched nuclear state

$$\mu_I \equiv \langle IM_I = I|\mathcal{M}^{(1)}_0|IM_I = I\rangle. \qquad (28)$$

We list the moments for the isotopes of interest in Table 1. The electronic part of the coupling for a point-like nucleus is given by

$$\mathcal{T}^{(1)}_\lambda = i\sqrt{2}\left(\boldsymbol{\alpha} \cdot \mathbf{C}^{(0)}_{1\lambda}\left(\hat{\mathbf{r}}\right)\right)/r^2, \qquad (29)$$

where $\mathbf{C}^{(0)}_{1\lambda}(\hat{\mathbf{r}}) = (4\pi/3)^{1/2}\,\mathbf{Y}^{(0)}_{1\lambda}(\hat{\mathbf{r}})$ is the normalized vector spherical harmonic (Varshalovich et al., 1988).

Using the Wigner–Eckart theorem, the matrix element of the hyperfine interaction in Equation (26) may be simplified to

$$\langle \gamma'\,(IJ')\,FM_F|H_{\rm HFI}|\gamma\,(IJ)\,FM_F\rangle = \delta_{FF'}\delta_{M_F M'_F} \times (-1)^{I+J'+F}\langle I\,||\mathcal{M}^{(1)}||\,I\rangle\langle n'J'||\mathcal{T}^{(1)}||nJ\rangle \begin{Bmatrix} I & I & 1 \\ J & J' & F \end{Bmatrix}. \tag{30}$$

Now we turn to the derivation of the hyperfine quenching rate. The rate of spontaneous emission for an E1 transition is given by the Fermi golden rule

$$A_{a\to b} = \frac{4\alpha^3}{3}\omega^3_{ab}\left|\langle a|\mathbf{D}|b\rangle\right|^2, \tag{31}$$

where $\omega_{ab} = E_a - E_b$ is the transition frequency. Summing over all possible momenta F_b and magnetic quantum numbers M_b of the final state, while disregarding small F-dependent energy correction, one obtains the rate

$$A_{a\to b} = \frac{4\alpha^3}{3}\,\omega^3_{ab}\,\frac{1}{2F_a+1}\sum_{F_b}\left|\langle a||D||b\rangle\right|^2. \tag{32}$$

For the case at hand, the initial state is the HFI-perturbed $nsnp\,^3P_0$ state decaying to the ground $ns^2\,^1S_0$ state. Taking into account Equation (26), we arrive at the hyperfine quenching rate

$$A_{\rm HFI}\left(nsnp\,^3P_0 \to ns^2\,^1S_0\right) = \frac{4\alpha^3}{27}\omega^3_0\mu_I^2\,\frac{I+1}{I}\left|\sum_{\gamma'}\frac{\langle ns^2\,^1S_0||D||\gamma'J'\rangle\langle\gamma'J'||\mathcal{T}^{(1)}||nsnp\,^3P_0\rangle}{E\,(\gamma'J') - E\left(nsnp\,^3P_0\right)}\right|^2. \tag{33}$$

Notice that because of the angular selection rules, the total electronic angular momentum of the intermediate states is limited to $J' = 1$.

4.2 Results and Conclusions

We carry out numerical evaluation of the HFI-induced rate, Equation (33), in several logical steps. First, we solve the CI + MBPT eigenvalue problem (see Section 2) and determine the ground and the $nsnp\,^3P_0$ state wave functions and energies. At the next step, we evaluate the sum over the intermediate states using the Sternheimer–Dalgarno–Lewis method, as discussed in Section 2.2.

The values of the sums over intermediate states grow larger for heavier atoms. This is because of increasing matrix elements of the hyperfine interaction (see Table 3). Further, a direct investigation of the sums shows that the contributions of both $nsnp\,^3P_1$ and $nsnp\,^1P_1$ intermediate states are comparable. Qualitatively, the triplet state is separated from the metastable states by a small fine-structure interval, but its E1 matrix element with the singlet ground state vanishes nonrelativistically. For the singlet state, the situation is reversed; compared with the triplet contribution, the involved energy denominator is much larger, but the electric-dipole matrix element is allowed.

In Table 7, we present our ab initio relativistic CI + MBPT results for the transition rates. Based on a better than 1% accuracy of the ab initio hyperfine constants (Table 3) and energy levels (Porsev et al., 2001, 1999a), we expect that the computed hyperfine quenching rate is accurate within at least a few percent. In Table 7, the CI + MBPT values are also compared with the results from the literature. For Mg, the hyperfine quenching rates for the $^3P_0$ state were estimated more than four decades ago by Garstang (1962) (this was motivated by astrophysical applications). Our result is in a reasonable agreement with his values and with previous, less complete, estimates for ^{87}Sr (Katori et al., 2003) and Yb isotopes (Porsev et al., 2004).

It is worth mentioning one more process that can potentially lead to a shortening of lifetimes of the metastable states. As demonstrated by Yasuda and Katori (2004), the blackbody radiation (BBR) induced decay rate of the $5s5p\,^3P_2$ state for Sr is equal to 8.03×10^{-3} s^{-1} at 300 K. Our order-of-magnitude estimate of the BBR quenching for Mg, Ca, and Yb shows that at room temperature ($T = 300$ K), the BBR quenching is negligible compared with the rates caused by the vacuum fluctuations of the electromagnetic field ($T = 0$). The reader, however, should be cautioned that the BBR rate strongly depends on the ambient temperature and it may become important, for example, if a hot oven is used as a source of atoms.

Table 7 The hyperfine E1-quenching rates for the metastable $^3P_0$ states in sec^{-1}. The rates are compared with values from the literature. Our CI + MBPT results were previously published in (Porsev & Derevianko, 2004). The notation $y[x]$ means $y \times 10^x$.

Atom	F	CI + MBPT	Other
^{25}Mg	5/2	4.44[−4]	4.2[−4][1]
^{43}Ca	7/2	2.22[−3]	
^{87}Sr	9/2	7.58[−3]	6.3[−3][2]
^{171}Yb	1/2	4.35[−2]	5.0[−2][3]
^{173}Yb	5/2	3.85[−2]	4.3[−2][3]

[1]Garstang (1962), [2]Katori et al. (2003), [3]Porsev et al. (2004).

To summarize the main results of this section, the resulting natural widths of the $^3P_0 - {}^1S_0$ clock transition are 0.44 mHz for ^{25}Mg, 2.2 mHz for ^{43}Ca, 7.6 mHz for ^{87}Sr, 43.5 mHz for ^{171}Yb, and 38.5 mHz for ^{173}Yb. These narrow widths translate into the high-resonance quality factors characteristic of the lattice-based optical clocks.

5. HYPERFINE-INDUCED VECTOR LIGHT SHIFT IN THE $^3P_0$ STATE

The second-order light shift involves two interactions with the laser field. The product of two interactions $(D \cdot \mathcal{E})(D \cdot \mathcal{E}^*)$ may be recoupled into the scalar, vector (axial), and tensor components of the dynamic polarizability (these are irreducible tensors of rank 0, 1, and 2 acting in the electronic space). Because of the angular selection rules, for the $J = 0$ clock states, only the scalar polarizability is of relevance and it was the focus of our discussion in Section 3. The hyperfine interaction, nevertheless, removes the spherical symmetry of the atoms and leads to residual vector, $\alpha^A_{\gamma F}(\omega)$, and tensor, $\alpha^T_{\gamma F}(\omega)$ a.c., polarizabilities. These may affect the performance of the clock: the vector light shift may cause a small Stark-shift dependence on the polarization of the trapping light.

To determine the effect of the HFI on the a.c. polarizability, we carry out an analysis in the third-order perturbation theory. We apply the Floquet formalism (Section 3.1) with respect to a combined operator

$$V = V_{\rm HFI} + V_{E1}(t)\,.$$

The third-order energy shift of the atomic energy level reads

$$E_a^{(3)} = \sum_{b,c\neq a} \frac{V_{ab}V_{bc}V_{ca}}{\left(E_b^{(0)} - E_a^{(0)}\right)\left(E_c^{(0)} - E_a^{(0)}\right)} - V_{aa}\sum_{b\neq a}\frac{V_{ab}V_{ba}}{\left(E_b^{(0)} - E_a^{(0)}\right)^2},$$

where matrix elements are evaluated with respect to the dressed basis and inner products involve time-averaging. The relevant terms (involving two E1 laser-atom interactions and one HFI coupling) are

$$E_a^{(3)} = \sum_{b,c\neq a} \frac{(V_{\rm HFI})_{ab}(V_{E1})_{bc}(V_{E1})_{ca}}{\left(E_b^{(0)} - E_a^{(0)}\right)\left(E_c^{(0)} - E_a^{(0)}\right)} + \sum_{b,c\neq a} \frac{(V_{E1})_{ab}(V_{\rm HFI})_{bc}(V_{E1})_{ca}}{\left(E_b^{(0)} - E_a^{(0)}\right)\left(E_c^{(0)} - E_a^{(0)}\right)}$$
$$+ \sum_{b,c\neq a} \frac{(V_{E1})_{ab}(V_{E1})_{bc}(V_{\rm HFI})_{ca}}{\left(E_b^{(0)} - E_a^{(0)}\right)\left(E_c^{(0)} - E_a^{(0)}\right)} - (V_{\rm HFI})_{aa}\sum_{b\neq a}\frac{(V_{E1})_{ab}(V_{E1})_{ba}}{\left(E_b^{(0)} - E_a^{(0)}\right)^2}.$$

Notice that we work in the dressed atom picture, i.e., the states a, b, c are products of atomic and photonic states. Also $(V_{E1})_{aa} = 0$ because of the

parity/angular/photon number selection rules leading to a simplification of the last term. Explicitly, after the time averaging, Equation (13), (now a, b, c are the "bare" atomic states and the matrix elements are computed using the traditional inner products)

$$
\begin{aligned}
E_a^{(3)}(\omega) &= T_a(\omega) + C_a(\omega) + B_a(\omega) + O_a(\omega),\\
T_a(\omega) &= \sum_{b,c\neq a} \frac{(V_{\mathrm{HFI}})_{ab}\, v_{bc}^{(+)} v_{ca}^{(-)}}{\left(E_b^{(0)} - E_a^{(0)}\right)\left(E_c^{(0)} - \omega - E_a^{(0)}\right)}\\
&\quad + \sum_{b,c\neq a} \frac{(V_{\mathrm{HFI}})_{ab}\, v_{bc}^{(-)} v_{ca}^{(+)}}{\left(E_b^{(0)} - E_a^{(0)}\right)\left(E_c^{(0)} + \omega - E_a^{(0)}\right)},\\
C_a(\omega) &= \sum_{b,c\neq a} \frac{v_{ab}^{(+)}\,(V_{\mathrm{HFI}})_{bc}\, v_{ca}^{(-)}}{\left(E_b^{(0)} - \omega - E_a^{(0)}\right)\left(E_c^{(0)} - \omega - E_a^{(0)}\right)}\\
&\quad + \sum_{b,c\neq a} \frac{v_{ab}^{(-)}\,(V_{\mathrm{HFI}})_{bc}\, v_{ca}^{(+)}}{\left(E_b^{(0)} + \omega - E_a^{(0)}\right)\left(E_c^{(0)} + \omega - E_a^{(0)}\right)},\\
B_a(\omega) &= \left[T_a(\omega)\right]^*,\\
O_a(\omega) &= -(V_{\mathrm{HFI}})_{aa} \sum_{b\neq a} \frac{v_{ab}^{(+)} v_{ba}^{(-)}}{\left(E_b^{(0)} - \omega - E_a^{(0)}\right)^2}\\
&\quad - (V_{\mathrm{HFI}})_{aa} \sum_{b\neq a} \frac{v_{ab}^{(-)} v_{ba}^{(+)}}{\left(E_b^{(0)} + \omega - E_a^{(0)}\right)^2}.
\end{aligned}
$$

If we represent these contributions diagrammatically, then $T_a(\omega)$, $C_a(\omega)$, and $B_a(\omega)$ can be treated as the top, center, and bottom diagrams, respectively. The naming convention reflects the position of the HFI in the diagram. $O_a(\omega)$ combines other corrective terms; for the case at hand, the $O_a(\omega)$ term is irrelevant since the expectation value $(V_{\mathrm{HFI}})_{aa} = 0$ for $J = 0$ states.

We carry out the angular reduction of these diagrams. We find that the magnetic-dipole HFI does not bring in neither the scalar nor the tensor contribution: there is only the vector component of the a.c. polarizability. In principle, the tensor contribution to $J = 0$ polarizability might appear because of the electric-quadrupole moment of the nucleus; the strength of this interaction is typically two orders of magnitude smaller than that of the magnetic HFI and we neglect this effect. The final result simplified for the $J = 0$ states reads

$$
\delta E_a = -\left(\frac{1}{2}\mathcal{E}\right)^2 \mathcal{A}\, \alpha_{\gamma F}^{A}(\omega)\, \frac{M_F}{2I},
$$

M_F being the projection of F (i.e., the projection of the nuclear spin I for $J = 0$). The degree of the circular polarization is defined in terms of $\mathcal{A} = \sin 2\theta$ for an electromagnetic wave $\mathcal{E} = \mathcal{E}\mathbf{e}_x \cos\theta \cos(\omega t - kz) + \mathcal{E}\mathbf{e}_y \sin\theta \sin(\omega t - kz)$. The shift is expressed in terms of the vector polarizability

$$\alpha^A_{\gamma F}(\omega) = -\sqrt{\frac{2}{27}}\left\{C^{(1)}_{1,1}(\gamma J, \omega) + 2T^{(1)}_{1,1}(\gamma J, \omega)\right\},$$

where the dynamic reduced sums are expressed in terms of the reduced matrix elements of the dipole operator and the HFI coupling

$$T^{(K)}_{J',J''}(\gamma J, \omega) = \mu_I \sum_{\gamma'} \sum_{\gamma'' \neq \gamma} \langle \gamma J || \mathcal{T}^{(1)} || \gamma'' J'' \rangle \langle \gamma'' J'' || D || \gamma' J' \rangle \langle \gamma' J' || D || \gamma J \rangle \times \left(\frac{1}{E - E''} \frac{1}{E - E' + \omega} + (-1)^K (\omega \to -\omega) \right),$$

$$C^{(K)}_{J',J''}(\gamma J, \omega) = \mu_I \sum_{\gamma' \gamma''} \langle \gamma J || D || \gamma' J' \rangle \langle \gamma' J' || \mathcal{T}^{(1)} || \gamma'' J'' \rangle \langle \gamma'' J'' || D || \gamma J \rangle \times \left(\frac{1}{E - E' + \omega} \frac{1}{E - E'' + \omega} + (-1)^K (\omega \to -\omega) \right).$$

In these formulas, E is the energy of the state of interest. Notation $(-1)^K(\omega \to -\omega)$ means that the preceding term is multiplied by $(-1)^K$ and ω is replaced by $-\omega$. For $J = 0$, the selection rules require $J' = J'' = 1$ for both reduced sums.

Analyzing these expressions numerically in the CI + MBPT approach, we find that the vector polarizability of the $6\,^3P_0$ state of Yb is much larger than that for the ground state, as in the case of Sr (Katori et al., 2003). For Sr, Katori et al. (2003) estimated the vector polarizability by adding HFS correction to the energy levels of intermediate states. Our analysis is more complete and we find that the dominant effect is not because of corrections to the energy levels, but it is rather because of perturbation of the 6^3P_0 state by the HFS operator. The resulting values of $\alpha^A_{6^3P_0}(\omega^*)$ are -0.10 a.u. for ^{171}Yb and 0.075 a.u. for ^{173}Yb. Recently, the value $\alpha^A_{6^3P_0}(\omega^*)$ for ^{171}Yb was experimentally found to be -0.08 (Lemke et al., 2009) in very good agreement with the theoretical result. In practice, this translates to requiring $\mathcal{A} < 10^{-6}$ at laser intensities of 10 kW/cm^2 for keeping the induced clock shifts below the mHz level.

6. ZEEMAN EFFECT

When an atom is placed in the magnetic field, magnetic moments of its electrons and nuclei interact with the magnetic field, leading to the familiar Zeeman effect. The advantage of the $J = 0$ levels used in the lattice clocks is that because of their scalar nature, to the lowest order in the field strength, they are not Zeeman-shifted. However, if we include the nuclear spin into the analysis, the linear Zeeman shift does appear because the total angular momentum F no longer vanishes in general. Qualitatively, the linear Zeeman shift appears for $I \neq 0$ because of the nuclear magnetic moment. This moment contributes both directly (through the coupling of the magnetic moment with the B-field) and indirectly. The indirect contribution is because of the mechanism of the HFI mixing, which brings in contribution of $J \neq 0$ levels with a large electronic magnetic moment. The two corrections are of the same order of magnitude.

We will present the discussion in terms of the so-called Lande g-factors g_F. It is introduced by considering the lowest-order perturbation by a sufficiently weak B-field,

$$\delta E_{M_F} = \langle FM_F|H_B|FM_F\rangle = \mu_B\, g_F B\, M_F,$$

the direction of the B-field being chosen as the quantization axis.

The direct contribution of the nuclear moment to the atomic g-factor is well known, see e.g., Haken and Wolf (1994). For the $J = 0$ level, it simplifies to

$$\delta g^n_{F=I} = -\frac{1}{I}\left(\frac{m_e}{m_p}\right)\left(\frac{\mu_I}{\mu_N}\right)$$

and involves the ratio of the electron and proton masses. The ratio μ_I/μ_N is simply the nuclear magnetic moment expressed in nuclear magnetons. Notice that the textbook derivation of the above expression implies that the magnetic field acting on the nuclear magnetic moment is the same as the externally applied field. Generally, this is not the case, as the currents induced inside the atom by external fields tend to shield the fields. This effect is usually parameterized in terms of the shielding constant σ: $B_{\text{nuc}} = (1-\sigma)B_{\text{external}}$. Values for the shielding factors σ for closed shell are listed in Kolb et al. (1982), indicating that the $\delta g^n_{F=I}$ may be modified by as much as a few percent. The shielding depends on the electronic state and should be different for the two clock states. This parallels the "chemical shift" effect in nuclear magnetic resonance. We are not aware of evaluation of the shielding correction for any of the atoms of interest to the lattice clocks. Considering that even the early clock experiments (Boyd et al., 2006) were

able to measure the differential g-factors to a 0.5%-level accuracy, such calculations may become of relevance.

Now we turn to the indirect contribution of the nuclear magnetic moment to the atomic g-factor. We consider an atom placed in the uniform magnetic field $\mathbf{B}$. The vector potential because of this field $\mathbf{A} = (\mathbf{B} \times \mathbf{r})/2$ determines the coupling

$$H_B = (\boldsymbol{\alpha} \cdot \mathbf{A}) = \sum_\lambda (-1)^\lambda \mathcal{S}^{(1)}_\lambda B_{-\lambda},$$

with the irreducible tensor operator of rank 1 defined as

$$\mathcal{S}^{(1)}_\lambda = \frac{i}{\sqrt{2}} \left(\boldsymbol{\alpha} \cdot \mathbf{C}^{(0)}_{1\lambda}\left(\hat{\mathbf{r}}\right)\right).$$

Nonrelativistically, the interaction H_B reduces to

$$H^{(NR)}_B = \mu_B \, \mathbf{B} \cdot \left(\mathbf{L} + g_e \mathbf{S}\right), \tag{34}$$

where $g_e \approx 2.0023$ is the g-factor of the electron (the quoted value also includes radiative QED corrections, which are beyond the present consideration).

Neglecting coupling of the nuclear spin to the B-field, we obtain

$$g^e_F = \frac{1}{\mu_B M_F} \langle FM_F | \mathcal{S}^{(1)}_0 | FM_F \rangle.$$

Nonvanishing correction to the g-factor arises because of HFI-induced admixture to wave functions. This is the same mechanism that causes the $^3P_0$ state to decay radiatively (see Section 4). The first-order correction $|\,(IJ)\,; FM_F\rangle^{(1)}$ to the wave function is given by Equation (26), leading to the correction to the g-factor

$$\delta g^e_F \, \mu_B M_F = 2 \sum_{\gamma' J'} \frac{\langle \gamma\,(IJ)\,; FM_F | \mathcal{S}^{(1)}_0 | \gamma'\,(IJ')\,; FM_F \rangle \langle \gamma'\,(IJ')\,; FM_F | H_{\rm HFI} | \gamma\,(IJ)\,; FM_F \rangle}{E\,(\gamma' J') - E\,(\gamma J)}$$

When restricting the summation over intermediate states, we took into account the scalar character of $H_{\rm HFI}$. The operator $\mathcal{S}^{(1)}_\lambda$ involves only electronic degrees of freedom; this restricts the intermediate electronic

momentum to $|J-1| \le J' \le J+1$. For the $J=0$ state, $F=I$ and the nonvanishing HFI matrix element is

$$\langle (I,J=1)\ F\, M_F|H_{\rm HFI}|\,(I,J=0)\,FM_F\rangle = \left(\frac{\mu_I}{\mu_N}\right)\left(\frac{I+1}{3I}\right)^{1/2}\frac{\alpha}{2m_p}\langle \gamma' J'=1||\mathcal{T}^{(1)}||\gamma\, J=0\rangle.$$

The matrix elements of the interaction with the external B-field are most easily evaluated in the nonrelativistic approximation. The nonrelativistic operator is diagonal with respect to the radial part of the wave function, implying that the only intermediate state that would admix to the $nsnp\,^3P_0$ state is the state $nsnp\,^3P_1$ of the same fine-structure multiplet. This leads to

$$\delta g_F^e = -\frac{2\sqrt{2}}{3\,I}\,(g_e-1)\left(\frac{\mu_I}{\mu_N}\right)\frac{\alpha}{2m_p}\,\frac{\langle nsnp\,^3P_1||\mathcal{T}^{(1)}||nsnp\,^3P_0\rangle}{E\left(nsnp\,^3P_1\right)-E\left(nsnp\,^3P_0\right)}. \qquad (35)$$

While using this expression, one should be careful with the relative phase convention between the $^3P_1$ and $^3P_0$ states: both states are assumed to nominally arise from the traditional coupling of S and L to their respective J with the same radial part of the total wave function. We emphasize that Equation (35) was obtained using the nonrelativistic expression for the B-field coupling, Equation (34), whereas the relativistic calculations are required for the HFI coupling, which is primarily accumulated near the nucleus.

Now we carry out CI + MBPT numerical estimates for Yb. Here the CI + MBPT value of the HFI matrix element is $\frac{\alpha}{2m_p}\langle {}^3P_1||\mathcal{T}^{(1)}||{}^3P_0\rangle = 6522$ MHz , and the fine-structure splitting has the value of 703.6 cm^{-1}. Numerical results for the nuclear δg_F^n and the electronic δg_F^e corrections to the g-factor are given in Table 8. One should observe that both corrections are of a comparable size. When analyzing the *differential* g-factors for the clock transition, one should keep in mind that δg_F^n factors are essentially the same for the ground and the excited state (the only difference is because

Table 8 Lande g-factors for the $^3P_0$ state of fermionic isotopes of Yb. The values are from Porsev et al. (2004). δg_F^n are the nuclear and δg_F^e are the electronic corrections. The total δg is the sum of the two δg-factors.

Isotope	μ_I/μ_N	I	δg_F^e	δg_F^n	δg, Total
171	0.4919	1/2	-2.9×10^{-4}	-5.4×10^{-4}	-8.3×10^{-4}
173	−0.6776	5/2	7.9×10^{-5}	1.5×10^{-4}	2.3×10^{-4}

of the "chemical shift" for the two levels), whereas in the nonrelativistic approximation, the g_F^e of the ground state vanishes. The computed values imply that mHz shifts would be produced by μG magnetic fields. Fields can readily be calibrated and stabilized to this level using magnetic shielding.

7. BLACKBODY RADIATION SHIFT

Considering advantages of optical lattice clocks, here we investigate an important systematic effect of the blackbody radiation on the frequency of the $^3P_0 - {}^1S_0$ clock transition. The current SI definition of the second explicitly involves atomic clock operating at the absolute zero of temperature (Taylor, 2001). Although the present definition of the second is based on the microwave Cs clock, one may anticipate that the rapidly progressing optical lattice clocks may be used to redefine the unit of time in the future. Beyond the metrologically important BBR correction to the clock frequency, the BBR shifts also affect the error balance of the clocks: a nonuniform distribution of the temperature inside the clock chamber may lead to the effective broadening of the lines (Boyd et al., 2006; Takamoto et al., 2005).

Presently, the BBR is the leading source of systematic errors in the best optical lattice clocks, and there are dedicated efforts (see e.g., Middelmann et al. [2010]) to measure the BBR clock shifts in the lattice clocks.

In a laboratory environment with an ambient temperature T, one needs to introduce the T-dependent BBR correction to the observed frequency. Even in Cs, the value of the BBR shift was a subject of a recent controversy (Angstmann et al., 2006; Beloy et al., 2006; Levi et al., 2004). Here we setup the relativistic multipolar theory of the BBR shifts, and using techniques of many-body relativistic atomic structure, we compute the BBR shift for Mg, Ca, Sr, Yb (Porsev & Derevianko, 2006b), and Hg (Hachisu et al., 2008) and evaluate uncertainties of the calculations. This section is mostly based on our paper (Porsev & Derevianko, 2006b) and provides additional details.

As summarized in Table 9, the resulting fractional uncertainties in the clock frequencies at $T = 300\,\mathrm{K}$ are *large*, ranging from 2×10^{-19} for Hg to 3×10^{-16} for Yb.

The main conclusions of this section are (1) the present uncertainty in our computed BBR shift is an obstacle on the way towards the projected 10^{-18} accuracy goal (except for Hg); (2) because of T^4 scaling of the BBR shift, it may be beneficial to operate at cryogenic temperatures; (3) if operating at room temperatures, high-precision (0.02%-accurate for Sr)

Table 9 Blackbody radiation shift for clock transitions between the lowest energy $^3P_0$ and the $^1S_0$ states in divalent atoms. $\delta\nu_{\rm BBR}$ is the BBR shift at $T = 300\,$K with our estimated uncertainties. ν_0 is the clock transition frequency, and $\delta\nu_{\rm BBR}/\nu_0$ is the fractional contribution of the BBR shift. The last column lists fractional errors in the absolute transition frequencies induced by the uncertainties in the BBR shift.

Atom	$\delta\nu_{\rm BBR}$ (Hz)	ν_0 (Hz)	$\delta\nu_{\rm BBR}/\nu_0$	uncertainty
Mg	−0.258(7)	6.55×10^{14}	-3.9×10^{-16}	1×10^{-17}
Ca	−1.171(17)	4.54×10^{14}	-2.6×10^{-15}	4×10^{-17}
Sr	−2.354(32)	4.29×10^{14}	-5.5×10^{-15}	7×10^{-17}
Yb	−1.25(13)	5.18×10^{14}	-2.4×10^{-15}	3×10^{-16}
Hg	−0.181	11.3×10^{14}	-1.6×10^{-16}	2×10^{-19}

measurements of the BBR shifts or related quantities are required; (4) Mg-based clock is one of the least susceptible to BBR; compared with Sr, the Mg BBR shift is an order of magnitude smaller (see Table 9). Additionally, we develop a general relativistic theory of the BBR shift caused by multipolar components of the radiation field.

7.1 Multipolar Theory of the Blackbody Radiation Shift

The BBR shift is caused by perturbation of the atomic energy levels by the oscillating thermal radiation. Both atomic levels involved in the clock transition are perturbed and the overall BBR correction is a difference of the BBR shifts for the two levels. We find that determining shift for the upper $^3P_0$ level requires certain care. This level is a part of the ^3P_J fine-structure manifold, $J = 0, 1, 2$. The separation between the levels in the manifold is comparable to the characteristic wave number of the BBR radiation, $208.51\,{\rm cm}^{-1}$, at $T = 300\,$K, and contributions of the BBR-induced magnetic-dipole and electric-quadrupole transitions to the levels of the manifold may be enhanced. Taking these induced transitions into account requires going beyond the conventional electric-dipole approximation (Farley & Wing, 1981).

Considering a potential importance of the multipolar contributions, here we derive the relevant formulas for the BBR-induced energy shifts. Although we show that the $M1$ and $E2$ contributions can be neglected at the present level of uncertainty for the dominant $E1$ shift, incorporating M1 multipoles will be required when the lattice clocks reach their projected 10^{-18} accuracy level.

We start with the usual box quantization for the photon field and expand the magnetic potential inside the box of side L over the plane

waves (see, e.g., Friedrich [2004])

$$\mathbf{A}\,(\mathbf{r},t) = \sum_{\lambda} q_\lambda \mathbf{A}_\lambda \mathrm{e}^{-i\omega_\lambda t} + c.c.$$

with

$$\mathbf{A}_\lambda = \frac{1}{L^{3/2}} \boldsymbol{\varepsilon}_\lambda \mathrm{e}^{i(\mathbf{k}_\lambda \cdot \mathbf{r})}.$$

A periodic boundary condition is imposed on $\mathbf{A}\,(\mathbf{r},t)$, effectively quantizing the modes, $k_\lambda = \omega_\lambda/c$. In the Gaussian units and the Coulomb gauge, the electron-field interaction Hamiltonian reads

$$H' = (\boldsymbol{\alpha}\cdot\mathbf{A}) = \frac{1}{L^{3/2}} \sum_{\lambda} q_\lambda v_\lambda^{(-)} \mathrm{e}^{-i\omega_\lambda t} + \frac{1}{L^{3/2}} \sum_{\lambda} q_\lambda^* v_\lambda^{(+)} \mathrm{e}^{+i\omega_\lambda t}$$

with $v_\lambda^{(\pm)} = (\boldsymbol{\alpha}\cdot\boldsymbol{\varepsilon}_\lambda)\,\mathrm{e}^{\mp i(\mathbf{k}_\lambda\cdot\mathbf{r})}$. We are interested in the time evolution of atomic states caused by these oscillating fields. To this end, we expand the atomic wave function $\psi\,(t)$ over the complete set of stationary states $\left|k\right\rangle$ of the atom

$$|\psi\,(t)\rangle = \sum_k c_k\,(t)\,\mathrm{e}^{-iE_k t}\,\left|k\right\rangle,$$

where the time-dependent amplitudes satisfy a set of coupled equations

$$i\frac{\mathrm{d}}{\mathrm{d}t} c_k\,(t) = \sum_p \mathrm{e}^{i\omega_{kp}t} H'_{kp}\,(t)\,c_p\,(t).$$

Here $\omega_{kp} = E_k - E_p$ and $H'_{kp} \equiv \langle k|H'|p\rangle$ are the matrix elements of the Hamiltonian H'.

To solve this set of equations, we employ the secular approximation. Indeed, the perturbing field is weak and we assume that it does not lead to large population transfer from the initial (perturbed) state $\psi_g\,(t)$. On the r.h.s. of the equation for the excited (perturbing) state amplitude, we may neglect contributions of other excited states

$$\begin{aligned} i\frac{\mathrm{d}}{\mathrm{d}t} c_{k\neq g}\,(t) &\approx \mathrm{e}^{i\omega_{kg}t} H'_{kg}\,(t)\,c_g\,(t) \\ &= \frac{1}{L^{3/2}} \sum_{\lambda} \left\{ q_\lambda \left[v_\lambda^{(-)}\right]_{kg} \mathrm{e}^{i(\omega_{kg}-\omega_\lambda)t} + q_\lambda^* \left[v_\lambda^{(+)}\right]_{kg} \mathrm{e}^{i(\omega_{kg}+\omega_\lambda)t} \right\} c_g\,(t). \end{aligned}$$

We expect that the reference state amplitude follows $c_g(t) = c_g(0) \exp\left[-i\delta E_g t\right]$, where the light shift $\delta E_g \ll \left(\omega_{kg} \pm \omega_\lambda\right)$. Under this assumption, we may disregard the time-dependence of $c_g(t)$ while integrating the above equations. The resulting amplitudes for the excited states adiabatically follow the reference state amplitude

$$c_{k\neq g}(t) = X_{kg} c_g(t),$$
$$X_{kg} = \frac{1}{L^{3/2}} \sum_\lambda \left\{ q_\lambda \frac{\left[v_\lambda^{(-)}\right]_{kg}}{\omega_{gk} + \omega_\lambda} \mathrm{e}^{i\left(\omega_{kg} - \omega_\lambda\right)t} + q_\lambda^* \frac{\left[v_\lambda^{(+)}\right]_{kg}}{\omega_{gk} - \omega_\lambda} \mathrm{e}^{i\left(\omega_{kg} + \omega_\lambda\right)t} \right\}.$$

We substitute this solution into the time-dependent equation for the $c_g(t)$ amplitude, arriving at

$$i\frac{\mathrm{d}}{\mathrm{d}t} c_g(t) = \delta E_g c_g(t),$$
$$\delta E_g = \sum_k \mathrm{e}^{i\omega_{gk}t} H'_{gk}(t) X_{kg}.$$

As the next step, we carry out statistical averaging of the above expression over the field amplitudes q_λ and q_λ^*. The only nonvanishing combinations are

$$\langle q_\lambda q_\lambda^* \rangle = \frac{2\pi}{\alpha^2} \frac{1}{\omega_\lambda} \bar{n}_{\omega_\lambda},$$

where the mean occupation number for photons is

$$\bar{n}_\omega = \frac{1}{\exp(\omega/T) - 1}.$$

Therefore,

$$\delta E_g = \frac{\alpha}{4\pi^2} \mathrm{P.V.} \int_0^\infty \mathrm{d}\omega\, \omega\, \bar{n}_\omega \sum_\varepsilon \int \mathrm{d}\Omega_k \sum_p \left\{ \frac{\left[v^{(+)}\right]_{gp} \left[v^{(-)}\right]_{pg}}{\omega_{gp} + \omega} + \frac{\left[v^{(-)}\right]_{gp} \left[v^{(+)}\right]_{pg}}{\omega_{gp} - \omega} \right\},$$

where we made a transition $\sum_\lambda \to \left(\frac{L}{2\pi}\right)^3 \sum_\varepsilon \int\int \mathrm{d}\Omega_k k^2 \mathrm{d}k$ in the limit of $L \to \infty$. The quantity P.V. $\int \mathrm{d}\omega$ stands for the Cauchy's principal value of the integral; as elucidated by Farley and Wing (1981), it is required for a proper treatment of nominally divergent resonant contributions.

So far, the derivation paralleled the method discussed, for example, in Farley and Wing (1981) for the electric-dipole transitions. At this point,

we focus on multipolar fields. While evaluating matrix elements of operators $v^{(\pm)}$, we make use of the multipolar expansion of $\boldsymbol{\epsilon} e^{i(\mathbf{k}\cdot\mathbf{r})}$ in vector spherical harmonics, Equation (19). To simplify the light-shift expression, we employ the following property of the harmonics

$$\sum_{\varepsilon} \int \mathrm{d}\Omega_k \left(\mathbf{Y}^{(\lambda')^*}_{J'M'} \left(\hat{\boldsymbol{k}} \right) \cdot \boldsymbol{\varepsilon} \right) \left(\mathbf{Y}^{(\lambda)}_{JM} \left(\hat{\boldsymbol{k}} \right) \cdot \boldsymbol{\varepsilon} \right) = \delta_{JJ'} \delta_{\lambda\lambda'} \delta_{MM'}.$$

As a result, we find that the BBR shift is a sum over independent multipolar contributions

$$\delta E_g = \sum_{J\lambda} \delta E_g^{(J\lambda)}, \tag{36}$$

where $\lambda = 0$ is for magnetic (MJ) and $\lambda = 1$ is for electric (EJ) multipolar amplitudes. The individual multipolar shifts are

$$\delta E_g^{(J\lambda)} = -\pi \frac{J+1}{J[(2J-1)!!]^2} \alpha^{2(J-1)} \mathrm{P.V.} \int_0^\infty \mathrm{d}\omega\, \omega^{2(J-1)}\, u_\omega(T)\, \bar{\alpha}_g^{(J\lambda)}(\omega), \tag{37}$$

where $\alpha_g^{(J\lambda)}(\omega)$ are the generalized dynamic multipolar scalar polarizabilities

$$\bar{\alpha}_g^{(J\lambda)}(\omega) = \frac{2}{2J+1} \sum_{p,M} \left| \langle p | \, q_{JM}^{(\lambda)} \, | g \rangle \right|^2 \frac{\omega_{pg}}{\omega_{pg}^2 - \omega^2}. \tag{38}$$

Here the transition operator was expressed in terms of the multipole moments $q_{JM}^{(\lambda)}$ of Section 3. The polarizabilities $\bar{\alpha}_g^{(J\lambda)}(\omega)$ are proportional to the scalar polarizabilities, Equation (23) of Section 3. Here for convenience, we pulled out frequency-dependent prefactor for clarifying the following derivation.

A cursory examination of Equations (37) and (38) reveals that compared with 2^J multipole, the contribution of 2^{J+1} multipole is suppressed by a factor of α^2. Also for the same J, the magnetic contribution is α^2 weaker than that of the EJ photons. As in the theory of multipolar radiative transitions, the E(J+1) and the MJ contributions are of the same order in α. To illuminate the T-dependence of contributions of individual intermediate states, we recast the BBR shifts into the following form, where J_g is the total angular momentum of the reference state and $\langle g || q_J^{(\lambda)} || p \rangle$ is the reduced matrix element, and we separate out factor of α^2 for MJ matrix elements:

$$\delta E_g^{(J\lambda)} = -\frac{(\alpha T)^{2J+1}}{2J_g+1} (\alpha^2)^{\lambda-1} \sum_p (\alpha^2)^{1-\lambda} \left| \langle g || q_J^{(\lambda)} || p \rangle \right|^2 F_J\left(\frac{\omega_{pg}}{T} \right), \tag{39}$$

with the universal functions ($x = \omega/T$)

$$F_J(y) = \frac{1}{\pi}\frac{J+1}{J\,(2J+1)\,!!\,(2J-1)\,!!}P.V.\int_0^\infty \left(\frac{1}{y+x}+\frac{1}{y-x}\right)\frac{x^{2J+1}}{e^x-1}\mathrm{d}x. \quad (40)$$

The universal functions $F_J(y)$ are multipolar generalizations of function $F(y)$ introduced by Farley and Wing (1981) in the $E1$ case. We computed F_J functions using standard integration routines built-in into Mathematica. A plot of $F_J(y)$ for several J may be found in Porsev and Derevianko (2006b). F_J rapidly change around $y \sim 1$ and slowly fall off for $y \gg 1$. Depending on the value of excitation energy, $\omega_{pg} = y\,T$, a particular intermediate state may introduce either negative or positive BBR shift. F_J are broad distributions and have comparable values for $|y| \lesssim 20$.

The limit $y \gg 1$ corresponds to the case when the transition energy is much larger than T. Here $|y| \gg 1$, $F_J(y) \propto 1/y$. If all virtual transitions satisfy this requirement, then the leading contribution to the multipolar BBR shift can be expressed in terms of static polarizabilities

$$\delta E_g^{(J\lambda)} = -\frac{\zeta(2J+2)(2J+2)!}{2\pi J\,[(2J-1)\,!!]^2}\,\alpha^{2J+1}T^{2J+2}\tilde{\alpha}_g^{(J\lambda)}(0), \quad (41)$$

where ζ is the Riemann zeta-function. As the scaling factor, $\alpha^{2J+1}T^{2J+2}$, is expressed in atomic units, we observe that as multipolarity J increases by one, in addition to the usual α^2 suppression, there is a temperature suppression factor of $\left(k_B T/E_h\right)^2$. For $T = 300\,\mathrm{K}$, this suppression is sizable, as $\left(k_B T/E_h\right)^2 \approx 9.0 \times 10^{-7}$.

7.2 BBR Shift for the Clock Transition in Divalent Atoms

Below we apply the developed formalism to compute the BBR shift for the ${}^1S_0 - {}^3P_0$ clock transition in divalent atoms. We will assume that the atoms are at the ambient temperature of $T = 300\,\mathrm{K}$. Both clock levels experience the BBR shift and the total shift is the difference between the individual shifts, $\delta\nu_{\mathrm{BBR}} = \delta\nu_{\mathrm{BBR}}({}^3P_0) - \delta\nu_{\mathrm{BBR}}({}^1S_0)$.

Consider first the BBR shift of the ground ${}^1S_0$ state. Here transition energies of various multipolar transitions to the upper levels are much larger than T, i.e., we are in the $y \gg 1$ limit. Here compared with the dominant $E1$-induced shift, the contribution of $M1$ transitions is suppressed by $\alpha^2 \sim 10^{-4}$ and $E2$ by $\alpha^2\left(k_B T/E_h\right)^2 \sim 10^{-10}$. Higher order multipoles are suppressed even more. As to the retardation effects in $E1$ matrix elements, we expect that they would be suppressed by a factor of $\alpha^2\left(k_B T/E_h\right)^2 \sim 10^{-10}$. Nevertheless, since the fractional contribution of the BBR shift to the clock

frequency is at 5×10^{-15} level (see Table 9), one would need to introduce the $M1$ corrections at the projected accuracy of 10^{-18}.

For the $^3P_0$ levels, the characteristic thermal photon frequency is comparable to the fine-structure intervals for the ^3P_J manifold. The $^3P_0$ level is connected by M1 transition to the $^3P_1$ level and by $E2$ transition to the $^3P_2$ level. For these transitions, the values of the relevant functions $F_J \sim 1$, thus $\delta E_g^{(M1)} \sim \alpha^2 (\alpha T)^3$ and $\delta E_g^{(E2)} \sim (\alpha T)^5$, while $\delta E_g^{(E1)} \sim \alpha^3 T^4/\omega_{^3D_1-{}^3P_0}$. Qualitatively, we anticipate that $M1$ and $E2$ contributions are suppressed by factors of 10^{-3} and 10^{-11}, respectively. (Notice that $\omega_{^3D_1-{}^3P_0} \approx 2 \times 10^{-2} E_h$.) Our numerical estimate, on the basis of the transitions inside the fine-structure manifold, leads to the following values of the BBR shifts for Sr: $|\delta E_g^{(M1)}| \approx 2.4 \times 10^{-5}$ Hz and $|\delta E_g^{(E2)}| \approx 2.5 \times 10^{-8}$ Hz. Since the $E1$ BBR shift for Sr is ~ 2 Hz, the $M1$ and $E2$ contributions can be neglected at the present 1%-level of accuracy of our calculations.

We find that although the thermal photon energy is close to the fine-structure intervals, the induced multipole BBR shifts are not amplified. The main reason is that the BBR energy distribution is broad: the functions F_J have comparable values for a wide range of excitation energies, $|\omega| \lesssim 20\,T$. For example, for the Sr $^3P_0 - {}^3D_1$, $E1$ transition $F_1 \approx 0.16$, whereas for the $^3P_0 - {}^3P_1$, $M1$ transition $F_1 \approx -0.41$, and for the $^3P_0 - {}^3P_2$ $E2$ transition $F_2 \approx -0.36$. For such a broad distribution, the multipolar BBR shift is determined by the prefactor in Equation (39) resulting in a suppression of multipoles beyond $E1$.

Based on the above discussion, we may exclusively focus on the electric-dipole ($J = 1, \lambda = 1$) contribution to the BBR shift. From our general expressions, we obtain an approximate formula,

$$\delta E_g^{(E1)} \approx -\frac{2}{15}(\alpha\pi)^3 T^4 \alpha_g^{(E1)}(0)\,[1+\eta]\,, \tag{42}$$

$$\eta = \frac{(80/63)\pi^2}{\alpha_g^{(E1)}(0) T} \sum_p \frac{|\langle p||q_1^{(1)}||g\rangle|^2}{(2J_g+1)y_p^3}\left(1 + \frac{21\pi^2}{5y_p^2} + \frac{336\pi^4}{11y_p^4}\right). \tag{43}$$

Here $y_p = \omega_{pg}/T$ and $\alpha_g^{(E1)}(0)$ is the traditional static dipole polarizability. To arrive at the above equation, we used the asymptotic expansion

$$F_1(y) \approx \frac{4\pi^3}{45y} + \frac{32\pi^5}{189y^3} + \frac{32\pi^7}{45y^5} + \frac{512\pi^9}{99y^7},$$

which has an accuracy better than 0.1% for $|y| > 10$. η represents a "dynamic" fractional correction to the total shift.

7.3 Numerical Results

The leading contribution to the BBR shift is determined by the static $E1$ polarizability. We have evaluated these polarizabilities in Section 2 using relativistic many-body procedure. The results of calculations for the static electric-dipole polarizabilities for the $ns^2\,{}^1S_0$ and $nsnp\,{}^3P_0$ states are presented in Table 5. The discussion of the accuracy of our results is given in Section 2.2.

With the computed polarizabilities, we find the BBR shifts with Equation (42). The "dynamic" correction η is negligible for the ${}^1S_0$ states, but is needed for the ${}^3P_0$ calculations. Indeed, for the ground state, the smallest excitation energy $E_{^1P_1} - E_{^1S_0}$ is equal to 21698 cm^{-1} for Sr. At $T = 300\,\mathrm{K}$, the characteristic value of y is $\sim$100 for all the atoms. By contrast, for the ${}^3P_0$ clock level, the transitions to the nearby ${}^3D_1$ level (see Figure 1) involve smaller energies. For Sr, the relevant energy is only 3841 cm^{-1} corresponding to characteristic value of $y \sim 20$. At this value, the "static polarizability" approximation has only a few percent accuracy. While evaluating η, we find it sufficient to truncate the summation over intermediate states at the lowest energy excitation. This "dynamic" correction contributes to the BBR shift of the ${}^3P_0$ state at 0.1% level in Mg, 1% in Ca, 2.7% in Sr, and 0.7% in Yb. Notice that since the clock BBR shift is obtained by subtracting BBR shifts of the individual levels, the "dynamic" correction contributes at an enhanced 5% level in Sr.

Finally, we combine the BBR shifts of the individual clock levels and arrive at the overall BBR corrections summarized in Table 9. Our computed BBR shift for Sr, −2.354(32) Hz, is in agreement with an estimate by Takamoto et al. (2005) of −2.4(1) Hz. The uncertainties are better than 3%, except for Yb where the uncertainty is 10%. These uncertainties are large compared with the projected 10^{-18} fractional accuracy of the lattice-based clocks (see Table 9).

At room temperatures, the uncertainties in BBR shifts seem to be a major factor in the error budget of these clocks. At the projected 10^{-18} fractional accuracy, the required accuracies (e.g., 0.02% for Sr) in determining BBR shifts are beyond the presently demonstrated capabilities of atomic calculations and related polarizability measurements.

If any experimental (theoretical) progress is achieved (for instance, if sufficiently accurate values of the dipole matrix elements such as $\langle {}^3P_0|D_0|{}^3D_1\rangle$ become available), the uncertainties in the BBR shifts because of $E1$ polarizabilities can be reduced. In this case, the accurate calculation of the BBR shift contributions from $M1$ and $E2$ transitions will be needed using the formalism developed in this section. At present, the uncertainties of the $E1$ polarizabilities are so large that the projected 10^{-18} fractional accuracy of the optical lattice clocks seem to be difficult to attain (if the future definition of the second involves atoms at $T = 0$ K). In any case,

the BBR contribution has to be taken into account when evaluating uncertainties because of either spatial or temporal fluctuations of the thermal radiation.

8. RAYLEIGH HEATING RATES

Clock atoms are trapped in an optical lattice; the scattering of lattice photons causes heating because of scattered photon recoil. Below we show that at the magic wavelength, the heating rates for $J = 0$ clock levels are expressed in terms of dynamic polarizability of Section 3. Moreover, we demonstrate that at the magic wavelength, the heating rates for both clock levels are the same.

To estimate the heating rate, we need to evaluate the rate of Rayleigh scattering. According to Equation (59.5) of Berestetskii et al. (1982), the differential cross section for nonresonant Raman scattering from the initial state i to the final state f reads (notice that the original equation has a typo—it should be ω_{k1} instead of ω_{k2} in the equation)

$$\frac{\mathrm{d}\sigma_R}{\mathrm{d}\Omega_s} = \frac{\omega_l \omega_s^3}{c^4} \left| \sum_k \left(\frac{\langle f \left| \varepsilon_s^* \cdot \mathbf{D} \right| k \rangle \langle k \left| \varepsilon_l \cdot \mathbf{D} \right| i \rangle}{\hbar\,(\omega_{ki} - \omega_l)} + \frac{\langle f \left| \varepsilon_l \cdot \mathbf{D} \right| k \rangle \langle k \left| \varepsilon_s^* \cdot \mathbf{D} \right| i \rangle}{\hbar\,(\omega_{ki} + \omega_s)} \right) \right|^2,$$

where ω_l and ε_l are the frequency and (linear) polarization of the laser light and ω_s and ε_s are those for the scattered light.

We are interested in the elastic Rayleigh process where the atom remains in the initial state after the scattering event and $\omega_s = \omega_l$. Since the clock states are spherically symmetric, $J_i = J_f = 0$ for both clock levels, and the derivation is simplified. By choosing the z-axis along the laser polarization ε_l, we arrive at

$$\frac{\mathrm{d}\sigma_R}{\mathrm{d}\Omega_s} = \frac{\omega_l^4}{c^4} \left[\alpha_i^{(E1)}(\omega_l)\right]^2 \sum_{\varepsilon_s} \left(\varepsilon_s^* \cdot \varepsilon_l\right) \left(\varepsilon_l^* \cdot \varepsilon_s\right),$$

where $\alpha_i^{(E1)}(\omega_l)$ is the electric-dipole dynamic polarizability of the atomic state i (see Section 3). The polarization sum $\sum_{\varepsilon_s} \left(\varepsilon_s^* \cdot \varepsilon_l\right) \left(\varepsilon_l^* \cdot \varepsilon_s\right) = \sin^2\theta$, where θ is the angle between laser polarization and $\hat{k}_s$. Integrating over angles, we arrive at the total cross section,

$$\sigma_R = \frac{8\pi}{3} \frac{\omega_l^4}{c^4} [\alpha_i^{(E1)}(\omega_l)]^2. \tag{44}$$

For a laser of local intensity I_L, this cross section leads to the heating rate

$$\gamma_h = \frac{8\pi}{3} \frac{\omega_l^3}{\hbar c^4} [\alpha_i^{(E1)}(\omega_l)]^2 I_L.$$

Notice that since $\alpha^{(E1)}_{^1S_0}(\omega_m) = \alpha^{(E1)}_{^3P_0}(\omega_m)$ at the magic wavelength, the heating rates for the both clock states are the same.

For example, for Yb clock at the magic wavelength, the values of a.c. polarizability for both states are equal to 160 a.u. (see Figure 3). For a laser intensity of 10 kW/cm^2, the resulting rate is in the order of 10^{-2} sec^{-1} (we took into account that the maximum of intensity in an optical lattice, where the atoms are trapped, is four times larger than I_L).

9. SUMMARY

In this review, we presented a detailed evaluation of a number of important atomic-structure parameters affecting design and ultimate accuracy of optical lattice clocks. The calculations were carried out using ab initio relativistic many-body methods of atomic structure. Overall, we find that the calculations are reliable and the underlying formalism provides a clear systematic way on improving theoretical accuracy further. In particular, we evaluated the hyperfine-induced transition widths of the clock transitions, multipolar and vector a.c. polarizabilities, static polarizabilities, "magic" trapping wavelengths, hyperfine-induced g-factors, and blackbody radiation shifts. Among the remaining parameters, one of the important systematic effects is because of hyperpolarizability, i.e., contribution to the Stark shifts *quartic* in the atom-laser interaction (Katori et al., 2003). Evaluation of this quantity is discussed in detail in Taichenachev et al. (2006b)

ACKNOWLEDGEMENTS

This work was supported in part by the U.S. National Science Foundation and an U.S. NIST precision measurement grant. The work of S.G.P. was also supported by the Russian Foundation for Basic Research under Grant No. 11-02-00943-a.

REFERENCES

Angstmann, E. J., Dzuba, V. A., & Flambaum, V. V. (2006). Frequency shift of the cesium clock transition due to blackbody radiation. *Physical Review Letters*, *97*, 040802.

Arnold, M., Bergmann, E., Bopp, P., Dorsch, C., Kowalski, J., Stehlin, T., et al. (1981). Hyperfine structure and nuclear moments of odd calcium isotopes by laser and radiofrequency spectroscopy. *Hyperfine Interactions*, *9*, 159.

Baillard, X., Fouche, M., Le Targat, R., Westergaard, P. G., Lecallier, A., Chapelet, F., et al. (2008). An optical lattice clock with spin-polarized ^{87}Sr atoms. *European Physical Journal D*, *48*, 11–17.

Barber, Z. W., Hoyt, C. W., Oates, C. W., Hollberg, L., Taichenachev, A. V., & Yudin, V. I. (2006). Direct excitation of the forbidden clock transition in neutral ^{174}Yb atoms confined to an optical lattice. *Physical Review Letters*, *96*, 083002.

Barber, Z. W., Stalnaker, J. E., Lemke, N. D., Poli, N., Oates, C. W., Fortier, T. M., et al. 2008. Optical lattice induced light shifts in an Yb atomic clock. *Physical Review Letters*, *100*, 103002.

Beloy, K., Safronova, U. I., & Derevianko, A. (2006). High-accuracy calculation of the blackbody radiation shift in the ^{133}Cs primary frequency standard. *Physical Review Letters*, *97*, 040801.

Berestetskii, V. B., Lifshitz, E. M., & Pitaevskii, L. P. (1982). *Quantum electrodynamics* (2nd ed.). Oxford: Pergamon Press.

Bjorken, J. D., & Drell, S. D. (1964). *Relativistic quantum mechanics*. Mcgraw-Hill College, New York, San Francisco, Toronto, and London.

Bowers, C. J., Budker, D., Freedman, S. J., Gwinner, G., Stalnaker, J. E., & DeMille, D. (1999). Experimental investigation of the $6s^2\,{}^1S \rightarrow 5d6s\,{}^3D_{1,2}$ forbidden transitions in atomic ytterbium. *Physical Review A*, *59*, 3513–3526.

Boyd, M. M., Zelevinsky, T., Ludlow, A. D., Foreman, S. M., Blatt, S., Ido, T., et al. (2006). Optical atomic coherence at the 1-second time scale. *Science, 314*, 1430–1433.

Budick, B., & Snir, J. (1969). Hyperfine structure of the $6s6p\,{}^1P_1$ level of the stable ytterbium isotopes. *Physical Review*, *178*, 18.

Campbell, G. K., Ludlow, A. D., Blatt, S., Thomsen, J. W., Martin, M. J., Miranda, M. H. G. d., et al. (2008). The absolute frequency of the ^{87}Sr optical clock transition. *Metrologia, 45*, 539–548.

Clark, D. L., Cage, M. E., Lewis, D. A., & Greenlees, G. W. (1979). Optical isotopic shifts and hyperfine splittings for Yb. *Physical Review A*, *20*, 239.

Dalgarno, A., & Lewis, J. T. (1955). The exact calculation of long-range forces between atoms by perturbation theory. *Proceedings of the Royal Society of London Series A*, *223*, 70.

Degenhardt, C., Binnewies, T., Wilpers, G., Sterr, U., Riehle, F., Lisdat, C., et al. (2003). Photoassociation spectroscopy of cold calcium atoms. *Physical Review A*, *67*, 043408.

Derevianko, A., Johnson, W. R., Safronova, M. S., & Babb, J. F. (1999). High-precision calculations of dispersion coefficients, static dipole polarizabilities, and atom-wall interaction constants for alkali-metal atoms. *Physical Review Letters*, *82*, 3589–3592.

Derevianko, A., & Katori, H. (2011). Physics of optical lattice clocks. *Reviews of Modern Physics*, *83*, 331–348.

Derevianko, A., Obreshkov, B., & Dzuba, V. A. (2009). Mapping out atom-wall interaction with atomic clocks. *Physical Review Letters*, *103*, 133201.

Drozdowski, R., Ignasiuk, M., Kwela, J., & Heldt, J. (1997). Radiative lifetimes of the lowest $^3P_1$ metastable states of Ca and Sr. *Zeitschrift fur Physik D*, *41*, 125.

Dzuba, V. A., & Derevianko, A. (2010). Dynamic polarizabilities and related properties of clock states of the ytterbium atom. *Journal of Physics B*, *43*, 074011.

Dzuba, V. A., Flambaum, V. V., & Kozlov, M. G. (1996). Combination of the many-body perturbation theory with the configuration-interaction method. *Physical Review A 54*, 3948–3959.

Dzuba, V. A., Kozlov, M. G., Porsev, S. G., & Flambaum, V. V. (1998). Using effective operators in calculating the hyperfine structure of atoms. *Zhurnal Eksperimental'noi i Teoreticheskoi Fiziki, 114*, 1636–1645, [Sov. Phys.–JETP **84** 461, (1997)].

Farley, J. W., & Wing, W. H. (1981). Accurate calculation of dynamic Stark shifts and depopulation rates of Rydberg energy levels induced by blackbody radiation. Hydrogen, helium, and alkali-metal atoms. *Physical Review A*, *23*, 2397–2424.

Friedrich, H. S. (2004). *Theoretical atomic physics* (2nd ed.). Berlin: Springer.

Froese Fischer, C., Tachiev, G., & Irimia, A. (2006). Relativistic energy levels, lifetimes, and transition probabilities for the sodium-like to argon-like sequences. *Atomic Nuclear Data Tables, 92*, 607.

Garstang, R. G. (1962). Hyperfine structure and intercombination line intensities in the spectra of magnesium, zinc, cadmium, and mercury. *Journal of the Optical Society*, *52*, 845.

Godone, A., & Novero, C. (1992). Lifetime measurement of the Mg I intercombination line. *Physical Review A*, *45*, 1717–1721.

Grundevik, P., Gustavsson, M., Lindgren, I., Olsson, G., Robertsson, L., Rosen, A., et al. (1979). Precision method for hyperfine-structure studies in low-abundance isotopes: the quadrupole moment of ^{43}Ca. *Physical Review Letters*, *42*, 1528.

Hachisu, H., Miyagishi, K., Porsev, S. G., Derevianko, A., Ovsiannikov, V. D., Pal'chikov, V. G., et al (2008). Trapping of neutral mercury atoms and prospects for optical lattice clocks. *Physical Review Letters*, *100*, 053001.

Haken, H., & Wolf, H. C. (1994). Physics of atoms and quanta. Springer, Berlin and New York.

He, M., Therkildsen, K. T., Jensen, B. B., Brusch, A., Thomsen, J. W., & Porsev, S. G. (2009). Isotope shifts of the $(3s3p)\,^3P_{0,1,2} - (3s4s)\,^3S_1$ Mg I transitions. *Physical Review A*, *80*, 024501.

Heider, S. M., & Brink, G. O. (1977). Hyperfine structure of ^{87}Sr in the $^3P_2$ metastable state. *Physical Review A*, 16, 1371.

Hong, T., Cramer, C., Nagourney, W., & Fortson, E. N. (2005). Optical clocks based on ultranarrow three-photon resonances in alkaline earth atoms. *Physical Review Letters*, *94*, 050801.

Hong, F.-L., Musha, M., Takamoto, M., Inaba, H., Yanagimachi, S., Takamizawa, A., et al. (2009). Measuring the frequency of a Sr optical lattice clock using a 120 km coherent optical transfer. *Optics Letters*, *34*, 692–694.

Husain, D., & Roberts, C. J. (1986). Energy pooling from Ca[4s4p(^3P_J)] and Ca[4s3d($^1D_2$)] studied by time-resolved atomic emission following pulsed dye-laser excitation. *Journal of the Chemical Society, Faraday Transactions*, *282*, 1921.

Husain, D., & Schifino, J. (1984). Kinetic study of Sr(5^3P_J) by time-resolved emission, $5\,^3P_1 \rightarrow 5\,^1S_0 + h\nu(\lambda = 689.3\,\text{nm})$, following dye-laser excitation. *Journal of the Chemical Society, Faraday Transactions*, *280*, 321.

Johnson, W. R. (1988). Relativistic random-phase approximation. *Advances in Atomic Molecular and Optical Physics*, *25*, 375.

Johnson, W. R., Plante, D. R., & Sapirstein, J. (1995). Relativistic calculations of transition amplitudes in the helium isoelectronic sequence. *Advances in Atomic Molecular and Optical Physics*, *35*, 255.

Katori, H. (2002). Spectroscopy of strontium atoms in the Lamb–Dicke confinement. In P. Gill (Ed.), *Proc. 6th symposium frequency standards and metrology* (pp. 323–330). Singapore: World Scientific.

Katori, H., Takamoto, M., Pal'chikov, V. G., & Ovsiannikov, V. D. (2003). Ultrastable optical clock with neutral atoms in an engineered light shift trap. *Physical Review Letters*, *91*, 173005.

Kohno, T., Yasuda, M., Hosaka, K., Inaba, H., Nakajima, Y., & Hong, F.-L. (2009). One-dimensional optical lattice clock with a fermionic ^{171}Yb isotope. *Applied Physics Express*, *2*, 072501.

Kolb, D., Johnson, W. R., & Shorer, P. (1982). Electric and magnetic susceptibilities and shielding factors for closed-shell atoms and ions of high nuclear charge. *Physical Review A*, *26*, 19–31.

Kozlov, M. G., & Porsev, S. G. (1999a). Effective hamiltonian for valence electrons of an atom. *Optika i Spektoskopiya*, *87*, 384–389, [*Optika i Spektoskopiya* **87** 352, (1999)].

Kozlov, M. G., & Porsev, S. G. (1999b). Polarizabilities and hyperfine structure constants of the low-lying levels of barium. *European Physical Journal D*, *5*, 59–63.

Kozlov, M. G., Porsev, S. G., & Johnson, W. R. (2001a). Parity non-conservation in thallium. *Physical Review A*, *64*, 052107.

Kozlov, M. G., Porsev, S. G., & Tupitsyn, I. I. (2001b). High accuracy calculation of $6S \rightarrow 7S$ parity nonconserving amplitude in Cs. *Physical Review Letters*, *86*, 3260.

Kwong, H. S., Smith, P. L., & Parkinson, W. H. (1982). Laser-excitation technique for the measurement of absolute transition probabilities of weak atomic lines. Physical Review A, *25*, 2629–2640.

Le Targat, R., Baillard, X., Fouché, M., Brusch, A., Tcherbakoff, O., Rovera, G. D., et al. (2006). Accurate optical lattice clock with ^{87}Sr atoms. *Physical Review Letters*, *97*, 130801.

Lemke, N. D., Ludlow, A. D., Barber, Z. W., Fortier, T. M., Diddams, S. A., Jiang, Y., et al. (2009). Spin-1/2 optical lattice clock. *Physical Review Letters*, *103*, 063001.

Lemonde, P. (2009). Optical lattice clocks. *European Physical Journal - Special Topics*, *172*, 81–96.

Levi, F., Calonico, D., Lorini, L., Micalizio, S., & Godone, A. (2004). Measurement of the blackbody radiation shift of the ^{133}Cs hyperfine transition in an atomic fountain. *Physical Review A*, *70*, 033412.

Lindgren, I., & Morrison, J. (1986). *Atomic many–body theory* (2nd ed.) Berlin: Springer–Verlag.

Ludlow, A. D., Boyd, M. M., Zelevinsky, T., Foreman, S. M., Blatt, S., Notcutt, M., et al. (2006). Systematic study of the ^{87}Sr clock transition in an optical lattice. *Physical Review Letters*, *96*, 033003.

Lundin, L., Engman, B., Hilke, J., & Martinson, I. (1973). Lifetime measurements in Mg I–Mg IV. *Physica Scripta*, *8*, 274.

Lurio, A. (1962). Hyperfine structure of the ^3P states of ^{67}Zn and ^{25}Mg. *Physical Review*, *126*, 1768.

Malossi, N., Damkjær, S., Hansen, P. L., Jacobsen, L. B., Kindt, L., Sauge, S., et al. (2005). Two-photon cooling of magnesium atoms. *Physical Review A*, *72*, 051403.

Manakov, N. L., Ovsiannikov, V. D., & Rapoport, L. P. (1986). Atoms in a laser field. *Physics Reports*, *141*, 319–433.

Middelmann, T., Lisdat, C., Falke, S., Vellore Winfred, J. S. R., Riehle, F., & Sterr, U. (2010). Tackling the blackbody shift in a strontium optical lattice clock. *Instrumentation and Measurement, IEEE Transactions, 60*, 2550-2557. http://ieeexplore.ieee.org/xpl/RecentIssue.jsp?punumber=19 ArXiv:1009.2017.

Mitroy, J., & Bromley, M. W. J. (2003). Semiempirical calculation of van der Waals coefficients for alkali-metal and alkaline-earth-metal atoms. *Physical Review A*, *68*, 052714.

Moore, C. E. (1971). *Atomic energy levels. Vol. I-III. NBS, National Standards Reference Data Series – 35, U.S.* Washington, DC: GPO.

Patil, S. H. (2000). A simple model potential description of the alkaline earth isoelectronic sequences. *European Physical Journal D*, *10*, 344.

Porsev, S. G., Beloy, K., & Derevianko, A. (2010). Precision determination of weak charge of ^{133}Cs from atomic parity violation. *Physical Review D*, *82*, 036008.

Porsev, S. G., & Derevianko, A. (2002). High-accuracy relativistic many-body calculations of van der Waals coefficients C_6 for alkaline-earth atoms. *Physical Review A*, *65*, 020701(R).

Porsev, S. G., & Derevianko, A. (2004). Hyperfine quenching of the metastable $^3P_{0,2}$ states in divalent atoms. *Physical Review A*, *69*, 042506.

Porsev, S. G., & Derevianko, A. (2006a). High-accuracy calculations of dipole, quadrupole, and octupole electric dynamic polarizabilities and van der Waals coefficients C_6, C_8, and C_{10} for alkaline-earth dimers. *Zhurnal Eksperimental'noi i Teoreticheskoi Fiziki, 129*, 227, [*Soviet Physics-JETP* **102** 195, (2006)].

Porsev, S. G., & Derevianko, A. (2006b). Multipolar theory of blackbody radiation shift of atomic energy levels and its implications for optical lattice clocks. *Physical Review A*, *74*, 020502(R).

Porsev, S. G., Derevianko, A., & Fortson, E. N. (2004). Possibility of an optical clock using the $6\,^1S_0 \rightarrow 6\,^3P^o_0$ transition in ^{171,173}Yb atoms held in an optical lattice. *Physical Review A*, *69*, 021403(R).

Porsev, S. G., Kozlov, M. G., Rakhlina, Yu. G., & Derevianko, A. (2001). Many-body calculations of electric-dipole amplitudes for transitions between low-lying levels of Mg, Ca, and Sr. *Physical Review A*, *64*, 012508.

Porsev, S. G., Rakhlina, Yu. G., & Kozlov, M. G. (1999a). Calculation of hyperfine structure constants for ytterbium. *Journal of Physics B*, *32*, 1113–1120.

Porsev, S. G., Rakhlina, Yu. G., & Kozlov, M. G. (1999b). Electric-dipole amplitudes, lifetimes, and polarizabilities of the low-lying levels of atomic ytterbium. *Physical Review A*, *60*, 2781–2785.

Riehle, F., et al. (2003). Optical frequency standard based on cold calcium atoms, talk at the Second Workshop on Cold Alkaline-Earth Atoms, September 11-13, Copenhagen, Denmark.

Santra, R., Arimondo, E., Ido, T., Greene, C. H., & Ye, J. (2005). High-accuracy optical clock via three-level coherence in neutral bosonic ^{88}Sr. *Physical Review Letters*, *94*, 173002.

Santra, R., Christ, K. V., & Greene, C. H. (2004). Properties of metastable alkaline-earth-metal atoms calculated using an accurate effective core potential. *Physical Review A*, *69*, 042510.

Savukov, I. M., & Johnson, W. R. (2002). Combined configuration-interaction and many-body-perturbation-theory calculations of energy levels and transition amplitudes in Be, Mg, Ca, and Sr. *Physical Review A*, *65*, 042503.

Smith, W. W., & Gallagher, A. (1966). Radiative lifetime of the first $^2P_{3/2}$ state of ionized calcium and magnesium by the Hanle effect. *Physical Review*, *145*, 26–35.

Sternheimer, R. M. (1950). On nuclear quadrupole moments. *Physical Review*, *80*, 102.

Taichenachev, A. V., Yudin, V. I., Oates, C. W., Hoyt, C. W., Barber, Z. W., & Hollberg, L. (2006a). Magnetic field-induced spectroscopy of forbidden optical transitions with application to lattice-based optical atomic clocks. *Physical Review Letters*, *96*, 083001.

Taichenachev, A. V., Yudin, V. I., Ovsiannikov, V. D., Pal'chikov, V. G., 2006b. Optical lattice polarization effects on hyperpolarizability of atomic clock transitions. *Physical Review Letters*, *97*, 173601.

Takamoto, M., Hong, F. L., Higashi, R., & Katori, H. (2005). An optical lattice clock. *Nature (London)*, *435*, 321–324.

Takamoto, M., Hong, F. L., Higashi, R., Fujii, Y., Imae, M., & Katori, H. (2006). Improved frequency measurement of a one-dimensional optical lattice clock with a spin-polarized fermionic ^{87}Sr isotope. *Journal of the Physical Society of Japan 75*, 104302.

Takamoto, M., & Katori, H. (2003). Spectroscopy of the $^1S_0$ - $^3P_0$ clock transition of Sr in an optical lattice. *Physical Review Letters*, *91*, 223001.

Takasu, Y., Komori, K., Honda, K., Kumakura, M., Yabuzaki, T., & Takahashi, Y. (2004). Photoassociation spectroscopy of laser-cooled ytterbium atoms. *Physical Review Letters*, *93*, 123202.

Taylor, B. N. (Ed.). (2001). *The international system of units (SI)*. Gaithersburg, Maryland: U.S. Government Printing Office..

Varshalovich, D. A., Moskalev, A. N., & Khersonskii, V. K. (1988). *Quantum theory of angular momentum*. Singapore: World Scientific.

Yasuda, M., & Katori, H. (2004). Lifetime measurement of the P_2 metastable state of strontium atoms. *Physical Review Letters*, *92*, 153004.

Yasuda, M., Kishimoto, T., Takamoto, M., & Katori, H. (2006). Photoassociation spectroscopy of ^{88}Sr: reconstruction of the wave function near the last node. *Physical Review A*, *73*, 011403.

This page intentionally left blank

CHAPTER 10

Confinement-Induced Resonances

Vanja Dunjko[a], **Michael G. Moore**[b], **Thomas Bergeman**[c], and **Maxim Olshanii**[a]

[a]*Department of Physics, University of Massachusetts Boston, Boston, MA 02125, USA*
[b]*Department of Physics and Astronomy, Michigan State University, East Lansing, MI 48824, USA*
[c]*Department of Physics and Astronomy, University of Stony Brook, SUNY, Stony Brook, NY 11794-3800, USA*

Contents

Advances in Atomic, Molecular, and Optical Physics, Volume 60, Copyright © 2011 Elsevier Inc.
ISSN 1049-250X, DOI: 10.1016/B978-0-12-385508-4.00010-3.

Abstract Confinement-induced resonances (CIRs) arise when particle scattering takes place in the presence of an external potential that spatially confines the motion of the particles. One finds that for some combinations of the values of the parameters governing the collision—the scattering energy, the parameters that govern the confining potential, and the parameters that govern the interatomic potential—the scattering cross section reaches the unitary limit: this is CIR. We provide details on one paradigmatic case of CIR and review the types of CIRs that have so far been studied theoretically and, more recently, experimentally. The rich variety of examples suggests that CIRs arise under generic confining conditions and that therefore we should expect to continue encountering new examples of them.

1. INTRODUCTION

Although confinement-induced resonances (CIRs) properly belong to the physics of two-particle scattering, they were discovered—and much work on them continues to be done—within the context of many-body physics of ultra-cold atomic gases (Bloch et al., 2008). In their initiating works, for example, Olshanii (1998) and Petrov et al. (2000a) considered ultracold Bose gases in strongly anisotropic harmonic traps, in which the motion of atoms was effectively confined to a line or to a plane, respectively. Experimentally, atomic traps are created by superimposing one or more (depending on the desired dimensionality of the trap) counterpropagating laser beams. The light is slightly off-resonant and causes the atoms to experience an AC Stark shift. The interference of the laser beams creates an optical standing wave, which leads to spatial variation

in the AC Stark shift experienced by the atoms, and thus to a dipole force. With Gaussian beams, the end result is a trapping potential that is approximately harmonic near the potential minimum (Grimm et al., 2000). Low-dimensional (low-D) confinement happens when the typical kinetic energy of an atom is much less than the energy difference between the ground and the first excited state of the confining potential; in many-body systems, one requires that both the chemical potential and the temperature ($k_B T$) be less than that energy difference (Moritz et al., 2003). If these conditions are satisfied, then the motion of the atoms is "frozen" in the ground state of the confining potential, and therefore limited to the unconfined directions.

The main motivation for the initial studies was that, broadly speaking, in low-D, strongly correlated many-body regimes are easier to study than in 3D (Tolra et al., 2004). The initiating papers sought to develop approximate theories, "effective low-D" theories, in which the frozen-out degrees of freedom are eliminated. The details of the confinement enter a low-D theory only parametrically, e.g., determining the value of the coupling constant in the effective low-D interaction potential.

At this point, we may give a preliminary definition of a confinement-induced resonance (CIR): a CIR is a unitarity-bound-saturating local maximum in the scattering cross section as one varies the confinement strength while keeping all the other parameters fixed.

In more detail, one starts with a two-body scattering problem in 3D with the confining potential present. The boundary condition is such that, asymptotically far in the unconfined directions, the state is a product of the ground state of the confining potential and of some free-space solution in the unconfined directions. (Here, one must further impose appropriate boundary conditions for the free-space solution, usually either periodic or of the form "incoming plane wave plus a scattered wave"; for an example, see Equation [33]). One finds that, when viewed as a function of whatever parameter governs the strength of the confinement (with all other parameters held fixed), the scattering cross section exhibits at least one local maximum. Now, the conservation of probability sets an upper limit on how large the scattering cross section can possibly get, the so-called unitarity bound (Capri, 2002, p. 437). If the local maximum actually saturates this bound, i.e., if it is as large as the conservation of probability allows, then this maximum is called a CIR.

As we said, the real goal is usually to eliminate the confined degrees of freedom from the theory. A well-constructed effective low-D theory will also feature a CIR, although the agreement with the full 3D theory as to the location of the CIR may be only approximate. For example, in the full 3D theory, there is usually a weak dependence on the scattering energy, which may disappear in the low-D effective theory (e.g., compare Equations [78] and [79] below). An important feature of effective low-D theories

is that the low-D effective interaction potential changes from repulsive to attractive as one crosses the CIR, as evidenced in the change of the sign of the low-D coupling constant. Indeed, some sources take this sign change to be the definition of a CIR (e.g., Bloch et al. [2008]).

Returning now to the historical background: as we said, the main motivation for the early (and much of the later) work on atomic gases in confining potentials was not two-body physics, but rather many-body physics. Not only are (as we said) strongly correlated many-body regimes more easily studied in low-D, but also many interesting and important phases of matter exist only in low dimensions. In either case, ultra-cold atoms seemed to promise a uniquely clean and controllable setting for study—a promise on which they have since more than delivered, as Bloch et al. (2008) have reviewed in great detail. For example, Olshanii (1998) was suggesting that an ultra-cold Bose gas confined to 1D can be a realization of the Tonks-Girardeau gas (TG gas, the 1D gas of hard-core, or impenetrable, bosons [Girardeau, 1960; Tonks, 1936]). The TG gas has at least three remarkable properties: first, it is an integrable many-body quantum system (Girardeau, 1960); second, it is the bosonic member of a pair of systems (one Bose, one Fermi) manifesting a type of Bose–Fermi equivalence (Girardeau, 1960); and third, it is a bosonic Luttinger liquid (Haldane, 1981a,b). For each of these three properties, the TG gas is famous for being one of the simplest systems to exhibit it. The experimental realization of the TG gas using ultra-cold atoms came several years after the initial proposal (Kinoshita et al., 2004; Paredes et al., 2004).

The two-body scattering theory enters the story—in these initial studies, as well as in many subsequent ones—because a key approximation in the derivation of the effective low-D theories is that only binary collisions between atoms matter. As we said, the scattering cross section depends on (among other parameters) the strength of the low-D confinement. In cases of harmonic confinement, this strength is usually parametrized through the length of the confining harmonic oscillator, $a_\perp$ in Equation (65) and a_z in Equation (97), below; the smaller the length, the stronger the confinement. This much was as anticipated—low-D physics should parametrically depend on the details of the confinement. What was *not* anticipated was that this dependence should include resonant behavior, the CIR: namely, that $a_\perp$ and a_z could be adjusted, while keeping all the other parameters constant, so that the low-D two-body scattering takes place at the unitary limit (i.e., so that the cross section saturates the unitarity bound [Braaten & Hammer, 2007]).

At least to its discoverer (M. Olshanii), this unexpected effect initially seemed spurious. It seemed that as one tunes any one of the relevant parameters (keeping the other parameters constant) closer and closer to the value that should result in a CIR, one should also leave the domain of validity of the low-D theory. If so, then as far as the low-D theory

is concerned, the CIR itself is unphysical. What did seem safe to claim was that the mean-field many-body coupling changed sign as one tuned $a_\perp$ through the would-be resonance. Only several years later was it confirmed, through numerical study and additional theoretical work, that the scattering resonance is not spurious and actually does happen; we discuss this below in Sections 3.7, 3.11, and 3.12.

Because of the suspicions of spuriousness, the original paper (Olshanii, 1998) never suggested that the CIR could be used to reach the regime of hard-core, TG Bose gas. It turns out that the figure of merit for reaching this regime, γ, is the ratio between the two-particle interaction strength and the 1D atomic density (namely, $\gamma = (m/\hbar^2)\, g_{1D}/n_{1D}$, where n_{1D} is the particle 1D density and g_{1D} is the 1D coupling constant; the 1D two-body interaction potential has the form $V(z_1, z_2) = g_{1D}\,\delta(z_2 - z_2)$). The original suggestion for reaching the TG regime was rather to decrease the density, and this was precisely the route followed by Kinoshita et al. (2004) in their experimental realization. In contrast, Paredes et al. (2004) used an optical lattice to increase the effective mass, which also enters the figure of merit.

It turned out, however, that CIR can be used to achieve the hard-core regime after all. This was accomplished by Haller et al. (2009), whose work is at the same time the first experimental demonstration of a CIR in an effectively 1D system (see Section 5.1, below). Interestingly, here, many-body properties serve as probes for detecting and studying the CIR (Haller et al., 2010). Slightly before the work of Haller et al., Lamporesi et al. (2010) observed the CIR in scattering between one unconfined atomic species, and one that is confined to move only in 2D (see Section 5.2).

Much subsequent work on CIR, say in the context of optical latices (Section 4.2) and higher partial waves (Section 4.4), remains incidental to the development of two-body effective theories that are principally meant to be included into many-body analysis. Other developments, however, such as those of Peano et al. (2004) in Section 4.3 and Naidon et al. (2007) in Section 4.5, as well as the experimental studies of Haller et al. (2010) and (in large part) of Lamporesi et al. (2010), had no overt many-body motivations.

2. CONFINEMENT AND EFFECTIVE THEORIES

Consider quantum-mechanical particles in three spatial dimensions, but subject to a one-body external potential $U_{3D}(\vec{r})$ that effectively confines the particle motion to a subspace $\mathcal{S}$ of reduced spatial dimensionality. Let the collisions between the particles be governed by a 3D, pairwise, short-range (i.e., decaying faster than $1/r^3$ at large distances [Landau & Lifshitz, 1991, §132]) interparticle potential $V_{3D}(\vec{r}_1, \vec{r}_2)$. To understand how spatial

confinement works, let us first consider the case of noninteracting particles, $V_{3D} = 0$. If there is to be confinement, the presence of U_{3D} should result in two classes of single-particle eigenstates: those that are spatially localized around the low-dimensional subspace $\mathcal{S}$ and those that are not. Importantly, there should be an energy gap ΔE_{cnf} between the two classes, with the localized class having the lower energy. We are interested in cases where the localization is so strong that in the Hilbert space spanned by the class of localized states, there is simply no dynamics in the spatial directions that are orthogonal to $\mathcal{S}$.

As an example (still with $V_{3D} = 0$), take the external potential U_{3D} to be isotropically harmonic in the x- and y-directions but flat in the z-direction: $U_{3D}(r_x, r_y, r_z) = \frac{1}{2}m\omega_\perp^2(r_x^2 + r_y^2)$, where m is the particle mass and $\omega_\perp$ is the characteristic frequency of the harmonic oscillator. Our "subspace of reduced dimensionality" $\mathcal{S}$ will turn out to be just the z-axis, resulting in an effective 1D system. The motions in the longitudinal (z) and transverse (x and y) directions decouple. The transverse problem is just a 2D isotropic harmonic oscillator with the energy gap $\hbar\omega_\perp$ (which will turn out to be ΔE_{cnf} in this case) between its ground and first excited states. The class of eigenstates that are spatially localized around the z-axis (which is the subspace $\mathcal{S}$ in this case) consists of states that are each a product of a plane wave in the z-direction, and of the ground state of the transverse harmonic oscillator (which is a Gaussian of half-width $\sqrt{\frac{\hbar}{m\omega_\perp}}$). In the Hilbert space spanned by this class, there is no dynamics in the transverse directions, because transversely one is always in the ground state.

Returning to the case of general U_{3D}, let us reintroduce the interparticle potentials V_{3D}. Consider initial conditions such that the energy gap ΔE_{cnf} is large compared with typical collision energies. There will still be no dynamics in the spatial directions orthogonal to the low-dimensional subspace $\mathcal{S}$, *except possibly at the very moment of collision*. During collision, the interaction energy may become comparable to the energy gap; put another way, we may not neglect the matrix elements of the interparticle potential involving one localized and one nonlocalized state. Still, except at the very point of collision (it is appropriate to speak of a "point"of collision because V_{3D} is assumed to be short ranged), the particle motion becomes "frozen" to the low-dimensional subspace $\mathcal{S}$. In such a situation, one can in principle derive low-dimensional equations of motion for such a system (meaning, equations of motion that only involve spatial coordinates internal to $\mathcal{S}$), valid at collision energies much lower than ΔE_{cnf}. Importantly, all of the complications that exist at the point of collision add up to a single effect: namely, that the strength of the interactions in the effective theory is a nonobvious function of the parameters of the underlying 3D theory. In particular, the correct low-dimensional equations of motion cannot be obtained by simply integrating out the spatial directions orthogonal to

the low-dimensional subspace $\mathcal{S}$. Although the effective Hamiltonian that results from such integrating out does generally have the correct functional form, nevertheless, the strength of the interparticle interaction in this Hamiltonian may be incorrect. The reason is that the integrating-out procedure neglects the virtual transitions, which take place during collisions, to the high-energy nonlocalized states. When these virtual transitions are taken into account, one finds that the scattering amplitude, considered as a function of the 3D parameters, in general has peaks in its modulus squared for certain values of the parameters. These peaks are not predicted by the Hamiltonian obtained through simple integrating-out procedure. Moreover, at these peaks, the modulus squared of the scattering amplitude reaches the absolute maximum allowed by unitarity. These peaks are termed CIR.

3. THE CIR IN EFFECTIVELY 1D SYSTEMS

Even though this is a review paper, we feel it is worthwhile to present at least one example of CIR in a self-contained manner and in detail. The example we have chosen is the confinement to 1D by transverse 2D-isotropic harmonic potential. We have two reasons: one is to explain certain basic concepts that are common to nearly all CIRs, but that are best explained on a specific example. The other reason is that many works on other CIRs make references to and even use results derived for the CIR in effectively 1D systems.

3.1 The Underlying 3D Theory

Let us examine how the scenario outlined in Section 2 plays out in the example of harmonic transverse confinement. The full two-particle Hamiltonian is separable in relative and center-of-mass coordinates, and the Hamiltonian for the relative motion becomes

$$\widehat{H}_{3D} = -\frac{\hbar^2}{2\mu}\frac{\partial^2}{\partial z^2} + \widehat{H}_\perp + V_{3D}(\vec{r}_1, \vec{r}_2), \tag{1}$$

where the transverse Hamiltonian $\widehat{H}_\perp$ may be written in polar coordinates as

$$\widehat{H}_\perp = -\frac{\hbar^2}{2\mu}\left(\frac{\partial^2}{\partial\rho^2} + \frac{1}{\rho}\frac{\partial}{\partial\rho} + \frac{1}{\rho^2}\frac{\partial^2}{\partial\phi^2}\right) + \frac{1}{2}\mu\omega_\perp^2\,\rho^2. \tag{2}$$

Here, ρ, ϕ, and z are cylindrical coordinates of the relative displacement vector $\vec{r} = \vec{r}_1 - \vec{r}_2$, where $\vec{r}_1$ and $\vec{r}_2$ are the position vectors of particles 1 and 2, respectively; $\mu = m_1 m_2/(m_1 + m_2)$ is the reduced mass,

whereas m_1 and m_2 are the masses of the two particles. In our case, $m_1 = m_2$ (let us call this common mass m_0) and so $\mu = m_0/2$. The harmonic potential $\frac{1}{2}\mu\omega_\perp^2\rho^2$, characterized by the transverse trap frequency $\omega_\perp$, provides the transversal 2D-isotropic harmonic confinement. Since $\widehat{H}_\perp$ commutes with the angular momentum along the z-axis, $\hat{L}_z = -i\hbar\,\partial/\partial\phi$, we may work with their common eigenstates. They can be labeled $|n, m\rangle_\perp$ according to the radial and azimuthal quantum numbers n and m:

$$\widehat{H}_\perp\,|n, m\rangle_\perp = \hbar\omega_\perp(2n + |m| + 1)\,|n, m\rangle_\perp, \tag{3}$$

$$\widehat{L}_z\,|n, m\rangle_\perp = \hbar m\,|n, m\rangle_\perp, \tag{4}$$

where n and m independently assume the values

$$n = 0, 1, 2, \ldots, \infty, \quad \text{and} \quad m = 0, \pm1, \pm2, \ldots, \pm\infty. \tag{5}$$

The eigenfunctions are well-known:

$$\langle\rho, \phi|n, m\rangle_\perp = \sqrt{\frac{n!}{\pi a_\perp^2 (n + |m|)!}}\, \mathrm{e}^{-\frac{1}{2}\rho^2/a_\perp^2}\ (\rho/a_\perp)^{|m|}\ \mathrm{e}^{im\phi}\ L_n^{(|m|)}\left(\rho^2/a_\perp^2\right), \tag{6}$$

where

$$a_\perp = \sqrt{\frac{\hbar}{\mu\omega_\perp}} \tag{7}$$

is the transverse harmonic oscillator length, and $L_j^{(k)}(x)$ are the generalized Laguerre polynomials, e.g., $L_0^{(k)}(x) = 1$, $L_1^{(k)}(x) = 1 + k - x$, etc.

We will take the 3D interparticle potential to be given by the Fermi-Huang pseudopotential, an approximation standard in physics of ultracold gases: $V_{3D}(\vec{r}_1, \vec{r}_2) = V_{\text{F-H}}(\vec{r}_2 - \vec{r}_2)$, where the action of $V_{\text{F-H}}$ on a wave function represented in spherical coordinates as $\Psi(r, \theta, \phi)$ is given by

$$V_{\text{F-H}}(\vec{r})\Psi(\vec{r}) = g_{3D}\,\delta^3(\vec{r})\,\frac{\partial}{\partial r}\Big(r\,\Psi(r, \theta, \phi)\Big), \tag{8}$$

$$g_{3D} = \frac{2\pi\hbar^2 a_{3D}}{\mu}; \tag{9}$$

here, a_{3D} is the 3D scattering length (Huang, 1987). The pseudopotential correctly describes the scattering off of any realistic short-range potentials with scattering length a_{3D} provided that (1) only s-wave scattering matters, and (2) the scattering energy is small enough, i.e., the wave vector k

of the incident wave satisfies $\left|a_{3D}k\right| \ll 1$; see Leggett (2001, Section IV) for a discussion of the validity of Fermi-Huang pseudopotential in the context of ultra-cold quantum gases. To understand the role of the "regularizing operator" $\frac{\partial}{\partial r}(r\,\cdot)$ in Equation (8), we note that (as we will show in a moment) a wave function $\Psi(\vec{r})$ will be a solution to a Schrödinger equation with the pseudopotential in Equation (8) if and only if Ψ satisfies the Bethe–Peierls boundary condition, or "contact condition," (Bethe & Peierls, 1935; Wigner, 1933)

$$\Psi(\vec{r}) = A(1/r - 1/a_{3D}) + \mathcal{O}(r) \quad \text{as } r \to 0^+, \tag{10}$$

where A may be a function of θ and ϕ. Note that for functions that satisfy

$$\Psi(\vec{r}) = A/r + B + \mathcal{O}(r) \quad \text{as} \quad r \to 0^+ \tag{11}$$

we have $\delta^3(\vec{r})\frac{\partial}{\partial r}[r\Psi(r)] = \delta^3(\vec{r})B$; we refer to B as the *regular part* of $\Psi(r)$ as $r \to 0^+$. So *on the space of functions that satisfy Equation (11)*, the regularizing operator $\frac{\partial}{\partial r}(r\cdot)$ removes the term that would otherwise result in a divergence once the delta function sets r to zero. (There are other operators that can do the same job; see Olshanii and Pricoupenko [2001].) When $V_{\text{F-H}}$ acts on a function which has $A = 0$ (i.e., functions of the form of Equation [11] that are nevertheless finite at $r = 0$), the regularizing operator has no effect and can be dropped.

To see the equivalence of the pseudopotential in Equation (8) and the contact condition in Equation (10), recall that $-1/(4\pi r)$ is the Green's function of the 3D Laplacian, so $\nabla^2(1/r) = -4\pi\delta^3(\vec{r})$. Substituting a wave function satisfying Equation (11) into the Schrödinger equation and realizing that the terms proportional to the 3D delta function must cancel among themselves, we get Equation (10) in the form $A + B\,a_{3D} = 0$.

In our consideration of the scattering problem, we will be considering an incident wave that factorizes into longitudinal and transverse parts, with the longitudinal wave vector k and the transverse quantum numbers n and m (almost always we will be interested only in the transverse ground mode, $n = m = 0$): $\langle\vec{r}|\Psi_0\rangle = \langle\rho,\phi|n,m\rangle_\perp e^{ikz}$. This is the form that the eigenstates of $\widehat{H}_{3D}$ from Equation (1) would have if the interparticle potential were zero—and it is nonzero only at the origin.

Since the value of $|n,m\rangle_\perp$ at the origin is given by

$$\langle\vec{r} = 0|n,m\rangle_\perp = \delta_{m,0}\frac{1}{\sqrt{\pi}a_\perp}, \tag{12}$$

the incident wave is nonzero at the origin only for $m = 0$. Given that the scattering potential has zero-range, it has no effect on incident waves that are zero at the origin, and thus only incident waves with zero-angular

momentum will scatter (an analog of s-wave scattering in unconfined 3D problems), for any incident energy. For realistic potentials, a similar result holds for low-energy scattering, which (not coincidentally) is also the regime in which they can be approximated by a zero-range potential.

If the scattering particle is in the transverse ground mode, then the energy of the scattering process is

$$E = E_G + \frac{\hbar^2 k^2}{2\mu}, \tag{13}$$

where $E_G = \hbar\omega_\perp$ is the ground-state energy of the system, equal to the ground-state energy of the confining potential. The first excited state of the confining potential is at $2\hbar\omega_\perp$. We will be interested in situations when $\frac{\hbar^2 k^2}{2\mu}$ is much less than $\hbar\omega_\perp$, in which case we expect that the scattering particles will not leave the transverse ground state (except virtually, at the single point of collision). The exact solution of the problem will allow us explicitly to compute the probability $W_{\leftarrow n}(k)$ that after a collision of two particles with the relative momentum k and relative transverse excitation n (see Equation [4]), the particles will *not* remain in the same transverse state (Moore et al., 2004). It will turn out that for particles in the ground transverse state, $n = 0$, this probability vanishes, just as physical intuition suggests; see Equation (73) below and the discussion that follows it. Our aim is to eliminate the inert transverse degrees of freedom from the scattering problem. This will result in a 1D theory, with z the only variable.

Let us recall the main features of 1D theories.

3.2 General Features of 1D Scattering

In 1D scattering, there are just two kinds of partial waves: even and odd. The asymptotic form of the scattering wave function is thus

$$\psi(z) \sim e^{ikz} + f_{\text{even}}(k)\, e^{ik|z|} + f_{\text{odd}}(k)\, \text{sign}(z)\, e^{ik|z|}. \tag{14}$$

Since in our case the 3D potential is zero-range, we expect that interactions in our effective 1D theory will also be zero-range, in which case the odd scattering amplitude f_{odd} must be zero: the odd component of the wave function is zero at the origin, and thus a zero-range scatterer at the origin cannot have any effect.

We may also consider a different sort of boundary conditions, namely one where $\psi(z)$ is an even function. One reason why even-wave scattering wave functions are of interest is that the 1D even-wave scattering phase $\Delta(k)$ is defined using their asymptotic form, which is always

$$\psi(z) \sim \sin[k|z| + Q(k))] \quad \text{as } z \to \pm\infty, \tag{15}$$

where $Q(k)$ is some function of k but not of z. By definition, the scattering phase in any particular case *is* just this function: $\Delta(k) = Q(k)$. The important concept of the 1D scattering length is then defined through

$$a_{1D} = \lim_{k \to 0^+} \left[-\frac{d}{dk} \Delta(k) \right], \tag{16}$$

although it can also be read off from the scattering amplitude, see Equation (19).

3.3 Unitarity and CIR

The integrated equation of continuity in 1D reads

$$\int_a^b \frac{\partial}{\partial t} |\psi(z, t)|^2 \, dz = \int_a^b \frac{\partial}{\partial z} j(z, t) \, dz = j(b, t) - j(a, t), \tag{17}$$

where

$$j(z, t) = \frac{\hbar}{2 m i} \left[\psi^*(z, t) \frac{\partial}{\partial z} \psi(z, t) - \psi(z, t) \frac{\partial}{\partial z} \psi^*(z, t) \right]$$

is the probability flux. In a time-independent situation, we have $j(b) - j(a) = 0$. In the case of scattering with the asymptotic form of Equation (14) with $f_{\text{odd}} = 0$, we may use that form to evaluate $j(+\infty) - j(-\infty)$. This, too, should be zero, which results in the "unitarity relation" $\left| f_{\text{even}}(k) \right|^2 = \text{Re} f_{\text{even}}(k)$. It immediately follows that

$$\frac{1}{f_{\text{even}}} = \frac{f_{\text{even}}^*}{\left| f_{\text{even}}(k) \right|^2} = \frac{f_{\text{even}}^*}{\text{Re} f_{\text{even}}} = 1 - i \frac{\text{Im} f_{\text{even}}}{\text{Re} f_{\text{even}}},$$

in other words, that the complex-valued function f_{even} must be parametrizable by a single real-valued function h_{real} (which is $-\text{Im} f_{\text{even}} / \text{Re} f_{\text{even}}$) through

$$f_{\text{even}}(k) = -\frac{1}{1 + i h_{\text{real}}(k)}. \tag{18}$$

One can show that the small-k expansion of $h_{\text{real}}(k)$ includes the 1D scattering length, Equation (16), in the leading order:

$$h_{\text{real}}(k) = k a_{1D} + \mathcal{O}(k^2). \tag{19}$$

Let us consider now the modulus squared of the scattering amplitude, $|f_{\text{even}}|^2$. Unitarity, i.e., the representation in Equation (18), shows that $|f_{\text{even}}|^2 = 1/\left(1 + h_{\text{real}}^2\right)$. Therefore, unitarity implies that $|f_{\text{even}}|^2$ is at most 1, attained when $h_{\text{real}} = 0$; this maximum is called the *unitarity bound*, and if a scattering process saturates this bound, it is said to take place at the *unitary limit*. There is no a priori guarantee that $h_{\text{real}}(k)$ ever vanishes for $k > 0$. But h_{real} depends on a number of parameters, including the strength of the confinement (e.g., $a_\perp$ for transverse 2D-isotropic harmonic confinement). If, as the confinement strength is varied with all the other parameters (e.g., k and $a_{3\text{D}}$) being held fixed, h_{real} either crosses or touches zero at a point, the corresponding maximum of $|f_{\text{even}}|^2$ is a CIR. From Equation (19), we may expect that for small k, the CIR happens approximately when $a_{1\text{D}} = 0$; we will confirm this expectation in Equation (76), below.

3.4 Properties of the 1D Zero-Range Potential

The low-D effective theory may or may not lend itself to a formulation in terms of a low-D Hamiltonian with a low-D effective potential. For example, we will see below that in the case of 1D harmonic confinement, one does get an effective 2D description, but encoding this description into a 2D potential is tricky. As it turns out, in the present case of 2D harmonic confinement, we will eventually get a nice effective 1D delta-function potential of the form

$$V_{1\text{D}}(z) = g_{1\text{D}}\,\delta(z), \tag{20}$$

and so it makes sense to review its properties. One begins by realizing that if a wave function $\psi(z)$ is to satisfy the 1D Schrödinger equation with the delta-function potential, then the second derivative of ψ must produce a delta function at zero, so that ψ itself is continuous at zero but its first derivative is not. The delta-function potential thus gives a jump condition on the derivative. To get this condition, we integrate the equation

$$-\frac{\hbar^2}{2\mu}\frac{\partial^2}{\partial z^2}\psi(z) + g_{1\text{D}}\,\delta(z)\,\psi(z) = E\,\psi(z)$$

in a small window $z \in [-\epsilon, \epsilon]$ and then take the limit $\epsilon \to 0^+$. Because of the continuity of $\psi(z)$ at $z = 0$, the term proportional to E vanishes and we obtain

$$\lim_{\epsilon\to 0^+}\left[\psi'(\epsilon) - \psi'(-\epsilon)\right] = \frac{2\mu}{\hbar^2}\,g_{1\text{D}}\,\psi(0) = -\frac{2}{a_{1\text{D}}^{\delta}}\,\psi(0). \tag{21}$$

Here,

$$a_{1D}^{\delta} = -\frac{\hbar^2}{\mu g_{1D}} \tag{22}$$

will turn out to be the 1D scattering length for the potential in Equation (20), see Equation (25) and the text that follows. As in the 3D case, Equation (10), we may express the jump condition of Equation (21) as a contact condition on the wave function:

$$\psi(z) = \psi(0)\,(1 - |z|/a_{1D}^{\delta}) + \mathcal{O}(z^2) \quad \text{as } z \to 0. \tag{23}$$

It is the absolute value in z that generates the delta function. Indeed, if $f(z)$ is a twice-differentiable function, we have

$$\frac{\mathrm{d}^2}{\mathrm{d}z^2} f(|z|) = f''(|z|) + 2f'(0)\,\delta(z), \tag{24}$$

where we used $\frac{d}{dz}|z| = 2\theta(z) - 1$ and $\frac{d}{dz}\theta(z) = \delta(z)$, with $\theta(z)$ the step function (0 if $z < 0$ and 1 if $z > 0$).

Away from zero, the wave function $\psi(z)$ must satisfy the free Schrödinger equation, and so it must be a superposition of incoming and outgoing plane waves. However, the jump condition says that the superpositions for $z > 0$ and for $z < 0$ will not be analytic continuations of each other. To fix the form of the superpositions, in addition to the jump condition, one needs another condition that the wave function must satisfy; this additional condition will determine the physical meaning of the final solution. Our first scattering solution will come from requiring that $\psi(z)$ be even; from this solution, we can read off the 1D even-wave scattering phase $\Delta(k)$ and determine the 1D scattering length, see Equations (15) and (16). An independent motivation is that from the two-body perspective, bosonic symmetry requires that the wave function in relative coordinate be even. Up to normalization, the even-wave scattering wave function works out to be

$$\psi(z) = \left[\, b(k) - i\,\mathrm{sign}\,(z)\right] \mathrm{e}^{ikz} + \left[\, b(k) + i\,\mathrm{sign}\,(z)\right] \mathrm{e}^{-ikz} \tag{25}$$

$$= \mathcal{A}\,\sin\left[k|z| + \Delta^{\delta}(k)\right]. \tag{26}$$

Here, $b(k) = \frac{\hbar^2 k}{\mu g_{1D}}$, $\Delta^{\delta}(k) = \arctan b(k)$ is the scattering phase, and $\mathcal{A} = 2/\cos\Delta^{\delta}(k)$. Note that for general short-range 1D interaction potentials, the form $\psi(z) \sim \sin[k|z| + \Delta(k)]$, i.e., the form of Equation (15), only holds for large $|z|$. But for zero-range 1D potentials, this form turns out to be correct for all z; in other words, for a zero-range scatterer at the origin, any

nonzero z is already asymptotically far from the origin. The 1D scattering length is then given by $a_{1D} = \lim_{k\to 0^+}[-\Delta'(k)]$, Equation (16), which gives Equation (22). We then also have $b(k) = -a_{1D}^{\delta} k$.

Another useful type of additional condition that we may require of our wave function is that the superpositions of plane waves that make up $\psi(z)$ match asymptotically the form in Equation (14); obviously, from this type of scattering solution, we will be able to read off the scattering amplitude. Once again the asymptotic form will turn out to be the form of the full solution,

$$\psi(z) = e^{ikz} + f_{even}(k)\, e^{ik|z|}, \quad \text{all } z, \tag{27}$$

since the scatterer has zero range. We get

$$f_{even}^{\delta}(k) = -\frac{1}{1 + i k a_{1D}^{\delta}}, \tag{28}$$

so that $h_{real}^{\delta}(k) = k a_{1D}^{\delta}$; this is consistent with the general result that $h_{real}(k) = k a_{1D} + \mathcal{O}(k^2)$, Equation (19).

The scattering amplitude has a pole for $k = i/a_{1D}^{\delta}$. On general grounds, a pole of the scattering amplitude at $k = i\kappa$ with $\kappa > 0$ corresponds to a bound state with energy $-\hbar^2\kappa^2/(2\mu)$; thus, the 1D delta-function potential supports a bound state whenever $a_{1D} > 0$, which means $g_{1D} < 0$, see Equation (22). Away from the origin, the bound state satisfies the free Schrödinger equation but must decay to zero at infinity, and so it must be $\sim e^{-\kappa z}$ for $z > 0$ and $\sim e^{\kappa z}$ for $z < 0$; in other words, $\sim e^{-\kappa|z|}$. The constant κ may be read off either from Equation (23) or from the fact that the energy must match that predicted from the pole of the scattering amplitude. Either way, the normalized bound-state wave function and its energy read

$$\psi_B(z) = \frac{1}{(a_{1D}^{\delta})^{1/2}} e^{-|z|/a_{1D}^{\delta}}, \quad E_B = -\frac{\hbar^2}{2\mu}\frac{1}{(a_{1D}^{\delta})^2}, \tag{29}$$

again provided $a_{1D} > 0$ ($g_{1D} < 0$).

We see that for 1D delta-function potential, a CIR would correspond to the vanishing of a_{1D}^{δ}, that is, to a divergence in g_{1D}. From the jump condition in Equation (21), we see that a diverging g_{1D} means that a scattering wave function must go to zero at $z = 0$. For if not, if $\psi(0) \neq 0$, then the right-hand side, $\frac{2\mu}{\hbar^2} g_{1D}\, \psi(0)$, would be infinite as $g_{1D} \to \pm\infty$. But the left-hand side, $\lim_{\epsilon\to 0^+}[\psi'(\epsilon) - \psi'(-\epsilon)]$, would not be: away from the origin, the wave function must satisfy a Schrödinger equation without the delta potential, with standard finite-energy boundary conditions

such as those in Equation (14), and such a problem cannot have any solutions whose derivatives diverge at zero. Clearly, both types of scattering solutions we considered, $\psi(z) = \mathcal{A} \sin\left[k|z| + \Delta^{\delta}(k)\right]$ and $\psi(z) = \exp(ikz) + f^{\delta}_{\text{even}}(k) \exp(ik|z|)$, become zero at $z = 0$ if $a^{\delta}_{\text{1D}} = 0$, since then $\Delta^{\delta}(k) = -\arctan(a^{\delta}_{\text{1D}} k) = 0$ and $f^{\delta}_{\text{even}}(k) = -1$.

In two-body language, we have a wave function that vanishes for zero separation between the scattering particles, which are, therefore, said to have *hard cores*. In many-body setting, the limit $g_{\text{1D}} \to +\infty$ results in a regime called the Tonks-Girardeau (TG) gas of hard-core bosons (Girardeau, 1960; Tonks, 1936). The limit $g_{\text{1D}} \to -\infty$ is called the super-Tonks gas, introduced and studied by Astrakharchik et al. (2005) (see also Sec. 5.1).

3.5 Preliminary Step in Building an Effective 1D Theory: Simple Integrating Out

We proceed with a preliminary, heuristic analysis of the elimination of the transverse degrees of freedom from our problem with 2D confinement, Equation (1). As we said, since the 3D potential is zero-range, the interactions in our effective 1D theory will also be zero-range, and we assume that we can describe them using the 1D zero-range potential $g_{\text{1D}}\,\delta(z)$, which according to Equations (19) and (28) should be true at least for low energies. All that remains is to determine the value of the coupling constant g_{1D}. The incident wave is taken to have the factorized form $\Psi(\vec{r}) = \phi_0(\rho)\,\psi(z)$, where $\phi_0(\rho) = \exp(-\rho^2/2a_\perp^2)/(a_\perp\sqrt{\pi})$ is the transverse ground state. The function $\psi(z)$ is expected to be the solution to a problem with 1D delta-function potential, so it should satisfy the contact condition in Equation (23). But then $\Psi(\vec{r})$ is finite at the origin, and so it does not satisfy the contact condition in Equation (10) as the true solution to the 3D scattering problem would have to. We conclude that in the true solution, the requisite $1/r$ divergence at the origin must somehow come from an admixture of transversely excited states.

Let us figure out under what conditions we are justified in neglecting the admixture of transversally excited states. What we need is for the confining potential to be approximately flat on the length scale relevant for 3D scattering. This would suggest the condition $|a_{\text{3D}}| \ll a_\perp$. The same can be guessed from dimensional analysis: there are only three length scales in the problem: a_{3D}, $a_\perp$, and $1/k$. When $a_{\text{3D}} = 0$, there is no admixture at all, and so the condition under which the admixture may be neglected must involve a_{3D}. We have already found the meaning of the comparison of a_{3D} to $1/k$: when $|a_{\text{3D}}|\,k \ll 1$, then the 3D pseudopotential approximation is valid. Therefore, the validity of neglecting the admixture must involve the remaining parameter, $a_\perp$, just as we had guessed. Below, we will be able to confirm from the exact solution that $|a_{\text{3D}}| \ll a_\perp$ is indeed the correct condition; see the text following Equation (79).

Plugging our factorized $\Psi(\vec{r})$ into the Schrödinger equation with $\widehat{H}_{3D}$ from Equation (1), we see that the terms apart from the interparticle potential return the same factorized form back (remember that $\phi_0(\rho)$ is an eigenstate of $\widehat{H}_\perp$). As we have noted above, the 3D Schrödinger equation with nonzero interactions is *not* exactly satisfied by any state of this factorized form; but we will assume that $|a_{3D}|/a_\perp \ll 1$ and that therefore we may neglect the admixture of excited transverse waves, so that the factorized form of $\Psi(\vec{r})$ does satisfy the equation approximately:

$$-\frac{\hbar^2}{2\mu}\frac{\partial^2}{\partial z^2}\phi_0(\rho)\,\psi(z) + \widehat{H}_\perp\,\phi_0(\rho)\,\psi(z) + g_{3D}\,\delta^3(\vec{r})\,\frac{\partial}{\partial r}\Big(r\,\phi_0(\rho)\,\psi(z)\Big) \approx E\,\phi_0(\rho)\,\psi(z).$$

We may now eliminate the ρ and ϕ coordinates by applying $_\perp\langle 0,0| = \int_0^{2\pi} d\phi \int_0^\infty \rho\, d\rho\, \phi_0^*(\rho)$ to both sides of this equation. Everywhere except at the interaction term, we simply get the normalization integral for $\phi_0(\rho)$, which is 1. Turning now to the interaction term: since $\Psi(\vec{r})$ is finite at the origin, the regularizing operator has no effect, and so we get

$$\int_0^\infty d\rho\, 2\pi\rho\, |\phi_0(\rho)|^2\, \frac{2\pi\hbar^2 a_{3D}}{\mu}\,\delta^3(\vec{r})\,\psi(z) = g_{1D}^{\text{int}}\,\delta(z)\,\psi(z), \tag{30}$$

where

$$g_{1D}^{\text{int}} = \frac{2\hbar^2 a_{3D}}{\mu a_\perp^2}, \tag{31}$$

with the corresponding 1D scattering length obtained via Equation (22):

$$a_{1D}^{\text{int}} = -\frac{a_\perp^2}{2a_{3D}}. \tag{32}$$

In this way we have obtained an effective 1D Schrödinger equation, where only the z coordinate appears, and where the 1D potential is given by $g_{1D}^{\text{int}}\,\delta(z)$, with g_{1D}^{int} from Equation (31).

This completes the preliminary heuristic analysis. So far, we have found no CIRs; however, what we did is valid only for $|a_{3D}| \ll a_\perp$. We now turn to a more careful analysis, which will reveal our first example of a CIR.

3.6 An Exact 1D Effective Theory

Our goal is to model the longitudinal behavior of the 3D system in the presence of transversal harmonic confinement, as described by the Hamiltonian in Equation (1). Remarkably, this 3D problem admits of an *exact*

solution (Moore et al., 2004; Olshanii, 1998). This exact solution can then be matched to the asymptotic scattering form; as in the previous two sections, this form should hold if we take the longitudinal kinetic energy $\hbar^2 k^2/(2\mu)$ to be small when compared with $\hbar\omega_\perp$, and $|z|$ to be so large that $k|z| \gg 1$. Again only even partial waves (1D analog of *s*-wave scattering) should matter, and we write

$$\Psi(z, \rho) \sim \left\{ e^{ikz} + f_{\text{even}}(k; a_{3D}, a_\perp)\, e^{ik|z|} \right\} \phi_0(\rho), \qquad |z| \gg 1/k, \tag{33}$$

where f_{even} is the scattering amplitude for even partial waves. To obtain the exact solution, we expand the 3D wave function in the $|n, m\rangle_\perp$ eigenstates of the transverse Hamiltonian $\widehat{H}_\perp$, see Equation (3). In fact, according to the discussion following Equation (12), only the $\phi_n(\rho) = \langle \rho, \phi | n, m = 0 \rangle_\perp$ states are relevant:

$$\Psi(z, \rho) = \sum_{n=0}^{\infty} \psi_n(z)\, \phi_n(\rho), \qquad \text{all } z. \tag{34}$$

We substitute this expansion in the Schrödinger equation $\widehat{H}_{3D}\, \Psi(z, \rho) = E\, \Psi(z, \rho)$, with $\widehat{H}_{3D}$ given in Equation (1), and impose the boundary condition in Equation (33). The boundary condition is appropriate if the energy E is less than $3\hbar\omega_\perp$, the energy of the first $m = 0$ excited transverse state, $|n = 1, m = 0\rangle_\perp$ in Equation (3). Note that although our principal interest is in situations when E is *much* less than $3\hbar\omega_\perp$, for now we merely assume that it is *less* than that. The transverse ground state energy is $\hbar\omega_\perp$, so

$$E = \hbar^2 k^2/(2\mu) + \hbar\omega_\perp \quad \text{with} \quad \hbar^2 k^2/(2\mu) < 2\hbar\omega_\perp. \tag{35}$$

Because $\Psi(z, \rho)$ satisfies a Schrödinger equation with the regularized pseudopotential in Equation (8), it must satisfy the contact condition in Equation (10). We will be most interested in the behavior of $\Psi(z, \rho)$ at $\rho = 0$. Since $r = (\rho^2 + z^2)^{1/2}$, the contact condition reads

$$\Psi(z, \rho = 0) = A(1/|z| - 1/a_{3D}) + \mathcal{O}(z) \quad \text{as } z \to 0. \tag{36}$$

We will be interested in the regular part of the wave function at $z = 0$, $\rho = 0$, which we denote by η. The simplest way to obtain it is to read it off as the z-independent term in the expansion of $\Psi(z, \rho = 0)$ about $z = 0$. More formally, we have $\eta = \frac{\partial}{\partial r}[r\, \Psi(\vec{r})]_{r\to 0^+} = \frac{\partial}{\partial z}\, [z\, \Psi(z, \rho = 0)]_{z\to 0^+}$, where we used $\frac{\partial}{\partial r} = (\rho/r)\frac{\partial}{\partial \rho} + (z/r)\frac{\partial}{\partial z}$. The contact condition in Equation (36) may be expressed as

$$\eta = -A/a_{3D} \quad \text{with} \quad A = \lim_{z\to 0^+}[z\, \Psi(z, \rho = 0)]. \tag{37}$$

At the level of the individual terms entering the infinite sum in Equation (34), what must happen is the following. Clearly, it is the action of the kinetic part of $\widehat{H}_{3D}$ onto $\Psi(z,\, \rho = 0)$ that must produce a regularized delta function, which then cancels the one coming from the pseudopotential in Equation (8). Moreover, since the transverse states $\phi_n(\rho)$ are analytic at $\rho = 0$, the delta function must come from the action of $-\frac{\hbar^2}{2\mu}\frac{\partial^2}{\partial z^2}$ on (at least some of) the longitudinal functions $\psi_n(z)$. From Section 3.4, we know that these functions of a single variable can indeed produce 1D delta functions, provided $\psi_n(z) = A + B|z| + \mathcal{O}(z^2)$, cf. Equations (23) and (24). Motivated by the wave functions we found in Section 3.4 (Equations [25], [27], and [29]) and Equation (24), we make the ansatz (which we will confirm in Equations [46] and [47] below) that for each ψ_n there is a function $p_n(z)$ such that

$$\psi_n''(z) = p_n(z) + \mu_n \delta(z), \quad p_n(z) \text{ finite at } z = 0, \tag{38}$$

for some μ_n. Let us denote the functions $p_n(z)$ by $\mathcal{R}\psi_n''(z)$ ("the regular part of $\psi_n''(z)$"). The Schrödinger equation can then be written as

$$\sum_{j=0}^{\infty} \left[-\frac{\hbar^2}{2\mu}\, \mathcal{R}\psi_j''(z)\, \phi_j(\rho) + \psi_j(z)\, \widehat{H}_\perp \phi_j(\rho) \right] + \Omega = E \sum_{j=0}^{\infty} \psi_j(z)\, \phi_j(\rho), \tag{39}$$

where

$$\Omega = \sum_{j=0}^{\infty} [\mu_j \phi_j(\rho)\, \delta(z)] + g_{3D}\, \delta(z)\, \frac{\delta(\rho)}{\pi\rho}\, \eta \tag{40}$$

contains the terms proportional to delta functions. Here, η is the regular part of the wave function at $z = \rho = 0$, see the text following Equation (36), and we have used the representation $\delta^3(\vec{r}) = \delta(z)\, \delta(\rho)/(\pi\rho)$.

As we said, Ω must be zero on its own, because it contains all the delta functions in the equation. We will return to that requirement shortly; for now, we assume that it is zero, and apply $\int_0^\infty 2\pi\rho\, d\rho\, \phi_n^*(\rho)$ to both sides of Equation (39). The orthonormality of the transverse wave functions $\phi_n(\rho)$ gives separate equations for each n. Away from $z = 0$, $\mathcal{R}\psi_n''(z) = \psi_n''(z)$, and we have just the free Schrödinger equations

$$-\frac{\hbar^2}{2\mu}\frac{\partial^2}{\partial z^2}\, \psi_n(z) + (2n+1)\hbar\omega_\perp \psi_n(z) = E\, \psi_n(z), \quad z \neq 0, \tag{41}$$

so that $\psi_n(z)$ is a superposition of exponentials $\mathrm{e}^{\pm\kappa_n z}$, with κ_n's (which may be complex-valued) to be determined presently. As in Section 3.4,

the superposition for $z < 0$ may be different from the one for $z > 0$, i.e., the wave function for $z < 0$ need not be the analytic continuation of the wave function for $z > 0$, because the Schrödinger equation contains a delta function at zero. Using Equation (35), we get that $\kappa_0 = i\,k$, whereas for each $n > 0$ one gets a real-valued κ_n:

$$\kappa_n = \sqrt{\frac{2\mu}{\hbar^2}\left(2n\hbar\omega_\perp - \frac{\hbar^2 k^2}{2\mu}\right)} = \frac{2}{a_\perp}\sqrt{n+\epsilon}, \quad n = 1, 2, \ldots, \tag{42}$$

$$\epsilon = -a_\perp^2\, k^2/4 = -\frac{E - \hbar\omega_\perp}{2\hbar\omega_\perp}, \quad -1 < \epsilon < 0 \quad \text{(cf. Equation [35])}. \tag{43}$$

The boundary condition in Equation (33) implies that

$$\psi_0(z) = \mathrm{e}^{ikz} + f\,\mathrm{e}^{ik|z|}, \tag{44}$$

as in Equation (27), from which it also follows that for $n > 0$, $\psi_n(z)$ must vanish as $z \to \pm\infty$. Thus, we obtain bound states:

$$\psi_n(z) = a_n\,\mathrm{e}^{-\kappa_n|z|}, \qquad n \geqslant 1, \tag{45}$$

compare with Equation (29). Note that without interactions, i.e., the delta function, the functions $\psi_n(z)$ would have to be analytic through $z = 0$, and so would for $n > 0$ have to be of the form $a\,\mathrm{e}^{-\kappa_n z} + b\,\mathrm{e}^{\kappa_n z}$ for all z. But this can vanish at both $-\infty$ and $+\infty$ only if $a = b = 0$; so we see explicitly that a wave function $\Psi(z, \rho)$ satisfying our boundary conditions can contain an admixture of transversely excited states only if there are interactions.

Now we make sure that Ω from Equation (40) is zero. From Equation (24), it follows that

$$-\frac{\hbar^2}{2\mu}\frac{\partial^2}{\partial z^2}\psi_n(z) = \begin{cases} \frac{\hbar^2 k^2}{2\mu}\,\psi_0(z) - i\,\frac{\hbar^2}{\mu}\,kf\,\delta(z), & n = 1, \quad (46) \\ -\frac{\hbar^2\kappa_n^2}{2\mu}\,\psi_n(z) + \frac{\hbar^2}{\mu}\,a_n\,\kappa_n\,\delta(z), & n \geqslant 1, \quad (47) \end{cases} \tag{48}$$

which is consistent with our ansatz in Equation (38). The equation $\Omega = 0$ becomes

$$-i\,\frac{\hbar^2}{\mu}\,kf\,\delta(z)\,\phi_0(\rho) + \sum_{n=1}^{\infty}\frac{\hbar^2}{\mu}\,a_n\,\kappa_n\,\delta(z)\,\phi_n(\rho) + g_{3\mathrm{D}}\,\delta(z)\,\frac{\delta(\rho)}{\pi\rho}\,\eta = 0; \tag{49}$$

now we apply $\int_0^\infty 2\pi\rho\, d\rho\, \phi_j^*(\rho)$ to both sides of Equation (49). Orthonormality of the functions $\phi_n(\rho)$ gives

$$f = -i\,2\sqrt{\pi}\,\frac{a_{3D}}{a_\perp}\,\eta\frac{1}{k} \tag{50}$$

$$a_n = -2\sqrt{\pi}\,\frac{a_{3D}}{a_\perp}\,\eta\,\frac{1}{\kappa_n}, \tag{51}$$

where we have used the fact that $\phi_n(\rho = 0) = 1/(a_\perp\sqrt{\pi})$ for all n, see Equation (12).

We plug the results in Equations (44), (45), (42), (50), and (51) into the expansion in Equation (34). At $\rho = 0$, we have

$$\Psi(z,\,\rho = 0) = \frac{1}{a_\perp\sqrt{\pi}}\,\mathrm{e}^{ikz} - i\,\frac{2}{k}\,\frac{a_{3D}}{a_\perp^2}\,\eta\,\mathrm{e}^{ik|z|} - \frac{a_{3D}}{a_\perp}\,\eta\,\Lambda(x,\,\epsilon), \tag{52}$$

with $\epsilon = -a_\perp^2\,k^2/4$ as in Equation (43), $x = 2|z|/a_\perp$, and

$$\Lambda\,(x,\,\epsilon) = \sum_{n=1}^{\infty}\frac{\mathrm{e}^{-x\sqrt{n+\epsilon}}}{\sqrt{n+\epsilon}}. \tag{53}$$

Note that the first two terms in Equation (52) match the asymptotic form of Equation (33), while the function Λ decays to zero at for large $|z|$. On the other hand, it is the function Λ that contains the admixture of transversally excited states. Further, the contact condition in Equation (37) says that the wave function must diverge at $z = 0$, $\rho = 0$. As all the functions $\psi_n(z)$ and $\phi_n(\rho)$ that enter the sum in Equation (34) are finite at the origin, it follows that the requisite divergence must come from the divergence of the infinite sum. In terms of Equations (52) and (53), it means that the divergence at $z = 0$, i.e., at $x = 0$, must come from Λ. This is indeed the case, as is easy to see from Equation (53).

Our main interest is to obtain the scattering amplitude f. According to Equation (50), we therefore need to find η, the regular part of the wave function at $z = \rho = 0$ (see the text following Equation [36]). Note that in the expression in Equation (52), some of the regular terms (such as the second one) are themselves expressed in terms of η. Thus, when we set the regular part of the wave function (which is η) to the sum of all the regular terms, η will appear on both sides—we will get an equation for it (see Equation [64] below).

We will now isolate the divergence at $z = 0$ from the sum in Equation (53). A divergence occurs already at the level of a related integral, $\int_0^\infty \mathrm{e}^{-x\sqrt{\nu}}/\sqrt{\nu}\,d\nu = 2/x$, and so we may hope that the difference between

the sum and the integral is finite at zero. Let Λ_N be the N-th partial sum for Λ. We add and subtract to it the integral

$$\int_1^N \frac{e^{-x\sqrt{v+\epsilon}}}{\sqrt{v+\epsilon}}\,dv = 2\,\frac{e^{-x\sqrt{1+\epsilon}} - e^{-x\sqrt{N+\epsilon}}}{x}$$

(note that many other integrals would work just as well), and take the limit $N \to \infty$. We also add and subtract $2/x$ and write the result as

$$\Lambda(x, \epsilon) = 2/x + \widetilde{\Lambda}(x, \epsilon) \tag{54}$$

with

$$\widetilde{\Lambda}\,(x, \epsilon) = -\frac{2}{x} + 2\,\frac{e^{-x\sqrt{1+\epsilon}}}{x} + \lim_{N\to\infty}\left(-2\,\frac{e^{-x\sqrt{1+\epsilon}} - e^{-x\sqrt{N+\epsilon}}}{x} + \sum_{n=1}^{N}\frac{e^{-x\sqrt{n+\epsilon}}}{\sqrt{n+\epsilon}}\right). \tag{55}$$

The point of this is that the limit $x \to 0^+$ of $\widetilde{\Lambda}$ is finite, and is all we will need to extract η:

$$\Lambda(x, \epsilon) = 2/x + \widetilde{\Lambda}(0^+, \epsilon) + \text{terms that vanish at } x = 0, \tag{56}$$

where

$$\widetilde{\Lambda}(0^+, \epsilon) = \lim_{N\to\infty}\left(\sum_{n=1}^{N}\frac{1}{\sqrt{n+\epsilon}} - 2\sqrt{N+\epsilon}\right). \tag{57}$$

If the sum in Equation (57) went from $n = 0$ rather than from $n = 1$, it would be the $s = 1/2$ case of the Hurwitz zeta function :

$$\zeta(s, \alpha) = \lim_{N\to\infty}\left[\left(\sum_{n=0}^{N}\frac{1}{(n+\alpha)^s}\right) - \frac{1}{1-s}\,\frac{1}{(N+\alpha)^{s-1}}\right]. \tag{58}$$

The representation above is valid when $\mathrm{Re}(s) > 0$ and $-2\pi < \arg(n+\alpha) \leqslant 0$ (Apostol, 1976). The Riemann zeta function is the special case with $\alpha = 1$:

$$\zeta(s) = \zeta(s, 1). \tag{59}$$

For $s = 1/2$, Equation (58) gives

$$\zeta(1/2, \alpha) = \lim_{N\to\infty}\left[\left(\sum_{n=0}^{N}\frac{1}{\sqrt{n+\alpha}}\right) - 2\sqrt{N+\alpha}\right], \tag{60}$$

where $\sqrt[\uparrow]{}$ and $\sqrt[\downarrow]{}$ denote two different branches of the square root: $\sqrt[\uparrow]{|z|e^{i\phi}} = \sqrt{|z|}e^{i\phi/2}$ for $0 \leqslant \phi < 2\pi$, and $\sqrt[\downarrow]{|z|e^{i\phi}} = \sqrt{|z|}e^{i\phi/2}$ for $-2\pi < \phi \leqslant 0$.

There are two ways to relate the sum in Equation (57) to $\zeta(1/2, \epsilon)$: first, we may reinterpret $n + \epsilon$ as $(n-1) + (1+\epsilon)$, which gives

$$\widetilde{\Lambda}(0^+, \epsilon) = \zeta(1/2, 1+\epsilon). \tag{61}$$

Secondly, we may add and subtract the missing $n = 0$ term, obtaining

$$\widetilde{\Lambda}(0^+, \epsilon) = \zeta(1/2, \epsilon) - 1/\sqrt[\downarrow]{\epsilon}. \tag{62}$$

Since $\epsilon = -a_\perp^2 k^2/4$, we have $1/\sqrt[\downarrow]{\epsilon} = -2i/(|k|a_\perp)$.

Another way to make sense of the sum in Equation (57) is to use the expansion $1/\sqrt{n+\epsilon} = 1/\sqrt{n} + \sum_{j=1}^{\infty} c_j \epsilon^j / n^{j+1/2}$, with $c_j = (2j-1)!!(-1)^j/(2^j j!)$. One obtains the $N \to \infty$ limit of $\left(\sum_{n=1}^{N} 1/\sqrt{n} - 2\sqrt{N+\epsilon}\right) + \sum_{j=1}^{\infty} c_j d_j(N) \epsilon^j$, with $d_j(N) = \sum_{n=1}^{N} 1/n^{j+1/2}$. According to Equation (60), the first two terms add up to $\zeta(1/2, 1) = \zeta(1/2)$ (see Equation [59]), whereas according to Equation (58) with $s = j + 1/2 > 1$, the limit of $d_j(N)$ is $\zeta(j+1/2, 1) = \zeta(j+1/2)$. Let us write the result in the form

$$\widetilde{\Lambda}(0^+, \epsilon) = \sum_{j=0}^{\infty} b_j(1/2)\, \epsilon^j \tag{63}$$

with $b_j(s) = \frac{(-1)^j}{j!} s(s+1)(s+2)\cdots(s+j-1)\,\zeta(j+s)$. Rane (1993) has proven that for any complex number $s \neq 1$, the series $\sum_{j=0}^{\infty} b_j(s)\,\epsilon^j$ converges uniformly and absolutely on every compact subset of the complex plane with $|\epsilon| < 1$, and that the series also converges for $\epsilon = 1$ if $0 < \mathrm{Re}\, s < 1$. Plugging the series into Equation (62) then yields the $s = 1/2$ case of the expansion $\zeta(s, x) = x^{-s} + \sum_{j=0}^{\infty} b_j(s)\, x^j$.

Returning to Equation (52), we express the function Λ through Equation (56), which gives

$$\Psi(z, \rho = 0) = -\frac{a_{3D}\,\eta}{|z|} + \underbrace{\frac{1}{a_\perp\sqrt{\pi}} - i\frac{2}{k}\frac{a_{3D}}{a_\perp^2}\,\eta - \frac{a_{3D}}{a_\perp}\,\eta\,\widetilde{\Lambda}(0^+, -a_\perp^2 k^2/4)}_{\text{regular part of } \Psi(r \to 0^+)\ = \eta} + \mathcal{O}(z). \tag{64}$$

Note that the form of the singular term is just that required by the contact condition in Equation (37). As expected, the other terms enter an equation for η, which is easily solved; the scattering amplitude follows by Equation (50). It will be useful to express $\widetilde{\Lambda}(0^+, \epsilon)$ through the Hurwitz zeta

function, via Equation (62). The result is

$$f_{\text{even}}(k;\, a_{3\text{D}},\, a_\perp) = -\frac{i}{\frac{a_\perp k}{2}} \frac{1}{\left[\frac{a_\perp}{a_{3\text{D}}} + \zeta(1/2, -\frac{a_\perp^2 k^2}{4})\right]}. \tag{65}$$

This form is most convenient for finding bound-state energies, as we will do below in Section 3.9. If we wish to extract the 1D scattering length $a_{1\text{D}}$ that appears in Equation (19), then it is better to write $\widetilde{\Lambda}(0^+,\, \epsilon)$ in terms of the expansion in Equation (63), where we single out the constant term: $\widetilde{\Lambda}(0^+,\, \epsilon) = \zeta(1/2) + \widetilde{\mathcal{L}}(\epsilon)$, with

$$\widetilde{\mathcal{L}}(\epsilon) = \sum_{j=1}^{\infty} b_j(1/2)\, \epsilon^j. \tag{66}$$

We get

$$f_{\text{even}}(k;\, a_{3\text{D}},\, a_\perp) = -\frac{1}{1 + i\left[a_{1\text{D}}\, k - \frac{a_\perp k}{2}\, \widetilde{\mathcal{L}}\left(-\frac{a_\perp^2 k^2}{4}\right)\right]}, \tag{67}$$

where

$$a_{1\text{D}} = \frac{a_\perp}{2}\,(C - a_\perp/a_{3\text{D}}) = a_{1\text{D}}^{\text{int}}\left(1 - C\ \tfrac{a_{3\text{D}}}{a_\perp}\right) \tag{68}$$

is the 1D scattering amplitude, see Equation (19), with

$$C = -\zeta(1/2) = 1.4603\ldots, \tag{69}$$

and where $a_{1\text{D}}^{\text{int}} = -a_\perp^2/(2a_{3\text{D}})$ is the result of the integrating-out procedure, Equation (32). The expression for the 1D scattering length, Equation (68), is arguably the key result of the whole analysis.

In terms of $h_{\text{real}}(k)$ introduced in Equation (18), we have found

$$h_{\text{real}}(k;\, a_{3\text{D}},\, a_\perp) = a_{1\text{D}}\, k - \frac{a_\perp k}{2}\, \widetilde{\mathcal{L}}\left(-\left(\frac{a_\perp k}{2}\right)^2\right) \tag{70}$$

$$= a_{1\text{D}}\, k + \mathcal{O}\left(\left(\frac{a_\perp k}{2}\right)^3\right), \tag{71}$$

with $a_{1\text{D}}$ given by Equation (68) and $\widetilde{\mathcal{L}}(\alpha)$ given by Equation (66); note the agreement with Equation (19). On the other hand, one can use Equation (61) to show that

$$h_{\text{real}}(k;\, a_{3\text{D}},\, a_\perp) = -\frac{a_\perp k}{2}\left[\frac{a_\perp}{a_{3\text{D}}} + \zeta\left(1/2,\, 1 - \frac{a_\perp^2 k^2}{4}\right)\right] \tag{72}$$

This form is convenient for identifying the CIR, which we will do in the next section.

In Moore et al. (2004), we relaxed the assumption that the scattering energy is below the first excited transverse level, Equation (35), and computed the kinetic coefficients governing the transitions between various transverse levels. The most important is the probability of transversely inelastic collision, $W_{\leftarrow n}(k)$. This is the probability that after a collision of two particles with the relative momentum k and relative transverse excitation n (see Equation [4]), the particles will *not* remain in the same transverse state:

$$W_{\leftarrow n}(k) = \frac{2}{\sqrt{\mathcal{E}_t}} \frac{\eta(\mathcal{E}) - 1/\sqrt{\mathcal{E}_t}}{[\frac{a}{a_\perp} + \zeta(1/2, 1 - \delta\mathcal{E})]^2 + \eta^2(\mathcal{E})}, \tag{73}$$

where

$$\mathcal{E}_t = (ka_\perp/2)^2 = \frac{E - E_{\text{transv}}}{2\hbar\omega_\perp}, \tag{74}$$

$E_{\text{transv}} = \hbar\omega_\perp(2n+1)$ is the transverse energy of particles with relative transverse excitation n (see Equation [3]; recall that we only consider cases with $m = 0$), $\mathcal{E} = n + \mathcal{E}_t$, $\delta\mathcal{E} = \mathcal{E} - \lfloor\mathcal{E}\rfloor$ $(0 \leqslant \delta\mathcal{E} < 1)$, and $\eta(\mathcal{E}) = \sum_{n'=0}^{\lfloor\mathcal{E}\rfloor} 1/\sqrt{\mathcal{E} - n'}$; here $\lfloor x\rfloor$ is the greatest integer less than x.

When $n = 0$ and $0 < \mathcal{E}_t \ll 1$ (see Equation [13] and the discussion that follows it), we have $\mathcal{E} = \mathcal{E}_t$, $\lfloor\mathcal{E}\rfloor = 0$, $\delta\mathcal{E} = \mathcal{E}_t$, $\eta(\mathcal{E}) = 1/\sqrt{\mathcal{E}_t}$, and thus $W_{\leftarrow n}(k) = 0$.

3.7 CIR for the Exact Scattering Amplitude

The condition for CIR is that there be a combination of values of $k > 0$, a_{3D}, and $a_\perp$ for which $h_{\text{real}}(k; a_{3D}, a_\perp)$ vanishes. We also require $a_\perp^2 k^2/4 < 1$ so that we remain one dimensional, see Equations (43) and (35). From Equation (72), the condition for CIR is therefore

$$\zeta\left(1/2,\, 1 - \frac{a_\perp^2 k^2}{4}\right) = -\frac{a_\perp}{a_{3D}} \quad \text{and} \quad 0 < a_\perp^2 k^2/4 < 1 \quad \text{(the exact CIR condition)}. \tag{75}$$

As we will discuss in more detail in Section 3.9, $\zeta(1/2, x)$ for $0 < x < 1$ is a monotonically decreasing function, diverging to $+\infty$ for small x as $1/\sqrt{x}$, reaching zero for $x = 0.3027\ldots$, and continuing to $\zeta(1/2) = -1.4603\ldots$ for $x = 1$; compare with Equations (84–86) below. Thus given a k in the range of interest indicated, $a_\perp/a_{3D}$ can be adjusted so that there is a CIR at that k. On the other hand, given $a_\perp$ and a_{3D}, there will be a CIR for some k in the range of interest only if $a_\perp/a_{3D} < -\zeta(1/2) = C = 1.4603\ldots$.

Of greatest interest is the case of small k, $0 < a_\perp^2 k^2/4 \ll 1$. Here, the existence of a CIR follows already from Equation (71)—which says that as $k \to 0^+$, $h_{\rm real}(k; a_{\rm 3D}, a_\perp)$ tends to $k a_{\rm 1D}$ faster than $k a_{\rm 1D}$ itself tends to zero—and from Equation (68), which says that depending on $a_\perp/a_{\rm 3D}$, $a_{\rm 1D}$ may be positive or negative. Say $a_{\rm 1D}$ is positive for some $a_{\rm 3D}^+$ and $a_\perp^+$ and negative for some $a_{\rm 3D}^-$ and $a_\perp^-$. Then for some small enough $k_0 > 0$, we will have $h_{\rm real}(k_0; a_{\rm 3D}^+, a_\perp^+) > 0$ and $h_{\rm real}(k_0; a_{\rm 3D}^-, a_\perp^-) < 0$. By continuity, there are some intermediate values of $a_{\rm 3D}$ and $a_\perp$ for which $h_{\rm real}(k_0; a_{\rm 3D}, a_\perp) = 0$.

For small k, Equation (75) becomes

$$a_\perp/a_{\rm 3D} = C - \frac{1}{2}\,\zeta(3/2)\left(\frac{a_\perp k}{2}\right)^2 + \mathcal{O}\left(\left(\frac{a_\perp k}{2}\right)^4\right) \quad \text{(exact CIR condition, small } k\text{)}. \tag{76}$$

At $k = 0$, we have $a_\perp/a_{\rm 3D} = C$, which is precisely the point when $a_{\rm 1D} = 0$, see Equation (68). But $a_{\rm 1D} = 0$ is the condition for CIR within the theory with an effective 1D delta-function potential, to which we will turn in the next subsection.

However, while still remaining exact, one may write down a 1D differential equation, satisfied by the scattering solution, which is almost a Schrödinger equation except that the potential-like term depends on the energy. From Equation (44), we see that $\psi_0(z = 0) = 1 + f$, which we use to we rewrite the delta-function term in Equation (46) as $-i\,\frac{\hbar^2}{\mu}\,k\,\frac{f}{1+f}\,\delta(z)\,\psi_0(z)$. But then that equation becomes

$$-\frac{\hbar^2}{2\mu}\,\frac{\partial^2}{\partial z^2}\,\psi_0(z) + g(E)\,\delta(z)\,\psi_0(z) = E\,\psi_0(z), \tag{77}$$

with

$$g(E) = \frac{\hbar^2}{\mu}\,\frac{2\,a_{\rm 3D}}{a_\perp^2}\,\frac{1}{1 + \zeta\left(1/2,\, 1 - \frac{a_\perp^2 k^2(E)}{4}\right)\frac{a_{\rm 3D}}{a_\perp}}. \tag{78}$$

Here, $k(E)$ is defined as usual through $E = \frac{\hbar^2 k^2}{2\mu} + \hbar\omega_\perp$, and we have used Equations (72) and (18). The above equations immediately suggest regimes when we may have a bona fide 1D effective potential, as we discuss next.

3.8 Effective 1D Potential for Low Scattering Energies

A great advantage of having an effective potential at one's disposal is that one may readily incorporate it into many-body theories. In the present case, such a potential is easily obtained (compare with the second paragraph of Section 4.1). We simply identify the regimes when we can neglect

the E-dependence in $g(E)$ in Equation (78). Our energy interval of interest is $0 < a_\perp^2 k^2/4 < 1$ (see Equations [43] and [35]); if the highest energy of interest $k_{\max}$ is still so small that $a_\perp^2 k_{\max}^2/4 \ll 1$, the zeta function may simply be replaced by $\zeta(1/2)$, and we obtain a 1D delta-function potential valid for any value of $|a_{3D}|$. From the coupling constant and Equation (22), we obtain the corresponding a_{1D}, which is the same as what we found in Equation (68). Alternatively, we may use the known exact value for a_{1D} in Equation (68) as a starting point. In Equation (71), we neglect the terms beyond the leading order in $a_\perp k/2$. But then the resulting 1D scattering amplitude, Equation (18), assumes the form in Equation (28). We conclude that the scattering is well-described by a 1D delta-function potential $g_{1D}\,\delta(z)$ whose scattering length a_{1D}^{δ} is given by a_{1D} from Equation (68). Equation (22) then gives the coupling constant. Either way, we get

$$g_{1D} = -\frac{\hbar^2}{\mu a_{1D}} = \frac{2\hbar^2 a_{3D}}{\mu a_\perp^2}\,\frac{1}{1 - C a_{3D}/a_\perp}, \quad 0 < a_\perp^2 k^2/4 \ll 1. \tag{79}$$

Note that $g_{1D}{=}g_{1D}^{\text{int}}/(1{-}Ca_{3D}/a_\perp)$, where g_{1D}^{int} is the result of the integrating-out procedure, Equation (31).

On the other hand, Equation (78) also says that we can have an effective 1D potential that is valid all the way up to some $a_\perp^2 k_{\max}^2/4 \lesssim 1$, provided $\left|\zeta(1/2,\, 1 - \frac{a_\perp^2 k^2(E)}{4})\frac{a_{3D}}{a_\perp}\right| \ll 1$. Using the expansion given in Equation (84) below, this works out to the condition $\frac{|a_{3D}|}{a_\perp} \ll \sqrt{1 - a_\perp^2 k_{\max}^2/4}$; this is the regime of "small" $|a_{3D}|$ when the integrating-out procedure gives the correct result, Equation (31).

Within the theory with the coupling constant given in Equation (79), the scattering amplitude manifests a CIR—reaches the unitary limit whenever $a_{1D} = 0$. According to Equation (68), this happens whenever

$$\frac{a_\perp}{a_{3D}} = C \approx 1.4603 \quad \text{(the "}\delta\text{-CIR" condition).} \tag{80}$$

From Equation (76), the δ-CIR condition agrees with the exact one up to first order in k. At δ-CIR, g_{1D} diverges and so within the theory with a delta-function potential, we have hard-core bosons; see the end of Section 3.4. There is no CIR in the theory with the coupling constant g_{1D}^{int}.

So far we have been discussing scattering; now we turn to bound states.

3.9 Exact Results for Bound-State Energies

Bound states are crucial to the description of the CIR as a Feshbach resonance, the subject of the next section. In an unconfined system where particle interaction is well-described by the regularized pseudopotential,

Equation (8), a two-particle bound-state exists only if a_{3D} is positive:

$$\Psi^{B}_{3D\,\delta}(\vec{r}) = e^{-r/a_{3D}}/(r\sqrt{2\pi a_{3D}}), \quad E^{B}_{3D\,\delta} = -\hbar^2/(2\mu a^2_{3D}), \tag{81}$$

where $\vec{r}$ is the relative displacement vector. Regal et al. (2003) has verified this fact experimentally. In contrast, as we will see shortly, theory predicts that in the presence of transverse confinement there should be a bound state for any sign of a_{3D}. This key feature has been experimentally confirmed by Moritz et al. (2005).

It is easy enough to construct bound states using the results in Section (3.6): the energy is now less than $\hbar\omega_\perp$, Equation (42) is valid for $n = 0$, and instead of Equations (44) and (46), we extend Equations (45) and (47), respectively, to $n = 0$. Repeating much the same steps as before, we arrive at the analog of Equation (52):

$$\Psi(z,\, \rho = 0) = -\frac{a_{3D}}{a_\perp}\,\eta \sum_{n=0}^{\infty} \frac{e^{-x\sqrt{n+\epsilon}}}{\sqrt{n+\epsilon}}, \qquad x = 2|z|/a_\perp. \tag{82}$$

Note that $\epsilon = -(E - \hbar\omega_\perp)/(2\hbar\omega_\perp) = a_\perp^2\,\kappa^2/4$ is now positive, where $E = \hbar\,\omega_\perp - \frac{\hbar^2\kappa^2}{2\mu}$. To isolate the singularity in the infinite sum, we use the same integral as before, except with $\nu = 0$ as the lower bound. As in Equation (64), the singular term has the form required by the contact condition in Equation (37). The regular part of $\Psi(z,\, \rho = 0)$ as $z \to 0$ is just $-(a_{3D}/a_\perp)\eta\,\zeta(1/2,\, \epsilon)$; but this is η, and so we get that the bound-state energy E^{B}_{1D} is the solution to the equation

$$\zeta(1/2,\, \epsilon) = -\frac{a_\perp}{a_{3D}}, \quad \text{where } \epsilon = -\frac{E^{B}_{1D} - \hbar\omega_\perp}{2\hbar\omega_\perp} > 0. \tag{83}$$

An alternative method of finding the bound-state energy is to analytically continue the scattering amplitude into the complex k-plane, and locate the pole lying on the positive imaginary axis, $k = i\,\kappa$, $\kappa > 0$. The bound-state energy is obtained by plugging this purely imaginary value into Equation (13), $E = \hbar\,\omega_\perp + \frac{\hbar^2 k^2}{2\mu}$. We use the expression for the exact scattering amplitude in Equation (65); note that in the course of analytic continuation in k one should not cross the branch cuts of the zeta function, and so one must keep to the first quadrant, $0 \leqslant \mathrm{Arg}\,(k) \leqslant \frac{\pi}{2}$. We find that the location of the pole is given precisely by Equation (83).

Now $\zeta(1/2,\, x)$ for $x > 0$ is a monotonically decreasing function; as x increases from 0 to $+\infty$, $\zeta(1/2,\, x)$ monotonically decays from $+\infty$ to $-\infty$.

We have

$$\zeta(1/2,\, x) = 1/\sqrt{x} + \zeta(1/2) + \mathcal{O}(x) \quad 0 < x \ll 1 \tag{84}$$

$$\zeta(1/2,\, 0.3027\ldots) = 0 \tag{85}$$

$$\zeta(1/2,\, x) = -2\sqrt{x} + \frac{1}{2\sqrt{x}} + \mathcal{O}(1/x^{3/2}) \quad x \gg 1; \tag{86}$$

for Equation (84) see the text following Equation (63); for Equation (86) see Paris (2005). Therefore, Equation (83) always has a solution–and the system always has a bound state, in contrast to the unconfined 3D problem–for any value of a_{3D}. In terms of the "energy-dependent potential" in Equation (77), using the identity $\zeta(1/2,\, 1+\epsilon) = \zeta(1/2,\, \epsilon) - 1/\sqrt[\downarrow]{\epsilon}$, see Equations (61) and (62), we see that for energies satisfying Equation (83), we have $g(E^{\mathrm{B}}_{1D}) = -\frac{\hbar^2}{\mu}\frac{a_{3D}}{a_\perp}\kappa$, which is consistent with Equation (47). In particular, $g(E^{\mathrm{B}}_{1D})$ is always negative, as it must be for the 1D delta-function potential in Equation (77) to support a bound state (see the paragraph preceding Equation [29]).

As $a_\perp/a_{3D} \to \infty$ (equivalently, $|E^{\mathrm{B}}_{3D\,\delta}| \gg \hbar\omega_\perp/2$), the 3D and 1D bound states must be basically the same, since the confining potential is then energetically negligible as well as flat on the length scale of the state (which is, of course, a_{3D}; compare with the discussion in the second paragraph of Section 3.5). As far as Equation (83), the limit $a_\perp/a_{3D} \to +\infty$ means then we can replace the zeta function on the left-hand side by the expansion in Equation (86). As anticipated,

$$E^{\mathrm{B}}_{1D} = E^{3D\,\delta}_{\mathrm{B}} + \mathcal{O}(1/(a_\perp/a_{3D})^2) \;\text{ when }\; \tfrac{a_\perp}{a_{3D}} \to +\infty, \tag{87}$$

where $E^{\mathrm{B}}_{3D\,\delta} = -\hbar^2/(2\mu a^2_{3D})$, Equation (81). In the context of Section 4.7 below, Equation (87) describes the "BEC" limit: when the theory is applied to confined nonidentical fermions, the tightly bound state corresponds to a $\uparrow\downarrow$ dimer, a compound boson. A gas of $\uparrow$ and $\downarrow$ fermions may, at low temperatures, become a Bose–Einstein condensate of such dimers (in the homogenous 1D case it is really a quasi-condensate, provided dimer–dimer interactions are weak; if they are strong, one has the Tonks-Girardeau gas mentioned at the end of Section 3.4 [Astrakharchik et al., 2004c; Fuchs et al., 2004; Petrov et al., 2000b; Recati et al., 2005; Tokatly, 2004]).

Next we consider the opposite limit, $a_\perp/a_{3D} \to -\infty$. Instead of using Equation (84), we look for the pole of the scattering amplitude, Equation (18). We solve $1 + ih_{\mathrm{real}} = 0$. using the expansion in Equations (70) and (66). We can see the that a_{1D} is now a better expansion variable, because $a_{1D}k$ is equal to a series with a two-order gap (k and k^2) between the leading and subleading orders, producing a correspondingly accurate leading-order

solution for $k^2 \sim E_{\rm B}^{\rm 1D,\delta} - \hbar\omega_\perp$. We get

$$E_{\rm B}^{\rm 1D,\delta} = \hbar\omega_\perp - \frac{\hbar^2}{2\mu a_{\rm 1D}^2} + \mathcal{O}((a_\perp/a_{\rm 1D})^5) \quad \text{when} \quad \frac{a_\perp}{a_{\rm 1D}} \to 0^+ \quad \left(\frac{a_\perp}{a_{\rm 3D}} \to -\infty\right), \tag{88}$$

Note that $-\hbar^2/(2\mu a_{\rm 1D}^2)$ is the energy of the bound state of the 1D effective potential in Equation (20), see Equation (29), with the coupling constant given in Equation (79).

It is interesting to look at how well the 1D effective potential predicts the bound-state energy as $a_\perp/a_{\rm 3D}$ is increased from $-\infty$ to $+\infty$. The bound-state energy given by the effective potential is correct to 1% for $a_\perp/a_{\rm 3D} = -5$. When $a_\perp/a_{\rm 3D} = 0$, the discrepancy is 55%; finally, at $a_\perp/a_{\rm 3D} = 1.4603\ldots$ the predicted bound-state energy is $-\infty$, Equation (80), whereas the true energy is $E_{\rm 1D}^{\rm B} = -\hbar\omega_\perp$, corresponding to $\epsilon = 1$ in Equation (83). As $a_\perp/a_{\rm 3D}$ is increased even further, the effective delta potential does not support bound states–as discussed in the paragraph preceding Equation (29), the 1D delta-function potential supports a bound state only if $a_{\rm 1D} > 0$ ($g_{\rm 1D} < 0$)–while true bound-state energies get deeper without bound, as we saw in Equation (87).

In the context of Section 4.7 below, Equation (88) describes the "BCS" limit. In this case, a 1D gas of $\uparrow$ and $\downarrow$ fermions at low temperatures becomes a gas of weakly bound $\uparrow\downarrow$ dimers–Cooper pairs (Fuchs et al., 2004)–whose spatial extent ($a_{\rm 1D}$) is much larger than the average interparticle spacing (Krivnov & Ovchinnikov, 1974).

3.10 CIR as a Feshbach Resonance

In Bergeman et al. (2003), we emphasized that the CIR is a Feshbach resonance, occurring when the energy of a bound state of the asymptotically closed channels (i.e., the excited transverse modes) coincides with the continuum threshold of the open channel (lowest transverse mode).

Following the Feshbach–Fano partitioning method, we divide the space of our problem into channels. The full Hamiltonian is $\widehat{H}_{\rm 3D} = \widehat{H}_z \otimes \widehat{I}_{d\perp} + \widehat{I}_{dz} \otimes \widehat{H}_\perp + \widehat{V}_{\rm F\text{-}H}$, see Section 3.1, where $\widehat{I}_{d\perp}$ and $\widehat{I}_{dz}$ are the identity operators in the transverse and longitudinal spaces, respectively. Because the only states that matter are those whose transverse angular momentum is zero (see the paragraph following Equation [12]), we take our whole space to be spanned by states of the form $|\psi_n\rangle|n\rangle_\perp$, where $|\psi_n\rangle$ is any state in the unconfined direction, $\langle z|\psi_n\rangle = \psi_n(z)$, whereas $|n\rangle_\perp = |n,0\rangle_\perp$ are the $m = 0$ eigenstates of the transverse Hamiltonian $\widehat{H}_\perp$, see Equation (3). The ground channel (g-channel) is the subspace spanned by states $|\psi_\alpha\rangle|0\rangle_\perp$; its complement is the excited channel (e-channel). Projectors to the g- and e-channels are $\widehat{P}_g = \widehat{I}_{dz} \otimes |0\rangle_{\perp\perp}\langle 0|$ and $\widehat{P}_e = \widehat{I}_{dz} \otimes \sum_{n=1}^{\infty} |n\rangle_{\perp\perp}\langle n|$, respectively.

We see that $\widehat{P}_g + \widehat{P}_e = \widehat{I}_d$, the identity on the whole space, while $\widehat{P}_g^2 = \widehat{P}_g$, $\widehat{P}_e^2 = \widehat{P}_e$, and $\widehat{P}_g\widehat{P}_e = \widehat{P}_e\widehat{P}_g = 0$. Now we write the Schrödinger equation as $\widehat{H}_{3D}\,(\widehat{P}_g + \widehat{P}_e)|\Psi\rangle = E\,|\Psi\rangle$ and act–from the left—on both sides of it first by $\widehat{P}_g$ and then by $\widehat{P}_e$. We obtain a system equivalent to the original equation:

$$\widehat{H}_g\,|\Psi_g\rangle + \widehat{V}_{ge}\,|\Psi_e\rangle = E\,|\Psi_g\rangle \qquad g\text{-channel equation} \tag{89}$$

$$(\widehat{H}_e - E)\,|\Psi_e\rangle = -\widehat{V}_{eg}\,|\Psi_g\rangle \qquad e\text{-channel equation,} \tag{90}$$

where $|\Psi_g\rangle = \widehat{P}_g|\Psi\rangle$, $\widehat{H}_g = \widehat{P}_g\widehat{H}_{3D}\widehat{P}_g$, $\widehat{V}_{ge} = \widehat{P}_g\,\widehat{H}_{3D}\,\widehat{P}_e$, and so on. Note that $\widehat{P}_g\,\widehat{H}_{3D}\,\widehat{P}_e = \widehat{P}_g\,\widehat{V}_{\text{F-H}}\,\widehat{P}_e$, and similarly for $\widehat{P}_e\,\widehat{H}_{3D}\,\widehat{P}_g$. Thus in real-space representation, $\widehat{V}_{ge}$ and $\widehat{V}_{eg}$ have zero range and are located at the origin.

As we will see below, $\widehat{H}_g$ and $\widehat{H}_e$ have continuum thresholds at E_{C_g} and E_{C_e}, respectively, separated by a gap $\Delta = E_{C_e} - E_{C_g} > 0$; also $\widehat{H}_e$ supports a bound state $|\Psi_B\rangle$ of energy E_B. We are considering incident waves whose total energy E is above the continuum threshold of $\widehat{H}_g$ but below that of $\widehat{H}_e$: $E_{C_g} < E < E_{C_e}$, compare with Equation (35). Therefore, the g-channel equation $\widehat{H}_g|\Psi\rangle = E|\Psi\rangle$ supports scattering solutions, whereas the corresponding e-channel equation (with the same energy) does not; we say that the g-channel is open and the e-channel, closed.

Resonances in the g-channel are now easy to spot: they occur whenever $(\widehat{H}_e - E)\,|\Psi_e\rangle$ in Equation (90) is zero at the origin (i.e., when its projection onto $\langle z|\langle\rho,\phi|$ is). This is because $\widehat{V}_{eg}$ is *not* zero at the origin, and so $|\Psi_g\rangle$ must be, which is equivalent to there being an infinitely strong zero-range scatterer at the origin.

To make the preceding more concrete, let us apply $\langle z|_\perp\langle 0|$ to both sides of Equation (89). We see that $\widehat{H}_g$ becomes precisely the Hamiltonian obtained in Section 3.5; what is new here is the coupling to the e-channel:

$$\left[-\frac{\hbar^2}{2\mu}\frac{\partial^2}{\partial z^2} + g_{1D}^{\text{int}}\,\delta(z)\right]\psi_0(z) + g_{ge}\,\delta(z)\frac{\partial}{\partial z}\left[z\Psi_e(z,\,\rho=0)\right]_{z\to 0^+} = (E - \hbar\omega_\perp)\psi_0(z), \tag{91}$$

where $g_{ge} = \frac{\hbar^2}{\mu}\frac{2\sqrt{\pi}a_{3D}}{a_\perp}$, and g_{1D}^{int} is the 'bare' coupling constant from Equation (31). Away from $z = 0$, Equation (91) is a free Schrödinger equation for $\psi_0(z)$, and so any scattering solution must be of the form in Equation (27), $\psi_0(z) = e^{ikz} + f_{\text{even}}(k)\,e^{ik|z|}$. And now if Equation (90) says that $\psi_0(z=0) = 0$, then $f_{\text{even}}(k) = -1$, i.e., the scattering amplitude is at its unitary limit.

In our system—and even more generally, as we will see—when $(\widehat{H}_e - E)\,|\Psi_e\rangle$ becomes zero at the origin, it accomplishes this in the most obvious way: by $|\Psi_e\rangle$ being an eigenstate of $\widehat{H}_e$ with energy E. Because the

continuum threshold of $\widehat{H}_e$ is above E, $|\Psi_e\rangle$ must be a bound state of $\widehat{H}_e$. It is intuitively plausible that $\widehat{H}_e$ should support a bound state at least for some range of parameters (imagine there was just one excited transverse state and consider the Schrödinger equation with the delta-function scatterer, compare with Equation (45) and the text that follows it). Below we will show that in our system, $\widehat{H}_e$ always has a bound state.

In fact, the existence of a bound state of $\widehat{H}_e$ is all we need to assume to show that for a zero-range scatterer, there must be a scattering resonance in the g-channel. So let $|\phi_e^{\mathrm{B}}\rangle$ be a bound state of $\widehat{H}_e$, of some energy E_e^{B}; let $|\Psi^{\mathrm{E}}\rangle$ be the scattering solution of energy E, and let $|\Psi_g\rangle = \widehat{P}_g|\Psi^{\mathrm{E}}\rangle$ and $|\Psi_e\rangle = \widehat{P}_e|\Psi^{\mathrm{E}}\rangle$. We claim that if E is set to E_e^{B}, then there is a scattering resonance. We will prove this by showing that if $E = E_e^{\mathrm{B}}$, then there is a solution $|\Psi_e\rangle$, $|\Psi_g\rangle$ of the system in Equations (89) and (90) such that, first, $|\Psi_g\rangle$ vanishes at the origin, and second, $|\Psi_e\rangle = a\,|\phi_e^{\mathrm{B}}\rangle$ for some constant a. We can show this by assuming $|\Psi_e\rangle = a\,|\phi_e^{\mathrm{B}}\rangle$ as an ansatz, and showing that a constant a can be found so that the system is indeed solved. In Equation (90), the ansatz gives zero for the left-hand side, which implies (by the reasoning we outlined above) that $|\Psi_g\rangle$ must be zero at the location of the potential. Turning to Equation (89), we see that $|\Psi_g\rangle$ satisfies $\widehat{H}_g|\Psi_g\rangle = E|\Psi_g\rangle$ except at the location of the potential, where the action of $\widehat{H}_g$ produces a finite zero-range object at the location of the potential (see Equation [24]). In terms of the discussion at the end of Section 3.4 and Equation (21), the product $g_{1\mathrm{D}}\,\psi(0)$ remains finite even though $\psi(0) \to 0$). But $\widehat{V}_{ge}|\Psi_e\rangle$ is also a zero-rage object at that location, so the two can be made to cancel by an appropriate choice of a, and we are done.

In our system, we can explicitly demonstrate the scenario just outlined. Let $|\widetilde{\Psi}_{3\mathrm{D}}^{\mathcal{E}}\rangle = \sum_{n=0}^{\infty} |\widetilde{\psi}_n^{\mathcal{E}}\rangle|n\rangle_\perp$ be the bound state of $\widehat{H}_{3\mathrm{D}}$ (recall that $\widehat{H}_{3\mathrm{D}}$ always has a bound state, see Section 3.9), whose energy $\mathcal{E} = -\hbar^2\kappa^2/4 + \hbar\omega_\perp$ is given by Equation (83); let $|\Psi_{3\mathrm{D}}^E\rangle = \sum_{n=0}^{\infty} |\psi_n^E\rangle|n\rangle_\perp$ be a scattering state of $\widehat{H}_{3\mathrm{D}}$ of energy E, and let $|\Psi_e^E\rangle = \widehat{P}_e|\Psi_{3\mathrm{D}}^E\rangle$ and $|\Psi_g^E\rangle = \widehat{P}_g|\Psi_{3\mathrm{D}}^E\rangle$. Note that $|\Psi_g^E\rangle$ and $|\Psi_e^E\rangle$ by construction are the solutions of the system in Equations (89) and (90).

The statement is that when $E = \mathcal{E} + 2\hbar\omega_\perp$, then $|\Psi_e^E\rangle$ is in fact a bound state of $\widehat{H}_e$ with $\widehat{H}_e|\Psi_e^E\rangle = E\,|\Psi_e^E\rangle$. Once this is shown, the arguments outlined above kick in, i.e., it follows that the left-hand side of Equation (90) is zero, and thus $|\Psi_g^E\rangle$ must be zero at the origin, so that there is indeed a resonance.

To prove the statement we will need two facts. The first fact is that

$$|\widetilde{\psi}_n^{\mathcal{E}}\rangle = a\,|\psi_{n+1}^E\rangle \quad n = 0,\, 1,\, 2,\ldots \quad \text{provided} \;\; \mathcal{E} = E - 2\hbar\omega_\perp, \tag{92}$$

where a is the same for all n. To see this, recall the construction of the bound-state solution as given in the text surrounding Equation (82). In

the present case, E and $\mathcal{E}$ are separated precisely by the transverse level spacing, and thus if κ_n^E are the quantities in Equation (42) for the scattering state, while $\kappa_n^{\mathcal{E}}$ are the corresponding quantities for the bound state, we have $\kappa_n^{\mathcal{E}} = \kappa_{n+1}^E$ for $n \geqslant 0$; Equations (45) and (51) then establish Equation (92), with a the ratio of the regular parts (η's) of $|\widetilde{\Psi}_{3\mathrm{D}}^{\mathcal{E}}\rangle$ and $|\Psi_{3\mathrm{D}}^E\rangle$ for $\rho = 0, z \to 0$.

The second fact is a peculiar property of confinement by a 2D harmonic oscillator: the 'excited' Hamiltonian $\widehat{H}_e$ and the full Hamiltonian $\widehat{H}_{3\mathrm{D}}$ can be transformed to each other via a simple "level-shifting" transformation

$$\widehat{H}_e = \widehat{A}^\dagger \widehat{H}_{3\mathrm{D}} \widehat{A} + 2\hbar\omega_\perp \widehat{P}_e, \quad \text{where } \widehat{A}^\dagger = \widehat{I}_{d_z} \otimes \sum_{n=0}^{\infty} |n+1\rangle_{\perp\perp}\langle n|. \tag{93}$$

Note that $\widehat{A}^\dagger \widehat{A} = \widehat{P}_e$ and $\widehat{A}\widehat{A}^\dagger = \widehat{I}_d$. If it were not for the presence of the interparticle potential in $\widehat{H}_{3\mathrm{D}}$, Equation (93) would be trivial: it would use no more than the fact that the eigenenergies of $E_n^\perp$ of $\widehat{H}_\perp$ (corresponding to the states $|n\rangle_\perp$) satisfy $E_{n+1}^\perp = E_n^\perp + 2\hbar\omega_\perp$. The potential term, however, produces

$$\sum_{n=1}^{\infty}\sum_{k=1}^{\infty} \langle n|\widehat{V}|k\rangle \; |n\rangle\langle k|$$

within $\widehat{H}_e = \widehat{P}_e \widehat{H}_{3\mathrm{D}} \widehat{P}_e$, and

$$\sum_{n=1}^{\infty}\sum_{k=1}^{\infty} \langle n{-}1|\widehat{V}|k{-}1\rangle \; |n\rangle\langle k|$$

within $\widehat{A}^\dagger \widehat{H}_{3\mathrm{D}} \widehat{A}$ (here "$|j\rangle\langle k|$" is a shorthand for $\widehat{I}_{d_z} \otimes |j\rangle_{\perp\perp}\langle k|$). These two double sums must be the same if Equation (93) is to hold. Luckily, (i) $\widehat{V}$ is located at the origin and has zero range, and (ii) all $m = 0$ eigenfunctions of the 2D harmonic oscillator have the same value at the origin, see Equation (12). It follows that the two double sums are the equal after all, and so Equation (93) does hold.

Armed with these two facts, we can finally prove the statement that when $E = \mathcal{E} + 2\hbar\omega_\perp$, then $|\Psi_e^E\rangle$ is a bound state of $\widehat{H}_e$ with energy E. Starting with $\widehat{H}_{3\mathrm{D}}|\widetilde{\Psi}_{3\mathrm{D}}^{\mathcal{E}}\rangle = \mathcal{E}\,|\widetilde{\Psi}_{3\mathrm{D}}^{\mathcal{E}}\rangle$, we act by $\widehat{A}^\dagger$ on both sides and insert $\widehat{A}\widehat{A}^\dagger = \widehat{I}_d$ after $\widehat{H}_{3\mathrm{D}}$. In the resulting equation, we write $\widehat{A}^\dagger \widehat{H}_{3\mathrm{D}} \widehat{A}$ as $\widehat{H}_e - 2\hbar\omega_\perp \widehat{P}_e$, see Equation (93). Then, we use the fact that $\widehat{P}_e \widehat{A}^\dagger = \widehat{A}^\dagger$, and the result says that $\widehat{A}^\dagger|\widetilde{\Psi}_{3\mathrm{D}}^{\mathcal{E}}\rangle$ is an eigenstate of $\widehat{H}_e$ with energy $\mathcal{E} + 2\hbar\omega_\perp$, in other words, with energy E. Finally, from Equation (92) it follows that $\widehat{A}^\dagger|\widetilde{\Psi}_{3\mathrm{D}}^{\mathcal{E}}\rangle = a\,\widehat{P}_e|\Psi_{3\mathrm{D}}^E\rangle$, and thus $\widehat{P}_e|\Psi_{3\mathrm{D}}^E\rangle$, which is $|\Psi_e^E\rangle$, is an eigenstate of $\widehat{H}_e$ with

energy E, as claimed. And now all the previous arguments follow: we note that the left-hand side of Equation (90) is zero, so that $|\Psi_g^E\rangle$ must be zero at the origin, etc.; we have a resonance.

We have just shown that the g-channel resonance occurs whenever the scattering energy E is above the bound-state energy $\mathcal{E}$ by $2\hbar\omega_\perp$. Now, $\mathcal{E}$ satisfies $\zeta(1/2, -\frac{\mathcal{E}-\hbar\omega_\perp}{2\hbar\omega_\perp}) = -\frac{a_\perp}{a_{3D}}$, see Equations (83) and (43); upon substituting $\mathcal{E} = E - 2\hbar\omega_\perp$, we get that a resonance occurs whenever $\zeta(1/2, 1 - \frac{E-\hbar\omega_\perp}{2\hbar\omega_\perp}) = -\frac{a_\perp}{a_{3D}}$, thereby recovering the exact result in Equation (75).

For low-energy scattering, $0 < (E - \hbar\omega_\perp)/(2\hbar\omega_\perp) \ll 1$, and we see that the resonance occurs when the bound-state energy of $\widehat{H}_e$ is $E \approx \hbar\omega_\perp$. This is in accordance with the general expectation that the Feshbach resonance should occur approximately when the bound-state energy of the closed channel crosses the continuum threshold of the open channel, and corresponds to the δ-CIR criterion in Equation (80).

In a more formal development, one would introduce an inverse of the operator $(\widehat{H}_e - E)$, let us call it $\mathcal{G}_e^E$. Equation (90) gives $|\Psi_e\rangle = -\mathcal{G}_e^E \widehat{V}_{eg} |\Psi_g\rangle$, which we substitute into Equation (89) to get an equation involving only $|\Psi_g\rangle$, $\widehat{H}_g |\Psi_g\rangle - \widehat{V}_{ge}\, \mathcal{G}_e^E \widehat{V}_{eg} |\Psi_g\rangle = E |\Psi_g\rangle$. In our case, this would result in Equation (77). If $E_{C,g} < E \ll E_{C,e}$, one may obtain a genuine potential if we approximate $\mathcal{G}_e^E$ by $\mathcal{G}_e^{E_{C,g}}$, as was done in Section 3.8.

Finally, note that almost by definition, *any* problem with confined scattering should be describable within the paradigm of open and closed channels: a system is confined precisely because the next excited state of the confining potential is higher in energy than the incident wave. Results of this section suggest that $\widehat{H}_e$ generically has a bound state, and that therefore (at least in the case of zero-range potentials) in the g-channel there is a scattering resonance whenever the scattering energy equals the energy of that bound state. We conclude that scattering resonances should be a generic feature of confined systems.

3.11 Is CIR Spurious as Far as Low-D Two-Body Physics?

On the face of it, a resonance is a dramatic effect, of unknown robustness with respect to tampering with the underlying assumptions of the theory. The most obvious weak link is the pseudopotential approximation, Equation (8). Can the CIR exist in the regime when the pseudopotential approximation is valid?

As we showed in Bergeman et al. (2003), the answer is that it can. In fact, there are regimes where even the 1D effective theory—which we took in the form with an effective 1D delta-function potential, see Section 3.8—is both physically valid as well as correctly predicting a CIR. We considered

harmonically confined scattering in the presence of either the Lennard-Jones potential, or the spherical well potential, and numerically computed the interaction strength

$$g_{1D}^{\text{strength}} = \lim_{k\to 0^+} \frac{\hbar^2 k}{\mu} \frac{\text{Re}f_{\text{even}}(k)}{\text{Im}f_{\text{even}}(k)} \tag{94}$$

for various values of the control parameter $a_{3D}/a_\perp$ (note that Equation [94] is an identity if $f_{\text{even}}(k)$ and g_{1D}^{strength} are as they would be for a 1D delta-function potential, i.e., as in Equations [28] and [22], respectively). We then compared these values to the analytic prediction of the theory with an effective 1D potential, which simply says that g_{1D}^{strength} should equal g_{1D} given by Equation (79). The effective 1D theory predicts that g_{1D} diverges at CIR, and this is precisely what we saw numerically. The overall numerical agreement was very good below the resonance (as $a_{3D}/a_\perp$ is approaching the CIR value of $1/C$ from below); above the resonance, there were systematic deviations, which are due to the finite range of the 3D potentials; more on that in Section 4.5.

The second most obvious weak link is the assumption of harmonic confinement. What happens when this assumption is relaxed is the subject of Section 4.3.

3.12 Is CIR Spurious as Far as Many-Body Physics?

Because the effective 1D potential may be incorporated into many-body theories, it is possible to test the predictions of the 1D effective theory not only at two-body level but also at the quantum many-body level. In particular, Astrakharchik and collaborators (Astrakharchik et al., 2004a,b) considered a gas of five particles interacting through finite-range potentials. The particles were trapped strongly in the transverse direction and weakly in the longitudinal direction. They used two different types of 3D interparticle potentials: one was a purely repulsive hard-sphere potential, $V^{\text{HS}}(r) = \infty$ for $r < a_{3D}$ and zero otherwise; the other potential, which they called simply a "short-range" potential, was $V^{\text{SR}}(r) = -V_0/\cosh^2(r/r_0)$. Unlike the hard sphere potential, V^{SR} can support two-body bound states. These transversely confined 3D systems were to be compared with effective 1D systems of five particles in a longitudinal harmonic potential, with the particle interaction given by a pairwise delta-function potential. The observable quantity that was used for comparison was the many-body energy per particle, which was computed (using quantum Monte Carlo techniques) for both 3D systems (corresponding to either V^{HS} or V^{SR} being chosen as interparticle potential), and for two 1D systems with 1D delta-function potentials: one where the potential was $g_{1D}\,\delta(z)$, with g_{1D} given by Equation (79), and another where the 1D potential was

$g_{1D}^{int}\,\delta(z)$, with g_{1D}^{int} given by Equation (31). The results showed excellent agreement between the 3D system with V^{SR} potential and the 1D system with the potential $g_{1D}\,\delta(z)$, extending right through the CIR as one varied the governing parameter $\frac{1}{\sqrt{2}}\,a_{3D}/a_{\perp}$. The $g_{1D}^{int}\,\delta(z)$ potential showed good agreement only for small positive values of the governing parameter. The 3D system with hard-sphere potentials also deviated from the 3D system with V^{SR} potentials (and so from the 1D system with g_{1D} potential). What distinguishes the two 3D potentials is the presence or absence bound states, which, as we saw in Section 3.10, play a crucial role in the physical mechanism whereby the CIR is generated.

We should mention that at the many-body level, the CIR has been used to produce—in Monte Carlo numerical experiments as well as, recently, in experiments (see Section 5.1)—both the Tonks-Girardeau (TG) gas of hard-core bosons (Girardeau, 1960; Tonks, 1936), where $g_{1D} \to +\infty$, as well as the super-Tonks gas (Astrakharchik et al., 2005), where $g_{1D} \to -\infty$ (recall the discussion at the end of Section 3.4).

4. OTHER TYPES OF CIR

The above example of zero-range 3D scattering in the presence of 2D transversal harmonic potential, resulting in an effective 1D theory with 1D delta-function interparticle potential, was the first setting in which CIR was found (Bergeman et al., 2003; Olshanii, 1998). Here, the particles were bosons, but the results immediately carry over to the case of nonequal fermions (Fuchs et al., 2004; Tokatly, 2004).

4.1 CIR in Effectively 2D Systems

A related resonance occurs when the harmonic confinement exists in only one direction, so that the effective theory is 2D (Petrov et al., 2000a; Petrov & Shlyapnikov, 2001). The easiest way to see the CIR is once again to look at the scattering amplitude.

Our definition of CIRs makes sense even in the absence of effective low-D potentials, and this gives us an excuse to avoid the lengthy topic of 2D pseudopotentials. Nevertheless, here is an incomplete list of works that discuss these objects: Wódkiewicz (1991); Olshanii and Pricoupenko (2001); Idziaszek and Calarco (2006); Kanjilal and Blume (2006); Pricoupenko and Olshanii (2007); and Pricoupenko (2008).

In 2D, for short-range interactions, the asymptotic expression at large relative distances ρ for the scattering wave function is

$$\Psi(\rho) = e^{ik\rho} - \frac{i}{4} f_{2D}(k) H_0^{(1)}(k\rho), \tag{95}$$

where $H_0^{(1)}(x)$ $\left(\sim \sqrt{2/\pi}\, e^{-i\frac{\pi}{4}} \frac{e^{ix}}{\sqrt{x}} \text{ for } x \gg 1\right)$ is the first Hankel function, k is the amplitude of the scattering wave vector, related to scattering energy through $E(k) = \frac{\hbar^2}{2\mu}k^2$, $\mu = m/2$ is the reduced mass, and

$$f_{2D}(k) = \frac{2\pi}{i\frac{\pi}{2} - \ln\left(k\, R_{2D}\, e^{\gamma}/2\right)} \tag{96}$$

is the scattering amplitude. Here, $\gamma = 0.57721\ldots$ is the Euler–Mascheroni constant, and R_{2D} is the effective radius of the 2D potential (not to be confused with the effective range). The effective radius is sometimes called the "2D scattering length", for example by the very people who introduced it (Verhaar et al., 1984). Note that we cannot define the scattering length as in 3D (through the derivative of the phase shift with respect to k at $k = 0$) because the phase shift is proportional to $1/\ln k$ for small k and thus its derivative always diverges at $k = 0$. The meaning of R_{2D} is that both the bound and the scattering states must for small ρ have the asymptotic form $\Psi(\rho) = \text{const.} \ln \frac{\rho}{R_{2D}} + \mathcal{O}(\rho)$. The effective radius depends on the parameters of the underlying 3D system through (Pricoupenko and Olshanii, 2007)

$$R_{2D} = \frac{1}{e^{\gamma}/2}\sqrt{\frac{\pi}{B}}\, a_z \exp\left(-\sqrt{\frac{\pi}{2}}\frac{a_z}{a_{3D}}\right), \tag{97}$$

where $a_z = \sqrt{\frac{\hbar}{m\omega_z}}$ is the size of the harmonic potential responsible for 1D confinement, $U_{3D}(r_x, r_y, r_z) = \frac{1}{2}m\omega_z^2 r_z^2$, m is the particle mass, a_{3D} is the 3D scattering length, and $B = 0.9049\ldots$ is a numerical constant. The modulus squared of the scattering amplitude, $4\pi^2\left[\frac{\pi^2}{4} + \ln^2\left(k\, R_{2D}\, e^{\gamma}/2\right)\right]^{-1}$, has a maximum when the log-squared term is zero, that is, when

$$k\, R_{2D}\, e^{\gamma}/2 = 1; \tag{98}$$

this maximum is the CIR in the case of an effectively 2D system. Note that unlike in the case of an effectively 1D system, it is not obvious how to approximately remove the dependence on k (and so on the scattering energy) from the resonance condition.

4.2 3D Optical Lattices

Fedichev et al. (2004) have considered the scattering of a pair of atoms confined in an isotropic and uniform 3D optical lattice, considered within the tight-binding model.

The lattice is characterized by the depth V_0 of the lattice potential and by the lattice spacing d. Additionally, the WKB tunneling exponent between the neighboring wells is supposed to be small: $t_s = \sqrt{D_s}\omega/\pi$, with $D_s \ll 1$. Here, s labels the Bloch bands corresponding to the relative coordinate of the two particles (the lattice potential is separable to a good approximation), and $\omega^2 = V_0/(m\,d^2)$ is the curvature within a single lattice site, where m is the particle mass. The effective mass is given by $m_s = 2/(t_s\,d^2)$.

The interparticle potential has the 3D scattering length a_{3D}. The potential range is assumed short, and in particular shorter than either the lattice spacing or the size ℓ_0 of the ground state wave function in an individual optical well. The lattice spacing is also assumed to be small relative to the de Broglie wavelength of the colliding particles.

The result for lowest-band scattering, $s = 0$, is that at low energies the scattering amplitude $f_{s=0,s'=0}$ is given by

$$f_{00}(k) = \frac{4\pi}{m_0}\,\frac{1}{i\,k + 1/a_{\text{eff}}} \tag{99}$$

with the effective scattering length

$$a_{\text{eff}} = a_{3D}\left(\frac{d}{\ell_0}\right)^3 m_s\,\frac{1}{1 + a_{3D}/\ell_*}, \tag{100}$$

where $\ell_* = \frac{1}{4\ln 2}\,\ell_0\,\sqrt{D_0}$.

The authors also introduce the effective pseudopotential

$$V(\vec{r}) = \frac{4\pi\hbar^2}{m_s}\,a_{\text{eff}}\,\delta^3(\vec{r})\,\frac{\partial}{\partial r}\,r\;\cdot \tag{101}$$

acting on wave functions ψ_p of the pair of atoms averaged over many lattice sites.

The results in Equations (99) and (100) imply that for repulsive 3D interaction ($a_{3D} > 0$), as a_{3D} increases from zero to large values, a_{eff} increases from zero to the asymptotic universal limiting value $a_\infty = m_0\,\ell_*\,(d/\ell_0)^3$. The rate of growth of a_{eff} begins positive and then steadily decreases toward zero.

In the case of attractive 3D interactions ($a_{3D} < 0$), as the magnitude $|a_{3D}|$ increases from zero to large values, a_{eff} displays resonant behavior: it starts at zero and steadily becomes more and more negative, diverging to negative infinity when

$$|a_{3D}| = \ell_* \tag{102}$$

This is the CIR. As $|a_{3D}|$ increases past the resonant point, a_{eff} switches sign to positive and starts to steadily decay from positive infinity to the asymptotic value a_∞ mentioned above.

Just after the effective scattering length passes through resonance and switches its sign to positive, it is very large. Such a large and positive effective scattering length implies a pole in the scattering amplitude at $k = ip_*$ with $p_* = 1/a_{\text{eff}}$, which means that there is a bound state with binding energy $p_*^2/m_s = 1/(a_{\text{eff}}^2 m_s)$. The size of such a dimer is of the order of a_{eff}, and therefore very large, possibly extending over many sites. Such dimers are called Wannier–Mott molecules, in analogy to the Wannier–Mott excitons in semiconductors (Yu & Cardona, 2001).

Köhl et al. (2005) have observed a shift in the location of the Feshbach resonance in a quantum-degenerate Fermi gas in a 3D optical lattice, an effect they attribute to CIR.

Recently, Cui et al. (2010) have extended these studies to the situations where the approximation of separable potentials is not valid (see Section 4.3). Their approach, which uses the momentum-shell renormalization group (Kaplan et al., 1998), captures most dominating higher-band effects as well as all intraband scattering within the lowest band. The approach is valid for the study of resonances in deep lattices at small a_{3D}, as well as shallow lattices with large a_{3D}. When applied to 1D and 2D traps, the approach reproduces the results reported in the sections above.

Resonances correspond to the divergence of the scattering length of the Bloch wave, a_{Bloch}. For small a_{3D}, one has the simple result

$$\frac{a_{\text{Bloch}}}{a_L} = \frac{1}{4\pi}\left(\frac{t}{U_{\text{H}}} - \frac{\gamma}{16}\right)^{-1}, \tag{103}$$

where a_L is the lattice constant, t is the lattice hopping parameter, U_{H} the on-site interaction, and $\gamma \approx 4$; the CIR occurs at $t/U_{\text{H}} \approx -1/4$. Away from the limit of small a_{3D}, there are many resonances, but it would be beyond the scope of this review to go into details.

4.3 CIR in a System Where Center-of-Mass and Relative Coordinates are Not Separable

In the problems considered so far, the scattering problem was tractable in part because the center-of-mass and relative coordinates were separable. Peano et al. (2004) (see also Peano et al. [2005]) have considered a general situation of 2D confinement where such a separation was not possible. They found that as one tunes the 3D scattering length a_{3D}, generally a resonance occurs at every bound state (i.e., whenever the size of a given bound state is equal to a_{3D}, up to some multiplicative constants)

of the operator which is the projection of the full Hamiltonian to the subspace of states orthogonal to the open channel. The resonances tend to be extremely sharp, there can in principle be an infinite number of them, and most of them tend to appear for $a_{3D}/a_\perp \to 0$, where $a_\perp$ is the typical size of the 2D confinement. Quantitative analysis can generally only be done numerically. Aside from the pioneering effort of Peano et al. (2004), however, the topic of CIRs—and more generally of effective theories—in situations when the relative and the center-of-mass motions are not separable remains largely unexplored. However, recently Cui et al. (2010) have succeeded in analyzing resonance scattering in optical lattices without assuming separable potentials; see the Section 4.2.

4.4 Higher Partial Waves

So far we have considered only *s*-wave scattering. Resonances have been found for scattering of higher partial waves, both in the cases of 1D (Granger & Blume, 2004) and 2D confinement (Kanjilal & Blume, 2006; Pricoupenko, 2008) (see also Idziaszek and Calarco [2006] and Kim et al. [2005]). The general character of the resonances is similar to their *s*-wave counterparts, though the analysis becomes more involved. What becomes even more involved is the construction of effective low-dimensional theories. Since it is not clear if the dust has completely settled in this field, we refer the reader to the primary literature for details.

4.5 Effects of Finite Range of the Underlying Interaction

Naidon et al. (2007) have shown that the predictions of the effective 1D and 2D theories—in particular, the positions of the CIRs in Equations (80) and (98)—can be noticeably improved if one takes into account the finite range of the underlying potential. As before, one systematically matches the expansions of the effective and exact results. However, since now the finite range of the underlying potential is being taken into account, one can go up to second order in $r/a_\perp$. The main result is the following simple recipe: in the effective theory, one should replace all appearances of a_{3D} by

$$a_{3D}^{r_e}(k) = \frac{a_{3D}}{1 - (1/2)k^2 a_{3D} r_e}. \tag{104}$$

Here, r_e is the effective range of the underlying potential, and k is the collisional momentum, defined through $\hbar k = \sqrt{2(m/2)E_{3D}}$. The energy E_{3D} is the full energy of the collision, which in confined settings is dominated by the energy of confinement, rather than by the kinetic energy in the unconfined directions. Thus, as far as the effective low-dimensional theory is concerned, E_{3D} is constant, resulting in an improved effective potential.

4.6 CIR in the Scattering Off a Finite-Range Potential in a Multimode Waveguide

Gattobigio et al. (2010) have analyzed the interaction of a propagating guided matter wave with a localized potential (intuitively, a 'defect' in the waveguide) whose range is of the order of or larger than the harmonic oscillator length of the transverse confinement. Additionally, they do not assume that scattering energy is small—the matter wave does not necessarily propagate in a single mode. The calculations are set in 2D: one direction is unconfined, whereas the other is confined due to 1D harmonic potential. Using a treatment that is nonperturbative in the strength of the scattering potential, and the specific example of square potential, they find multiple scattering resonances. They explain the physical origin of these resonances as follows: when the incident wave is within the range of the scattering potential, there is a strong coupling between the transverse and longitudinal degrees of freedom. When the transverse excited modes get virtually excited, the longitudinal energy enters the range of values for which total reflection would occur in 1D. The understanding of the detailed structure of the transmission probabilities will require further study.

4.7 CIR in the Scattering of Dimers

In the context of the study of the BCS-BEC crossover (Fuchs et al., 2004; Tokatly, 2004) in a two-species Fermi gas with zero-range interactions between particles of unlike species, Mora et al. (2005) have treated the four-body problem under 2D confinement (resulting in 1D effective theory). In particular, they have studied dimer-dimer scattering by solving the full fermionic four-body problem under confinement.

They assume that atoms are of identical fermionic species with two spin states, labeled $\uparrow$ and $\downarrow$. They also assume that atoms interact only via a two-body *s*-wave interaction, which is modeled with a zero-range interaction, i.e., the Huang-Fermi pseudopotential of Equation (8). Within the zero-range approximation, interaction exists only between fermions in unlike spin states ($\uparrow\downarrow$). For fermions in like spin states ($\uparrow\uparrow$ or $\downarrow\downarrow$), the two-body wave function must be antisymmetric with respect to the exchange of particles, and so must be zero when the particle positions coincide. Thus, in the Schrödinger equation, the potential term $g_{3D}\,\delta^3(\vec{r})\,\frac{\partial}{\partial r}\big(r\,\Psi(\vec{r},\vec{R})\big) = g_{3D}\,\delta^3(\vec{r})\,\times$ regular part of $\Psi(\vec{r}=0,\vec{R})$ is zero because $\Psi(\vec{r}=0,\vec{R})$ is zero (here, $\vec{r}$ is the relative coordinate and $\vec{R}$ is the center-of-mass coordinate); and so there is no interaction between fermions in like spin states.

The four-body problem considered by Mora et al. (2005) involves two $\uparrow$ and two $\downarrow$ particles under 2D confinement (resulting in a 1D effective theory). The results of Section 3.9 imply that at the two-body level, one $\uparrow$ and one $\downarrow$ fermion always have a single bound state, called a 'dimer,' which is therefore a composite boson. Its binding energy Ω_B is determined through Equation (83), where we relabel ε by Ω_B; the longitudinal dimer size a_B is defined through $\Omega_B = [a_\perp/(2\,a_B)]^2$. In the "BEC" limit, $a_\perp/a_{3D} \to +\infty$ (see the text following Equation [87]), we have $a_B \approx a_{3D}$ (intuitively, a very small, compact dimer) and $\Omega_B \approx [a_\perp/(2\,a_{3D})]^2 \gg 1$; in the "BCS" limit, $a_\perp/a_{3D} \to -\infty$ (see the last paragraph of Section 3.9), we have $\Omega_B \approx (a_{3D}/a_\perp)^2 \ll 1$ and $a_B \approx a_\perp^2/(2\,|a_{3D}|)$ (intuitively, a very delocalized dimer). The 1D atom-atom scattering length is given by Equation (68), where we relabel a_{1D} by a_{aa}^{1D}.

Mora et al. (2005) consider the 3D four-body ($\uparrow\uparrow\downarrow\downarrow$) problem under confinement in the regime when the relative dimer-dimer momentum k is sufficiently small ($k\,a_\perp < 1$) so that the relative dimer-dimer motion is in the lowest transverse state when the dimers are far apart. The solution of the resulting dimer-dimer scattering problem shows that the scattering amplitude may be expanded in terms of a dimer-dimer 1D scattering length, a_{dd}^{1D}. For $|k\,a_{dd}^{1D}| \ll 1$ (but without any restrictions on the value of $a_\perp/a_{3D}$), one may introduce an effective 1D dimer-dimer delta-function potential, $V_{dd}^{1D} = g_{dd}^{1D}\,\delta(Z)$. Here, Z is the longitudinal component of $\vec{R} = [(\vec{x}_1 + \vec{x}_a) - (\vec{x}_2 + \vec{x}_b)]/\sqrt{2}$, the relative vector between the two dimers ($\vec{x}_{1,2}$ and $\vec{x}_{a,b}$ are the position vectors of the $\uparrow$ and $\downarrow$ particles, respectively). The coupling constant is given as in Equation (79), $g_{dd}^{1D} = -\hbar^2/(m_0 a_{dd}^{1D})$, with m_0 the mass of a single fermion.

In the BCS limit, one may solve the 1D four-body problem using Bethe ansatz. This analysis shows that even in the BCS limit, the dimers are not broken, and $a_{dd}^{1D} = a_{aa}^{1D}/2$. The treatment can be extended to the N-body case provided the 1D particle density n satisfies $n\,a_\perp < 1$. Because the dimers are not broken, the ground state can be bosonized, i.e., described as a gas of $N/2$ delta-function-interacting bosons, where the bosonic interaction has the scattering length $a_{aa}^{1D}/2$. The resulting Lieb-Liniger equations (Lieb & Liniger, 1963) for $N/2$ bosons in this case coincide with Yang-Gaudin equations (Gaudin, 1967; Yang, 1967) for N fermions with attractive interaction. Chen et al. (2010) have shown that the $N/2$-particle Bose system with attractive interactions and the N-particle attractive Fermi system can be mapped into each even when the interaction strengths are finite. It is even true that the mapping remains the same: the bosonic scattering length should be half the fermionic one, and the mass of a boson should be twice the mass of a fermion.

As long as $n\,a_\perp < 1$, the typical momenta k will satisfy $|k\,a_{dd}^{1D}| \ll 1$ even as one moves away from the BCS limit ($a_\perp/a_{3D} \to -\infty$, $a_{aa}^{1D} \to +\infty$) through

the crossover regime ($a_\perp/|a_{3D}| \approx 1$, which includes the atom-atom CIR at $a_\perp/a_{3D} = 1.4603\ldots$) and into the BEC limit ($a_\perp/a_{3D} \to +\infty$, $a_{aa}^{1D} \to -\infty$). Thus, the effective 1D dimer-dimer delta-function potential remains valid throughout. In the BEC limit, the dimer size a_B is much less than the size of transverse confinement ($a_B \approx a_{3D} \ll a_\perp$), and so the confinement has no effect on four-body collisions. Therefore, the 3D four-body theory developed in Petrov et al. (2004) and Petrov et al. (2005) becomes valid, and so one has 3D dimer-dimer scattering with the dimer-dimer scattering length $a_{dd}^{3D} \approx 0.6\, a_{3D}$. This results in $a_{dd}^{1D} = -a_{red,\perp}^2/[2\,(0.6\, a_{3D})]$, where $a_{red,\perp} = \sqrt{\hbar/(m_0\,\omega_\perp)}$ is the transverse oscillator length for dimers.

Notice that a_{dd}^{1D} is positive in the BCS limit and negative in the BEC limit; therefore, it should be zero for some intermediate value of $a_\perp/a_{3D}$, which means that we have a CIR for dimer-dimer scattering. An interesting question is whether this CIR happens at the same value of $a_\perp/a_{3D}$ (or, equivalently, of Ω_B, since the latter is a one-to-one function of the former) as the atom-atom CIR. Answering this question requires treating the dimer-dimer scattering problem away from the limiting cases $a_\perp/a_{3D} \to \pm\infty$, leading to a fairly complicated integral equation. The result is that the dimer-dimer CIR happens for $\Omega_B \approx 0.3$. This is different from the atom-atom CIR, which takes place at $\Omega_B \approx 1$ ($= 1$ in the theory with the effective 1D potential).

4.8 CIR in the Scattering in Mixed Dimensions

See Section 5.2.

5. EXPERIMENTAL REALIZATIONS

5.1 Experimental Study of CIR in Scattering in an Effectively 1D System

Haller et al. (2009) have experimentally realized the CIR in an effectively 1D system. In fact, they used the CIR as an engineering tool to realize a new state of matter—the super-Tonks gas (Haller et al., 2009). Immediately afterwards, they studied the CIR in its own right (Haller et al., 2010).

Both sets of experiments were conducted in Hanns-Christoph Nägerl's group in Insbruck. In the first set, the group studied an ultra-cold gas of cesium atoms in a 2D optical lattice, which formed an array of elongated tubes with an aspect ratio of between 100 and 1000. Atoms in each tube are very well described as a delta-function-interacting 1D Bose gas (Bloch et al., 2008). As we mentioned above, different values of the 1D two-body coupling constant, g_{1D}, result in different regimes of the gas. From Equation (79), we have that $g_{1D} = g_{1D}^{int}/(1 - Ca_{3D}/a_\perp)$, where $g_{1D}^{int} = 2\hbar^2 a_{3D}/(\mu a_\perp^2)$ is the result of the integrating-out procedure, Equation (31). Thus, if $a_{3D} \lesssim a_\perp/C$, then g_{1D} is large and positive, resulting in the Tonks-Girardeau (TG)

gas, whereas if $a_{3D} \gtrsim a_\perp/C$, then g_{1D} is large and negative, and one has the super-Tonks (sTG) gas. But a_{3D} may be adjusted experimentally via magnetic Feshbach resonance (FR) (Bloch et al., 2008); Nägerl's group used a combination of a broad and a narrow FR with poles at $B = -11.1$ G and $B = 47.78$ G and widths of about 29.2 G and 164 mG, respectively. Using the FR, a_{3D} could be tuned from 0 a_0 to over 4000 a_0 (where a_0 is the Bohr radius); the CIR value is $a_\perp/C = 1304\ a_0$. Thus, as one is ramping a_{3D} from the values below 1304 a_0 to the values above it (i.e., though the CIR), one should see the state of the gas change from TG to sTG. To detect the state of the gas, Haller et al. took advantage that the 1D coupling constant indeed passed through a CIR.

To detect the state of the gas, the Nägerl group took advantage of the weak harmonic confinement along the axial direction of the confining tubes. As it turns out, the frequency ω_D of the lowest dipole mode depends only on the confinement and not on the interparticle interaction, whereas the frequency ω_C of the lowest axial compressional mode depends on the atom–atom interaction (Menotti & Stringari, 2002). The figure of merit was chosen to be $R = \omega_C^2/\omega_D^2$. The theoretical prediction was that as one tunes g_{1D} from zero to positive infinity, R would change from 4 (ideal gas) to 3 (1D Thomas-Fermi regime), then back to 4 (TG regime, in which the density profile is the same as for the gas of noninteracting fermions) (Moritz et al., 2003). Values $R > 4$ correspond to the sTG regime (Astrakharchik et al., 2005), i.e., to large and negative values of g_{1D}. And indeed, as a_{3D} was being increased from zero (using the FR), one could see R starting from 4, dipping to 3, and increasing to 4 as a_{3D} approached the CIR point at 1304 a_0 from below. Then, as a_{3D} became larger than 1304 a_0, R increased beyond 4 up to a maximum of 4.5, after which it started decreasing again. The values of $R > 4$ are a clear signature of sTG regime; moreover, the switch from $R \leqslant 4$ to $R \geqslant 4$ happens exactly where theory predicts the CIR to be.

Additionally, the Nägerl group looked at particle loss and kinetic energy of the various regimes. They entered the TG regime adiabatically, to prevent the excitation of collective modes. The magnetic field was then ramped up to a specific value within 0.2 ms, and held there for the duration of $\tau = 10, 50, 100$, or 200 ms; the lowest value of τ was also the duration of the measurements of the R-values described in the previous paragraph. For $\tau = 10$ ms, the particle loss was virtually nil on the TG regime, starting to increase slightly as a_{3D} increases away from the CIR on the sTG side. Also very smooth—as a_{3D} passed through the CIR value—was the change in the kinetic energy of the gas. This was probed by measuring the axial width of the atomic cloud after release from the tubes, where the particle interactions are switched off immediately after the release.

For the larger values of τ, the particle loss changes rather discontinuously at the CIR, from lower values on the TG side to the higher values on the sTG side. The kinetic energy, in turn, develops a clear peak at the

CIR. The reason for these features is that sTG is really an excited state of the gas, lying above a family of lower-lying many-body excited states into which the system may decay. Also, at the two-body level, near the CIR there is a possibility of the formation of confinement-induced molecules in transversally-excited states of the confining potential (Bergeman et al., 2003). Finally, near the CRT, inelastic three-body collisions become significant (Weber et al., 2003), leading to molecule formation and to the conversion of the binding energy into kinetic energy, which in turn causes trap loss and heating. Figure 1a shows the rapid increase in the particle loss as the magnetic field (and thus a_{3D}) is increased through the point where the CIR is expected to occur. Moreover, as the transverse confinement $a_\perp$ is stiffened, we see a shift in the point at which the rapid particle

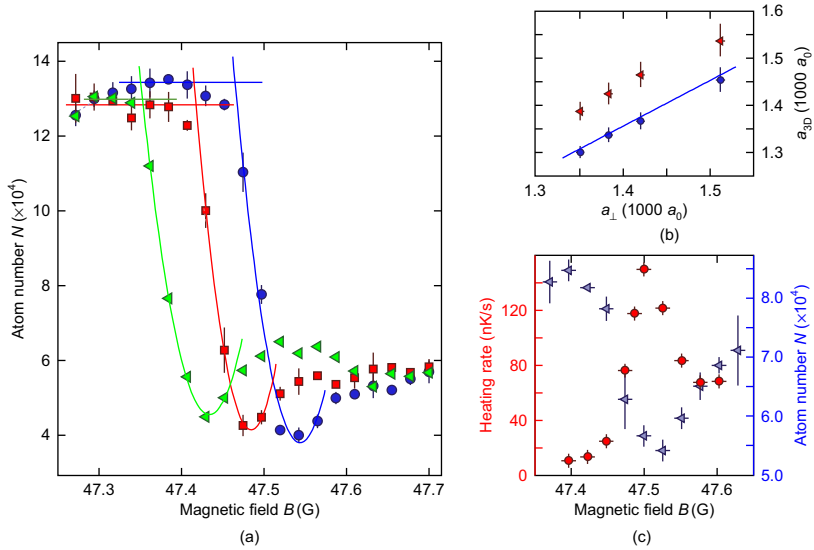

Figure 1 Particle loss and heating rates in the vicinity of a CIR, as observed in the experiment of Haller et al. 2010. (a) The number of atoms N remaining after $\tau = 200$ ms shows a distinct drop, or edge, when the magnetic field B is scanned across the CIR. As the transverse confinement is stiffened — $\omega_\perp = 2\pi \times x \times 14.2(2)$ kHz with $x = 0.84$ (circles), 0.95 (squares), and 1.05 (triangles)—the position of the edge shifts to the lower values of B. (b) The position of the edge (circles) as determined from the intersection point of a second-order polynomial fit to the minimum for N and the initial horizontal baseline as shown in (a), converted into values of a_{3D}. The position of the minimum (triangles) is also shown. (c) The heating rates near the CIR (circles); for comparison, N is also shown (triangles). Here, $\omega_\perp = 2\pi \times 12.0(2)$ kHz. The error bars correspond to 1σ statistical uncertainty. Reprinted figure with permission from Haller et al., Phys. Rev. Lett. **104,** 153203 (2010). Copyright (2010) by the American Physical Society.

loss begins, as expected for a CIR. Figure 1b shows a plot (the circles) of the value of a_{3D} corresponding to the onset of the rapid particle loss vs. the strength of the transverse confinement $a_\perp$, compared with the CIR prediction $a_{3D} = (1/C)\, a_\perp$ (the line); the two agree very well. However, since there is, at present, no detailed theory for the shape of the particle loss vs. the magnetic field curve, also plotted is the position of the minimum of that curve (the triangles), which is shifted accordingly. Figure 1c shows the increase in the heating rate as the CIR is crossed. To measure it, one keeps the system at a given a_{3D} for a time. One then reduces a_{3D} to 250 a_0 in 20 ms, switches off the lattice potential, and determines the release energy from the measurement of the momentum distribution in free-space expansion. The heating rate peaks at the magnetic field value that corresponds to the CIR.

Haller et al. (2010) have also studied what happens if the confinement is made more and more anisotropic, all the way up to converting the effectively 1D system into an effectively 2D one. In Section 3.10, we explained that CIR is a Feshbach resonance, occurring when the scattering energy is equal to the bound state energy of the full Hamiltonian shifted up by the energy gap between the ground and first excited state of the transverse potential. Now, the transverse energy levels can be labeled by quantum numbers n_1 and n_2 belonging to the two Cartesian directions of the 2D harmonic trap. The lowest states to which atoms scattering in their transversal ground state, (0, 0), can couple are (2, 0) and (0, 2). This is because only these states both preserve the parity of the total wave function (Kim et al., 2005) and have wave functions which do not vanish at the point of contact between the atoms (this latter requirement disqualifies the [1, 1] state). With anisotropy present, the degeneracy between the (2, 0) and (0, 2) states is lifted; the energy levels are split as $E_{n_1,n_2} = \hbar\omega_{\perp,1}(n_1 + n_2 + 1) + \hbar\Delta\omega(n_2 + 1/2)$, where $\Delta\omega = \omega_{\perp,2} - \omega_{\perp,1}$ is the anisotropy. The Feshbach mechanism would now predict two resonances, corresponding to the two near-in-energy excited states (2, 0) and (0, 2).

Since sharp features in the atom loss and the heating rate were established as experimental CIR signatures in Haller et al. (2009), the CIRs could now be detected simply by observing such features. For small anisotropy, the Nägerl group indeed observed two distinct values of the magnetic field for which there was a distinct increase in atom loss. However, as the anisotropy was increased, there appeared features, which Haller et al. identified as additional resonances, clustered near one of the two original split CIRs. The origin of these additional features is not yet clear. Haller et al. suggest that they may come from the opening of additional scattering channels, or from the circumstance that the confinement is sufficiently anharmonic for the parity conservation rule to be violated (Kim et al., 2005).

The greatest surprise was that one of the features identified as a CIR persisted for negative a_{3D} even in the limit of a 2D system. This is surprising because all workers agree that known theory predicts that in 2D the CIR occurs only for positive a_{3D} (Naidon et al., 2007; Petrov & Shlyapnikov, 2001); see Section 4.1. Haller and collaborators checked that the increase in the atom loss in the 2D, negative a_{3D} case is indeed the result of the confinement: they varied the confinement strength $a_{\perp,2D}$, and found that the position of the feature as a function of $a_{\perp,2D}$ satisfies the scaling $a_{\perp,2D} = C_{2D}\, a_{3D}$ with $C_{2D} \approx 1.19$ (recall that in the 1D case we have $a_{\perp} = C\, a_{3D}$ with $C \approx 1.46$; see Equation [80]). At present, there is no complete theory accounting for this behavior. We do know, however, that transverse anisotropy in the confinement cannot be the explanation (Peng et al. 2010). In fact, the very recent work of Sala et al. (2011) makes a strong case that what is important is the coupling of the relative and the center-of-mass motion due to the anharmonicities in the trapping potential.

5.2 Experimental Study of CIR in the Scattering in Mixed Dimensions

Using the technique of species-selective dipole potential (Catani et al., 2009; LeBlanc & Thywissen, 2007; Massignan & Castin, 2006), it is possible to study the scattering of an unconfined atomic species off of a confined one. Lamporesi et al. (2010) have implemented the 1D confinement (resulting in a 2D effective theory) of ^{41}K atoms, and studied their scattering with unconfined, fully 3D atoms of ^{87}Rb. They observed a series of up to five scattering resonances. These resonances disappear when both species are either unconfined or confined with potentials of equal harmonic frequencies. Experimentally, the resonances are detected as sharp peaks in the atom loss (the loss is due to the increase in the 3-body recombination rate at the resonance).

To obtain a theory of these resonances that is quantitatively valid, one must take into account the fact that the ^{41}K atoms have enough time during the experiment to delocalize over the lattice. In other words, one needs to account for the lattice band structure. The results are then in good agreement with the experiment, especially if the lattice strength is not too great. Notably, the Bloch wave theory predicts, and the experiment observes, resonances that are due to the coupling to odd harmonic oscillator levels; this would not be possible in the case of simple harmonic confinement, because it would violate the conservation of parity. On the other hand, for larger lattice strengths, there appear resonant features that are so far not accounted for by any theory.

6. FUTURE DIRECTIONS

Experience as well as worked-out theory suggests that resonances are to be expected generically when scattering takes place in the presence of an external potential that in some way limits the motion of particles. Thus, there is every reason to believe we will continue to encounter new examples of CIRs.

The experimental realizations of the CIRs have already demonstrated the usefulness of these resonances as tools in manipulating atoms, most spectacularly by allowing the creation in the laboratory of the super-Tonks gas (Haller et al., 2009)—a highly correlated, and highly excited but metastable many-body state. It is hard to predict in what way will the experimentalists use the CIRs next. To name just one possibility, one might consider the settings in which a CIR modifies the properties of another resonance—for example, the positions of the magnetic Feshbach resonances (Wouters et al., 2003; Yurovsky, 2005, 2006) and of the "optical" Feshbach resonances (Naidon & Julienne, 2006). Optical Feshbach resonances refer to the situation when photoassociation of atoms creates bound states of colliding atoms, by making them absorb a resonant photon; the presence of such bound states alters the scattering properties of the atoms. In addition to shifting the position of the Feshbach resonances, the presence of CIR may result in narrower lines, as it does for optical Feshbach resonances (Naidon & Julienne, 2006). Thus, CIRs could result in improved spectroscopic resolution.

The two experiments that have so far observed the CIRs (Haller et al., 2009; Lamporesi et al., 2010) have certainly opened up new theoretical challenges, of which perhaps the most urgent one is to explain the unexpected persistence, in the 2D limit, of the atom-loss feature for negative a_{3D}, in the experiments of Haller et al. (2010). Also, much theoretical work awaits in extending the efforts of Peano et al. (2004) and Cui et al. (2010) in making sense of the CIRs in the case of nonseparable confining potentials, and of Gattobigio et al. (2010) in the case of finite-range, realistic scattering potentials. Those who dare venture in these directions will almost certainly encounter a rich variety of new resonant effects and theoretical challenges.

REFERENCES

Apostol, T. M. (1976). *Introduction to analytic number theory*. Berlin: Springer.

Astrakharchik, G. E., Blume, D., Giorgini, S., & Granger, B. E. (2004a). Quantum Monte Carlo study of quasi-one-dimensional Bose gases. *Journal of Physics B*, *37*, S205.

Astrakharchik, G. E., Blume, D., Giorgini, S., & Granger, B. E. (2004b). Quasi-one-dimensional Bose gases with a large scattering length. *Physical Review Letters*, *92*, 030402.

Astrakharchik, G. E., Blume, D., Giorgini, S., & Pitaevskii, L. P. (2004c). Interacting fermions in highly elongated harmonic traps. *Physical Review Letters*, *93*, 050402.

Astrakharchik, G. E., Boronat, J., Casulleras, J., & Giorgini, S. (2005). Beyond the Tonks-Girardeau gas: strongly correlated regime in quasi-one-dimensional Bose gases. *Physical Review Letters*, *95*, 190407.

Bergeman, T., Moore, M. G., & Olshanii, M. (2003). Atom-atom scattering under cylindrical harmonic confinement: numerical and analytic studies of the confinement induced resonance. *Physical Review Letters*, *91*, 163201.

Bethe, H., & Peierls, R. (1935). Quantum theory of the diplon. *Proceedings of the Royal Society of London Series A*, *148*, 146.

Bloch, I., Dalibard, J., & Zwerger, W. (2008). Many-body physics with ultracold gases. *Reviews of Modern Physics*, *80*, 885.

Braaten, E., & Hammer, H.-W. (2007). Efimov physics in cold atoms. *Annalen der Physik (New York)*, *322*, 120.

Capri, A. Z. (2002). *Nonrelativistic quantum mechanics* (3rd ed.). Singapore: World Scientific.

Catani, J., Barontini, G., Lamporesi, G., Rabatti, F., Thalhammer, G., Minardi, F., et al. (2009). Entropy exchange in a mixture of ultracold atoms. *Physical Review Letters*, *103*, 140401.

Chen, S., Guan, X.-W., Yin, X., Guan, L., & Batchelor, M. T. (2010). Realization of effective super Tonks-Girardeau gases via strongly attractive one-dimensional Fermi gases. *Physical Review A*, *81*, 031608(R).

Cui, X., Wang, Y., & Zhou, F. (2010). Resonance scattering in optical lattices and molecules: interband versus intraband effects. *Physical Review Letters*, *104*, 153201.

Fedichev, P. O., Bijlsma, M. J., & Zoller, P. (2004). Extended molecules and geometric scattering resonances in optical lattices. *Physical Review Letters*, *92*, 080401.

Fuchs, J. N., Recati, A., & Zwerger, W. (2004). Exactly solvable model of the BCS-BEC crossover. *Physical Review Letters*, *93*, 090408.

Gattobigio, G. L., Couvert, A., Georgeot, B., & Guéry-Odelin, D. (2010). Interaction of a propagating guided matter wave with a localized potential. *New Journal of Physics*, *12*, 085013.

Gaudin, M. (1967). Un systeme a une dimension de fermions en interaction. *Physics Letters A*, *24*, 55.

Girardeau, M. (1960). Relationship between systems of impenetrable bosons and fermions in one dimension. *Journal of Mathematics and Physics (New York)*, *1*, 516.

Granger, B. E., & Blume, D. (2004). Tuning the interactions of spin-polarized fermions using quasi-one-dimensional confinement. *Physical Review Letters*, *92*, 133202.

Grimm, R., Weidemüller, M., & Ovchinnikov, Y. B. (2000). In B. Bederson & H. Walther (Eds.), Optical dipole traps for neutral atoms. *Advances in atomic molecular and optical physics* (Vol. 42, p. 95). London: Academic Press.

Haldane, F. D. M. (1981a). Demonstration of the 'Luttinger liquid' character of Bethe-ansatz-soluble models of 1-D quantum fluids. *Physics Letters A*, *81*, 153.

Haldane, F. D. M. (1981b). Effective harmonic-fluid approach to low-energy properties of one-dimensional quantum fluids. *Physical Review Letters*, *47*, 1840.

Haller, E., Gustavsson, M., Mark, M. J., Danzl, J. G., Hart, R., Pupillo, G., et al. (2009). Realization of an excited, strongly correlated quantum gas phase. *Science*, *325*, 1224.

Haller, E., Mark, M. J., Hart, R., Danzl, J. G., Reichsöllner, L., Melezhik, V., et al. (2010). Confinement-induced resonances in low-dimensional quantum systems. *Physical Review Letters*, *104*, 153203.

Huang, K. (1987). *Statistical mechanics*. New York: John Wiley & Sons.

Idziaszek, Z., & Calarco, T. (2006). Pseudopotential method for higher partial wave scattering. *Physical Review Letters*, *96*, 013201.

Kanjilal, K., & Blume, D. (2006). Coupled-channel pseudopotential description of the Feshbach resonance in two dimensions. *Physical Review A*, *73*, 060701(R).

Kaplan, D. B., Savage, M. J., & Wise, M. B. (1998). Two-nucleon systems from effective field theory. *Nuclear Physics B*, *534*, 329.

Kim, J. I., Schmiedmayer, J., & Schmelcher, P. (2005). Quantum scattering in quasi-one-dimensional cylindrical confinement. *Physical Review A*, *72*, 042711.

Kinoshita, T., Wenger, T., & Weiss, D. S. (2004). Observation of a one-dimensional Tonks-Girardeau gas. *Science*, *305*, 1125.

Köhl, M., Moritz, H., Stöferle, T., Günter, K., & Esslinger, T. (2005). Fermionic atoms in a three dimensional optical lattice: observing Fermi surfaces, dynamics, and interactions. *Physical Review Letters*, *94*, 080403.

Krivnov, V. Y., & Ovchinnikov, A. A. (1974). One-dimensional Fermi gas with interaction between electrons. *Zhurnal Éksperimental'naia Teorie Fizika 67*, 1568 [*Soviet Physics–JETP*, *40*, 781 (1975)].
Lamporesi, G., Catani, J., Barontini, G., Nishida, Y., Inguscio, M., & Minardi, F. (2010). Scattering in mixed dimensions with ultracold gases. *Physical Review Letters*, *104*, 153202.
Landau, L. D., & Lifshitz, E. M. (1991). *Quantum mechanics: Nonrelativistic theory* Vol. 3 of *Course of theoretical physics* (3rd ed.). Oxford: Pergamon.
LeBlanc, L. J., & Thywissen, J. H. (2007). Species-specific optical lattices. *Physical Review A*, *75*, 053612.
Leggett, A. J. (2001). Bose-Einstein condensation in the alkali gases: some fundamental concepts. *Reviews of Modern Physics*, *73*, 307.
Lieb, E. H., & Liniger, W. (1963). Exact analysis of an interacting Bose gas. I. The general solution and the ground state. *Physical Review*, *130*, 1605.
Massignan, P., & Castin, Y. (2006). Three-dimensional strong localization of matter waves by scattering from atoms in a lattice with a confinement-induced resonance. *Physical Review A*, *74*, 013616.
Menotti, C., & Stringari, S. (2002). Collective oscillations of a one-dimensional trapped Bose-Einstein gas. *Physical Review A*, *66*, 043610.
Moore, M. G., Bergeman, T., & Olshanii, M. (2004). Scattering in tight atom waveguides. *Journal of Physics IV France*, *116*, 69.
Mora, C., Komnik, A., Egger, R., & Gogolin, A. O. (2005). Four-body problem and BEC-BCS crossover in a quasi-one-dimensional cold fermion gas. *Physical Review Letters*, *95*, 080403.
Moritz, H., Stöferle, T., Günter, K., Köhl, M., & Esslinger, T. (2005). Confinement induced molecules in a 1D Fermi gas. *Physical Review Letters*, *94*, 210401.
Moritz, H., Stöferle, T., Köhl, M., & Esslinger, T. (2003). Exciting collective oscillations in a trapped 1D gas. *Physical Review Letters*, *91*, 250402.
Naidon, P., & Julienne, P. S. (2006). Optical Feshbach resonances of alkaline-earth-metal atoms in a one- or two-dimensional optical lattice. *Physical Review A*, *74*, 062713.
Naidon, P., Tiesinga, E., Mitchell, W. F., & Julienne, P. S. (2007). Effective-range description of a Bose gas under strong one- or two-dimensional confinement. *New Journal of Physics*, *9*, 19.
Olshanii, M. (1998). Atomic scattering in the presence of an external confinement and a gas of impenetrable bosons. *Physical Review Letters*, *81*, 938.
Olshanii, M., & Pricoupenko, L. (2001). Rigorous approach to the problem of ultraviolet divergencies in dilute Bose gases. *Physical Review Letters*, *88*, 010402.
Paredes, B., Widera, A., Murg, V., Mandel, O., Fölling, S., Cirac, I., et al. (2004). Tonks-Girardeau gas of ultracold atoms in an optical lattice. *Nature (London)*, *429*, 277.
Paris, R. B. (2005). The stokes phenomenon associated with the Hurwitz zeta function. *Proceedings of the Royal Society A*, *461*, 297.
Peano, V., Thorwart, M., Mora, C., & Egger, R. (2004). Shape resonances for ultracold atom gases in carbon nanotube waveguides. *cond-mat/0411517* .
Peano, V., Thorwart, M., Mora, C., & Egger, R. (2005). Confinement-induced resonances for a two-component ultracold atom gas in arbitrary quasi-one-dimensional traps. *New Journal of Physics*, *7*, 192.
Petrov, D. S., Holzmann, M., & Shlyapnikov, G. V. (2000a). Bose-Einstein condensation in quasi-2D trapped gases. *Physical Review Letters*, *84*, 2551.
Petrov, D. S., Salomon, C., & Shlyapnikov, G. V. (2004). Weakly bound dimers of fermionic atoms. *Physical Review Letters*, *93*, 090404.
Petrov, D. S., Salomon, C., & Shlyapnikov, G. V. (2005). Scattering properties of weakly bound dimers of fermionic atoms. *Physical Review A*, *71*, 012708.
Petrov, D. S., & Shlyapnikov, G. V. (2001). Interatomic collisions in a tightly confined Bose gas. *Physical Review A*, *64*, 012706.
Petrov, D. S., Shlyapnikov, G. V., & Walraven, J. T. M. (2000b). Regimes of quantum degeneracy in trapped 1D gases. *Physical Review Letters*, *85*, 3745.
Pricoupenko, L. (2008). Resonant scattering of ultracold atoms in low dimensions. *Physical Review Letters*, *100*, 170404.
Pricoupenko, L., & Olshanii, M. (2007). Stability of the two-dimensional Bose gases in the resonant regime. *Journal of Physics B*, *40*, 2065.

Rane, V. V. (1993). Dirichlet L-function and power series for Hurwitz zeta function. *Proceedings of the Indian Academy Science (Mathematical Sciences)*, *103*, 27.
Recati, A., Fuchs, J. N., & Zwerger, W. (2005). Boson-fermion resonance model in one dimension. *Physical Review A*, *71*, 033630.
Regal, C. A., Ticknor, C., Bohn, J. L., & Jin, D. S. (2003). Creation of ultracold molecules from a Fermi gas of atoms. *Nature (London)*, *424*, 47.
Tokatly, I. V. (2004). Dilute Fermi gas in quasi-one-dimensional traps: from weakly interacting fermions via hard core bosons to a weakly interacting Bose gas. *Physical Review Letters*, *93*, 090405.
Tolra, B. L., OHara, K. M., Huckans, J. H., Phillips, W. D., Rolston, S. L., & Porto, J. V. (2004). Observation of reduced three-body recombination in a correlated 1D degenerate Bose gas. *Physical Review Letters*, *92*, 190401.
Tonks, L. (1936). The complete equation of state of one, two and three-dimensional gases of hard elastic spheres. *Physical Review 50*, 955.
Verhaar, B. J., van den Eijnde, J. P. H. W., Voermans, M. A. J., & Schaffrath, M. M. J. (1984). Scattering length and effective range in two dimensions: application to adsorbed hydrogen atoms. *Journal of Physics A*, *17*, 595.
Weber, T., Herbig, J., Mark, M., Nägerl, H.-C., & Grimm, R. (2003). Three-body recombination at large scattering lengths in an ultracold atomic gas. *Physical Review Letters*, *91*, 123201.
Wigner, E. (1933). Über die Streuung von Neutronen an Protonen. *Zeitschrift fur Physik*, *83*, 253.
Wódkiewicz, K. (1991). Fermi pseudopotential in arbitrary dimensions. *Physical Review A*, *43*, 68.
Wouters, M., Tempere, J., & Devreese, J. T. (2003). Feshbach resonances in a quasi-two-dimensional atomic gas. *Physical Review A*, *68*, 053603.
Yang, C. N. (1967). Some exact results for the many-body problem in one dimension with repulsive delta-function interaction. *Physical Review Letters*, *19*, 1312.
Yu, P. Y., & Cardona, M. (2001). *Fundamentals of semiconductors*. Berlin: Springer.
Yurovsky, V. A. (2005). Feshbach resonance scattering under cylindrical harmonic confinement. *Physical Review A*, *71*, 012709.
Yurovsky, V. A. (2006). Properties of quasi-one-dimensional molecules with Feshbach-resonance interaction. *Physical Review A*, *73*, 052709.

Index

Page numbers followed by "*f*" indicate figures, "*t*" indicate tables, and "*n*" indicate footnotes.

This page intentionally left blank

CONTENTS OF VOLUMES IN THIS SERIAL

Volume 33

Volume 34

Supplements

Volume 58

Volume 59

This page intentionally left blank

This page intentionally left blank

This page intentionally left blank

This page intentionally left blank

This page intentionally left blank